Past the dripline: Bridging palaeoenvironmental records between sediments outside and inside Gledswood Shelter 1 (GS1), North Queensland, Australia

Mojca Zega

A thesis submitted for the Degree of
DOCTOR OF PHILOSOPHY
College of Science and Engineering
James Cook University

June 2024

STATEMENT OF ACCESS

I, the unsigned author of this thesis, understand that James Cook University will make it available for use within the University Library. I would also like to allow access to users under the Creative Commons Non-Commercial license (version 4).

All users consulting this thesis will have to agree to the following:

"In consulting this thesis I agree not to copy or closely paraphrase it in whole or in part without written consent of the author; and to make proper written acknowledgement for any assistance which I have obtained from it."

Beyond this, I do not wish to place any restriction on access to this thesis.

…… …… ……. ……29.06.2024……

(Signature) (Date)

DECLARATION

I declare that this thesis is my own work and has not been submitted in any form for another degree or diploma at any University or other institution of tertiary education.

Information derived from the published or unpublished work of others has been acknowledged in the text and a list of references given.

Every reasonable effort has been made to gain permission and acknowledge the owners of copyright material. I would be pleased to hear from any copyright owner who has been omitted or incorrectly acknowledged.

…… …… ……. ……29.06.2024……
(Signature) (Date)

''The task is unique for each individual

- just like each individual is unique,

and is different from moment to moment

- just as every moment is different.''

Viktor E. Frankl

Acknowledgements

This project was funded by the ARC Centre of Excellence for Australian Biodiversity and Heritage − CABAH and James Cook University, QLD, Australia. I would like to express my sincere gratitude to the Graduate Research School at James Cook University and my primary advisor, Prof. Michael Bird, for selecting me as a suitable candidate, awarding me a fully funded scholarship and providing financial support, overall assistance, and supervision throughout my candidature. I wish to thank the Aboriginal Traditional Owners, the Woolgar Valley Aboriginal Corporation (WVAC) − particularly Uncle Levin Keyes and Jasmine Keyes as well as the Hinze family and Prof. Lynley Wallis for allowing our presence on their Country and making this work possible.

I am immensely grateful to my wonderful supervisors and expert professionals, Prof. Michael Bird, Prof. Lynley Wallis, Assoc. Prof. Fiona Petchey, Dr. Christian Reepmeyer, and Dr. Robert Wasson, for their unwavering support and guidance throughout my journey. For assistance in the field I am very grateful to the Hinze family, Costijn Zwart, Michael Brand, Tina Nemec, Raul Hernandez Font, Xennephone Hadeen and Lauren Linnenlucke. Their commitment and positive attitude contributed importantly to the outcome of this study.

My gratitude to Dr. Zenobia Jacobs for generously sharing her knowledge and experience, as well as for her invaluable guidance and support in the field of optically stimulated luminescence (OSL) dating. I would like to acknowledge Prof. Keith Fifield for his guidance in navigating the intricate theory and equations of cosmogenic dating.

A huge thank-you goes to my colleague Rainy Comley at the Advanced Analytical Centre (AAC) at James Cook University (JCU) in Cairns for assisting me with the laboratory work, hypy and $\delta^{13}C$ analysis. I would also like to acknowledge Dr. Cassandra Rowe for her help with the phytolith extraction. I appreciate the support and assistance provided by Prof. Scott Smithers and Glen Blackstock with particle size analysis and Scott Merrington from Leica with phytolith microscopic analysis.

Many friends, as well as my family, who stood by my side throughout this long and intense journey. They held my hand during the highest and lowest moments and I would have never made it without them. I want to express a heartfelt THANK YOU to each and every one of you for believing in me. Last but not least, thank you, God, for protecting and accompanying me in this life experience.

Statement of contribution of others

Financial support	Research costs	Michael Bird, ARC Centre of Excellence for Australian Biodiversity and Heritage–CABAH			
	Stipend	James Cook University International Research Training Program Stipend (IRTPS)			
	Scholar extension	Michael Bird, ARC Centre of Excellence for Australian Biodiversity and Heritage – CABAH			
Fieldwork		Woolgar Valley Aboriginal Corporation (WVAC) Mojca Zega, Lynley Wallis, Costijn Zwart, Michael Brand, Tina Nemec, Raul Hernandez Font, Xennephone Hadeen, Lauren Linnenlucke			
Laboratory work		Mojca Zega, Rainy Comley, Réka-H. Fülöp, Tibi Codilean, Yasaman Jafari			
Intellectual support		Chapter 1	Chapter 2	Chapter 3	Chapter 4
	Conceptualization	Michael Bird Robert Wasson Mojca Zega	Michael Bird Robert Wasson Christian Reepmeyer Lynley Wallis Mojca Zega	Lynley Wallis Mojca Zega Michael Bird	Mojca Zega Michael Bird Lynley Wallis Christian Reepmeyer
	Methodology	Robert Wasson Michael Bird Mojca Zega Keith Fifield	Michael Bird Zenobia Jacobs Fiona Petchey Mojca Zega	Lynley Wallis Michael Bird Mojca Zega	Mojca Zega Michael Bird Lynley Wallis Robert Wasson Christian Reepmeyer
	Software	Keith Fifield Jack Koci Mojca Zega	Zenobia Jacobs Fiona Petchey Maria Rivera-Araya Mojca Zega	Mojca Zega	Mojca Zega Maria Rivera-Araya
	Investigation	Mojca Zega Robert Wasson Michael Bird	Mojca Zega Michael Bird	Mojca Zega Michael Bird	Mojca Zega Lynley Wallis Kelsey Lowe
	Writing–original draft	Mojca Zega	Mojca Zega	Mojca Zega	Mojca Zega
	Writing–review & editing	All authors	All authors	All authors	All authors

Abstract

Most Quaternary palaeoenvironmental studies from tropical Australia have focused on the coast and large water bodies, such as lakes, sinkholes and swamps. There is a need to extend investigations into drier regions, particularly the inland savannah that covers much of the northern portion of the continent. Yet, using terrestrial sediment profiles as palaeoenvironmental archives in such environments is complicated and complex. In contrast to lake and swamp sediments, the stratigraphic evidence from terrestrial contexts is often fragmented and establishing a reliable chronology is challenging. Consequently, inland investigations have favoured sediment deposits inside rockshelters. Rockshelters function as traps for sediments; therefore, their chronostratigraphic resolution is better, but the sedimentary record is space-confined and thus usually biased. Owing to the shielded and restricted space and long periods of use, deposits within rockshelters may be subjected to different natural events and post-depositional modification processes compared to areas outside their confines. Hence, numerous researchers have suggested that rockshelter investigations should expand beyond the 'dripline' to include sedimentary records from the surrounding environment. Yet such an approach still lacks proper implementation.

In this doctoral research, terrestrial sedimentary records from open-site deposits surrounding the Gledswood Shelter 1 (GS1) rockshelter in North Queensland were used, together with sedimentary records from the archaeological deposit inside GS1, to reconstruct geomorphic and sedimentologic processes as well as palaeoenvironmental changes. The GS1 rockshelter lies in the northern Australian semi-arid tropics, an area characterized by a monsoonal climate and open woodland savannah. GS1 is a small overhang situated at the base of a large sandstone outcrop formed as a result of cavernous weathering. The surroundings are dominated by quartzose sand deposits and outcrops of weathered Jurassic Hampstead sandstone in the form of rugged plateaus, scarps and residual hills. Archaeological research was undertaken at GS1 between 2006 and 2008, providing evidence of human activity for at least 38 ka (Kiloannus; 1ka = 1,000 years).

This research includes an examination of the site's geological and geomorphological context, the development of a chronology for open-site non-archaeological sediment deposits, vegetation reconstruction and a comparison of archaeological sedimentary records from inside GS1 with the non-archaeological deposits outside the site and in the surrounds. Fieldwork and laboratory methods involved surveying and sampling, digital elevation model (DEM) construction, particle size analysis, optical microscopy, cosmogenic 10Be nuclide analysis, single-grain optically stimulated luminescence (OSL) dating, radiocarbon dating (^{14}C) of macro- and microcharcoal (Stable Polycyclic Aromatic

Carbon–SPAC), phytolith analysis, carbon isotope $\delta^{13}C$ analysis, magnetic susceptibility analysis and age-depth modelling.

In terms of broad-scale geological evolution, the study area appears to be in the final erosional stage, characterized by slope retreat and reduced topography. Quartz-rich, fine to medium grained sands prevail, originating from the weathering of local sandstone, with substantial post-depositional mixing. The chronological results of the non-archaeological sediments surrounding GS1 indicate that they have been depositing for at least 15 ka. Quartz grains as old as 55 ka were measured in the OSL samples from outside GS1. The presence of these grains suggests that the sediments in the study area have been accumulating, eroding and re-depositing through several cycles of deposition and erosion for at least that long. The archaeological deposits from inside GS1 are at least 38 ka old, confirming the rockshelter functions as a sediment trap for at least this long without signs of any major disruption. ^{14}C dating of macro-charcoal gave comparable results for the archaeological sequence inside the rockshelter and the non-archaeological sedimentary sequence outside. Using OSL and ^{14}C macro-charcoal dates we constructed age-depth models for the non-archaeological sediments outside GS1 as well as for the archaeological sequence inside GS1. The models demonstrate a strong alignment and as a result we were able to establish a robust chronological framework for the study area.

Comparison of the sedimentary records from the sediments outside the GS1 rockshelter with those from the archaeological deposits inside GS1 provided a comprehensive geomorphic and sedimentologic understanding of the two archives. This allowed us to obtain a more reliable natural sedimentological signal and thereby clearly distinguish the anthropogenic signal in the shelter sediment sequence. The anthropogenic signal was particularly evident in the presence of iron concretion fragments, iron oxide nodules, sediment aggregates, coarse charcoal fragments and enhanced magnetic susceptibility in anthropogenically impacted archaeological deposits inside GS1. A difference was also observed in the vegetation reconstruction, as derived from phytolith and $\delta^{13}C$ analysis of the natural signal recorded in the non-archaeological open-site sediments outside GS1 and the anthropogenically impacted archaeological deposits inside, allowing us to produce a reliable palaeoenvironmental reconstruction of the study area. The vegetation reconstruction shows that savannah vegetation persisted throughout the Holocene, but tree cover was denser during the early Holocene, possibly indicating a wetter and warmer climate. In sediments from archaeological deposits inside GS1, however, a deviation in the phytolith assemblage was recorded, which was attributed to the impact of animal and human activity.

Finally, evidence of human agency around the exterior of the GS1 rockshelter, including an unusual stone line, missing stone artefacts in sediment profiles as well as possible human bioturbation effects, imply that expanding research beyond the dripline of rockshelters should become a routine

part of future work on analogous sites. This would represent a step forward in archaeological research quality as well as addressing the palaeoenvironmental record gap from northern Australia's semi-arid and arid interior.

Table of Contents

List of Tables

Terms and Abbreviations

Explanation of frequently used terms and abbreviations

ENSO	El Niño Southern Oscillation
hypy	hydrogen pyrolysis: a technique used for the isolation of SPAC from other organic matter in a sedimentary matrix and its subsequent quantification
ITCZ	The Intertropical Convergence Zone
GS1	Gledswood Shelter 1 – the given name of the archaeological rockshelter
GS1 site	interior of the Gledswood Shelter 1 representing the archaeological site
Inside GS1	refers to the sediment material obtained from the archaeological deposit located inside the GS1, in the area between the rear wall and the dripline
ka or kyr	Kiloannus = kiloyears = 1000 years
LGM	Last Glacial Maximum (~23–18 ka)
Ma	Million years
MS	Magnetic susceptibility
MIS	Marine Isotope Stage
Outside GS1	refers to the sediment material obtained from the non-archaeologic open-site deposit expanding south-southwest outside the GS1, beyond the dripline
open site	open air site
PyC	Pyrogenic Carbon
SPAC	Stable Polycyclic Aromatic Carbon

I. General Introduction

Regardless of the route the first Australian settlers travelled, the earliest archaeological sites on the continent should be in the tropical north (Birdsell, 1977). Recent evidence from Madjedbebe, an Aboriginal rockshelter located in Mirarr country of the Alligator Rivers region of the Northern Territory, north Australia, set a new minimum age for the arrival of anatomically modern humans in Australia to 65,000 years (Clarkson et al., 2017). For over 40 years, researchers have been debating the nature of the climatic and environmental conditions that the first settlers encountered (Bird et al., 2005, Hiscock, 2008, Moss and Kershaw, 2007, Williams et al., 2015), the routes they took (Bird et al., 2016, 2018, Bradshaw et al., 2021, Norman et al., 2018, O'Connell and Allen, 2012) and how they responded to sometimes extreme environmental changes they encountered from initial settlement onwards (Dortch et al., 2019, Hiscock and Wallis, 2005 , Veth, 1993, Williams et al., 2013). The nature and magnitude of the environmental impact of human arrival in Australia remains a fundamental unresolved issue in Australian prehistory.

Australia is the driest inhabited continent in the world. About half of the land mass is either arid or semi-arid. It spans the latitudinal range of 10–43°S, straddling climatic zones from the tropical north through the subtropics to the temperate zone in the south of the continent. The area experiencing each of these broad climate regimes varied considerably during the global climate cycles of the Quaternary (Fitzsimmons et al., 2013). Despite our broad understanding of the history of environmental change in Australia, particularly during the late Quaternary, the nature, extent, and timing of climate and landscape changes across the continent's vast semi-arid tropical north remain poorly resolved. Research has predominantly concentrated on wetter environments, containing larger lakes and swamps, the marine domain, the coastline and the continental shelf. Other sources of information include fluvial, estuarine, aeolian deposits, speleothem records and terrestrial rockshelters, all typically clustered in coastal areas, apart from a few rockshelters. This bias has led to large inland areas of northern Australia being significantly under-represented. The lack of data in drier regions away from the coast makes it challenging to evaluate how early humans responded to, and potentially modified, their biophysical environment. This, in turn, introduces uncertainty into the interpretation of paleoenvironmental change and the identification of potential refugia during times of climatic deterioration

Contributing to the knowledge gap is the very nature of the Australian semi-arid tropical interior itself, which is primarily characterised by open-site terrestrial sediments, typical Australian savannah vegetation and a monsoonal climate. Contrasting hot-wet and cooler-dry seasons have created unfavourable conditions for the accumulation of sediment and the preservation of organic proxies,

such as pollen or biomarkers such as alkanes (Bird et al., 2020), which are primarily used in palaeoenvironmental studies. Furthermore, the terrestrial sediments in Australian savannahs are typically unconsolidated, relatively homogenous and prone to bioturbation. Hence, the resolution of the sedimentary record can be lower compared to some marine or lacustrine deposits, and the stratigraphic evidence is often fragmented and incomplete (Davidson, 1935, Ward and Larcombe, 2003, Ward et al., 2005). In such circumstances, obtaining a reliable vegetation signal and establishing a reliable chronology for palaeoenvironmental reconstruction is challenging.

To address this challenge in Australia, as in analogous environments elsewhere, research has primarily focused on deposits inside rockshelters and caves, commonly in connection with archaeological excavations (e.g. Aubry et al., 2011, Dortch, 1986, Hovers et al., 2014, Oestmo et al., 2014, Rink et al., 2002, Sharon et al., 2014, Ulm, 2013, Ward et al., 2016). Rockshelters and caves function as sediment traps. The deposits that have accumulated within their confines are considered to represent relatively complete sequences that hold environmental signals in well-defined, discrete and datable contexts, directly associated with specific moments of the archaeological past (Butzer, 2008, Sandweiss and Kelley, 2012). Recently, however, an increasing number of studies, dominantly from outside Australia, have identified a research bias in solely focusing on caves and rockshelters. They have demonstrated that by extending the research to include areas beyond the dripline and connecting inside sequences with those outside, we can better understand the site function, human occupation and palaeoenvironmental data, even in challenging sedimentological settings (e.g. Angelucci et al., 2018, Barbieri et al., 2018, Kindermann et al., 2018, Uthmeier and Chabai, 2018, Ward, 2003, Ward et al., 2006).

In addition, the continuous improvement of methods for establishing precise chronological control for sedimentary deposits also contributes to addressing the challenges in palaeoenvironmental investigations of terrestrial open-site sediments (e.g. Athanassas and Wagner, 2016, Hajdas et al., 2021, Schaefer et al., 2022). Moreover, durable vegetation proxies, such as phytoliths and the carbon isotope composition of soil organic matter ($\delta^{13}C$), have successfully produced time series of vegetation change from terrestrial sediments in tropical regions worldwide. Examples include studies from Brazil (Alexandre et al., 1999, Calegari et al., 2013, 2017, Chueng et al., 2019, Coe et al., 2014, Desjardins et al., 1996), French Guiana (Watling and Iriarte, 2013), Africa (Bremond et al., 2017, Neumann et al., 2009, Sangen et al., 2011) and India (Tripathi et al., 2021). These studies used phytolith analysis and $\delta^{13}C$ values of organic matter to (i) establish their reliability as palaeovegetation proxies (Alexandre et al., 1999), to investigate the changing abundance of C_3 (tree) and C_4 (grass) species (Calegari et al., 2013, 2017, Coe et al., 2014), (ii) identify the major vegetation formations (Watling and Iriarte, 2013), (iii) determine past and present fluctuations of the

forest-savannah boundary (Desjardins et al., 1996), (iv) help the interpretation of geomorphological processes operating during particular palaeoclimates and to understand the variations in vegetation from which to infer climatic changes. (Chueng et al., 2019). The results suggest that phytolith analysis coupled with organic $\delta^{13}C$ values offers a valuable alternative as terrestrial environmental proxies for past environmental change in tropical settings, where high temperatures and variable rainfall challenge the preservation and integrity of many traditional palaeoenvironmental proxies.

I.1 Thesis Overview

This thesis forms part of the larger research program of the Australian Research Council-funded Centre of Excellence for Australian Biodiversity and Heritage–CABAH. One of the aims of CABAH is to provide the definitive long-term environmental records required to disentangle natural and anthropogenic drivers of palaeoenvironmental change before, during and after the peopling of Australia. The primary focus of this thesis is the reconstruction of past landscape and environment characteristics at a rockshelter site (Gledswood Shelter 1-GS1) in tropical North Queensland using records from terrestrial open-site sediments in the Australian savannah. Particular emphasis is placed on bridging the archaeological sequences inside the rockshelter with surrounding (beyond the dripline), non-archaeological sequences, outside the shelter. Four research questions are addressed in this thesis: (1) What were the main geologic and geomorphic processes that created the surrounding landscape and GS1? (2) What is the chronology of the non-archaeological sediments outside GS1? (3) How has the environment changed in the study area? (4) How do sedimentary records from deposits inside and outside GS1 complement or differ from each other and how does this contribute to a better, broader, understanding of sedimentary and palaeoenvironmental archives at the GS1 site?

This multi-layered thesis has been written as a series of individual manuscripts to be submitted as journal articles. It is organised into four standalone chapters, each representing an added 'layer' in the reconstruction of past landscape and environmental change at the GS1 site. This introductory chapter outlines the aims and objectives, focus and main approaches of the thesis as well as the geography of the area and previous research. Since this thesis focuses on archaeological rockshelter deposits and paleoenvironmental reconstruction, background information about the archaeological and palaeoenvironmental context is also included. Chapters 1–4 address each research question as listed above, with Chapters 1 and 2 focusing on non-archaeological open-site sediment sequences outside (beyond the drip line) GS1. In Chapters 3 and 4, the non-archaeological open-site sediment sequences outside GS1 are further correlated and integrated with archaeological sequences inside GS1. The Thesis Summary chapter summarizes the major findings of the thesis and demonstrates how

the aims and objectives were met. A single reference list is provided for all chapters following the Thesis Summary at the end.

This structure results in some repetition in the introductory sections of each chapter, such as the study area and sampling location details. However, since each paper has a different focus, this repetition is necessary. Moreover, the thesis covers various areas of knowledge. As such, each chapter includes relatively comprehensive theoretical background information, which will be rearranged or excluded for future publications. A brief introduction to the four chapters is listed as follows:

Chapter 1 (the landscape layer) *Geologic and geomorphic setting of the Gledswood Shelter 1 (GS1) site, North Queensland, Australia.* This chapter utilises geomorphology and sedimentology—particle size, optical microscopy, and cosmogenic nuclide techniques—to provide a geomorphic and geologic framework for the GS1 study area. This chapter is the first study to present a geomorphic and geologic context for the area where the GS1 is situated, which is crucial for a better understanding site formation processes.

Chapter 2 (the time layer) *Luminescence and radiocarbon chronologies of sediments at the Gledswood Shelter 1 (GS1) site, North Queensland, Australia*. This chapter presents the work undertaken to establish a reliable chronology for the terrestrial non-archaeological open-site sediments outside the GS1 shelter. The objective here is to produce solid chronological foundation for the sedimentary sequence outside the shelter using a two-method approach: single-grain optically stimulated luminescence (OSL) dating of quartz grains and radiocarbon dating of two charcoal fractions. This study has implications for better understanding how these two methods and their combination work together in analogous environments to deepen our understanding of the impact of post-depositional disturbance processes on single-grain OSL distribution patterns and how degradation and mixing can impact radiocarbon dates.

Chapter 3 (the vegetation layer) *Vegetation reconstruction at Gledswood Shelter 1 (GS1) site in North Queensland, Australia, combining phytoliths and $\delta^{13}C$*. This chapter presents a comprehensive analysis of palaeovegetation using phytoliths and $\delta^{13}C$ signatures in charcoal. The analysis includes non-archaeological sedimentary sequences outside GS1 and archaeological sequences inside the GS1 rockshelter to reconstruct changes in vegetation (and, by implication, climate) in the study area through time. This work also discusses the discrepancies in results between the inside and outside sample collections and suggests possible sources for these differences.

Chapter 4 (the integration layer) *Bridging palaeoenvironmental archives from outside to the inside: Gledswood Shelter 1 (GS1), North Queensland, Australia*. This chapter integrates the results obtained from both non-archaeological sedimentary sequences outside GS1 and archaeological inside

GS1 sedimentary sequences. It does this by comparing and correlating the findings established in Chapters 1, 2 and 3 with previous archaeological studies conducted inside GS1. Based on this integration, interpretation of site formation processes, palaeoenvironmental change and site significance is provided to improve our understanding of the drivers of change and observed differences between the two archives.

I.2 Study area context

I.2A Regional setting

The study area is based at Gledswood Shelter 1 (GS1) and its surroundings in the western foothills of the Gregory Range in inland North Queensland, approximately 130 km north of the small township of Richmond (Figure FI.1). The site lies within the traditional lands of the Woolgar Valley Aboriginal Corporation (WVAC), on Strathpark pastoral station, the homestead for which is located 10 km south of the GS1 site (Figure FI.2).

The topography of the broader area comprises low and gently undulating plains but locally includes strongly dissected plateaus and outcrops of Jurassic sandstone and conglomerate. The vegetation is primarily open woodland and grassland, that is to say, broadly typical Australian semi-arid savannah. Meandering its way across the sandy plains, around 1.6 km south of the GS1, is the Norman River, with headwaters in the Gregory Range to the east (Figure FI.2).

Figure FI.1: Study area (red circle) location.

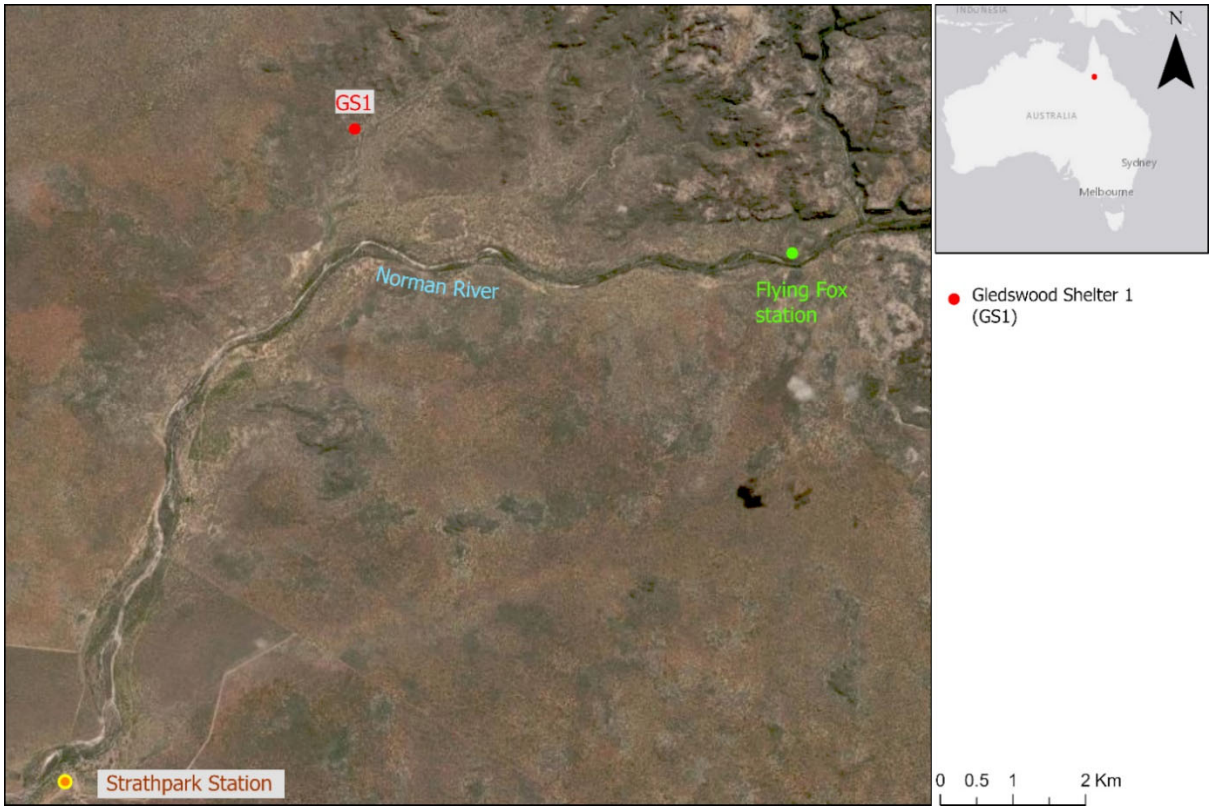

Figure FI.2: The study area with marked locations: Gledswood Shelter 1 (GS1), Norman River, Flying Fox Hydro Station (now abandoned), and Strathpark Station.

I.2B Climate and Hydrology

The study area lies within the northern Australian semi-arid tropics, characterised by a short, hot, wet season and a longer, cooler dry season. Daytime temperatures are relatively high all year round, averaging 36°C in summer (November–April) and 26°C in winter (May–October) (Source: Australian Government, Bureau of Meteorology Portal, Site name: Richmond Post office). The region experiences a low annual rainfall (median 432.5 mm) and high evaporation (average~3000 mm) (Source: Australian Government, Bureau of Meteorology Portal, Site name: Richmond Post Office).

Surface water is typically abundant during the wet summer season but becomes extremely scarce during the dry winter months. The hydrology of the region is, therefore, dominated by ephemeral river systems, with significant episodic flooding during the wet season (November–April) and minimal (often subsurface) or no flow during winter (May–October). A twenty-year Norman River water level and discharge record shows high water levels and discharges during the wet seasons, periodically exceeding 4 m in height (250 Cumecs) (Figure FI.3), followed by extremely low water levels and zero discharge during the dry season (source: Queensland Government, Water Monitoring Information Portal, Historic Streamflow Data, 916002A, referred to as Norman_R Strathpark). This pattern is typical for a monsoon-driven river in the region. The data were measured at the Flying Fox

hydro station on the right bank of the Norman River, approximately 6 km southeast of the GS1 site, and operated from 1968 to 1988 (Figure FI.2).

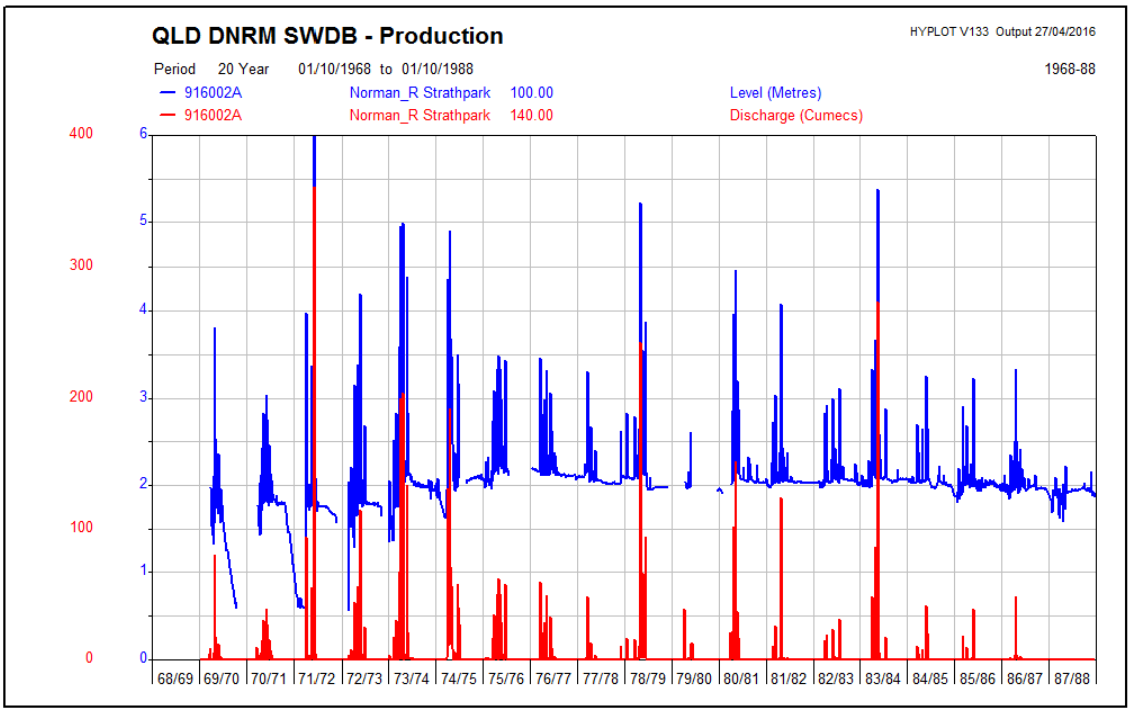

Figure FI.3: A twenty-year Norman River water level and discharge data measured at the former Flying Fox Hydro Station

The seasonal variability is typical of the present climate of much of tropical northern Australia and is governed largely by the annual migration of the Intertropical Convergence Zone (ITCZ) (Reeves et al., 2013a) (Figure FI.4). The ITCZ is a tropical zone, often called the monsoon trough in the Southern Hemisphere. On satellite images, the ITCZ appears as a band of clouds, usually thunderstorms that encircle the globe, migrating seasonally north and south of the equator. The ITCZ follows the sun and migrates north during the Northern Hemisphere summer and south during the Southern Hemisphere summer, thus influencing the tropical north Australian region most strongly during the Austral summer, from November to March (Kershaw and van der Kaars, 2012, Reeves et al., 2013a). During this period, the ITCZ migrates roughly 15° southward into northern Australia, bringing the summer monsoon rains. Tropical cyclones also occur in the summer months, often embedded in the monsoon trough that can penetrate the continent as significant rain-bearing depressions (Figure FI.4–right). During the winter months—June through September—the ITCZ moves northward over Southeast Asia, resulting in a dry winter in the northern Australian region. The ITCZ effect is modulated by the influence of the El Nino Southern Oscillation (ENSO) (Figure FI.4–right), especially in northern and eastern Australia, which introduces pronounced interannual variability to the Australian climate (Allan, 1988, Allan et al., 1996).

The northeast of Australia also receives moisture from the humid south-easterlies, sourced from the Coral Sea and equatorial Pacific (Figure FI.4–left), which extend the summer wet season in the adjacent continental areas. The Great Dividing Range in the northeast of the continent acts as a barrier to easterly rain, creating a rainshadow of the inland tropical Australian savannah (Sturman and Tapper, 1996) where the study area is located.

Additionally, the Australian continent is placed latitudinally between the heat of the equatorial tropics from the Indo-Pacific Warm Pool (IPWP) and the cool waters of the Southern Ocean (Figure FI.4). This latitudinal position results in several large-scale controls on the climate, such as the ITCZ, the Sub-tropical High-Pressure Belt or the Australian subtropical ridge, the major ocean currents, fronts, and winds (see Figure FI.4). Being unaffected by major topographic barriers, the mean climatic conditions across Australia primarily respond to the seasonal zonal circulation resulting in continental heating/cooling and therefore seasonally variable land-sea temperature contrast (Gimeno et al., 2010).

I.2C Previous research

GS1 is a small south-facing overhang at the base of a large sandstone outcrop (Figure FI.5). The interior floor area is approximately 15 $m^{2,}$ and the shelter roof is 3–5 m high. The overhanging sandstone outcrop extends about 8 m above the shelter and provides protection for a sandy and vegetation-free floor, except for sparse grasses and occasional low herbs. The southern outlook faces a lightly wooded sandy plain, extending beyond the dripline and further away from the outcrop to the south and west.

Lynley Wallis and her team have been conducting research at GS1 since 2006 (Wallis, 2008). Between 2006 and 2008 a total of 6 m^2 (six 1 m^2 squares) were excavated and the maximum depth to bedrock is approximately 250 cm in the shelter. The archaeologists worked in arbitrary 5 cm layers ('spits'), from which numerous stone artefacts, ochre and wood charcoal were recovered. Owing to poor preservation conditions, they did not retrieve significant amounts of bone or other organic remains. Apart from six squares inside GS1, the team also excavated five test pits outside GS1 to a fixed maximum depth of 120 cm, not always reaching bedrock. These test pits served to enable collection of sediment samples for comparison of records from inside and outside GS1 in future palaeoenvironmental and archaeological research.

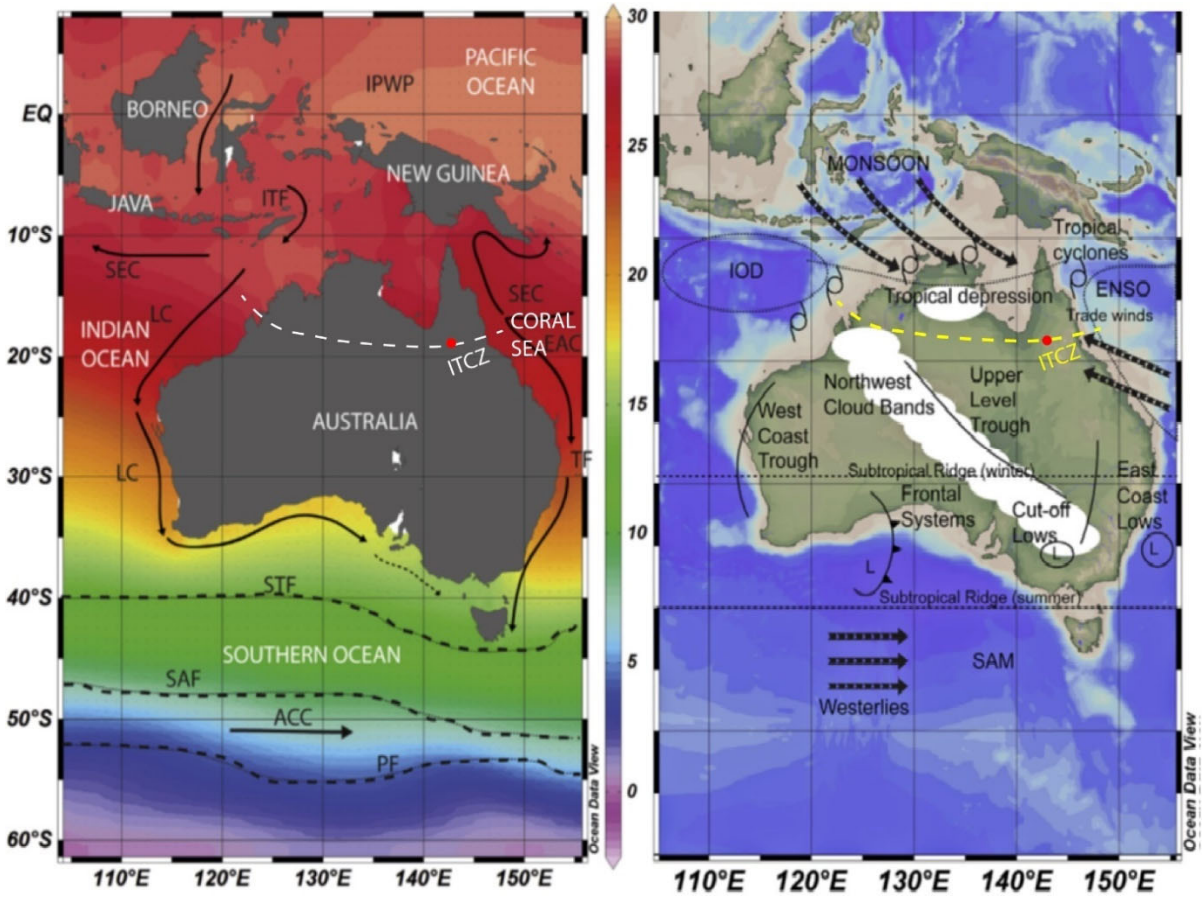

Figure FI.4: The large-scale controls on the Australian climate. **Left:** The map shows average modern sea surface temperatures and the major oceanographic features. Solid lines represent the major currents – IPWP: Indo-Pacific Warm Pool, ITF: Indonesian Throughflow, SEC: South Equatorial Current, LC: Leeuwin Current, EAC: East Australian Current, ACC: Antarctic Circumpolar Current. The mean positions of the major fronts are shown in dotted lines – TF: Tasman Front, STF: Subtropical Front, SAF: Subantarctic Front, PF: Polar Front. **Right:** The map shows the major features of the modern climate of the Australian region – ITCZ: Inter-tropical Convergence Zone, ENSO: El Niño Southern Oscillation, IOD: Indian Ocean Dipole, SAM: Southern Annular Mode. Red circle marks the GS1 site. Both images adopted from Reeves et al. (2013b)

Wallis et al. (2009) published an initial report on the GS1 excavations which focused on establishing a chronology based on radiocarbon dates from macro charcoal collected inside GS1. In this initial paper, the occupation date for the shelter was estimated to be 28,419±320 BP (before present), uncalibrated. Subsequent calibration using OxCal v 4.2 (Ramsey et al., 2010) against SHCal13 (Hogg et al., 2013) and IntCal13 (Reimer et al., 2013) and the addition of more dated radiocarbon samples have pushed the site back to about 38 ka (Kiloannus; 1ka = 1,000 years) (Wallis et al., 2014a).

Following the initial report, multiple papers (Lowe et al., 2016, 2018, Lowe and Wallis, 2020), unpublished reports (Wallis, 2008, Wallis et al., 2014a, 2014b) and an honours thesis (Keys, 2009) were produced. Several analyses were conducted, including particle size and shape, optical microscopy, quantification of organic matter (by Loss on Ignition [LOI]), biologically available phosphorous (P), FTIR and μ-FTIR on loose sediments as well as quantification of the cultural materials

(artefacts and charcoal) (Lowe et al., 2018). Particular emphasis was placed on the analysis of sediment magnetic properties to determine the onset of Pleistocene human settlement at GS1 (Lowe et al., 2016) and ground penetrating radar (GPR) to determine sediment depths (Lowe and Wallis, 2020).

Overall, the chronological, archaeological and geoarchaeological data indicate that GS1 was occupied from approximately 38 ka, through and beyond the Last Glacial Maximum (LGM). Lowe et al. (2018) stated that the resultant dataset highlighted the benefit of using a multi-proxy approach to understand sandstone settings in analogous environments better. The analyses and results from this large body of previous research are brought into this thesis where appropriate to compare the sedimentary archives inside the shelter with the results obtained in this thesis from outside the shelter, as discussed more in detail in the following chapters.

Figure FI.5: First image: a bird's eye view of the outcrop where GS1 formed and its surroundings (size of the tarpaulin is approx. 2.7 x 4m); **Second image:** a closer view of the GS1.

I.2D Archaeological context

The significance of the tropical north in Australian prehistory

Since the first humans set foot in northern Australia, approximately 65,000 years ago, and for most of the period of human occupation, the Australian continent was part of Sahul, the combined Pleistocene landmass comprising today's mainland Australia, Tasmania, New Guinea and the Aru Islands (Figure FI.6). Lower sea levels exposed an extensive area of the north of the Australian continent—today a submerged shelf—connecting the Kimberley, Arnhem Land and Cape York Peninsula regions into one vast area separated only by the great Lake of Carpentaria (Figure FI.6).

For decades, considerable debate has surrounded the role these now partially submerged northern areas may have played in early human arrival on the continent and, in particular, in human dispersal into the semi-arid and arid north interior as well as towards the south (e.g. Allen and O'Connell, 2008, Bird et al., 2018, 2019b, Bowdler, 1977, Bradshaw et al., 2021, Kealy et. al, 2018, Norman et al., 2018, O'Connell et al., 2018, O'Connor, 2007, O'Connor and Veth, 2000, Veth et al., 2017, Wild, 1986). In this regard, numerous models proposed different pathways and drivers of human dispersal throughout the Australian continent, such as woodland-riverine corridors (Horton, 1981, Tindale, 1981), foraging resource availability/depletion (O'Connell and Allen, 2012, 2015), food access

(Smith, 2005) and palaeohydrological corridors (dispersal along well-watered routes) (Bird et al., 2016), all of which were variably dependent on a matrix of biogeographic (Veth, 1993), ecological/climatic (Veth et al., 2000) and sociological/technological (Lourandos and Ross, 1994) factors. These postulates were summarised into conceptual models that view the vast interior of the continent as a mosaic of potential oases, corridors and barriers, with the viability of a specific region for occupation or transit also depending on the trajectories of environmental change (Hiscock and Wallis, 2005, Smith, 1993, 2013, Veth, 1993). Based on this concept, archaeologists inferred that in response to climatic instability in the terminal Pleistocene, human populations contracted to oases 'refugia', well-watered ranges and major riverine systems, most notably around the LGM (~23–18 ka) (Dortch et al., 2019, Hiscock, 1988, Hiscock and Wallis, 2005 , O'Connor et al., 1993, Slack et al., 2018, Veth, 1993).

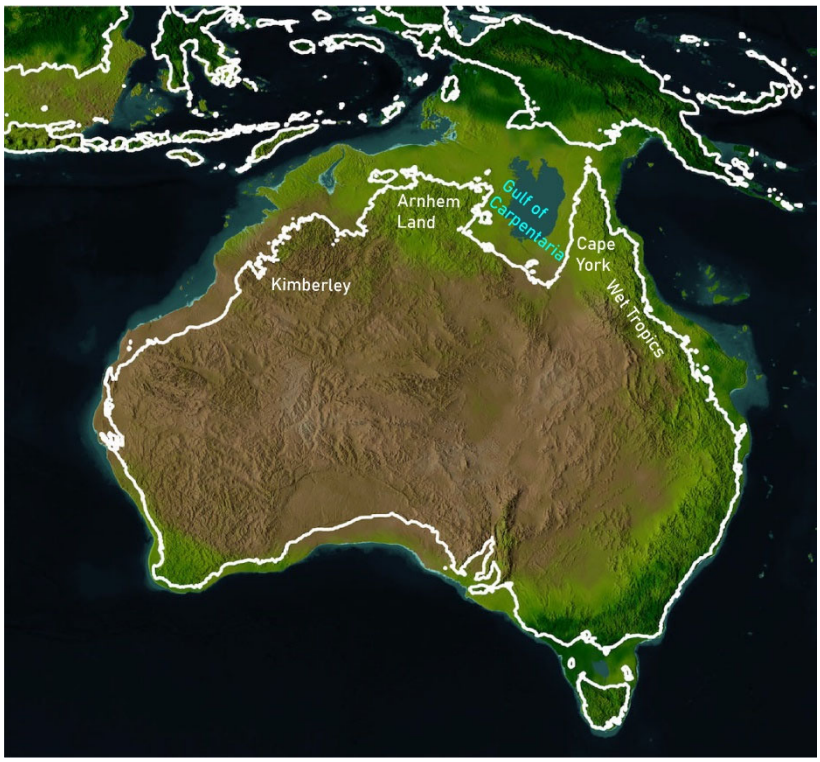

Figure FI.6: The palaeocontinent of Sahul, from Bradshaw et al. (2021). Note the exposed extensive lands at the north of the continent along with the shelf, which is today submerged.

These archaeological models were evaluated by Williams et al. (2013) with emphasis on human responses to climate change in the Late Pleistocene in Australia, who established that some regions could be considered refugia as study results showed they were preferred by people through the LGM and the terminal Pleistocene. Of these areas, some are consistently highlighted as of importance to people, including the Gulf Plains and Einasleigh Uplands in northeastern Australia, based on bioregions

(Thackway and Cresswell, 1995) that correspond to the Gulf Country and North and Far North Queensland (Figure FI.7), including the area of GS1.

Other areas were used less consistently but still contain several periods of activity, including those of the Central and North Kimberley and the Arnhem Plateau in the north. Additionally, the study identified several areas that were abandoned and/or never used that can be considered 'barriers' in accordance with the examined models. Overall, the results from Williams et al. (2013) correlated well with the earlier models proposed by Veth (1993) and highlighted a number of regions that were probably refugia during periods of climatic instability (Figure FI.7). These areas should therefore form a focus of more detailed future archaeological and palaeoenvironmental research as they potentially hold evidence for early human entry points to Australia and corridors to the continent interior, but also for their role as refugia during periods of climatic deterioration throughout the Late Pleistocene.

In contrast, the archaeological and palaeoenvironmental record that was not submerged by the rising sea levels during the flooding of Sahul in the early Holocene (~10 ka ago) is dominated by sandstone and limestone rockshelters in the Kimberley, Arnhem Land and Wet Tropics (Williams et al., 2015) and by lake, fluvial, marine sediments and corals from the northern coastal area (Figure FI.8). However, large inland areas of the Gulf of Carpentaria, Cape York Peninsula, Northern Territory and North Queensland are scarcely represented in either archaeological or palaeoenvironmental archives (Figure FI.8).

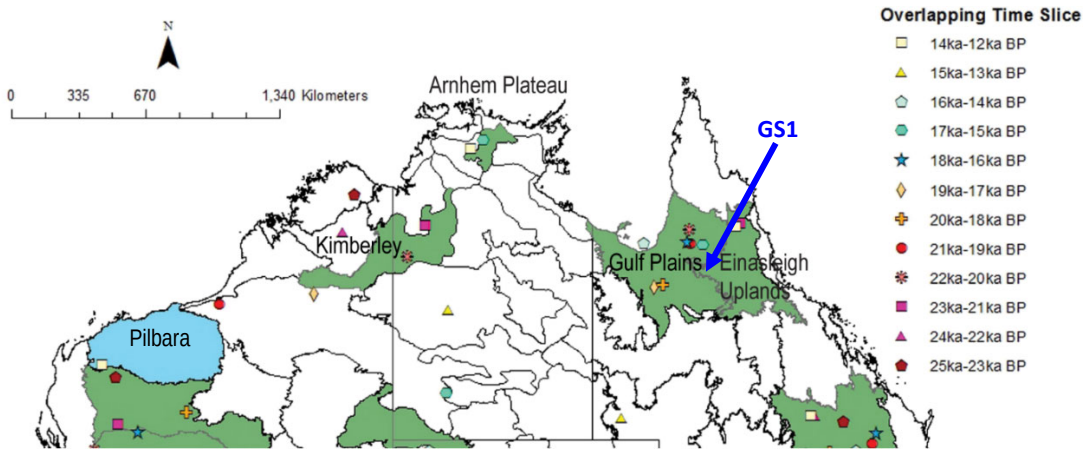

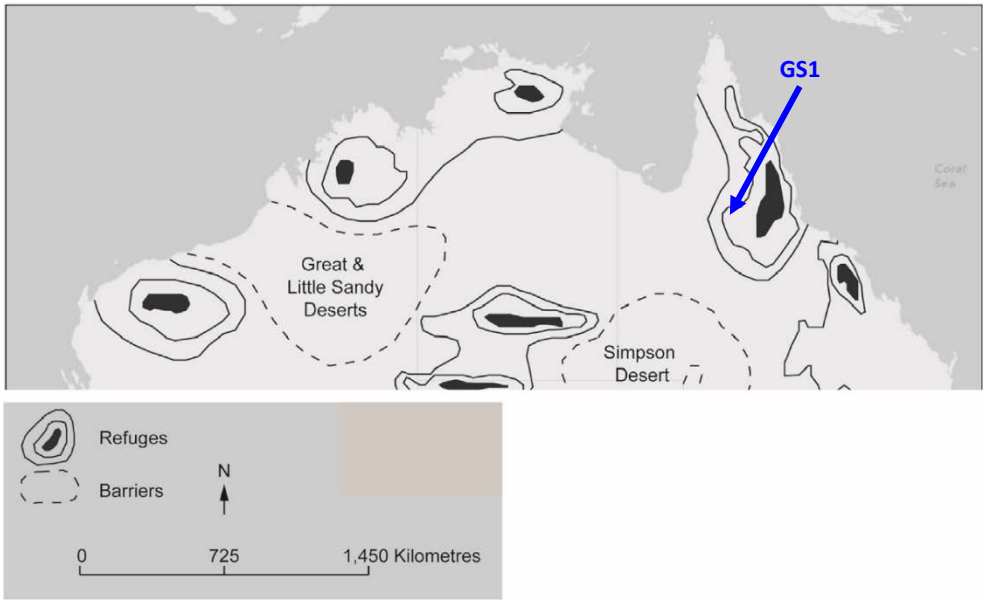

Figure FI.7: Upper: map showing likely refugia (green) based on bioregions after Thackway and Cresswell (1995) and the analysis undertaken by Williams et al. (2013); **Bottom:** Map of refugia, barriers and corridors for human occupation through the Last Glacial Maximum after Veth (1993).

The lack of archaeological knowledge for the inland tropical north has led to debates about peopling and settlement patterns and strategies, which continue with minimal supporting evidence. In addition, the limited understanding of localised palaeoenvironmental conditions has hindered researchers from rigorously interrogating competing hypotheses. In most cases, investigations must rely on sedimentary archives of low stratigraphic resolution, such as dunes, playas, river terraces, caves and rockshelters, which, while potentially discontinuous, broadly preserve records of past human and environmental responses to climatic change (Fitzsimmons et al., 2013). Despite unfavourable research conditions, numerous authors (Reeves et al., 2013a, Ulm, 2013, Williams et al., 2013) emphasized an urgent need to extend the palaeoenvironmental record into the Australian savannah region, which represents the majority of the tropical environments of the north. However, a ten-year data comparison shows that the situation regarding the palaeoenvironmental and archaeological record from the inland tropical north has not changed significantly (Figure FI.8). This thesis addresses the gap by focusing on landscape formation and palaeoenvironmental reconstruction at an inland tropical archaeological rockshelter site in North Queensland.

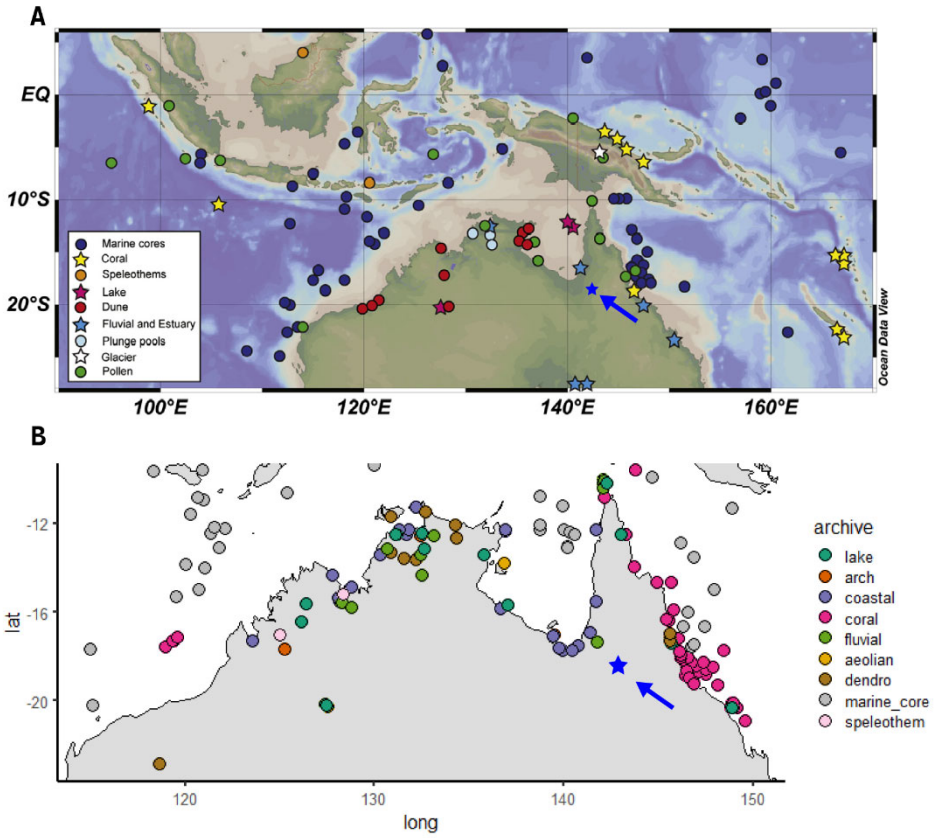

Figure FI.8: Palaeoenvironmental archives from the Australian tropical north. A) from Reeves et al. (2013a) and B) courtesy borrowed from Wall A. (2023, unpublished work). The blue star with the arrow marks the location of the GS1 rockshelter.

Regional framework

The GS1 study site lies adjacent to a number of archaeologically significant areas: Cape York Peninsula to the north, the Gulf Country to the northwest, Riversleigh and Mt. Isa to the west, while to the south are the Mitchell Grass Downs and to the southeast are the basalt-capped sandstones of the Upper Flinders region (Figure FI.9). The latter also referred to as the 'North Queensland highlands' by initial researchers (Morwood and Godwin, 1982, Morwood, 1990, 1992).

The earliest systematic archaeological investigations in the region were undertaken by Morwood and Godwin (1982), who conducted surveys across a widespread area between Hughenden and Torrens Creek in the south to Georgetown and Croydon in the north (Figure FI.9). These surveys recorded the presence of numerous sites in the region, primarily rockshelter art/occupation sites, some axe-grinding grooves, hearths and open artefact scatters. This initial work suggested a strategic position of the surveyed area in archaeological terms for the distribution of specific cultural traits. It was followed by a more detailed investigation that included a number of excavations immediately north of Hughenden (Morwood, 1990, Morwood, 1992, 2002), on Esmeralda Station near Croydon (Gorecki et al., 1992), on Middle Park Station 30 km south of the GS1 site (Cooke, 1995), and around

Sandy Creek south of Cloncurry (Davidson et al., 1993) as well as further west at Lawn Hill–Boodjamulla (Hiscock, 1988) and Riversleigh (Slack et al., 2004) (Figure FI.9). Excavations at Mickey Springs 34 rockshelter, located 67 km northeast of Hughenden in Mickey Gorge (a tributary of the Flinders River) (Figure FI.9), revealed occupation dated to about 10 ka (Morwood, 1990, p.13). Occupation in three other shelters in the area (Mickey Springs 33 and 31 and Quippenburra Cave) also dated to the mid- and late Holocene. In the Selwyn Ranges, 120 km south of Cloncurry, the Cuckadoo Shelter yielded a maximum date of 15,270±210 yrs BP, providing further evidence for the occupation of the inland north Queensland upland area since at least the terminal Pleistocene (Davidson et al., 1993). Further afield, excavations of two cave sites at Lawn Hill–Boodjamulla gave ages of first occupation around 18 ka BP (Hiscock, 1988). Whereas radiocarbon dating results from two excavated sites adjacent to the Gregory River at Riversleigh (Figure FI.9), just south of the Lawn Hill caves, showed an age of ~15 ka BP at the OLH midden site and suggested continuous occupation from at least 35 ka ago of the GRE8 rockshelter (Slack et al., 2004).

Figure FI.9: Map of North Queensland. The blue square marks the GS1 site and the adjacent archaeologically significant areas: Cape York (N), Gulf Country (NW), Riversleigh and Mt. Isa (W), Mitchell Grass Downs (S), Upper Flinders (SE).

Overall, the studies showed that the regional archaeological record of inland north Queensland is dominated by surface scatters of stone artefacts, often associated with hearths, followed by rockshelters, typically in sandstone outcrops, containing abundant stencilled rock art. Axe grinding grooves and grinding surfaces are also very common in geologically suitable areas. The upland areas

were occupied by at least the terminal Pleistocene, 15 ka, probably as early as 35 ka, corroborating the proposition that the uplands country experienced early occupation and, in at least some places, afforded better-watered refuges capable of supporting human populations through the LGM. There also appears to be some evidence for a suite of mid-Holocene changes, including more regular use of sites, a broader range of activities (i.e. the introduction of seed-grinding technology), a shift in rock art styles and an increase in local population and productivity (Gorecki and Grant, 1994, Gorecki et al., 1992, 1996, Morwood, 1992, 2002).

Following the initial work, the majority of archaeological investigations in the area continue to focus on identifying new sites and their regional distribution. Excavations have concentrated predominantly on GS1 rockshelter (Keys, 2009, Lowe and Wallis, 2020, Lowe et al., 2016, 2018, Wallis et al., 2009, 2014a), open-hearth sites along Flinders River and Woolgar River (Wallis et al., 2004a, 2004b), axe grinding grooves on Woolgar River and its tributaries (Munt, 2013) and skeletal remains in the low-lying plains country—the Mitchell Grass Downs—south of Richmond (Domett et al., 2006) (Figure FI.9). These investigations, however, have not produced dates beyond the last 2 ka, apart from the 38 ka BP occupation age obtained from the archaeological sequence inside GS1. Besides the scientific research, a number of cultural heritage management surveys were undertaken in the Mitchell Grass Downs (Bird, 1997, 1998, 1999, 2000, Crothers, 1997, Davidson and Fife, 1994, Davidson et al., 1991, Spencer, 1994) related to various activities planned in the area by different corporations and institutions. As the number of sites excavated and dated in the Norman River and Woolgar River area is very low, the connection of these sites with those in the neighbouring low-lying plains and upland areas remains unclear. So does the possibility that the area of Norman River was indeed a refuge during the LGM.

I.2E Palaeoenvironmental context

Today, northern tropical Australia experiences a mild dry winter with moderate strength southeasterly trade winds. Moisture is brought in from the north by the summer monsoon, which provides most of the annual precipitation in the wet season between December and March (Bowler et al., 2001). As these rains penetrate inland from the north, mean annual rainfall decreases to the south, although low-pressure troughs and cyclones can generate significant episodic rainfall in the continental interior (Hesse et al., 2004). The climate in the region is governed mainly by the seasonal movement of the Intertropical Convergence zone (ITCZ) (Figure FI.4). The climate boundary of the monsoon tropics, however, cannot be rigorously defined. The boundary is mobile from year to year in the present day and is likely to have been in the past, with climate zones shifting by multiple degrees

of latitude during past glacial and interglacial times throughout the Quaternary period (Metcalfe and Nash, 2012).

Below, I present an overview of environmental change in the Australian tropical north across various significant late Quaternary timeframes, with a focus on climate. The overview is summarized from earlier works (Bowler, 1976, Donnelly and Wasson, 1989, Hesse et al., 2004, Nanson et al., 1992, Thomas et al., 2001, Webster and Streten, 1978) as well as more recent significant contributions in this region (Burrows et al., 2016, De Deckker et al., 2019, Fitzsimmons et al., 2013, Kershaw and van der Kaars, 2012, Moss et al., 2017, Reeves et al., 2013a, Reeves et al., 2013b, Williams et al., 2015). The section is divided into three parts: 1) Before the LGM, 2) The LGM, and 3) After the LGM, where the LGM marks a global change in climate, which serves as a turning point for this overview.

Before the LGM

Palaeoenvironmental evidence from the tropical north is comparable with other parts of Australia in showing recognizable, alternating wet and dry episodes superimposed on a clear drying trend over at least the last 300 ka (Burrows et al., 2016, Hesse et al., 2004, Nanson et al., 1992). These episodes are generally recorded as enhanced runoff records in the form of extensive alluvial sand deposits indicating stronger precipitation and wetter climate in interglacial stages and as a diminished presence of water in the landscape enabling expanded dune building in dry phases, the glacial stages (Bowler et al., 2001, English et al., 2001, Nanson et al., 1992).

In the Gilbert River system in northeast Queensland (Figure FI.10), extensive luminescence dating supported by some U-Th ages yielded a record of fluvial activity dating back to 130 ka (Nanson et al., 1991, Nanson et al., 2005). Basal sands indicate that the most marked fluvial episode occurred during the last interglacial (MIS 5e,c), extending to about 85 ka (Kershaw and van der Kaars, 2012). Whereas evidence of several phases of lake floor dunes and reworking of shoreline deposits into dune fields have been recorded at Lake Gregory (Bowler et al., 2001) and also Lake Lewis (English et al., 2001) in periods of increased aridity and limited fluvial activity, such as MIS 5b,d and MIS 4 (Figure FI.10).

During the following stage, MIS 4 global sea level was reduced by ~100 m and the extent of glaciers in high-elevation parts of Sahul was more significant compared to the LGM (Barrows et al., 2001, Williams, 1996), sea-surface temperatures were lower and the dust signal record increased (De Deckker et al., 2019). These glacial conditions peaked at around 65 ka. Northern Australian lakes were apparently dry during MIS 4 (Hesse et al., 2004), although evidence suggests that in the Gilbert River system in northeast Australia (Figure FI.10) late Austral summer moisture peaked at ~65 ka (Kershaw and van der Kaars, 2012). This might be because the ITCZ during MIS 4 extended further south over

Australia (Wang et al., 2001) and this southward shift may have peaked around 65 ka (Miller et al., 2016). By ~59 ka, the conditions at sea and on land progressively returned to those recorded before the sea-level drop and drop in temperature. The significant climatic changes during the MIS 4 glacial period coincide with the earliest human occupation of Sahul at about 65 ka, based on evidence from the Madjedbebe rockshelter (Clarkson et al., 2017) (Figure FI.10). These uncertain and harsh conditions must have represented a serious challenge for the early humans entering the north of Australia at the time.

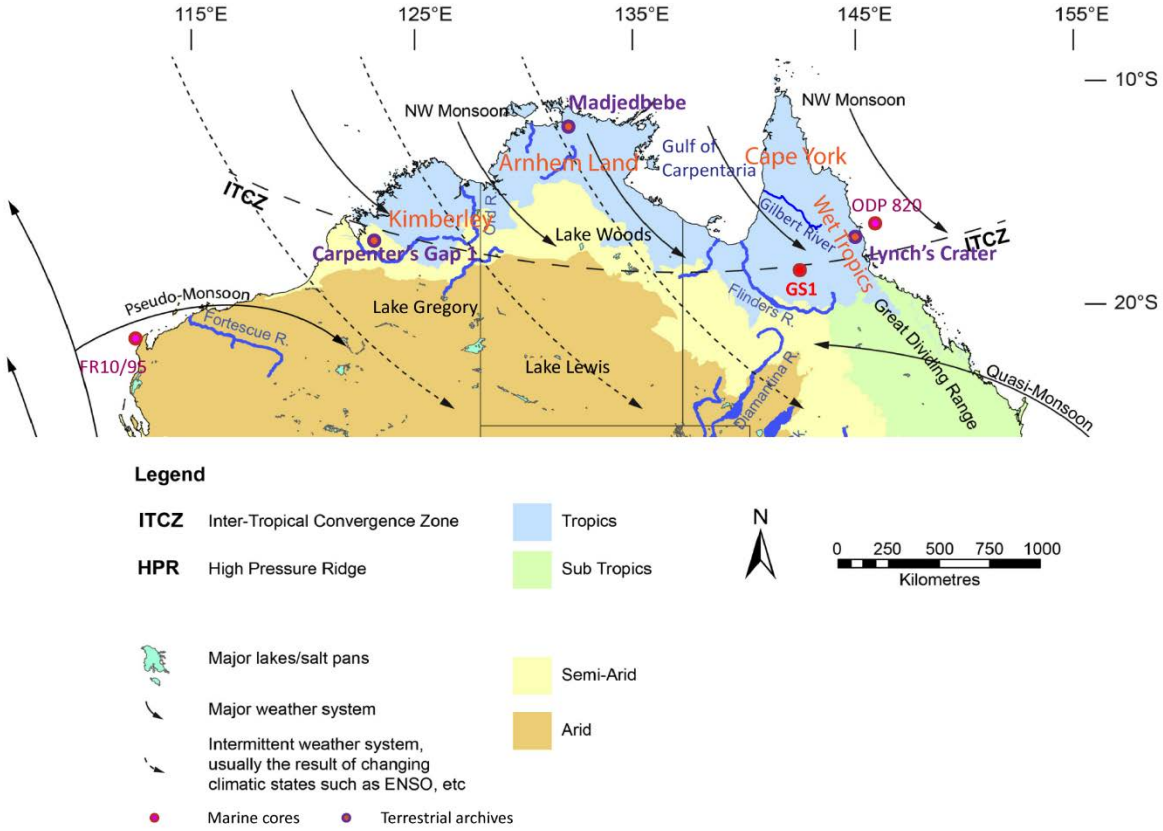

Figure FI.10: Map of tropical north Australia's main modern day climatic classifications and systems (after Williams et al. (2015). Lakes, rivers, marine cores and archaeological sites referred to in the text are also shown. The width of major rivers has been exaggerated for visibility.

At the beginning of MIS 3 (~55 ka), the Australian tropics returned to warmer and wetter conditions. A recent 60 ka record of environmental change for the Wet Tropics comes from a marine core ODP 820 study (Moss et al., 2017) (Figure FI.10). Based on these records, a sea-level transgression from MIS 4 to MIS 3 is reflected in a relatively high abundance of mangroves from at least 58 to 50 ka ago, also supported by lower carbonate concentrations indicating greater terrestrial inputs and a decrease in foram $\delta^{18}O$ value. There is, however, a notable absence of a solid climate signal for MIS 3 in tropical north Australia (Kershaw and Nanson, 1993, Thomas et al., 2001), especially in the north semi-arid savannah interior. The main reference for late Quaternary environmental change in northeast

Australia and beyond is provided by Lynch's Crater on the Atherton Tableland in North Queensland (Figure FI.10). Lynch's Crater is a crater of volcanic origins filled with at least a 60 m deep sequence of lake and peat sediments that contains one of the most complete environmental records of the last two glacial-interglacial cycles on the continent (Kershaw, 1974, 1976, 1978, 1986, Kershaw et al., 2007, Turney et al., 2001). The revised comparison between the Lynch's Crater and the ODP 820 records shows a charcoal peak at around 44 ka, followed by a more sustained increase in burning from 40 ka, a possible indicator of increased human activity.

The late MIS 3 period from ~40 to 30 ka appears to have been broadly characterized by relatively cool and wet conditions evident in pollen, lake, fluvial and speleothem records of the northern Australian region (Reeves et al., 2013a) (Figure FI.8). The ODP 820 marine core record, on the other hand, shows an increase in dry rainforest taxa from around 40 ka and suggests a trend to drier conditions in the Wet Tropics (Moss et al., 2017). The authors, however, explain that the relatively high percentages of ferns combined with reduced grass pollen abundance do not support the evidence of drier conditions and it may be that increased variability was the central environmental influence at the time.

In comparison to the present day, late MIS 3 indicates cooler climatic conditions in the northeast tropics. Wet conditions, however, are evident throughout most of the region due to decreased evaporation under these cooler conditions (Bowler and Wasson, 1984, Galloway, 1965). Both the lake level and speleothem records from the tropical north show a close correlation between effective precipitation and regional insolation through the late MIS 3 up to the early glacial period (35–22 ka) (Reeves et al., 2013a). There is no evidence of a strong monsoon penetrating the Australian mainland at this time (Devriendt, 2011, Lewis et al., 2011, Reeves et al., 2013a); however, there is, some evidence for a short-lived expansion of rainforest taxa in North Queensland ~26–24 ka (Moss and Kershaw, 2007, Moss et al., 2017) implying increased effective moisture.

Leading up to the LGM, much of inland Australia periodically had large permanent lakes in catchments with lakes that are presently dry or ephemeral (Bowler et al., 1976, 2012, Cohen et al., 2011, 2012, Fitzsimmons et al., 2013). Relatively high lake stands prevailed in the tropical north (Veth et al., 2009) and temperate regions (Bowler and Hamada, 1971, Coventry, 1976). Cool and humid conditions are inferred, with increased effective precipitation (Kemp and Rhodes, 2010). It is important to note that despite this comparatively wet period, it was dwarfed by the wet intervals of MIS 5 (Cohen et al., 2011, 2012, Nanson et al., 1992). Lake systems at all scales maintained perennial conditions through to or intermittently up to ~30 ka, coeval with peaks in river activity (Fitzsimmons

et al., 2013). Eventually, regardless of the drivers, lake levels appear to have fallen earlier in the north than in the south of the continent.

The LGM

The LGM occurs in MIS 2 (~22–18 ka) and is a period of universally cooler and drier conditions. Palaeoecological data from northern Australia support dry conditions during the LGM, with the disappearance of palm trees (indicators of wetter climates) from the phytolith record in Carpenter's Gap 1 (Wallis, 2001) and evidence of a drier vegetation assemblage from Indian Ocean deep-sea marine core FR10/95 pollen record (van der Kaars and De Deckker, 2002) in the Kimberley (Figure FI.10). Although pollen records reveal universally drier conditions in conjunction with cooler temperatures for much of the lowland regions of tropical Australasia during the LGM, unambiguous evidence for drier glacial conditions is missing. In contrast, plunge pool and fluvial records of northern Australia reveal that the LGM was characterized by episodic and sometimes extreme rainfall events but with dry conditions in northwestern Australia and south of the Gulf of Carpentaria (Reeves et al., 2013a). In this period, the monsoon is considered inactive or greatly weakened.

In the Coral Sea marine core, ODP 820, extreme conditions during the last glacial in the Wet Tropics are marked in the sedimentary and pollen records. In the sedimentary data, the driest conditions are recorded by a sand layer and more positive foram $\delta^{18}O$ values as well as increased carbonate abundances in the record during the LGM (Moss et al., 2017). The pollen record demonstrates drier conditions through the disappearance of the freshwater aquatic taxa, a reduction in rainforest and mangrove taxa, as well as a more open landscape, with increased representation of grass and a decline in sclerophyll arboreal taxa (Moss et al., 2017). Moreover, the authors suggest that in this period, low charcoal values may indicate little burning activity, probably the result of a marked reduction in fuel loads associated with lower woody biomass.

After the LGM

During the deglacial period toward the end of MIS 2, warmer conditions returned on both land and sea. This initially brought greater precipitation to Indonesia and then to northern Australia with the expansion and intensification of the monsoon due to the southward migration of the ITCZ (Reeves et al., 2013a). The first evidence of warming following the LGM comes from the sea-surface temperature (SST) increase in the Coral Sea at around 20 ka, with 80% of the deglacial warming achieved at about 18 ka (Tachikawa et al., 2009). Generally, warming in the Indian Ocean lagged behind the Pacific Ocean, not commencing until ~15 ka (Martínez et al., 1999). The decline in ice volume reflected in foram $\delta^{18}O$ values, due to increased temperature and decreased salinity, occurred rapidly from 18–15 ka in the east, but lagged in the seas to the northwest of Australia, where it

commenced around 15 ka. Despite an expansion in Lake Carpentaria from 18 ka, the northern plunge pools were considered non-functioning and Lake Gregory may have been dry (Reeves et al., 2013b). The post-LGM arid phase appears to have prevailed in the north until 14 ka when the monsoon resumed (Spooner et al., 2005, Wyrwoll and Miller, 2001).

SSTs rose significantly again at the end of the deglacial period, associated with peak flooding of the continental shelf, re-initiation of coral reef growth and the development of large estuarine systems. This period coincides with the early stages of MIS 1 and is marked by rapidly rising sea levels and extensive mangrove forest expansion over the shelf (Grindrod et al., 1999, 2002). In marine core ODP 820 the highest levels of mangroves were recorded during this period (Moss et al., 2017). Open environments are still well represented in the ODP 820 record with the continued dominance of grasses. Rainforest taxa in the Wet Tropics greatly declined, but an increase in sclerophyll arboreal taxa, with a peak in Melaleuca, possibly indicates the formation of local paperbark swamps behind the mangroves (Moss et al., 2017).

In most archives from tropical Australia, evidence of cooling during Younger Dryas chronozone (12.9–11.7 ka) is not discernible, overlapping with the time when the intensification of the austral summer monsoon occurred (Kuhnt et al., 2015, Tibby, 2012). In a recent study from Lake Barrine, close to Lynch's Crater in the Wet Tropics (Figure FI.10), brGDGT compounds were used to reconstruct mean annual air palaeo-temperatures and the analysis recorded a potential slight decrease in temperature during the Younger Dryas (Li et al., 2023).

In the early Holocene (~11.5−8 ka), warmer and wetter conditions were established across tropical Australia, the sea level peaked and Sahul no longer existed as a single continent (Figure FI.6). The trade winds re-invigorated, the monsoon was at its maximum through this time, with the ITCZ in a southward position with its effects on rainfall extending into the Australian continent. By 8 ka, SSTs and the continental land mass had reached essentially modern values in the tropical regions (Lewis et al., 2013, Petherick et al., 2013, Reeves et al., 2013a).

Wet conditions are evidenced by the active plunge pools in north Australia and vegetation similar to the modern day in northeast Australia by 9 ka, with the establishment of rainforest taxa in the Wet Tropics (Reeves et al., 2013a). There is an increase in charcoal in the north at 8 ka, associated with a switch from grass-dominant to rainforest taxa in the northeast (Mooney et al., 2011, Moss and Kershaw, 2007). The mangrove swamps and estuaries along the eastern seaboard had been established along with the renewed growth of the Great Barrier Reef (Moss et al., 2017, Reeves et al., 2013a). Evidence from the ODP 820 marine core (Figure FI.10) also exhibits a sharp increase in major complex rainforest taxa and fern spores as well as reductions in sclerophyll canopy and ground layer

taxa around 9.5 ka ago, indicating a substantial increase in rainfall (Moss et al., 2017). According to the authors, the vegetation landscape stabilized around 8.5 ka ago with a dominance of complex rainforest developed under high rainfall and temperature. While this refers to the coastal Wet Tropics and hinterland, this implies increased effective moisture further inland in the savannah regions.

Human populations began to expand from ~12 ka and more so from ~8–6 ka, corresponding to increased temperatures and rainfall as the Australian monsoon strengthened and peaked (Griffiths et al., 2009, Wyrwoll and Miller, 2001, Wyrwoll et al., 2000). The mid-Holocene period represents the maximum temperature in terrestrial records throughout the Australasian region, yet it was expressed in different places at different times (Li et al., 2023, Reeves et al., 2013b).

Through the late Holocene, increasing variability with enhanced periods of drier conditions was the overall characteristic of much of the Australian tropics, which is indicative of ENSO being more frequently in the El Niño mode. The evidence comes from coral (e.g. Gagan et al., 2004, McGregor and Gagan, 2004, Tudhope et al., 2001) and speleothem (Griffiths et al., 2009, 2010a,b) records in the north as well as evidence of the reactivation of dunes and dust deposits in the northern, interior and temperate regions (e.g. Fitzsimmons and Barrows, 2010, Fitzsimmons et al., 2007, Marx et al., 2009, 2011, Shulmeister and Lees, 1995). This is consistent with arguments for an at least periodically weakened monsoon after this time (Lees, 1992b, Wyrwoll and Miller, 2001) and has been attributed to the late Holocene weakening of the Walker circulation over the tropics (Shulmeister, 1999). Across much of the continent, the fluvial activity decreased (e.g. Cohen and Nanson, 2007), as evidenced by lower interior lake levels (e.g. De Deckker, 1982, Wilkins et al., 2013).

To conclude, Figure FI.11 provides an illustrated synthesis of palaeoenvironmental change in tropical northern Australia during the late Quaternary.

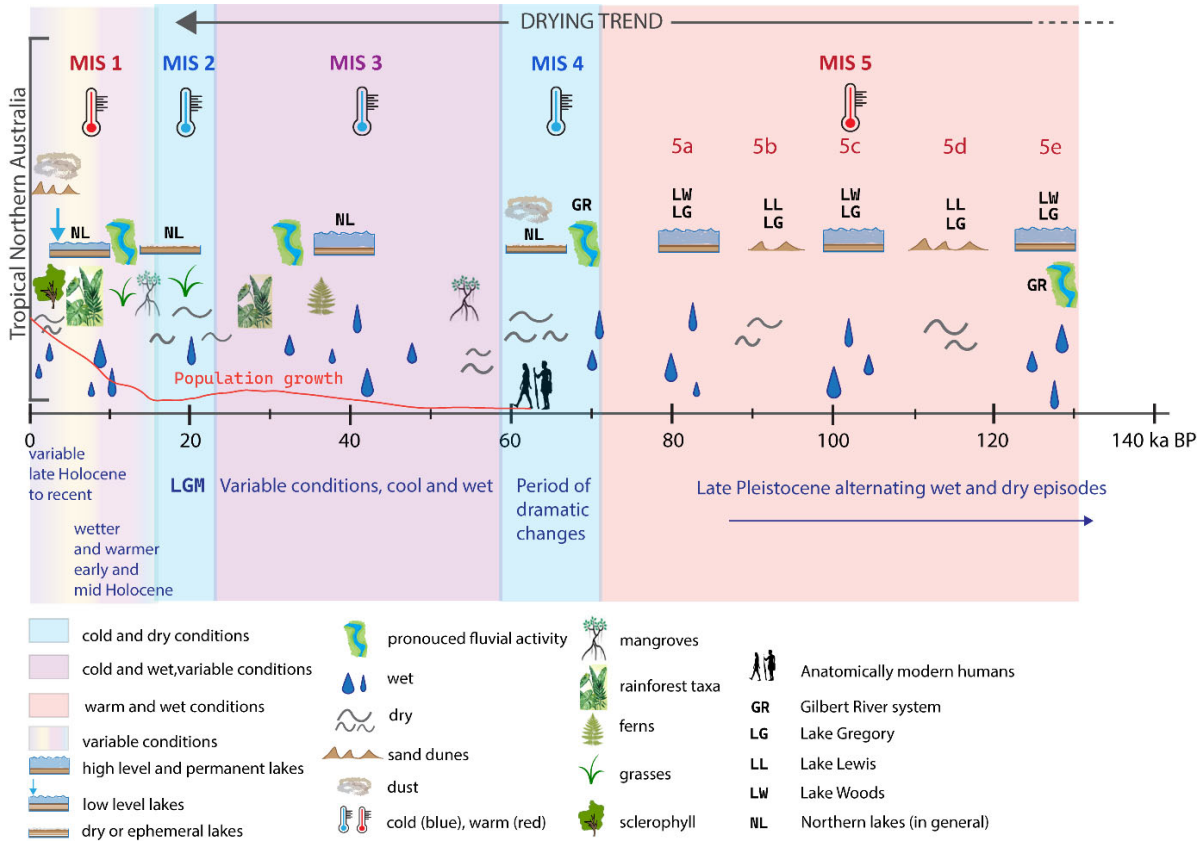

Figure FI.11: A synthesis of late Quaternary palaeoenvironmental change in Australian tropical north from MIS 5 to MIS 1. The conditions are represented in comparison to the previous and following periods. For illustrative purposes, bigger drops depict stronger precipitation. Human silhouettes are included to show what conditions the first humans, according to Clarkson et al. (2017), would have encountered. The population growth line is placed solely for interpretative purposes, to illustrate the decrease in population numbers during the LGM, and the subsequent rapid expansion in the Holocene, based on Williams et al. (2015) (authors do not provide any numbers).

Chapter 1 Geologic and geomorphic setting of the Gledswood Shelter 1 (GS1) site, North Queensland, Australia

Mojca Zega[1,2], Michael Bird[1,2], Robert Wasson[1], Keith Fifield[3], Lynley A. Wallis[4], Jack Koci[1]

[1]College of Science and Engineering, James Cook University, QLD, Australia

[2]ARC Centre of Excellence of Australian Biodiversity and Heritage CABAH

[3]Department of Nuclear Physics, The Australian National University, Canberra, ACT, Australia

[4] Griffith Centre for Social and Cultural Research, Griffith University, Nathan, Australia

Statement of contribution of others:

MZ, MB and RW designed the study. MZ conducted the field work, did most of the laboratory work, the data analysis and drafted the manuscript. RW and MB provided support with the interpretation of results. KF advised about fieldwork sampling for ^{10}Be cosmogenic nuclide analysis, coordinated the ^{10}Be cosmogenic nuclide laboratory analysis and provided support with the interpretation of results. JK constructed the digital elevation model and provided support with interpretation. All authors edited the manuscript.

Abstract

Northern Australia comprises stable, extensively weathered landforms dating back to the Precambrian era as well as more recent dynamic sediments that have shaped Quaternary alluvial deposits, sand dunes and estuarine sediments. Geomorphically, these materials are distributed in particular ways, knowledge of which improves our understanding of their formation processes.

This study is one of the few conducted in tropical north Australia that focuses on the immediate surroundings of an archaeological rockshelter, Gledswood Shelter 1 (GS1), to better understand of the formation processes and past landscape conditions. GS1 is an archaeological rockshelter site situated in the semi-arid savannah inland in North Queensland, in the vicinity of the Norman River. The surface consists of weathered Jurassic sandstone pediments, rugged outcrops, sand plains and fluvial deposits. Two sampling locations were selected: 1) the non-archaeological open-site sediment deposits extending south of the GS1 dripline (referred to as 'Outside GS1'), and 2) the river terraces exposure along the nearby Norman River, to establish a geologic and geomorphic context to the GS1 site and investigate the past dynamics of the Norman River. GPS data and drone images were acquired for geomorphic analysis and to construct a digital elevation model (DEM). Multiple sediment and rock samples were collected from excavated pits, auger holes and river terraces for particle size analysis and optical microscopy. ^{10}Be cosmogenic nuclide analysis was applied to estimate denudation rates and exposure ages.

A comparison of sediment and rock samples demonstrates that the local sediments originate from the weathering of Jurassic Hampstead sandstone, the underlying lithology across the wider area. The sediments from both sampling sites predominantly consist of fine and medium sand. The sediment and rock samples were classified as sub-litharenite and quartz-dominated lithic greywacke. Evidence of post-deposition disturbances, clay illuviation and redoximorphic features were recorded by macro- and microscopic optical analysis. The calculated denudation rates of 8–11 mmka^{-1} Outside GS1 indicate a slowly denuding surface and the estimated exposure ages show that the area surrounding the GS1 site has been exposed to surface cosmic rays for at least 70 ka. The evidence suggests that the sediments outside GS1 have been episodically, in cycles, accumulated, moved around, removed and redistributed by gravitational processes, precipitation and bioturbation. At the Norman River site, the stratigraphic evidence indicates 'fill-cut terrace' form, suggestive of periodic shifts in river dynamics from aggrading to incising, induced by changes in water discharge and sediment load at the upstream end of the Norman River.

1.1 Introduction

Landscape processes can be considered in terms of entropy, as a measure of the deposition, erosion, degradation or disorganization of material in a depositional environment by physical, chemical, biological or anthropogenic activity (Ward and Larcombe, 2003, pg. 1225). It is virtually impossible to account for all the various processes and combinations of processes that influence the formation of a site. In response, Ward and Larcombe (2003) suggest that investigating and quantifying some of the most significant processes in an area can contribute greatly to a deeper understanding of site formation. They highlighted the need for a greater emphasis on of process studies in connection with archaeological site research throughout northern Australia.

The Gledswood Shelter 1 (GS1; see Wallis et al., 2009) is an archaeological rockshelter in north inland tropical Queensland. It lies approximately 1.6 km north of the Norman River, in a typical Australian semi-arid savannah (Figure F1.1). The wider area is composed of two distinct geomorphological elements: rugged plateaus and residual hills of dark, dissected sandstone up to a few tens of meters high stretching to the north and east, with lowland sandy plains adjoining the Norman River to the south and west. The residual outcrops (Migoń et al., 2020) are confined mainly to residual hills, scarp retreats and tablelands of the Gregory Ranges that fringe the area on the east side (Figure F1.1). At the base of the backing escarpments and residual hills, stretching to the south and west, are the gently sloping, timbered sand plains, named Strathpark Plains, which flank the Norman River. A view of the area is shown in Figure F1.1 and the images of the described geomorphological elements are given in Figures F1.2a and F1.2b.

This study aims to provide more detailed insights into the geologic and geomorphic characteristics of the area where the GS1 archaeological site has formed. The main research was carried out in the area where the GS1 is located, immediately beyond the GS1 rockshelter dripline, to understand the development of the geologic and geomorphic structure of the GS1 rockshelter's surroundings. The geogenic processes that have been operating at the site in the late Pleistocene and Holocene were also investigated, particularly the last 50 ka (Kiloannums; 1ka = 1,000 years) as the time frame of relevance to early human presence on the former mega-continent of Sahul (mainland Australia, Tasmania, New Guinea and Aru Islands, joined at times of lowered sea level) and now Australia. Additionally, a subsidiary project was conducted on the Norman River terraces to obtain initial information on the dynamics of the river channel as well as water and sediment discharge in the past. These records can offer insights into past environmental conditions in the region, thereby complementing the data obtained at the GS1 site from previous archaeological studies. As an initial step, a summary of the geologic and geomorphic evolution of the region is given below.

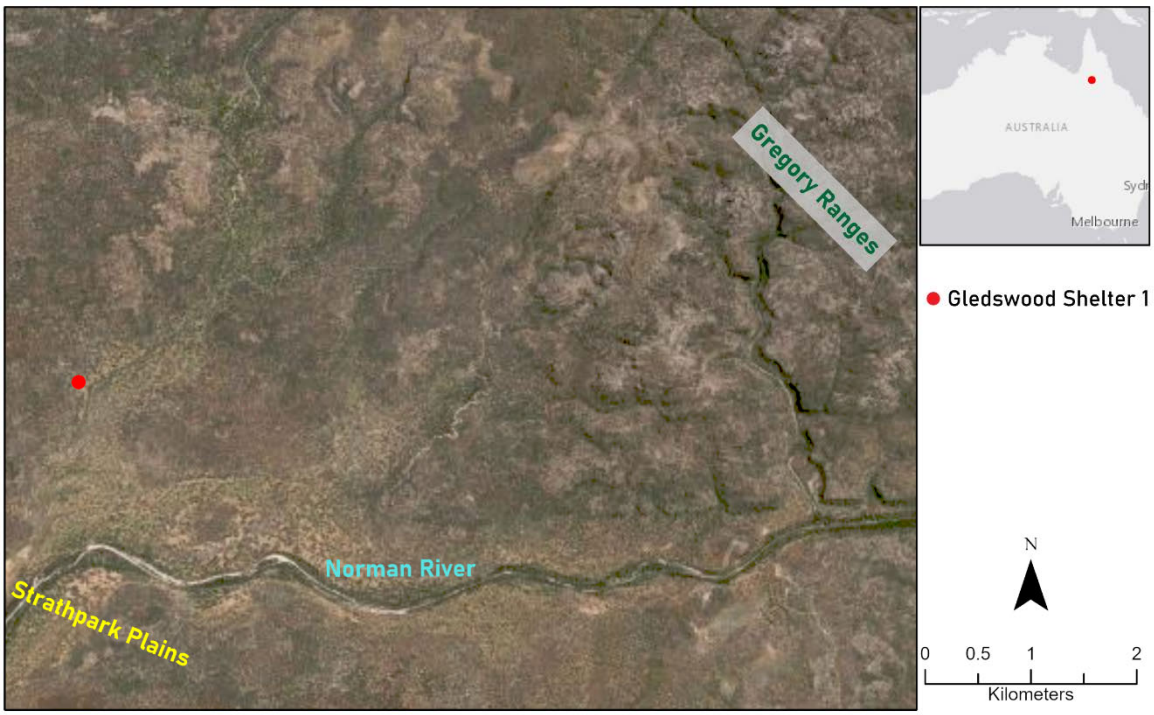

Figure F1.1: The wider area where Gledswood Shelter 1 (GS1) is situated. The red circle marks GS1 located at a topographic boundary between the foothills of the Gregory Ranges to the east and the Strathpark plains sloping gently to the west and south. About 1.6 km to the south of GS1 flows the Norman River, whose headwaters are in the Gregory Ranges and which drains westward into the Gulf of Carpentaria.

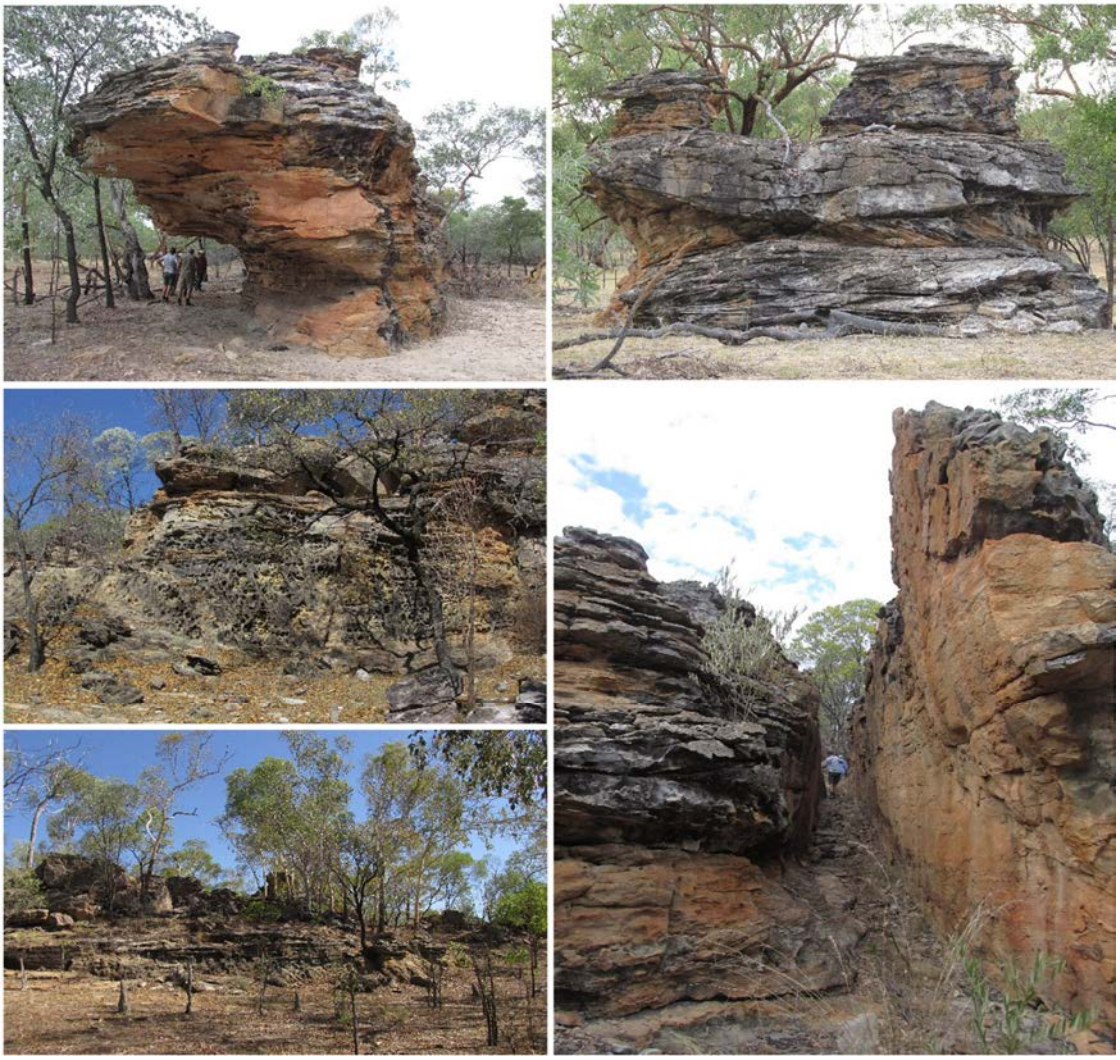

Figure F1.2a: Rugged residual hills and outcrops spread of dissected, cross-bedded sandstone found in the area of study.

Figure F1.2b: **Top:** scarp retreats and dissected plateaus of Gregory Ranges. **Middle:** an image showing the transition from residual hill slopes on the right to the Strathpark Plains on the left and Norman River in-between. **Bottom:** the gently undulating, timbered Strathpark Plains that flank the Norman River.

1.1.1 Geologic background

For a significant part of the past, the Australian northeast's geology was driven by subduction along a long-lived convergent margin on the eastern side of the continent. This subduction zone was active from the early Cambrian (~510 Ma) until, at minimum, the Late Triassic (~230 Ma), but possibly up to the Late Cretaceous (~100 Ma) (Hoy and Rosenbaum, 2017, Hoy et al., 2018, Tucker et al., 2016, Veevers, 2006, Wainman et al., 2015, 2018a,b). Collision and subduction controlled the rise of the

orogens to the east from the Cambrian to Triassic Periods and the subsidence and formation of sedimentary basins in the region afterwards (Todd, 2020). These sedimentary basins belong to two major groups in connection to the time of their formation: the older 'Carboniferous to Triassic' basins and the overlying 'Jurassic to Cretaceous' basins (Todd, 2020). The latter are often considered parts of a single superbasin system called the Great Artesian Basin. Within this structural framework, the position of the GS1 rockshelter is on the Euroka Arch, a ridge that separates two 'Jurassic to Cretaceous' sedimentary basins, the Eromanga Basin to the south and the Carpentaria Basin to the north (Figure F1.3). Buried beneath the Eromanga Basin lies the older Galilee Basin, which is part of the 'Carboniferous to Triassic' basin group.

1.1.1.1 The Galilee Basin: Carboniferous to Late Triassic (~320-230 Ma)

The Galilee Basin developed between the late Carboniferous and Middle Triassic (de Caritat and Braun, 1992). During the late Carboniferous to early Permian, glaciogenic fluvial and lacustrine sediments were deposited in the Galilee Basin (Gray, 1977, Jones, 2004) followed by non-deposition or non-preservation throughout the middle Permian, ~270–260 Ma (Allen and Fielding, 2007a, Evans, 1980, Phillips et al., 2017a, Van Heeswijck, 2004, 2010). Widespread deposition resumed in the late Permian, dominated by volcanolithic fluviatile sandstones, carbonaceous shales and coals (Allen and Fielding, 2007a, b, Phillips et al., 2017a). In the Early to Middle Triassic coal formation ceased and a shift to slightly drier fluvial-dominated sandstone and pedogenic floodplain shales is documented (Balfe, 1979, Gray, 1977).

Sedimentary deposition into the Galilee Basin ceased in the early Late Triassic (~235–230 Ma) as a result of a large-scale deformation and uplift of the eastern Australian convergent margin. This uplift was followed by a period of tectonic stability during the Late Triassic and into the Early Jurassic. The stratigraphic boundary marking the contact between the Galilee and Eromanga Basins is, therefore, characterized as a paraconformable surface (Todd, 2020), with parallel strata on either side of the unconformity and little apparent erosion of the contact. The position and extent of the Galilee Basin is shown in Figure F1.4.

1.1.1.2 The Eromanga Basin, the Carpentaria Basin, the Euroka Arch and the formation of the Jurassic Hampstead Sandstone: Jurassic to Cretaceous (~201-100 Ma)

Following Late Triassic tectonic stability, the younger Eromanga and Carpentaria Basins started to evolve in the region coevally. Localized sedimentary deposition was initiated in places in the latest Triassic, whereas widespread deposition of these sedimentary basins commenced in the Early Jurassic (Draper and Mines, 2002).

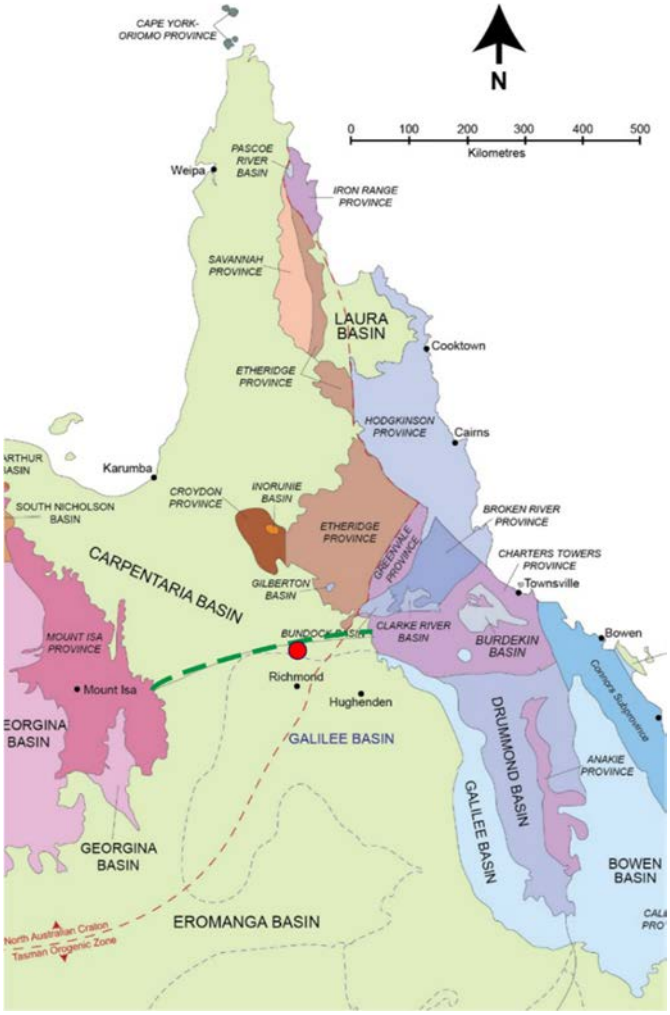

Figure F1.3: Geologic structural framework of Queensland, Australia showing the positions of Palaeozoic and Mesozoic sedimentary basins and orogenic belts. from Todd (2020). The green colour represents the Mesozoic basins, all other colours represent the Palaeozoic structures. Light grey dotted lines indicate portions of Carboniferous to Triassic basins that are buried beneath the Jurassic to Cretaceous basins. The red circle marks the GS1 area of study, the dark green dashed line marks the Euroka Arch

The Euroka Arch is a structural boundary between the Carpentaria Basin to the north and the Eromanga Basin to the south (Figure F1.3, Figure F1.6). It represents a passive basement high on either side of which subsidence occurred, but upon which deposition was generally continuous (Smart et al., 1980). The Euroka Arch consists of a core of pre-Mesozoic rocks across which the Jurassic-Cretaceous rocks of the Carpentaria Basin continue into the Eromanga Basin. The Eromanga Basin overlies the older - Galilee and Cooper Basins and covers 1.2 million km^2 across Queensland and South Australia as well as parts of the Northern Territory and New South Wales. The saucer-shaped Eromanga Basin is commonly described as an intracratonic sag basin (Cook et al., 2013). The process and timing of its formation remain unclear, which is often the case with cratonic basins (Allen and Armitage, 2012,

Middleton, 1989). Most of the existing hypotheses about its formation, however, imply that an active convergent margin was located along the eastern Australian continental margin during the Jurassic (Todd, 2020). This supports the theory mentioned earlier about the eastern subduction zone being active until the Cretaceous (see section 1.1.1).

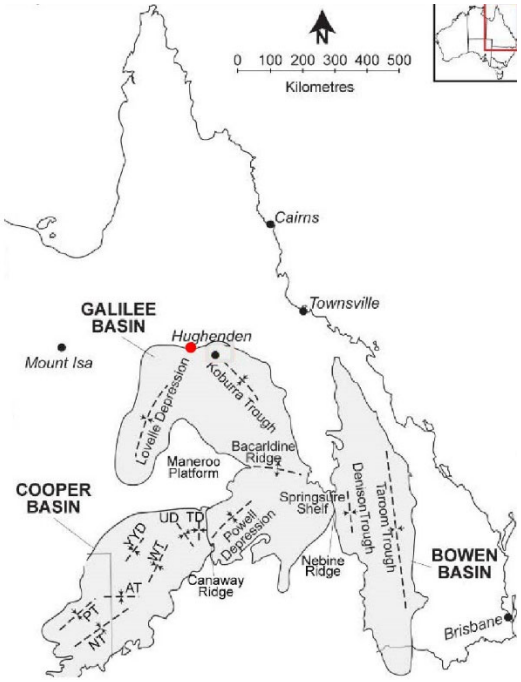

Figure F1.4: Position and extent of the Galilee Basin as well as the other two contemporary basins - the Cooper and Bowen Basin, from Todd (2020). The red circle marks the GS1 study area

From the Early Jurassic to Early Cretaceous the sedimentary infill of the Eromanga Basin was dominated by continental depositional systems consisting of highly permeable fluvial sandstones and carbonaceous floodplain deposits (Balfe, 1979, Draper and Mines, 2002, Wainman et al., 2015). The only exception is represented by two short-lived episodes of marine influence recorded in the Eromanga Basin deposits during this period, one in the Early Jurassic (Bianchi et al., 2018, La Croix et al., 2019, Wang et al., 2019) and another in the Late Jurassic (Wainman and McCabe, 2019). During this long period, the Late Jurassic Hampstead Sandstone, which constitutes the plateaus scarps, residual hills and outcrops in the GS1 area, was deposited in the north of Eromanga Basin and in the Carpentaria Basin (Smart and Senior, 1980).

Lithologically, the Hampstead Sandstone is described as fine, medium and coarse quartzose sandstone with some pebbly beds and conglomerate, strongly cross-bedded and interbedded micaceous siltstone, mudstone and very fine sandstone (Smart and Senior, 1980). The sandstone is grey to brown or white in places. The formation is massive and cliff-forming. The dark tone and strong

jointing visible on air and satellite photos (Figure F1.5) distinguish it from the overlying Loth Formation (Smart et al., 1971). The latter also belongs to the Late Jurassic period and conformably overlies the Hampstead Sandstone in Eromanga and Carpentaria Basins. In outcrop, the Loth Formation is predominantly white, soft, locally ferruginized sandstone and siltstone, less resistant than the adjacent formations and therefore differential erosion has formed a prominent topographic bench on top of the Hampstead Sandstone. Together the Hampstead Formation and the Loth Formation form a continuous sequence known as the Eulo Queen Group (Smart et al., 1971, Smart and Senior, 1980).

Figure F1.5: The dark tone and the strong jointing of the Jurassic Hampstead Sandstone

In the Early Cretaceous (Aptian, ~120 Ma), a marine transgression blanketed the Eromanga Basin in shallow marine mudstones (Cook et al., 2013). The Euroka Arch remained a relatively stable area between the sagging Carpentaria and Eromanga Basins throughout the Early Cretaceous (Smart et al., 1980). In the Late Cretaceous the sea retreated and deposition continued through a progressive shift to continental depositional systems (e.g. Tucker et al., 2017) until a switch to an extensional regime beginning ~83 Ma. Rifting of the eastern Australian margin led to isostatic rebound and created significant relief in the form of the present-day Great Dividing Range and its northern section, the Einasleigh Uplands, thereby terminating deposition that filled and closed the Eromanga Basin (Cook et al., 2013). Figure F1.6 shows the position and extent of the Eromanga and Carpentaria Basins with the location of GS1 marked.

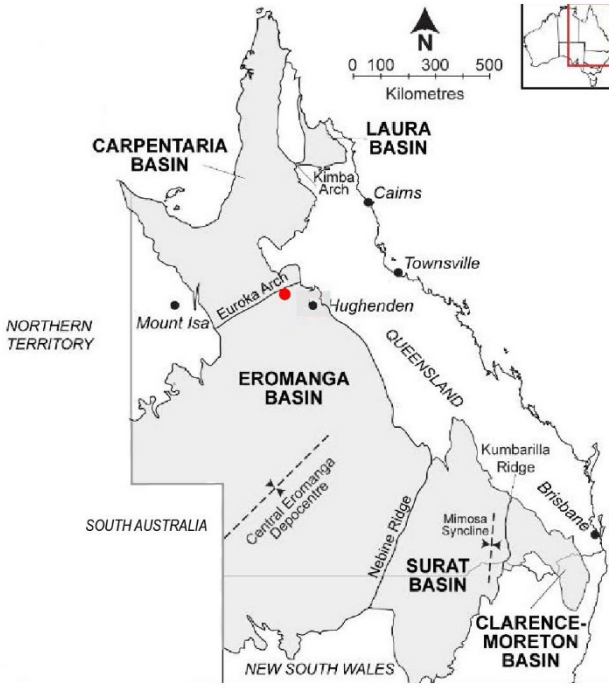

Figure F1.6: The position and extent of the Eromanga and Carpentaria Basin, from Todd (2020). The red circle marks the GS1 study area.

1.1.1.3 The Karumba Basin and geomorphic cycles: Cainozoic, Tertiary and Quaternary (~65 Ma – recent)

The uplift and warping of the highlands on the east margin of the Australian continent in the Late Cretaceous and early Tertiary initiated the development of the Karumba Basin, a dominantly Cainozoic, epicratonic basin superimposed on the Mesozoic Carpentaria Basin and northmost parts of the Eromanga basin (Bain & Draper, 1997, Grimes, 1979, Smart et al., 1980) (Figure F1.7). The Tertiary and Quaternary period of the Australian northeast is hence controlled by activity in the Karumba Basin. The basin originated due to changes in tectonic dynamics (e.g. Smart et al., 1980, Twidale, 1966) on the eastern continental margin and its development can be divided into three major cycles, each characterized by a similar sequence of erosional, depositional and weathering events.

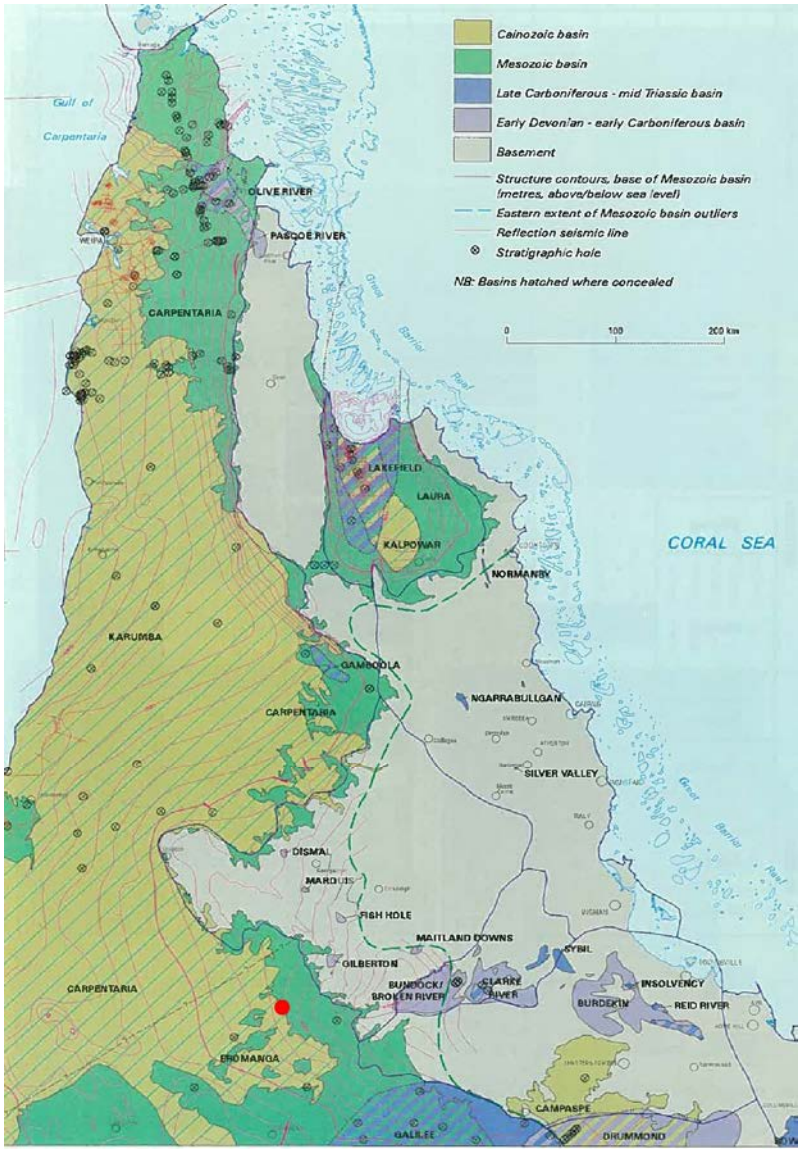

Figure F1.7: The position and extend of the Cenozoic Karumba Basin (olive green colour). The Mesozoic Eromanga and Carpentaria Basins shown in dark green colours and outcrops of Palaeozoic basins in blue and purple. The picture is from Bain & Draper (1997). The red circle marks the GS1 study area.

In general, each cycle in the evolution of the Karumba Basin started with uplift or some other event during which times erosion occurred in the higher, uplifted areas and the eroded material was transported and deposited in the lower, downwarped areas (e.g. Grimes, 1979, Smart et al., 1980). As the depositional area expanded or shifted, it buried parts of the erosional area to form a diachronous unconformity surface. Erosion and deposition continued until the uplands were worn down and the geopotential energy of the system was reduced. The final or passive phase of a cycle is equivalent to the 'old age stage' of a geomorphic cycle during which both erosion and deposition are reduced and a more or less stable planar surface results. This terminal surface was generally deeply weathered.

The weathering of the stable surface continued until renewed tectonism or some other event initiated the next cycle of erosion and deposition.

The basic cycle, however, was often modified by subsidiary events, resulting in several episodes in either phase of the main cycles. The three cycles recognized in the Karumba Basin are: 1) the *Bulimba Cycle* (Early to Middle Tertiary, ~65(?)–30 Ma) during which the Bulimba Formation accumulated and the terminal Aurukun Surface formed, 2) the *Wyaaba Cycle* (Middle Tertiary to Pliocene, ~30–5 Ma) during which the Wyaaba Beds and other deposits were laid down and the terminal Kendall Surface formed; and finally, the present *Claraville Cycle* which began in Pliocene times and it is continuing (e.g. Bain & Draper, 1997, Grimes, 1979, Grimes and Doutch, 1978, Smart et al., 1980). The geological evolution of the study area from Palaeozoic to Quaternary is illustrated in Figure F1.8.

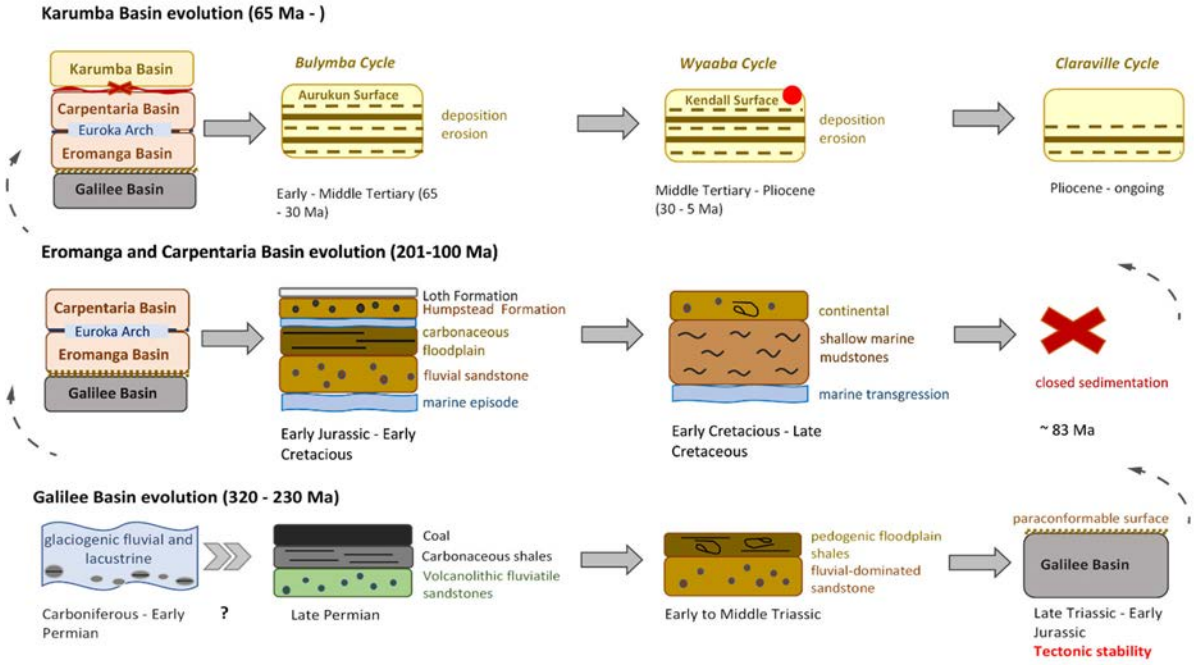

Figure F1.8: A figurative representation of the geological evolution of the study area, from the oldest Palaeozoic Galilee Basin at the bottom and the youngest Karumba Basin at the top. The red circle represents the evolution cycle stage at the GS1 study area.

A detailed description of these cycles, their corresponding deposits and terminal surfaces is provided in various contributions (e.g. Bain & Draper, 1997, Grimes and Doutch, 1978, Grimes, 1979, Smart et al., 1980, and citations therein) but exceeds the purpose of this chapter. In connection with the Karumba Basin evolution, it is relevant to this study that the GS1 area is located within the Strathpark Plain (Perry et al., 1964) (Figure F1.9). The Strathpark Plain belongs to a group of narrow lateritic plains that occur as marginal strips between the depositional plains and the erosional areas from which the deposits were derived (Grimes and Doutch, 1978). Hence, these plains are little

disturbed remnants of old land surfaces, in particular, the early Kendall Surface. The Kendall Surface is of Pliocene age and represents the planation surface preserved in the interfluves, developing as a depositional surface towards the end of the Wyaaba Cycle. The surface has undergone some erosional modification since its formation, having been lateritised, ferricreted and silicified in some places (Grimes, 1979).

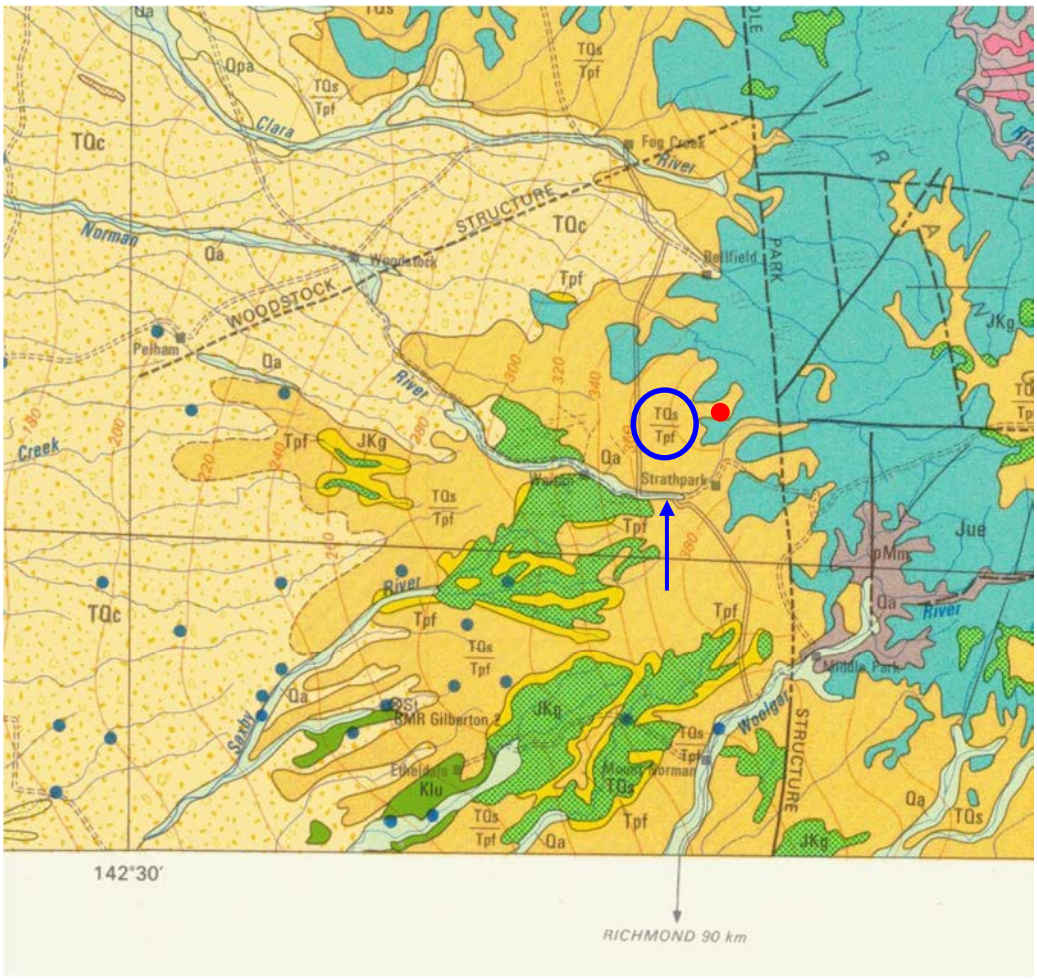

Figure F1.9: The position and classification of Strathpark Plain and GS1 within the Karumba Basin evolution cycles. The detail was taken from the map published in Smart et al. (1980). The red circle marks the GS1 study area. The arrow identifies the Norman River meandering through the Strathpark Plain. The dark yellow coloured unit with encircled symbol TQs/Tpf covering the Strathpark Plain and the GS1 indicates quartzose sands with minor gravel, clay and silt that form the deep weathered Kendall surface. The yellowish orange spotted TQc area further west, marks the Claraville beds, belonging to the last cycle in Karumba basin evolution. The blue colour unit marked Jue on the east of GS1 represents the slopes and plateaus of Jurassic quartzose sandstone, siltstone and conglomerate – the Gregory Ranges. The GS1 position at the topographic boundary between the slopes on the east and the Strathpark Plain on the south and west is evident. The green colour marks the outcrops of upper Jurassic-Lower Cretaceous sandstone (the Gilbert River Formation), while the pink and brown colours represent the outcropping old Palaeozoic and Precambrian units. The numbered orange contours mark the height of the terrain above the sea level and the number at the bottom of the map indicates the geographical longitude.

The Strathpark Plain and the study area are currently experiencing the passive part of the evolution cycle as the relief of the area is reduced and the terminal planation surface develops. These surfaces can have both erosional and depositional components, the former being most common near the margins of a sedimentary basin (Grimes, 1979), such as the Strathpark Plain situated in the transitional area between the Karumba Basin and the footslopes of the Einasleigh Uplands. Subsidiary changes in erosion and deposition in the study area are therefore limited to a local level.

1.1.2 Geomorphic background

The geologic background described above defines the context for the geomorphic processes that resulted in the formation of the study area, contributing to the landscape we perceive today. The position of GS1 within the geologic and geomorphic structures generates an array of long-term processes that constantly reform and shape the site. The Euroka Arch, although buried deep underneath the Cainozoic Karumba Basin deposits, contributes to the general structural stability of the area, as it appears to have been left upstanding as the two Mesozoic sedimentary basins sagged away from it (Smart et al., 1980). The Gregory Ranges footslopes (rising on the east and the Strathpark Plain expanding to the south and west along with the Norman River) give the site a distinct transitional character between the higher and lower lands. Perry et al. (1964) described these highlands as dissected and rugged plateaus and stepped scarps of the Torwood Land System and the lowlands as the Strathpark Land System, a very gently undulating plain. Although their pioneering work still represents an important reference source, the Land System classification is generally not in use anymore in light of new findings and approaches. Gravitational processes, rock denudation, sediment transport and deposition induced by weathering, precipitation and fluvial transport during the monsoon as well as by drought and wind in the dry season are the major factors that shape the area today.

1.2 Materials and Methods

1.2.1 Field survey, drone imagery, GPS data and sampling

Field survey was performed in July 2018, October 2018, May 2019 and July 2020 for sample and data collection. Aerial imagery was obtained in May 2019 and July 2020 using the Mavic 2 Pro/Zoom drone flown at a height of 51 m with camera angle at nadir and Pix4D software. Images were collected in a single grid pattern with 70% forward overlap and 60% side overlap. Rhino 750 GPS units were used for GPS data collection and a Hemisphere S321 for DGPS data collection. Drone imagery along with GPS and DGPS data were used to produce maps in ArcGIS Pro. Agisoft PhotoScan Professional

(v4.1) was used to stitch the drone images together and produce a high-resolution digital elevation model (DEM) and ortho-photo mosaic of the study area.

Two locations were selected for sediment sampling and named as follows:

1. **Outside GS1:** representing the non-archaeological open-site sediment deposit expanding up to 73 m south and southwest beyond the GS1 shelter dripline (Figure F1.10), and

2. **Norman River site:** representing a profile exposed in a meander bend at the Norman River, approximately 1.6 km south of the GS1 (Figure F1.10). This location was chosen as a subsidiary site to provide information about past changes in water and sediment discharge dynamics.

The collected samples are described below and the complete sample catalogue is given in Table T1.1.

1.2.1.1 Bulk sediment samples

Altogether, 47 bulk sediment samples were collected for sedimentologic analysis, 45 from the Outside GS1 site and 2 from the Norman River site. At the Outside GS1 site, bulk sediment samples were collected at various distances from the GS1 shelter's dripline and from various depths to investigate changes in studied parameters, i.e. colour, particle size and microscopic features, with distance from the GS1 rockshelter and with depth. At the Norman River site, we were able to collect two bulk samples (along with other samples) to obtain essential information about the sedimentological characteristics of the larger sediment-contributing area. Information about the samples' distance, depth and performed analyses are provided in Table T1.1.

1.2.1.1.1 Outside GS1

In 2008, five off-site shovel test pits (TP01, TP02, TP03, TP04, TP05) were excavated at the Outside GS1 site by L. Wallis' team (Lowe et al., 2018) and made available for the current analysis (Figure F1.11). The maximum depth of these pits was 120 cm, regardless of the depth of the bedrock, apart from TP04, in which bedrock was reached at around 100 cm below surface. Multiple bulk sediment samples were collected at various depths for laboratory analyses. Of these, 20 samples were analysed in this study (Table T1.1).

During fieldwork in 2019 and 2020, two additional pits (PA_10-M and C_1-CR) and ten augers holes (PA_1-M, PA_2-M, PA_3-M, PA_5-M, PA_5-M, PA_6-M, PA_7-M, PA_8-M, PA_9-M and PA_11-M) were excavated (Figure F1.11). From these, 25 bulk sediment samples were collected for this study (Table T1.1), 10 were scraped from the profile using a hand trowel, 11 were collected by a hand auger and 4 were collected from the core head. The sampling was designed to observe changes in sediment characteristics with respect to the depth of the sediment deposit and increasing distance from the

GS1 shelter's dripline. The locations of all pits and augers are given in Figure F1.11 and examples of excavations and profile sampling are shown in Figure F1.12.

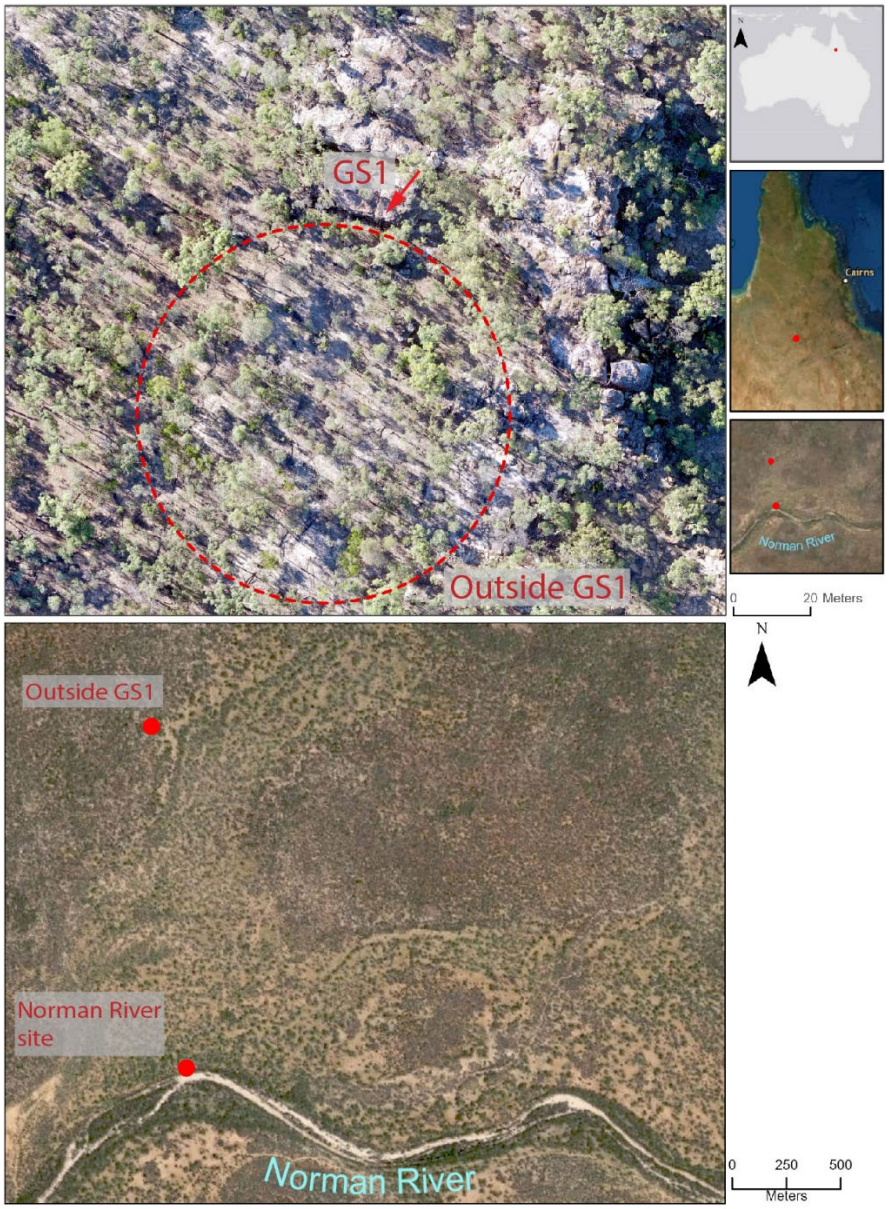

Figure F1.10: The two sampling sites. **Upper:** Outside GS1, the dashed red circle marks the sediment deposit expanding south from the GS1, the GS1 marks the Gledswood Shelter 1 and the red arrow points to the GS1 shelter's dripline. On the small maps to the right the red dot marks the study area. **Bottom:** Norman River site marked with the red circle on the northern riverbank, the second red circle located north from the river marks the GS1 for the purpose of orientation, with scale provided in the lower right.

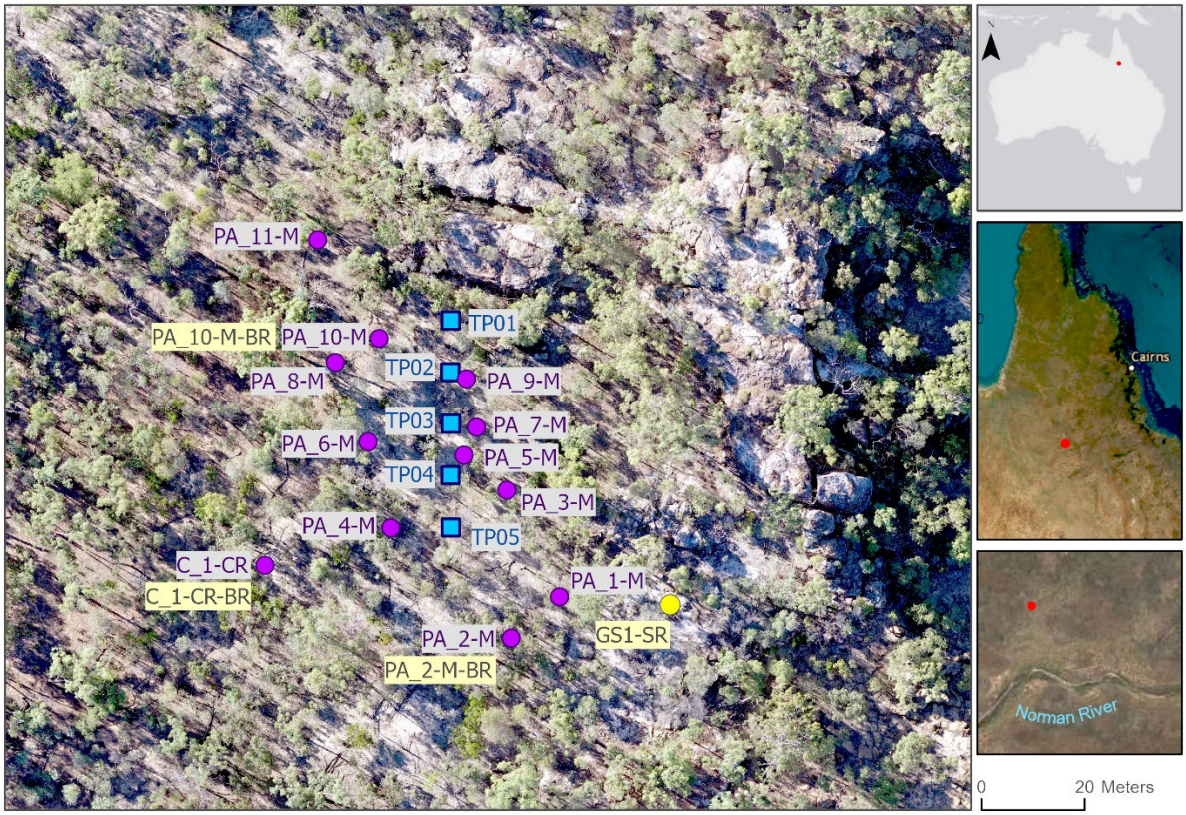

Figure F1.11: Sampling locations, pits and augers, Outside GS1. The test pits excavated in 2008 are labelled blue, the pits and augers excavated in 2019 and 2020 are labelled purple. Yellow label marks the locations of four rock samples, which correspond to two pits, one auger and one surface rock collected for petrography and ^{10}Be cosmogenic nuclide analysis (see sample catalogue Table T1.1).

Figure F1.12: Examples of augers and pit excavations and samples collection from a profile Outside GS1. a-d) auger holes: PA_1-M, PA_3-M, PA_9-M, e-f) pit PA_10-M, south face: excavation and bulk sampling.

1.2.1.1.2 Norman River site

At the Norman River site profile four distinguishable units were recognised. They were marked A, B, C and D, where A represents the uppermost unit and D represents the lowest unit (Figure F1.13). Bulk sediment samples were collected from the top of Unit A and the bottom of Unit D.

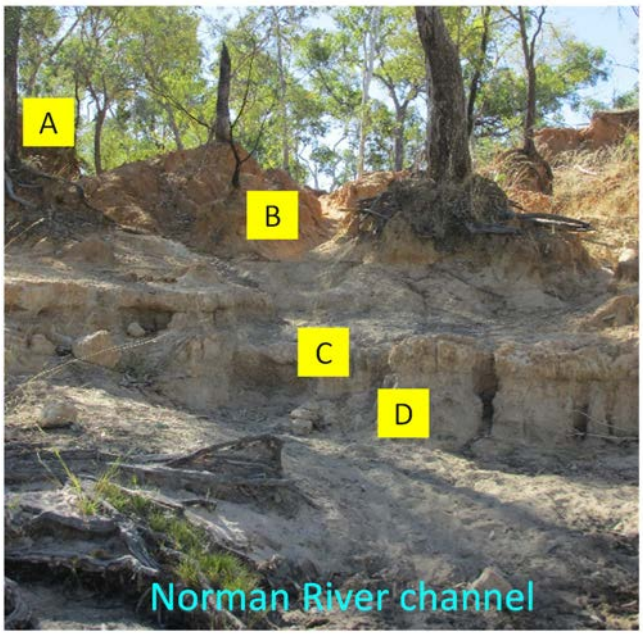

Figure F1.13: The four units (A–D) at the Norman River site profile. Bulk sediment samples were collected from units A and D, hardened sediment units B and C were sampled for petrographic thin sections.

1.2.1.2 Petrographic samples

Nine samples were collected for optical microscopic petrographic analysis (Table T1.1). Out of these, seven samples were collected Outside GS1 and two at the Norman River site to investigate the sediment provenance and evidence of syn-depositional and post-depositional processes.

1.2.1.2.1 Outside GS1

Outside GS1, four sediment samples from the south face of the pit PA_10-M were collected for sediment thin sections (PA_10-M 1, PA_10-M 2, PA_10-M 3, PA_10-M 4) (Figure F1.11), using a rapid on-site method (Asscher and Goren, 2016). We applied Luci Clear Casting Resin, Crystal Clear–Bubble free Resin, and Hardener to impregnate and cut out the four sediment blocks from the profile.

In addition, three rock samples were also collected for rock thin sections, as follows:

1) bedrock at the bottom of the pit PA_10-M, depth ~170 cm (PA_10-M-BR),

2) bedrock at the bottom of auger PA_2-M, depth 25 cm (PA_2-M-BR) and

3) exposed surface rock sample (GS1-SR).

Samples details are given in Table T1.1. Sampling locations are shown in Figure F1.11 and the rapid on-site method for sediment petrographic samples is shown in Figure F1.14.

1.2.1.2.2 Norman River site

At the Norman River site, two samples were collected for optical petrographic analysis, one from unit B and one from unit C (Figure F1.13). Both units were firm enough to be sampled without the need for impregnation.

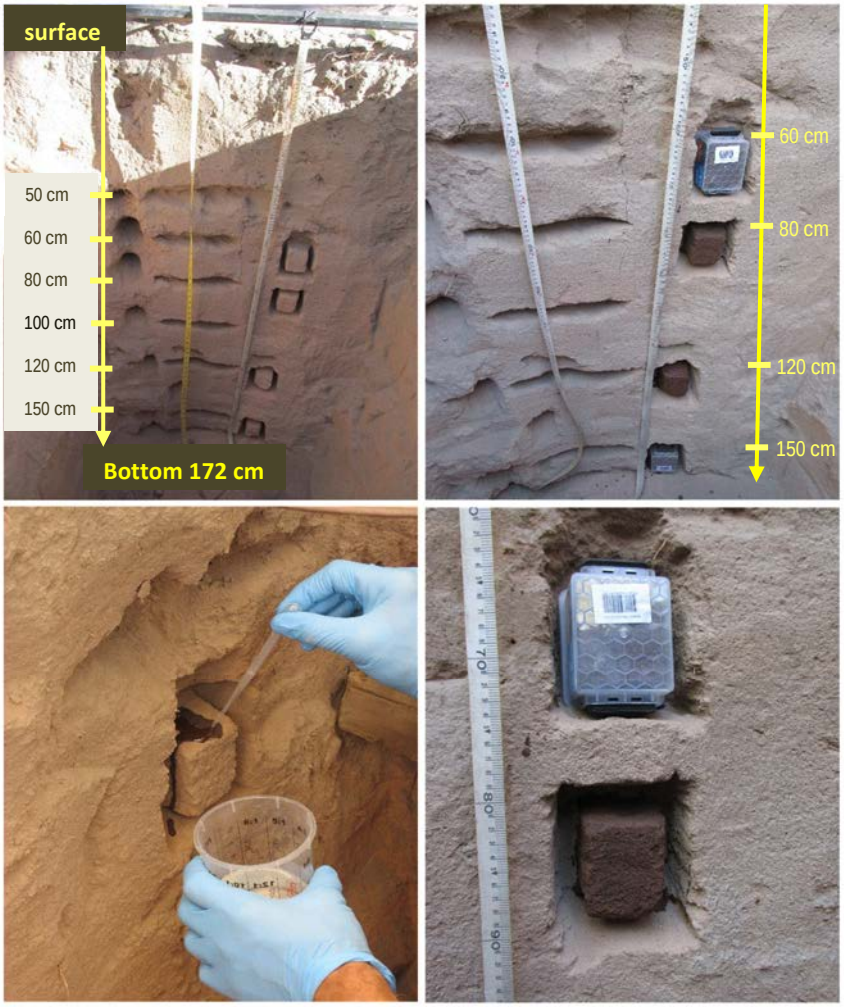

Figure F1.14: Rapid on-site method used in pit PA_10-M Outside GS1 for sediment optical microscopic petrographic analysis.

1.2.1.3 Sample collection for cosmogenic nuclide ^{10}Be measurements

Outside GS1 only, three rock samples, ~2–3 cm thick, were collected for cosmogenic nuclide denudation rate measurements to obtain information about the general ground lowering rate at the site. Two samples were cut from the bedrock at the bottom of the two pits:

1) bedrock from pit PA_10-M, at depth ~170 cm: PA_10-M-BR,

2) bedrock from pit C_1-CR, at depth ~85 cm: C_1-CR-BR

and one rock sample was cut from the exposed surface rock:

3) surface sample: GS1-SR.

Shielding effects on cosmogenic dose rates were calculated online via CRONUS-Earth using azimuths measured in the field with a standard compass.

The sampling locations are shown in Figure F1.11, sample details are given in Table T1.1 and the sampling procedure is shown in Figure F1.15.

Figure F1.15: Sample collection for cosmogenic denudation rate measurements. a-b) bedrock in pit PA_10-M-BR (depth ~170 cm), c-d) exposed surface rock GS1-SR, e,f) bedrock pit C_1-CR-BR (depth ~85 cm).

Table T1.1 Sample Catalogue

Sample ID	Sampling site	Sampling method	Depth (cm)	Distance from GS1 dripline (m)	Sample form	Particle size (µm) D_{50}	D_{10}	$D_{[4,3]}$	Colour Munsell Chart
PA_1-M	GS1 site	auger	10	68	bulk	241	71.8	245	10YR 5/2 (greyish brown)
PA_2-M	GS1 site	auger	25	73	bulk	266	64	271	10YR 5/2 (greyish brown)
PA_3-M	GS1 site	auger	50-60	45	bulk	235	37.2	239	10YR 5/2 (greyish brown)
PA_4-M	GS1 site	auger	30-37	52	bulk	234	56.4	239	10YR 5/2 (greyish brown)
PA_5-M	GS1 site	auger	15	37	bulk	244	93.3	252	10YR 5/2 (greyish brown)
PA_6-M	GS1 site	auger	50-60	37	bulk	270	12.7	267	10YR 6/3 (pale brown)
PA_7-M	GS1 site	auger	55-65	32	bulk	243	66.1	246	10YR 6/3 (pale brown)
PA_8-M	GS1 site	auger	122-140	29	bulk	236	51.5	240	10YR 6/6 (reddish yellow)
PA_9-M	GS1 site	auger	150-160	22	bulk	224	2.38	218	7.5YR 7/3 (pink)
PA_10-M 42	GS1 site	pit PA_10-M	42-43	19	bulk	237	49.8	242	10YR 5/3 (brown)
PA_10-M 50	GS1 site	pit PA_10-M	50-52	"	bulk	223	28.9	224	10YR 5/3 (brown)
PA_10-M 60	GS1 site	pit PA_10-M	60-65	"	bulk	245	48.1	249	10YR 5/4 (yellowish brown)
PA_10-M 65	GS1 site	pit PA_10-M	65-67	"	bulk	266	55.4	269	10YR 5/4 (yellowish brown)
PA_10-M 80	GS1 site	pit PA_10-M	80-82	"	bulk	244	74.3	249	7.5YR 6/4 (light brown)
PA_10-M 100	GS1 site	pit PA_10-M	100-105	"	bulk / core	242	74.8	247	7.5YR 6/6 (reddish yellow)
PA_10-M 102	GS1 site	pit PA_10-M	100-102	"	bulk	235	4.38	230	7.5YR 6/6 (reddish yellow)
PA_10-M 120	GS1 site	pit PA_10-M	120-122	"	bulk	264	34	266	7.5YR 6/6 (reddish yellow)
PA_10-M 150	GS1 site	pit PA_10-M	150-152	"	bulk	264	38.1	266	7.5YR 6/6 (reddish yellow)
PA_10-M 160	GS1 site	pit PA_10-M	160-162	"	bulk	232	24.3	233	7.5YR 6/6 (reddish yellow)
PA_10-M 172	GS1 site	pit PA_10-M	168-172	"	bulk	276	11	275	7.5YR 6/4 (light brown)
PA_11-M 60	GS1 site	auger	60 ±5	25	bulk	275	99.3	281	10YR 5/3 (brown)
PA_11-M 140	GS1 site	auger	140-160	"	bulk	232	71.2	237	7.5YR 6/4 (light brown)
TP01 0	GS1 site	pit TP01	0	10	bulk	264	109	274	10YR 5/2 (greyish brown)
TP01 40	GS1 site	pit TP01	40	"	bulk	261	84.2	267	10YR 5/2 (greyish brown)
TP01 60	GS1 site	pit TP01	60	"	bulk	220	7.17	218	10YR 5/3 (brown)
TP01 80	GS1 site	pit TP01	80	"	bulk	253	48	255	10YR 6/3 (pale brown)
TP01 120	GS1 site	pit TP01	120	"	bulk	241	4.99	237	7.5YR 6/3 (light brown)
TP02 20	GS1 site	pit TP02	20	20	bulk	255	86.5	261	10YR 5/2 (greyish brown)
TP02 40	GS1 site	pit TP02	40	"	bulk	263	71.3	266	10YR 5/2 (greyish brown)
TP02 60	GS1 site	pit TP02	60	"	bulk	256	65.6	260	10YR 5/3 (brown)
TP02 100	GS1 site	pit TP02	100	"	bulk	262	128	266	10YR 6/4 (light yellowish brown)
TP02 120	GS1 site	pit TP02	120	"	bulk	267	86.6	271	7.5YR 6/4 (light brown)
TP03 60	GS1 site	pit TP03	60	30	bulk	218	30.3	220	10YR 6/2 (light brownish grey)
TP03 120	GS1 site	pit TP03	120	"	bulk	202	2.25	201	7.5YR 7/3 (pink)
TP04 20	GS1 site	pit TP04	20	40	bulk	241	68.8	246	10YR 5/2 (greyish brown)
TP04 80	GS1 site	pit TP04	80	"	bulk	257	115	263	10YR 6/3 (pale brown)
TP05 0	GS1 site	pit TP05	0	50	bulk	252	58.3	257	10YR 6/2 (light brownish grey)
TP05 40	GS1 site	pit TP05	40	"	bulk	241	29.6	241	10YR 5/3 (brown)
TP05 60	GS1 site	pit TP05	60	"	bulk	224	26	224	10YR 6/3 (pale brown)
TP05 80	GS1 site	pit TP05	80	"	bulk	253	97.8	257	10YR 6/3 (pale brown)
TP05 100	GS1 site	pit TP05	100	"	bulk	249	20.9	248	10YR 7/3 (very pale brown)
TP05 120	GS1 site	pit TP05	120	"	bulk	263	47	264	10YR 7/3 (very pale brown)
C_1-CR 100	GS1 site	pit C_1-CR	100	68	bulk / core	261	58.3	264	10YR 6/4 (light yellowish brown)
C_1-CR 135	GS1 site	pit C_1-CR	135	"	bulk / core	253	44.7	256	10YR 7/3 (very pale brown)
C_1-CR 200	GS1 site	core C_1-CR	200	"	bulk / core	241	35.9	241	10YR 7/3 (very pale brown)
RT_1-CR	Norman River site	profile	unit A	NA	bulk	227	23.2	253	7.5YR 5/8 (strong brown)
RT_3-CR	Norman River site	profile	unit B	NA	hard sample	NA	NA	NA	7.5YR 5/6 (strong brown)
RT_2-CR	Norman River site	profile	unit C	NA	hard sample	NA	NA	NA	10YR 8/1 (white to light grey)
RT_4-CR	Norman River site	profile	unit D	NA	bulk	156	10.7	200	10YR 8/3 (very pale brown)

Sample ID (additional samples)	Depth (cm)
Petrography sediment samples	
PA_10-M 1	64-71.8
PA_10-M 2	82.8-90.8
PA_10-M 3	124-130.4
PA_10-M 4	153.2-161
RT_2-CR	NA
RT_3-CR	NA
Petrography rock samples	
GS1-SR	surface
PA_2-M-BR (bedrock)	25
PA_10-M-BR (pit bedrock)	170
^{10}Be Cosmogenic analysis	
GS1-SR	surface
PA_10-M-BR (pit bedrock)	170
C_1-CR-BR (pit bedrock)	85
purple samples were collected by Zega's team	
blue samples were collected by Walli's team	

1.2.2 Sedimentology analysis

1.2.2.1 Colour and particle size

Sediment colour was determined using Munsell soil colour charts (1994) on dry, untreated sediment samples. Particle size analysis was carried out using a laser diffraction particle sizing technique on a Malvern Mastersizer MS3000 analyser in the Earth and Environmental Sciences Laboratory facility at James Cook University, Townsville, QLD, Australia. Laser diffraction measures particle size distributions by measuring the angular variation in the intensity of light scattered as a laser beam passes through a dispersed particulate sample. Large particles scatter light at small angles relative to the laser beam and small particles scatter light at large angles. The angular scattering intensity data is then analysed to calculate the size of the particles responsible for creating the scattering pattern, using the Mie theory of light scattering. Due to machine requirements, the samples were first dry sieved using an 850 µm sieve. We applied the wet dispersion approach and water as a dispersant. The particle size is reported as a volume equivalent sphere diameter.

1.2.2.2 Petrographic analysis

Four block samples of impregnated sediment from the pit PA_10-M and two samples of Norman River B and C units were wrapped in bubble wrap, placed to sit tight in plastic boxes and sent to VanPetro, Vancouver Petrographics, Canada for thin section preparation. Petrographic analysis of the thin sections was carried out using a Motic petrographic microscope under transmitted and polarized light, following the classification and description of Pettijohn, Potter & Siever (2012) and Folk (1980). Images of the microscopic sections were taken using a Cannon 600D DSLR camera.

1.2.2.3 Cosmogenic nuclide methods

1.2.2.3.1 General principles

Cosmogenic nuclide methods can provide direct, quantitative information about the exposure, burial and denudation of the earth's surface. Cosmogenic nuclide methods rely on the measurement of minute amounts of cosmogenic nuclides in a wide variety of natural samples, such as surface rocks, sediments, ice, rain, ocean water and meteorites. Cosmogenic nuclides form when surface rocks are exposed to the open sky and therefore cosmic radiation. High-energy cosmic radiation, mostly protons born in supernovae, enter the Earth's atmosphere and trigger a cascade of particle reactions. These reactions create secondary cosmic rays, predominantly neutrons and muons, that impact the Earth's surface. The collisions between these particles and target atoms, such as oxygen, silicon, potassium, calcium and iron, in near-surface minerals of exposed rocks, cause these atoms to fragment (a process known as spallation), resulting in the creation of new nuclides – terrestrial cosmogenic nuclides (Lowe

and Walker, 2015, Schaefer et al., 2022). These accumulate in the exposed surface of rocks and their abundance is directly related to the time of rock exposure to cosmic ray activity (Figure F1.16). Hence, the measurement of the concentration of cosmogenic nuclides in rock surface samples can provide an estimate of the time of exposure of that surface. This is the basis of cosmogenic nuclide dating, also known as terrestrial in-situ cosmogenic nuclide dating or surface exposure dating. The technique description varies according to the cosmogenic nuclides that are measured and the location of the sample used for dating (details in: Gosse and Klein, 2020)

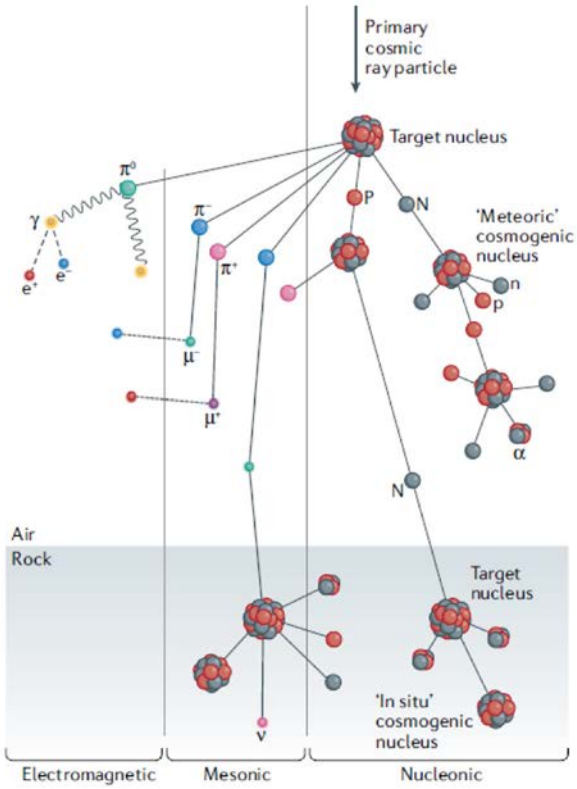

Figure F1.16: Cosmogenic nuclide formation in surface rocks due to cosmic radiation, from Schaefer et al. (2022).

The Earth is constantly bombarded by cosmic rays, however, cosmogenic nuclide production is not the same nor constant across the Earth's surface. In traversing the atmosphere, the flux of secondary particles steadily decreases when approaching the Earth's surface, resulting in nuclide production rates in surface rocks being lower at lower altitudes (Ivy-Ochs and Kober, 2008). In other words, the cosmic ray flux decreases at lower altitude as air pressure and the shielding effect of the atmosphere increase (Stone, 2000). Moreover, most cosmic ray particles are deflected by the Earth's magnetic field. Only the highest-energy cosmic rays can penetrate the atmosphere and eventually reach the surface. These particles encounter the greatest resistance when travelling perpendicular to

the field and penetrate most easily when travelling in the same direction. As a consequence, cosmic ray intensity and cosmogenic nuclide production are highest at the poles and decrease toward the equator (Gosse and Phillips, 2001, Ivy-Ochs and Kober, 2008). Production rates at sea level at the equator are about half what they are at the poles (Ivy-Ochs and Kober, 2008). Additionally, as the Earth's magnetic field waxes and wanes in strength over time, the amount of cosmic radiation entering the atmosphere and reaching the surface also rises and falls. Therefore, the cosmogenic nuclide production rates vary on Earth spatially and temporally owing to variations in the geomagnetic field and atmospheric shielding, which results in a temporally varying dependence on latitude and altitude.

Calculating cosmogenic nuclide production rates at a sample site requires: (i) a scaling function that describes the variation of the production rate with time, location and elevation, and (ii) a reference production rate at a particular time and place. Several physical models have been presented for the scaling of production rates (see discussion in Balco et al., 2008). For example, in their latest review, Schaefer et al. (2022) use the latitude and altitude scaling factors based on Lifton-Sato-Dunai (LSD) (Lifton et al., 2014) and Lal/Stone (Stone, 2000). In any case, it is crucial to use the same scaling formalities used for calculating the original production rate for all other calculations as well.

In surface rocks, only certain minerals are suitable to measure cosmogenic nuclides, such as quartz for ^{10}Be, ^{26}Al, ^{14}C and ^{21}Ne, pyroxene and olivine for ^{3}He and ^{21}Ne, and feldspar and pyroxene for ^{36}Cl. These minerals are ubiquitous in the Earth's surface rocks, allowing for widespread application of cosmogenic nuclide techniques. The rates of production of cosmogenic nuclides are relatively well known (Balco, 2020a, Gosse and Phillips, 2001, Ivy-Ochs and Kober, 2008, Ivy-Ochs et al., 1997), as are the half-lives of the radioactive isotopes (^{10}Be, ^{26}Al, ^{14}C, ^{36}Cl). Thus, by measuring the concentration of cosmogenic nuclides in rock samples and accounting for production rate and half-lives, an estimate of exposure age, time of burial and erosion or denudation rate can be obtained, depending on the sample context.

1.2.2.3.2 Cosmogenic nuclide surface exposure and denudation rate evaluation

Cosmogenic nuclides can be particularly useful in the quantitative evaluation of the rate of erosion or denudation (Bierman and Caffee, 2002, Cockburn and Summerfield, 2004, Lal, 1991, Von Blanckenburg, 2005). In this study, we use the denudation rate to evaluate the loss of material from a surface, which includes both physical erosion and chemical weathering (solution loss). Denudation rates can be calculated from measurements of in situ-produced cosmogenic nuclides. The key to quantifying denudation rates using surface concentrations of cosmogenic nuclides is the changes in production rate with depth, since denudation involves progressively bringing up to the surface rock that was previously buried (Cockburn and Summerfield, 2004). This is possible under the assumption

that denudation is steady and that denudation has been taking place for an extended period compared to a denudation time scale (e.g. Cockburn and Summerfield, 2004, Darvill, 2013, Schaefer et al., 2022).

In a continuously eroding rock outcrop after a long period, the production of nuclides will equal the removal of nuclides at the surface by denudation. Hence, the surface nuclide concentration of an eroding bedrock is inversely proportional to the denudation rate, as a result of constant production, losses by denudation and radioactive decay (in the case of radioactive nuclides) (Cockburn and Summerfield, 2004, Von Blanckenburg, 2005). Under these circumstances, a measured surface concentration of cosmogenic nuclides in an eroding rock outcrop can be accurately modelled (e.g. Lal, 1991, Nishiizumi et al., 1986) and has been used to establish site-specific denudation rates in different geomorphic contexts (see: Cockburn and Summerfield, 2004, Table 3, pg. 22). The calculated rates represent total denudation, which includes both physical erosion and solution loss.

Routine measurement of cosmogenic nuclides, as well as their use for determination of exposure histories and denudation rates, became possible after the development of accelerator mass spectrometry (AMS) and noble gas mass spectrometry between 1970 and 1980 and as of very recently, atom trap trace analysis (ATTA) (Schaefer et al., 2022). These technical developments enabled the measurement of exceedingly low nuclide concentrations. To measure cosmogenic nuclide abundance in surface rocks, high-purity mineral separates must be produced from the whole rock, ranging from tens of milligrams to 50-100 g in mass (Schaefer et al., 2022). In this study, we used ^{10}Be concentrations for denudation rate evaluation, with ^{26}Al also measured as a control. ^{10}Be and ^{26}Al are the two most widely used radioactive isotopes in cosmogenic dating and quartz remains the most commonly used mineral for ^{10}Be and ^{26}Al analyses as both isotopes can be extracted by dissolving a single quartz mineral separate from a rock or sediment sample (Ivy-Ochs and Kober, 2008, Schaefer et al., 2022).

- *Sample preparation and measurement of cosmogenic nuclides ^{10}Be and ^{26}Al*

Rock samples collected for cosmogenic nuclide ^{10}Be and ^{26}Al measurements Outside GS1 were prepared and analysed at the University of Wollongong and the Department of Nuclear Physics and Accelerator Applications, The Australian National University, Canberra.

Rock samples were first crushed and sieved and then sent to the University of Wollongong for further sample preparation involving quartz purification, carrier addition and complete sample dissolution in hydrofluoric acid (HF), isolation of Be and Al using column chromatography, and conversion to Be and Al oxides ready for accelerator mass spectrometry (AMS) (Figure F1.17). The 250-500 µm fraction was purified to clean quartz by a combination of magnetic separation, froth flotation, and chemical leaching with dilute HF (to remove meteoric Be). Purity was checked by

measuring Al concentration by Inductively Coupled Plasma Optical Emission Spectroscopy (ICP-OES), where values <200 ppm indicate sufficient purity.

^{9}Be and ^{27}Al carriers were added and a weighed amount of purified quartz dissolved in concentrated hot HF. This study used 30 g of purified quartz from the surface bedrock sample and 60 g for the two bedrock samples. An aliquot of this solution was taken for 'definitive' ^{27}Al measurement by ICP-OES. Measured concentrations were 80 -100 ppm. Be and Al were extracted by separation on an ion-exchange column, precipitated as $Be(OH)_2$ and $Al(OH)_3$, then fired at 850°C to convert to oxides BeO and Al_2O_3.

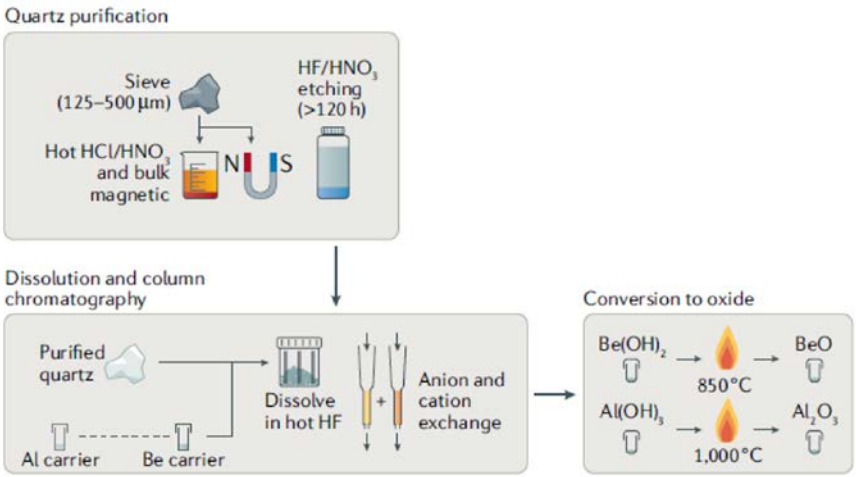

Figure F1.17: Sample preparation protocol for in-situ produced ^{10}Be and ^{26}Al cosmogenic nuclide analysis, simplified. Prior to complete HF dissolution, the sample may undergo sequential leaching steps to separate various Be fractions (adapted from Schaefer et al., 2022, pg. 5). For a more detailed step by step procedure see Corbett et al. (2016b, pg. 26).

At this stage samples were sent to ANU for measurement. BeO was mixed with Nb (~1:4) and pressed into stainless steel sample holders. Al_2O_3 was mixed with silver (~1:2) and pressed into copper sample holders. ^{10}Be/^{9}Be ratios were measured by AMS using the 14UD Pelletron accelerator, as follows:

a. BeO^- negative ions were extracted from the ion source. Typical beam currents are 3-5 µA.
b. Injected into the accelerator operating at 8 MV.
c. The molecular ions are dissociated in a gas stripper canal in the terminal, using nitrogen gas, which also removes electrons from the Be atoms.
d. With $^{10}BeO^-$ ions injected, 27 MeV $^{10}Be^{3+}$ ions are selected after the second stage of acceleration. ^{10}Be ions are counted in a gas ionization detector after a gas-filled magnet (using Ar gas). This very effectively removes interfering ^{10}B ions.

e. Periodically, the $^{9}BeO^{-}$ beam is injected and the beam current of $^{9}Be^{3+}$ ions is measured in an off-axis Faraday cup after the high-energy analysing magnet.

Measured $^{10}Be/^{9}Be$ ratios were normalized relative to the NIST standard, assumed $2.79x10^{-11}$.

Similarly, $^{26}Al/^{27}Al$ ratios were measured by AMS using the 14UD Pelletron accelerator at the ANU, as follows:

a. AlO^{-} negative ions extracted from the ion source. Typical beam currents are 3-5 μA.
b. Injected into accelerator operating at 13.5 MV.
c. The molecular ions are dissociated in a gas stripper canal in the terminal using nitrogen gas, which also removes electrons from the Al atoms.
d. With $^{26}AlO^{-}$ ions injected, 103 MeV $^{26}Al^{7+}$ ions are selected after the second stage of acceleration. ^{26}Al ions are counted in a gas ionization detector after a gas-filled magnet (using N_2 gas). This effectively removes most of the interfering ^{26}Mg ions and the detector discriminates against the residual ^{26}Mg ions.
e. Periodically, the $^{27}AlO^{-}$ beam is injected and the beam current of $^{27}Al^{7+}$ ions is measured in an off-axis Faraday cup after the high-energy analysing magnet.

Finally, the results were processed using the online University of Washington cosmogenic isotope calculator CRONUS-Earth (https://hess.ess.washington.edu/) to calculate the denudation rates.

1.3 Results

1.3.1. Geomorphology, drone imagery and digital elevation model (DEM)

Field survey, drone imagery and elevation modelling revealed that the landscape is strongly governed by varying erosional, depositional and weathering features. Dissected and strongly weathered residual outcrops and scarps of Jurassic Hampstead sandstone are patchily covered by accumulated sediments. Escarpments and collapsed slopes fringe the expanding sand plains against the upland areas. Plane surfaces of exposed smooth bedrock appear in stretches on the west and northwest side of the GS1 outcrop and on the southern fringe of the sediment deposit Outside GS1 (Figure F1.18). Outcrops of the Loth Formation, which overlies the Hampstead sandstone, were not observed in the study area. Drone imagery and the constructed DEM with recorded geomorphic elements Outside GS1 are shown in Figure F1.18.

At the Norman River site, the field survey, inspection of the satellite imagery and geological map showed a distinct wide channel structure (P) located next to the current river channel on the north

side (Figure F1.19). A tributary channel structure (T) joining the Norman River from the north was also noted and inspected (Figure F1.19). The two-channel structures (P and T) showed no signs of active water flow, channel incision, flooding or visible connection with the contemporary Norman River channel. We therefore presume that the channel structure (P) is a paleochannel of the Norman River and the tributary (T) is a former Norman River tributary.

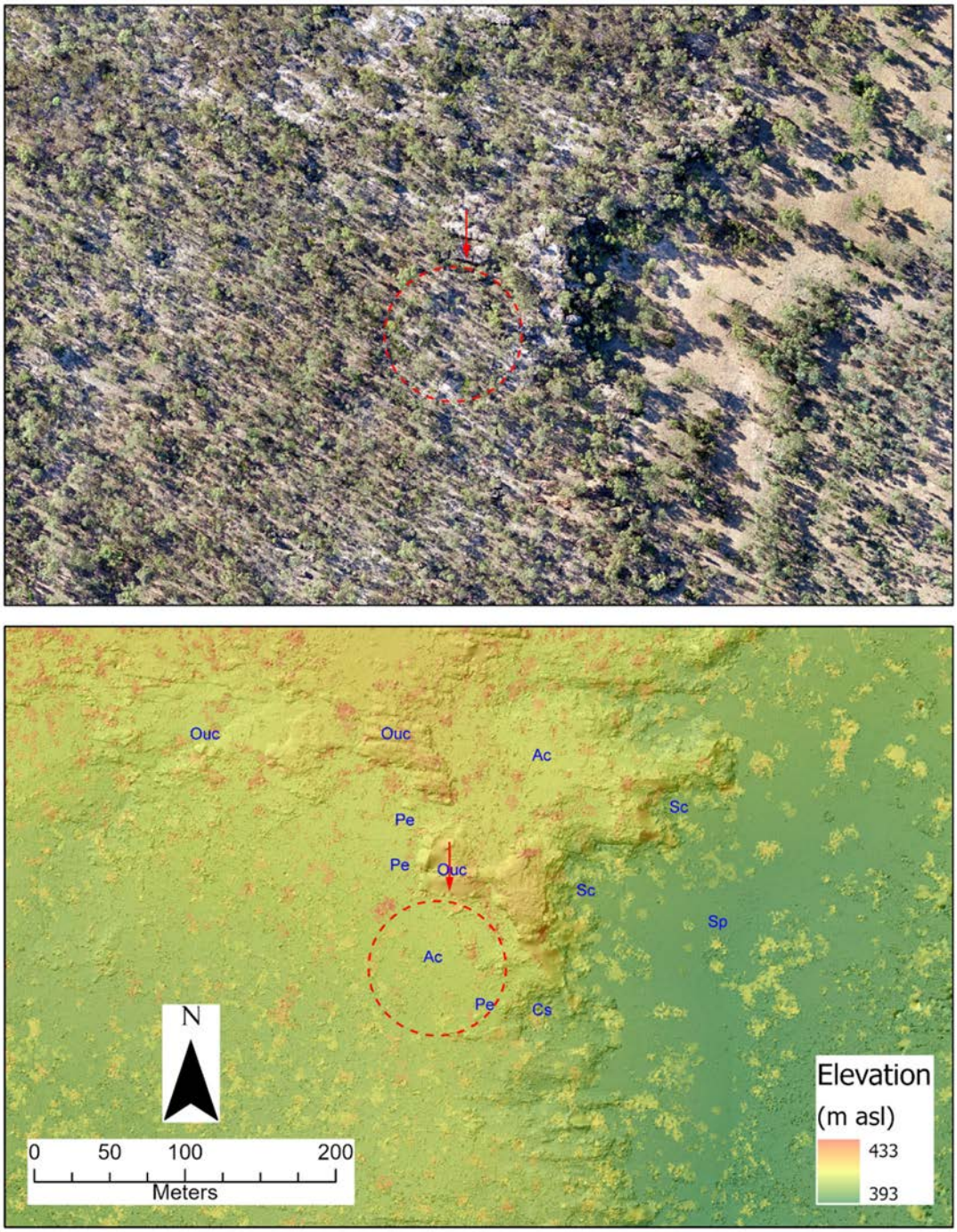

Figure F1.18: Upper: drone image of the study area. Red arrow points to the GS1 dripline, red dashed circle marks the Outside GS1 sediment deposits. **Bottom:** DEM constructed from the upper drone image. Ac-accumulated sediment, Cs-collapsed slope, Ouc-outcrop, Pe-plane bedrock exposures, Sc-scarp, Sp-sand plain.

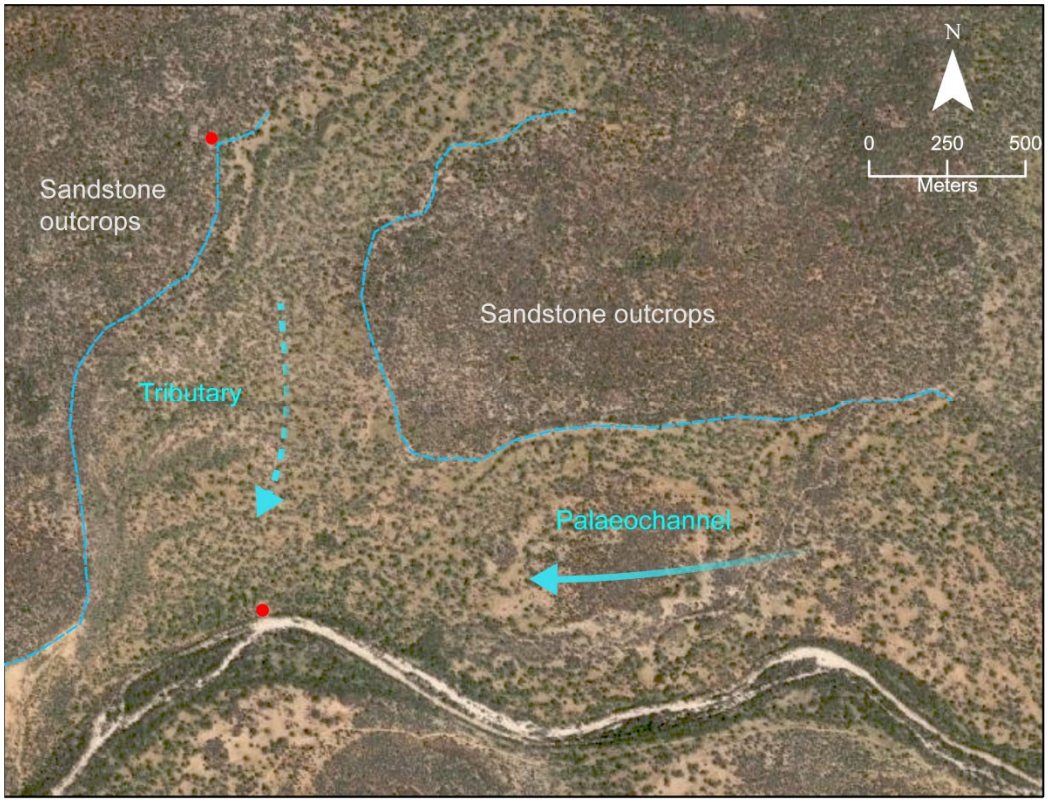

Figure F1.19: A view of the Norman River. The palaeochannel and the tributary channel are marked along with the areas of sandstone outcrops. Two red dots mark the two sampling sites at this study, the Outside GS1 on north and the Norman River site to the south.

1.3.2 Stratigraphy and sedimentology Outside GS1

1.3.2.1 Pit PA_10-M stratigraphy

Pit PA_10-M was located 19 m southwest of the GS1 dripline (Figure F1.11). The maximum pit depth was 172 cm. The measured depth ranged from 172–162 cm because the bedrock at the pit bottom was dipping towards the northeast, in the direction of GS1, at an angle of 3–4°. The excavated pit faces were south, east, west and north (henceforth called pit profiles). The exposed profiles were homogeneous, without any visible changes in stratigraphy. No palaeosols or silcretes were noted. There was, however, a gradual change in the colour of the sediment, from greyish and greyish brown in the upper 40 cm to pale brown, pinkish or pale orange below 65 cm (Figure F1.20b).

Evidence of post-depositional disturbance in the form of circular and ellipsoidal structures with crust rims was documented in the south profile (Figure F1.20a). Also, a line of rocks was recorded at a depth of 100–115 cm in three profiles (east, south and west), (Figure F1.20b). The single rocks were from ~2–10 cm long.

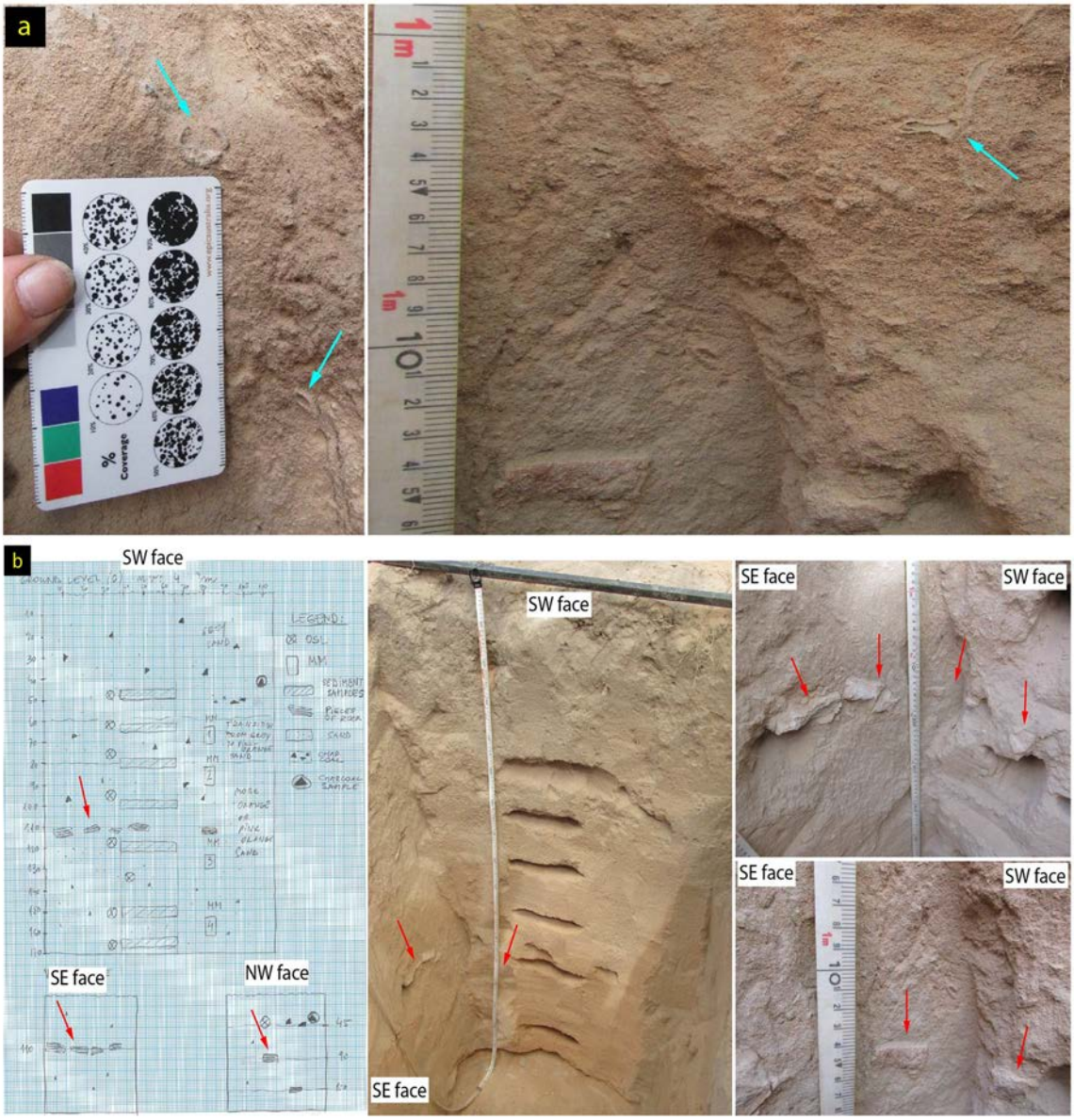

Figure F1.20: Profiles in pit PA_10-M. **a:** Post-deposition disturbance, light blue arrows point to noticed structures; **b:** Left: fieldwork sketch of the pit profiles. Middle and right: line of rocks recorded in south (S), southeast (SE) and northwest (NW) profile, red arrows pointing to single rocks. Note: the gradual change from greyish to pale brighter brown and pale orange in sediment colour with depth on the middle image.

1.3.2.2 Pit C_1-CR stratigraphy

Pit C_1-CR was located the furthest away, 65 m, from the GS1 dripline (Figure F1.11). No stratigraphy was apparent in the pit, apart from a gradual change in sediment colour. At the beginning of the excavation, the depth to the pit bedrock was 85 cm, but after the bottom of the pit was enlarged, a parallel opening appeared in the bedrock, approximately 22 cm wide (Figure F1.21). During a subsequent coring into the opening, a depth of 220 cm was reached.

Figure F1.21: A parallel opening in the bedrock in the pit C_1-CR. The opening is approximately 22 cm wide and 65 cm long.

1.3.2.3 Sediment colour

Munsell colour results are given in Table T1.1. They are consistent in both the pits and auger samples. The sediments are generally darker, greyish brown (10YR 5/2), from the surface to 40 cm depth. At depths 40–80 cm they gradually change to a lighter colour, either pale brown (10YR 6/3), brown (10YR 5/3) or yellowish brown (10YR 5/4). At depths below 100 cm, the colour changes gradually again, hues vary between reddish yellow (7.5YR 6/6), light brown (7.5YR 6/4, 6/3), light yellowish brown (10YR 6/4), very pale brown (10YR 7/3) and pink (7.5YR 7/3).

1.3.2.4 Particle size distribution

Fine (62.5−250 µm) and medium (250−500 µm) sand-sized particles are the dominant fractions in all analysed sediment samples, constituting 80−90% of the total. The median grain size Dx (50) ranges from 202 to 276 µm and the mean grain size D [4,3] (volume mean diameter) ranges from 201 to 281 µm. Clay (<3.9 µm) and silt (3.9−62.5 µm) particles make up to 15% of the samples, except for a few samples where they reached 20% (Table T1.1). Coarse sand (500−1000 µm) accounts for less than 6%. Apart from some minor trends in particle distribution patterns, such as a lower proportion of clay particles is generally detected in samples from shallow depths (0–20 cm), no obvious trends were observed in any fraction, either in relation to sample depth or sample distance from the GS1 dripline.

The grain size distribution results (D_{50}, D_{10}, $D_{[4,3]}$) of bulk sediment samples are given in Table T1.1. The particle size results for samples Outside GS1 are presented in Figure F1.22 in pie charts per fraction. Additionally, a few selected results are also shown in size distribution graphs in Figure F1.23, as provided by Mastersizer 3000 software.

A

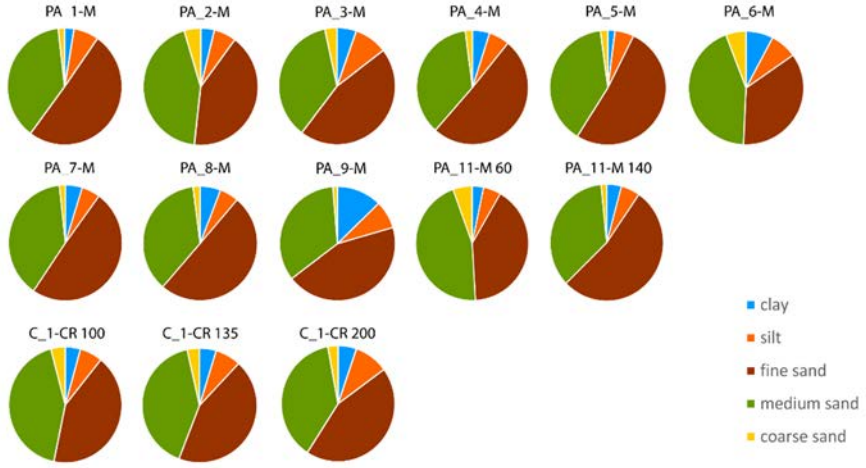

Particle size	PA_1-M	PA_2-M	PA_3-M	PA_4-M	PA_5-M	PA_6-M	PA_7-M	PA_8-M	PA_9-M	PA_11-M 60	PA_11-M 140
clay	2.64%	3.87%	5.37%	4.97%	1.95%	7.65%	4.79%	5.82%	12.57%	3.25%	4.21%
silt	7.06%	6.27%	9.16%	5.94%	5.30%	7.53%	5.25%	5.36%	7.85%	5.05%	5.40%
fine sand	50.48%	41.64%	45.81%	50.63%	51.57%	35.52%	49.43%	50.12%	44.10%	40.76%	53.14%
medium sand	37.99%	43.58%	36.28%	36.40%	39.08%	43.60%	38.83%	36.72%	34.20%	45.44%	35.65%
coarse sand	1.83%	4.64%	3.38%	2.06%	2.10%	5.70%	1.70%	1.98%	1.28%	5.50%	1.60%

C_1-CR 100	C_1-CR 135	C_1-CR 200
4.33%	4.70%	5.25%
6.47%	7.21%	9.71%
42.45%	43.93%	44.15%
42.62%	40.68%	37.99%
4.13%	3.48%	2.90%

B

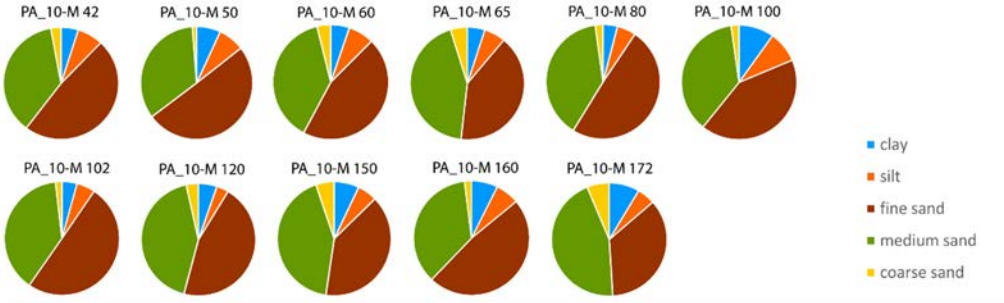

Particle size	PA_10-M 42	PA_10-M 50	PA_10-M 60	PA_10-M 65	PA_10-M 80	PA_10-M 100	PA_10-M 102	PA_10-M 120	PA_10-M 150	PA_10-M 160	PA_10-M 172
clay	4.85%	6.91%	5.23%	4.99%	4.06%	4.25%	9.83%	5.22%	7.07%	7.32%	8.50%
silt	7.25%	7.54%	7.17%	6.03%	5.35%	5.20%	8.81%	3.42%	5.61%	6.64%	5.05%
fine sand	48.20%	50.32%	45.37%	40.75%	49.38%	50.15%	42.11%	45.46%	39.68%	48.14%	35.45%
medium sand	36.85%	33.98%	38.39%	43.45%	38.98%	38.60%	37.00%	42.45%	42.42%	35.94%	44.75%
coarse sand	2.85%	1.25%	3.84%	4.78%	2.23%	1.80%	2.25%	3.45%	5.22%	1.96%	6.25%

C

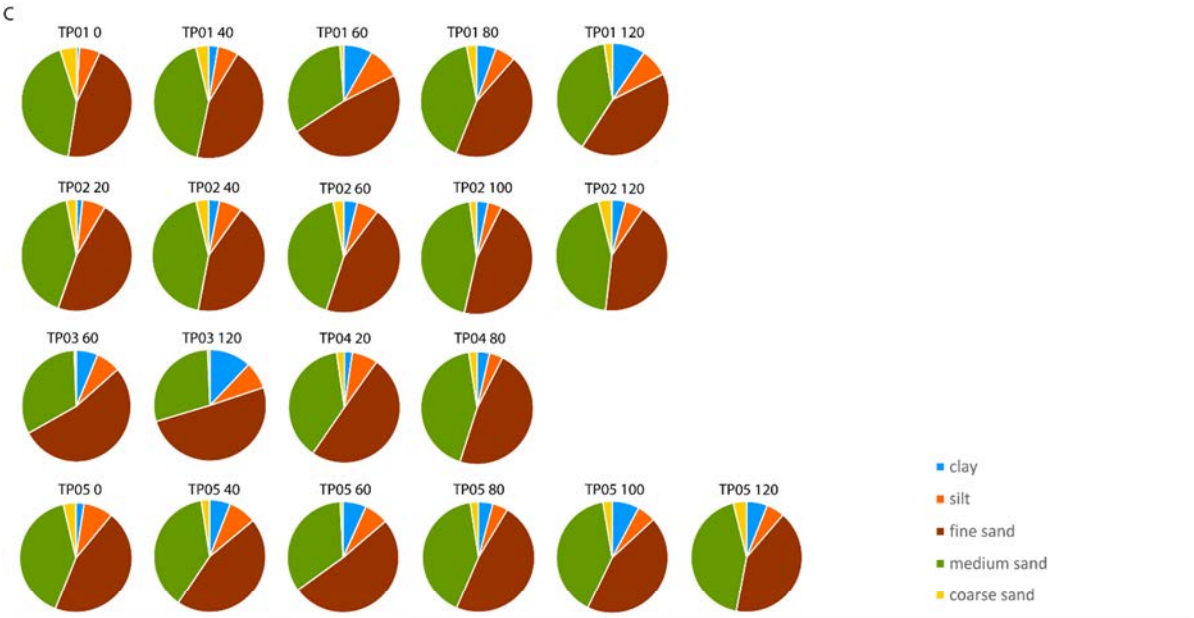

Particle size	TP01 0	TP01 40	TP01 60	TP01 80	TP01 120	TP02 20	TP02 40	TP02 60	TP02 100	TP02 120
clay	0.80%	2.74%	8.25%	5.59%	9.40%	1.71%	3.11%	3.88%	3.27%	4.01%
silt	6.10%	6.04%	9.20%	5.82%	8.18%	6.77%	6.57%	6.22%	4.05%	5.31%
fine sand	45.53%	44.62%	48.30%	44.64%	41.55%	46.93%	43.28%	44.88%	46.22%	42.47%
medium sand	42.73%	42.85%	33.10%	41.06%	38.42%	41.63%	43.45%	42.00%	44.44%	44.36%
coarse sand	4.84%	3.75%	1.15%	2.89%	2.45%	2.96%	3.59%	3.02%	2.02%	3.85%

Particle size	TP03 60	TP03 120	TP04 20	TP04 80	TP05 0	TP05 40	TP05 60	TP05 80	TP05 100	TP05 120
clay	6.38%	11.97%	2.31%	3.56%	2.35%	5.98%	6.75%	4.13%	7.85%	6.06%
silt	7.22%	7.85%	7.47%	3.89%	8.50%	8.07%	7.01%	4.44%	5.37%	5.26%
fine sand	53.38%	50.50%	49.76%	47.48%	45.11%	45.45%	51.30%	47.81%	44.00%	41.65%
medium sand	32.38%	28.98%	38.21%	42.69%	40.44%	38.04%	34.14%	41.27%	40.07%	43.15%
coarse sand	0.64%	0.70%	2.25%	2.38%	3.60%	2.46%	0.80%	2.35%	2.71%	3.88%

Figure F1.22: Particle size distributions of sediment samples Outside GS1 in pie charts, numbers are also given under the graphics. **A**: Particle size distribution in auger holes and pit C_1-CR, **B:** Particle size distribution in pit PA_10-M, **C:** Particle size distribution in test pits TP01−TP05.

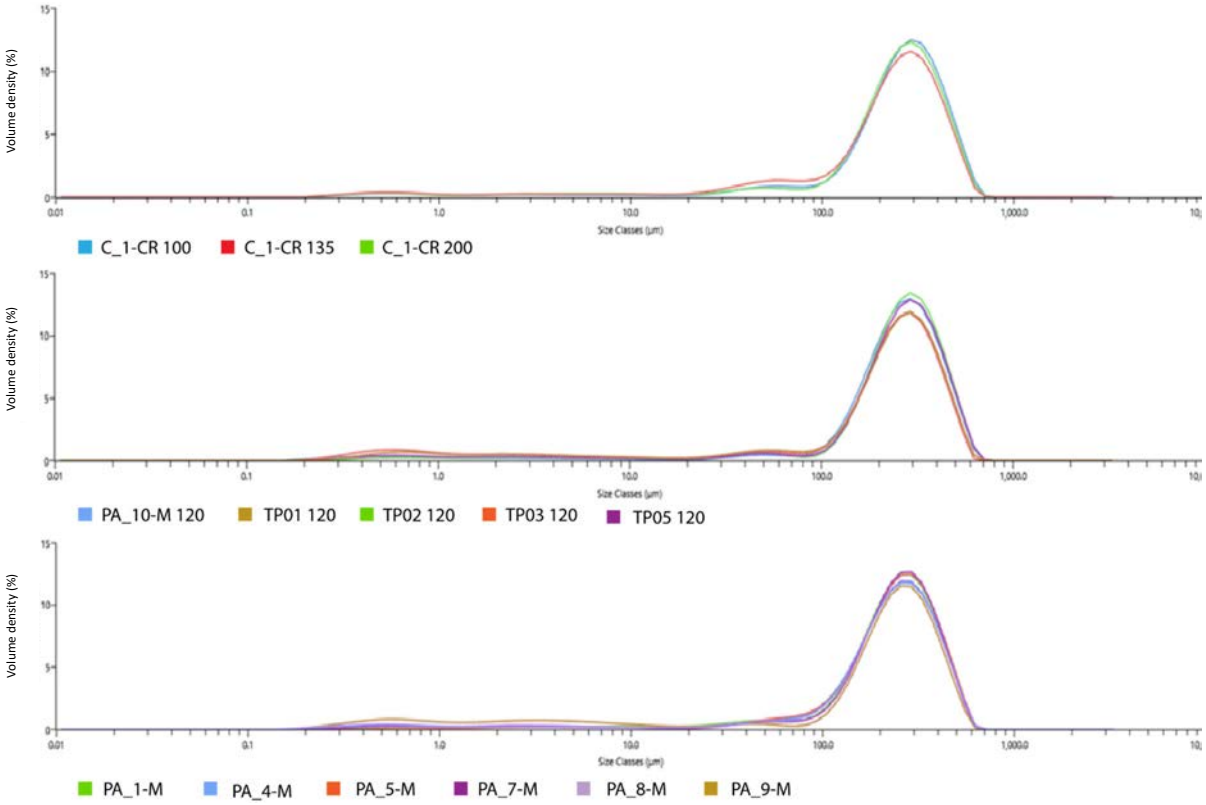

Figure F1.23: The selected grain size distribution graphs; Size Classes µm 0.01−10,000 are shown on the x-axis and the Volume density (%) of particle sizes on the y-axis

1.3.2.5 Petrography, optical microscopy

- *Sediment samples*

Mineral grains in the four sedimentary petrographic thin sections are typically sub-angular to sub-rounded, subordinately angular and rounded, and moderately sorted. They range in size from coarse to fine sand (the largest is 3.25 mm, most grains are size <0.4 mm). The samples are texturally sub-mature. Petrography results are given in Table T1.2. Figure F1.24 shows the sampling profile and the microscopic texture of the samples.

Quartz is the dominant mineral (~80%) across all samples but is most abundant in the thin sections from the upper part of the profile. Feldspars are of minor abundance, occurring as K-feldspar and rarely plagioclase grains. Lithic fragments are sparse and composed of chert, quartzite, sandstone and siltstone. The matrix typically consists of silt- and clay-sized materials, present in all samples in low abundances (<15%) (Figure F1. 25a). Iron oxides at moderate abundance occur in the matrix. In sample PA_10-M 3, collected at a depth of 124−130.4 cm, authigenic clays (pseudomatrix) were observed. They predominantly occur as pore linings and pore fillings (Wilson and Pittman, 1977) formed in what appears to be the infilled rim of a former burrow (Figure F1.25b−e). Amphibole, pyroxene, tourmaline, zircon, rutile, mica and chlorite are present as accessory minerals (Figure F1.25g−l). Cross sections of

root remains were also observed (Figure F1.25f). Importantly, the grain size characteristics and matrix abundance match the particle size analysis results (section 1.3.2.4).

Table T1.2 Petrography results

Sample ID	Sample origin	Depth (cm)	Classification*	Texture **	Sorting
PA_10-M 1	pit sediment	64-71.8	sublitharenite	submature	moderately
PA_10-M 2	pit sediment	82.8-90.8	sublitharenite	submature	moderately
PA_10-M 3	pit sediment	124-130.4	sublitharenite	submature	moderately
PA_10-M 4	pit sediment	153.2-161	sublitharenite	submature	moderately
RT_2-CR	river terrace sediment	NA	quartz dominated lithic greywacke	submature	poorly
RT_3-CR	river terrace sediment	NA	quartz dominated lithic greywacke	submature	poorly
GS1-SR	surface rock	surface	sublitharenite	submature	moderately
PA_2-M BR	auger bedrock	25	sublitharenite	submature	moderately
PA_10-M BR	pit bedrock	170	sublitharenite	submature	moderately

* Classification after Dott modified by Pettijohn, Potter & Siever (2012)

** Texture after Folk (1980)

The quartz fraction is dominated by monocrystalline grains, some of which display an undulose extinction, indicating a metamorphic protolith (Figure F1.26a). Polycrystalline quartz is also represented, some being semi-composite with undulose extinction (Figure F1.26b,c), which also suggests a metamorphic and/or plutonic source (Pettijohn et al., 2012, pg. 300, Scholle, 1979). Microcrystalline quartz−chert and metamorphic quartz or quartzite are also present in low abundance in all samples (Figure F1.26d,e,i). Phytoliths were also detected. Additionally, quartz detrital grains with an authigenic overgrowth originating from an episode prior to the last deposition of the grains were observed (Figure F1.26f). Compared to quartz and lithic grains (Figure F1.26g,h,ii), K-felspar grains in thin section are generally highly weathered and show significant alteration (Figure F1.26j,k). Mineral grains typically have a thin coating containing iron oxides and occasionally clay-to-silt-sized material, responsible for the more intense orange colour at the edges (Figure F1.25a, F1.26f,g,l). The coatings exhibited internal layering, particularly in deeper profiles (PA_10-M 3 and PA_10-M 4).

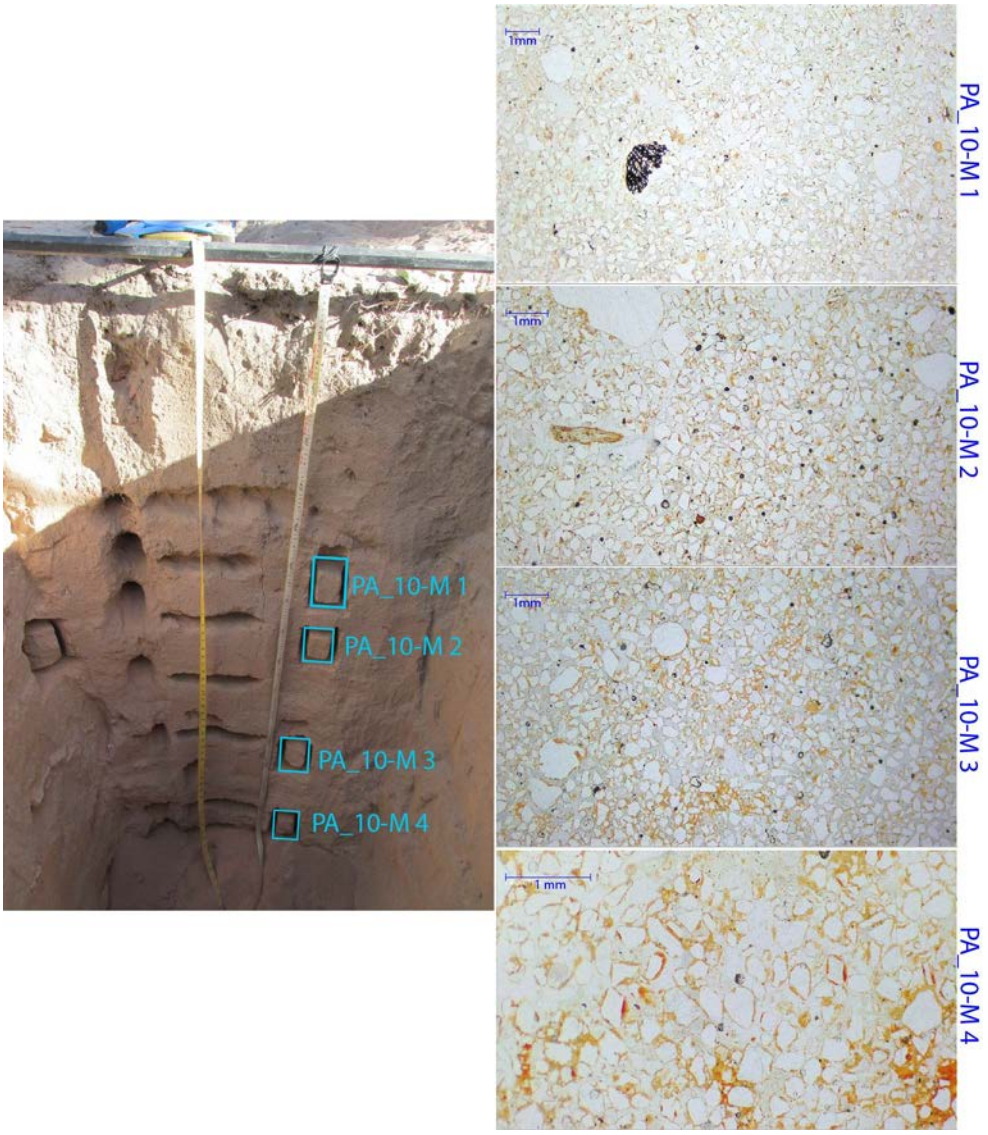

Figure F1.24: Pit PA_10-M south profile. **Right side:** blue squares mark the locations of collected sediment petrography samples; **Left side:** microscopic images of corresponding sediments in thin sections showing moderately sorted submature texture and predominantly subangular to subrounded grains as well as subordinately angular and rounded grains. The scale on the images is 1 mm.

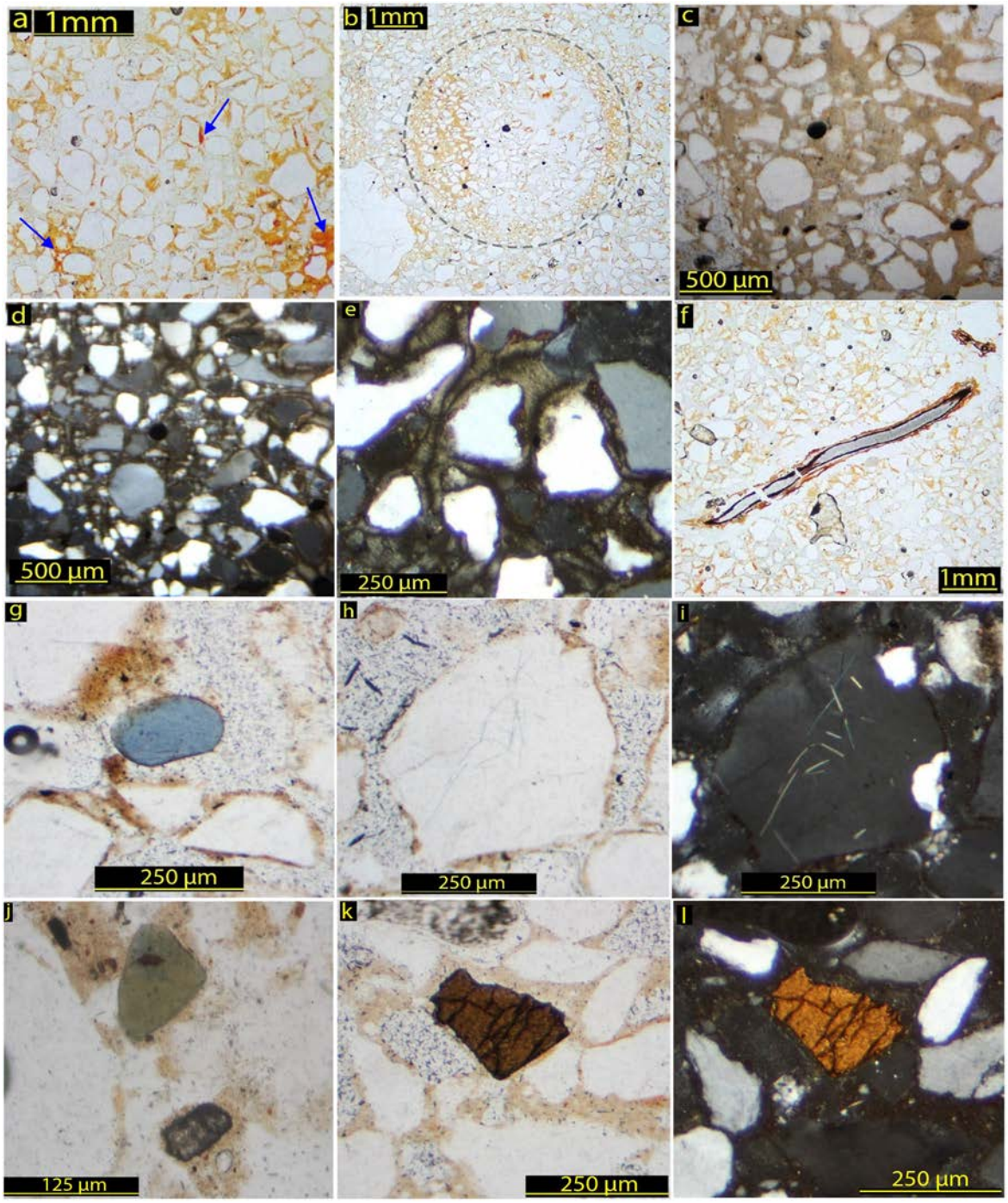

Figure F1.25: Components identified in four sediment petrographic thin sections. **a)** Matrix, clay and silt sized material, appears as yellowish to brownish coatings surrounding mineral grains (PPL). Blue arrows point to strong orange coloured iron oxides. Crescent layered coatings are also visible in the area marked by the blue arrow on the right side; **b)** Marked with dashed line the rim of a former burrow or tunnel infilled with clay matrix (PPL); **c)** Detrital and authigenic clay matrix filling the burrow rim shown on picture b, a closer view (PPL); **d,e)** Authigenic clays in the matrix that fills the burrow rim shown on picture b were identified under crossed Nicols (XN); **f)** cross section of a root in decomposition process (PPL); Accessory minerals: **g)** tourmaline (PPL), **h,i)** mica inclusions in a quartz grain (PPL, XN), **j)** chlorite and zircon (PPL), **k,l)** amphibole (PPL, XN).

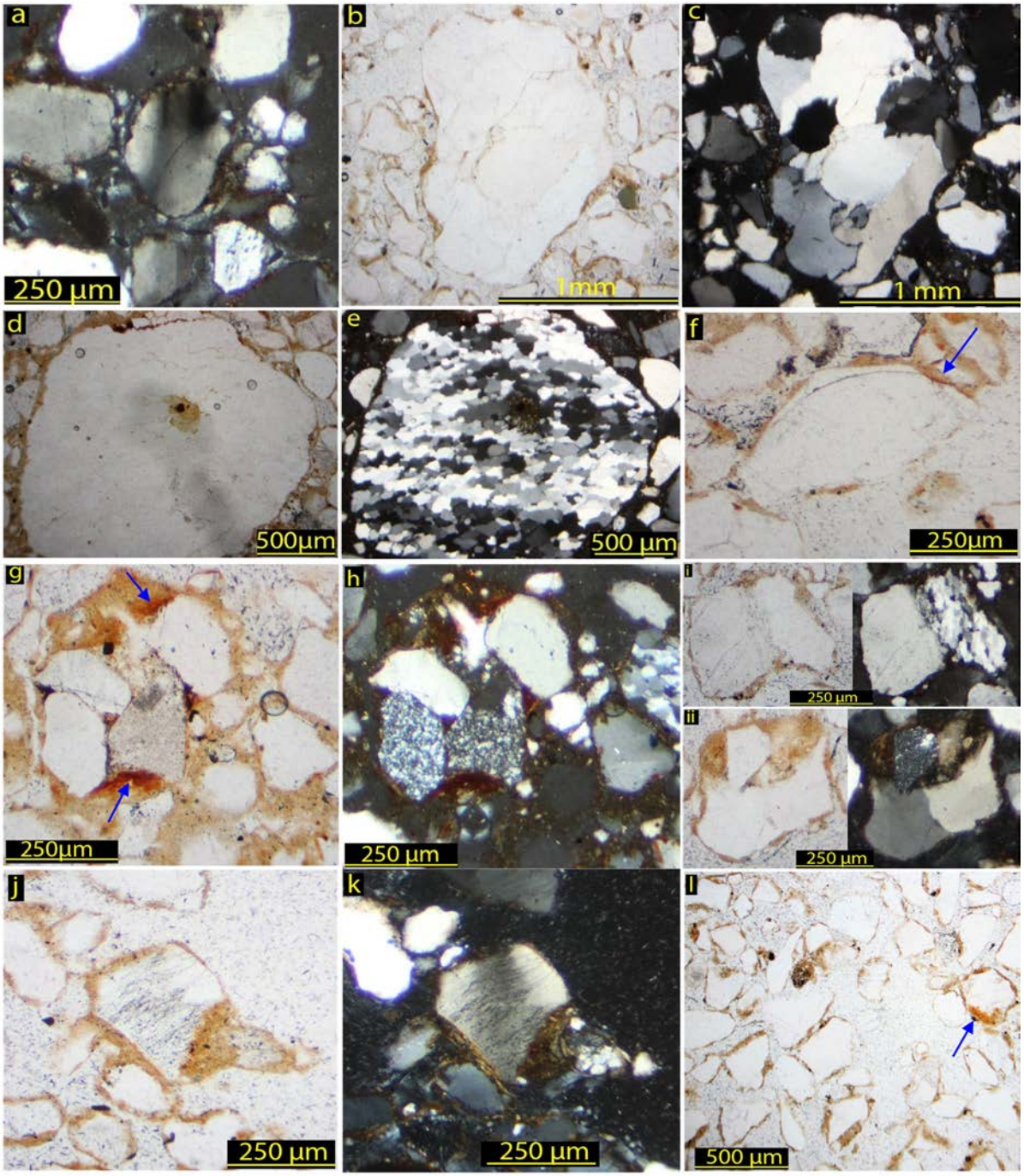

Figure F1.26: Assorted mineral grains identified in sediments by optical microscopic analysis. Blue arrows mark the strong yellow-orange coloured iron oxides in orange-brown clay coatings and matrix. **a)** Quartz undulose extinction (XN); **b,c)** Polycrystalline quartz grain (PPL,XN); **d,e)** Metamorphic quartz grain, quartzite (PPL,XN); **f)** Authigenic overgrowth on a detrital quartz grain (PPL). The well-rounded nucleus is outlined by a thin layer of inclusions (probably clay and iron oxides) on its surface. The authigenic overgrowth shows euhedral crystal shape; **g,h)** Lithic sandstone grain composed by quartz, chert, clay and silt (PPL,XN); **i)** Quartz grain composed by two cemented parts – a monocrystalline quartz (left side) and quartzite (right side) (PPL, XN); **ii)** Lithic sandstone grain (PPL,XN); **j,k)** Feldspar grain with clay coatings (PPL, XN); **l)** Mineral grains with clay coatings (PPL);

- *Rock samples*

In thin section, the three rock samples from Outside GS1 display the same mineralogical and textural characteristics as the sediment samples described above. Samples are moderately sorted and

texturally sub-mature. Quartz is the dominant mineral and is present in various forms, as mono, poly, microcrystalline (chert) and metamorphic quartz. Lithic grains and feldspars are also present, although compared to quartz, they are significantly less abundant (Figure F1.27 d−f). In rock samples, however, the clay-to-silt matrix is present, but mineral grains do not exhibit the clay and iron-oxide coatings around the edges found in the unconsolidated sediments.

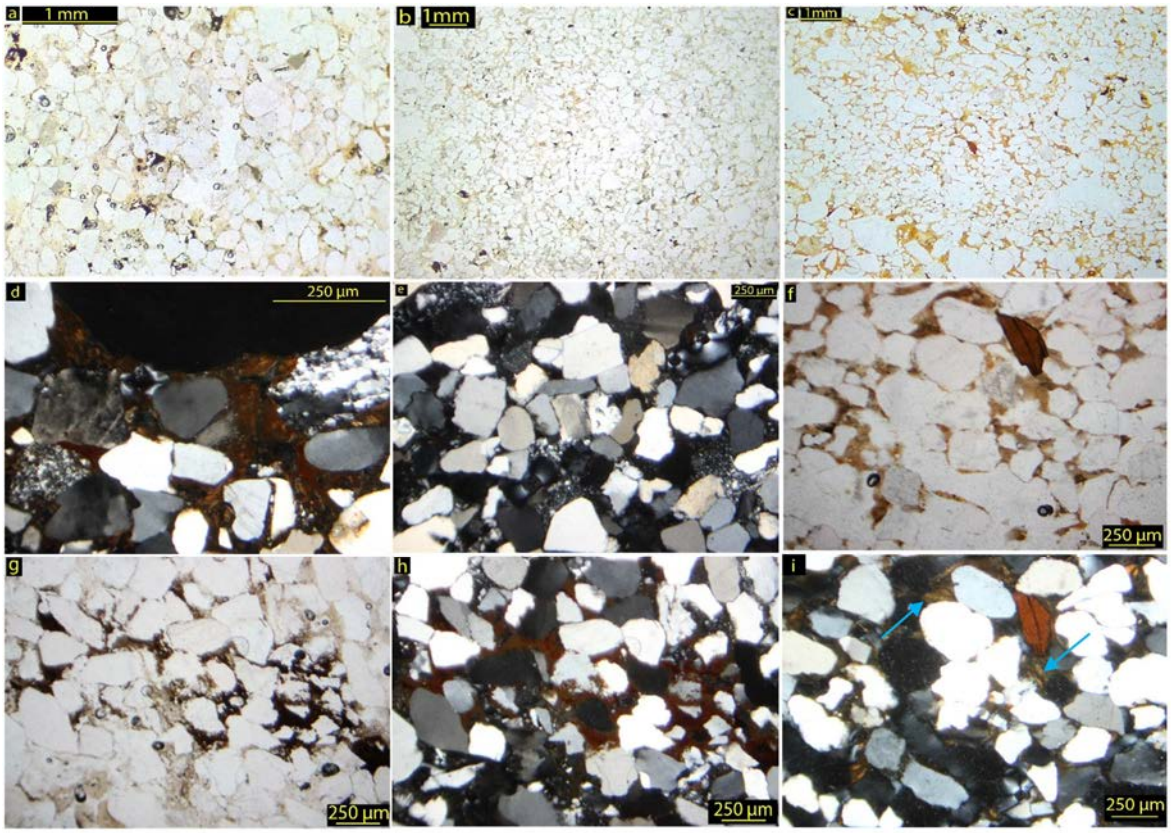

Figure F1.27: Rock samples in thin section. **a)** Surface rock sample (GS1-SR) (PPL); **b)** Pit PA_2-M bedrock sample (PA_2-M-BR, depth 25 cm) (PPL); **c)** Pit PA_10-M bedrock sample (PA_10-M-BR, depth 170 cm) (PPL). Note the matrix is evidently pale in colour at surface and shallow covered rock samples (a,b) compared to deep buried rock sample (c); **d)** Mineral grains (quartz, metamorphic quartz, chert, clay-silt matrix) (XN); **e)** Mineral composition of PA_2-M-BR under crossed Nicols (note: quartz, chert, feldspar, metamorphic quartz) (XN); **f)** Clay matrix, altered feldspar and amphibole in rock sample PA_10-M-BR (PPL); **g,h)** Presence of hematite in clay matrix in surface rock sample GS1-SR (PPL,XN); **i)** Figure (f) under crossed Nicols, blue arrows pointing to authigenic clays.

Matrix is present in low abundance (<20 %) and consists of dark brown to pale orange coloured clay- and silt-sized material. In the surface rock sample (GS1-SR) and shallow covered rock sample (PA_2-M BR, depth 25 cm), the matrix is considerably paler in colour compared to the pit PA_10-M-BR bedrock sample taken at a depth of 170 cm (Figure F1.27a−c). Authigenic clays (pseudomatrix) were also observed in the PA_10-M-BR rock sample (Figure F1.27i). A very dark brown to opaque matrix was observed in the surface rock sample (GS1-SR) that was attributed to hematite (Figure F1.27d,h).

1.3.3 Stratigraphy and sedimentology at the Norman River site

1.3.3.1 Stratigraphy

Four stratigraphic units (designated A, B, C, and D) were documented at the Norman River meander bend exposure (Figure F1.28). They are described as follows:

A. The upper unit is reddish brown, loose sandy and silty material, approximately 150 cm thick, named 'the top red unit'.
B. Underneath lies 'the mottled transition unit'. It is a reddish to orange-brown hardened sediment layer approximately 183 cm thick, with strong reddish mottles and areas of pale, low chroma colour.
C. An approximately 65 cm thick whiteish, sparsely mottled hardened sediment named 'the white crust unit' was documented below the transition unit.
D. The bottom unit ('the bottom grey unit') is constituted by light grey to brown loose sand material with sparse mottles.

For units B and C, the term hardened sediment is used as a general term for any indurated zone resulting from cementation at or below a land surface as a part of a weathering process. The mottles present in units B, C and D are identified as redoximorphic features. They form by the reduction and oxidation of Fe and Mn compounds. The term redoximorphic features replaced the former expressions ''mottles'' and ''low chroma colours'' in Soil Taxonomy (Stoops et. al, 2018). Macroscopically, the redoximorphic features appear in units C and D as redox concentrations masses (soft bodies like mottles), coarse (5 to <20 mm), yellowish red and irregular (after Schoeneberger et al., 2012) (Figure F1.29 left). In unit B, the surface looks reddish brown, but when cleaned using a shovel, areas of low chroma colour appear on a fresh exposure (Figure F1.29 right). This could be due to redox depletion along a root channel or reduced matrix occurrence (Stoops et. al, 2018, Vepraskas, 2015).

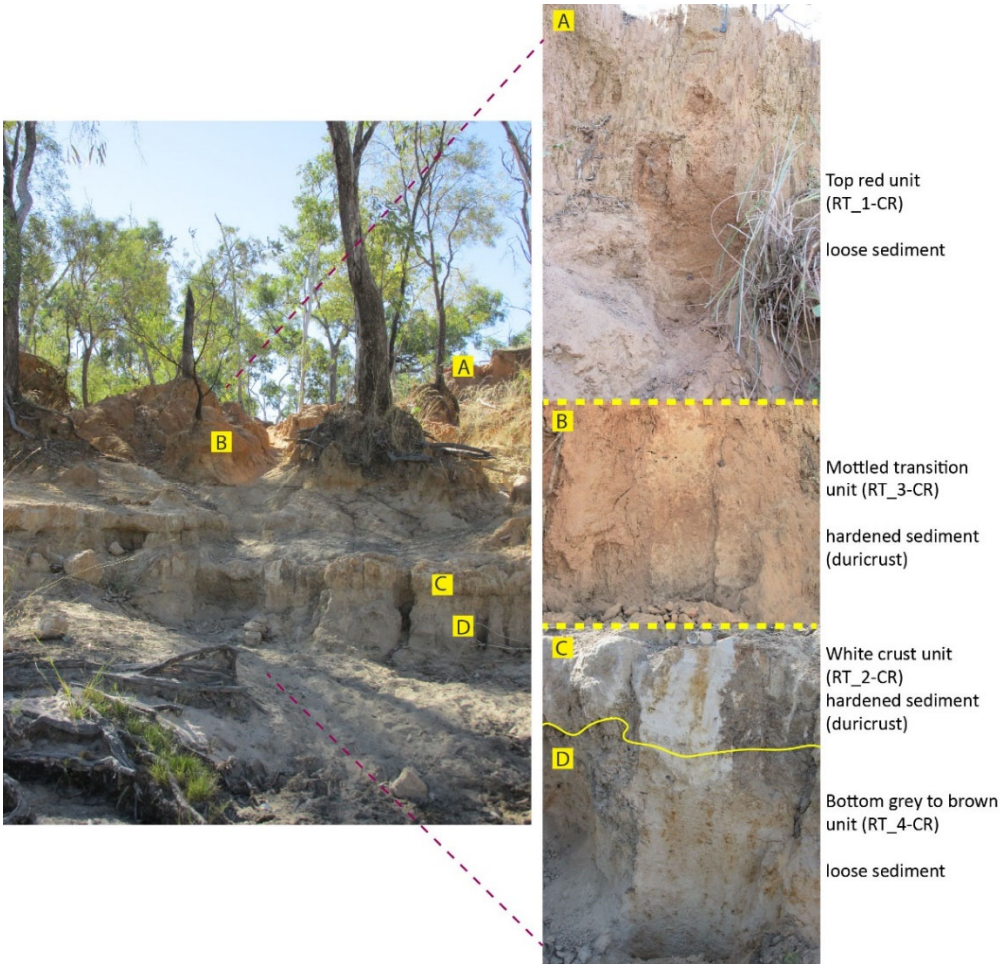

Figure F1.28: Four stratigraphic units at Norman River site. The dashed yellow line marks the constructed boundary between the units for the purpose of presentation, the solid yellow line marks the actual boundary between the C and D unit in nature.

Figure F1.29: Redoximorphic features. **Left:** redox concentrations−masses or soft bodies; **Right:** redox depletion or reduced matrix.

1.3.3.2 Sediment colour

Sediments at Norman River site exhibit colours as follows (Figure 1.28): unit A strong brown (7.5YR 5/8), unit B strong brown (7.5YR 5/6), C is white to light grey (10YR 8/1-7/1) and D very pale brown (10YR 8/3).

1.3.3.3 Particle size distribution

In the two bulk sediment samples from the Norman River site, from units A and D, fine and medium sand fractions are dominant (Table T1.1, Figure F1.13, Figure F1.30). They account for ~78% in unit A and ~65% in the lowest unit D. Clay-sized particles make up less than 5%, whereas silt-sized particles are more abundant at 10–23%. The coarse sand fraction represents 6% and 8% in units A and D respectively. The median grain size Dx (50) in the upper A unit was 227 µm and the mean grain size D [4,3] was 253 µm, which falls in the same range as Outside GS1 size distributions (Figure F1.22). On the other hand, Unit D exhibited a slightly different grain size distribution, with parameters Dx (50) at 156 µm and D [4,3] at 200 µm and a wider span. The latter is shown on the size distribution graph in Figure F1.31.

Results of sedimentological analyses from the Norman River site are summarised in Tables T1.1 and T1.2.

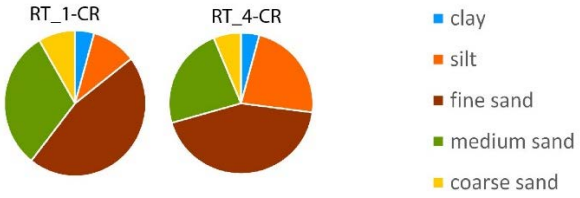

Particle size	RT_1-CR	RT_4-CR
clay	4.36%	4.12%
silt	10.17%	22.93%
fine sand	46.08%	43.50%
medium sand	30.96%	23.28%
coarse sand	8.43%	6.17%

Figure F1.30: Grain size distribution in unit A (RT_1-CR) and D (RT_4-CR) in pie charts; numbers are also given under the graphics.

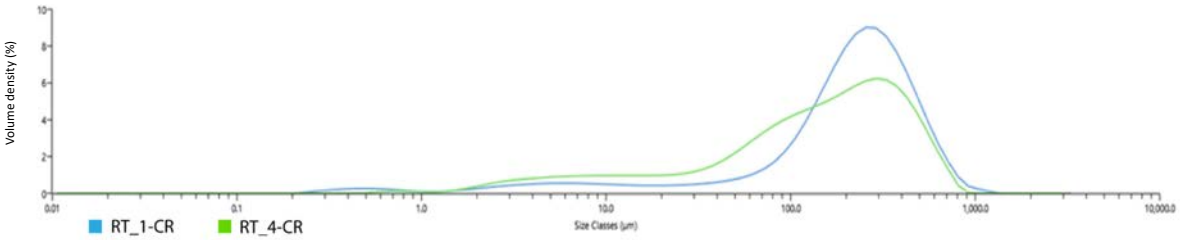

Figure F1.31: Grain size distribution graphs in the A and D Norman River units; Size Classes µm 0.01−10,000 are shown on the x-axis and the Volume density (%) of particle sizes on the y-axis

1.3.3.4 Petrography, optical microscopy

Mineral grains in the sediment samples from units B and C (Table T1.2: RT_3-CR and RT_2-CR) are angular to rounded, with the majority being sub-angular to sub-rounded. They are poorly sorted and texturally immature (Figure F1.32). The mineralogical composition is very similar to the sediment samples from Outside GS1. Quartz is the dominant mineral (~70%), followed by lithic grains and feldspars, the latter occurring as K-feldspar and plagioclase. Lithic grains are composed of sandstone, siltstone and mudstone. The quartz fraction is typically represented by mono, poly to microcrystalline (chert) and metamorphic quartz. Some quartz grains show signs of recrystallization. Accessory minerals are typically mica and amphibole; small opaque grains and tourmaline were also present. In general, mineral grains appear highly weathered and altered. Mineral composition, texture and other components of the sediments that constitute units B and C are shown in Figure F1.32.

The matrix component in the Norman River samples is more abundant (>20%) compared to the Outside GS1 samples, composed of clay and silt material that in colour ranges from pale yellow and brown to strong orange (Figure F1.32). Iron oxides are present in the clay matrix as well as authigenic clays in the form of pore fillings between the grains and pseudomorphous replacements (Wilson and Pittman, 1977) (Figure F1.32d,e). Crescent-shaped, layered coatings around primary grains were also observed (Figure F1.32f). Under the microscope, redoximorphic features occur as Fe/Mn coatings and infillings as well as redox depletion zones or Fe oxide depleted groundmass (after: Stoops et. al, 2018, Table 1, p. 428) (Figure F1.32g).

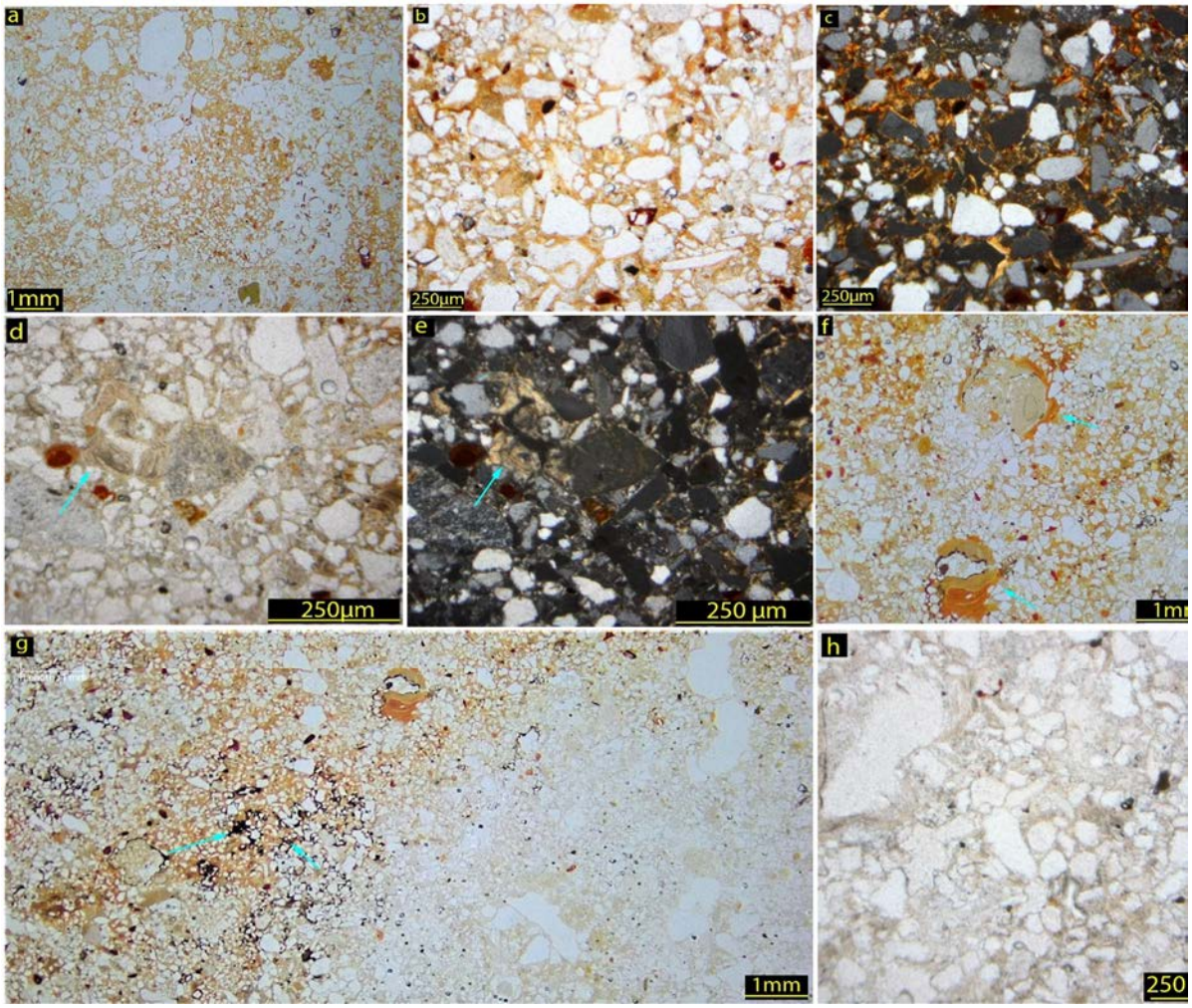

Figure F1.32: Norman River sediments unit B and C in thin section. **a)** Poorly sorted, immature texture (PPL); **b,c)** Mineral composition under PPL and XN, quartz, chert, lithic grains, silt, isotropic grains, clay matrix; **d,e)** Blue arrows mark the authigenic clays, pseudomorphous replacement under PPL and XN; **f)** Crescent, layered coatings in unit C marked by blue arrows, multiple layers representing multiple episodes (PPL); **g)** Redoximorphic features in unit C, blue arrows marking Fe/Mn coatings and infillings, note also the pale right half of the figure representing a redox depletion zone or Fe oxide depleted groundmass (PPL); **h)** Zoom-in into the redox depletion zone or depleted groundmass on the image (g).

1.3.4 Cosmogenic nuclide ^{10}Be concentrations, denudation rates and minimum exposure time

Cosmogenic nuclide ^{10}Be concentrations in quartz from three rock samples (PA_10-M-BR, C_1-CR-BR, GS1-SR) are given in Table T1.3. ^{26}Al/^{10}Be values are also provided as a double check (where ^{26}Al:^{10}Be=6.75:1), showing a very good alignment of both isotopes. The calculated denudation rates and the minimum exposure age calculations for estimating the length of time that the rock sample has been exposed at or near the Earth's surface are also provided in Table T1.3. Figure F1.33 recalls the field sampling locations Outside GS1.

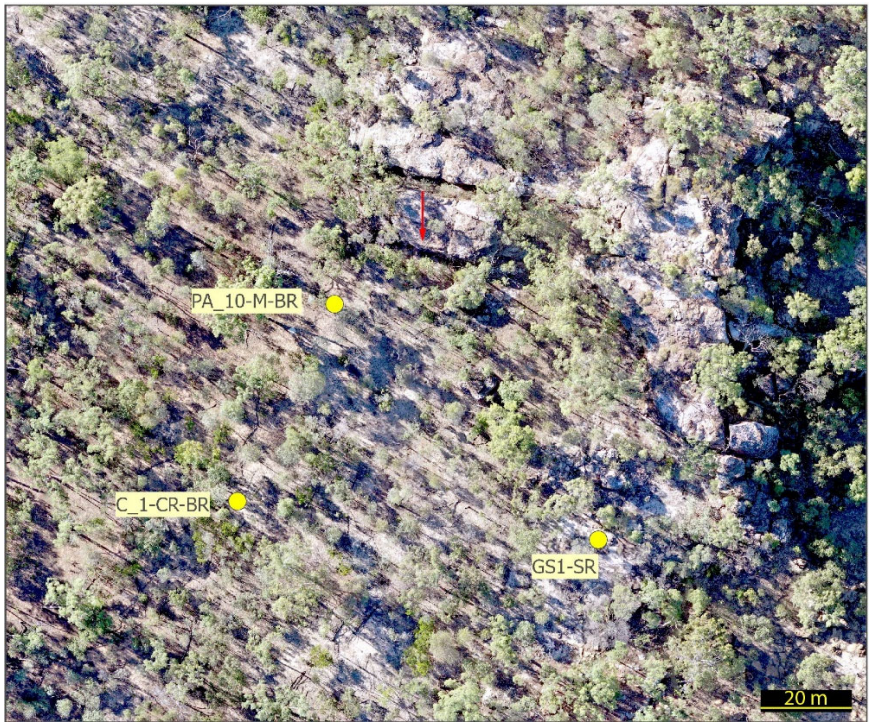

Figure F1.33: Sampling locations for ^{10}Be cosmogenic nuclide analysis. Red arrow indicates the GS1 dripline. In pits PA_10-M-BR and C_1-CR-BR the sample was cut from buried bedrock at depths of 170 cm and 85 cm, respectively. At the GS1-SR location, the sample was cut from the surface rock.

^{10}Be concentrations ranged from 1.97 to 2.73 x 10^5 atoms g^{-1} (Table T1.3), with the lowest concentration measured in the bedrock sample PA_10-M-BR, from the greatest depth ~170 cm, and the highest concentrations measured in the bedrock sample C_1-CR-BR, located at depth 85 cm.

Table T1.3 ^{10}Be concentration data for surface and pit bedrock samples Outside GS1 and calculated denudation and minimum time of exposure

Sample ID	Sample origin	Depth (cm)	Altitude (m asl)	^{10}Be concentration (10^4 atoms g-1)	^{26}Al/^{10}Be	Max. denudation rate * (mm ka^{-1}) Lm	Min. exposure age * (years)
GS1-SR	surface rock	surface	409	22.2 ± 0.8	6.36	9.96	56141 ± 2051
C_1-CR	pit bedrock	85	411	27.3 ± 0.7	6.63	8.05	69263 ± 4394
PA_10-M BR	pit bedrock	170	412	19.7 ± 0.6	6.87	11.3	49739 ± 1534

* The 10Be concentrations, max. denudation rate and exposure ages were calculated using U.Washington cosmogenic isotope calculator online program CRONUS-Earth Time-dependent Lm scaling (Balco 2020b) was used with max. denudation rates. The max. denudation rates were calculated under the assumption of no burial and no inherited concentrations; the min. exposure ages were calculated under the assumption of no burial, no inherited concentrations and no denudation.

The concentrations of cosmogenic radionuclides are a function of exposure time and denudation rate and can be expressed as (Lal, 1991):

$$N = \frac{P}{(\lambda+\frac{\rho\varepsilon}{\Lambda})}\left[1 - e^{-\left(\lambda+\frac{\rho\varepsilon}{\Lambda}\right)t}\right] + N_0 e^{-\lambda T} \quad (1)$$

N = concentration of cosmogenic radionuclide (atom/g)

P = production rate (atom/g^{-1}yr^{-1})
λ = decay constant of the nuclide (yr^{-1})
Λ = attenuation length, the exponential absorption depth dependence of cosmogenic nuclide production (g/cm^{-2})
ρ = rock density (g/cm^{3})
ε = erosion (denudation) rate (cm/yr)
t = exposure age (yr)
T = burial age (yr)
N_0 = inherited concentration

With measured cosmogenic nuclide concentrations from a rock sample, equation (1) is typically used to calculate either the denudation rate or exposure age. Under the assumption of prolonged (t=∞) exposure where the concentration has reached a steady-state value and does not contain inherited concentrations of cosmogenic radionuclides (N_0=0), the equation used to calculate the constant denudation rate can be written as:

$$\varepsilon = \frac{\Lambda(\frac{P}{N} - \lambda)}{\rho} \quad (2)$$

The results allow the calculation of denudation rates range of 8.05−11.3 mMyr^{-1} (8.05–11.3 mmka^{-1}), using a time-dependent Lm scaling (Balco, 2020b) (Table T1.3). The lowest denudation rate, 8.05 mmka^{-1}, derives from rock sample C_1-CR-BR from 85 cm depth, whereas the highest, 11.3 mmka^{-1}, was calculated for the rock sample PA_10-M-BR from 170 cm depth.

Under the assumption that there has not been denudation since exposure (ε=0), and there are no contain inherited cosmogenic radionuclides (N_0=0), equation (1) can be used to calculate the minimum exposure age, expressed as:

$$t = -\frac{1}{\lambda} \ln\left(1 - \frac{N\lambda}{P}\right) \quad (3)$$

Calculated minimum exposure times (t) at three rock samples from Outside GS1 (Table T1.3) showed the longest minimum exposure age 69.3 ±4.4 ka for the rock sample with the highest ^{10}Be concentration C_1-CR-BR, taken from bedrock at a depth of 85 cm. The shortest minimum exposure time, 49.7±1.5 ka, was estimated for the deepest rock sample PA_10-M-BR, today buried at a depth of 170 cm under sand sediment. The rock sample that is today exposed at the surface (GS1-SR) showed a minimum exposure age of 56.1±2 ka.

Finally, to make the equation (2) or (3) valid, two other conditions must be satisfied: (i) the surface production rate (P) is constant through time and (ii) the surface is continuously exposed to the cosmic-ray flux and has not been buried after exposure (T=0). For many actual geological cases, however, it is hard to judge whether the assumptions behind the equations are met from field observations. In this study, the assumptions are not fully met since the two pit bedrock samples are currently buried under 85 cm and 170 cm of sand. Therefore, in these cases, the calculated exposure ages represent minima and denudation rates are maxima.

1.4 Discussion and conclusions

1.4.1 Outside GS1

1.4.1.1 Stratigraphic and sedimentological evidence

Sedimentological characteristics of the non-archaeological open-site sediments Outside GS1 reflect the local rock characteristics, fine to medium and coarse quartzose sandstone with interbeds of siltstone, mudstone and very fine sandstone (Smart and Senior, 1980). This is evident in the particle size analysis (section 1.3.2.4) by the dominance of fine and medium sand with subordinate coarse sand, clay and silt as well as in the optical microscopy, by dominant quartz presence over lithics and feldspars, low clay-silt matrix abundance (<20%) and sub-mature texture (section 1.3.2.5). The variety of quartz forms, monocrystalline grains with normal and undulose extinction, semi-composite quartz, polycrystalline, chert and metamorphic quartz, emphasises the geologically old and heterogenous nature of the source rocks contributing the Hampstead Sandstones. Features like feldspar alteration, authigenic overgrowth and recrystallization indicate the material was exposed to multiple cycles of diagenesis, weathering, transport and deposition. Therefore, the accumulated sediment at the GS1 is a major result of chemical weathering and physical erosion (i.e. denudation) of the surrounding Jurassic Hampstead sandstone. This is consistent with the geological evolution of the region, which was subjected to multiple cycles of erosion, deposition and weathering throughout Tertiary and Quaternary times (section 1.1.1). A certain amount of sediment movement and transport has probably occurred due to bioturbation, gravitation, wind and precipitation, although evidence of sediment transport by wind or water was not recorded.

The coatings that surround quartz, feldspar and lithic grains in sediment thin sections are related to pedogenic processes, including clay illuviation. The coatings are predominantly composed of clay material, in which iron-oxides and internal layering occasionally occur. The coatings and the internal layering tend to increase with depth. The latter is common in clay illuviation, the process associated with the removal of clay from upper horizons and its redeposition as clay coatings and infillings in deeper horizons (Stoops et. al, 2018). In this process, the water from atmospheric precipitation mobilises the clay from the surface horizons and the suspensions infiltrates the sediment through macro voids.

There are many factors required for the mobilisation of clay to occur. First, clay dispersion is needed because most clay particles are aggregated in small clusters up to 250 µm. Several factors affect clay dispersion, including the type of clay minerals, the particle size, pH, the types of cations present (affects clay absorption), the electrolyte concentration in the soil solution and the organic

matter content. Once dispersed and mobilised, the clays are transported as solid particles in suspension, controlled mainly by the quantity of percolating water and the porosity of the sediment. Clay redeposition within a sediment profile occurs when: (i) the infiltration of the suspension stops because the water supply has stopped due to the end of precipitation, or, for example percolating water can be hindered by active roots at the depth of high root concentration (Runge, 1973), (ii) a level of minimum microporosity is reached, (iii) a rise in the electrolyte concentration, due to a change in pH or enriched levels of iron and aluminium compounds, causes clays to flocculate (Dorronsoro and Aguilar, 1988), or finally (iv) a decrease in water velocity (Stoops et. al, 2018). In the analysed thin sections, the presence of iron oxides in clay coatings may indicate flocculation occurred, although a combination of multiple described factors cannot be excluded, considering the intermittent wet-dry monsoonal conditions and the presence of savannah vegetation (tree roots) in the study area.

The clay illuviation process may repeat in the following wet periods, resulting in an increasingly thick clay coating on particles at depth. Layered coatings thus indicate different phases of clay illuviation. The thickness of clay coatings formed on sandy material is a direct function of the clay concentration of the suspension, which implies, in this type of material, that the higher the clay concentration the thicker the clay coatings (Stoops et. al, 2018, pg. 384). The general low thickness of clay coatings in this study, therefore, confirms low clay presence (<15%), which increases with profile depth as the clay was removed from upper to deeper horizons during multiple wet periods. Clay illuviation was one of the first pedogenic processes to be recognised and documented in microscopy of soils and sediments (e.g. Agafonoff, 1936, Frei and Cline, 1949, Kubiëna, 1943) and it has been widely studied since. Under a microscope, pure clay coatings are pale in colour and greyish, but the presence of iron oxides gives them the yellowish to reddish colour, which is the case in this study. As in most cases, iron oxides probably originated from alteration and weathering of iron bearing minerals, such as biotite, pyroxenes and amphiboles. Thus, the pale colour of the clay matrix noted in rock samples (GS1-SR, PA_2-M-BR; Figure F1.27a,b) most probably indicates the absence of iron oxides in the process of deposition and diagenesis.

In relation to climate conditions, clay illuviation has been observed in sediments and soils from many climates, even in areas experiencing low temperatures. Indeed, snow melt water was found to be responsible for the formation of clay coatings and layered clay coatings in surficial sediments of the Transantarctic Mountains (van der Meer and Menzies, 2011, van der Meer et al., 1993). Therefore, the interpretation of clay coatings as proxies in palaeoclimatic studies is highly questionable and not applicable for the time being.

Apart from allogenic clays forming the matrix and clay coatings, authigenic clays were also noted in sediment thin sections (Figure F1.25d,e). They occur as pore linings and pore fillings. Authigenic

clays are common in sand sediments and sandstones and they form either as a direct precipitate from formation waters or through reactions between precursor materials (e.g. feldspars) and the contained water (Wilson and Pittman, 1977). In general, an authigenic origin can be distinguished on the basis of clay composition, structure, morphology and distribution (Wilson and Pittman, 1977). In this case, the distinctly different characteristics of the authigenic clays under the microscope, such as the concentric colour zonation under crossed Nicols (Figure F1.25e), the radial arrangement of the detrital grain surfaces and the regular aggregate morphology, caused them to be easily distinguished from the allogenic component.

1.4.1.2 Post-deposition disturbances and the stone line

Signs of post-depositional disturbance were documented during fieldwork in pit PA_10-M, in the form of circular, oval and ellipsoidal crusts (Figure F1.20a). They are evidence of bioturbation, most probably fossil remains of root and/or termite activity, both very typical of, and common in, Australian savanna regions. Furthermore, according to the Stoops et. al (2018 and citations therein), the origin of crescent-shaped layered coatings and infillings, as observed also at this study (Figure F1.25a), is unclear but they have often been linked to bioturbation as a result of earthworm and/or termite activity.

Bioturbation by root and termite activity can relocate particles in sediment and soil profiles upward and downward after deposition, causing substantial post-depositional mixing. This mixing can have a significant impact on the interpretation of some analyses, for example OSL dating, radiocarbon dating or artefact distribution (e.g. Gabet et al., 2003, Phillips and Marion, 2006, Williams, 2019, Williams et al., 2021). The presence of signs of bioturbation in pit PA_10-M implies that the stratigraphic integrity of the sediment deposit is most probably disrupted to some degree and this should be adequately considered in the interpretation of all analyses. The effects of post-deposition disturbance on sediment particles and the geochronological, isotopic and phytolith analyses undertaken Outside GS1 are presented in Chapter 2 and Chapter 3 of this study.

The origin of the stone line noted in pit PA_10-M (Figure F1.20b) is difficult to determine. Subsurface stone lines or stone layers are isolated layers of gravel-sized rock fragments that appear as a two-dimensional 'line of stones' in a gully or excavated pit profile (Johnson, 1989, Williams et al., 2021). A stone layer may be one stone thick and thus appear as a "stone line" or several stones thick and appear as a "stone zone". They occur in sediments and soils in many parts of the world but are especially common in the seasonally wet tropical regions of Asia, Africa, Australia and South America (Johnson, 1989, Williams, 2019, Williams et al., 2021). Stone lines can form in a number of ways, in particular by (a) selective dissolution of bedrock material or dissolution from quartz veins by

subsurface flow (Braucher et al., 2004, Nehren et al., 2016), (b) residual surface accumulations that were later covered by colluvial, fluvial or aeolian sediments (e.g. Fairbridge and Finkl Jr, 1984, Lichte and Behling, 1999, Morrás et al., 2009, Ojanuga and Wirth, 1977, Parizek and Woodruff, 1957, Ruhe, 1959), (c) parallel retreat of hill slopes (Ségalen, 1969), (d) buried terrace gravels (Rohdenburg, 1982, Veit and Veit, 1985), (e) episodic mass movements, such as soil creep and mudslides (Eargle, 1940, Moeyersons, 1989, Ruhe, 1959, Tricart, 1972) or the swelling of clay soils (Mabbutt, 1965, Moeyersons et al., 2006), (f) bioturbation, the burrowing and selective size-sorting activities of earthworms, ants, termites and other fauna (e.g. Bird et al., 2002, Johnson, 1989, Nehren et al., 2016, Nye, 1955, Ruhe, 1959, Smith et al., 2020, Williams, 2019). In some cases, people may also be involved (e.g. Wallis et al., 2004b, Wesley et al., 2018). Most stone layers, however, are pedogenically-produced by bioturbation (Johnson, 2006).

Due to the variety of processes that can lead to the formation of stone lines, Vogt (1966) and Thomas (1974) emphasized their polygenetic origin, discounting a universal explanation of their development. Stocking (1978: 121) highlighted that ''similar stone lines may be formed as a result of different combinations of environmental circumstance. '' After forty years of research, the processes leading to the formation of stone lines are still controversial (Braucher et al., 2004, Nehren et al., 2016). The controversy is mainly between autochthonists proposing an in-situ chemical weathering genesis (e.g. Lecomte, 1988) and allochthonists explaining the presence of stone lines by mechanical transporting processes resulting from large-scale erosive cycles (e.g. Fölster et al., 1971).

The stone line documented Outside GS1 in pit PA_10-M, at a depth of 100-115 cm, was initially thought to be of anthropogenic origin, or more precisely, that it represents sub-surface dispersed hearth remains, which are very common in the wider area (Wallis et al., 2004b). Yet, no macroscopic charcoal pieces were found along with the apparent heat retainers and no dark, charcoal rich sediment unit or red stained layer was found underneath the stone line, which could confirm this initial hypothesis. Alternatively, stone lines are interpreted as the basis of the active bioturbation zone, following the biomantle concept formulated by Johnson (1990). A biomantle is a differentiated zone in the upper part of soils produced primarily by bioturbation aided by subsidiary processes, where subsurface stone lines can occur. They can form, for example, via uprooting under an open woodland on a stable geomorphic surface (Johnson, 1990, pg.89, Fig.5), but in most cases, stone lines were linked with subsurface faunal activities, associated with earthworms, termites, ants and gophers (Johnson, 1990, Johnson et al., 2005, Williams, 2019, Williams et al., 2021). In many parts of the tropics, termites and ants are the dominant agents of bioturbation. Under their inexorable and relentless 'bio-sorting' the stones are slowly displaced from the surface downward and become concentrated as the ubiquitous basal stone layer of tropical soils (Johnson, 1990, Johnson et al., 2005, Smith et al., 2020,

Williams, 2019). Therefore, the stone line in pit PA_10-M could have been formed by bioturbation. Additionally, Nehren et al. (2013), in their study from the Brazilian tropics, suggest that the formation of stone layers by bioturbation can only occur under open grassland or savannah vegetation, because the dense and relatively deep root system of rainforests prevents stone layer formation. Their study and others imply that stone layers may provide a climate-genetic interpretation under certain circumstances (Maley et al., 2018, Nehren et al., 2013 and citations therein).

At this point, it is impossible to reach a discrete conclusion regarding the formation of the stone line in pit PA_10-M. Considering the diagnostic criteria for termite stone layers as suggested by Smith et al. (2020), the evidence in pit PA_10-M does not satisfactorily fulfill those criteria. For example, despite the direct evidence of termite activity in the profile (Figure F1.20, F1.25b), the evidence of an overlying fine-grained mantle with the profile fining upwards was not observed. Furthermore, substantial evidence of pedogenesis in the form of clay illuviation and mineral authigenesis was observed underneath the stone line, not above it as indicated by Smith et al. (2020). It might be that the stones in the pit PA_10-M are the remains of some other structure used in an Indigenous open camps in the past, such as a support for a sleeping platform or similar (e.g. Wesley et al., 2018). On the other hand, it might be a combination of processes, such as a cracked rock slab where individual pieces were parted and moved downward by the weight of the accumulating sediment as well as bioturbation. Additional field inspection might provide interesting insights.

1.4.1.3 ^{10}Be cosmogenic nuclide evidence

The ^{10}Be cosmogenic nuclide results provide information about the sediment deposit and dynamics Outside GS1. The three rock samples, when compared, showed the lowest ^{10}Be concentration in the deepest bedrock sample PA_10-M-BR (170 cm) (Table T1.3, Figure F1.33, Figure F1.15a,b). This is consistent with cosmic ray bombardment being the strongest at the surface. Therefore, samples at increasing depth will contain progressively decreasing nuclide concentrations, according to the normal attenuation of cosmic radiation (Anderson et al., 1996, Repka et al., 1997). Thus, the ^{10}Be concentration should be the highest in the exposed surface rock sample GS1-SR (Figure F1.33, Figure F1.15c,d). Yet, the ^{10}Be concentration was the highest in the bedrock sample C_1-CR-BR collected at a depth of 85 cm in pit C_1-CR (Table T1.3, Figure F1.33, Figure F1.15e,f). This result suggests that the GS1-SR location, which is currently exposed, was once protected from cosmic ray bombardment by over-burden that is not now present. Additionally, the site that experienced the most intense cosmic ray bombardment and remained closest to the surface for the longest duration is the buried bedrock site C_1-CR, located at a depth of 85 cm.

In the calculation procedure for obtaining exposure ages and denudation rates the basic assumption is that the surface has not been buried since exposure (section 1.3.4). This is even though two of the three measured rock samples are now buried, i.e. sample C_1-CR-BR under 85 cm and sample PA_10-M-BR under 170 cm of sediment. Under this assumption, the measured nuclide activities imply that the sample with the highest ^{10}Be concentrations will reflect the highest (longest) minimal exposure age. According to the calculations, the bedrock sample C_1-CR showed an exposure age of 69.3±4.4 ka, followed by the surface bedrock sample GS1-SR 56.1±2 ka and the pit bedrock sample PA_10-M BR 49.7±1.5 ka (Table T1.3). Uncertainties included, there is approximately 20±5 ka difference between the highest and the lowest minimal exposure time. These results imply a similar exposure history for all three bedrock locations (GS1-SR, C_1-CR-BR and PA_10-M-BR). All three locations exhibit similar exposure times and short, relatively recent burial events; short and recent as understood in terms of geology and the production of ^{10}Be cosmogenic nuclides. Following these results, the bedrock outside GS1 has been exposed to cosmic rays on the surface or buried under shallow sediment for roughly 70 ka.

The calculated denudation rate range, 8.5–11.3 mmka^{-1} (Table T1.3), aligns well with denudation rates reported in analogous, semi-arid and arid environments in Australia and the world; for example, in quartzite and sandstone summit surfaces and slopes from Flinders Ranges, South Australia (6.3−11.4 mmka^{-1}) (Heimsath et al., 2010, Quigley et al., 2007), in exposed sandstone surfaces from Tin Camp Creek, Arnhem Land, north Australia (6.3−11.4 mmka^{-1}) (Heimsath et al., 2009), in basalts in northwest (NW) Tibet (11 mmka^{-1}) (Kong et al., 2007) and in sediments and surface clasts from the Namib desert in Africa (5−16 mmka^{-1}) (Fujioka and Chappell, 2011). The rates are consistent with the median denudation rates (14.5 mmka^{-1}) measured along the East Australian passive continental margin (Codilean et al., 2021). These rates are similar to those found in other post-orogenic, tectonically-passive landscapes with a calculated global median of 12.4 mmka^{-1} (Codilean et al., 2021) and generally indicate a slowly eroding landscape (Fujioka and Chappell, 2011, Kong et al., 2007). Kong et al. (2007) compared the low denudation rates from their study in arid NW Tibet with various arid regions worldwide that, on the contrary, exhibited high denudation rates, such as ~30 mmka^{-1} or even >500 mmka^{-1} (Foster et al., 1994). They found out that those regions were all tectonically active. Furthermore, very high denudation rates (>3000 mmka^{-1}) were determined at their study location in arid NW Tibet during an earlier, tectonically intense stage in the Early Pliocene (Kong et al., 2007). Based on these findings, they concluded that tectonic activity plays a more significant role in modifying denudation rates than climate shifts. A similar argument was proposed previously by Lal et al. (2003), Bierman and Nichols (2004) and Riebe et al. (2001) in their studies on landscape changes worldwide.

The argument that low denudation rates are related to low tectonic activity aligns relatively well with the current state at the Outside GS1 sampling location. Particularly considering the geomorphic and geological evolution of the region (Karumba Basin, section 1.1.1.3), which is currently experiencing the passive part of the evolution cycle with diminished tectonic activity and reduced relief. Codilean et al. (2021) found that denudation rates along the East Australian margin correlate with topographic metrics, suggesting that topography exerts the main control on rates of landscape lowering in this tectonically passive setting. Considering the calculated maximum denudation rates Outside GS1 and the calculated minimum exposure times (Table T1.3), it can be inferred that it takes approximately 51 ka for 500 mm of rock to be 'released into the surrounding environment through denudation'.

1.4.1.4 Geomorphic evidence

The geomorphic evidence suggests that the GS1 rockshelter and the immediate surrounding area are on an erosion remnant, a residual hill (Migoń et al., 2020). The GS1 outcrop is a dissected and deeply weathered residual outcrop of Jurassic Hampstead sandstone, crisscrossed by numerous cracks and joint lines (Figure F1.18). These have been subjected to solution weathering as subsurface and surface processes, producing deep openings along the major drainage lines, like those shown in outcrops in Figure F1.2a. Between these erosion lines, the bedrock has weathered into the remnant flat-topped block outcrop. Micro differences in the composition of the sandstone layers have also facilitated differential weathering rates, resulting in the sculpting of the outcrop.

Exposed plane and smooth bedrock surfaces that were observed on the west and northwest of the GS1 outcrop as well as on the south fringe of the Outside GS1 sediment deposits (Pe in Figure F1.34) bear resemblance to mantled and bare rock pediments, as described by Twidale (2014), albeit on a significantly smaller scale. They are presumably erosion surfaces. Soluble parts were removed by dissolution while solid particles were physically detached and then removed by gravitational processes, rain wash or the combination of both, exposing a plane and smooth bedrock surface. The DEM of the study area in Figure F.34 also shows that a larger portion of the GS1 outcrop is exposed on the east side, where it is fringed by steep scarps. In contrast, the middle and west sides are lower in elevation, more denuded and covered by sediment. The sediment deposit Outside GS1 expands and deepens towards the southwest. Additionally, at the southeast edge of the site a backwaring slope is evident, a probable effect of a slope collapse, marked by blue arrows and a dashed blue circle in Figure F1.34.

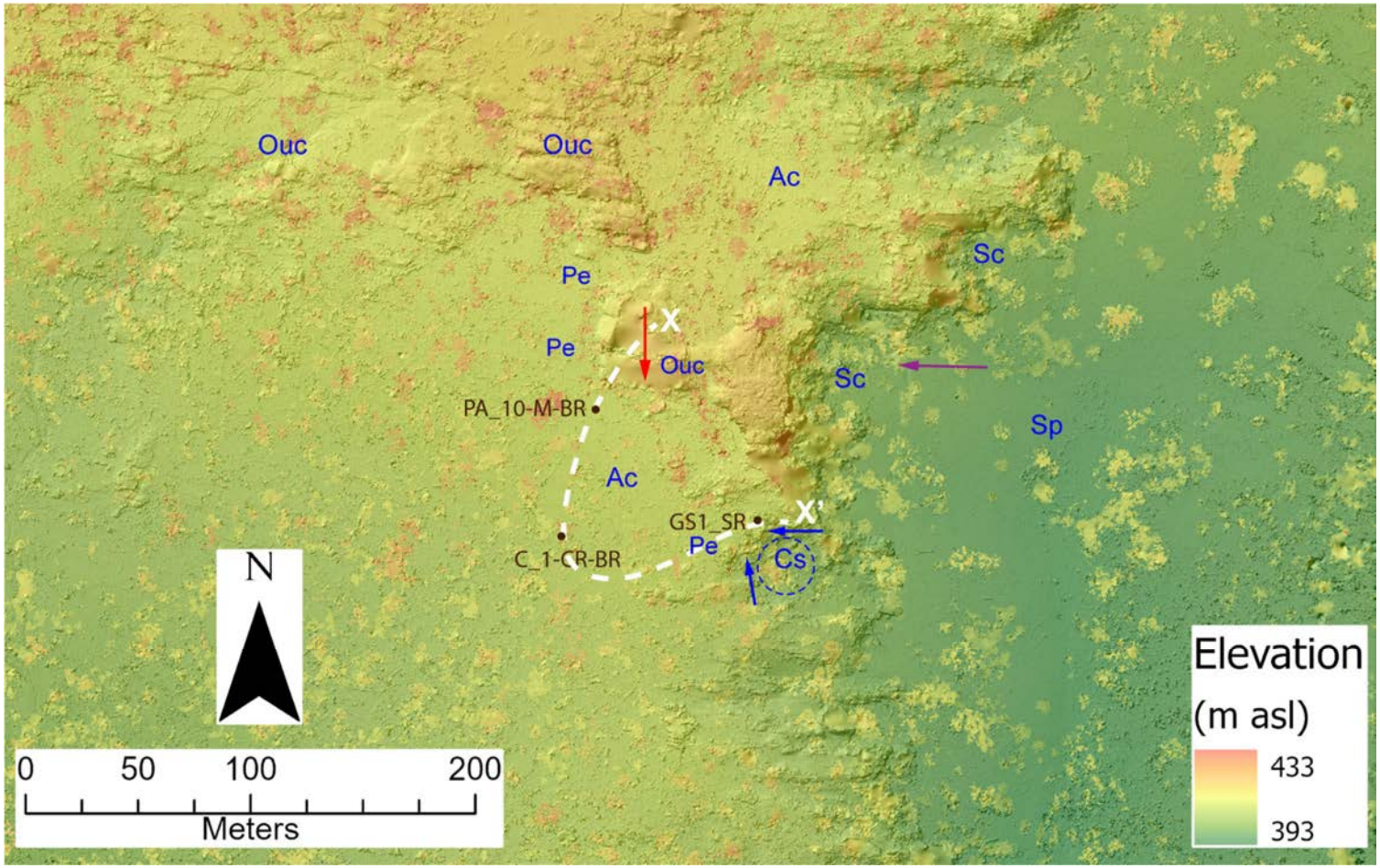

Figure F1.34: DEM of the study area. Red arrow indicates the GS1 dripline. Purple arrow indicates the scarps on the east edge of the outcrop, blue arrows indicate the backwaring slope and the dashed blue circle marks the slope collapse area. Dark brown dots indicate the ^{10}Be cosmogenic nuclide sampling locations. Ac-accumulated sediment, Cs-collapsed slope, Ouc-outcrop, Pe-plane bedrock exposures, Sc-scarp, Sp-sand plain. The X-X' white dashed line marks the profile used to describe the scenario in Figure F1.35.

Changes in local geomorphology resulting from slope collapse and backward erosion, can have significant impacts on the morphology and formation processes of a site. However, the direct evidence of these processes is typically randomly preserved and frequently either removed or deeply buried. Figure F1.35 illustrates a reconstruction of a hypothetical cycle of geomorphic events further in the distant past for the Outside GS1 sampling site. This reconstruction is based on evidence from site morphology, geomorphic processes, sediment dynamics and ^{10}Be cosmogenic nuclide data.

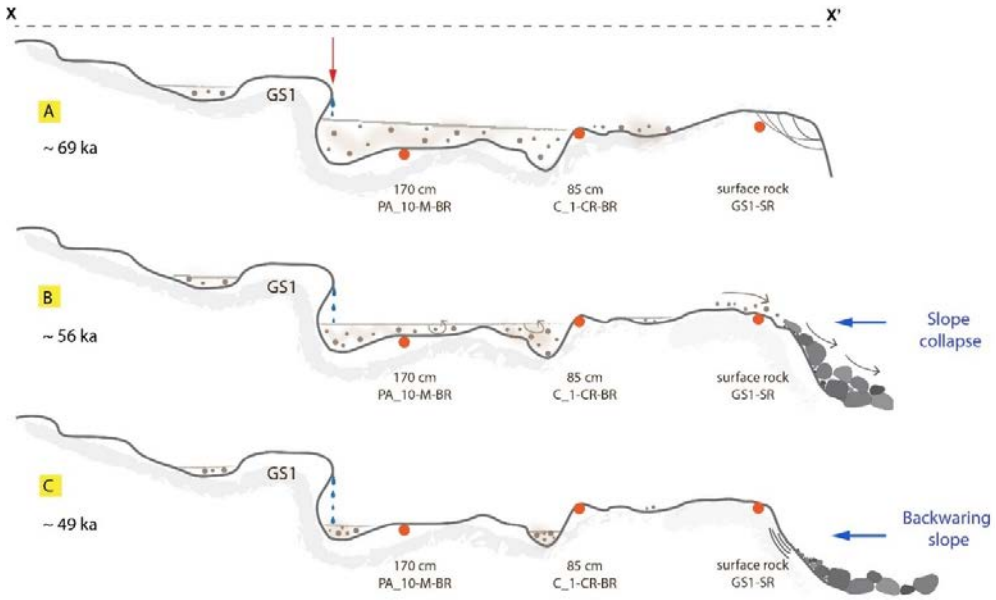

Figure F1.35: The reconstruction of a hypothetical cycle of geomorphic changes at the Outside GS1 sampling location. X-X' dashed line outlines the profile position in Figure F1.35, the red arrow indicates the GS1 rockshelter's dripline. **A:** ~69 ka ago, the escarpment on the southeast edge was higher, forming a rock blockage and the sediment deposit was uneven and deeper on the north side, but shallower on the southwest where the bedrock at C_1-CR-BR was exposed. The bedrock at PA_10-M-BR and GS1-SR was shielded from cosmic rays. **B:** around ~56 ka, the southeast escarpment margin collapsed, the GS1-SR bedrock was exposed and the ^{10}Be production commenced due to cosmic ray bombardment. Gradual reduction of sediment deposit by slope wash and sediment redistribution happened, due to changes in site morphology and very likely also changes in climate. **C:** about ~49 ka most of the bedrock was exposed and most of the accumulated sediment removed. The ^{10}Be production commenced also in the bedrock at PA_10-M-BR. After the collapsed slope stabilised backwaring began on the exposed slope area. Eventually, the sediment removal ceased, and the new accumulation cycle began.

Based on the ^{10}Be calculated exposure times (Table T1.3), approximately 69 ka, ago the escarpment on the southeast of the Outside GS1 sampling location (GS1-SR location) was higher, forming a rock blockage for the sediment (Figure F1.35A). Most of the Outside GS1 was covered by an uneven sediment deposit that was shallower or absent at the southwest where the ^{10}Be cosmogenic nuclide production in the bedrock C_1-CR-BR commenced in quantities that allow measurement. The possibility of past exposure of the C_1-CR-BR location is also supported by the parallel opening in the bedrock at the

fieldwork site (Figure F1.21). Similar parallel openings of various dimensions can be found in outcropping sandstone areas around the study area (Figure F1.2a right bottom). The two other locations were shielded from cosmic rays, either embedded in solid rock (GS1-SR) or buried under deep sediment (PA_10-M-BR).

After the slope collapse (Figure F1.35B), the GS1-SR location was exposed at the surface which allowed the ^{10}Be cosmogenic nuclide production in the surface rock GS1-SR to commence. The change in slope morphology and possible climatic effects set off a gradual reduction in sediment deposit, by slope wash or wind blow, causing a redistribution of the sediment in the study area.

Over time, the collapsed material stabilized at the slope bottom and the backward erosion began on the exposed slope area (Figure F1.35C). At the Outside GS1 location, much sediment was removed and accumulated sediment was limited to the lower parts of existing depressions. Much of the bedrock was exposed and the ^{10}Be cosmogenic nuclide production commenced in quantities that allow measurement also in the bedrock at location PA_10-M-BR, which is today covered by 170 cm of sediment. After some time, a new cycle of accumulation eventually began. Before reaching its current state, additional sediment redistribution likely occurred Outside GS1 throughout millennia, influenced by gravitational processes and climatic conditions.

The depths of pits and auger holes at the Outside GS1 sampling location (Table T1.1) enable the delineation of the distribution of bedrock in the subsurface, as shown in Figure F1.36. Only the pits and auger holes excavated by Zega's team (Table T1.1, purple circles in Figure F1.11) were included because they were dug all the way to the bedrock. The test pits excavated by Wallis's team in 2008 were not dug to the bedrock, but to a defined depth of 120 cm (Table T1.1, blue squares in Figure F1.11); therefore, they were not included in the delineation. Figure F1.36 shows that sediment deposit Outside GS1 occurs on an uneven and undulating subsurface composed of dipping bedrock layers, bedrock slabs and depressions or basins. A general shallowing of the depth from the surface to bedrock occurs as the distance from the dripline increases. Beyond 40 m from the dripline, this depth is <50 cm, although the results from pit C_1-CR (bedrock at 85 cm 68 m beyond the dripline) indicate that there is also significant lateral variation in depth to bedrock. The uneven subsurface suggests the uneven deposition of sediment and the potential for post-depositional disturbances to occur. These include sediment mixing caused by slipping or washing of sediment from higher bedrock levels into depressions.

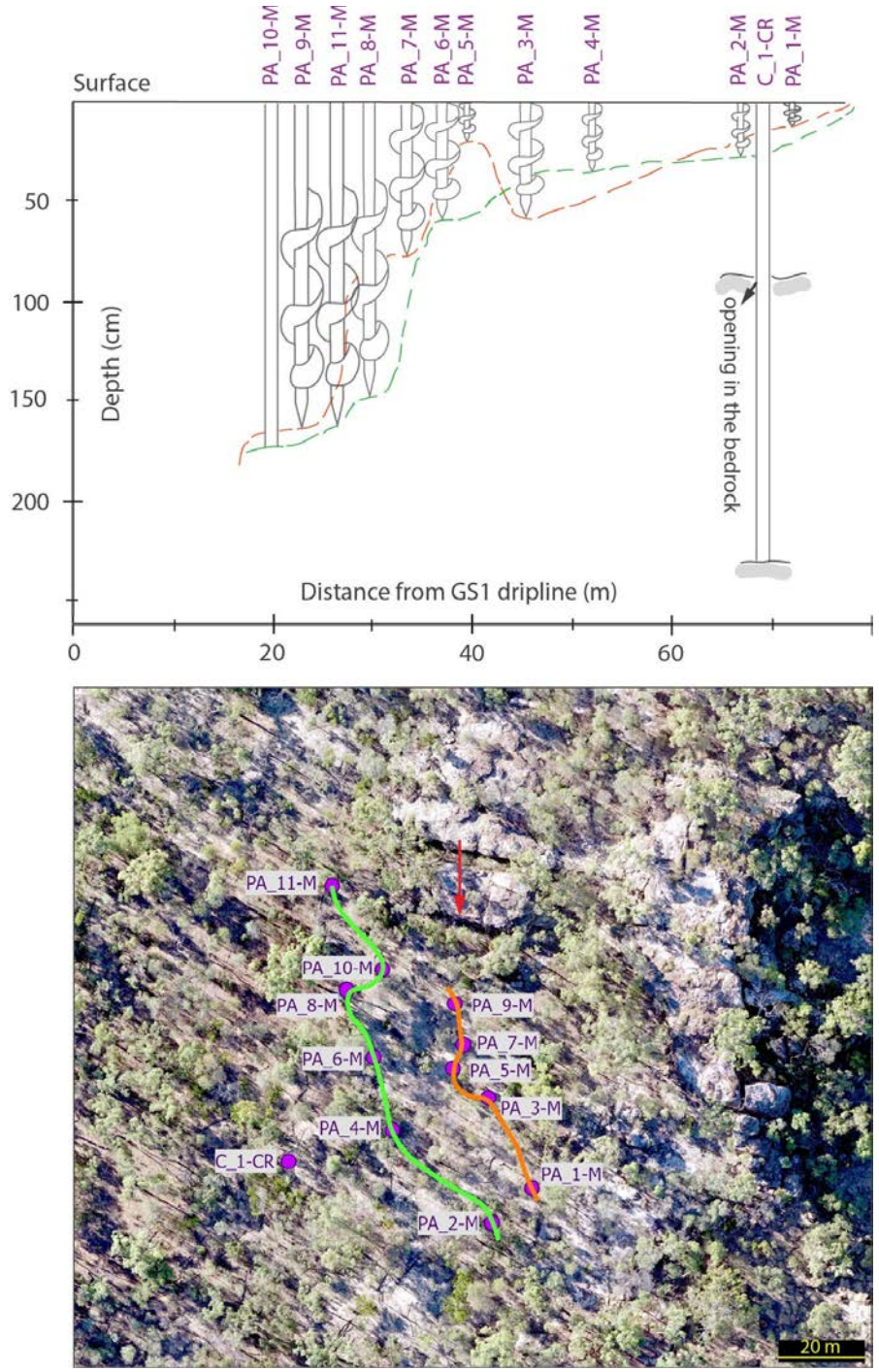

Figure F1.36: Top: undulating and uneven subsurface bedrock of the sediment deposit Outside GS1 demonstrated in depth profile of pits and auger holes in relation to distance from the GS1 dripline. The orange dashed line connects the auger holes on the east line, the green dashed line connects the pit and auger holes on the west line of the sampling locations. **Bottom:** the locations of the two pits and ten augers on field linked by the east and west contour. Note: due to pit C_1-CR off-set position and peculiar bedrock opening at 85 cm it could not be connected to the two lines. Its structure, however, along with the two constructed contours confirms that the subsurface bedrock is dipping towards the west and that the sediment cover is thickening in the same direction.

In summary, the non-archaeological sediment deposit at the Outside GS1 site originated in situ by rock denudation and ex-situ by movement of colluvium derived from the weathering of adjacent outcrops and scarps. The sediment Outside GS1 has been deposited, redeposited and redistributed through time by gravitational movement, slope wash and bioturbation. The findings indicate a complex and dynamic setting despite the missing evidence. The area most likely experiences periods of sediment stripping and periods of accumulation of sediment at unknown intervals. The Outside GS1 location has been exposed to these geomorphic events for approximately 70 ka at least, as determined by the cosmogenic ray exposure age calculation. A visual summary of the results obtained in this study from the Outside GS1 location is provided in Figure F1.37. To conclude, estimating the chronology of sediment accumulation Outside GS1 will provide information about when the last stripping event ended and consequently, when the current cycle of sediment accumulation began (refer to Chapter 2 of this thesis).

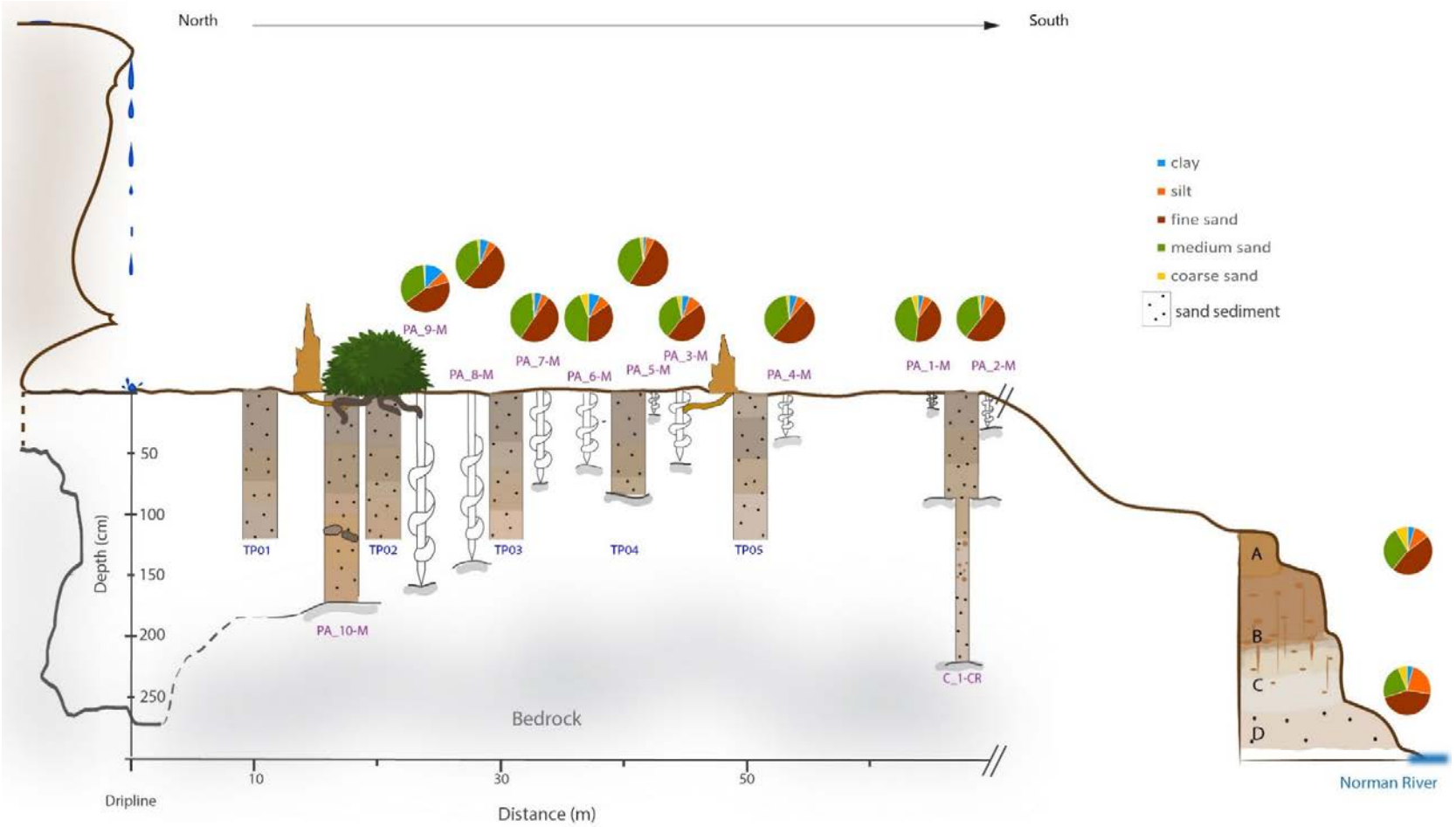

Figure F1.37: A visual summary of this study. Left side, the outline of the GS1 with the dripline. To represent the colour of sediments in pits the Munsell chart colours were transferred in RGB. The general particle size distribution is shown in form of pie charts only for auger holes and Norman River terraces due to transparency reasons. They exhibit the general trend. Note the stone line in pit PA_10-M, the root and termite post-deposition disturbances and the uneven subsurface bedrock as shown by pits and auger holes. Also note the default depth 120 cm of pits TP01-05, apart from TP04 (~100 cm). Due to its position (side-behind GS1) PA_11-M is missing.

1.4.3 Norman River site

1.4.3.1 Stratigraphic and sedimentological evidence

The sedimentological analyses of the Norman River stratigraphic units demonstrate that the sediments originate from the main bedrock that constitutes the wider area, the Jurassic Hampstead sandstone. Recapping, four stratigraphic units, A, B, C and D, were identified from the exposed terraces in a meander bend at the Norman River site, out of which the uppermost A and the lowermost D units consisted of loose sand, whereas the two middle units B, C of hardened sediment (section 1.3.3.1, Figure F1.28). The upper units were reddish to strong brown, while lower units exhibited pale colours. According to Ollier (1988), the weathering profiles can usually be divided into two major zones: the upper, unsaturated zone and the lower zone, which is saturated with groundwater. These correspond to a red, oxidized upper zone, and a pale white to green reduced zone. The top of the saturated zone is the water table, the level of which may fluctuate with storms, with seasons, or in response to longer term changes in climate. At the Norman River site unit C likely marks the level of the former saturated zone. This would explain the distinct change in colour between units B and C.

At least periodically, water-saturated and reduced conditions at the Norman River site are also confirmed by redoximorphic features−mottles and low chroma colours, visible in the field with the naked eye, as well as under the microscope (Figures F1.28, F1.29, F1.32). Redoximorphic features are formed by reducing, translocating and oxidizing iron and manganese compounds in the soil after water saturation and desaturation (Soil Science Society of America, 2001, Vepraskas, 2015). For redoximorphic features to form, specific conditions have to be established: (i) saturation of soil or sediment with stagnant, anaerobic (oxygen-depleted) water, (ii) presence of sufficient organic matter (e.g. from root exudates) and microorganisms (bacteria), and (iii) soil or sediment temperatures above biological zero (5^{o}C) to allow biological activity (Vepraskas, 2015, Vepraskas and Vaughan, 2016). It is not unusual that different types of features may be found in the same unit, thus reflecting past and current hydrology (Stoops et. al, 2018 and citations therein). The redoximorphic features in this study suggest higher river water levels and alternating conditions between periods of stagnant water and desiccation. Floodplain alluviation probably caused occasional water saturation and reduced conditions in sediment layers.

Stratigraphic and redoximorphic evidence indicates that the water levels were higher in the past. The processes that accumulated the Norman River stratigraphic units were fluviatile, sediment particles were subjected to fluvial transport and fluvial deposition. The majority of the particles are subrounded to

subangular in shape, indicating that the fluvial transport did not last long enough to round the particles fully.

1.4.3.2 Geomorphologic evidence

Recently, the Norman River has been incising, exposing the studied profile in the meander bend. The site geomorphology, however, shows that prior to incising, the river was aggrading. The observed river terraces, palaeochannel and tributary channel (section 1.3.1, Figure F1.19) all provide evidence of at least one antecedent phase of river aggradation. The field survey showed that these two channels are no longer active, regardless of the wet or dry season. Only a few signs of occasional water flow were found in the tributary channel, disappearing into sediments after a short distance.

Since the Norman River has been incising, the stream channel has lowered. The sediments deposited during the period of aggradation have been exposed as terraces, described in this study as stratigraphic units A, B, C and D. Additionally, the lowermost stratigraphic unit D exhibited a difference in particle size distribution pattern compared to A, B and C units at the Norman River site (Figure F1.31). Compared with other units, the particle size distribution pattern in unit D shows a higher contribution from the finer component (silt), suggesting a lower flow strength. This indicates that the strength of the Norman River flow was lower during the deposition of the lowermost unit D. Then, it increased during the deposition of units C, B and A until a shift in the river's dynamics occurred from aggrading to incising.

A fluvial terrace represents the former floodplain of a river that was abandoned when the river incised to a lower level (e.g. Bull, 1990, Charlton, 2007, Harden, 2004, Schumm, 1977). The surface of the former floodplain is known as the terrace tread, while the slope that rises to the tread is generally referred to as the terrace scarp, berm, or riser (Ritter et al., 2002). Geomorphologically, the Norman River profile matches a *fill-cut* terrace or *cut-in-fill* terrace form, as described by Larson et al. (2015, Figure 6.B, p.422) or Schirmer (2020, Figure 21.(b), p.17). A stream valley is initially filled with alluvium, a period of floodplain formation, followed by a subsequent incision of the stream channel into this floodplain (Figure F1.38). In this formation type, the highest terrace in a valley filled with alluvium, called a fill terrace, is depositional in origin, whereas fill-cut terraces are inset within this fill terrace and are erosional in origin, representing further incision events (Larson et al., 2015, Oshebi et al., 2017, Schirmer, 2020). Thus, the fill-cut terrace is classified as an erosional terrace (Schirmer, 2020). At the Norman River site the highest terrace is represented by the paleochannel (unit A) and the other stratigraphic units (B,C and D) represent the fill-cut terraces.

Fluvial fill-cut terraces represent sites of transient sediment storage along river channels and are, therefore, an important component of the sediment-routing system (Allen, 2008). They are generated by variations in river-bed elevations due to sediment deposition followed by river incision into the formerly deposited sediments (Bull, 1990). In palaeoenvironmental reconstruction, changes in river dynamics, namely aggradation and incision, tend to reflect changes in water discharge and sediment load at the upstream end of the river (e.g. Buffington, 2012, Lane, 1955) or changes in river base level at the downstream end (e.g. Merritts et al., 1994, Shen et al., 2012).

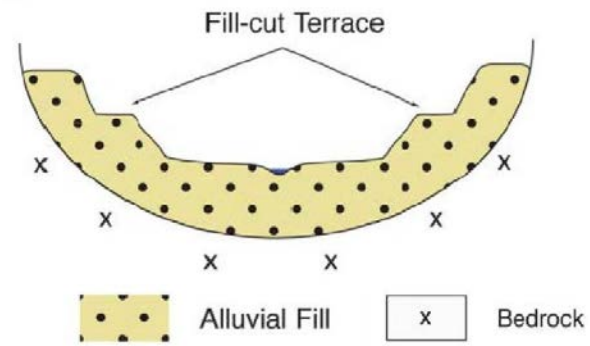

Figure F1.38: Fill-cut terrace form after Larson et al. (2015).
It is considered an erosional landform.

Tofelde et al. (2019) tested three potential mechanisms of fill-terrace cutting and sediment export in connection to changed conditions: (1) an increase in water discharge (Q_w), (2) a reduction in sediment load ($Q_{s,in}$), and (3) a fall in base level. They used a set of seven physical experiments in a braided channel system in non-cohesive sediment. The results showed that an increase in Q_w, a decrease in $Q_{s,in}$ or a drop in base level, would trigger river incision and terrace cutting combined with an instantaneous reduction in channel width (Tofelde et al., 2019). At the Norman River site, one or a combination of two of these changes are responsible for initiating the shift in Norman River dynamics from aggradation to incision. An increase in the length and intensity of the monsoon season could have resulted in higher water discharge in the Norman River. On the other hand, a decrease in rainfall due to a weakened monsoon could have led to a reduction in sediment supply at the upstream end. However, more research is necessary to investigate which condition(s) are responsible for the change in dynamics of the Norman River. This would provide a much better understanding of past and present environmental conditions at the local and regional levels. This thesis returns to these issues in the following chapters (refer to Chapters 2 and 3).

1.5 Acknowledgements

The authors express their gratitude to the Traditional Owners, represented by Woolgar Valley Aboriginal Corporation and especially Uncle Lavin Keyes, Jasmine Keyes and Tameika Keyes as well as Helen Smith and William Smith for their partnership, guidance and help. The authors are very thankful to the Hinze family for their generous support and assistance throughout the fieldwork. The authors would like to thank Costijn Zwart, Michael Brandt, Tina Nemec, Raul Hernandez Font, Xennephone Hadeen and Lauren Linnenlucke for their invaluable help with field work. Their commitment and positive attitude contributed importantly to the outcome of this study. Many thanks to Réka-H. Fülöp & Tibi Codilean for their help with ^{10}Be cosmogenic nuclide laboratory analysis as well as to Scott Smithers at James Cook University in Townsville and Glen Blackstock, Micron Scientific Australia, for their help and support with particle size analysis.

Chapter 2 Luminescence and radiocarbon chronologies of sediments at the Gledswood Shelter 1 (GS1) site, North Queensland, Australia

Mojca Zega[1,2], Michael Bird[1,2], Zenobia Jacobs[2,3] Fiona Petchey[2,4], Maria Rivera-Araya[2,5], Christian Reepmeyer[2,6], Robert Wasson[1], Lynley A. Wallis[7]

[1]College of Science and Engineering, James Cook University, Cairns, QLD, Australia

[2]ARC Centre of Excellence of Australian Biodiversity and Heritage CABAH

[3]OSL Dating Laboratory, University of Wollongong, Wollongong, NSW, Australia

[4]Radiocarbon Dating Laboratory, University of Waikato, Hamilton, New Zealand

[5]Department of Environment and Science, Queensland Government, Australia

[6]Deutsches Archäologisches Institut, Kommission für Archäologie Außereuropäischer Kulturen (KAAK), Bonn, Germany

[7]Griffith Centre for Social and Cultural Research, Griffith University, Nathan, Australia

Statement of contribution of others:

MZ, MB, CR, RW and LW designed the study. MZ conducted the field work, the laboratory works partly (hypy), the data analysis and drafted the manuscript. LW liaised with Aboriginal Traditional Owners to facilitate the study. ZJ advised in relation to fieldwork sampling for OSL dating, conducted the OSL analysis and provided support with the results and interpretation. FP advised in relation to fieldwork sampling for radiocarbon dating, carried out the radiocarbon dating and provided support with the results and interpretation. MB coordinated part of the laboratory work (hypy) and provided an overall support with the results and interpretation. MRA carried out the age-depth modelling. All authors edited the manuscript.

Abstract

Chronology is fundamental to palaeoenvironmental reconstruction. It bridges the gap between geomorphologic/sedimentologic evidence and the timing of environmental change. Palaeoenvironmental reconstructions from terrestrial sediments in open savannah contexts are rare in Australia because their stratigraphic evidence is often fragmented, post-depositionally mixed and generally incomplete. In contrast to lake or swamp deposits, establishing a reliable chronology of events from terrestrial sediments at open sites remains an experimental process with an uncertain outcome.

This study establishes a geochronological framework for terrestrial, non-archaeological open-site sediments deposited outside the Gledswood Shelter 1 (GS1) site, beyond the shelter dripline. GS1 is an archaeological rockshelter located inland in semi-arid tropical savannah near the Norman River in North Queensland, Australia. Two sampling locations were selected for this study: 1) the non-archaeological open-site sediment deposits which extend south-southwest beyond the GS1 dripline and are referred to as 'Outside GS1', and 2) a river terrace exposure along the nearby Norman River referred to as the 'Norman River site'. We used single-grain optically stimulated luminescence (OSL) dating of quartz grains and Accelerator Mass Spectrometry (AMS) radiocarbon dating of two fractions of charcoal (macro-charcoal and SPAC-Stable Polycyclic Aromatic Carbon), to develop a chronology for selected sediment sequences. Altogether, sediment samples from five pits, one auger hole and two river terraces were measured. In addition to age estimation of the selected sediment sequences, we also investigated the reliability of the applied methods and the degree to which the results are in accord across techniques.

The OSL results from the open-site deposit Outside GS1, in general, indicate that sediment has been accumulating for at least 15 ka. However, the presence of quartz grains older than 50 ka in some samples indicates that some of the sediment pool is at least that old. The equivalent dose (De) distribution graphs from Outside GS1 samples showed substantial scatter. Therefore, statistical models were applied, to reduce the scatter and obtain a more reliable chronological result. The De distribution graphs and evidence obtained through fieldwork were used to identify the most likely agents of scatter, predominantly attributed to post-depositional sediment mixing caused by bioturbation, specifically termite and plant activity. The radiocarbon (^{14}C) ages obtained from macro-charcoal samples at the Outside GS1 sampling site conformed with OSL results. In contrast, the ages obtained from SPAC were inconsistent. The oldest date obtained from SPAC is ~5 ka, which proved to be substantially younger compared to ages obtained with OSL dating. Overall, the ^{14}C results obtained from SPAC in this study question the applicability of this fraction for dating in field settings where significant mobility and mixing

of fine material can occur. The oldest terrace age estimation is ~40 ka at the Norman River site. The De distribution graphs showed less scatter suggesting that less post-depositional mixing occurred in sediments at the Norman River site.

The OSL and macro-charcoal ^{14}C dating results were applied to build an age-depth model for the non-archaeological open-site sediments outside GS1 and the sedimentation rates were calculated. Based on calculations sedimentation rates were noticeably lower during the early to mid-Holocene than in the late Holocene, which might indicate climate change.

This comparative dating attempt provided valuable insights into the performance of the methods used, the complexity of disturbance in terrestrial sediments at open sites and how these complexities affect dating results. It also has implications for future studies conducted in analogous environments with similarly complex histories.

2.1 Introduction

Terrestrial sediments in open savannah contexts cover a vast area of northern Australia. They contain important records of Australian climate and human prehistory, but they are notoriously difficult to date. The majority of chronologies for tropical Australia are derived from rockshelter contexts (e.g. Bird et al., 2002, Clarkson et al., 2015, David et al., 2007, O'Connell and Allen, 2004, O'Connor, 1995, Roberts et al., 1998, Wood et al., 2016), followed by records from marine cores (e.g. Dunbar et al., 2000, Holbourn et al., 2005, Jorry et al., 2008, Linsley et al., 2010, Martínez et al., 1999, Moss et al., 2017, Spooner et al., 2011, Stott et al., 2007, van der Kaars and De Deckker, 2002), lake sediments (e.g. Rivera-Araya et al., 2022, Rowe et al., 2019, Shipton et al., 2021), fluvial terraces (e.g. Croke et al., 2011, Jones et al., 2003, Murray et al., 1992, Nanson et al., 1991, 1993, 2005, Nott and Price, 1994, 1999, Nott et al., 1996, Veth et al., 2009) and sand dunes (Hutton et al., 1984, e.g. Lees et al., 1990, 1992, 1995, Shulmeister and Lees, 1992). However, most of the available records focus on coastal areas and the wet parts of the tropics, neglecting the large semi-arid interior. Bridging this gap is not a straightforward process.

Rockshelters represent a focal point of Quaternary research in Australia and the main sites for establishing chronologies for the peopling of Sahul (O'Connell and Allen, 2004, 2015, O'Connell et al., 2018). The obtained chronologies are, however, confined to the interior space of the rockshelters and typically do not extend to locations beyond the dripline. Areas surrounding rockshelters, where sediment records can potentially provide additional information, present an opportunity to establish new open-site

chronologies. These can subsequently be linked to chronologies from rockshelters, thereby contributing more fully to our understanding of change in the semi-arid interior of northern Australia.

This study describes an attempt to establish the chronology of non-archaeological open-site terrestrial sediment deposits from the area surrounding an archaeological rockshelter. The Gledswood Shelter 1 (GS1; see Wallis et al., 2009) is a rockshelter located in the semi-arid inland of North Queensland, with sandy sedimentary deposits contiguous with, and expanding southward from, the dripline (Figure F2.1). The area is covered by a typical Australian savannah. The geography is given in the introduction (Chapter I.2A,B) and the geologic and geomorphic settings of the site are examined in Chapter 1.

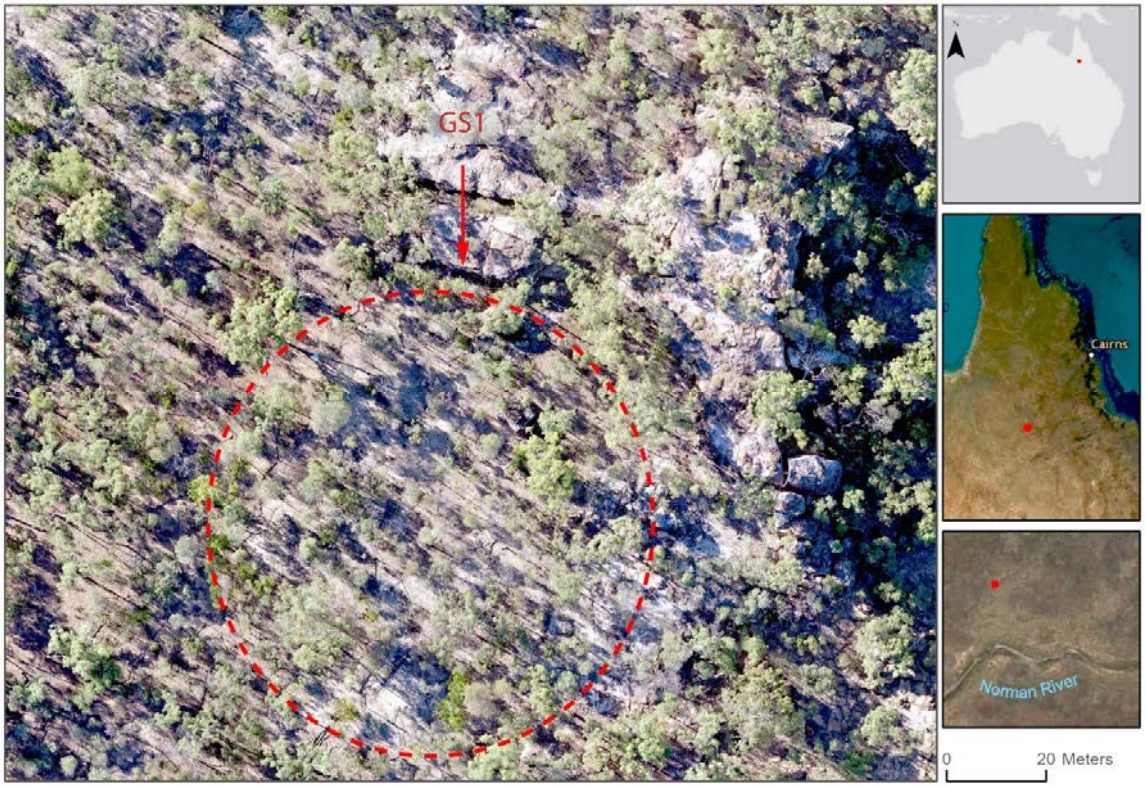

Figure F2.1: Aerial image showing the Gledswood Shelter 1 (GS1) site and the adjacent sediment deposits. The dashed line marks the non-archaeological sediment deposits expanding southward beyond the GS1 dripline, the red arrow points to the dripline; at the bottom right the reference scale for the image. The maps on the right show the location on a bigger scale.

In these field settings, sediments tend to have an unknown history of stability and disturbance. Dating the sediments is challenging and selecting the most suitable method does not ensure a reliable outcome. Each of the dating methods currently employed in Quaternary research has its own distinctive set of limitations, leading to uncertainties in interpretation (Lowe and Walker, 2015). Given the

characteristics of the study area, i.e. quartzose sandy deposits (see Chapter 1), we used the single-grain optically stimulated luminescence (OSL) of quartz grains and radiocarbon dating of charcoal to develop a geochronological framework for the sediment sequences. We applied a two-method approach to cross-check the results, investigate the reliability of chosen methods in this field setting and observe the degree to which the results are, or are not, in accord across techniques. The following paragraphs provide a brief insight into the general principles, advantages and constraints of the two dating methods applied to this study.

2.1.1 Single-grain Optically Stimulated Luminescence (OSL) dating

2.1.1.1 General principles

Luminescence dating is a geochronological technique used for age determination of Quaternary materials, such as soils and sediments from different environmental settings as well as archaeological artefacts. It is a set of analytical methods that measure the time elapsed since sediments, more precisely quartz and feldspar minerals in sediments, were last exposed to daylight. When sediments are buried and protected from sunlight at normal environmental temperatures, the energy in minerals begins to accumulate, induced by naturally occurring radioactivity. All sediments contain trace amounts of radioactive isotopes of elements, such as potassium (^{40}K), uranium (^{238}U) and thorium (^{232}Th). These slowly decay over time. The ionizing radiation they produce is absorbed by mineral grains in sediments, such as quartz and potassium feldspar along with cosmic radiation. This charge remains within the grains in structurally unstable ''electron traps''. The instant the sediments are exposed to light or heat, for example, on the ground surface, the mineral grains emit the energy accumulated during the burial stage in the form of a luminescence signal. Once exposed to sunlight or a light/heat emitting body in a laboratory, any accumulated luminescence signal within the mineral grains is erased (optically bleached or thermally annealed) until completely removed (zeroed) (Preusser et al., 2008). By measuring the energy of the emitted luminescence signal, it is possible to determine for how long the mineral grains were hidden from daylight and with knowledge of the dose-rate of environmental radioactivity (i.e. background radiation of the location where the sample was buried), calculate the time of burial.

Luminescence methods can be applied to samples ranging in age from a few years to hundreds of thousands of years. Therefore they can cover a time interval that encompasses important turning points in Quaternary history (Jacobs and Roberts, 2007). Luminescence dating includes thermoluminescence and optical dating, for which the principles are the same, the techniques differ in how the luminescence signal

is stimulated in the laboratory, i.e. by heat (thermo) or by light (optical). The choice of luminescence method depends on the availability of suitable minerals, the time period of interest, and the nature of the target event. In this study we used OSL to date quartz grains.

OSL is generally used to determine burial ages for sediments and associated fossils and artefacts in the range of ~10 years to ~100 ka for quartz and up to ~300 ka for feldspar (Aitken, 1998, Athanassas and Wagner, 2016, Duller, 2004, Jacobs and Roberts, 2007, 2015, Preusser et al., 2008, Roberts et al., 2015). The OSL age equation consists of two parts (1):

(1)

$$Age\ (ka) = \frac{Equivalent\ dose\ \boldsymbol{De}\ (Gy) *}{Environmental\ dose\ rate\ \boldsymbol{Dr}\ (Gy\ kyr^{-1})}$$

* *Gy is Gray, where 1 Jkg^{-1} = 1 Gy*

The numerator De represents the energy stored by the mineral grains since they were last exposed to sunlight. The denominator, Dr, is the rate at which the radiation energy was supplied, i.e. the background radiation in the material surrounding the grains to a distance of around 30 cm. The numerator (i.e. stored energy) is termed the Equivalent dose (De), it is measured in the laboratory and reported in Gray (Gy), the international unit for absorbed dose (Jacobs et al., 2022). The denominator (i.e. the rate at which the energy is supplied) is referred to as the Environmental dose (Dr) and reported as Gy/ka (Grays per thousand years) (Jacobs et al., 2022).

2.1.1.2 Environmental dose rate Dr

Dr represents the rate of inducing radioactivity from all the radiation sources to the grains from the surrounding material over the same time span (Roberts et al., 2015). These sources are (Figure F2.2):

a) Internal: alpha particles (α−radiation) emitted by radioactive inclusions internal to the grains,
b) External: the beta particle (β–radiation) and gamma-ray (γ–radiation) dose rates emitted by the decay of natural uranium (^{238}U), thorium (^{232}Th) and potassium (^{40}K) from neighbouring grains, and
c) Cosmic: protons, neutrons, electrons, muons, etc.−particles reaching the Earth's surface from space.

There are three ways to determine the Dr:

a) measuring directly in the sediment using dosimeters,

b) measuring alpha, beta and gamma dose rates using radiation counting devices and

c) measuring the relevant nuclides activity and/or concentration and estimating the Dr using well-established conversion factors (Adamiec and Aitken, 1998, Preusser et al., 2008, Roberts et al., 2015).

In practice, most laboratories use the last c) approach.

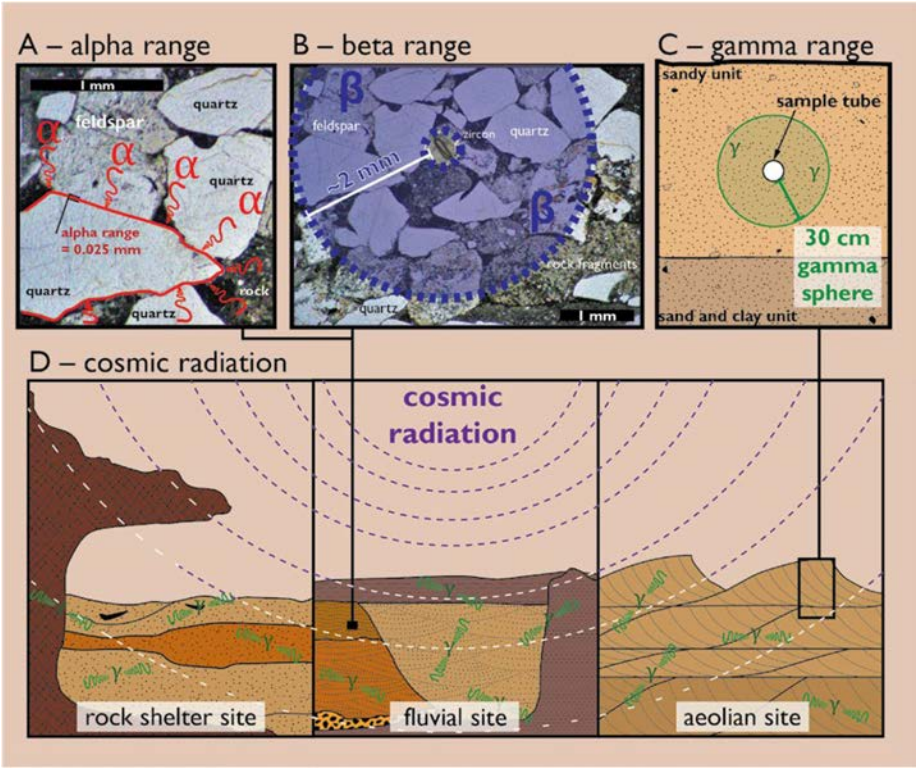

Figure F2.2: Different types of ionizing radiation. A-internal; B and C-external from neighbouring grains; D-cosmic. Note: the difference in the impact range for different radiation (A,B,C) as well as the impact of cosmic radiation (D) at different field settings, e.g. a rockshelter's roof shielding the sediments from the impact of cosmic radiation and the decrease of cosmic radiation with depth (from: Jacobs et al., 2022, 66)

Lastly, interstitial water in the sediment deposit absorbs some radiation energy that would otherwise have reached the grains (Aitken, 1985). Therefore, an estimate must be made of the sample water content integrated over the entire burial period, usually by measuring the water content in the modern sample. Some uncertainty is assigned to each estimate, sufficient to adequately cover the fluctuations in the mean water content over the investigated time span (Roberts et al., 2015). In most cases, the Dr is constant.

2.1.1.3 Equivalent dose De

De represents the sum of the radiation energy the surrounding material accumulated in mineral grains while buried and shielded from light. Mineral grains store energy in the form of an increasing number of electrons trapped at defects in their crystal structure. The number of trapped electrons increases over time due to induced radioactivity. Light sensitive traps can be bleached (zeroed) in a few seconds when the mineral grains are exposed to light again. This way, the OSL 'clock' is reset upon exposure to light (Figure F2.3).

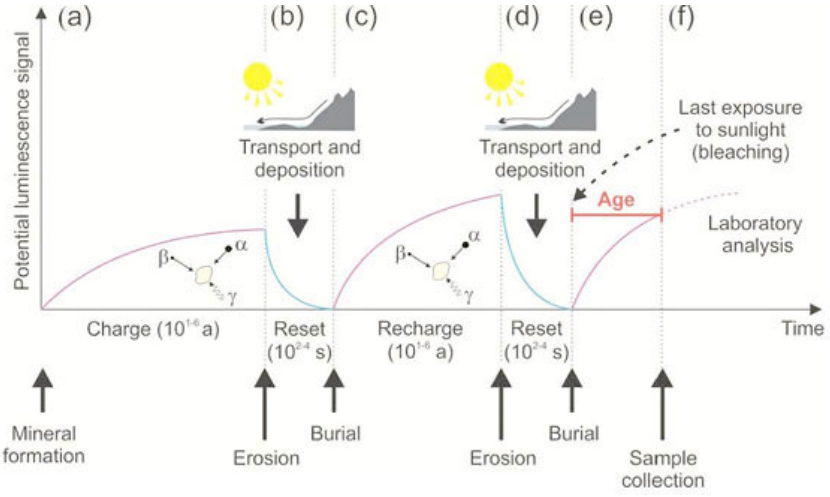

Figure F2.3: Principles of luminescence dating; (a) Luminescence is acquired in mineral grains with exposure to ionizing radiation and trapping of electrons (b) The luminescence for grains is bleached by exposure to sunlight with erosion and transport (c) With burial and exposure to ionizing radiation free electrons are stored in charge defects within grains crystal lattice (d) Further light exposure of grains with erosion and transport bleaches the luminescence (e) The grains are buried again and luminescence is acquired with exposure to ionizing radiation (f) Careful sampling without light exposure and measuring of the luminescence signal in the laboratory will yield a De (from: Mellett, 2013)

When quartz or feldspar grains are exposed to sunlight or photon stimulation in the laboratory, the electron traps are quickly depleted by giving a rise to an emitted OSL signal. De is, therefore, a measure of the energy stored since the traps were last emptied by sunlight. The released OSL signal must be converted into a reliable estimate of De to obtain useful information about the burial age of mineral grains.

2.1.1.3.1Single-grain vs. Single-aliquot and Multi-aliquot procedures

The procedures to estimate the De have changed over time. Early procedures in the 1990s involved taking measurements of the OSL signal from many subsamples, or aliquots, of each sample and then combining the measurements to obtain a single estimate of De (Duller, 2008). This is known as the multi–

aliquot procedure, where an aliquot is a sample of grains mounted on a disk. The disadvantage of this method is that it cannot distinguish between well-bleached and insufficiently bleached samples. The latter can result in an age error, particularly in depositional environments where not all the mineral grains were exposed to daylight long enough for any pre-existing signal to be zeroed, such as rivers, glaciers or archaeological deposits (Duller, 2004, 2008, Hu et al., 2019, Jacobs and Roberts, 2007, Roberts, 2008). For this reason, the multiple-aliquot methods have eventually been replaced by single-aliquot methods.

In a single-aliquot procedure all the measurements necessary to determine De are undertaken using a single subsample or aliquot (Jacobs and Roberts, 2007). This approach allows the generation of replicate measurements of De for the same aliquot, thereby facilitating the recognition of sample contamination or inconsistency. The aliquot size can vary from tens to hundreds to thousands of grains, referred to as micro-, small, medium and large single-aliquot, respectively.

The single-grain OSL technique is a version of the single aliquot method where an aliquot is an individual grain and the De is estimated from the OSL signal produced by a single-grain. Single-grain OSL dating, of quartz grains in particular, is widely used for dating sediments. Intrinsic advantages of single-grain over any other luminescence dating method are especially important when dealing with partially bleached samples and those affected by post-depositional mixing. The measurement of single grains maximizes the probability of finding those that had been bleached at deposition, significantly improving the precision of a sampler's final age estimate (Olley et al., 1999).

Finally, once De and Dr are estimated, the optical ages are calculated with equation (1) in calendar years and more precisely in sidereal years. There is no need for subsequent calibration, such as that required to convert radiocarbon years to sidereal years (refer to section 2.1.2.4).

2.1.2 Radiocarbon dating

Radiocarbon dating uses the decay of a radioactive isotope of carbon (^{14}C) to date objects containing carbon-bearing material. Due to the ^{14}C half-life, it applies to a small proportion of Quaternary time, to the last 55 ka BP, but it has been the most widely used of all radiometric techniques.

2.1.2.1 General principles

^{14}C atoms are continually produced by secondary cosmic rays in the upper atmosphere. Free neutrons from nuclear reactions in the upper atmosphere collide with other atoms and molecules. One effect is the displacement of protons from stable nitrogen (^{14}N) atoms to produce ^{14}C atoms (Figure F2.4). ^{14}C atoms are rapidly oxidized to carbon dioxide (CO_2) and mixed with other CO_2 molecules throughout

the atmosphere. These molecules are absorbed by the ocean and assimilated by living organisms to become part of all organic and inorganic carbon-bearing materials. Once fixed in the organic tissues of plants via photosynthesis and in animal tissues through the food chain, the ^{14}C concentration used to build new tissues will be in isotopic equilibrium with the contemporary atmosphere (environment) for as long as the organism is alive (Libby et al., 1949). This means a steady state exists for the organism's lifetime between the ^{14}C uptake and decay, whereby ^{14}C decays back to stable ^{14}N by emitting a ß-particle (electron) (Figure F2.4).

Upon death, the uptake from the environment stops and the only remaining process is the ß - decay of ^{14}C within the organic tissues, thereby starting the radiocarbon clock (t_0). As the initial ^{14}C content decays with a half-life of 5730±40 ($t_{1/2}$) years, the remaining content ^{14}C provides a measure of time elapsed from death (t_0) (Hajdas et al., 2021, Lowe and Walker, 2015). Given the ^{14}C half-life rate, the simple limit to radiocarbon dating is from 500 to approximately 55,000 years, before and after these, there is not enough radioactivity to be measured. Originally, the half-life of ^{14}C calculated by Libby, who developed the method, was 5568±30 years but was subsequently more accurately determined as 5730±40 years. However, because a large number of ^{14}C dates were published before the new half-life determination, Libby's value for the half-life is used to maintain consistency with early radiocarbon testing results. This is corrected during conversion to calendar ages (refer to section 2.1.2.4). This is the base for age determination using the radioactive carbon isotope ^{14}C.

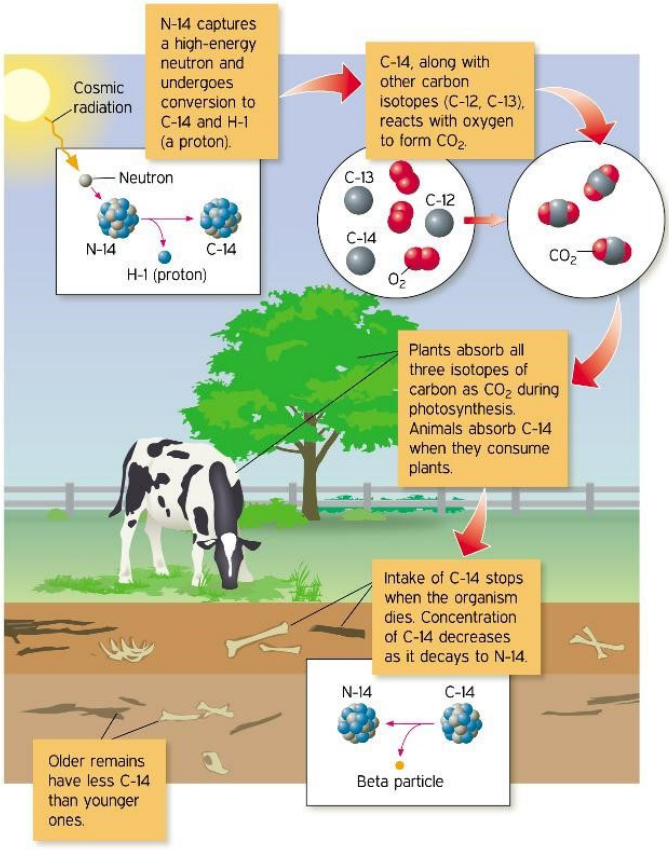

Figure F2.4: Life cycle of ^{14}C; Formation of ^{14}C atoms from ^{14}N induced by cosmic radiation their incorporation (absorption) into living organisms and eventually decay to stable ^{14}N by emission of ß-particles (image from: Blog, 2013)

2.1.2.2. ^{14}C measurement techniques

In the atmosphere, the ^{14}C content is the lowest, compared to the other two stable carbon isotopes (^{12}C and ^{13}C). Most of the carbon on Earth accounts for ^{12}C (98.9 %), while the $^{14}C/^{12}C$ ratio is approximately 10^{-12}, in other words, for every one trillion atoms of ^{12}C in a living organism, there is only one atom of ^{14}C (Hajdas et al., 2021, Lowe and Walker, 2015). Therefore, extremely sensitive equipment is required to detect the remaining ^{14}C activity in organic materials. For this, two approaches are used:

a) ß−counting techniques, which involve the detection and counting of ß emissions from ^{14}C atoms over a period of time to determine the rate of emissions and hence the activity of the sample, and
b) Accelerator Mass Spectrometry (AMS), which uses particle accelerators as mass spectrometers to determine the isotope ratio of ^{14}C relative to that of the stable isotopes of carbon (^{14}C /^{12}C or $^{14}C/^{13}C$). The age is then determined by comparing this ratio with a standard of known ^{14}C content.

The AMS technique was demonstrated in 1977 (Bennett et al., 1977, Nelson et al., 1977, Purser et al., 1977) and is today the most used technique in radiocarbon analysis. It resulted in much shorter measurement times, from days to tens of minutes, and reduced sample material, from grams to micrograms of carbon. Figure F2.5A shows a figurative representation of the AMS radiocarbon analysis process and AMS instrumental set-up.

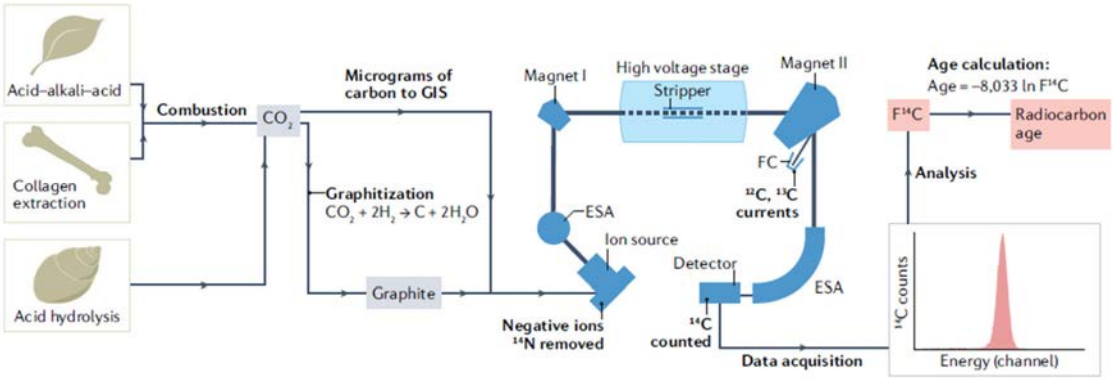

Figure F2.5: AMS radiocarbon analysis procedure and instrumentation. Carbon bearing samples are first pretreated according to the sample specifics. The purified material is combusted to CO_2, which is then either graphitized or, when microgram sized (gas in source, GIS), transferred directly into the sputtering ion source of the accelerator system−AMS. The AMS system consists of the following parts: an ion source that generates negative ions, electrostatic analysers (ESAs) that bend the ions' trajectories depending on their energy to charge ratio, a low-energy magnetic analyser (Magnet I) which separates pre-accelerated ions, a high voltage stage (stripper) that brakes up molecules and changes the charge of ions from negative to positive, a high-energy magnetic analyser (Magnet II) that separates molecular fragments from the required ^{14}C and the stable carbon isotopes, and a detector (Faraday cup−FC) where the stable carbon isotopes are measured. The second ESA is used for further filter atomic ions allowing detection of ^{14}C by single ion detecting techniques. Obtained isotope ratios are compared with those from reference materials analysed under the same measurement conditions in order to calculate the normalised fraction of ^{14}C ($F^{14}C$) and radiocarbon age. (adopted from: Hajdas et al., 2021)

2.1.2.3 Sources of error in radiocarbon age determination

In radiocarbon dating, age determination relies on the assumption that atmospheric ^{14}C concentrations have not varied significantly over time. However, this is not the case. Comparisons between dendrochronological (tree-ring) chronologies and radiocarbon dating series indicate that atmospheric ^{14}C activity has fluctuated markedly in the past, apparently in a quasi-periodic manner (Sonett and Finney, 1990). On a longer time scale, comparisons between ^{14}C AMS determinations and uranium isotopes on carbonate materials, such as cave speleothems and corals, indicate that radiocarbon dates underestimate true age by as much as 3.5 ka at 20 ka BP (BP=Before Present, where present equals the year 1950, refer to section 2.1.2.4 for detail), with even greater discrepancies beyond 25 ka BP (Hughen et al., 2004). These divergences mean variations in atmospheric ^{14}C production rate as well as

fluctuations in Earth's carbon reservoirs' exchange rates that impact the radiocarbon dates and should, therefore, be evaluated.

2.1.2.3.1 Changes in atmospheric ^{14}C production rate

Of particular significance for long-term atmospheric variations in ^{14}C concentrations are the variations in the strength of the Earth's geomagnetic field and changes in the intensity of solar activity (Stuiver et al., 1991). For example, a reduction in the strength of the solar wind would enable more cosmic rays to enter the atmosphere, increasing ^{14}C production (van Geel et al., 2003). Similarly, palaeomagnetic records suggest a close connection between changes in the Earth's geomagnetic field and ^{14}C production. More radiocarbon is produced during periods of low geomagnetic field intensity and less during periods of high magnetic field intensity (Muscheler et al., 2005). Changes in the production rate impact the exchange of radiocarbon between the Earth's main carbon reservoirs.

2.1.2.3.2 Carbon exchange reservoirs: Terrestrial sediments

On Earth, most carbon is stored in rocks and sediments, while the rest is found in the atmosphere, ocean, freshwater and living organisms. They are referred to as carbon exchange reservoirs (Aitken, 2003), or sources and sinks, through which carbon cycles. Once the atmospheric ^{14}C is oxidized to CO_2 and mixed in the atmosphere the exchange with other carbon reservoirs takes place (Figure F2.6). The different elements of the carbon exchange reservoir vary in how much carbon they store and how long it takes for the ^{14}C generated by cosmic rays to mix with them thoroughly (Figure F2.6). This affects the ratio of ^{14}C to ^{12}C in the different reservoirs and, therefore, the radiocarbon ages of samples that originated in each reservoir (Bowman, 1990). Earth's carbon exchange reservoirs and fluxes are shown in Figure F2.6. The following section focuses only on the role of terrestrial sediments as a carbon exchange reservoir, which is relevant to this study.

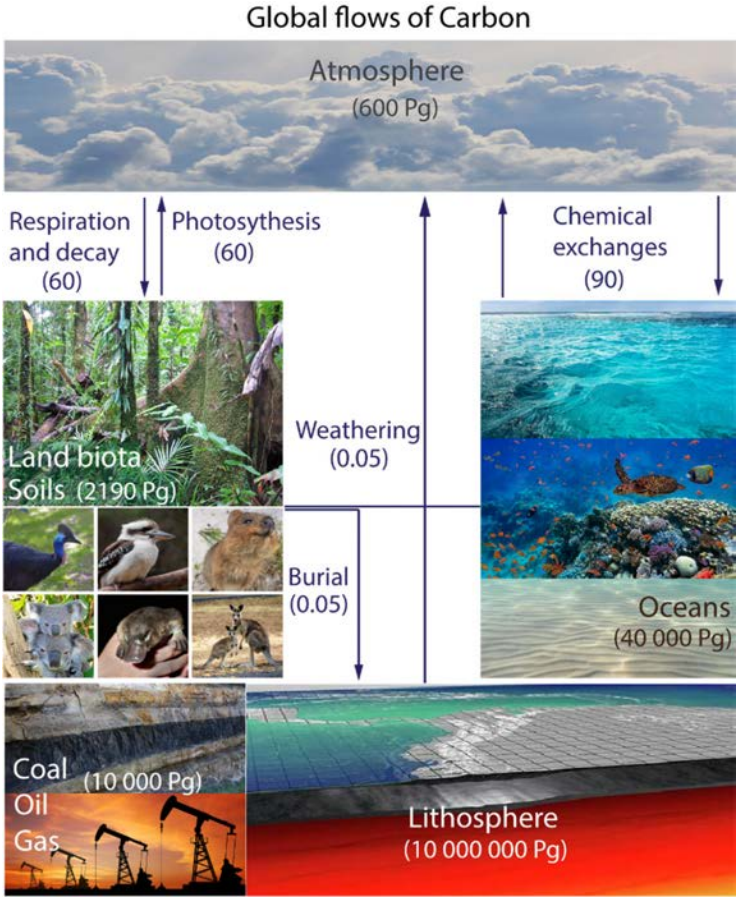

Figure F2.6: Carbon exchange reservoirs and fluxes. Simplified preindustrial carbon budget diagram, prior to humans adding significant carbon dioxide to the atmosphere. The boxes are reservoirs for carbon, numbers associated with reservoirs are in units of Petagrams Pg (10^{15} grams) of carbon stored. The largest reservoir is the lithosphere. Part of the organic carbon, the remains of organisms, has accumulated in the Earth's crust limestone and coral as well as fossil fuels (coal, gas, and petroleum). The arrows on the diagram indicate fluxes (or movement) of carbon between reservoirs. Numbers associated with fluxes are in units of Petagrams per year (Pg/a). Each flux arrow has a sink and a source component. A sink is a removal mechanism and takes carbon out of a reservoir and a source is a mechanism that adds carbon to a reservoir. Modified from: ATMO336 (UA, 2022).

Sediments, including soils, can contain both organic and inorganic carbon in many different forms with many different ages and inbuilt reservoir effects; for example, as fresh organic matter in the form of roots and humic acids, as dead organic matter in the form of charcoal and as inorganic carbonate minerals (Bird, 2007). Sediments are dynamic systems receiving organic and inorganic carbon over long periods of time. Unreliable dates due to contamination can occur because younger or older carbon has been added to the sediment sample material due to, for example, bioturbation or infiltration (Lowe and Walker, 2015,

pg. 277). The continual addition of carbon throughout the development of a sediment profile means that the measured radiocarbon age can result in an average age (Pessenda et al., 1997, 2001). This can prevent the establishment of a radiocarbon age for the sediment profile. However, sediments are a complex mix of many different components and meaningful results have been obtained in the last decades through the application of several inventive approaches. Some of these include dating and comparing different organic components from the same profiles (Pessenda et al., 2001), isolating specific fractions to determine the rate at which they are cycled (Trumbore and Zheng, 1996), modelling the measured ^{14}C content of soil organic matter (Wang et al., 1996) and verifying radiocarbon dates from sediments against results obtained from other dating methods (Dalsgaard and Odgaard, 2001, David et al., 2007).

Pyrogenic carbon (PyC), Charcoal and Stable Polycyclic Aromatic Carbon (SPAC) in terrestrial sediments

In terrestrial sediments, burnt organic matter is one of the most important materials for radiocarbon dating, particularly in savannah environments where fires occur regularly (Bird and Ascough, 2012, Bird et al., 2015, Conedera et al., 2009, Libby, 1955). Pyrogenic carbon (PyC) is a general term used to describe thermochemically altered (pyrolyzed) carbon, derived from the incomplete combustion of organic matter during biomass burning and the consumption of fossil fuels (Bird and Ascough, 2012, Bird et al., 2015). Other partly equivalent terms for PyC include charcoal, black carbon, soot, char and biochar. Rather than a single combustion product, the components that make up PyC form part of a 'combustion continuum' (Hedges et al., 2000, Masiello, 2004), which represents a wide range of compounds of varying reactivity, from lightly charred plant material to highly condensed soot and microcrystalline graphite (Figure F2.7) (Bird et al., 2015). We used charcoal and Stable Polycyclic Aromatic Carbon (SPAC) (Figure F2.7) as the target compounds from which we obtained ages for sediment profiles in this study. The term 'charcoal' is often used to describe a PyC component of macroscopic material resulting from incomplete combustion of woody plant tissue (Bird, 2007). It is highly resistant to decomposition and can persist in the environment over millennia (Ascough et al., 2018, Bird and Gröcke, 1997, Cope and Chaloner, 1980, Eckmeier et al., 2009, Pessenda et al., 2001, Skjemstad et al., 1996). Whereas SPAC is a highly resistant and homogeneous microscopic form of charcoal that forms at combustion temperature range 400–600°C (Figure F2.7) (Ascough et al., 2020, Bird et al., 2015, Fig. 3, pg. 281).

The significant production rate of PyC in fires and its environmental persistence make PyC both abundant and ubiquitous in the natural environment (Bird et al., 2015, Coppola and Druffel, 2016, Cotrufo et al., 2016, Reisser et al., 2016, Santín et al., 2016). PyC, however, potentially contains all the components of the 'combustion continuum' (Figure F2.7) and it is extremely unlikely, in the context of its

environmental persistence, that all PyC components will be preserved in the same way in similar natural conditions (Ascough et al., 2018, Bird, 2007, pg. 2951). PyC stability is better understood as a 'degradation continuum' where the more stable and resistant PyC components, such as some forms of charcoal, including SPAC, are likely to persist in suitable depositional environments for longer periods (Ascough et al., 2020, Bird et al., 2015). For this reason, charcoal is among the most frequently used carbon-bearing materials in radiocarbon dating.

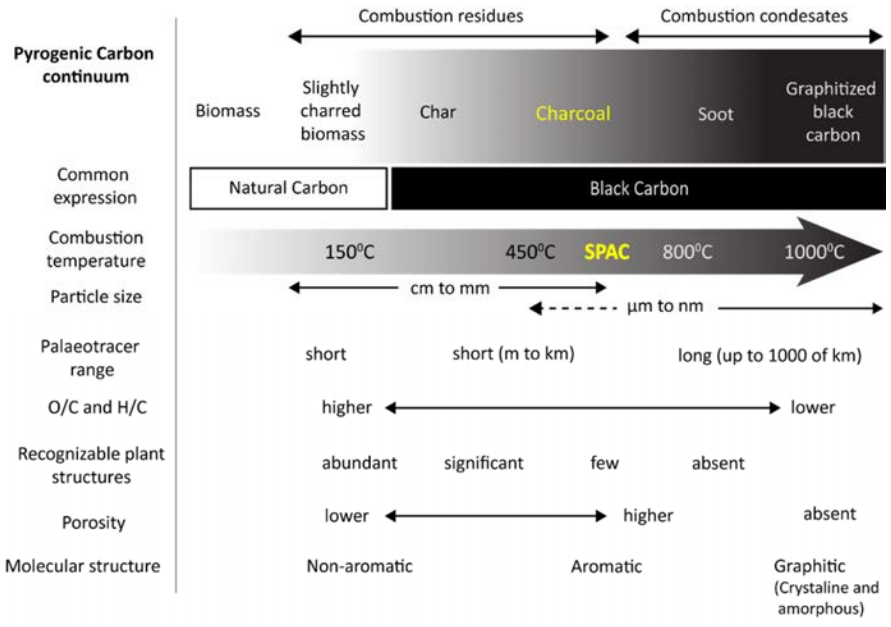

Figure F2.7: The combustion continuum used to describe the multiple forms of PyC to be found in the environment. The two components used in this study are marked in yellow. Note the position of SPAC. Modified after Hedges et al. (2000), Masiello (2004) and Schimmelpfennig ang Glaser (2012).

The age of a charcoal fragment does not date a fire event, but the average age of carbon in the plant structure (at the time of death) and the time of a fire. The two events often coincide closely, particularly in the case of burnt grass or leaves, but not always, for example, in the case of long-dead fallen timber where inbuilt age could be several centuries (Eckmeier et al., 2009). In the case of a fire event, all organic material exposed to fire is affected, i.e. decaying plants, living plants, previously charred biomass, etc. Hence, dating a pool of charcoal particles (macro or micro) delivers a mean age of charcoal in the assemblage that is dated. Moreover, charcoal produced during a single fire event is not necessarily found in the same sediment horizon. Particles can undergo relocation via physical transport and bioturbation, which influences the age distribution in a sediment profile. This is particularly important because charcoal dating is often used to reconstruct a chronology of events by stratigraphic association in

palaeoenvironmental and archaeological studies. The age of an event or events is deduced from a stratigraphic correlation between the charcoal component that is dated and an artefact or a change in the sedimentary composition or the stratigraphic superposition. Processes like bioturbation and water percolation through a profile can result in vertical translocation of particles with negligible (Pessenda et al., 2001) or significant effect on apparent age of a stratigraphic unit (Araujo, 2013, Bird et al., 2002). The latter becomes more likely as charcoal particle size decreases and sediment particle size increases (Bird, 2007).

Ultimately, the resistance of charcoal to physical, biological and chemical decomposition is influenced by several factors. These include the combustion conditions (Baldock and Smernik, 2002), the nature of the surrounding environment and charcoal compounds' physical and chemical recalcitrance (Krull et al., 2006). They undergo initial surface oxidation that makes them susceptible to decomposition (Eckmeier et al., 2009). Over time, the external and internal structures of charcoal will eventually break down (Bird et al., 2002, Cohen-Ofri et al., 2006). During the decomposition process, older degraded charcoal carbon or inorganic carbon products in the depositional environment (Hockaday et al., 2006) or the contamination of micropores in charcoal with younger organic carbon (Alon et al., 2002) can alter the ^{14}C ages and compromise the reliability of radiocarbon measurements. To ensure that the measured radiocarbon activity is directly related to the radiocarbon activity of the sample at the time of death, a series of pretreatments need to be applied during laboratory processing (refer to section 2.2.3.2.1) to remove younger and older organic and inorganic carbon from the sample.

2.1.2.4 Calibration of the radiocarbon timescale

Calibration is the final step in radiocarbon dating of a sample. The raw radiocarbon date must be calibrated, i.e. converted to 'calendar' or sidereal years. This is because the radiocarbon activity of the atmosphere has varied in the past (refer to section 2.1.2.3.1). The age is calibrated using a curve (Hogg et al., 2020, Reimer et al., 2020) based on measurements of ^{14}C from samples of independently known age appropriate to the sampling location; in this study, for example, to the terrestrial environment in the tropical semi-arid monsoonal region of the southern hemisphere. The most widely used technique uses Bayesian statistical chronological models available in different calibration software, such as OxCal, BCal and MatCal. The calibrated radiocarbon age is referred to in calendar years counted backward from 1950, such that 1950 equals 0 cal BP, the time before the nuclear testing (agreed convention based on the publication of the technique by Libby (1961)). The accuracy of a calibrated date is limited by the precision

of the radiocarbon date, the available calibration data and our knowledge of natural variations in ^{14}C (Hajdas et al., 2021).

2.2 Material and Methods

2.2.1 Study area

For this study, two sampling locations were selected:

1. **Outside GS1:** representing the terrestrial non-archaeological open-site sediment deposits expanding south-southwest beyond the GS1 shelter dripline (Figure F2.8), and

2. **Norman River site:** representing a profile of river terraces exposed in a meander bend at the Norman River, approximately 1.6 km south of the GS1.

The role of the Norman River site in this study is subsidiary, to obtain general information about the ages of the terraces and an insight into the timing of changes in river dynamics from which some inferences about hydroclimate can be made. The study area and sampling locations are shown in Figure F2.8 and the sample details are summarised in Table T2.1. Dating samples were collected during fieldwork in 2019 and 2020. Altogether, 15 samples were selected for OSL and 15 for radiocarbon dating. Both OSL and ^{14}C samples were taken at some locations but not in all instances.

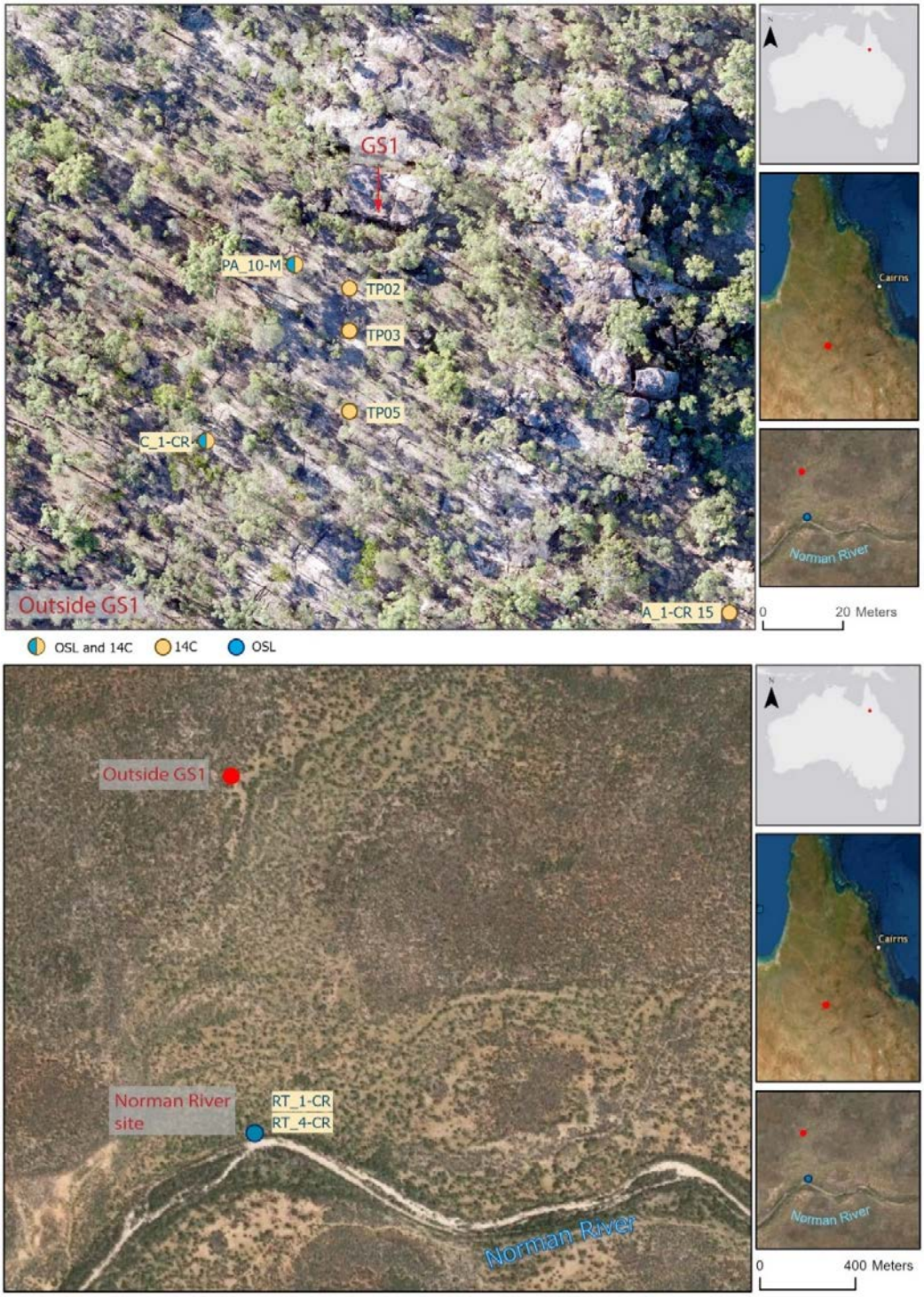

Figure F2.8: The sampling locations. **Top:** Outside GS1 sampling site, mix-coloured circles represent locations where samples were taken for both OSL and ^{14}C analysis (PA_10-M and C_1-CR); the orange circles represent the ^{14}C sampling locations only; the blue circles mark the location where only OSL samples were collected, the red arrow points to the GS1 dripline; on the smaller maps right side the red dot marks the GS1 area. **Bottom:** Norman River site where only OSL samples were collected. The metres scales belong to the main map in both cases.

Table T2.1 Sampling details

Sample ID	Sampling location	Sampling pit face	Depth (cm)	Distance from GS1 dripline (m)	OSL	^{14}C macro-charcoal	^{14}C SPAC	Date of sample collection
PA_10-M 42	pit	NW face	42-43	19	metal tube	individual piece		July 2020
PA_10-M 50	pit	SW face	50-52	"	metal tube			July 2020
PA_10-M 65*	pit	SW face and NE face	65-67	"	metal tube	individual piece		May 2019 and July 2020
PA_10-M 71	pit	SW face	71	"		individual piece		July 2020
PA_10-M 80	pit	SW face	80-82	"	metal tube	individual piece		July 2020
PA_10-M 102	pit	SW face	100-102	"	metal tube		bulk sediment	July 2020
PA_10-M 120	pit	SW face	120-122	"	metal tube		bulk sediment	July 2020
PA_10-M 135	pit	SW face	135-137	"	metal tube			July 2020
PA_10-M 150	pit	SW face	150-152	"	metal tube			July 2020
PA_10-M 160	pit	SW face	160-162	"	metal tube			July 2020
PA_10-M 172	pit	SW face	168-172	"	metal tube		bulk sediment	May 2019
C_1-CR 100	pit	NW face	100	68			bulk sediment	July 2020
C_1-CR 118	pit	SE face	118	"	metal tube			July 2020
C_1-CR 135	pit	SE face	135	"			bulk sediment	July 2020
TP02 40	pit	NA	40	20			bulk sediment	August 2008
TP02 120	pit	NA	120	"			bulk sediment	August 2008
TP03 60	pit	NA	60	30			bulk sediment	August 2008
TP05 60	pit	NA	60	50			bulk sediment	August 2008
TP05 120	pit	NA	120	"			bulk sediment	August 2008
RT_1-CR 124	river terrace - Unit A		124 (from terrace top)	NA	metal tube			July 2020
RT_4-CR 60	river terrace - Unit D		60 (from terrace top)	NA	metal tube			July 2020
A_1-CR 15	auger		109	NA			bulk sediment	July 2020

* three paralel OSL samples were taken for the purpose of reliabilty check

2.2.2 Single-grain OSL dating

2.2.2.1 Sample collection

The study area was initially sampled in May 2019. Based on the preliminary results, financial budget and time constraints, two pits and two river terraces were eventually selected for OSL sampling. The objective was to capture a range of depths in the sediment deposit expanding south from the GS1 dripline (Figure F2.1). The two river terraces were included to obtain general information about the river dynamics, i.e. periods of aggradation vs. incising. Sample collection included (Figure F2.7, Table T2.1):

- Pit PA_10-M, 18.5 m southwest of the GS1 dripline, 12 samples,
- Pit C_1-CR, 68 m southwest of the GS1 dripline, 1 sample, and
- River terraces RT_1-CR, at Norman River 1.6 km south of the GS1 site, 2 samples.

Pit PA_10-M contains homogeneous quartzose sand that constitutes the sandy deposit extending south from the GS1 dripline (Figure F2.8). The pit was selected for OSL dating because it was the deepest pit Outside GS1 at 172 cm deep. The pit C_1-CR contained the same homogeneous quartzose sand and was located the furthest away, 68 m southwest of the GS1 dripline. It was selected to track changes with the

increasing distance from the GS1 dripline. The river terraces constitute four distinguishable units, out of which the topmost (unit A) and the bottommost unit (unit D) were selected for OSL dating (Figure F2.9). An accurate description of Norman River terraces is given in section 1.3.3 (Chapter 1).

Figure F2.9: OSL sample collection. **Top:** pit PA_10-M covered by tarps during sampling and the south profile−holes on the right are from metal tubes. **Middle:** Norman River topmost terrace unit A. **Bottom:** Norman River bottom terrace unit D, the arrow and the circle show the location of the collected OSL samples

OSL samples were collected from the cleaned exposure profile using metal tubes, 2 cm in diameter and ~20 cm in length. The sediment deposits in all cases were uniform, without visible stratification and the tube diameter was chosen with the possibility of very low accumulation rates in mind. During the sampling process the pits were covered with dark tarpaulin and red cling wrap was placed on a head torch to prevent the bleaching of the signal. Once collected, the samples were immediately sealed with light-proof plastic upon extraction. The tubes were filled tight to keep the sediment fill in place and avoid mixing. A 15 ml plastic tube of sediment was collected from each sampling hole for Dr determination.

Table T2.1 provides sample IDs, pit profiles, and depths below the surface. Figure F2.9 shows sample locations from pit PA_10-M's south profile and the Norman River terraces.

2.2.2.2 Sample preparation

All 15 samples were prepared and measured in the OSL dating laboratory at the University of Wollongong in NSW, Australia, following routine optical dating procedures (Aitken, 1998, Wintle, 1997). The sediments all consist of quartzose sand, therefore, quartz grains were used for single-grain OSL dating. The samples were first sieved for a range of sand-sized grain fractions. Quartz grains of 180−212 µm in diameter were recovered and purified using standard procedures. The selected fraction was initially treated with 10% hydrochloric acid (HCl) for carbonate removal and subsequently with 10% hydrogen peroxide (H_2O_2) to remove the organic matter. Sodium polytungstate heavy liquid separation was applied to separate the quartz grains from feldspars.

The quartz grains were then etched using 40% hydrofluoric acid for 45 min to dissolve any remaining feldspar grains present in the quartz separates and remove the α–irradiated layer around each grain surface. After etching, the quartz grains were rinsed in HCl again to remove precipitated fluorides and then sieved again. Finally, the grains were carefully positioned one by one on five aluminium discs, each containing 100 holes, resulting in 500 grains from each sample being measured.

2.2.2.3 Equivalent dose (De) determination

De measurements were made between January and March 2021 using a single-aliquot regenerative-dose (SAR) procedure (Galbraith et al., 1999, Murray and Wintle, 2000, 2003). The SAR procedure involves measuring the OSL signals from the natural dose (Ln−the dose that the sample accrued during burial) and from a series of regenerative doses (Lx−radiation doses administered to the same mineral grain in the laboratory) that adequately bracket the De value. The procedure can be divided into two parts. Initially, an estimate of Ln signal and Lx signals is made. The second part estimates test dose signals Tn and Tx for sensitivity correction. These signals are obtained in the form of an OSL decay curve. Then, the sensitivity-corrected luminescence response for natural (Ln/Tn) and regenerative (Lx/Tx) doses is projected to the response curve to obtain an estimate of De for each quartz grain. A representation of a natural OSL decay curve and a SAR generated dose response curve for De determination is shown in Figure F2.10.

OSL measurements were made on an automated Risø TL-DA-20 luminescence reader equipment with a focused green (532nm) laser for single-grain stimulation (Bøtter-Jensen et al., 2003). Luminescence emissions were detected using an Electron Tubes Ltd 9235QA photomultiplier tube. The OSL signals were

detected through Hoya U-340 filters. Single-grain measurements were made using aluminium discs containing 100 holes, each 300 µm in diameter and 300 µm deep. Irradiations were carried out inside each luminescence reader using $^{90}Sr/^{90}Y$ beta sources that have been calibrated using a range of known gamma-irradiated quartz samples. Spatial variations in beta dose rate to individual grain positions were taken into account for De determination (Ballarini et al., 2006).

Grains were preheated at 260°C for 10 s prior to optical stimulation by an intense, green (532 nm) laser beam for 2 s at 125°C, with laser power set to 90%. A fixed test dose (~9 Gy), preheated at 160°C for 5 s, was given to each natural and regenerative dose, and the induced OSL signals (Tn and Tx) were used to correct for any sensitivity changes during the SAR sequence. A duplicate regenerative dose was included in the sequence to check on the adequacy of this sensitivity correction and a 'zero regenerative dose' (0 Gy) measurement cycle was included to monitor the extent of any 'recuperation' induced by the preheat treatment. To check the possible contamination of the acid-etched quartz grains by other mineral inclusions, the OSL IR depletion ratio test was applied (Duller, 2003) to each grain at the end of the SAR sequence, using an infrared exposure of 40 s at 50°C.

Ln, Lx, Tn and Tx values were estimated from the first 0.22 s of OSL decay, with the mean count recorded over the last 0.3 s subtracted as background. Sensitivity-corrected (Lx/Tx) dose response curves were constructed from the Lx and Tx OSL signals, using a general-order kinetic (GOK) function (Guralnik et al., 2015). The sensitivity-corrected natural OSL signal (Ln/Tn) was then projected on to the fitted dose response curve to obtain the De by interpolation (Figure F2.10). All data analyses, including curve fitting, De determination and error estimations, were achieved using the functions implemented in the R-package 'numOSL' (Peng et al., 2013).

Not every grain yields useful information on absorbed dose (Jacobs and Roberts, 2007). Most grains have inherent luminescence properties that make them unsuitable. The latter are identified based on known characteristics and rejected. A series of quality-assurance criteria (Jacobs et al., 2006a, Li et al., 2017) have been developed to identify and reject such grains objectively, ensuring all accepted grains provide reliable estimates.

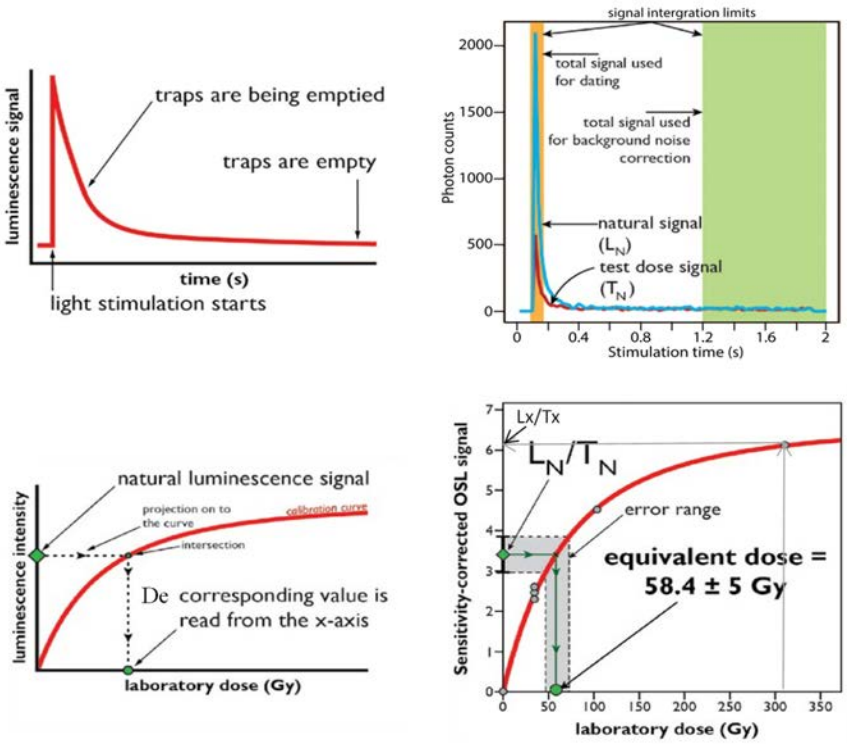

Figure F2.10: OSL decay and response curves. **Top:** a typical OSL decay curve. Note the representation of Ln and Tn signal on the right explanatory graph. **Bottom:** a representation of the dose-response curve or calibration curve for a single-grain of quartz De estimation. Note, the final De is estimated by projecting the natural luminescence signal (green square, Ln/Tn) onto this curve and the corresponding value is read from the x-axis. The calibration curve is constructed from a series of known radiation doses (Lx) and test doses (Tx) administered to the same mineral grain in the laboratory. (adopted from: Jacobs et al., 2022)

2.2.2.4 Environmental dose rate (Dr) determination

To calculate an OSL age, it is assumed that the present-day radionuclide activities and dose rates have prevailed throughout the period of sample burial at each sampling location. For Dr measurements, we used the separate samples collected into 15 ml plastic tubes from the holes' walls left after removing metal tubes.

The beta dose rate commonly contributes most of the total dose rate (Roberts et al., 2015). Beta particles can penetrate up to ~3 mm through sediment (Figure F2.2), so their ionising radioactivity can substantially affect on the calculated Dr over small distances. Inductively-coupled plasma mass spectrometry (ICP-MS) was used to measure the uranium (^{238}U, ^{235}U) and thorium (^{232}Th) content, combined with inductively coupled plasma optical emission spectroscopy (ICP-OES) to measure the potassium (^{40}K) content (Preusser et al., 2008, Roberts et al., 2015). The method measures the individual

radionuclide concentrations and converts them to dose rates using well-established conversion factors (Preusser et al., 2008, Roberts et al., 2015).

The external alpha dose rate contribution was made negligible by etching away the alpha-irradiated outer rim (see section 2.2.2.2 Sample preparation) and the internal alpha dose from inclusions inside the quartz grains is generally so low that it was assumed negligible.

Cosmic radiation typically accounts for only a small fraction of the total dose rate (Roberts et al., 2015). It was calculated following Prescott and Hutton (1994) and adjusted for geomagnetic longitude, latitude, altitude, depth, and sediment density (assumed to be 1.8 g/cm^3). The beta, gamma, and cosmic-ray dose rates were adequately corrected for long-term water contents.

2.2.3 Radiocarbon dating

2.2.3.1 Sample collection

Only the Outside GS1 sampling site was selected for radiocarbon dating. Samples were collected on different fieldwork occasions, first in August 2008 by Wallis's team and later in May 2019 and July 2020 by Zega's team (Table T2.1). Samples for radiocarbon dating were obtained to isolate two different fractions: the macro-charcoal, where macroscopic particles (>0.5 cm) were collected individually, and the collection of bulk sediment for dating of SPAC (Figure F2.11, Table T2.1). Sampling locations include (Figure F2.8, Table T2.1):

- Pit PA_10-M, 18.5 m southwest of the GS1 dripline, 7 samples (4 macro-charcoal and 3 bulk samples),
- Pit TP02, 20 m south of the GS1 dripline, 2 bulk samples,
- Pit TP03, 30 m south of the GS1 dripline, 1 bulk sample,
- Pit TP05, 50 m south of the GS1 dripline, 2 bulk samples,
- Pit C_1-CR, 65 m southwest of the GS1 dripline, 2 bulk samples, and
- Auger hole A_1-CR 15, 150 m southeast of GS1 dripline under the escarpment, 1 bulk sample.

Macro-charcoal samples (Table T2.1) were photographed in-situ and documented (Figure F2.11). They were then carefully extracted from the profile, wrapped in aluminium foil and placed in plastic tubes. Bulk sediment samples were collected in plastic bags. All bags and tubes were labelled and securely packed for transportation to the laboratory facilities.

Figure F2.11: Documentation and collection samples for radiocarbon dating. **Top left:** macro-charcoal as found in the west profile of pit PA_10-M. **Top right:** macro-charcoal, white cover marks the position of OSL tube. **Bottom left:** macro-charcoal samples sent for dating. **Bottom right:** bulk sediment samples.

2.2.3.2 Laboratory methods

2.2.3.2.1 Sample pretreatment

Charcoal, due to its large surface area and porous nature, is a sorbent for a range of organic and inorganic compounds. In a natural terrestrial environment, contamination may happen through exposure to soil or sediment solutions containing organic compounds, such as carbohydrates, amino acids, phenolics (Pietikäinen et al., 2000) and microbial colonisation (Zackrisson et al., 1996) and the exchange with carbonates (Demeyer et al., 2001, Hatté et al., 2001).

For macro-charcoal, the pretreatment techniques, such as acid-base-acid (ABA) and acid-base oxidation (ABOX), focus removing contaminants that can be bound to external and internal surfaces (e.g. Alon et al., 2002, Bird et al., 1999a, 1999b, De Vries and Barendsen, 1954, Gillespie et al., 1992, Hatté et al., 2001). In contrast, SPAC is molecular-scale fraction that cannot be physically separated from other particles, hence, hydrogen pyrolysis (hypy) technique centres isolating SPAC from other organic matter in a sedimentary matrix and its subsequent quantification (e.g. Ascough et al., 2009, 2010, Bird, 2007, Conedera et al., 2009, Hammes et al., 2007, Masiello, 2004, Meredith et al., 2012, Schmidt et al., 2001, Wurster et al., 2012, 2013).

This study used the ABA pretreatment to process four macro-charcoal samples (Figure F2.12). The samples were cleaned and washed in 1M HCl at 80°C for 1 hr; 1M NaOH at 80°C for 30 mins; 1M HCl at 80°C for 1hr; 80°C, MilliQ™ water for 5 mins (pH>5), sonicated, then dried at 80°C. The supernatant was removed after each step by pipette. The chemical concentrations, number of NaOH treatments (which continues until the colour is no longer transferred from the sample to the liquid), temperature and length of pretreatment will vary depending on the quantity and condition of the sample.

To eliminate other carbon compounds in the bulk sediments and keep the SPAC fraction only, the SPAC samples were pre-treated using hypy (Figure F2.12). The procedure was performed at the Advanced Analytical Centre, James Cook University, Cairns, Australia. Hypy is an established method for PyC analysis (Ascough et al., 2009, Wurster et al., 2012, 2013, 2021). The technique works in the temperature range of 500–560°C to convert most organic matter to volatile products, which enables rapid isolation and quantification of SPAC in the sample (Bird et al., 2015). Samples were first sieved at 425 µm. Due to the low PyC content of all samples, heavy liquid floatation was applied to increase the micro-PyC mass content needed for AMS (> 0.3 mg). Approximately 250 mg of the sediment was mixed with a Mo catalyst using an aqueous methanol solution of ammonium dioxydithiomolybdate, sonicated and dried at 60°C overnight. The catalyst weight was ca. 10% of the sample weight, which gave a nominal loading of 1% Mo. The insert sample/catalyst mixture was placed in a reactor, pressurized with H_2 to 150 bar with a purge gas flow of 5 L min^{-1} and heated at 300°C min^{-1} to 250°C and then at 8°C min^{-1} to final 550°C, held for 5 min. Labile carbon is removed during the hypy reaction, and the remaining carbon is composed of a stable form with greater than seven condensed aromatic rings, referred to as SPAC (Bird et al., 2015, Wurster et al., 2013, 2015), which was then used in AMS analysis.

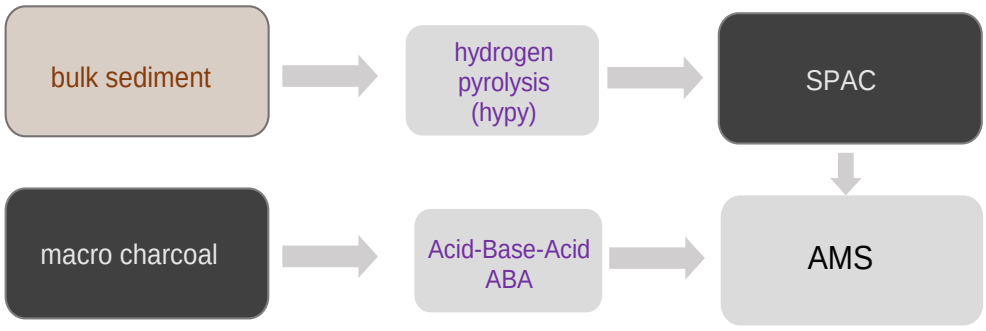

Figure F2.11: Carbon fractions and corresponding pretreatment techniques

2.2.3.2.2 AMS procedure

AMS radiocarbon age determinations on macro-charcoal and SPAC were undertaken at the University of Waikato Radiocarbon Dating Laboratory, New Zealand. The AMS Processing Technical Report (Waikato Radiocarbon Dating Laboratory, 2017) provides a detailed step-by-step report on the applied procedure and instruments. The lab reported 14C precision uncertainties (~±15 at Modern) including contributions from the normalizing standards, the background subtraction, the scatter in the repeated runs on each sample, and counting statistics.

2.2.3.2.2 Calibration

All samples were calibrated to calendar years (cal BP) using the OxCal Program (https://c14.arch.ox.ac.uk/oxcal.html) and the northern calibration curve IntCal20 (Reimer et al., 2020), with 0 calibrated years before present representing 1950 AD. The northern hemisphere calibration was chosen due to the influence of northern hemisphere air masses on the tropical north of Australia, when the Inter Tropical Convergence Zone (ITCZ) moves southwards during the Australian-Indonesian summer monsoons, resulting in cross-equatorial air flow into northern Australia from the northern hemisphere (Hogg et al., 2020). Although the study area is located slightly south of the current ITCZ, its position has been changing over time and it is rather unclear where to place the zonal boundaries at different times in the past. Therefore, the choice of calibration curve remains a matter of individual research decision.

2.3 Results

2.3.1 Single-grain OSL dating

The OSL dating results are presented in Table T2.2. The statistical models used to calculate the optical ages and estimates of over-dispersion (OD) are also included. The distribution of De estimated values for all 15 samples are displayed as radial plots (Galbraith, 1988) in Figure F2.13. The number of grains accepted and the applied models are also shown on the plots.

In radial plots, each point represents a single quartz grain for which a De value can be read by extending a horizontal line from the 'Standardised estimate' axis on the left side across the point to intersect the radial axis on the right. The uncertainty of this estimate is shown in the form of relative standard error in % and precision by extending a vertical line from the point to intersect the horizontal axis at the bottom of the plot. In such plots, the most precise estimates fall to the right and least precise to the left. The label 'N' stands for the number of quartz grains accepted after applying the rejection criteria.

In single-grain OSL dating, it is common for the data to spread due to the natural variability of mineral grains and other complicating factors, such as random errors, which affect measurements in unpredictable ways (Jacobs et al., 2022). Over-dispersion (OD), also denoted as σ_b, is used to quantify the degree of the spread present in a De distribution of a sample. OD is usually expressed as a percentage and refers to the relative standard deviation of the distribution of true De values from a central De value after accounting for various measurement uncertainties (Galbraith and Roberts, 2012, Galbraith et al., 2005). The OD value on its own, however, does not say anything about the pattern of a De distribution. Instead, a high over-dispersion value (>20%) indicates the possible reasons for the additional scatter should be investigated (Jacobs et al., 2022). Hence, OD is applied in combination with De distribution patterns and knowledge of the context (Jacobs and Roberts, 2007).

The radial plots of most samples exhibit significant scatter in the estimated De values (Figure F2.13). The OD values calculated using the central age model (CAM, Galbraith et al., 1999–further explanation given below) range between 67±6% (sample PA_10-M_135-137) and 134±12 % (sample RT_4-CR) (Table T2.2), well above the global average for fully bleached and undisturbed single-grain De datasets (20±1%; Arnold and Roberts, 2009). To obtain more information about possible reasons for the additional scatter, three statistical modelling approaches were used:

1. nMAD CAM was applied where there is a clear cluster of ages that make up the main population of grains with a few discrete outliers (Figure F2.13B,C,D,E,G,H,I,J N,O). Statistical outliers were identified using the 'Normalised median absolute deviation' (nMAD) method (Rousseeuw and Croux, 1993, Rousseeuw et al., 2006), shown in the radial plots as open triangles. The remaining values, shown as filled circles, were then combined using the weighted mean by applying the 'Central age model' (CAM) of Galbraith et al. (1999). The CAM assumes that the De estimates for all grains are centred on some average value of De and the estimated standard error takes account of any over-dispersion. This weighted mean estimate of the burial dose is usually similar to the median or geometric mean.
2. FMM, the 'Finite mixture model' (FMM) of Roberts et al. (2000) was used where discrete components were present (Figure F2.13F,K) and post-depositional mixing was identified as the most likely reason for over-dispersion. To run the FMM it is necessary first to tell the model how many mixing components you think there may be and what the OD of each of these components might be. To do this, we used a standard statistical test combination of 'maximum log likelihood' and 'Bayes Information Criterion' (Jacobs et al., 2022). Once the optimum components and the OD were determined, the FMM estimated the weighted average of each component using CAM at a

predetermined OD (σ_b in the radial plots). These models are complicated but have been shown to work successfully in composite datasets (David et al., 2007, Jacobs et al., 2006b, 2008, 2011, Sivia et al., 2004).

3. MAX, CAM and MAM, the 'Maximum age model' (MAX) and 'Minimum age model' (MAM) were used along with the 'Central age model' (CAM) where the spread was very broad and no clear target population was visible (Figure F2.13A,C,D,L,M). An estimate of over-dispersion must be added to the relative standard error of each De value prior to running any of the three models. The MAX age model has not been used much (Jacobs et al., 2022) and it is most appropriate for estimating the burial dose of sediment samples thought to contain grains bleached after burial. If we assume a normal (Gaussian) distribution of De values, the MAX age model assumes that the highest population of De values represents grains that have not been bleached after burial (Jacobs and Roberts, 2007, Olley et al., 2006). Opposite, the MAM is usually applied when insufficient or heterogeneous bleaching is thought to cause over-dispersion of single-grain De values (Arnold et al., 2009, Galbraith et al., 1999). This model assumes that the lowest population of De values represents those grains completely bleached before deposition.

Table T2.2 (Age [ka]) provides the final De values determined using these approaches. OSL age estimates considered to be most reliable are shown in bold. Uncertainties on the ages are given at 1σ (the standard error of the mean) and were calculated by combining, in quadrature, all known and estimated sources of random and systematic error. The calculated nMAD CAM OD values after rejecting outliers using nMAD vary between 20−69 % (Table T2.2−provided in parentheses next to OD values).

Table T2.2 OSL results

No.	Sample ID	Depth	Grain size	Water	Dose rate - Dr (Gy/kyr)			Total Dr	De	Procedure	Model	OD	Age
		(cm)	(μm)	(%)	Beta	Gama	Cosmic		(Gy)			(%)	(ka)
1	PA_10-M 42	42-43	180-212	3 ± 1 (1)	0.27 ± 0.01	0.37 ± 0.01	0.212	0.87 ± 0.04	7.6 ± 1.1	SAR (Q)	CAM	127 ± 10	8.7 ± 1.3
									1.1 ± 0.2		MIN		**1.2 ± 0.2**
									48.9 ± 7.2		MAX		55.9 ± 8.6
2	PA_10-M 50	50-52	180-212	3 ± 1 (1)	0.26 ± 0.01	0.36 ± 0.01	0.211	0.87 ± 0.04	1.8 ± 0.1	SAR (Q)	nMAD CAM	87 ± 8 (43)	**2.0 ± 0.2**
3	PA_10-M 65.7/1*	65-67	180-212	3 ± 1 (1)	0.27 ± 0.02	0.42 ± 0.02	0.21	0.92 ± 0.06	2.96 ± 0.15	SAR (Q)	nMAD CAM	72 ± 5 (46)	**3.2 ± 0.3**
4	PA_10-M 65.7/2*	65-67	180-212	3 ± 1 (1)	0.28 ± 0.02	0.47 ± 0.05	0.21	0.99 ± 0.06	2.56 ± 0.14	SAR (Q)	nMAD CAM	79 ± 6 (51)	**2.6 ± 0.2**
5	PA_10-M 65-67*	65-67	180-212	3 ± 1 (1)	0.27 ± 0.01	0.37 ± 0.01	0.209	0.89 ± 0.04	2.5 ± 0.2	SAR (Q)	nMAD CAM	79 ± 7 (65)	**2.9 ± 0.3**
6	PA_10-M 80	80-82	180-212	3 ± 1 (1)	0.26 ± 0.01	0.37 ± 0.01	0.207	0.87 ± 0.04	3.4 ± 0.2	SAR (Q)	FMM-1 (78%)	76 ± 6 (33)	**3.9 ± 0.3**
									16.9 ± 1.6		FMM-2 (22%)		19.4 ± 2.1
7	PA_10-M 102	100-102	180-212	3 ± 1 (1)	0.25 ± 0.01	0.33 ± 0.01	0.204	0.81 ± 0.04	5.9 ± 0.3	SAR (Q)	nMAD CAM	75 ± 6 (38)	**7.3 ± 0.5**
8	PA_10-M 120	120-122	180-212	3 ± 1 (1)	0.29 ± 0.01	0.41 ± 0.02	0.202	0.94 ± 0.04	10.1 ± 0.5	SAR (Q)	nMAD CAM	78 ± 7 (34)	**10.8 ± 0.7**
9	PA_10-M 135	135-137	180-212	3 ± 1 (1)	0.31 ± 0.01	0.41 ± 0.02	0.2	0.95 ± 0.04	12.5 ± 0.7	SAR (Q)	nMAD CAM	67 ± 6 (44)	**13.2 ± 0.9**
10	PA_10-M 150	150-152	180-212	3 ± 1 (1)	0.29 ± 0.01	0.40 ± 0.02	0.198	0.92 ± 0.04	11.7 ± 1.3	SAR (Q)	nMAD CAM	116 ± 12 (69)	**12.7 ± 1.5**
11	PA_10-M 160	160-162	180-212	3 ± 1 (1)	0.35 ± 0.01	0.47 ± 0.02	0.196	1.04 ± 0.04	12.0 ± 1.1	SAR (Q)	FMM-1 (54%)	96 ± 7 (39)	**11.5 ± 1.2**
									35.9 ± 4.6		FMM-2 (28%)		34.5 ± 4.6
									2.5 ± 0.4		FMM-3 (18%)		2.4 ± 0.4
12	PA_10-M 172	168-172	180-212	3 ± 1 (1)	0.33 ± 0.02	0.51 ± 0.05	0.195	1.07 ± 0.06	15.6 ± 1.4	SAR (Q)	CAM	84 ± 6	**14.6 ± 1.5**
									4.10 ± 0.45		MIN		3.8 ± 0.5
									54.4 ± 6.1		MAX		50.9 ± 6.4
13	C_1-CR 118	118-120	180-212	3 ± 1 (1)	0.27 ± 0.01	0.38 ± 0.01	0.2	0.89 ± 0.04	4.4 ± 0.06	SAR (Q)	CAM	105 ± 9	4.9 ± 0.7
									1.4 ± 0.02		MIN		1.6 ± 0.2
									11.9 ± 1.6		MAX		**13.5 ± 1.9**
14	RT_1-CR 124	124	180-212	3 ± 1 (1)	0.48 ± 0.02	0.51 ± 0.02	0.2	1.22 ± 0.04	13.2 ± 0.3	SAR (Q)	nMAD CAM	75 ± 5 (20)	**10.9 ± 0.5**
15	RT_4-CR 60	60	180-212	3 ± 1 (3)	0.39 ± 0.01	0.35 ± 0.01	0.15	0.92 ± 0.03	36.4 ± 1.2	SAR (Q)	nMAD CAM	134 ± 12 (22)	**39.7 ± 2.1**

* Paralel samples **B -** most probable age estimates, based on the context, comparison and age depth model are marked in bold

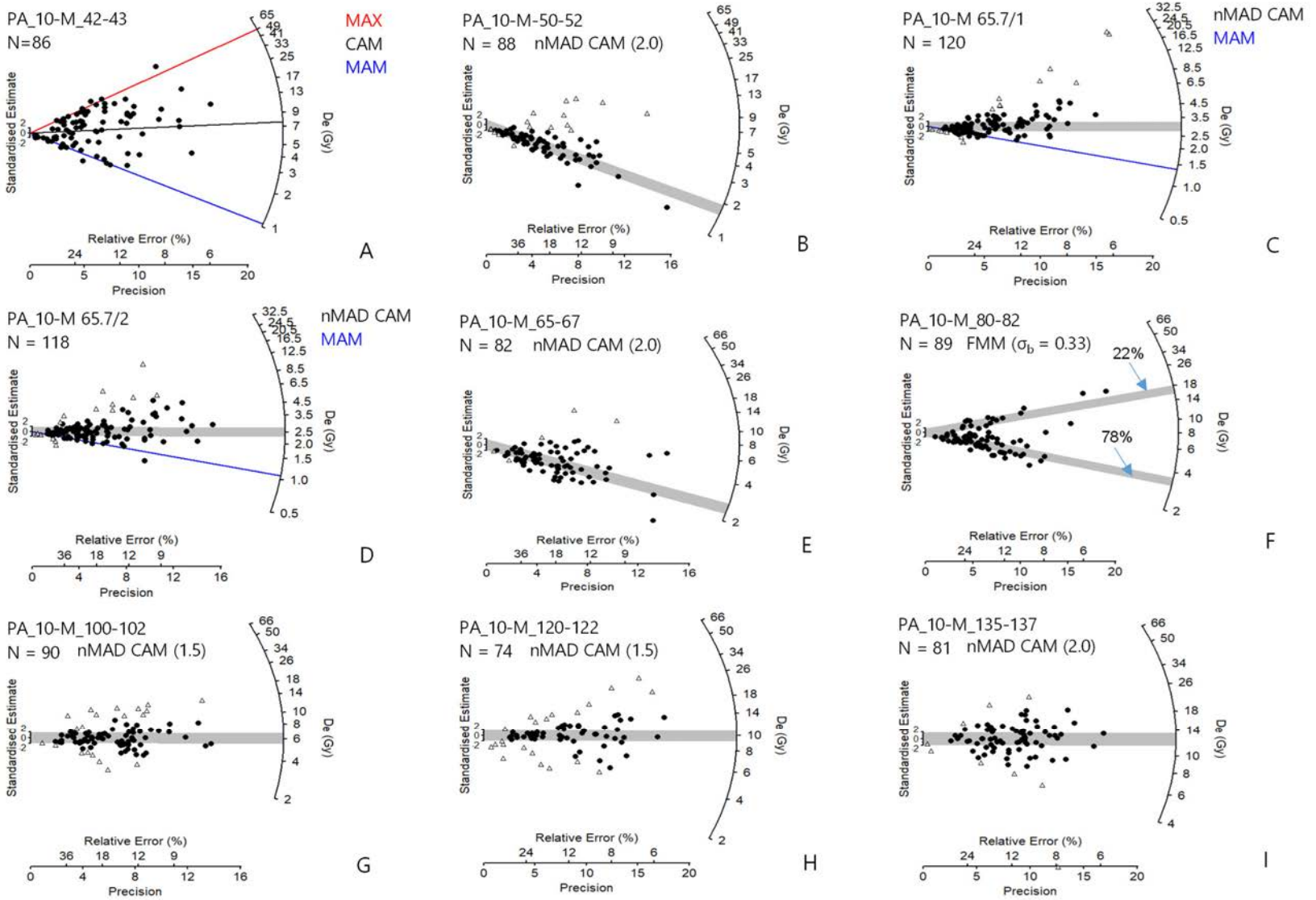
PA_10-M_42-43
N=86
MAX
CAM
MAM
A
PA_10-M-50-52
N = 88 nMAD CAM (2.0)
B
PA_10-M 65.7/1
N = 120
nMAD CAM
MAM
C
PA_10-M 65.7/2
N = 118
nMAD CAM
MAM
D
PA_10-M_65-67
N = 82 nMAD CAM (2.0)
E
PA_10-M_80-82
N = 89 FMM (σb = 0.33)
22%
78%
F
PA_10-M_100-102
N = 90 nMAD CAM (1.5)
G
PA_10-M_120-122
N = 74 nMAD CAM (1.5)
H
PA_10-M_135-137
N = 81 nMAD CAM (2.0)
I
Standardised Estimate
De (Gy)
Relative Error (%)
Precision

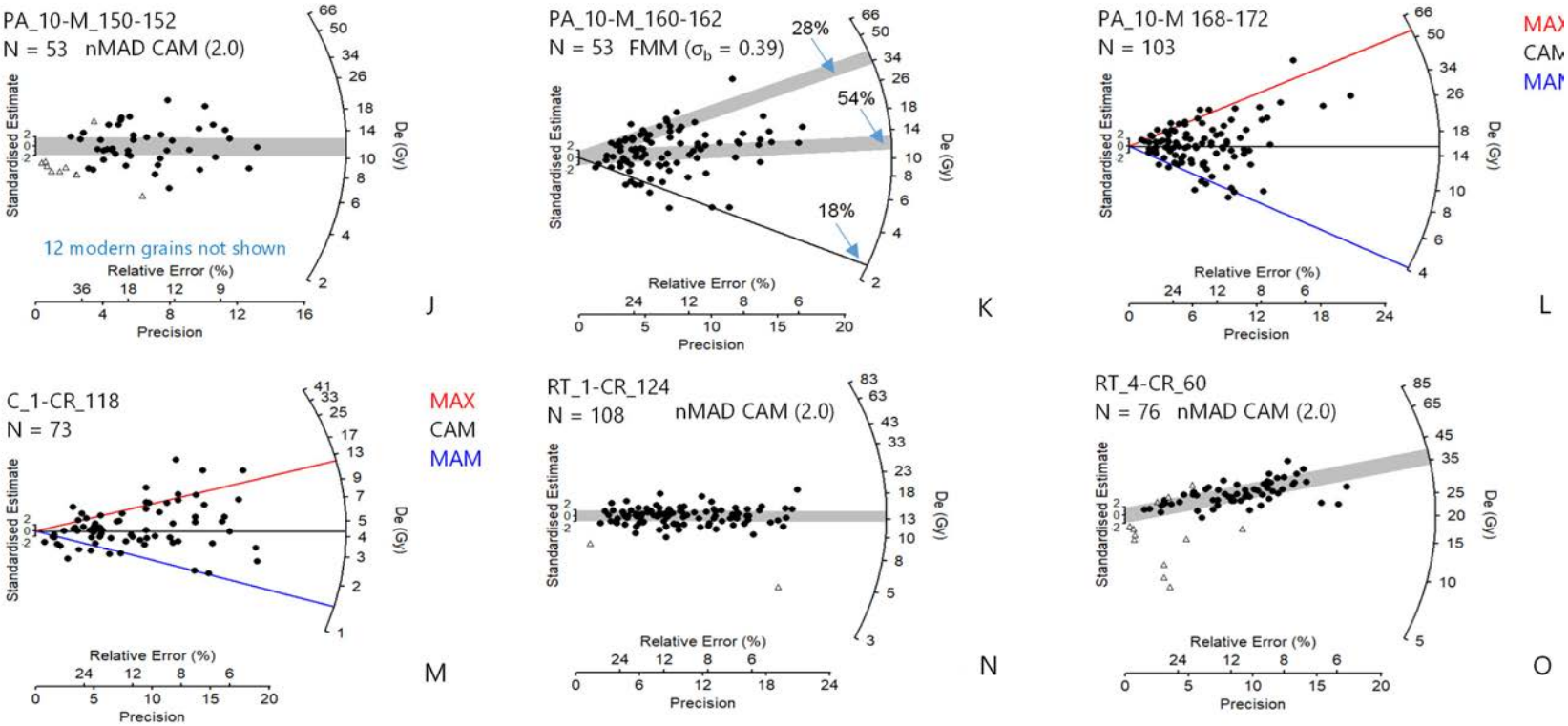

Figure F2.13: De distribution radial plots. The sample ID and the number of accepted grains (N) are in the top right of each plot, the applied models are given either next to N or in the top left. Filled circles mark the measured grains included in the final age estimation, open triangles mark the statistical outliers identified by nMAD model and excluded from the final age estimation. The ±1σ uncertainties are shown as a grey ribbon and a small vertical scale (2-0-2) in the middle left of the plots. Relative error (%) and precision are shown at the bottom of each plot. Note: (J) the '12 modern grains not shown' indicates zero or negative De values that cannot be shown on a radial plot.

The final OSL chronology of the analysed sediment profiles is shown in Figure F2.14 and is summarised as follows:

- Pit PA_10-M (Table T2.2, Figure F2.13 A−L, Figure F2.14a, Figure F2.8 top)

After modelling, the OSL age estimates from the pit PA_10-M showed a time span from the late Holocene, 2 ka in the upper 50 cm of the profile, to late Pleistocene >12 ka in the deeper parts (130–172 cm).

For the upper most sample, depth 42–43 cm and in the bottommost samples at depths 160–162 cm and 170–172 cm the OSL dates were inconclusive, even after modelling; Sample ID: PA_10-M_42-43, PA_10-M_160-162 and PA_10-M_170-172 (Table T2.2, Figure F2.13A,K,L). The De estimates of these three samples ranged from 1.2±0.2 to 55.9±8.6 ka (at depth 42–43 cm) and from 2.4±0.4 to 50.9±6.4 ka (at depths 160–162 cm and 168–172 cm). Quartz grains older than 50 ka were present in the top and bottom of the pit profile, along with grains younger than 2 ka and those aged between the two extremes. The most reliable dates of these samples, marked bold in Table T2.2, were chosen based on the depositional context and by correlation with other age estimates in the profile.

The results for sample PA_10-M_80-82, collected at depth 80–82 cm (Figure F2.13F, Table T2.2) indicated post-depositional mixing with two distinct populations of quartz grains after applying the FMM; 78% of grains belonging to a younger population 3.9±0.3 ka and 22% grains accounting for an older population age of 19.4±2.1 ka.

- Pit C_1-CR (Table T2.2, Figure F2.13M, Figure F2.14b, Figure F2.8 top)

Only one sample, at depth 118 cm, was used for OSL dating from this pit. The results show a fair amount of scatter, which is why MAX, CAM an MAM modelling were applied. The De distribution remained inconclusive even after modelling (Figure F2.13M). The most probable OSL age estimate (13.5±1.9 ka, Table T2.2) is, however, in good agreement with the OSL age from the pit PA_10-M at the same depth.

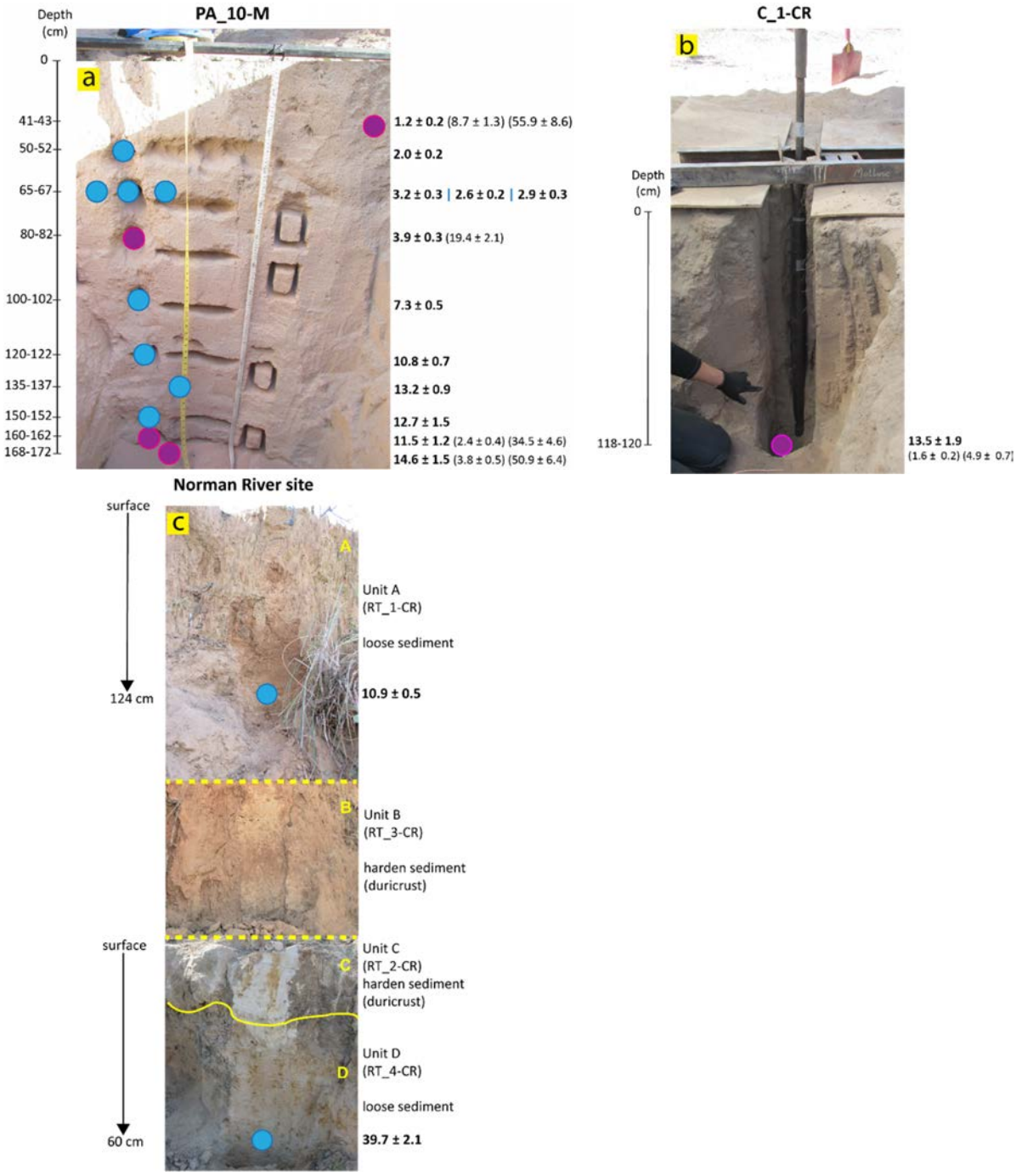

Figure F2.14: OSL chronology results from sediment sequences in this study: **a)** Pit PA_10-M, **b)** Pit C_1-CR, **c)** Norman River site. Depths are given on the left, OSL ages are given on the right in ka. Locations where OSL samples were collected are shown as blue and purple circles. Blue circles represent samples that gave more reliable ages after statistical modelling, purple circles are samples where the results remained inconclusive. For the latter, the more probable ages are given in bold, while other age spans are given in brackets. Figure c) was adjusted to show the whole sequence of Norman River terraces; the thick dashed yellow line marks the constructed boundary between units B and C for the purpose of presentation and the smooth yellow line marks the real boundary between units C and D as seen in the natural profile.

- Norman River site samples: RT_1-CR and RT_4-CR (Table T2.2, Figure F2.13N,O, Figure F2.14c, Figure F2.8 bottom)

The oldest age of 39.7±0.7 ka was estimated for the sample RT_4-CR 60 (Figure F2.13O), representing the Norman River bottom terrace (unit D) (Figure F2.14c). The topmost unit A showed an age estimate of 10.9±0.5 ka (Figures F2.13N, F2.14c), consistent with the Pleistocene–Holocene transition. Samples were collected from the lowest and the topmost terraces to provide a time frame for deposition at the currently exposed terraces.

2.3.2 Radiocarbon dating

A total of 15 radiocarbon dates were obtained from five pits and one auger hole from 12 different depths Outside GS1 (Figure F2.8 top). Four dates were measured on macro-charcoal and the reminder on SPAC. The results are shown in Table T2.3 and Figure F2.15.

The calibrated ages of the four macro-charcoal samples ranged from 2247±90 to 4064±81 cal BP at corresponding depths of 42 cm and 71 cm (Table T2.3, Figure F2.15). In general, the ^{14}C ages obtained from macro-charcoal samples showed a good alignment with the OSL ages obtained from the same depths in the same pit PA_10-M profile.

The calibrated ages of the 11 SPAC samples exhibited ages that ranged between 1474±61 and 5243±194 cal BP (Table T2.3, Figure F2.15). In general, the ^{14}C ages obtained from SPAC did not show a good alignment, not within the same pit, nor between different pits (Figure F2.15). A comparison of the ^{14}C ages of SPAC with those from macro-charcoal indicated no distinctive correlation pattern between the two. However, the inconsistency between the results of the two charcoal fractions seems to increase with the distance from the GS1 dripline (Figure F2.15). Additionally, the oldest ^{14}C age obtained was 5243±194 cal BP from sample C_1-CR 100 at a depth of 100 cm (Table T2.3, Figure F2.15), which is significantly younger compared to the oldest OSL age estimate (14,600±1500, Table T2.2) obtained at Outside GS1 sampling site.

Table T2.3 Radiocarbon dating results

Sample ID	Depth (cm)	Sample origin	%C	Conventional ^{14}C dates (BP)	Calibrated age (cal BP)	Loaded weight (mg)
PA_10-M 42	42	macro charcoal	67.87	2247 ± 19	2247 ± 90	4.0
PA_10-M 65	65.7	macro charcoal	66.48	3366 ± 26	3591 ± 99	3.4
PA_10-M 71	71	macro charcoal	67.68	3715 ± 20	4064 ± 81	4.6
PA_10-M 81	81	macro charcoal	59.33	3538 ± 20	3807 ± 85	4.2
PA_10-M 102	100-102	SPAC	0.78	3312 ± 16	3525 ± 44	100.0
PA_10-M 120	120-122	SPAC	2.28	2912 ± 15	3058 ± 92	26.0
PA_10-M 172	168-172	SPAC	0.45	3899 ± 60	4334 ± 183	32.0
A_1-CR 15	109	SPAC	1.64	1921 ± 15	1817 ± 72	25.0
C_1-CR 100	100	SPAC	0.52	4553 ± 41	5234 ± 194	36.0
C_1-CR 135	135	SPAC	0.54	2883 ± 84	3051 ± 268	15.0
TP02 40	40	SPAC	0.56	2667 ± 15	2796 ± 45	80.0
TP02 120	120	SPAC	0.54	4130 ± 16	4675 ± 140	105.0
TP03 60	60	SPAC	2.28	3502 ± 14	3768 ± 68	30.0
TP05 60	60	SPAC	1.35	2365 ± 15	2383 ± 42	67.0
TP05 120	120	SPAC	0.76	1609 ± 15	1474 ± 61	118.0

The SPAC age result from test auger hole A_1-CR 15 was 1817±72 cal BP at a depth of 109 cm (Figure F2.15). This auger hole was placed in a former tributary channel of the Norman River (Smart, 1973), located east and underneath the escarpment where the GS1 has formed (Figure F2.8 top). The location was selected in an attempt to obtain additional chronologic control for the area of study. The plan was to excavate a pit after the auger hole. The location, however, was unsuitable for a pit, owing to the presence of many fresh roots and large rocks within a depth of a few tens of centimetres. Thus, we could not pursue this attempt any further in the time available.

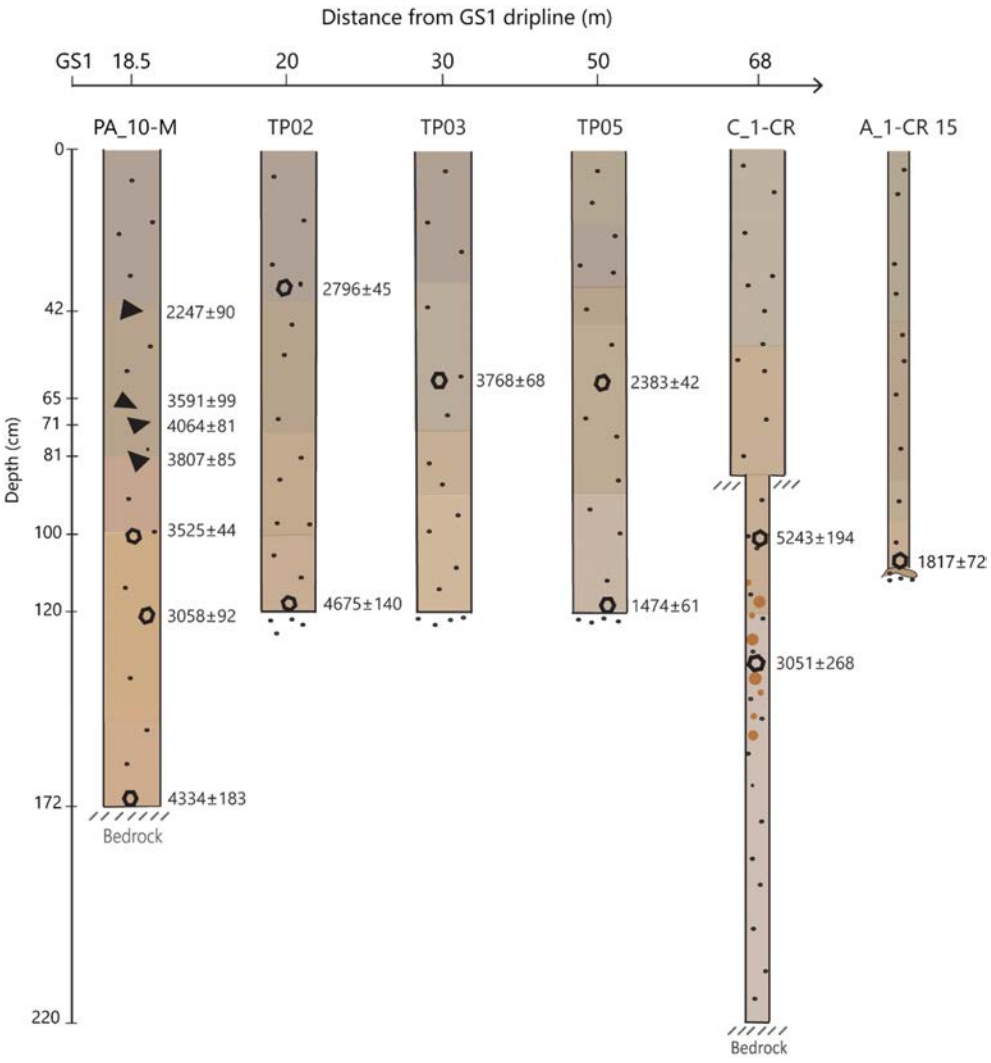

Figure F2.15: Radiocarbon dating results from sediment sequences in selected pits and auger hole. Four macro-charcoal samples are shown as black triangles, SPAC samples are shown as black rings. Reddish-orange circles represent iron-oxides found in bulk sediment samples. Calibrated radiocarbon dates (cal BP) are given on the left side of the pits, depths are given on the right. Depths are in proportion, distances from the GS1 dripline are informative. The narrowing of C_1-CR at depth 85 cm represents the transition from pit to core (see Chapter 1 for details).

2.3.3 Age-depth model

An age-depth model was constructed using the *rbacon* software package with Bayesian statistics (Blaauw and Christen, 2011). The model was built using the twelve most reliable OSL age estimates and the four macro-charcoal radiocarbon dates from profile PA_10-M demonstrating good overall consistency (Table T2.2 in bold, Table T2.3). The age-depth model was produced by 9.46 million Markov Chain Monte Carlo (MCMC) iterations with prior information: accumulation (acc.) shape=1.5 and acc. mean=100 for the

gamma distribution. Age modelling was run to achieve a 1 cm final resolution and was further used for calculating the cm/ka sedimentation rate.

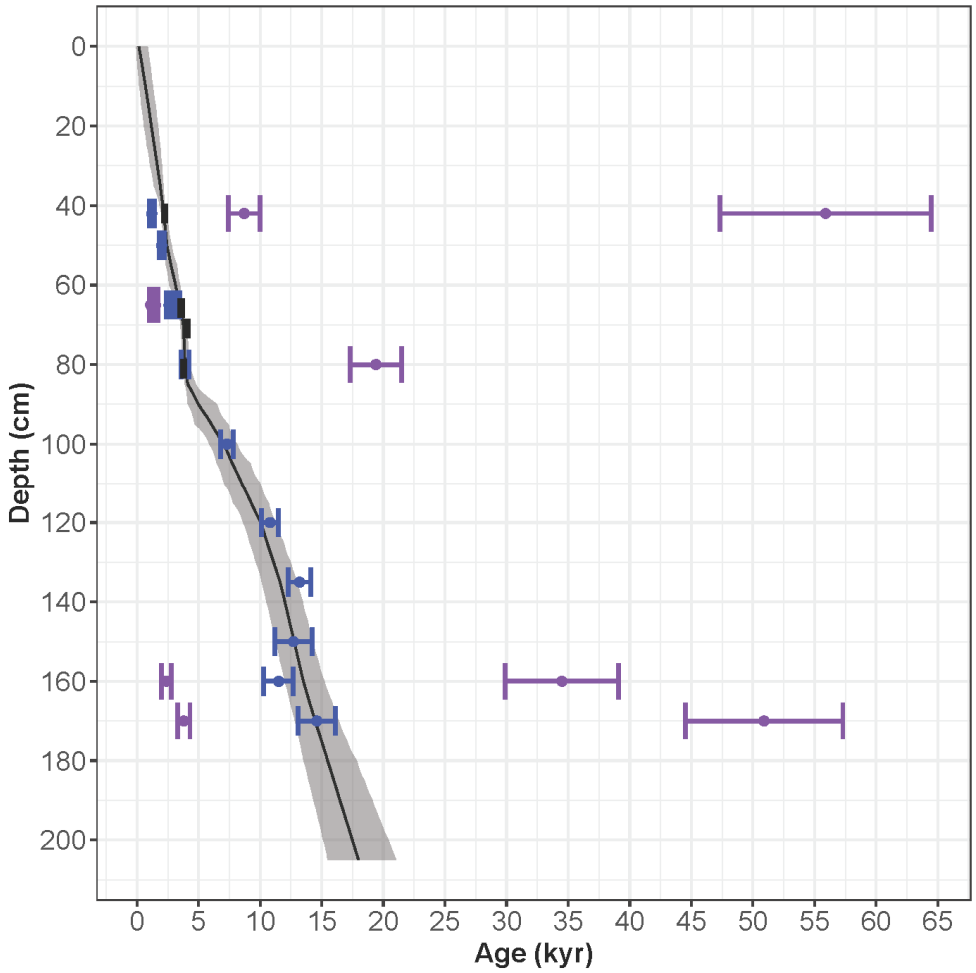

Figure F2.16: Age-depth model from the PA_10-M pit profile constructed using Bayesian age modelling with rbacon package in R. The 12 OSL age estimates are shown in blue and the 4 macro-charcoal radiocarbon dates are shown as black bars. kyr=ka. Purple bars (outliers) represent the younger and older grain populations in those OSL samples that were inconclusive.

2.4 Discussion

2.4.1 OSL evidence

The OSL evidence indicates that the sand deposit Outside GS1 (Figure F2.1 dashed circle) has been accumulating for at least 15 ka. Sediments derive from weathering of the Jurassic Hampstead sandstone that forms the outcrops, escarpments and exposed bedrock in the area (Chapter 1, section 1.4.1). The

overdispersion (OD) of De distributions, shown as scatter on radial plots (Figure F2.13), suggests a dynamic deposition history. Statistical models were applied to reduce the OD (section 2.3.1), which did not produce a satisfactory result for five samples, shown as purple circles in Figures F2.14a,b and F2.17. This further indicates a dynamic environment where post-depositional mixing takes place.

In addition, substantially older quartz grains, with luminescence signals above 30 ka and above 50 ka, were present in the majority of the OSL samples collected Outside GS1. The contributing sediment pool to the profile must, therefore, at least in part, be significantly older, having been accumulating and relocating in the surrounding area of GS1 for over 50 ka. This observation supports the geomorphic and sedimentologic evidence discussed in the first chapter of this thesis that suggests that the GS1 study area likely experiences cycles of sediment removal and sediment accumulation at unknown but recurrent intervals. Based on the OSL evidence the last accumulation cycle commenced approximately 15 ka ago.

The OSL ages obtained from the Norman River terraces indicate that favourable conditions for river terrace aggradation have persisted in the area for most of the past 40 ka. The oldest currently exposed river terrace (unit D) dates 39.7±2.1 ka and the youngest terrace (unit A) dates 10.9±0.5 ka, which coincides with the transition period between Pleistocene and Holocene (Figure F2.14c). Unit A sample was taken at a depth of 124 cm from the surface (Figure F2.14 c). There are no visible sedimentologic changes, such as changes in colour, grain size, texture or structure, in the unit A profile, therefore, we assume the aggradation was roughly constant without notable disturbance or interruption. The unit A OSL result indicates that after the start of the Holocene, the Norman River experienced an additional aggradation of 124 cm before shifting to the incision we observe today (Figure F2.17).

2.4.2 Radiocarbon evidence

Macro-charcoal samples have yielded the most reliable ^{14}C-based ages in this study. Their stratigraphic positions in the PA_10-M pit profile are known and the coarser particles are the least likely to suffer from significant post-depositional movement. The ^{14}C-based ages obtained on macro-charcoal samples also exhibit good stratigraphic coherence as do the OSL ages obtained from the same sections in the pit PA_10-M (Figure F2.17).

On the other hand, the ^{14}C-based ages on SPAC, did not follow a consistent age-depth trend, nor were they in agreement with the OSL ages. The SPAC results showed a general disagreement between themselves, whether within the same sediment sequence or between different sequences (Figure F2.17). The inconsistency in the SPAC ^{14}C-based ages seems to increase with the distance from the GS1 dripline.

Figure F2.17 illustrates the single-grain OSL and ^{14}C chronologies for the two sampling locations, Outside GS1 and Norman River site, along with other findings relevant to this study.

Discrepancies in ^{14}C results when using macro- and microcharcoal[1] have been observed before, for example, in terrestrial archaeological contexts (Asscher and Boaretto, 2019, Bird et al., 2002), eolian sequences (Feng et al., 2013), alluvial and colluvial sediments (Schroedter et al., 2013), soils in Amazonia (Saldarriaga and West, 1986, Santos et al., 2000) and even in the same soil samples (Eckmeier et al., 2009). Several reasons have been suggested for this. The differences in the ^{14}C-based ages obtained from macro- and microcharcoal samples are generally explained by charcoal heterogeneity, charcoal recalcitrance and charcoal particle relocation.

A single macro-charcoal particle dates a single event in time. In contrast, a microcharcoal sample (e.g. SPAC in bulk sediment) is a mixture of different biomass compounds from various fire events, potentially with different ^{14}C ages (Eckmeier et al., 2009). For this reason, data from macro-charcoal and microcharcoal fractions are not comparable and microcharcoal ages should not complement existing chronologies based on macro-charcoal data, as noted by Eckmeier et al. (2009). This finding has also been corroborated in this study.

The oldest ^{14}C age obtained in this study is 5243±194 cal BP from SPAC sample C_1-CR 100 at a depth of 100 cm (Table T2.3, Figure F2.17). In most cases, the SPAC ^{14}C ages are significantly younger than anticipated from other dates obtained at similar stratigraphic levels. It has been recognised that tropical hot and moist conditions, along with monsoonal climates, deleteriously influence the preservation state of charcoal (Bird et al., 2002, Higham et al., 2009). Nonetheless, several robust ^{14}C chronologies on charcoal collected within rockshelters in tropical north Australia prove that macro-charcoal can preserve for tens of thousands of years (e.g. Bird et al., 2002, Clarkson et al., 2015, David et al., 2007, 2017, Maloney et al., 2018, Turney et al., 2001, Whitau et al., 2017). Moreover, the ^{14}C dates obtained by Wallis (Wallis et al., 2009) on macro-charcoal from the archaeological deposit inside the GS1 rockshelter yielded calibrated ages of about 38,000 years BP (Wallis et al., 2014a). It was, therefore, reasonable to expect that charcoal from the immediate proximity of the GS1 rockshelter should provide comparably old ages.

[1] SPAC is considered a form of microcharcoal

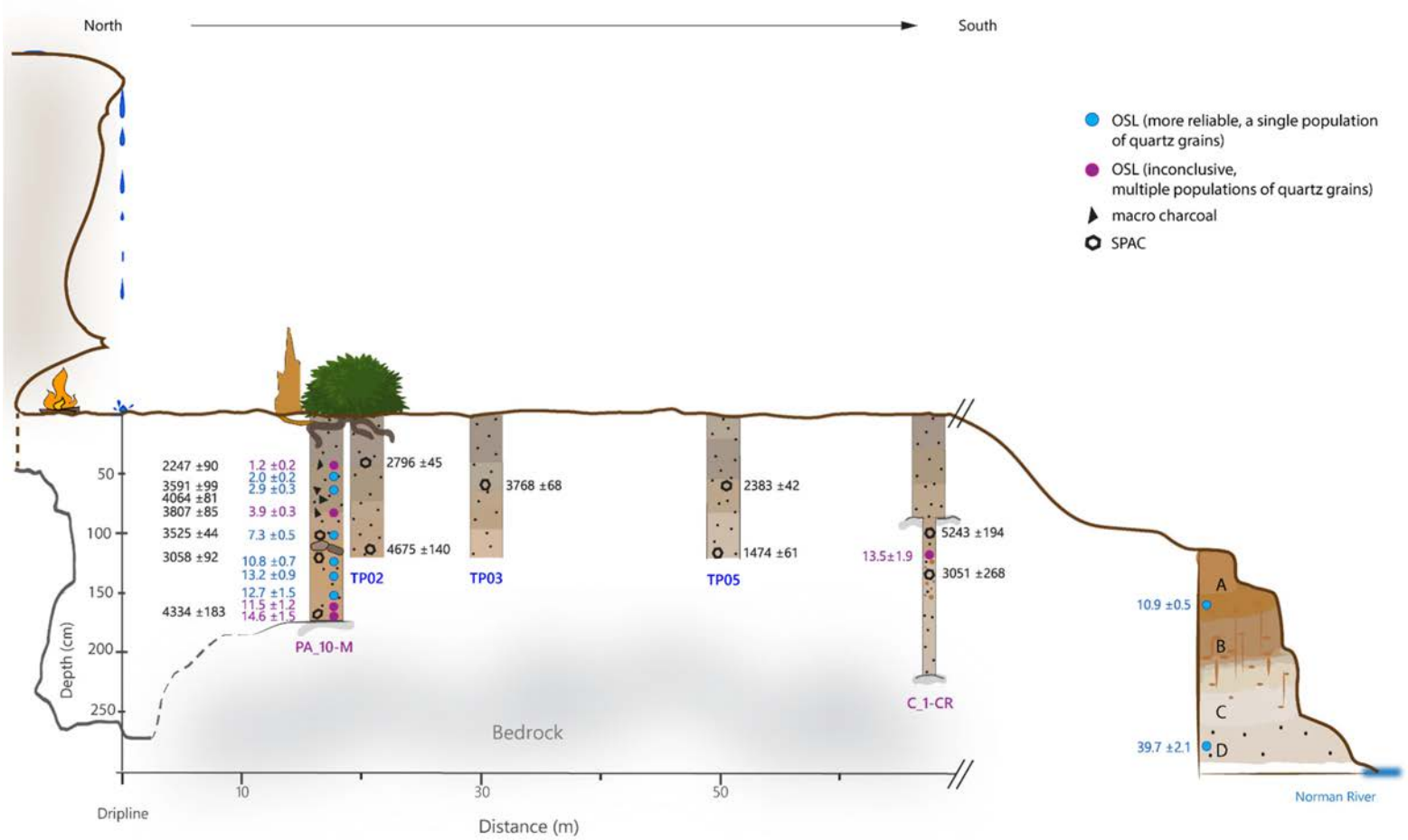

Figure F2.17: Chronologies in the study area, Outside GS1 and the Norman River site. On the left, the outline of the GS1 rockshelter. OSL ages are shown as blue and purple circles and corresponding numbers in ka. Purple are samples with less reliable result, where the age was determined on the overall context. Radiocarbon dates are shown in black, macro-charcoal samples as triangles and SPAC as rings, with corresponding ages in black. In pit PA_10-M note the good alignment of macro-charcoal ages with OSL ages. Bioturbation is shown as termite and root channels. Depth and distance are in proportion for the Outside GS1 location but not for the Norman River terraces, as marked by //.

The absence of these older ^{14}C ages in the non-archaeological open-site sediments outside the GS1 rockshelter, compared to those from the interior archaeological deposits, indicates that the charcoal present in the outside sediments was exposed to significantly less favourable preservation conditions in the seasonally wet, porous sandy sediments. As a result, coarse macro-charcoal was largely broken down into finer resistant SPAC-like material highly susceptible to vertical, and downward translocation by infiltrating rainwater (similar to the movement of clay particles through the illuviation process, refer to Chapter 1, section 1.4.1.1). The translocation of fine particles led to a mixing of SPAC of a variety of ages throughout the profile and a reduction in the maximum age obtainable because of the mixing of younger and older SPAC particles from higher sedimentary levels into lower layers. This is because smaller and lighter SPAC particles are easier to move downward through a relatively coarse and porous sand sediment profile, by percolating water. Therefore, the reduction in measured ^{14}C SPAC age is partly due to a mixture of SPAC of different ages and partly a result of decomposition processes due to less favourable preservation conditions outside GS1. These processes cause older material to be further comminuted in size, limiting the amount that can be dated. This, in turn, suggests that SPAC radiocarbon dates that are younger than OSL dates in the same profile section are more likely to indicate mixing downwards of fine material than an erroneous OSL date.

2.4.3 Post-depositional mixing and implications for the chronology

The occurrence of substantial post-deposition mixing in the open-site sand deposits Outside GS1 (Figure F2.17) is indicated by the scatter on the De radial plots (Figure F2.13) and the inconsistency and reduction of ^{14}C SPAC age results (Figure F2.15). Soil and sediment post-deposition disturbances are a regular natural occurrence and the most common causes in the tropics are raindrop impact, surface runoff, soil creep, water percolation, subsurface lateral eluviation and bioturbation (Williams, 1976). These processes move particles around laterally and vertically and can mix sediments efficiently enough to impact the outcomes of both OSL and ^{14}C dating.

2.4.3.1 Physical factors

Raindrop impact in the seasonally wet tropics is maximum at the start of the wet season, when plant cover is minimal and rainfall intensity from convection and monsoon storms is often very high. In semi-arid savannah, tree canopies provide little protection since they cover only about 15% of the ground, are often sparse and do not influence overland flow (McIvor et al., 1995). Moreover, they may also increase the drop size and the energy per mm rainfall available for erosion (Brandt, 1988, Bridge and Ross, 1983). Particle displacement by raindrop impact is proportional to total raindrop momentum (Williams,

1969). In general, kinetic energy calculated from a measurement of drop sizes has been successfully related to the amount of splash erosion and, therefore, the displacement of particles (Brandt, 1988). Consequently, raindrop impact is the primary cause of particle detachment, which makes them more vulnerable to surface runoff.

Different forms of water transport, such as surface runoff, eluviation, creep and subsurface lateral flow, are related to sloping land, the influence of gravity, water percolation and sediment (im)permeability (Williams, 2019). Erosion by surface runoff or slope wash comprises detachment of particles by raindrops, particle movement by rain splash and particle transport by runoff. In native savannah woodlands, the surface runoff increases with the size of the rainfall event and it is influenced by ground cover (McIvor et al., 1995). The ground cover of tall to mid-height annual and perennial grasses is characteristically sparse during the first downpours, which herald the wet season, but increases rapidly once the groundwater content is replenished (Williams, 1969). The cover reduces the amount of particles detached by raindrops, increases the flow depth and reduces the flow velocity (McIvor et al., 1995).

2.4.3.2 Bioturbation

Following the early work published by Wood and Johnson (1978) and Cahen and Moeyersons (1977), the role of bioturbation in post-depositional particle movement through soil and sediment profiles has presented a major challenge (Araujo, 2013, Balek, 2002, Bateman et al., 2003, 2007a, 2007b, Leigh, 1998, O'Connell et al., 2018, Williams, 2019, Williams et al., 2021). Particularly in terrestrial sediments, bioturbation complicates the measurement of reliable OSL doses, causes radiocarbon ages to have no direct relation with the sequence in the profile where they were obtained and leads to questions relating to whether artefacts are in their original position (Araujo, 2013, Cahen and Moeyersons, 1977, Kristensen et al., 2015, McBrearty, 1990, Smith et al., 2020, 2021, Williams, 2019, Wood and Johnson, 1978). Some forms of bio-disturbance of the sediment profile are very obvious and well documented, such as mammal burrowing or the impact of tree-fall and accompanying root-throw (Johnson, 1989, 1993, Gabet et al., 2003, Paton et al., 1995, Schaetzl and Follmer, 1990). Others, mainly connected to the activity of termites, ants and earthworms, are much more subtle and difficult to recognize, though equally important.

Various studies have confirmed that termites and ants in the tropics play the same part in soil turnover and soil fertility as earthworms in temperate regions (Viles et al., 2021, Williams, 2019 and citations therein). Thanks to the ability of termites to digest cellulose, they play a major role in the dynamics of the savannah ecosystem by consuming woody biomass (Andersen, 2005, Williams, 2019). Particles can be displaced horizontally by underground tunnels and animals pushing their way through

the sediment. Evidence shows that both termites and ants can move finer particles and mineral grains upward and downward in a profile (e.g. Araujo, 2013, Lee and Wood, 1971, Rink et al., 2013, Williams, 2019). Upward, resulting from mound or nest building and downward, caused either by deliberate downward movement of particles or through the collapse and subsidence of termite mounds (Bird et al., 2002−and citations therein, Halfen and Hasiotis, 2010, Johnson et al., 2014, Rink et al., 2013, Williams, 2019).

Ant and termite bioturbation can have two possible adverse effects on age estimation: underestimation of particle ages due to subterranean transport of younger particles downward and overestimation due to transport of older particles upward. In OSL dating, various research implies that the effects of bioturbation by ants, especially over extended time periods, can be a significant contributor to the overdispersion of De, beyond values that can be associated with incomplete zeroing at burial (Halfen and Hasiotis, 2010, Rink et al., 2013, Viles et al., 2021). Nonetheless, researchers agree that careful analysis of single-grain OSL De distributions can still yield satisfactory dates from mixed sediments, where the sedimentary context and climatic characteristics of the area are well understood (Bateman et al., 2003, Gliganic et al., 2015, Kristensen et al., 2015).

Sediment is also influenced by the post-depositional effects of plants. Plants, trees particularly, can mix sediments in many ways: through root expansion during growth, with decay and infilling of former root channels, by settling of particles due to water extraction by roots, by plant movements during severe storms and by tree-fall or uprooting (Gabet et al., 2003, Schaetzl et al., 1989). Roots penetrate the soil or sediment and as they elongate and expand in diameter, they form a cylindrical sheath around the root that pushes away the sediment. The increase in size is promoted by the imbibition of water, which can exert enormous pressures on the surrounding sediment, sufficient to break up bedrock (Gabet et al., 2003). For example, the roots of Eucalyptus and wattle trees can reach several meters in depth to get to water in savannahs (Moore, 2005). When a root dies it decomposes and leaves behind an empty space, eventually filled by sediment caving in from above. Brimhall et al. (1992) investigated the vertical mixing of soils and performed experiments with a pseudoroot buried vertically in a sandy matrix. It turned out that cyclic inflation and deflation of the pseudoroot caused the surface material to become mixed within the soil column and the mixing depth increased with the number of inflation-deflation cycles.

In the case of uprooting, an uprooted tree falls over and the root mass with attached substrate rotates up, leaving a pit in the ground. As the root mass decays, the substrate accumulates underneath, mixing with the surface sediment in and around the pit, forming a mound. The relief of pit and mound

features becomes more diffuse with time until evidence of the event completely disappears, leaving behind a mixed sediment layer of a thickness that depends on the rooting depth and consequent root wad thickness (Jungers et al., 2009). Phillips and Marion (2006) showed that physical displacement of soil by root growth, tree uprooting and infilling of tree stump holes are significant processes that maintain a continuously mixed surface biomantle.

Considering the various post-depositional effects of bioturbation on OSL dating some researchers attempted a different approach. They used the impacted OSL data from mixed sediment or soil profiles to identify and quantify sediment mixing (David et al., 2007, Gliganic et al., 2015, 2016, Heimsath et al., 2002, Johnson et al., 2014, Kristensen et al., 2015, Stockmann et al., 2013, Wilkinson et al., 2009). By utilizing visual signs and calculating mixing rates, a few of these studies quite confidently attributed the sediment mixing predominately to plant bioturbation (floralturbation), such as displacement by root growth, uprooting and tree stump hole infilling (e.g. Gliganic et al., 2016), or termite activity (Johnson et al., 2014, Kaste et al., 2007). In some of these studies, the mixing processes were found to be strongest at the surface and become more diffuse with depth (Gliganic et al., 2015, 2016, Stockmann et al., 2013, Wilkinson et al., 2009). For example, Johnson et al. (2014) noted that termite activity seemed to mirror the vertical distribution of roots. They concluded this to be possible since termites are distributed relative to the abundance of their food source, including dead root material.

It is difficult, however, to attribute the sediment mixing to one specific agent (Smith et al., 2021) unless the signs are very clear, for example, as in Gliganic et al. (2016). So far, there have been few attempts to collect field data that evaluates the impact of a range of different agents on sediment mixing and their impact on the reliability of dates obtained on the sediments. Kaste et al. (2007) calculated mixing rates from measurements of short-lived radionuclides, suggesting that the short-timescale processes of termite mixing may be the dominant agent compared to long-timescale processes such as uprooting. The mixing due to termite activity goes on for a few years before the mounds are abandoned (Williams, 2019), while mixing due to an uprooting may continue for several hundred or even thousand years (Schaetzl and Follmer, 1990).

2.4.3.3 Towards a better comprehension of the chronologic results in the study area

The ground in front of the GS1 rockshelter is flat and hosts typical open woodland savannah vegetation (Figure F2.1). The absence of sloping land at the site suggests that the possible impact of physical disturbances like creep and surface runoff on sediment mixing has been negligible. Additionally, there are no visible signs of past floods or water transport at the site or in the profiles. In terms of

subsurface flow as a possible major agent of post-depositional mixing, there was no visual proof of lateral relocation of particles in the profiles, such as particle size gradations or preferential particle orientation. Similarly, the raindrop effect and water percolation are difficult to confirm without evidence, such as particle sorting or the formation of impermeable surface crusts due to raindrop impact (Williams, 1969). However, the subsurface at the Outside GS1 location is uneven, undulating and composed of broken bedrock parts, bedrock slabs and depressions filled with sediment (Lowe and Wallis, 2020,Chapter 1 section 1.4.1.4). Consequently, the sediment Outside GS1 also accumulated unevenly between the depressions, bedrock cracks and bedrock slabs, which might have resulted in sporadically mixed sequences. This might explain the presence of intrusive younger quartz grains in the lower parts of the PA_10-M pit profile (Table T2.2 No.11,12), but it does not explain the presence of reworked older quartz grains (>19 and >50 ka) in the uppermost and middle part of the profile (Table T2.2: No.1,6).

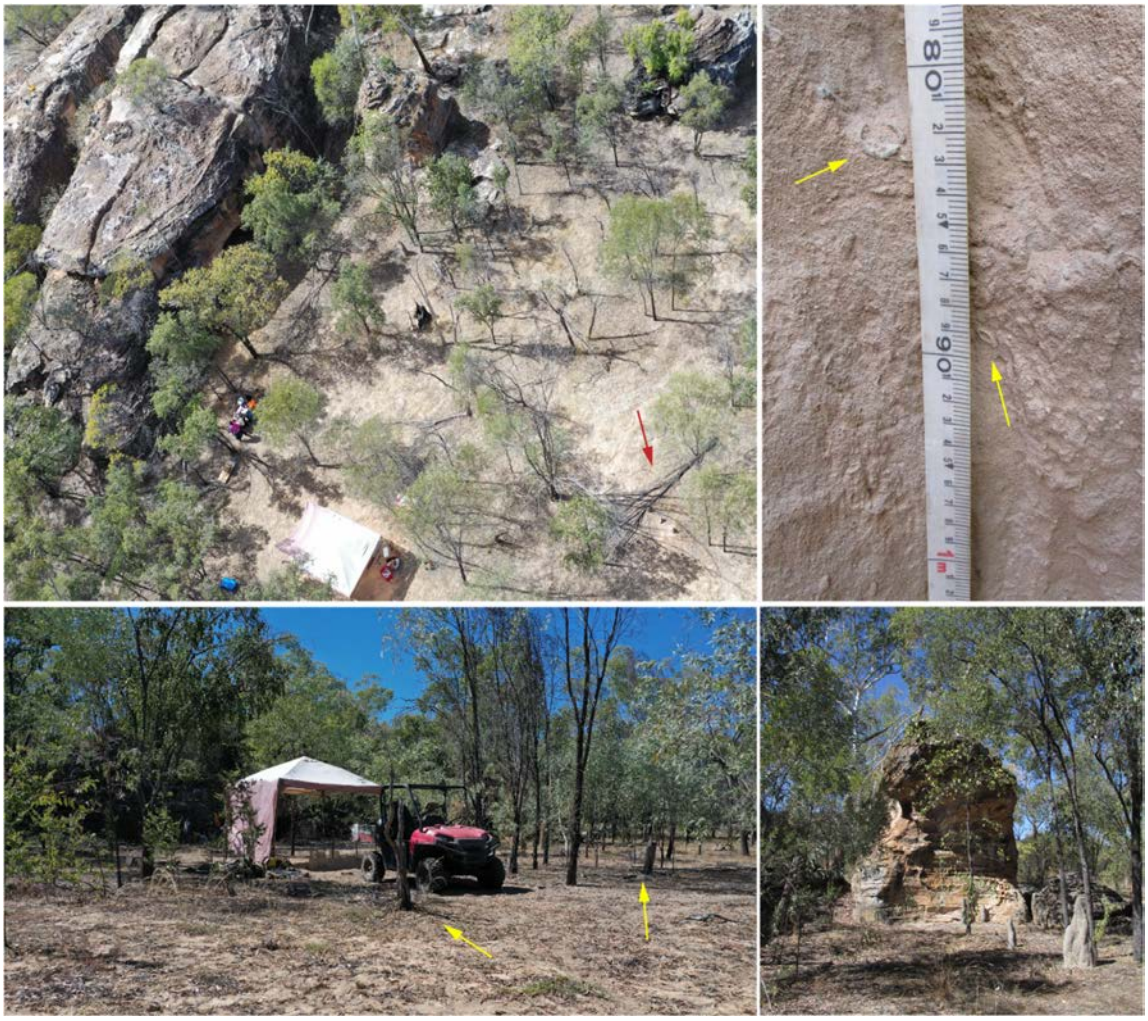

Figure F2.18: Evidence of bioturbation in the study area. **Top left:** the sandy deposits in front of GS1, GS1 roof seen in the top left corner, the arrow pointing to fallen trees (possible uprooting) and termite mounds - bottom right three in a diagonal; **Top right:** detail from pit PA_10-M profile, arrows pointing to root and/or burrows trace fossils; **Bottom left:** arrows pointing to tree stumps; **Bottom right:** termite mounds.

On the other hand, sparse termite mounds, ant activity, trees, fallen trees and tree stumps were prominent at the surface Outside GS1 (Figure F2.18). Additionally, root trace fossils were documented in the PA_10-M pit profile (Figure F2.18). This evidence suggests sediment mixing due to bioturbation is the dominant cause of the observed overdispersion of De distributions associated with the OSL results. It is highly probable that SPAC particles, similarly to quartz grains, were also subjected to mixing and relocation due to bioturbation. Nonetheless, the absence of older SPAC (>5243±194 years) cannot be adequately explained by bioturbation only and implies that even resistant PyC was removed by degradation over millennial timescales, at least in the non-archaeological open-site sediments Outside GS1 beyond the GS1 dripline.

In general, however, the De distributions in this study suggest rather peculiar patterns of post-deposition mixing. For example, De distributions in the PA_10-M pit profile indicate that sediment mixing, or ''scatter'' on the radial plots, occurred throughout the profile at similar intensity in all samples (Figure F2.13 A−L or as OD in Table T2.2). Additionally, in some samples, quartz grains were older than the average (Table T2.2: No.1,6,11,12). These patterns are not comparable with observations in some studies, where based on De distributions, mixing processes due to termite or plant bioturbation were found to be greatest close to the surface and more diffuse with depth (Bateman et al., 2003, 2007a, Gliganic et al., 2016, Johnson et al., 2014, Stockmann et al., 2013, Wilkinson et al., 2009). They also do not comply with findings about post-depositional mixing due to ant activity where mixing was more intense in the upper part of the profiles, ~10−60 cm, and diminished gradually afterwards (Halfen and Hasiotis, 2010, Rink et al., 2013). However, these two studies were conducted in artificially formed profiles, while in the studied PA_10-M pit profile the surface has been gradually aggrading over the last 15 ka. This means all samples were once near the surface and subject to more intense bioturbation, possibly becaming more diffuse with increased depth over time. If so, we expect a similar sediment mixing pattern throughout the profile. In fact, we see a general mixing pattern that is constantly present in all sampled sections of the PA_10-M pit profile (in the form of 'scatter'), albeit along with sporadic pulses of severe mixing with significantly older quartz grains. This evidence suggests that post-depositional sediment mixing observed during this study is not a result of solely one factor but rather a combination of factors and possibly geogenic, biogenic or anthropogenic events that have yet to be identified.

Field evidence suggests that termites, ants, root expansion and tree throw are the dominant agents of mixing. However, the lack of data on how different agents of bioturbation reinforce and/or counteract each other prevents us from being more precise about how they impact the De distributions at single-grain OSL analysis. The mixing patterns in this study find corresponding similarities in *Scenario II*, as suggested by Bateman et al. (2003, pg.1170-1171). This scenario implies bioturbation at low sedimentation rates and in thin sedimentary packages in which the entire sediment column will be disturbed. In these circumstances, OSL ages still increase with depth but represent an intermediate age reflecting both the age of burial as well as the magnitude and timing of post-depositional mixing. If the latter has varied through time, age reversals can occur over shorter depths (Bateman et al., 2003). This can be observed in the PA_10-M results (Table T2.2 No.9,10,11). In the end, although these disturbed sites can still display increasing ages with depth, even when some stratigraphy is evident (not the case in this study), it may not be possible to determine the true burial age (Bateman et al., 2007a).

Scenario II (Bateman et al., 2003), however, does not explain the presence of the above mentioned 'intrusive age signals' in profile PA_10-M (Table T2.2: No.1,6,11,12). Profile sections with these intrusive signals are represented by inconclusive samples (shown as purple circles in Figure F2.14 a and Figure F2.17) where the following specifics were observed:

- Grains with the oldest (>50 ka) and the youngest (<2 ka) age signals were found together in the same sample (Table T2.2.: No.1,11,12). Sections with this characteristic represent the upper most and the lowermost part of the PA_10-M pit profile.
- In the middle of the profile (80−82 cm), two age groups of grains were extrapolated after applying the FMM model where the second population, 22% of grains, exhibited an older age signal 19.4±1.2 ka−with no linkage to any other age group in the profile (Table T2.2: No.6).
- Grains showing an age of ~34 ka were found throughout the profile, almost in all profile sections apart from the middle section of the profile at 80−82 cm and 100−102 cm (Figure F2.13F,G).

An in-depth examination of the radial plots (Figure F2.13) reveals that the samples from the upper part and the bottom of the PA_10-M pit profile (Figure F2.13A,K,L) show similar De distributions. The samples in the rest of the profile exhibited De distributions more similar to each other (Figure F2.13B,C,D,E,G,H,I,J), except the sample from the middle of the profile (PA_10-M 80) which showed a De distribution that differs from all others (Figure F2.13F). The sample from the pit C_1-CR (Figure F2.14b) also showed an inconclusive result and a radial plot similar to those from the top and bottom of profile PA_10-M (Figure F2.13K). We, therefore, suggest that the incoherent signals may reflect occasional

phases of intensified mixing due to a currently undefined mechanism that resulted in the infiltration of young and old grains from proximate sediment basins or older deposits into the profile column. Changes in deposition/erosion cycles or sporadic events, such as uprooting, could have driven this hypothetical mechanism. We note that the movement of old grains upward toward the surface must have been in 'clumps' of sediment such that the OSL signal was not bleached as a result of the movement. This is more consistent with root throw than movement by termites or ants.

Finally, the De distributions in samples from the Norman River terraces showed less scatter after nMAD CAM modelling, and were more conclusive. This suggests that post-depositional disturbance had significantly less impact on the sediments of the river terraces compared to sediment deposits Outside GS1. As trees are equally present at the upper river terrace (unit A) as Outside GS1, a possible explanation would be that water makes the sediments less suitable for termites or ants. It is also possible that the sediments at the Norman River site were bult up faster, so there was less time for bioturbation to occur before the sediments were buried to a depth where bioturbation is less intense. The bottom terrace, however, is overlayed by two significantly harder units that constitute a barrier for termite and ant activity as well as a challenge for root expansion.

2.4.4 Age-depth model and sedimentation rate

The age-depth model, based on OSL and macro-charcoal results from the PA_10-M profile (Figure F2.16), supports the formerly discussed *Scenario II* (Bateman et al., 2003). It shows that OSL ages still increase with depth, but they give an average result influenced by the age of burial and post-depositional mixing. At depths 135−137 cm and 150−152 cm, an age reversal is observed, which, according to Bateman et al. (2003, pg.1171), can happen when the post-depositional mixing has varied through time. Overall, the age-depth model supports the conclusion that the sand deposits south of the GS1 rockshelter have been accumulating for at least 15 ka.

The age-depth model was used to calculate the sedimentation rate for pit PA_10-M (Figure F2.19). The sedimentation rate appears to be the lowest in the period from the Pleistocene-Holocene transition to the end of the mid-Holocene, which corresponds to the depth range 135−80 cm in PA_10-M. In this period, the sedimentation rate initially dropped from ~9 cm/ka (at depth ~135 cm) down to ~6 cm/ka (at depth ~118 cm) in the early Holocene (Figure F2.19).

Around 4000 years ago (at ~80 cm below the surface), the sedimentation rate started to increase and has been significantly higher for the last 1500 years, exceeding 20 cm/ka. A similar steady increase in

sedimentation rate from late Pleistocene to late Holocene was observed by Ward et al. (2005) at Keep River in north Western Australia, although a significant drop in sedimentation rate during early and mid-Holocene was not mentioned in that study. The authors attributed the observed increase to enhanced monsoonal activity (Nanson et al., 1992, Shulmeister, 1999). A wetter climate in the early Holocene (Bird et al., 2002) would mean more vegetation, intensified runoff and water percolation, increased rootlet bioturbation and, therefore, a lower sedimentation rate during the early Holocene compared to the late Holocene, which is consistent with the results in this study.

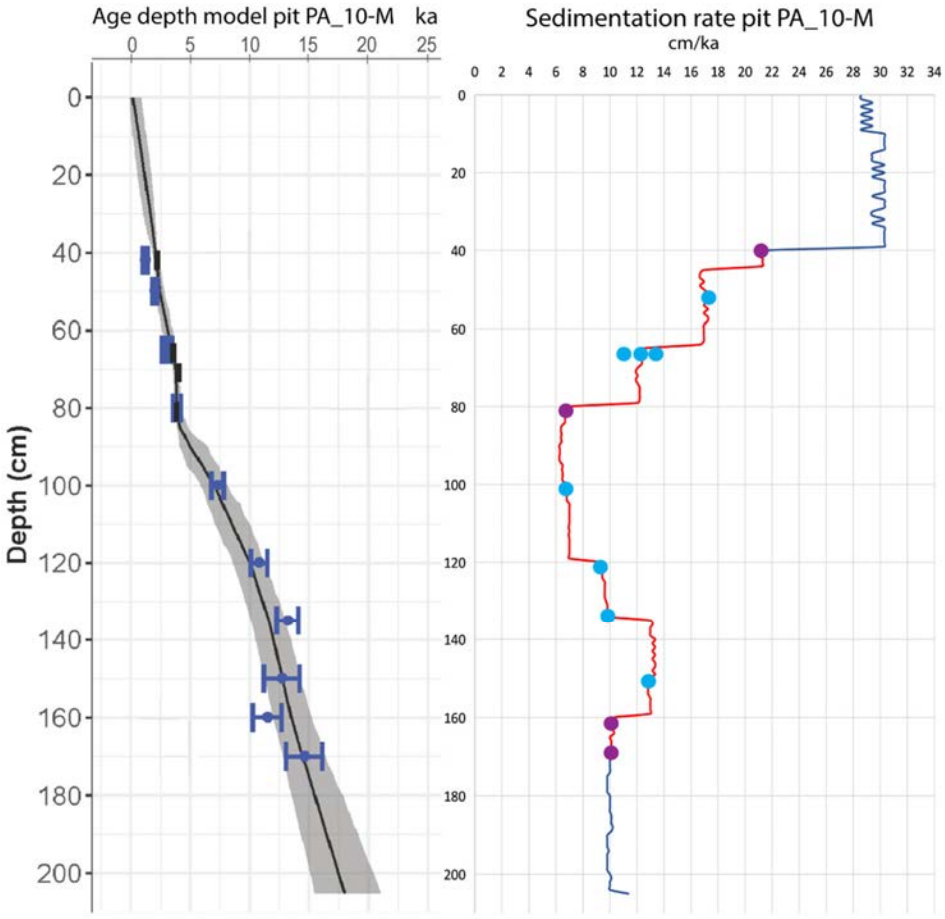

Figure F2.19: Age-depth model and sedimentation rate changes in PA_10-M pit profile through time. The graphs are placed so that the depths are at the same level, which allows a simultaneous observation of OSL age and the corresponding sedimentation rate. **Left:** Age-depth model constructed using Bayesian age modelling with rbacon package in R Chronology based on OSL and macro-charcoal ages. **Right:** Sedimentation rates calculated using the OSL ages modelled with rbacon. The part of the graph marked in red represents the sampled part of the PA_10-M profile, where the OSL ages were obtained. The blue part of the graph represents the part extrapolated by the model. The circles represent the OSL samples; as previously, the purple circles represent the samples of intensified mixing with intrusive ages (Figures F2.14a, F2.17). Note, the intensified mixing with incoherent ages is often connected with a significant increase in sedimentation rate.

(note by the author: only modelled OSL ages were used for the calculation of sedimentation rates).

To conclude, it appears (Figure F2.19 right) that the samples with incoherent ages (purple circles) occur after long periods of steady sedimentation, just before an increase in sedimentation rate. This observation, however, should be treated with caution because it might be biased by under-sampling and/or the applied Bayesian age modelling. Because the samples that showed multiple populations of quartz grains were recorded at both lower and higher rates of sedimentation, the undefined mechanism responsible for incoherent ages is independent of the sedimentation rate but might be dependent on the factors that induce the shift in sedimentation rate.

2.5 Conclusions

Developing a robust and reliable chronology from disturbed terrestrial sediments that characterize much of the Australian tropical savannah is challenging and complex. Single-grain OSL dating on quartz and radiocarbon dating on two charcoal fractions, macro-charcoal and SPAC, were used to obtain ages for two locations: 1) the terrestrial open-site non-archaeologic sediment deposit beyond the GS1 rockshelter dripline (named Outside GS1) and 2) the subsidiary Norman River terraces exposure (named Norman River site). Altogether, 15 OSL and 15 ^{14}C samples were collected from five pits excavated Outside GS1 and two terraces at the Norman River site. We examined the reliability of these techniques for dating terrestrial deposits from open sites in the Australian tropical savannah and observed how they agree. Several conclusions and implications for future studies can be drawn from this work:

- Single-grain OSL dating and ^{14}C dating of macro-charcoal produced the most reliable age results. The age-depth model constructed using these results showed that the non-archaeologic open-site sediment deposit Outside GS1 has been accumulating for at least 15 ka.
- In some samples Outside GS1 quartz grains older than 50 ka were mixed with the youngest grains (~1.2 ka). These samples were collected in the uppermost and lowermost sections of the PA_10-M pit profile located 19 m southwest beyond the GS1 dripline. This finding indicates that quartz grains from much older deposits were reworked into the younger deposits of pit PA_10-M without being bleached during the process. The configuration of older and younger sediment deposits and the mechanisms responsible for the transport and infiltration of significantly older quartz grains into younger deposits have yet to be fully resolved.

- The OSL age estimates, particularly those from Outside GS1 site, showed a lot of scatter in De distributions indicating post-depositional mixing. The observed overdispersion of De distributions implies a combination of mixing agents, of which some occur throughout the profile, while others are intermittent. Post-depositional mixing is, in large part, the result of bioturbation. Evidence of termite and ant activity as well as plant-turbation by tree roots, fallen trees and tree stumps were documented in sediments Outside GS1. A fair amount of work has already been published concerning the effects of bioturbation on De distributions in archaeological deposits (e.g. Araujo, 2013, Bateman et al., 2007b, Leigh, 1998, Williams, 2019, Williams et al., 2021), savannah soils (e.g. Johnson et al., 2014, Kristensen et al., 2015) as well as aeolian, fluvial and marine sands (e.g. Bateman et al., 2007a, Gliganic et al., 2015, 2016). Nonetheless, more research is needed to investigate the potential for single-grain OSL De distribution patterns to identify individual agents of post-depositional mixing, particularly bioturbation. In the future, it might be possible to use these approaches to identify the impact of human induced post-depositional mixing in sediments.
- The OSL age estimates from the Norman River terraces were more conclusive with less scatter in De. This might support the hypothesis that termites and ants are the dominant mixing agents at the Outside GS1 sampling site, since both tend to avoid excessive soil water.
- The OSL age derived from the lower portion of the youngest terrace (10.9±0.5 ka) suggests that, following the late Pleistocene-Holocene transition, sediment deposition at the Norman River site persisted for at least an additional 124 cm before the change in river dynamics occurred and the Norman River shifted to the current incising.
- The four radiocarbon dates obtained from macro-charcoal samples from the PA_10-M pit profile Outside GS1 aligned well with the OSL ages obtained from the same profile sections (Figure F2.17). This suggests that macro-charcoal was not subjected to significant relocation or deterioration and proved to be a reliable additional chronology proxy in this and probably analogous settings. However, the occurrence and preservation of macro-charcoal is too sporadic to be relied upon as the leading dating proxy.
- In contrast, the radiocarbon dates of SPAC samples proved unreliable, being inconsistent in the sediment sequences Outside GS1. The oldest date obtained from SPAC in pit C_1-CR was ~5 ka (Table T2.3, Figure F2.17). This is substantially younger than OSL ages. The overall inconsistency of SPAC dates and the lack of SPAC older than ~5 ka in open-site sediments Outside GS1 suggests the likelihood of significant translocation of fine SPAC up and down the loose, porous, sandy sedimentary sequence and a relatively rapid degradation of charcoal in this environment. This is

an important finding that should be addressed in the future to gain a better understading of macro-charcoal and SPAC dynamics in Australian semi-arid savannah open-sites.

- Low sedimentation rates and thin sedimentary packages allowed for the post-depositional disturbance of the whole sedimentary record of the PA_10-M pit profile Outside GS1. However, a significantly lower sedimentation rate during the early and mid-Holocene, in comparison to recent times (Figure F2.19), might indicate a change in climate between the mid- and late Holocene that impacted sediment deposition in the study area.

This is the first time that the combination of single-grain OSL and radiocarbon dating of macro-charcoal and SPAC have been used to date terrestrial sediment deposits at an open site. This study supports the conclusion that there is a lack of comprehensive understanding of the origins and cumulative effects of post-depositional sediment mixing as well as the dynamics of charcoal decay in sand deposits, which typically constitute the open sites of Australian northern savannahs. The study showed that the application of at least two independent dating methods as well as a good knowledge of the site characteristics and formation background, are essential in analogous contexts. Moreover, a large number of samples and multiple sampling locations should be planned, preferably in transects. Another possible method worth considering using in this context is cosmogenic nuclide dating (refer to Chapter 1 section 1.2.2.3.1). This preliminary research contributes to our knowledge of the complexities associated with the dating of typically disturbed terrestrial sand deposits in the open sites that constitute the majority of the northern Australian continent.

2.6 Acknowledgements

The authors express their gratitude to the Traditional Owners, represented by Woolgar Valley Aboriginal Corporation and their representatives, especially Uncle Lavin Keyes, Jasmine Keyes and Tameika Keyes as well as Helen Smith and William Smith for their partnership, guidance and help. The authors are very thankful to the Hinze family for their generous support and assistance throughout the field work. We also thank Costijn Zwart, Michael Brandt, Tina Nemec, Raul Hernandez Font for their invaluable help with fieldwork. Their commitment and positive attitude contributed importantly to the outcome of this study. The authors express special thanks to Yasaman Jafari and Rainy Comley for their guidance, assistance and support with sample preparation.

Chapter 3 Vegetation reconstruction at Gledswood Shelter 1 (GS1) site in North Queensland, Australia, combining phytoliths and $\delta^{13}C$ values

Mojca Zega [1,2], Michael Bird[1,2], Lynley A. Wallis[3]

[1]College of Science and Engineering, James Cook University, Cairns, QLD 4878, Australia

[2]ARC Centre of Excellence of Australian Biodiversity and Heritage CABAH

[3]Griffith Centre for Social and Cultural Research, Griffith University, Nathan, 4111, Australia

Statement of contribution of others:

MZ conducted the fieldwork laboratory and data analysis and drafted the manuscript. LW liaised with Aboriginal Traditional Owners to facilitate the study. LW did the fieldwork and laboratory work for the phytolith samples from inside Gledswood Shelter 1 (GS1), identified the current plant species in the study area and provided support and guidance to MZ in relation to phytolith identification and classification. MB assisted with the $\delta^{13}C$ part of the study. All authors designed the study and edited the manuscript.

Abstract

Reliable palaeovegetation reconstruction is vital for understanding past climate change and its impact on ecosystems, people and biodiversity. A standard approach to identify plant composition and variability over time is to use pollen. Unfortunately, pollen is not always available due to unfavourable preservation conditions, such as those in semi-arid and arid environments. Phytoliths, on the other hand, are durable and ubiquitous plant fossils that preserve well in very diverse sedimentary environments. They are common in many herbaceous and woody plants as well as in other angiosperms (flowering plants) and are particularly abundant and diverse in the grass family (Poaceae). Hence, phytoliths are a potential tool for the detection of changes in vegetation over time in contexts that lack conventional proxies. Similarly, charcoal or pyrogenic carbon is durable, ubiquitous and abundant in various natural environments. These characteristics likewise make pyrogenic carbon an excellent tool for palaeoenvironmental reconstruction via carbon isotope composition.

In this study, we combined phytolith analysis and $\delta^{13}C$ isotopic signatures from pyrogenic carbon, more precisely from Stable Polycyclic Aromatic Carbon (SPAC), to reconstruct past vegetation at the Gledswood Shelter 1 (GS1) archaeological site in North Queensland, Australia. SPAC is a highly resistant microscopic form of pyrogenic carbon, that can persist in the environment for millennia. We explored the usefulness of these two proxies to track vegetation changes through time in a sedimentary context of a terrestrial Pleistocene sand sheet in the Australian savannah. Sediments from the GS1 rockshelter interior ('Inside GS1'), and up to 73 m beyond the GS1 rockshelter dripline ('Outside GS1'), were collected for laboratory analysis. Given the divergent nature of the two types of record their comparability was also investigated.

The results revealed the persistence of savannah-type vegetation in the study area throughout the Holocene. According to phytolith indices, tree cover was denser during the early and mid-Holocene, compared to the more recent past. When compared, the results from the two locales exhibited differences between all proxies, suggesting a reliable palaeoenvironmental record cannot be provided by rockshelter interior deposits information alone. The combination of phytolith and $\delta^{13}C$ of organic carbon has been successfully applied before for vegetation reconstruction, but the $\delta^{13}C$ signature in SPAC has never been used to our knowledge. This study confirms the usefulness of this approach for vegetation reconstruction in semi-arid Australian savannah environments and discusses its constraints.

3.1 Introduction

Most reconstructions of past vegetation change in the tropical north of Australia derive from pollen and charcoal records. The studies have generally focused on wetter parts of the region that contain lakes and swamps, such as the Top End region in the Northern Territory (Bird et al., 2019a, Rowe et al., 2021, Shulmeister and Lees, 1995, Woodroffe et al., 1985), the Gulf of Carpentaria (Prebble et al., 2005), Cape York Peninsula (Luly et al., 2006, Rehn et al., 2021a), Torres Strait (Rowe, 2007), Lynch's Crater (Kershaw, 1981, Rule, 2020, Turney et al., 2006) and various marine cores (Moss et al., 2017, Moss and Kershaw, 2007, van der Kaars and De Deckker, 2002). There is an obvious need to extend research into the drier parts of northern Australia, particularly the savannahs that characterise most of the Australian tropics (Reeves et al., 2013a).

The harsh nature of semi-arid and arid Australia has resulted in a generally restricted, low preservation potential for conventional plant indicators, mostly pollen, but also spores and macrobotanics (e.g. seeds). Such remains do not preserve well in terrestrial sediments that are subjected to aerobic conditions and contrasting wet-dry seasonal climate shifts, as experienced in tropical monsoonal climates. It is, therefore, essential to develop new tools that will enable researchers to fill current gaps in the palaeoenvironmental record. In this regard, phytoliths and charcoal or pyrogenic carbon are generally well preserved in contexts where pollen is not and can contain palaeoenvironmental information in both morphology (e.g. Asscher and Boaretto, 2019, Enache and Cumming, 2006, Jensen et al., 2007, Mustaphi and Pisaric, 2014, Piperno, 1983, 2006, Rehn et al., 2019, 2021b, Smith et al., 1995, Strömberg et al., 2018) and stable isotope composition (e.g. Ascough et al., 2018, Bird et al., 2015, 2020, Carter, 2009, Fredlund, 1993, Hall et al., 2008, Kelly et al., 1991, Krull et al., 2003, Nelle et al., 2013, Parr and Sullivan, 2005, Santos and Alexandre, 2017, Song et al., 2016). Phytoliths have cautiously been adopted by researchers in Australia as an alternative source of palaeoenvironmental and palaeoecological data over the last several decades (Clark et al., 1992, Clarkson and Wallis, 2003, Florin et al., 2020, Fullagar and Wallis, 2012, Golson et al., 2003, Hayes et al., 2021, Moravek et al., 2013, Parr and Carter, 2003, Wallis, 2018, Wallis, 2003, Wallis, 2001, Wallis, 2000, Wallis, 2002). In North Queensland, however, only a few phytolith studies have been conducted, specifically on lake sediments at Long Pocket (Thorn, 2004) and from wet tropical forest soils on the Atherton Tablelands (Alexandre et al., 2012, Field et al., 2016).

The current study aimed to reconstruct past vegetation at the archaeological site of Gledswood Shelter 1 (GS1; see Wallis et al., 2009) using phytoliths and pyrogenic carbon. We used the stable carbon isotope signature $\delta^{13}C$ in a highly resistant microscopic form of pyrogenic carbon, defined as Stable

Polycyclic Aromatic Carbon (SPAC) (Ascough et al., 2018, Bird et al., 2015, McBeath et al., 2015). GS1 is located in inland North Queensland, approximately 1.6 km north of the Norman River, surrounded by typical Australian semi-arid savannah (Figure F3.1). The objective was to test the potential of phytolith analysis and $\delta^{13}C$ in SPAC ($\delta^{13}C_{SPAC}$) for palaeovegetation reconstruction in the Australian tropical savannah. For this purpose, two sets of samples were collected: 1) the first collection from a non-archaeological open-site sediment deposit expanding south-southwest of GS1, up to 73 m beyond the GS1 dripline, referred to as 'Outside GS1', and 2) a second collection from archaeological sediment deposit in the GS1 rockshelter interior, referred to as 'Inside GS1' (Figure F1.3).

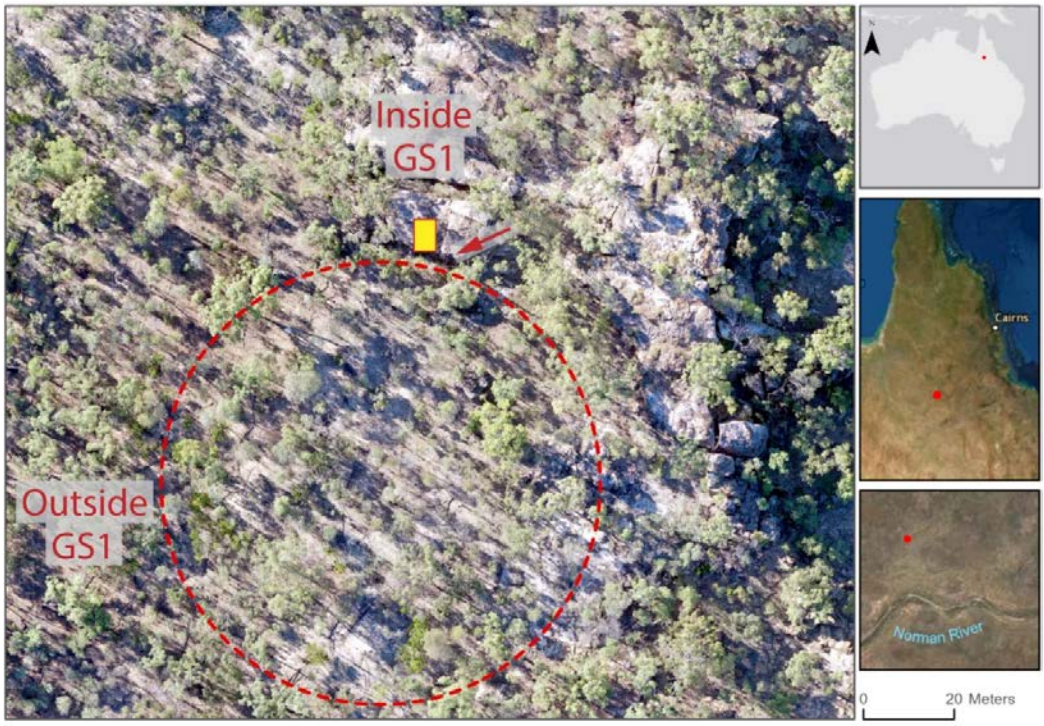

Figure F3.1: Gledswood Shelter 1 (GS1) study area. The yellow rectangle on the big map marks the archaeological sediment deposits inside the GS1 rockshelter–Inside GS1 sampling site and the dashed circle marks the non-archaeological open-site sediment deposits expanding southward beyond the GS1 dripline–Outside GS1 sampling site, the arrow indicates the GS1 dripline representing the demarcation between the Inside and Outside GS1. On the right, the red dot marks the position of the GS1 on a bigger scale.

In this study, the dripline is used to demark the boundary between the Inside GS1 and the Outside GS1 sediments, that is, between the archaeological deposits inside the GS1 rockshelter and the non-archaeological open-site sediment deposits extending beyond the GS1 dripline. Phytoliths and $\delta^{13}C_{SPAC}$ values were analysed in both sample collections to establish a palaeovegetation record. The second objective was to compare the results from both collections, inside GS1 and outside GS1, for similarities

and differences in phytolith assemblages and $\delta^{13}C_{SPAC}$ ranges, hypothesizing that the inside GS1 record is more likely to contain an anthropogenic signal. The purpose of the comparison was to see whether the two datasets confirm the same vegetation history, but also to determine whether the geomorphic form of the GS1 shelter operated as a sediment trap, and its possible role in acting as a human refugia that impacted the two proxies and, if so, how?

This study is, to our knowledge, the first in Australia to combine phytolith analysis and an $\delta^{13}C_{SPAC}$ isotopic signature from terrestrial sediments for palaeovegetation reconstruction. Phytoliths have been used several times before in combination with stable carbon isotope $\delta^{13}C$ for palaeovegetation reconstruction in other semi-arid regions, among the first by Fredlund and Tiezsen (1997) in South Dakota, USA, and Alexandre et al. (1999) in south-central Brazil. The authors found the approach useful for regions lacking lake sediments and preserved pollen records. Other researchers recently adopted this approach to investigate shifts in tree vs. grass vegetation predominance as well as changes in the position of the forest-savannah boundary, particularly in Brazil (e.g. Calegari et al., 2013, Calegari et al., 2017, Chueng et al., 2019, Coe et al., 2014), but also in tropical Africa (e.g. Bremond et al., 2017, Sangen et al., 2011) and parts of Asia (e.g. Li et al., 2021, Tripathi et al., 2021). In these studies, however, soil and/or sediment organic matter (SOM) was used as the source of carbon for $\delta^{13}C$ analysis rather than SPAC. Hence, the application of $\delta^{13}C_{SPAC}$ in combination with phytoliths in this study is novel. To provide essential theoretical background for the scientific approach used in this study, the following section contains an overview of the origins, formation and application of phytoliths and $\delta^{13}C_{SPAC}$. Additionally, it discusses their potential as proxies in palaeovegetation reconstruction.

3.1.1 Phytoliths

3.1.1.1 Origin and formation

Phytoliths (also known as plant opals, biogenic opal or opal phytoliths) are microscopic bodies of microcrystalline amorphous/opaline silica found in plants. The term derives from Greek, where *~phyto* means plant and *~lith* stone, hence 'plant-stones'. Plants produce phytoliths by secreting silica, obtained from ground water taken up into their tissues and cells, in the form of amorphous siliceous microstructures.

Charles Darwin was one of the first to write about the uniqueness of phytoliths. At the very beginning of his voyage, the *Beagle* stopped at Porto Praya off the northwest coast of Africa on the Cape Verde islands. In his notes, Darwin described a fine dust which was found to have slightly abraded the

astronomical instruments (Darwin, 1809-1882). Darwin wrote that this dust was a fairly common phenomenon in the region and, occasionally, it created such a haze that ships were rumoured to have run aground because of the poor visibility. It turned out that the dust was actually composed of phytoliths, though, it would take another 150 years before the scientific value of phytoliths began to be understood.

The weathering of silicate rocks, such as granite, sandstone or basalt, releases silicon, which with the addition of ground water forms monosilicic acid [$Si(OH)_4$] in soils (Jones and Handreck, 1967). Plants take up silicic acid through their roots along with water and various other nutrients they need for growth and development. During this process, in some plants the level of silicic acid will reach supersaturation, at which point it will be deposited it in their cells, spaces between cells and in other tissues in a solid form as amorphous silica or opaline silica ($SiO_2 \cdot nH_2O$) (Blackman, 1971, Epstein, 1999). The opaline silica thus deposited takes the shape of the surrounding tissue, forming microscopic bodies known as phytoliths (Figure F3.2). Phytoliths consequentially come in many different forms and shapes. In colour they are usually slightly transparent to slightly pink or grey, although colours can extend from brown to opaque and size can range from one to more than 100 micrometres.

Phytoliths are produced by most major groups of land plant taxa (Kondo, 1977) in almost every environment around the world, including many herbaceous and woody plants as well as other angiosperms (flowering plants), gymnosperms (conifers, cycads, Ginkgo, Gnetales) and pteridophytes (ferns). They are particularly abundant and diverse in monocotyledons, with the grass family (Poaceae) and palms serving as prime examples. Among dicotyledonous angiosperms, several plant families deposit abundant phytoliths, especially among tropical trees, vines and herbs. Nevertheless, not all plants produce phytoliths. The whole phytolith formation process is not fully understood (Hart, 2015, Piperno, 2006), though studies suggest that phytoliths might serve a range of structural, physiological and protective functions (Epstein, 1999).

3.1.1.2 Applicability and limitations

The biological function of phytoliths might be ambiguous, but their scientific significance certainly is not. Phytoliths are being increasingly applied in a wide range of fields from palaeontology, archaeology, and environmental science to nanotechnology (Neethirajan et al., 2009). In palaeoenvironmental reconstruction, they are particularly useful as proxies of the past vegetation cover because of their physiochemical durability (Rovner, 1971). Once a plant dies, phytoliths can dissolve under alkaline conditions (Alexandre et al., 1994, Alexandre et al., 1999, Cornelis et al., 2014, Opalinska and Cowling, 2015, Santos et al., 2018, White et al., 2012). However, in many cases, they are buried and preserved in

soils, sediments and archaeological deposits (Blackman, 1971) (Figure F3.2) where, when recovered, they can be used as palaeoenvironmental or archaeological indicators (e.g. Lewis, 1978, 1979, Pearsall, 1978, 1982, Piperno, 1983, Rovner, 1971).

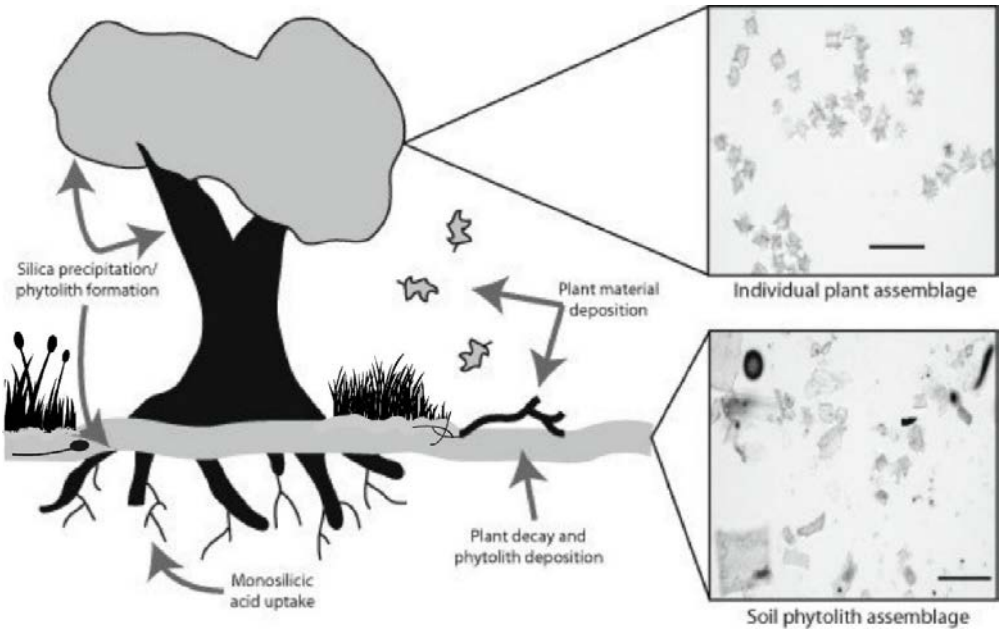

Figure F3.2: Phytoliths as proxies of the past. The figure shows the production and deposition cycle of phytoliths. Inset images on the right show examples of plant and sediment phytolith assemblages. Black bars in inset images are 20 µm. Image modified from Hyland (2014).

Deposition of silica often occurs at several sites within plant tissue, such as stomata, epidermal cells and trichomes, resulting in a *multiplicity* of different phytolith shapes (known as morphotypes) for each plant (Rovner, 1971, Piperno, 1988). After deposition, phytoliths adopt the relatively conserved shape of the cell types in which they form, such as those found in the epidermis, parenchyma or associated with the vasculature (e.g. stomata, tracheary elements, trichomes). Consequently, there is significant overlap in the shapes of the phytoliths formed within plants, even among taxa that are not closely related (Dunn et al. 2015), a phenomenon often referred to as *redundancy* (Rovner, 1971, Piperno, 1988). Here, it is important that grasses (*Poaceae*) produce different phytolith morphotypes compared to trees, shrubs and herbs (that is, Non-*Poaceae*). However, when it comes to determining higher taxonomic levels, phytoliths are not as diagnostic as pollen and attributing phytolith morphotype to a plant group is not a straightforward process. Various factors need to be taken into consideration in the process of classification, and multiplicity and redundancy represent a persistent challenge for researchers (Lu et al., 2006, Rashid et al., 2019, Vrydaghs et al., 2016). Furthermore, not all plants produce the same quantity

of phytoliths, meaning that the amount of a specific phytolith morphotype does not necessarily reflect the abundance of their producers (Piperno, 1988, 2006). Additionally, environmental factors, including temperature and precipitation, can alter the phytolith shape, content and size (Fishkis et al., 2009, Liu et al., 2021, Madella and Lancelotti, 2012). Despite these challenges, the field of phytolith research has grown enormously in the last few decades and a considerable amount of work has contributed to a better understanding and application of phytoliths as proxies of past environmental change (Hart, 2016, Rashid et al., 2019, Strömberg et al., 2018).

3.1.2 Carbon and $\delta^{13}C$ isotopic signature in plants

Of the three naturally occurring carbon isotopes two (^{12}C and ^{13}C) are stable and one (^{14}C) is radioactive. In total, 98.9% of the carbon circulating on Earth is ^{12}C, approximately 1.1% is ^{13}C and only 1 part in 10^{10} is ^{14}C (Lowe and Walker, 2015). In nature fractionation during biosynthesis reactions is standard and results in the enrichment of one isotope relative to the other. Generally speaking, these effects are very small but can be particularly significant, for instance, for radiocarbon dating. Moreover, isotope compositions engendered by fractionation are diagnostic of photosynthetic pathways (Farquhar et al., 1989, Fry and Sherr, 1989, Kohn, 2010). The ratio of stable carbon isotopes ^{13}C:^{12}C can therefore be interpreted as an isotopic 'signature' or 'fingerprint', providing information on the original source of the carbon. Once this fingerprint is imparted to a carbon-bearing substance, it remains the same as when it was formed, thereby representing a diagnostic key to substance origins. The ratio is referred to as a $\delta^{13}C$ (delta ^{13}C) value and is expressed as parts per thousand deviations from the VPDB international scale (per mil, ‰).

$\delta^{13}C$ values in nature vary widely as the carbon isotopic composition varies for different substances (e.g. Balesdent et al., 1987, Bird and Ascough, 2012, DeNiro and Epstein, 1978, Dickson and Coleman, 1990, Jasper and Gagosian, 1989, McCorkle et al., 1985, O'Leary, 1988, Oppo and Fairbanks, 1989, Tieszen and Boutton, 1989, Tieszen et al., 1983). Among terrestrial plants, the $\delta^{13}C$ varies from about -8 to -34‰ (Bender, 1971). The most significant differences derive from three different pathways that plants use during photosynthesis (C_3, C_4 and CAM) (Farquhar et al., 1980, Hatch, 1987, Sage, 2004). These pathways refer to the chemical processes and correspond to how plants fix atmospheric carbon (CO_2). The C_3 and C_4 pathways are the most widely distributed, while CAM plants (e.g. epiphytes and succulents) are uncommon except in arid regions (Ehleringer and Cerling, 2002, O'Leary, 1988, Osmond et al., 1973). C_3 photosynthesis is the ancestral pathway for carbon fixation and occurs in all taxonomic plant groups, utilized by most trees, shrubs, herbs, temperate grasses and lianas. Most plants use the C_3 pathway, which

discriminates strongly against ^{13}C, resulting in low $\delta^{13}C$ values (from -33 to -24‰). C_4 photosynthesis, alternatively, represents a relatively recent (approximately 8 Ma old) biochemical and morphological modification of the original C_3 pathway (Ehleringer and Cerling, 2002). Plants that use the C_4 pathway have higher $\delta^{13}C$ values, from -16 to - 10‰. The C_4 pathway occurs in the more advanced plant taxa and is especially common among monocots, such as grasses and sedges (Bird and Ascough, 2012, Ehleringer and Cerling, 2002, O'Leary, 1981, 1988). The C_4 pathway, however, is only advantageous for plants in environments with low CO_2 and/or high temperature. Therefore, C_4 plants are more common in the tropics and subtropics and a mixture of C_3 woody vegetation and C_4 grasses represents a typical pattern found in monsoon-dominated savannah environments but not in temperate or cold regions.

3.1.2.1 Pyrogenic Carbon and Stable Polycyclic Aromatic Carbon (SPAC)

Pyrogenic carbon, also known as charcoal, black carbon, soot, or biochar is a product of biomass burning, either natural or anthropogenic. Chemically, pyrogenic carbon represents a wide range of carbon-rich materials that form when biomass is exposed to temperatures above 300°C under conditions of restricted oxygen (Ascough et al., 2010, Bird, 2007). For example, when a savannah catches fire, trees burn alongside shrubs and grasses, including trunks, bark and branches, leaves, stems, nuts, fruits, resins and oils. Hence, pyrogenic carbon results from all biomass that was not fully combusted and has undergone physical and chemical alteration by exposure to high temperatures under conditions of low oxygen availability (Ascough et al., 2020). The degree of alteration the biomass sustains depends on fire intensity and burn time.

Fires have always been a feature of Australian tropical savannah dynamics. Fire events leave macro- and micro-particles of pyrogenic carbon dispersed ubiquitously in the environment. This material is generally very resistant to weathering and decay (Ascough et al., 2020, Bird et al., 2015) and some forms can persist in the environment for millennia or even tens of millions of years (e.g. Cressler, 2001). These characteristics make pyrogenic carbon one of the major tools for palaeoenvironmental reconstruction. The shape, size and abundance of pyrogenic carbon particles can be used as proxies for fire frequency (e.g. Aleman et al., 2018, Hawthorne et al., 2018, Rehn et al., 2021a, Rowe et al., 2021, Wurster et al., 2021). The geochemical measurement of the most inert fraction of pyrogenic carbon, measured as Stable Polycyclic Aromatic Carbon (SPAC), can also provide information about fire intensity (Wurster et al., 2012, 2013, 2021). For more information about pyrogenic carbon and SPAC formation, refer to section 2.1.2.3.2. The $\delta^{13}C$ value of SPAC ($\delta^{13}C_{SPAC}$) is indicative of the balance between the types of vegetation burnt in tropical savannah because, as mentioned previously, grasses utilize the C_4 photosynthetic pathway ($\delta^{13}C$

-16 to -10‰) while woody vegetation uses the C_3 pathway (-33 to -24‰). Hence, $\delta^{13}C_{SPAC}$ from pyrogenic carbon can provide information about what vegetation was burning during fire events in the past.

3.2 Materials and Methods

3.2.1 GS1 site background

The regional setting and climate of the study area are given in the introductory part of this thesis (chapter I.2A,B), with the geological evolution and geomorphic characteristics treated in depth in Chapter 1. To avoid repetition, only a brief summary of these is given below, where we focus instead on the extant plant composition of the area that deals with palaeovegetation reconstruction. Wallis recorded plant composition in the study area in 2006−2008. This study is complemented here with data from the Atlas of Living Australia ALA digital database (ALA, https://www.ala.org.au/) .

Figure F3.3: The study area with the red circle marking the GS1. The area is located at a topographic boundary between the foothills of the Gregory Ranges to the east and the gently sloping Strathpark Plains to the west and south. About 1.6 km to the south of GS1 flows the Norman River, whose headwaters are in the Gregory Ranges and which drains westward into the Gulf of Carpentaria.

The GS1 study area lies in the semi-arid Australian monsoonal tropics (Figure F3.3 right), characterised by a short, hot, wet season and a long cool, dry season. While surface water is abundant during the wet season, it becomes extremely scarce during the dry, when people must access subterranean streams or spring-fed waterholes. Geomorphologically, the area is located at a topographic

boundary, with the foothills of the Gregory Ranges (600−900 m asl) to the east, and the Strathpark Plains (300−400 m asl) sloping gently to the west and south (Figure F3.3). The foothill region is dominated by residual hills, scarp retreats and outcrops of quartzose Hampstead Jurassic sandstone. About 1.6 km to the south of the GS1 rockshelter is the Norman River, meandering its way across the Strathpark Plains, whose headwaters are in the Gregory Ranges and which drains westward into the Gulf of Carpentaria. The surrounding vegetation is primarily open woodland and grassland, and even today the region is generally regarded as rugged and difficult to access.

The sandy forest country of the Strathpark Plains is dominated by Georgetown box *(Eucalyptus microneura)*, lancewood *(Acacia shirleyi)* and Cooktown ironwood *(Erythophleum chlorostachys)*. Subordinately, the arboreal assemblage further includes quinine bush *(Petalostigma banksii)*, *Ficus* spp., paperbark *(Melaleuca* spp.), long fruited bloodwood *(Corymbia polycarpa)*, cocky apple *(Planchonia careya)*, white cypress pine *(Callitris glaucophylla)*, bean tree *(Bauhinia cunninghamii)*, lemon wood *(Dolichandrone heterophylla)*, arid peach *(Terminalia aridicola)*, *T. ferdinandiana*, *Dolichandrone alternifolia* subsp. *variabilis*, currant bush *(Carissa lanceolate)*, damson *(Terminalia* spp.*)*, starflower *(Calytrix leptophylla)* and *Acacia* spp. Groundcover is dominated by a combination of three-awn grass *(Aristida* spp.), ribbon grass *(Chrysopogon fallax)*, blue grasses *(Dicanthium* spp. and *Bothriochloa* spp.*)*, kangaroo grass *(Themeda australis)* and black speargrass *(Heteropogon contortus)*, with rocky areas dominated by spinifex *(Triodia* spp.). The majority of the listed grasses are C_4 plants, apart from the three-awn grass and spinifex, which can be either C_3 or C_4 species (Blood et al., 2015, Goergen and Daehler, 2001, Osborne et al., 2014).

The vegetation of the rugged, outcropping surfaces of the foothills comprises communities of variable structure generally dominated by lancewood *(Acacia shirleyi*) along with Cooktown ironwood *(Erythophleum chlorostachys)*, Georgetown box *(Eucalyptus microneura)* and various other *Eucalyptus* species. The ground surface is often bare or sparsely covered by short grasses, such as the commonly present three-awn grass and spinifex on rock-exposed surfaces.

Inside the dripline of the GS1 rockshelter the ground is sandy, supporting little or no vegetation. Figure F3.4a,b show the current vegetation in the study area.

Figure F3.4a: Current vegetation in the area of study. **Top left and right:** open woodland savannah of the Strathpark Plains. **Left:** the bare Inside GS1 ground. **Right middle:** grasses and shrubs growing on the rooftop of the GS1 rockshelter outcrop. **Right bottom:** open woodland savannah surrounding the GS1 rockshelter outcrop; note the baldachin set for fieldwork purposes.

Figure F3.4b: Current vegetation in the area of study. **Left:** the vegetation of the rugged, outcropping surfaces of the foothills. **Right:** *Melaleuca* dominated vegetation overgrowing the banks of the Norman River.

3.2.2 Phytolith analysis

Phytolith analysis involved field collection of bulk sediment samples from Inside GS1 and Outside GS1, followed by extraction of phytoliths from sediments and microscopic examination. A total of 44 bulk sediment samples were selected from pits and auger holes outside GS1, and 64 from the archaeological sequence inside GS1, Square C1 (Tables T3.1, T3.2). Sampling locations are shown in Figure F3.5. Archaeological excavations and sample collection from Inside GS1 were conducted by Wallis in 2006 and 2008 (Lowe et al., 2018, Wallis, 2008, Wallis et al., 2009). The pits and auger holes from the Outside GS1 sampling location comprise five test pits (TP01, TP02, TP03, TP04, TP05) excavated by Wallis in 2008 (Lowe et al., 2018) as well as two pits (PA_10-M and C_1-CR) and ten auger holes (PA_1-M, PA_2-M, PA_3-M, PA_5-M, PA_5-M, PA_6-M, PA_7-M, PA_8-M, PA_9-M and PA_11-M) excavated by Zega in 2019 and 2020 (Figure F3.5).

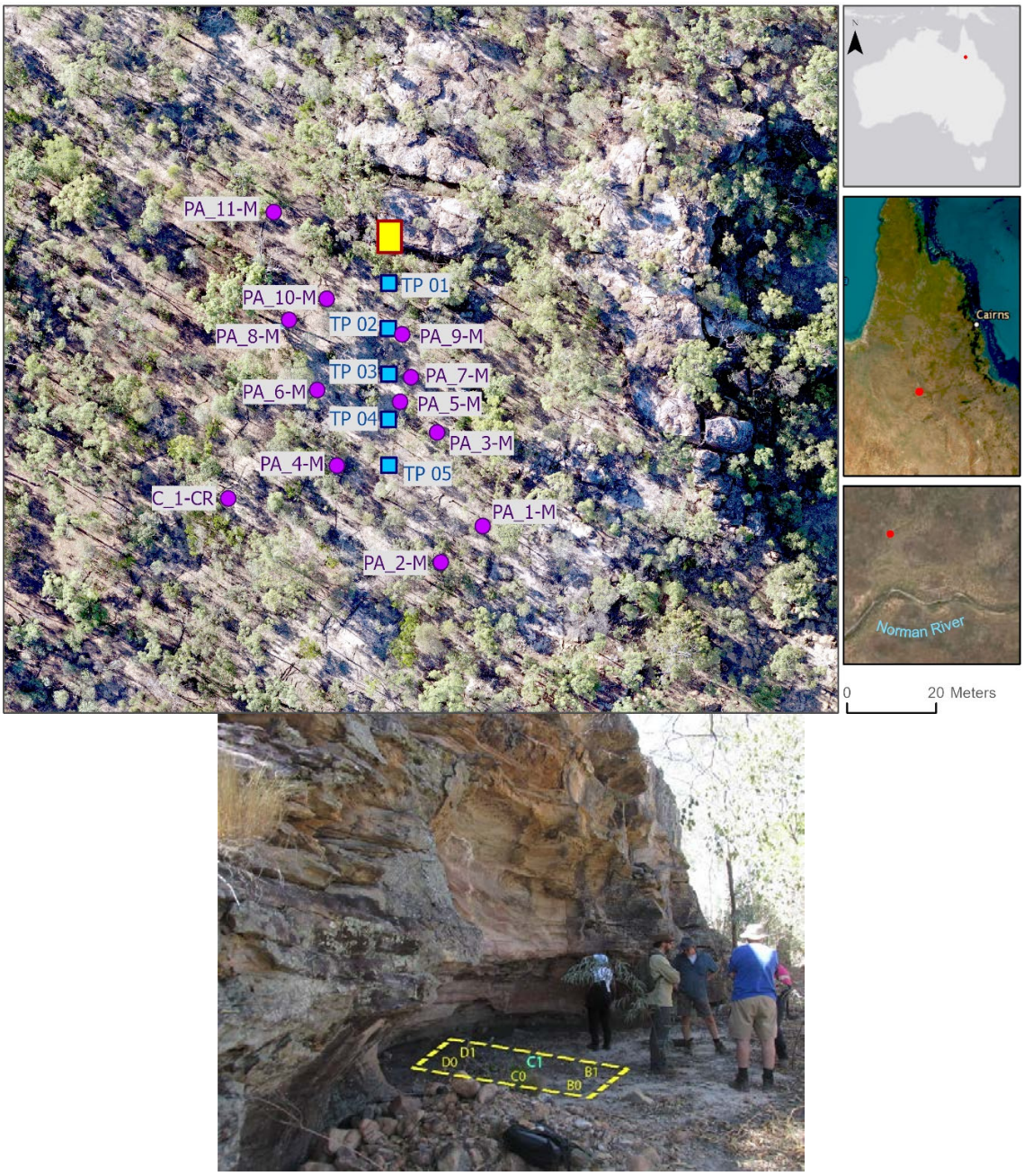

Figure F3.5: Sampling locations Outside GS1 and Inside GS1. **Top:** Pits and auger holes Outside GS1, blue squares mark the test pits excavated in 2008 by Wallis, purple circles mark the two pits and ten auger holes excavated by Zega in 2019 and 2020. The yellow rectangle marks the archaeological excavation Inside GS1. The red dot on the right marks the location of GS1 on a bigger scale. **Bottom:** A photograph from the Inside GS1−rockshelter interior, with marked archaeological squares. Samples from Square C1 were used in this study.

3.2.2.1 Phytolith extraction from sediments

We chose the heavy liquid separation process for the extraction of phytoliths, following the standard procedure described by Wallis (2000) and Aleman et al. (2013) with a few minor adaptations. First, the samples were sieved at 425 µm and left to dry overnight at 70°C. Then samples were placed in 50 ml plastic tubes and Calgon was added to promote clay dispersion. After mixing, they were left to settle overnight. The next step was to remove the organics by adding 30% hydrogen peroxide and placing the samples in a gently shaking water bath at 65°C. The hydrogen peroxide was topped up as necessary, until all reaction had ceased. Calgon was then re-added to further assist in the removal of the clay-sized particles. The Calgon step was repeated as many times as necessary until no clots of clay were seen with the naked eye. Phytoliths were then separated from other material by flotation in sodium polytungstate with a specific gravity of 2.3 (Figure F3.6). The heavy liquid was chosen because it is reusable and non-toxic (Hart, 1988, Madella et al., 1998). After extraction, phytoliths were placed in small plastic vials for the last step, and the sodium polytungstate solution was set aside for reclamation. The phytolith extraction protocol is provided in detail in Appendix A3.1.

3.2.2.2 Slides production

A number of different media are available for mounting phytoliths (Aleman et al., 2013, Piperno, 2006, Wallis, 2000). The only requirement is a refractive index of *ca.* 1.5, so the phytoliths can be easily distinguished against the background mount. For this study Eukitt UV was selected, as it is transparent, dries very quickly and causes no colour distortion under the microscope. It was very easy to work with, although a 3 min UV light exposure is needed for the slides to cure (Figure F3.6). Eukitt UV cures to a solid mount, hence phytoliths cannot be rotated to determine their overall three-dimensional morphology. In a permanent solid mount, however, phytoliths cannot migrate across the slide during examination, thereby potentially affecting counts. Moreover, individual phytolith coordinates can be recorded for referral at a later date and slides can be archived in an upright or horizontal position. Therefore, the usage of Eukitt UV was considered more appropriate than a non-solid mount. The slide preparation protocol is given in Appendix A3.1.

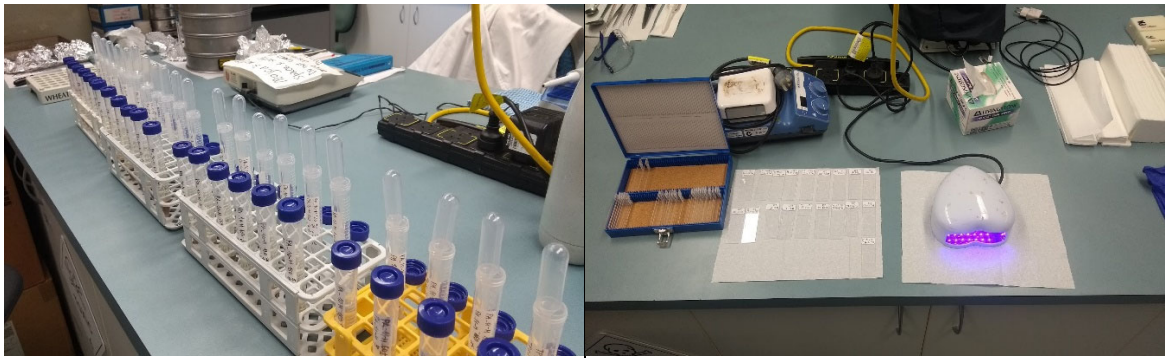

Figure F3.6: The heavy liquid step for phytolith extraction from sediments (left) and phytolith slide preparation (right).

3.2.2.3 Phytolith microscopic analysis and classification procedure

Phytoliths were observed and photographed using a Leica DM 750 transmitted light microscope with a fixed Leica ICC50 W camera and Leica LAS X (v.4.21) software. Additionally, to obtain an insight into the three-dimensional morphology of the phytoliths, 18 samples were inspected using a JEOL Scanning electron microscope JSM-5410LV.

Phytoliths were counted and sorted into groups based on their shape. In counting, the main objective is to recover the diversity of a given sample (Strömberg, 2009). Diversity is a combination of evenness (abundance of each taxon within a sample) and richness (number of taxa present), both of which provide the numbers from which to determine a representative phytolith assemblage, i.e. the minimum interpretative unit (Zurro, 2018). The appropriate count size should be determined for each study individually (Strömberg, 2009). In this study, the sample size of 100 (±20) was determined based on a clear domination of one morphotype class over another, test double counts and time constraints *versus* the project size and objectives. Only undamaged, preserved and distinctly shaped phytoliths were counted. Burnt, etched, damaged and irregularly shaped phytoliths were also recorded, along with charcoal and other bodies, such as Chrysophyta, diatoms and sponge spicules, but did not add to the number of counts.

During counting, phytoliths were first sorted using the author's shape descriptions. The shapes were subsequently arranged into morphotypes according to the latest International Code for Phytolith Nomenclature (ICPN) 2.0 (ICPT, 2019). A morphotype is defined as a group of individual specimens with the same morphological traits, such as shape, texture and size. Shapes that did not fit into any morphotype suggested in ICPN 2.0 were named and described accordingly by the author of this study. The classification procedure used in this study to fit the various observed shapes into selected 25 morphotypes as defined by ICPN 2.0 is given in Table T3.1. The general description of identified morphotypes is given in Appendix A3.2.

TiliaIT Software was used to collate and graph the phytolith results.

3.2.2.4 Phytolith indices

The phytolith morphotypes for the calculations of phytolith indices in this study were used only if the sample fulfilled the pre-condition that the assigned morphotype represented at least 5% of the total count in the analysed sample. In this way phytolith indices provide significant palaeoenvironmental inferences (Salgado et al., 2021). Two phytolith indices were used:

(1) D/P ratio, a widely applied index which uses the spheroid ornate morphotype, typically produced by tropical woody vegetation, to indicate tree cover (Strömberg et al., 2018); D stands for Dicotyledons (dicots, trees) and P (*Poaceae*, grasses) for phytolith grass morphotypes. The rationale is the lower the D/P value, the more open/grassy the habitat. After the classification (refer to Table T3.1), the D/P index for tree cover density determination was calculated using the relevant and representative morphotypes in this study as follows:

$$D/P = \frac{OVA_{ORN}+SPH_{ORN}+OVA_{ORN\_prob}+SPH_{ORN\_prob}}{BIL+ndGSSCP+PAP+RON+SAD} \quad (1)(2)$$

(2) FI-t index, used to study relative changes between grasses and non-grasses through time. The FI-t ratio represents the percentage of non-grass, i.e. ''forest indicator'' phytoliths, of all diagnostic phytoliths in a studied sample (Strömberg, 2003, 2005, Strömberg et al., 2007a, 2018). This index has been used broadly for tracking relative change in vegetation, i.e. the emergence of grass-dominated and presumably open habitats (Chen et al., 2015, Cotton et al., 2012, Strömberg, 2005, Strömberg et al., 2007a, 2018). The result is expressed in percentages. After the classification (refer to Table T3.1), the phytolith index FI-t was calculated using the relevant and representative morphotypes in this study as follows:

$$FI\text{-}t = FI/(FI+P) * 100\ (\%) \quad (2)(3)$$

[2] *The morphotype codes are provided in Table T3.1. The morphotypes in the formula were only used in the calculation when the 5% criterion was fulfilled. Grass morphotypes CRO, POL and TRZ never reached the 5% criterion and therefore are not included in the formula.*

[3] *The morphotype codes are provided in Table T3.1. The morphotypes in the formula were only used in calculation when the 5% criterion was reached. Forest indicator morphotype SPH_PSI_nod and grass morphotypes CRO, POL and TRZ never reached the 5% criterion and therefore are not included in the formula*

where $FI=\frac{(SPH_{PSI}+OVA_{PSI}+SPH_{ORN}+OVA_{ORN}+SPH_{PSI\_prob}+SPH_{ORN\_prob}+OVA_{PSI\_prob}+OVA_{ORN\_prob})}{TOTAL\ number\ of\ counts}$ and

$$P=\frac{(BIL+ndGSSCP+PAP+RON+SAD)}{TOTAL\ number\ of\ counts}$$

Since first proposed (Alexandré et al., 1997a), the D/P index used to estimate relative tree cover has been questioned and modified (Alexandré et al., 1997a), by including or excluding different morphotypes within both variables (e.g. Bremond et al., 2005, 2008, Mercader et al., 2011, Neumann et al., 2009, Strömberg, 2002). Ultimately, the D/P index has proven to be successful in tropical areas at low elevation (Barboni et al., 2007, Bremond et al., 2008, Mercader et al., 2011, Neumann et al., 2009, Strömberg et al., 2018). In contrast, the FI - t index has proven to be better used for tracking relative change in vegetation rather than reconstructing absolute tree cover (Strömberg, 2004, Strömberg et al., 2007a). In this study, we applied both indices to gain information about changes in habitat openness through time.

Table T3.1

Phytolith Classification used in this study

Phytolith shape as dscribed on counting sheets	Phytolith Morphotype as determined for classification	Code according ICPN 2.0	Vegetation type as used for phytolith analysis	Additional comments	References	Plate No.
Bilobate	Bilobate (GSSCP)	BIL	**Grasses (Poaceae)**			
Bilobate long waist (Aristida)						
Unilobe						
Cross	Cross (GSSCP)	CRO				
Quadrilateral small - short cell	Not-defined (GSSCP)	ndGSSCP				
Short cell (not defined)						
Short cell Elongate						
Short cell irregular						
Short cell with spikes					ICPT 2.0, 2019, Madella et al., 2005, and citations therein	Plate 3.1
Lobate (Polylobate)	Polylobate (GSSCP)	POL				
Rondel (short cell)	Rondel (GSSCP)	RON				
Bilobate no waist (Saddle)	Saddle (GSSCP)	SAD				
Short cell rectangular/ Trapezoid	Trapezoid (GSSCP)	TRZ				
Papillate	Papillate	PAP				
Elongate irregular	Elongate dentate	ELO_DET		ELO_DET is commonly formed in long cells in the epidermis of Poaceae leaves, precisely in the inflorescence of Poaceae.		
Elongate dentate/echinate/tuberculate						
Elongate nodulate/sinuate (Cyperus sp.)	Elongate sinuate	ELO_SIN	**Grasses (Poaceae) and Sedges (Cyperaceae)**	ELO_SIN likely attributed to Poaceae and Cyperaceae particularly in the presence of other typical morphotypes such as GSSCP, Papillate and Sedge plate.	ICPN 2.0 and citations therein; Metcalfe, 1960, Murungi and Bramford, 2020	Plate 3.2
Bulliform cell (Flabellate)	Bulliform Flabellate	BUL_FLA			Chen et al., 2020, ICPT 2.0, 2019, Madella et al., 2005	
Conical (squat cone) or Sedge plate	Sedge plate	SED	**Sedges (Cyperaceae)**		Murungi and Bramford, 2020, Wallis 2000	Plate 3.2
Ovate medium 12.5 - 25 µ	Ovate psilate	OVA_PSI	**Forest indicator (TSH)**	Ovate phytoliths along with trasitional forms from spheroidal to ellipsoidal smooth surface phytoliths are generally found in a wide range of arboreal and herbaceous monocots and dicots, although in low numbers. They have been used as part of 'forest indicators' class. Visual proboscis or stalk can represent a protrusion that marks a site of attachment to a host structure (Piperno 2006, pg. 39) or possibly a bended upper part of a cone or an exaggerated tubercula. The surface projections of the Ovate denatate shape in this study were eventually found more similar to tuberculate than to conical, therefore this shape was included in the Ovate ornate morphotype.	Amos, 1952; Alexandre et al., 1997, Barboni et al., 2007, Benvenuto et al. 2015, Bowdery et al., 2001, Bremond et al., 2005, 2008, Collura and Neumann 2017, Contreras et al. 2019, Cordova 2013, Crifo and Strömberg 2020, Esteban et al., 2017, Hart 2016, ICPT 2.0, 2019, Iriarte and Paz 2009, Kealhofer and Piperno 1998, Lu et al. 2006, Mercader et al., 2009, 2010, 2011, 2019, Novello et al., 2018, Piperno 1988, 2006 (pg. 39, 40), Premathilake et al. 2017, Runge 1999, Scurfield et al.,1974; Strömberg 2004, 2005, Strömberg et al., 2007, 2018, Teste et al, 2020, Wallis 2000, 2003, Watling and Iriarte 2013, Watling et al., 2020, Zucol et al. 2018, Zurro 2016	Plate 3.3
Ovate small < 12.5 µ						
Ovate irregular lemon shape						
Ovate with proboscis	Ovate psilate with prob	OVA_PSI_prob				
Ovate with proboscis small						
Ovate dentate	Ovate ornate	OVA_ORN	**Forest indicator (woody vegetatation)**			
Ovate irregular						
Ovate irregular Type B						

Ovate nodulate Ovate nodulate tuberculate Ovate nodulate Type B Ovate tuberculate	Ovate ornate	OVA_ORN	**Forest indicator (woody vegetatation)**	The Ovate ornate morphotype consisting of tiny granules or nodules (cauliflower like), which is sometimes spheroidal (SPH_ORN), but usually ellipsoid or irregular, can be specific for woody vegetation. Both morphotypes together are used as indicators for woody vegetation in the calculation D:P (Dicotleydon:Poaceae) index.		Plate 3.3
Ovate irregular with proboscis Ovate nodulate with proboscis Ovate tuberculate with proboscis	Ovate ornate with prob	OVA_ORN_prob		Visual proboscis or stalk can represent a protrusion that marks a site of attachment to a host structure (Piperno 2006, pg. 39) or possibly a bended upper part of a cone or an exaggerated tubercula. Ornamented ovate phytoliths can be also cystoliths.		
Potential Cystolith	Cystolith	CYS	**Forest indicator (TSH)**	Cystolith's phytoliths have been isolated and described from many families of dicot plants.	Piperno 1988, 2006, Runge, 1999	
Circular large > 25 µ Circular medium 12.5 - 25 µ Circular small < 12.5 µ Spheroidal large > 25 µ Spheroidal medium 12.5 - 25 µ Spheroidal small < 12.5 µ Subspheroidal large > 25 µ Subspheroidal medium 12.5 - 25 µ Subspheroidal small < 12.5 µ	Spheroid psilate	SPH_PSI	**Forest indicator (TSH)**	widely distributed in different tissues, organs and taxonomic groups; found also in seeds	Kondo et al. 1994, ICPT 2.0, 2019, Madella et al., 2005, Piperno 1988 (Fig. 6), 2006, Strömberg, 2004, 2005, Strömberg et al., 2018, Runge, 1999	Plate 3.4
Circular small Type B	Spheroid psilate with nodule	SPH_PSI_nod		Visual nodule can represent a tubercula, a papilla or a possible former attachment to a host structure or another spheroid; a possible non-phytolith confuser for Spheroid psilate with a nodule or collar are the Chrysophyte cysts		
Circular small with proboscis or nodule Subspheroidal with proboscis	Spheroid psilate with proboscis	SPH_PSI_prob		Small smooth spheroidal or subspheroidal phytoliths with a nodule or proboscis were also found in wood	Collura and Neumann, 2017	
Spheroidal granulate Spheroidal nodulate Spheroidal tuberculate Spheroidal tuberculate small Subspheroidal nodulate Subspheroidal nodulate tuberculate Subspheroidal tuberculate	Spheroid ornate	SPH_ORN	**Forest indicator (woody vegetatation)**	SPH_ORN occur in leaves, branches, trunks and fruits of woody eudicots as well as in vegetative structures of some herbaceous monocots. Used along with OVA_ORN as indicator for woody vegetation in the calculation D:P (Dicotleydon:Poaceae) index.	ICPT 2.0, 2019, Piperno, 2006	
Spheroidal tuberculate with proboscis Spheroidal medium with proboscis Spheroidal small with proboscis Subspheroidal tuberculate with proboscis	Spheroid ornate with proboscis	SPH_ORN_prob		Visual proboscis or stalk can represent a protrusion that marks a site of attachment to a host structure (Piperno 2006, pg. 39) or possibly a bended upper part of a cone or an exaggerated tubercula.		

Hair cell	Acute bulbosis	ACU_BUL	**Mix (Inconclusive)**	Hair cell phytoliths are largely found in grasses and sedges as well as in many dicots	ICPT 2.0, 2019, Mercader et al., 2009, Piperno 1983, 1988, 2006, Strömberg, 2003	Plate 3.5
Oblong	Acute bulbosis or Blocky	ACU_BUL or BLO				
Ovate large > 25 µ	Blocky	BLO	**Mix (Inconclusive)**	BLO are very common in leaves of Cyperaceae and Poaceae, but also in trees, herbs and shrubs.	ICPT 2.0, 2019	
Ovate enigmatic						
Polygonal						
Polyhedral						
Quadrilateral						
Quadrilateral irregular						
Rectangular						
Rectangular irregular						
Rectangular tuberculate						
Rectangular very large						
Rectangular with spikes						
Trapeziform						
Triangular						
Triangular irregular						
Reniform	Blocky or Ovate psilate	BLO or OVA_PSI	**Mix or Forest indicator (TSH)**			
Reniform irregular	Blocky or Ovate ornate	BLO or OVA_ORN	**Mix or Forest indicator (woody)**			
Reniform nodulate						
Reniform tuberculate						
Reniform with proboscis	Blocky or Ovate ornate with proboscis	BLO or OVA_ORN_prob				
Cylindrical	Elongate entire	ELO_ENT	**Mix (Inconclusive)**	ELO_ENT can result from the silification of cells within different plant tissues and organs - in lycophytes, conifers, monocots, dicots.	ICPT 2.0, 2019 and citation therein	
Elongate						
Elongate large (>25µm, obviously big)						
Elongate with curved ends Type C						
Elongate with a top Type D	Elongate entire veloate	ELO_ENT_VEL				
Acute	Acicular	ACI	**NA**	Morphotypes were named according to current Nomenclature, but were not further elaborated, because could not be associated with any plant group.	ICPN 2.0, 2019	Plate 3.6
Ameboidal	Ameboid	AME				
Arcuate (anchor, boomerang, arch)	Arcuate	ARC				
Claviform	Claviform	CLA				
Enigmatic	Enigmatic	ENI				

GSSCP = Grass Silica Short Cell Phytolith; TSH = Trees-Shrubs-Herbs; Mix = can result from different vegetation types; Poaceae = grasses; Cyperaceae = sedges; Dicotleydon = Dicots

3.2.3 $\delta^{13}C$ isotopic signature analysis and carbon quantification

The same 44 sediment samples from Outside GS1 that underwent phytolith analysis were also used for $\delta^{13}C_{SPAC}$ isotope analysis (Table T3.1). From Inside GS1, only 13 samples were analysed for $\delta^{13}C_{SPAC}$ (Table T3.2). The $\delta^{13}C$ value was obtained from in two forms of carbon: Total Organic Carbon (TOC) and Stable Polycyclic Aromatic Carbon (SPAC). Here, TOC represents the carbon in all organic matter present in the sample, i.e. particles of fresh roots, leaves, bark, resin, soils, organic carbon etc., whereas SPAC represents the particularly stable component of pyrogenic carbon that forms during combustion of the organic matter at 500–600°C, as described in section 3.1.2.1. The percentage of SPAC in TOC was also measured, to determine what amount of the organic matter in the analysed sample represents preserved combusted organic matter. Undertaking these measurements first required the isolation of SPAC from the TOC and then running the $\delta^{13}C_{TOC}$ and $\delta^{13}C_{SPAC}$ analysis.

3.2.3.1 Carbon quantification using the hydrogen pyrolysis method (hypy)

The SPAC component was isolated by hydrogen pyrolysis (hypy), an established method for quantifying SPAC (Ascough et al., 2009, Meredith et al., 2012, Wurster et al., 2012). With the application of the hypy method, labile carbon is removed, leaving a stable form of pyrogenic carbon with greater than seven condensed aromatic rings, referred to as SPAC. The hypy procedure and sample pretreatment are described in section 2.2.3.2.1 (Chapter 2). The SPAC proportions in samples were calculated from the losses following the hypy treatment. The SPAC component was then used for isotope composition analysis.

3.2.3.2 $\delta^{13}C_{TOC}$ and $\delta^{13}C_{SPAC}$ determination

Carbon abundances and isotope compositions of TOC and SPAC were measured via elemental analysis isotope ratio mass spectrometry (EA-IRMS) using a ThermoScientifc Flash EA with Smart EA option coupled via a Confo IV to a Delta VPlus mass spectrometer. Carbon abundances were determined using a TCD (Thermal Conductivity Device). Carbon isotope measurements are reported as per mil (‰) deviations from the VPDB (Vienna Pee Dee Belemnite) reference standard scale for $\delta^{13}C$ values. USGS-40 and two internal laboratory reference materials (Taipan, Chitin) were used within each analytical sequence for 3-point calibrations (normalization) of isotope delta-scale anchored to the VPDB scale. Internal standards were calibrated using USGS40 and USGS41 international reference materials (Figure F3.7). SPAC abundances were corrected for possible in situ production of SPAC during the hypy reaction, and errors estimated for carbon isotope composition.

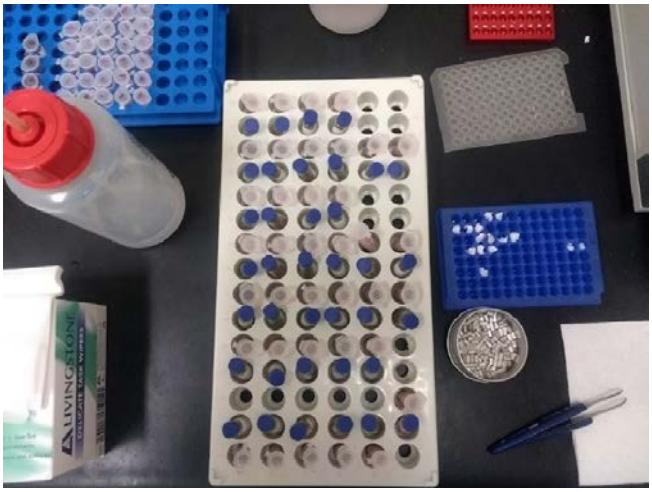

Figure F3.7: The preparation of sample inserts with standards for $\delta^{13}C$ measurement

3.2.4 Dating

Age estimations for the open-site, non-archaeological sediments expanding outside GS1 (Figure F3.8) were obtained with the Optically Stimulated Luminescence (OSL) method performed in the OSL Laboratory at the University of Wollongong, Australia, and by macro-charcoal radiocarbon dating conducted at the Waikato Radiocarbon Dating Laboratory in New Zealand. Radiocarbon dates for the archaeological deposit inside the GS1 rockshelter (Figure F3.9) were produced at the Australian National University in Canberra or the Waikato Radiocarbon Dating Laboratory in New Zealand. The dating methods and procedures applied in this study to obtain a chronology framework for the non-archaeological sediment deposit expanding outside GS1 (beyond the dripline) are explained in detail in Chapter 2.

3.3 Results

The phytolith and $\delta^{13}C$ results and other relevant information, are presented in Tables T3.2 and T3.3 and discussed below.

Table T3.2 Phytolith and $\delta^{13}C$ results from Outside GS1 dataset

Sample ID	Sampling method	Depth (cm)	Dripline distance (m)	SUM Phytoliths	SUM Irregular body	Chrysophytae cyst/ Spongie spicules/Diatoms	SUM Burned / Weathered Phytoliths	TOC in sample (%)	SPAC in sample (%)	SPAC in TOC (%)	$\delta^{13}C_{TOC}$ (‰)	$\delta^{13}C_{SPAC}$ (‰)	D/P	F/F-t (%)
PA_1-M	auger	10	68	**122**	11	0	7/0	0,88	0,10	11,08	-21,73	-21,99	0,31	58
PA_2-M	auger	25	73	**115**	1	1/0/0	1/0	0,61	0,05	8,44	-22,28	-21,55	0,31	48
PA_3-M	auger	50-60	45	**114**	13	0	1/2	0,42	0,06	15,18	-23,16	-21,58	0,34	64
PA_4-M	auger	30-37	52	**111**	15	0	4/4	0,43	0,05	11,09	-23,27	-21,59	0,50	63
PA_5-M	auger	15	37	**108**	16	0	3/9	0,72	0,16	22,62	-22,21	-21,47	0,88	70
PA_6-M	auger	50-60	37	**112**	10	1/1/0	2/14	0,21	0,03	15,18	-22,24	-22,17	1,96	72
PA_7-M	auger	55-65	32	**112**	7	0	5/11	0,25	0,04	17,33	-22,50	-22,21	2,25	76
PA_8-M	auger	122-140	29	26	4	0	3/3	0,11	0,03	26,22	-23,01	-23,99	NA	NA
PA_9-M	auger	150-160	22	**95**	15	0	4/21	0,12	0,03	26,41	-23,75	-24,54	2,64	81
PA_10-M 42	pit	42-43	19	**109**	19	0	3/20	0,34	0,07	19,46	-23,38	-22,39	5,80	88
PA_10-M 50	pit	50-52	"	**120**	10	0	1/1	0,30	0,05	16,27	-22,56	-22,02	5,62	87
PA_10-M 60	pit	60-65	"	**107**	23	1/0/0	2/14	0,21	0,03	15,77	-23,21	-22,49	1,52	72
PA_10-M 65	pit	65-67	"	**118**	9 *	0	2/7	0,25	0,04	15,94	-22,75	-21,62	3,73	83
PA_10-M 80	pit	80-82	"	**112**	19 *	0	1/11	0,19	0,03	14,32	-22,22	-21,07	3,47	83
PA_10-M 100	pit	100-105	"	**90**	19 *	0	3/15	0,11	0,02	21,50	-22,53	-22,72	2,33	81
PA_10-M 102	pit	100-102	"	73	13	0	0/20	0,12	0,02	20,34	-22,08	-21,46	NA	NA
PA_10-M 120	pit	120-122	"	**111**	19 *	0	1/18	0,12	0,02	20,32	-21,98	-20,12	2,67	78
PA_10-M 150	pit	150-152	"	10	0	0/0/1	0/0	0,14	0,03	18,32	-22,02	-20,34	NA	NA
PA_10-M 172	pit	168-172	"	**107**	9	0	4/18	0,22	0,05	21,97	-23,92	-22,11	1,44	72
PA_11-M 60	auger	60±5	25	**111**	23	1/0/0	2/26	0,26	0,05	20,33	-23,18	-22,06	2,64	82
PA_11-M 140	auger	140-160	"	9	1	0	0/3	0,11	0,03	24,03	-23,21	-22,34	NA	NA
TP01 0	pit	0	10	**107**	8 *	0	10/4	0,89	0,09	9,88	-24,02	-22,07	1,13	66
TP01 40	pit	40	"	**110**	9	0	1/15	0,59	0,10	16,47	-23,07	-22,30	0,83	60
TP01 60	pit	60	"	**108**	14	0	1/13	0,36	0,07	18,11	-22,97	-22,24	4,13	83
TP01 80	pit	80	"	**107**	11	0	1/22	0,23	0,04	16,72	-22,70	-22,56	6,22	90
TP01 120	pit	120	"	**112**	10	0	5/14	0,16	0,04	23,89	-23,19	-22,73	5,71	90
TP02 20	pit	20	20	**110**	15	2/0/0	5/2	0,43	0,05	12,65	-23,13	-21,75	0,72	57
TP02 40	pit	40	"	**109**	3	0	1/22	0,31	0,06	20,87	-23,37	-22,25	0,70	60
TP02 60	pit	60	"	**105**	11	0	0/14	0,26	0,05	17,40	-22,32	-22,20	2,00	73
TP02 100	pit	100	"	**85**	8	0	0/21	0,12	0,03	21,72	-22,69	-22,23	3,00	81
TP02 120	pit	120	"	**89**	13	0	2/25	0,10	0,03	27,19	-22,78	-22,12	5,29	90
TP03 60	pit	60	30	**110**	18	0/1/0	1/10	0,23	0,04	15,99	-21,46	-21,44	1,90	76
TP03 120	pit	120	"	47	4	0	1/16	0,13	0,02	18,18	-22,60	-22,53	NA	NA
TP04 20	pit	20	40	**115**	9	0	5/9	0,60	0,06	9,23	-22,86	-21,36	1,69	77
TP04 80	pit	80	"	**111**	2	1/0/0	3/23	0,19	0,03	18,32	-21,97	-21,29	2,88	87
TP05 0	pit	0	50	**112**	9	0/0/3	13/2	0,65	0,07	10,24	-24,02	-22,27	0,32	39
TP05 40	pit	40	"	**113**	9	1/0/0	1/11	0,30	0,06	19,02	-22,16	-21,98	2,42	82
TP05 60	pit	60	"	**110**	12	0	2/7	0,27	0,05	19,44	-22,19	-22,09	2,09	74
TP05 80	pit	80	"	**86**	4	0	4/20	0,16	0,03	19,85	-22,42	-21,58	8,25	94
TP05 100	pit	100	"	**116**	19	0	3/21	0,18	0,03	16,33	-21,50	-22,06	1,77	69
TP05 120	pit	120	"	**113**	15	0	8/11	0,27	0,04	15,95	-22,49	-22,45	1,75	70
C_1-CR 100	core head	100	68	**86**	12	0	0/13	0,15	NA	NA	-22,95	-21,88	13,00	94
C_1-CR 135	core head	135	"	**105**	17	0	1/16	0,15	0,03	22,02	-23,56	-22,39	3,50	83
C_1-CR 200	core head	200	"	**106**	20	0	0/11	0,12	0,01	11,39	-23,69	-21,33	NA (P=0)	NA (P=0)

D = Dicotleydons (Dicots); P = Poaceae (grasses); F = Forest indicators; t = time; NA = sample is not representative; * samples where geniculate irregular bodies were observed

Table T3.3 Phytolith and $\delta^{13}C$ results from Inside GS1 dataset

Sample ID	Sampling method	Depth (cm)	SUM Phytoliths	SUM Irregular body	Chrysophytae cyst/ Spongie spicules/Diatoms	SUM Burned / Weathered Phytoliths	TOC in sample (%)	SPAC in sample (%)	SPAC in TOC (%)	$\delta^{13}C_{TOC}$ (‰)	$\delta^{13}C_{SPAC}$ (‰)	D/P	F/F-t (%)
C1-01	spit	3,1	**115**	12	2/0/0	1/11	1,4	0,21	14,77	-24,53	-23,09	0,42	53
C1-02	spit	8,6	**118**	1	0	0/NA						0,86	92
C1-03	spit	13,6	**112**	8	0	0/20	2	0,82	41,13	-24,08	-23,64	0,92	84
C1-04	spit	18,9	**109**	10	1/1/0	1/NA						1,64	88
C1-05	spit	24,0	**116**	14	0	0/NA	1,8	1,25	69,54	-24,22	-23,91	4,25	92
C1-06	spit	28,4	**108**	9	1/0/0	0/14						3,17	93
C1-07	spit	32,8	**119**	19	0	0/NA						NA (P=0)	NA (P=0)
C1-08	spit	37,6	**110**	3	0	1/14						1,50	89
C1-09	spit	42,4	**110**	18	0	0/NA	1,39	0,36	25,82	-23,96	-23,57	4,25	92
C1-10	spit	47,2	**111**	0	0	0/NA						NA (P=0)	NA (P=0)
C1-11	spit	52,2	**106**	4	1/0/1	1/16						1,18	81
C1-12	spit	57,0	**118**	12	0	0/NA						1,07	85
C1-13	spit	61,5	**120**	4	0	0/15						4,86	93
C1-14	spit	66,3	**115**	18	0	0/NA	0,93	0,14	15,14	-23,32	-23,32	3,13	90
C1-15	spit	70,9	**118**	3	0/1/0	1/NA						1,50	94
C1-16A	spit	75,6	**107**	4	0	2/19						0,50	65
C1-16B	spit	75,6	**107**	3	0	0/38						NA (P=0)	NA (P=0)
C1-17A	spit	80,5	**116**	6	0	0/NA						1,31	87
C1-17B	spit	80,5	**110**	8	1/0/0	0/NA	0,68	0,10	14,44	-25,23	-22,80	2,44	90
C1-19	spit	88,7	**106**	17	0	0/NA						3,43	91
C1-20	spit	92,8	**106**	16	1/0/0	0/NA						2,67	93
C1-21	spit	96,6	**109**	13	0	0/13						0,52	64
C1-22	spit	100,6	**112**	4	2/0/0	0/20	0,54	0,12	22,14	-23,43	-22,91	0,88	83
C1-23	spit	105,5	**108**	2	0	2/31						0,77	69
C1-24	spit	110,5	**106**	8	0	0/NA						2,86	92
C1-25	spit	115,5	**115**	8	1/0/0	0/NA						NA (P=0)	NA (P=0)
C1-26	spit	120,4	**105**	5	0	0/64	0,46	0,11	23,38	-23,36	-22,67	4,80	94
C1-27A	spit	125,4	**105**	9	0	0/NA						NA (P=0)	NA (P=0)
C1-27B	spit	125,4	**84**	8	0	0/22						NA (P=0)	NA (P=0)
C1-28	spit	130,4	**86**	9	0	0/73						0,89	88
C1-29	spit	135,3	**104**	18	1/0/0	0/NA						2,00	89
C1-30	spit	140,4	29	2	0	0/NA						NA	NA
C1-31	spit	145,4	20	1	0	0/21						NA	NA
C1-32A	spit	149,6	14	0	0	0/NA						NA	NA
C1-32B	spit	149,6	16	4	0	0/NA						NA	NA
C1-33A	spit	156,3	26	3	0	0/30						NA	NA
C1-33B	spit	156,3	15	3	0	0/6						NA	NA
C1-34A	spit	163,4	26	4	0	0/NA	0,17	0,04	26,49	-23,45	-22,03	NA	NA
C1-34B	spit	163,4	13	2	0	0/NA						NA	NA
C1-35A	spit	168,5	6	1	0	1/NA						NA	NA
C1-35B	spit	168,5	33	13	0	0/NA						NA	NA
C1-36A	spit	173,5	14	1	0	0/10						NA	NA
C1-36B	spit	173,5	20	1	0	0/12	0,15	0,03	23,17	-23,34	-22,98	NA	NA
C1-37A	spit	178,8	**87**	17	0	0/NA						1,50	92
C1-37B	spit	178,8	31	13	0	0/NA						NA	NA
C1-38A	spit	183,5	3	0	0	0/4						NA	NA

C1-38B	spit	183.5	5	0	0	0/NA						NA	NA	
C1-39A	spit	187.9	0	0	0	0/NA						NA	NA	
C1-39B	spit	187.9	14	0	0	1/NA						NA	NA	
C1-40A	spit	193.0	6	1	0	0/NA						NA	NA	
C1-40B	spit	193.0	7	0	0	0/NA						NA	NA	
C1- 41A	spit	198.0	3	1	0	0/NA						NA	NA	
C1-41B	spit	198.0	0	1	0	0/1						NA	NA	
C1-42	spit	202.6	8	0	0	0/NA	0.08	0.02	25.17	-23.34	-25.08	NA	NA	
C1- 43	spit	207.3	4	1	0	0/NA						NA	NA	
C1-44	spit	212.5	5	0	0	0/NA						NA	NA	
C1-45	spit	218.2	3	0	0	0/NA						NA	NA	
C1- 46	spit	223.8	14	1	0	0/1						NA	NA	
C1-47	spit	228.3	10	6	0	1/NA						NA	NA	
C1-48	spit	232.1	11	0	0	0/NA	0.06	0.01	22.15	-23.99	-22.34	NA	NA	
C1- 49	spit	235.8	1	0	0/0/1	4/NA						NA	NA	
C1-50	spit	239.5	2	0	0	0/NA						NA	NA	
C1-51	spit	243.5	3	2	0	1/NA						NA	NA	
C1-52	spit	248.9	9	0	0	1/NA	0.10	0.02	18.00	-22.70	-23.16	NA	NA	

D = Dicotleydons (Dicots); P = Poaceae (grasses); F = Forest indicators; t = time; NA = sample is not representative

3.3.1 Phytolith results

In the non-archaeological open-site sediment samples Outside GS1, 4 of the 44 samples yielded less than 80 phytoliths for counting. The remaining 40 samples met the predetermined sample size of 100 (±20) (Table T3.2). In general, the abundance of phytoliths started to decline below 60 cm in depth, although no reliable relationship between phytolith abundance and depth was evident. For example, sample PA_9-M at 150 cm below the surface contained abundant phytoliths, while sample PA_8-M at 120 cm below the surface did not. Similarly, in pit PA_10-M, the samples were not representative at depths 102 cm and 150 cm, but they were representative at 120 cm and 162−172 cm. On average, the amount of weathered and damaged phytoliths is higher in the medium depth ranges, between 80 and 120 cm, with the exception of sample PA_10-M at 42 cm and PA_9-M at 140 cm depth. A total of 120 burned phytoliths were observed, along with a single sponge spicule and three diatoms (Table T3.2).

In contrast, in the archaeological sediment samples Inside GS1, phytoliths were abundant to 135.3 cm depth (sample C1-29) (Table T3.3). Below this depth, apart from C1-37A at a depth of 178.8 cm, all samples were devoid of representative phytoliths. Altogether, 32 samples met the predetermined sample size of 100 (±20) (Table T3.3). The abundance of weathered and/or damaged phytoliths does not follow any particular pattern, with the proportion of burned phytoliths being very low (Table T3.). Two sponge spicules and two diatom frustules were recorded.

3.3.1.1 Identified phytolith morphotypes

Phytoliths were classified into 25 morphotypes (classification: Table T3.1, morphotypes description: Appendix A3.2) that were in turn attributed to 5 vegetation groups:

- 9 morphotypes to grasses (*Poaceae*),
- 2 morphotypes to grasses (*Poaceae*) and/or sedges (*Cyperaceae*),
- 1 morphotype to sedges (*Cyperaceae*),
- 10 morphotypes to trees, shrubs and herbs. These are referred to as 'forest indicators' and
- 3 morphotypes were found to be inconclusive and were not attributed to any group in particular.

3.3.1.1.1 Grass Morphotypes (Plate P3.1)

Grass Short Silica Cell Phytoliths (GSSCP) include:

- Bilobate (BIL) (Plate P3.1a–d)
- Cross (CRO) (Plate P3.1f–h)

- Not-defined Grass Silica Short Cell Phytoliths (ndGSSCP) (Plate P3.1i–r)
- Polylobate (POL) (Plate P3.1s)
- Rondel (RON) (Plate P3.1t–y)
- Saddle (SAD) (Plate P3.1aa–ac)
- Trapezoid (TRZ) (Plate P3.1ad)

Bilobates were observed in all samples in both assemblages – Outside GS1 and Inside GS1. The proportions of Bilobates from Outside GS1 is significantly higher than the number in the Inside GS1 sample (Figures F3.8, F3.9), though in both many are broken and present as Unilobes. Few specimens with a particularly long castula were attributed to *Aristida* sp. (Plate P3.1a,b) (Wallis, 2000). Along with Bilobate, ndGSSCP is the most common grass morphotype in both assemblages (Figure F3.8, F3.9). The ndGSSCP morphotype consists of different grass silica short-cell phytoliths that are clearly grass affiliated but could not be attributed to other grass morphotypes. In both assemblages, Rondel is the third most frequently counted grass morphotype, following Bilobate and ndGSSCP (Figures F3.8, F3.9).

Cross phytoliths are present sporadically in both assemblages. However, more crosses were counted in samples Outside GS1 than Inside GS1 (Figure F3.8, F3.9). Polylobate, Saddle and Trapezoid morphotypes are generally poorly represented in both assemblages (Figure F3.8, F3.9).

Non-GSSCP grass morphotypes include:

- Papillate (PAP) (Plate 3.1ae–af)
- Elongate dentate (ELO_DET) (Plate 3.1ag–ai)

Papillates are rare in both assemblages (Outside GS1 and Inside GS1), while the presence of Elongate dentate is moderate and more frequent Outside GS1 (Figures F3.8, F3.9).

3.3.1.1.2 Grass and Sedge Morphotypes (Plate P3.2)

- *Bulliform flabellate (BUL_FLA) (Plate P3.2–d)*
- *Elongate sinuate (ELO_SIN) (Plate P3.2e–h)*

The Bulliform flabellate and Elongate sinuate morphotypes are rare and slightly more frequent Outside GS1 than Inside GS1 (Figure F3.8, F3.9).

3.3.1.1.3 Sedge Morphotypes (Plate P3.2)

- Sedge plate (SED_PLA) (Plate P3.2i–l)

Sedge plate was counted only in two samples Inside GS1 but was found to be more frequent in Outside GS1 assemblages (Figures F3.8, F3.9). A few specimens counted as 'Elongate with a top' or 'Elongate velloate' (Table T3.1) were also added to this morphotype based on Murungi and Bramford (2020, e.g. Plate II,13).

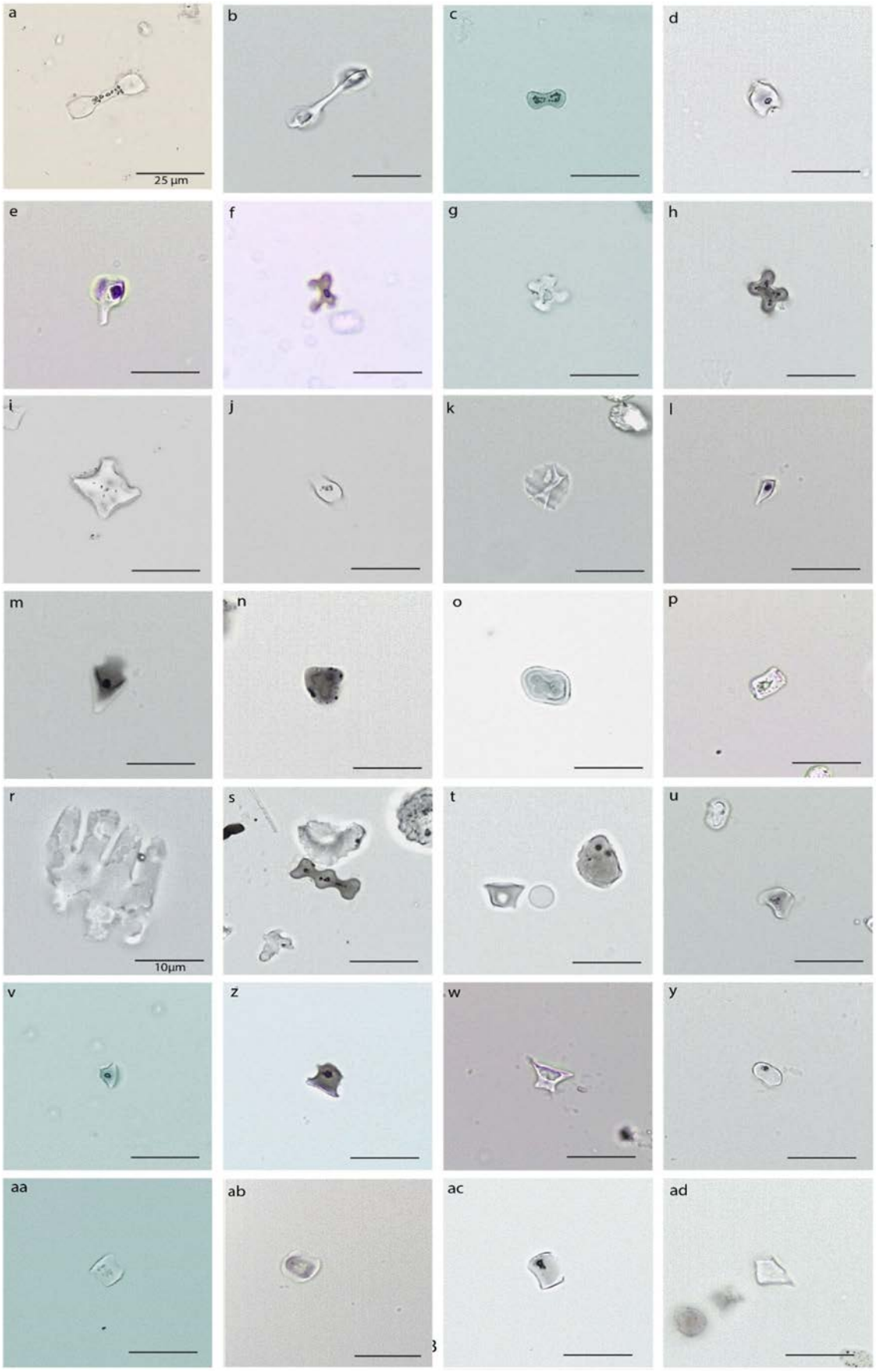
a
25 µm
b
c
d
e
f
g
h
i
j
k
l
m
n
o
p
r
10µm
s
t
u
v
z
w
y
aa
ab
ac
ad

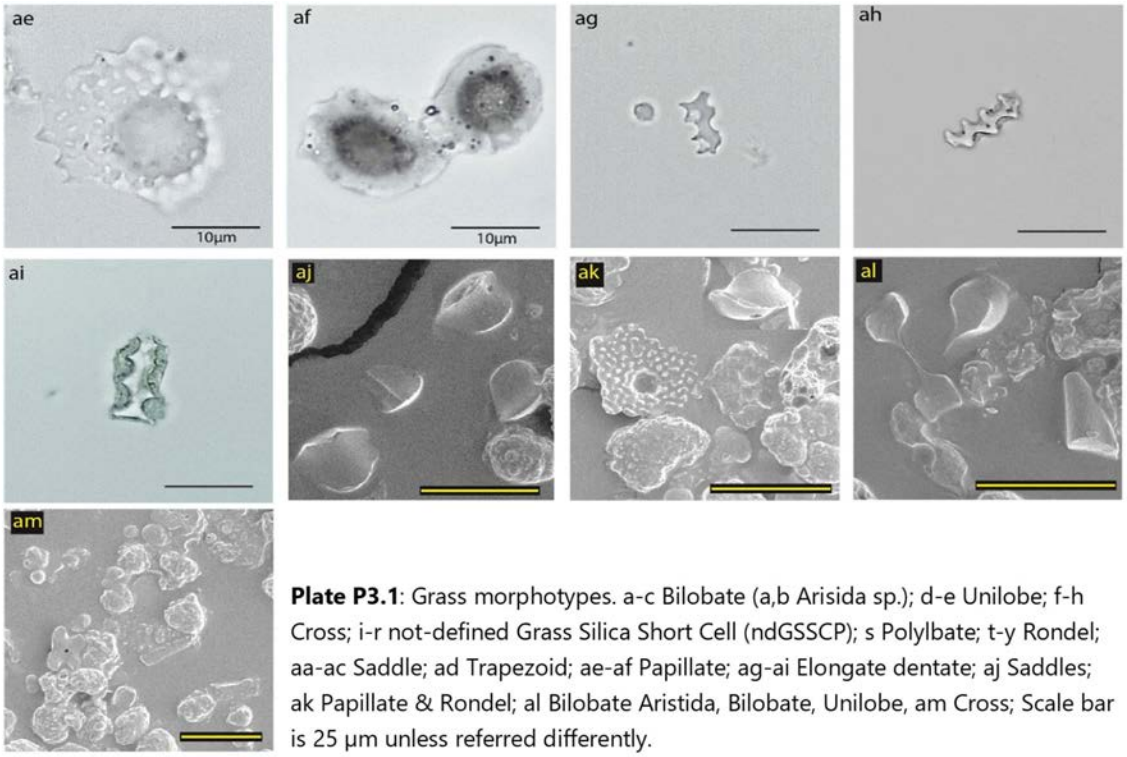

Plate P3.1: Grass morphotypes. a-c Bilobate (a,b Arisida sp.); d-e Unilobe; f-h Cross; i-r not-defined Grass Silica Short Cell (ndGSSCP); s Polylbate; t-y Rondel; aa-ac Saddle; ad Trapezoid; ae-af Papillate; ag-ai Elongate dentate; aj Saddles; ak Papillate & Rondel; al Bilobate Aristida, Bilobate, Unilobe, am Cross; Scale bar is 25 µm unless referred differently.

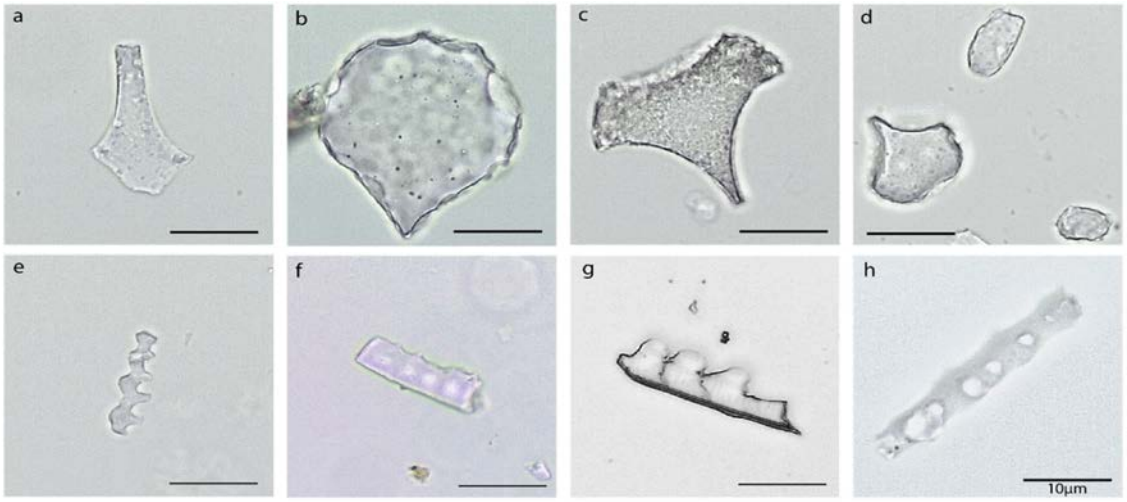

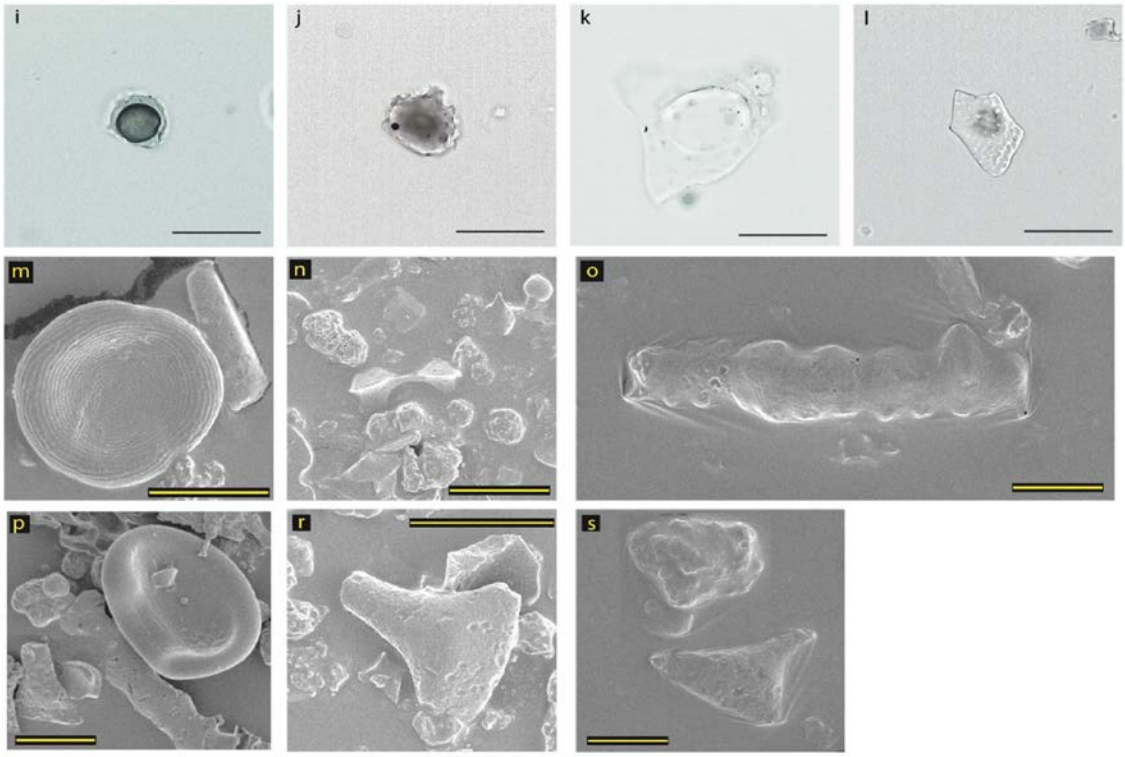

Plate P3.2: Grass and Sedge morphotypes. a-d Bulliform flabellate; e-h Elongate sinuate (f-h Cyprus sp., (Wallis, 2000)); Sedge morphotypes. i-l Sedge plate; m Sedge plate; n Sedge plates (two disk shapes in the middle); o Elongate sinuate; p Sedge plate; r-s Bulliform flabellate; Scale bar is 25 µm unless referred differently.

3.3.1.1.4 Tree, shrub and herb Morphotypes (Forest indicators) (Plate P3.3, P3.4)

Ovate morphotypes (Plate P3.3) include:

- Ovate psilate (OVA_PSI) (Plate P3.3a,b)
- Ovate ornate (OVA_ORN) (Plate P3.3c–e,g)
- Ovate psilate with proboscis (OVA_PSI_prob) (Plate P3.3f)
- Ovate ornate with proboscis (OVA_ORN_prob) (Plate P3.3f)
- Cystoliths (CYS) (Plate P3.3h,i)

The most frequent morphotype among all present in the Outside GS1 phytolith assemblages is Ovate ornate, outnumbering the second most common morphotype, Ovate psilate, by a factor of two (Figure F3.8). In the Inside GS1 assemblages, Ovate ornate and Ovate psilate are the most common among ovate morphotypes (Figure F3.9). Other ovate morphotypes are moderately common in both assemblages (Figures F3.8, F3.9).

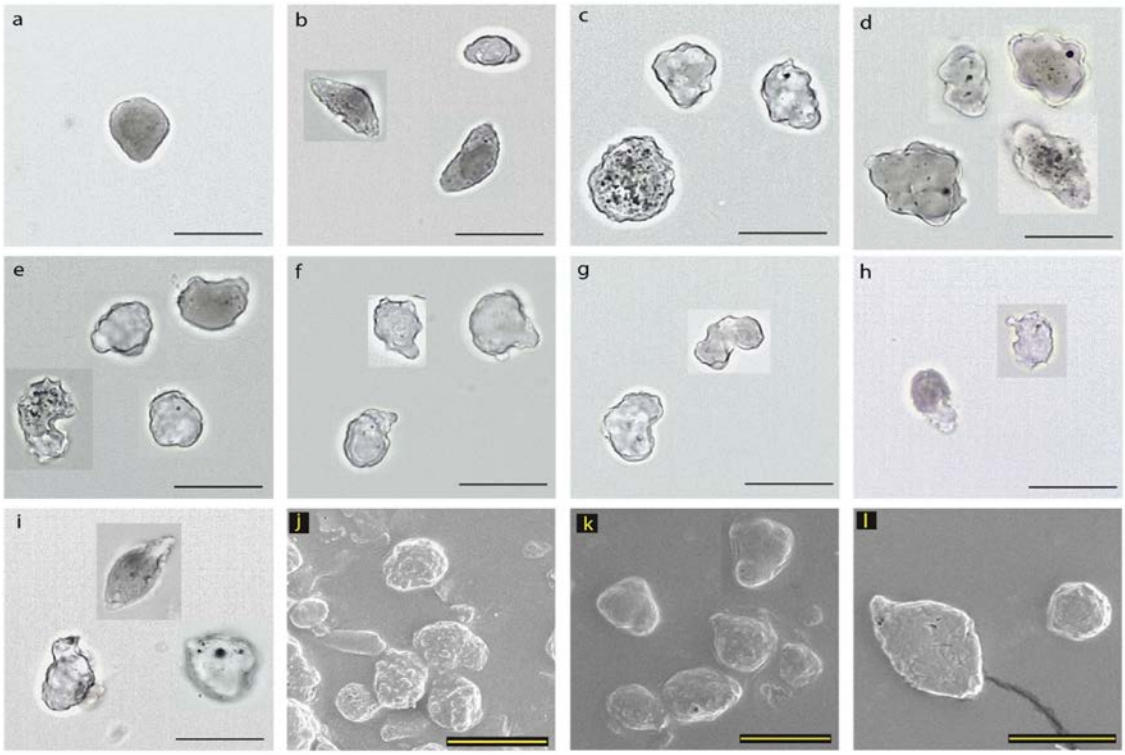

Plate P3.3: Ovate morphotypes Tree, shrub and herb (Forest indicators). a,b Ovate psilate; c,d Ovate ornate; e Ovate ornate and Ovate ornate with proboscis; f Ovate psilate with proboscis and Ovate ornate with proboscis; g Ovate ornate–reniform shape; h,I potential Cystoliths; j Ovate ornate; k Ovate psilate and Ovate ornate–nodulate; Ovate psilate with a stalk and Ovate psilate; Scale bar is 25 µm.

Spheroid morphotypes (Plate P3.4) include:

- Spheroid psilate (SPH_PSI) (Plate P3.4a–c)
- Spheroid psilate with nodule (SPH_PSI_nod) Plate (P3.4c)
- Spheroid psilate with proboscis (SPH_PSI_prob) (Plate P3.4f)
- Spheroid ornate (SPH_ORN) (Plate P3.4d,e)
- Spheroid ornate with proboscis (SPH_ORN with prob) (Plate P3.4f–g)
- Spheroid echinate (SPH_ECH) (Plate P3.4k)

The Spheroid psilate is the dominant morphotype in the Inside GS1 phytolith assemblages (Figure F3.9). In the Outside GS1 samples, Spheroid ornate and Spheroid psilate are the second most common morphotypes, following Ovate ornate and Ovate psilate (Figure F3.8). Other spheroid morphotypes are moderately common in both assemblages (Figures F3.8, F3.9). The Spheroid echinate morphotype is typically associated with palms (Arecaceae) (Benvenuto et al., 2015, ICPT, 2019, Piperno, 1988, 2006). In this study only one Spheroid echinate body was found under SEM (Plate 3.4,k), but none during phytolith

analysis. Therefore, this morphotype is not included as an actual morphotype in the classification procedure (Table T3.1).

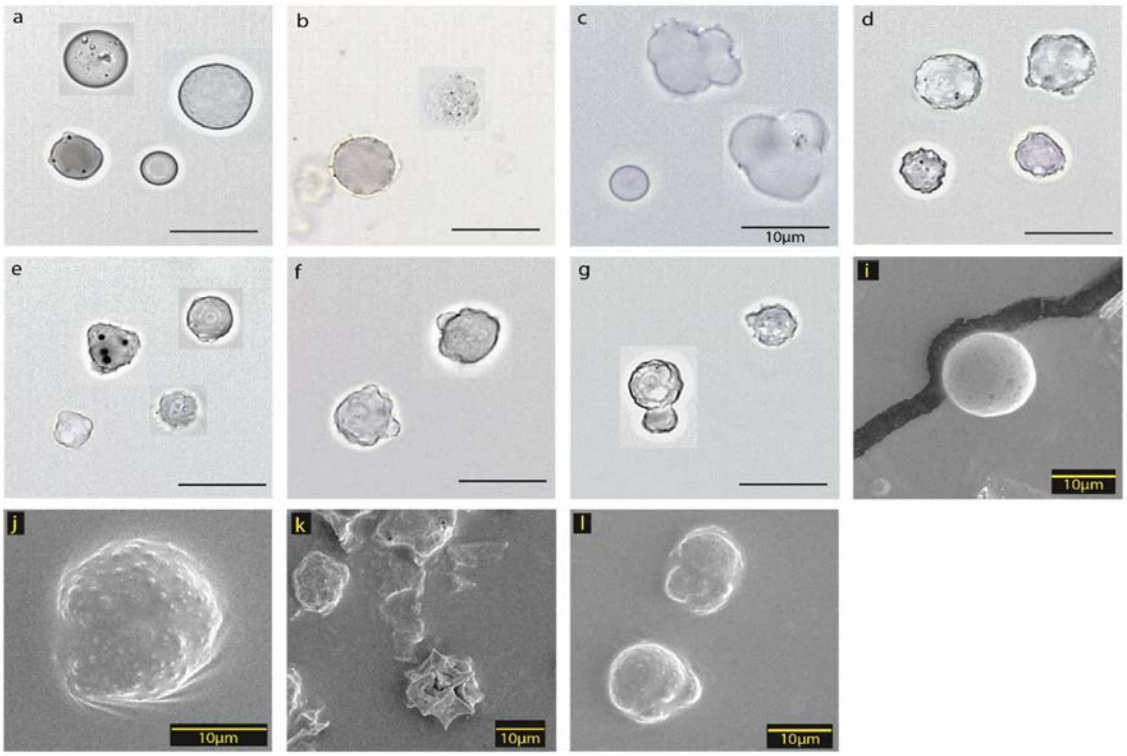

Plate P3.4: Spheroid morphotypes Tree, shrub and herb (Forest indicators). a,b Spheroid psilate; c Spheroid psilate and Spheroid psilate with nodule; d-e Spheroid ornate; f-g Spheroid psilate with proboscis and Spheroid ornate with proboscis; i Spheroid psilate; j Spheroid ornate; k Spheroid echinate, palm phytolith (at the bottom of the picture); l Spheroid ornate; Scale bar is 25 µm unless referred differently.

3.3.1.1.5 Non-diagnostic Morphotypes (Plate P3.5)

- Acute Bulbosus (ACU_BUL) (Plate P3.5a–c)
- Blocky (BLO) (Plate P3.5d–i)
- Elongate entire (ELO_ENT) (Plate P3.5j–k)

Blocky forms in this study come in different shapes, from quadrilateral and rectangular to oblong, sometimes with projections and slightly velloate edges. Surfaces are generally smooth or granulate. Blocky types and Elongate entire morphotypes are common in both Outside GS1 and Inside GS1 assemblages. The presence of Acute Bulbosus is relatively low (Figures F3.8, F3.9). The diagnostic value of these morphotypes is very low, therefore, they were not attributed to any specific plant group.

Plate P3.5:Non-diagnostic morphotypes. a-c Acute bulbosis, hair cell; d-i, l, o Blocky; j-k m, n Elongate entire; Scale bar is 25 µm unless referred differently.

The Outside GS1 phytolith assemblages are generally dominated by Ovate and Spheroid ornate morphotypes, both associated with forest indicators (tree, shrub and herb). On average, grass morphotypes make up around 23% of the phytolith assemblages in the Outside GS1, while potential sedge morphotypes make up less than 0.7%. The morphotype distribution diagram in Figure F3.8 shows the relative abundance of phytolith morphotypes per Outside GS1 sample, grouped into assigned vegetation types. Raw counts are given in Appendix A3.3.

The Inside GS1 phytolith assemblages are dominated by Spheroid and Ovate psilate morphotypes, followed by Ovate ornate, all morphotypes associated with forest indicators (tree, shrub and herb). Following these is the grass morphotype ndGSSCP, although in significantly lower quantities. Generally, grass morphotypes make up around 14.3% of the phytolith assemblages Inside GS1. Potential sedges represent less than 0.1%. The distribution diagram in Figure F3.9 shows the relative abundance of morphotypes per Inside GS1 sample, grouped into vegetation types. Raw counts are given in Appendix A3.4.

When compared, phytolith assemblages from Outside GS1 and Inside GS1 are both dominated by tree, shrub and herb morphotypes (Figure F3.10). While the Outside GS1 assemblages are dominated by the Ovate ornate morphotype, the Inside GS1 assemblages are dominated by Spheroid and Ovate psilate morphotypes. Neither assemblage demonstrates any significant variation in relative abundance as depth increases. Noticeably, more grass phytoliths were counted Outside GS1, particularly in samples higher in the profiles, from shallower depths (Figure F3.10). In general, grass and sedge morphotypes show a higher proportion in Outside GS1 assemblages than Inside GS1 (Figure F3.10). The surface (3 cm) sample from Inside GS1, however, aligns well with surface results from Outside GS1, where both supposedly reflect the current plant composition.

3.3.1.2 Other observations

Burned, etched or weathered phytoliths were present in the Outside GS1 and Inside GS1 assemblages (Tables T3.2, T3.3, Plate P3.6,a,b,e). Approximately half of the counts of weathered phytoliths from Inside GS1 are missing (marked as NA in column 7) because it was decided to count both types only after the study had progressed for some time without counting them.

Irregular bodies (Plate P3.6g,h) are those phytoliths that could not be assigned to any of the morphotypes. In general, they did not show any obvious pattern in their occurrence or abundance, occurring sporadically and randomly, apart from distinct geniculate-shaped phytoliths observed in a limited number of samples Outside GS1 (marked with a star in Table T3.2).

Chrysophyte cysts (Chrysophyceae stomatocysts), sponge spicules and diatoms frustules were rarely observed (Plate 3.6l–t) (Table T3.2, T3.3). While these organisms may provide insights into palaeoenvironmental conditions in certain contexts, their presence in this case is not in significant enough abundance to warrant further investigation.

Plate P3.6: a,b burned phytoliths; c,d etched Blockies; e etched and burned Elongate; f etched Elongate entire; g-h irregular bodies; i Acicular phytoliths (classified as morphotype but not assigned to a plant group, Table T3.1); j Arcuate phytoliths (classified, but not assigned to a plant group, Table T3.1); k Claviform (classified, but not assigned to a plant group, Table T3.1); l-n chrysophyte cysts; o diatoms; p sponge spicule; r-t chrysophyte cysts; Scale bar is 25 µm unless referred differently. Chrysophyte cysts can be best distinguished from Spheroid psilate by a distinct pore, sometimes with a collar, or resembling a proboscis or a flagella. Sponge spiculae can be usually distinguished from translucent elongates by a distinct axial canal, while diatoms tend to have a thick frustule with a very distinct ornamentation that distinguish them from phytoliths.

Outside GS1

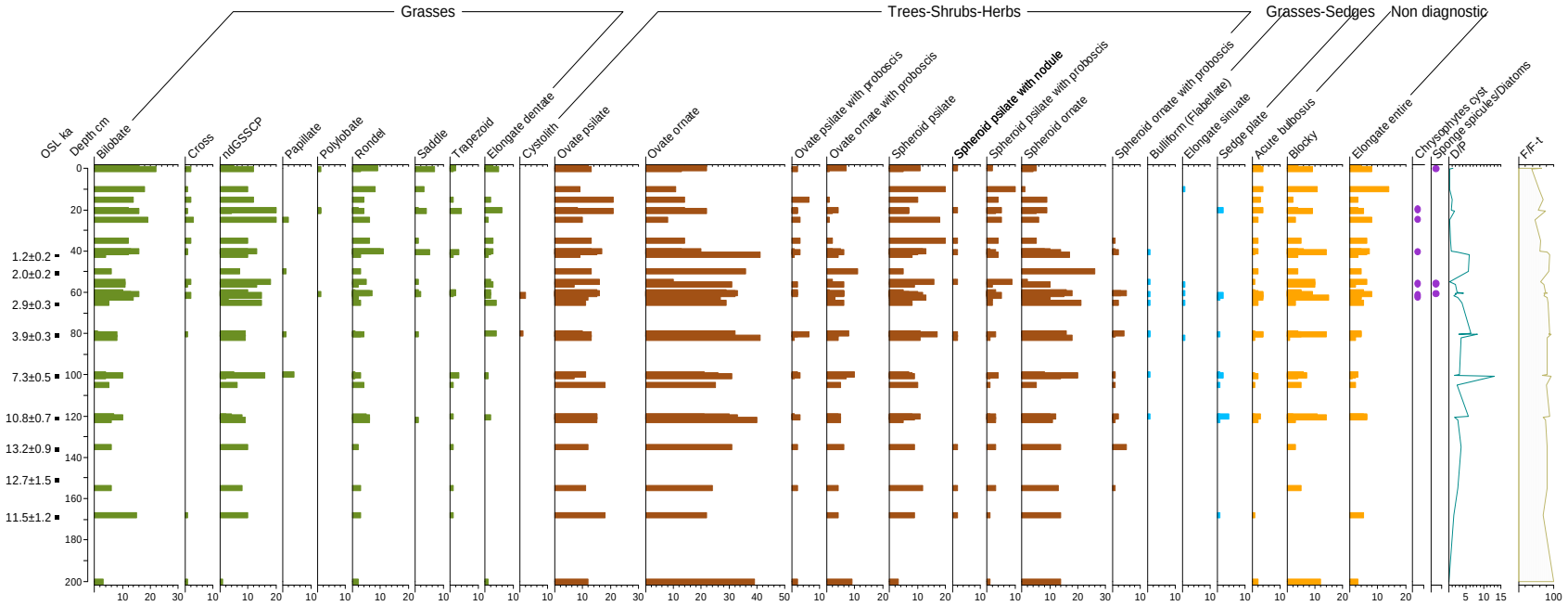

Figure F3.8: Diagram of phytolith assemblages Outside GS1 shown by morphotypes and vegetation types. OSL dates on the left are from the chronology results in Chapter 2. The number of samples included in the diagram analysis N=40. Phytolith indices are presented in the final columns on the right.

Inside GS1

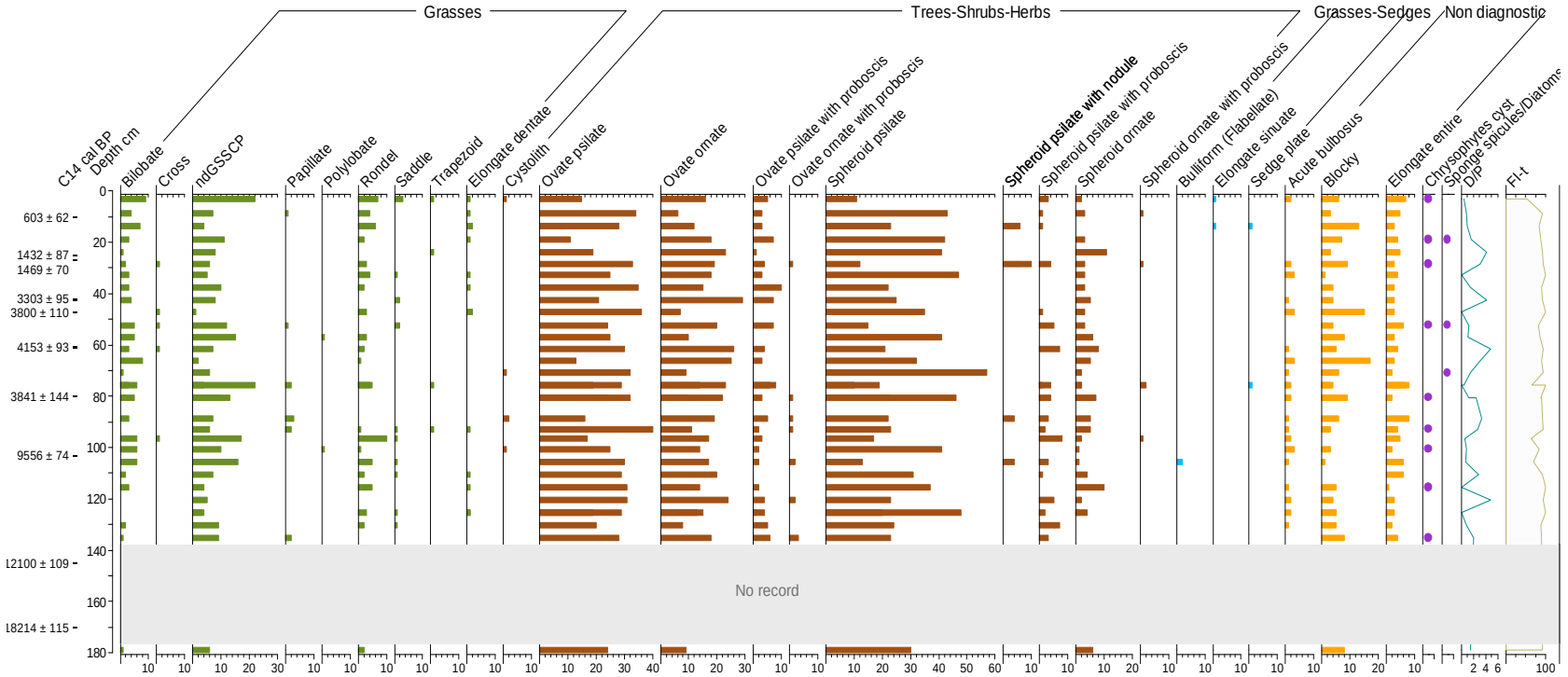

Figure F3.9: Diagram of phytolith assemblages Inside GS1 presented by morphotypes and vegetation types. ^{14}C ages on the left are taken from previous archaeological studies (Lowe et al., 2018, Wallis et al., 2014a). The number of samples included in the diagram analysis N=32. Phytolith indices are presented in the final columns on the right. The grey 'No record' area marks the depth gap where no phytolith representative samples were recorded (see Table T3.3).

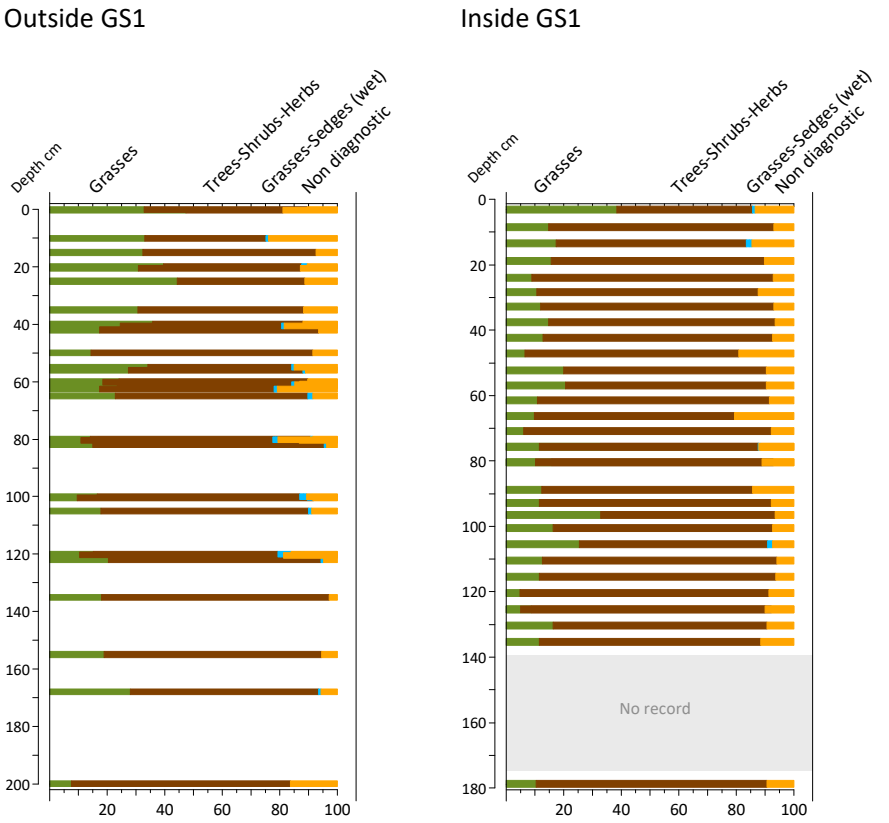

Figure F3.10: Percentage phytolith diagrams of collections Outside GS1 (left side; the number of samples included in the analysis N=40.) and Inside GS1 (right side; the number of samples included in the diagram analysis N=32.); the grey 'No record' zone marks the depth gap where no phytolith representative samples were recorded.

3.3.1.3 Phytolith indices

3.3.1.3.1 Outside GS1

The D/P index values in the non-archaeological Outside GS1 samples ranged from 0.3 to 13 (Table T3.2). Generally, the lowest D/P values correspond to depths between 0–40 cm and the D/P rises with increasing depth, reaching the highest values of 5.6–13 between depths 80–120 cm. At depths below 120 cm the Outside GS1 samples exhibit an erratic decrease in D/P values−2.6, 1.4 and 3.5, respectively (Table T3.2, Figures F3.8, F3.11). The FI-t results agree with D/P results. In alignment with the D/P, the FI-t index exhibits the lowest relative abundance (FI-t=40–65%) in forest indicators (tree-shrub-herb) at depths 0–40 cm. The FI-t then increases gradually with depth until reaching a maximum (FI-t ≥ 90%) at depths 80–120 cm. At depths below 120 cm the FI-t decreases again (FI-t=81, 72, 82%).

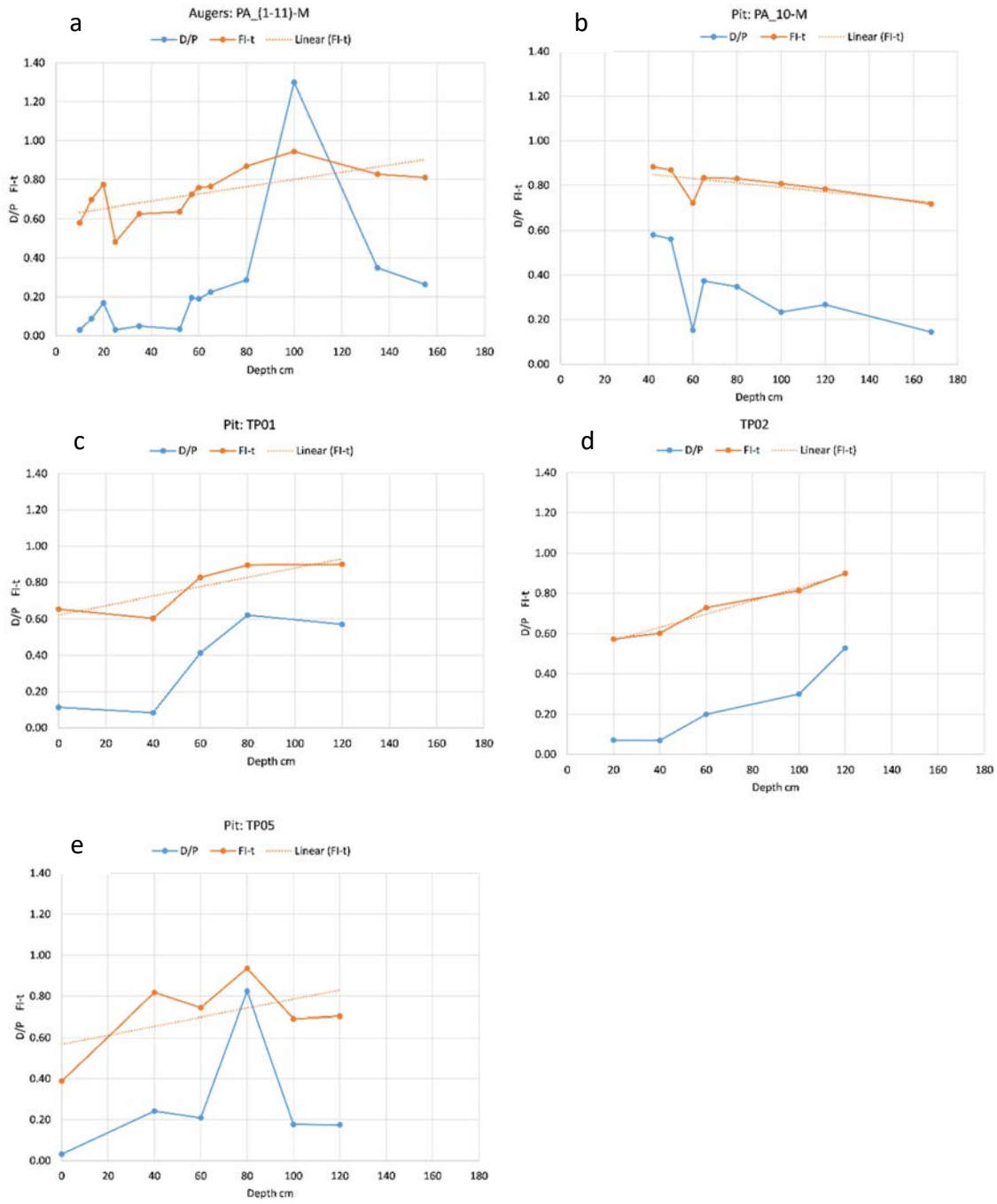

Figure F3.11: Phytolith indices as calculated in the Outside GS1 samples collection. D/P index (blue) and FI-t index (orange) results divided in five graphs; **a** showing the results in auger holes and showing results in pits. Note, the D/P values were divided by 10 and the FI-t values by 100 for the purpose of representation. The linear trend line is placed on the FI-t index.

The change in both phytolith indices in Outside GS1 assemblages is exhibited in Figure F3.8 on the right and Figure F3.11. To show the trend for both indices in the same samples on the same graphs in

Figure F3.11, the D/P values were divided by 10 and the FI-t values by 100. For clarity, the results for pits and auger holes are shown separately. Therefore, some graphs exhibit no value at depth of 0 cm because the first sample in the pit was collected at 20 cm or 40 cm (Figure F3.11a,b,d). One sample (C_1-CR 200) was inconclusive because neither grass nor woody morphotypes reached 5% representativeness, preventing D/P and FI-t from being calculated.

3.3.1.3.2 Inside GS1

Inside GS1, the D/P index values ranged from 0.4 to 4.8 (Table T3.3). The D/P index in phytolith samples from Inside GS1 exhibits a very erratic pattern, shifting from lower to high values over short intervals (Figure F3.9 right side, Figure F3.12). The lowest FI-t index (52%) from Inside GS1 comes from the upper 3 cm. Subsequently, all FI-t values along the profile exceed 64% (Table T3.2, Figures F3.9, F3.12). Six samples were inconclusive for both indices (Table T3.3). To illustrate the trend for both indices in the same samples on a single graph, the D/P values were divided by 10 and the FI-t values by 100, as shown in Figure F3.12.

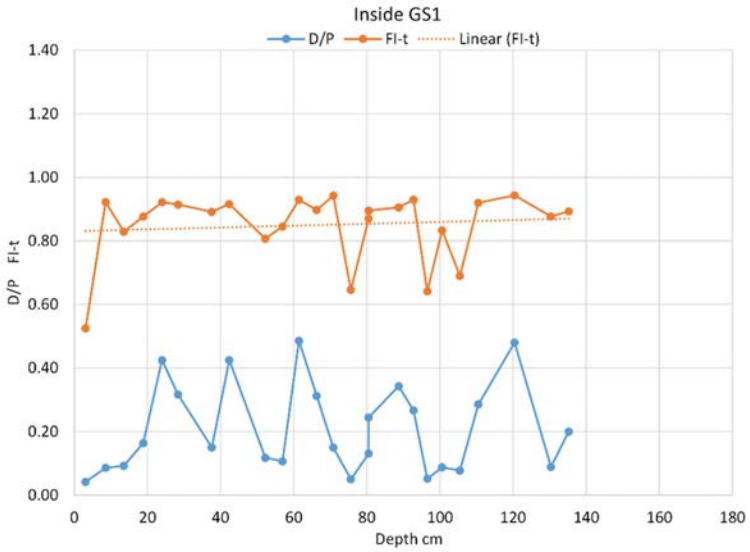

Figure F3.12: The phytolith indices as calculated in the Inside GS1 samples. D/P index (blue) and FI-t index (orange) results from Inside GS1.Note, the D/P values were divided by 10 and the FI-t values by 100. The linear trend line is placed on the F/F-t index and it shows basically no trend in time.

3.3.2 $\delta^{13}C$ value and carbon quantification results

3.3.2.1 $\delta^{13}C_{SPAC}$ and $\delta^{13}C_{TOC}$ analysis

The $\delta^{13}C_{SPAC}$ and $\delta^{13}C_{TOC}$ values range from -24.0 to -21.5‰ in both collections, Outside GS1 and Inside GS1 (Tables T3.2, T3.3). Results within this range are generally attributed to a mixture of C_3 and C_4 plants, which corresponds to a tropical savannah environment (Lloyd et al., 2008, Wurster et al., 2013, 2015). The differences between $\delta^{13}C_{TOC}$ and $\delta^{13}C_{SPAC}$ values are due to loss of the labile and semi-labile carbon fraction that was volatilized during the hypy procedure. The loss can be observed as lower amount of carbon in mg shown in columns TOC (mg) and SPAC (mg) in Tables T3.2 and T3.3.

In general, $\delta^{13}C_{SPAC}$ results show an obvious divergence between Outside GS1 and Inside GS1 from the modern ground level to approximately 100 cm below the surface (Figure F3.13). The $\delta^{13}C_{SPAC}$ values from Outside GS1 cluster at higher values than Inside GS1 (dashed line in Figure F3.13). Overall, the $\delta^{13}C_{SPAC}$ results from archaeological sediments Inside GS1 are lower than those from non-archaeological open-site sediments beyond the dripline (Figure F3.13).

Outside GS1, the $\delta^{13}C_{SPAC}$ values range from -21 to -22.7‰ across depths from 0−120 cm below the surface. Below 120 cm, the $\delta^{13}C_{SPAC}$ results show considerable variation (Table T3.2). However, they remain higher than -25‰ throughout. Inside GS1, the $\delta^{13}C_{SPAC}$ values range from a minimum of -23.9 to -22.6‰ in the upper 120 cm of the deposit (Table T3.3). Below 120 cm, the $\delta^{13}C_{SPAC}$ results show are inconsistent, alternating erratically between -22 and -25‰.

The $\delta^{13}C_{TOC}$ values exhibit a similar discrepancy to the one observed in $\delta^{13}C_{SPAC}$ between the sediment deposits Outside GS1 and Inside GS1, from the surface to approximately 120 cm below the surface. The $\delta^{13}C_{TOC}$ values, however, are generally lower compared to $\delta^{13}C_{SPAC}$ and inclined towards C_3 (trees and shrubs) vegetation in both collections. $\delta^{13}C_{TOC}$ results from Outside GS1 range from -21.5 to -23.9‰, while Inside GS1 they range from -22.7 to -25.2‰ (Tables T3.2 and T3.3). The comparison of $\delta^{13}C$ in TOC and SPAC in both sequences is shown in Figure F3.14.

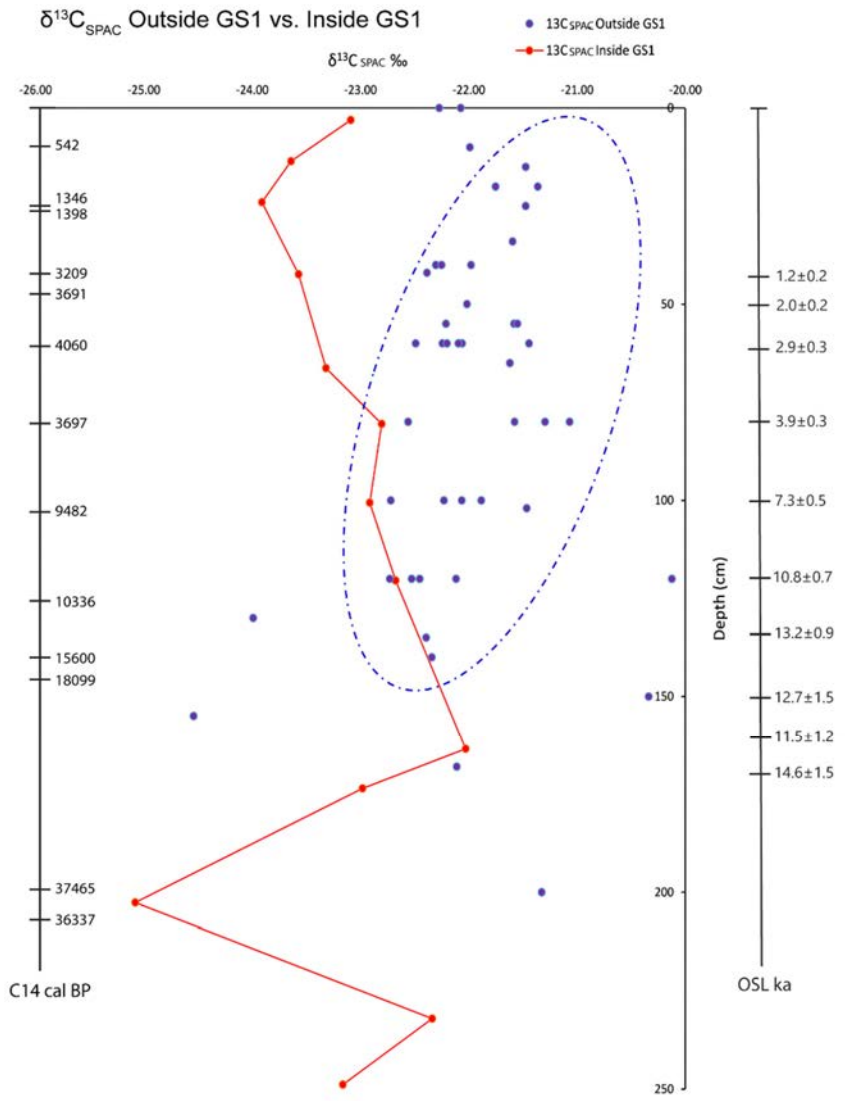

Figure F3.13: $\delta^{13}C_{SPAC}$ results Outside GS1 (blue dots) and Inside GS1 (red). The dashed line marks the cluster of higher $\delta^{13}C_{SPAC}$ values Outside GS1 compared to the values Inside GS1. Both collections exhibit unreliable result patterns below 120 cm. The OSL ka age scale on the right belongs to the Outside GS1 non-archaeological sediment deposit, the dates were taken from Chapter 2 in this thesis. The ^{14}C calBP dates on the left belong to the Inside GS1 archaeological sediment deposit and were adopted from the published archaeological studies (Lowe et al., 2018) and unpublished data (Wallis et al., 2014a).

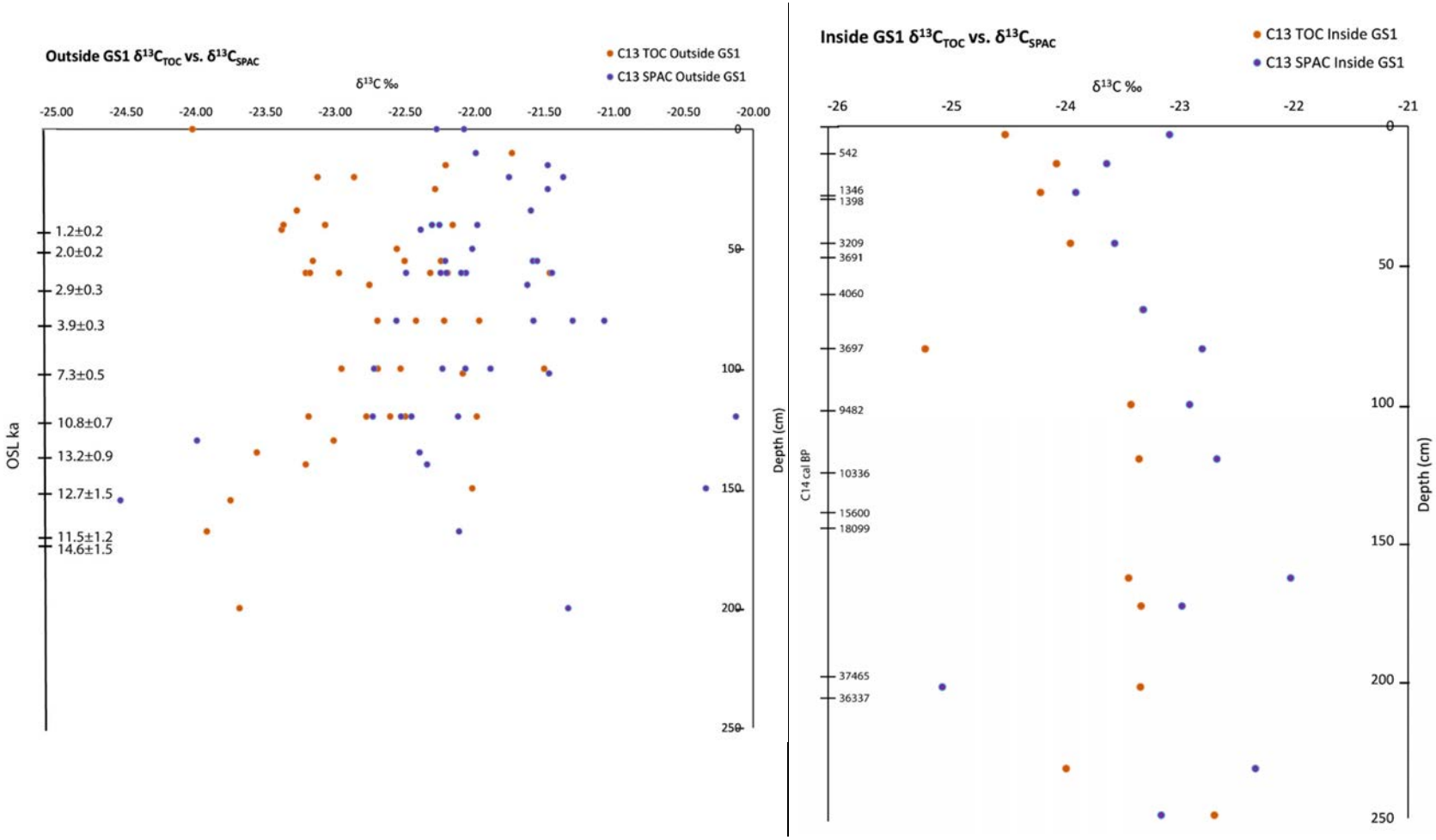

Figure F3.14: $\delta^{13}C_{TOC}$ *versus* $\delta^{13}C_{SPAC}$ Outside GS1(left) and Inside GS1 (right). The OSL ka age scale for the Outside GS1 sediment deposit was taken from Chapter 2 in this thesis. The ^{14}C cal BP in Inside GS1 archaeological deposit was adopted from the published archaeological studies (Lowe et al., 2018) and unpublished data (Wallis et al., 2014a).

3.3.2.2 Carbon quantification

The percentage of TOC in the analysed collections does not generally exceed 1%, except the four uppermost samples from Inside GS1 that exhibit significantly higher percentages of TOC compared to all other samples (Table T3.3 column TOC in sample, Figure F3.15a). The SPAC percentage in the analysed samples in both collections, in general, does not exceed 0.15% (Tables T3.2, T3.3 column SPAC in sample, Figure F3.15b). Analogous to the TOC values, the only exceptions are four distinguishably high peaks from samples Inside GS1, at 3.1 cm, 13.6 cm, 24 cm and 42.4 cm below the surface (Figure F3.15b).

Finally, SPAC as a component of TOC generally does not exceed 20% in Outside GS1 samples (Table T3.2 column SPAC in TOC, Figure F3.15c). This means combusted organic matter represents less than 20% of all organic matter in the analysed sediment samples. In contrast, Inside GS1 the percentage of SPAC in TOC exceeds 22% in most samples, with two samples, C1-03 (depth 13.6 cm) and C1-05 (depth 24 cm), having extraordinarily high SPAC peaks at 41% and 69% respectively (Table T3.3 column SPAC in TOC, Figure F3.15c).

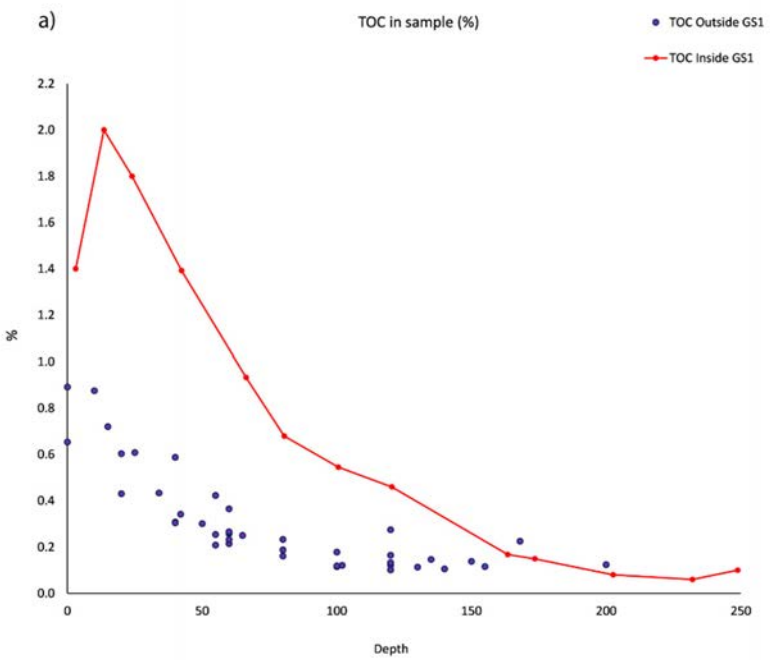

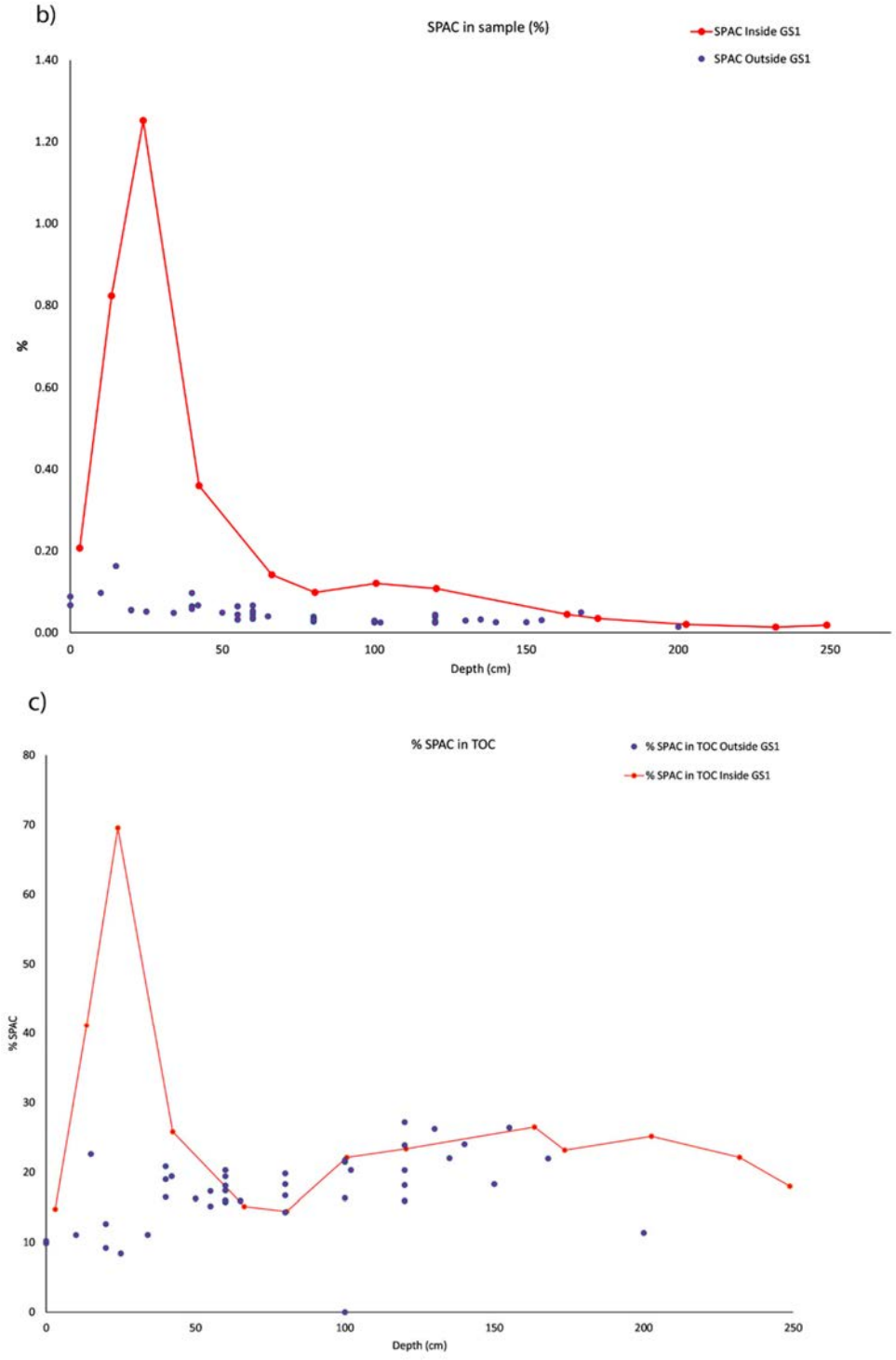

Figure F3.15: The TOC and SPAC content in analysed sediment samples from Outside GS1 and Inside GS1. **a)** the % of TOC in samples Outside GS1 (blue) vs. Inside GS1 (red).**b)** the SPAC % amount in samples Outside GS1 (blue) vs. Inside GS1 (red). **c)** the % amount of SPAC in TOC in samples Outside GS1 (blue) vs. Inside GS1 (red).

3.4 Discussion

3.4.1 Phytolith evidence

The phytolith assemblages Outside GS1 show an overall mixture of arboreal, herbaceous and grass morphotypes, typical of a savannah ecosystem, with a dominance of C_3 arboreal vegetation. This is demonstrated by a dominance of Ovate and Spheroid ornate morphotypes (Figure F3.8), both commonly regarded as representatives of woody vegetation in tropical areas, along with a continuous occurrence of C_4 grasses in fluctuating proportions (Bremond et al., 2017, Coe et al., 2014, Runge, 1999, Strömberg et al., 2018).

The Inside GS1 results show a dominance of different tree, shrub and herb morphotypes compared to those from Outside GS1 – Spheroid and Ovate psilate (Figure F3.9). Although the two dominant morphotypes differ from those Outside GS1, they too are associated with non-grass plants, arboreal and herbaceous vegetation, and are regarded as forest indicators (Strömberg, 2004, 2005, Strömberg et al., 2018). Moreover, spheroid psilate forms, in particular, have been occasionally associated with wood (Collura and Neumann, 2017, ICPT, 2019, Kondo et al., 1994, Piperno, 2006). The dominance of C_3 morphotypes Inside GS1 is evident (Figure F3.9). Nevertheless, C_4 grass morphotypes persist throughout the profile, even if sometimes in minute numbers.

In general, both phytolith collections are consistent with a savannah vegetation type. However, there are some differences in the phytolith assemblages between Outside GS1 and Inside GS1. Assuming that the Outside GS1 phytolith assemblages represent the natural vegetation signal in the study area, it is reasonable to infer that the Inside GS1 phytolith assemblages do not reflect an unmodified natural signal. Several factors can influence the deposition and sedimentation of phytoliths and, as a result, impact on the composition of the phytolith assemblage. Phytolith shape and size, for example, can play a significant role in phytolith transport and dissolution (Cabanes et al., 2011, Cabanes and Shahack-Gross, 2015, Lentfer et al., 2003b, Selkin et al., 2015, Strömberg, 2007, Strömberg et al., 2018). Or, for example, burned assemblages are less stable than unburned assemblages (Cabanes et al., 2011). The origin of vegetation, as reflected in the phytolith record, ultimately depends on various natural dispersal, transport and preservation mechanisms (Strömberg et al., 2018 and citations therein), including wind and water transport, colluvial erosion, animal activity and bioturbation, or they can result from human activity.

In this study, the variation in phytolith assemblages between the archaeological deposit Inside GS1 and the non-archaeological sediment deposit beyond the GS1 dripline (Outside GS1) could be due to

several factors, such as the morphology of the GS1 rockshelter, geomorphic and sedimentologic processes as well as animal and human activity. The morphology of a rockshelter can cause it to act as a sediment trap. As a result, the interior of a rockshelter, in this case GS1, may be subject to potential windblown or raindrop deposition of sediment particles, including phytoliths, from outside the shelter. Because small (<20 µm) phytoliths are preferentially moved around by wind compared to larger ones (Selkin et al., 2015, Strömberg et al., 2007b, 2018), they are more likely to accumulate inside such a 'sediment trap'. This might potentially influence the number of smaller and easily transported phytoliths, such as GSSCP and spheroids, Inside GS1.

As demonstrated by Wallis during fieldwork (2000, 2001), macropods, regular users of rockshelters in Australia, also occupied the GS1 interior based on the preservation of their faecal pellets. This would have contributed significantly to the accumulation of phytoliths Inside GS1, skewing the assemblages towards grasses (Dawson et al., 2004, Squires, 1982). While grass phytolith morphotypes could be attributed to macropods, macropoda cannot be responsible for the deposition of the dominating forest indicator morphotypes Inside GS1. Hence, the Inside GS1 phytolith assemblages most likely reflect the natural vegetation signal which includes substantial macropod influence, shown in the contribution of grass phytoliths, as well as anthropogenic influences, such as the purposeful accumulation of specific plants or plant components for food, fibre or bedding materials. This is demonstrated by the contribution of grass and tree indicator phytoliths in the Inside GS1 phytolith assemblages. Finally, it cannot be entirely excluded that the influence of wind and water on particle transport and the 'sediment trap' morphology of the GS1 rockshelter, impact the phytolith assemblage inside GS1. In this regard, however, further investigation is needed and some suggestions are provided in Thesis Summary (section II.2).

The small proportion of phytoliths deriving from sedges or inconclusively from sedges or grasses in both collections (Inside GS1 and Outside GS1) is not numerous enough to indicate a change in vegetation. However, they inform about the nature of microhabitats in the study area. Most likely, these phytoliths originate from the sedges populating shallow ponds that form on the flat tops of the sandstone outcrops (Figure F3.16). These depressions fill with water in the wet season, providing a microhabitat for water-loving plants. The presence of these phytoliths in sediments away from the ponds further suggests the transport of phytoliths in the local environment over several tens of metres.

A visual summary of the evidence from this study over the past 15 ka is given in Figure F3.17. The Inside GS1 archaeological deposit collection is illustrated inside the rockshelter, in front of the dripline,

and the Outside GS1 non-archaeologic sediments collection from seven pits and ten auger holes is displayed beyond the dripline.

Figure F3.16: Seasonal ponds formed on the flat top of the GS1 sandstone outcrop. The red arrow on the top image is pointing to the pond shown closer in the bottom image.

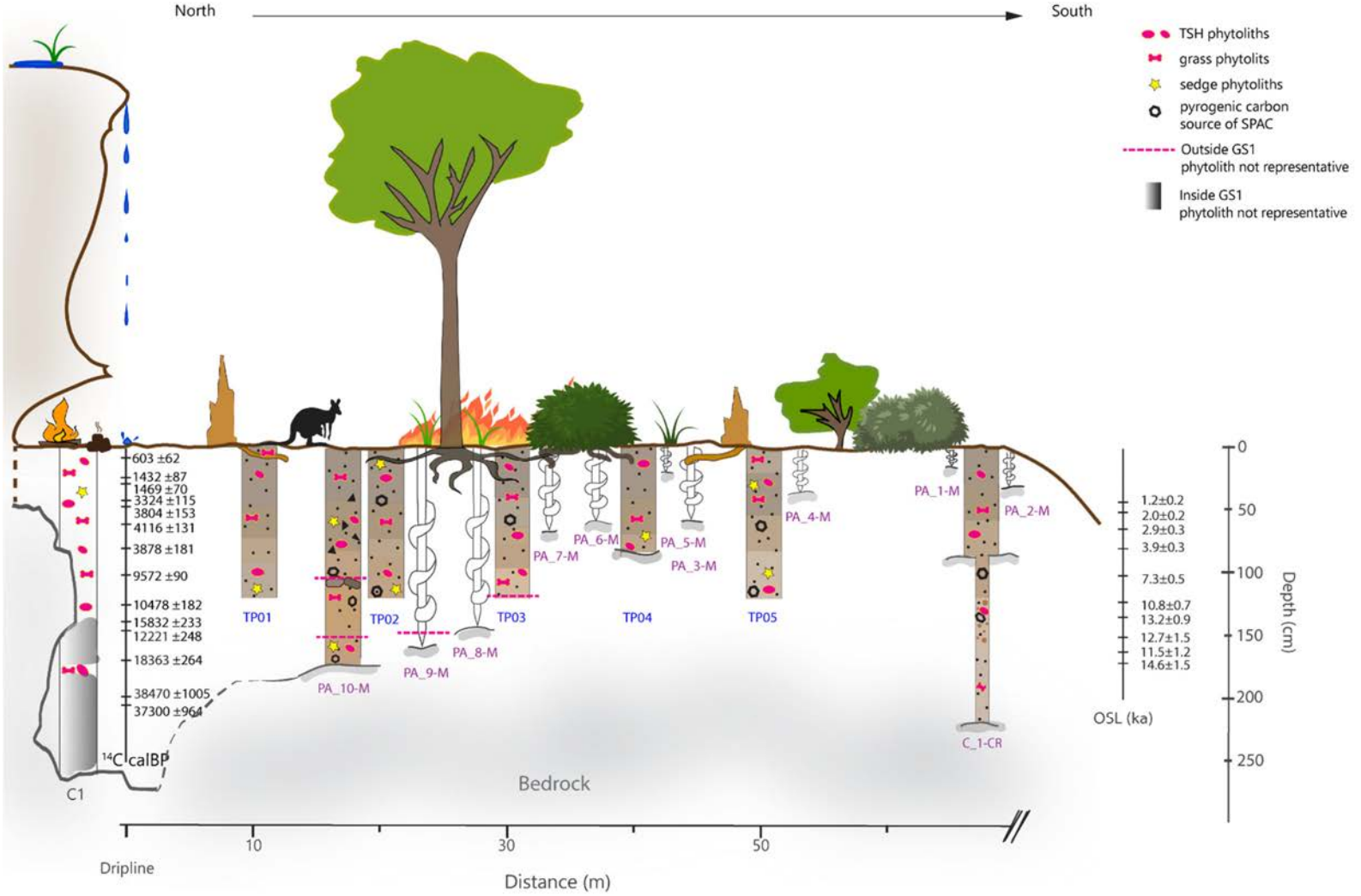

Figure F3.17: The reconstruction of past vegetation at the GS1 study area. The GS1 rockshelter dripline and the Inside GS1 phytolith collection is shown on the left. The Outside GS1 pits and auger holes are shown at correct distances beyond the GS1 rockshelter dripline. The savannah vegetation is shown along with other evidence, such as natural fire, hearth, bioturbation, kangaroo faecal pellets and a pond. In the legend: TSH=tree-shrub-herb phytoliths; the dashed pink line represents parts in Outside GS1 profiles where phytolith counts were not representative; the gradient rectangle Inside GS1 represents the part in square C1 where phytolith counts were not representative. The chronologies ^{14}C cal BP for the Inside GS1 archaeological deposit and OSL (ka) for the Outside GS1 sediments as explained in the text.

Another factor to consider is phytolith occurrence and abundance, i.e. presence/absence and presence of a representative amount of phytoliths in a sample (minimum 80 phytoliths in a sample, see section 3.2.2.3). Phytolith occurrence and abundance in this study exhibit no depth trend or pattern. By simple logic in undisturbed sediments, we would expect the amount of phytoliths to be representative to a certain depth and then diminish gradually with depth (Liu et al., 2019, Runge, 1999). Yet, the results of occurrence and abundance are inconsistent with depth, particularly Outside GS1. Inside GS1, the phytoliths show a continuous representative amount to a depth of 135 cm, below which phytoliths were generally poorly preserved, apart from one exception, at a depth of 178 cm (Table T3.2, sample C1-37A).

In samples Outside GS1 the discrepancies in phytolith occurrence and abundance along sediment profiles show that sediments were most probably disturbed and mixed after deposition. The transport characteristics of phytoliths in sediments and soils have been studied previously (Bremond et al., 2017, Fishkis et al., 2009, 2010, Hart and Humphreys, 1997, 2003, Liu et al., 2019, 2021, Madella and Lancelotti, 2012), yet the processes are unclear (Bremond et al., 2017, Strömberg et al., 2018). The potential drivers for vertical translocation are bioturbation, vegetation roots and soil fauna, percolating water, depositional environment (discussed in Chapter 2, section 2.4.3) and sediment properties (pH, ionic strength, organic matter content, grain size, sediment type) (Alexandre et al., 1997b, Bremond et al., 2017, Fishkis et al., 2010, Hart and Humphreys, 1997, 2003, Morales et al., 2011, Porubcan and Xu, 2011, Wallis, 2003).

The results show that smaller phytoliths, such as GSSCP, spheroids and elongates, are preferentially displaced compared to blocky or bulliform morphotypes (Fishkis et al., 2010, Liu et al., 2019, Locke, 1986). Studies also suggest that, along with the phytolith morphotype, mean annual precipitation, pH and soil clay content are the main factors influencing phytolith transport (Fishkis et al., 2009, 2010, Liu et al., 2019, 2021). They also indicate that phytolith transport is related to climatic factors, such as mean annual precipitation, rather than the phytolith type and that increased soil clay content promotes phytolith transport. Although the influence of these drivers is widely recognised it is not yet quantified, particularly in different environmental conditions (Fishkis et al., 2010, Strömberg et al., 2018). In tropical environments, as discussed in previous chapters, termites can significantly impact sediment mixing and particle movement (e.g. Runge, 1999, Williams, 2019, Williams et al., 2021). The presence of root and termite activity at the Outside GS1 study location (refer to: Chapter 1, section 1.4.1.2 and Chapter 2, section 2.4.3) along with the effects of monsoonal precipitation suggest that a proportion of the inconsistency in phytolith occurrence and abundance Outside GS1 could be at least partly attributed to

sediment transport and mixing due to these factors. Evidence of bioturbation has also been reported from GS1 shelter's interior (Lowe et al., 2018).

The number of counted burned phytoliths is significantly higher in non-archaeological sediment samples Outside GS1 compared to the archaeological sediment samples Inside GS1 (Tables T3.2, T3.3, Plate P3.6, a,b,e). Several studies suggest that the colour of phytoliths is a tool that can be used to indicate modification by fire (Albert and Cabanes, 2007, Boyd, 2002, Kealhofer, 1996, McMichael et al., 2012, Parr, 2006, Selkin et al., 2015). The dynamics of the effects of burning on phytoliths, however, are not clear. The quoted studies and results from elsewhere, for example, confirm that only a part or even no phytoliths manifested observable changes from burning after being subjected to fire (Elbaum et al., 2003, Kealhofer, 1996, Parr, 2006). Additionally, several studies have demonstrated during laboratory extractions that colour changes in phytoliths are uncommon when fire temperatures do not exceed 500^{o}C (Bowdery, 1989, Bowdery et al., 2001, Jones and Milne, 1963, Parr, 2006, Runge, 1998, Wallis, 2003). By observing the results of a lack of oxygen within a muffle furnace, Parr (2006) assumed that the discolouration of phytoliths might be linked to whether the oxidation process was complete or incomplete. The discolouration phenomenon, however, is poorly understood. Hence, it is unreliable to infer, for example, that past fires in the study area were low temperature or that the fire frequency was low, based solely on the paucity of burned phytoliths encountered in the samples.

Apart from colouration, some phytoliths from both collections showed distinct etching on the phytolith surface and/or on the margins (Tables T3.1, T3.2, Plate 3.6,c-f,i). This etching differs from the cavities typically observed with GSSCP (Alexandre et al., 2015) and is more similar to the dissolution features presented by Tombeur et al. (2020) from soils in Western Australia. Etched phytoliths were counted along with the weathered and damaged ones and no significant difference was observed between samples from Outside GS1 and Inside GS1. There were, however, two samples from Inside GS1 where the number of weathered phytoliths exceeded 60 (Table T3.2, samples C1-26 and C1-28, depth 120 and 130 cm, respectively), resulting in a similar amount of damaged and well preserved phytoliths present in these two samples.

Mild to severe etching of phytoliths in this study match the etching and dissolution features commonly described for phytolith weathering in a range of environments. Generally, the number of weathered phytoliths tends to increase with depth, although no clear depth trend has been confirmed (Runge, 1999, Sommer et al., 2012, Strömberg et al., 2018, Tombeur et al., 2020). Several factors affect the preservation of individual phytoliths in soils and sediments, including soil/sediment solution pH, the

presence of organic matter, the potential coating of the phytoliths and the phytolith geometry (i.e. morphotype) (Cabanes and Shahack-Gross, 2015, Kaczorek et al., 2019, Kendrick, 2005, Huang and Hardie, 2011, Strömberg et al., 2018). Studies of phytolith etching and dissolution have focused mainly on the role of phytoliths in the terrestrial biogeochemical silicon cycle (e.g. Alexandre et al., 1997b, Borrelli et al., 2008, Clarke, 2003, Derry et al., 2005, Fredlund and Tieszen, 1997, Kaczorek et al., 2019, Sommer et al., 2006, 2012, Tombeur et al., 2020) rather than on environmental or climate characteristics that could affect the etching and dissolution of phytoliths.

The etching observed in this study likely relates to individual phytolith morphotype characteristics (shape, size and structure density) and depth. Greater depths generally mean prolonged exposure to weathering factors and diagenesis. Apart from that, studies also indicate that thin, flattened and porous silica bodies with large surface areas, such as elongate morphotypes, are more readily impacted by dissolution compared to more compact and dense morphotypes, like GSSCP, spheroids or blockies (Borrelli et al., 2008, Hart and Humphreys, 2003, Strömberg et al., 2018−and citations therein). However, the high amount of phytolith dissolution in some of the Inside GS1 samples might be due to the extra water that comes off the shelter rooftop along the dripline in the wet season. This is something worth considering also because such high levels of dissolution do not occur further away from the shelter, i.e. Outside GS1.

The potential phytolith confusers, chrysophyta cysts, sponge spiculae and diatoms, when present even in small numbers, might still hint about events or conditions in the past. Chrysophyte algae for example mostly occur in slightly humic ponds, but they also thrive in moderately oligotrophic waters. In contrast to sponge spicules and diatom frustules, chrysophytes are not found in moist sediments and soils (Kristiansen, 2010). However, their ability to form stomatocysts allows cells to survive drought and other adverse environmental conditions (Nicholls and Wujek, 2003). Although it is unclear if the seasonal water ponds on the GS1 outcrop rooftop in the wet season (Figure F3.16) represent a potential seasonal habitat for chrysophytes, this cannot be excluded. Outside water bodies, the most obvious dispersal method of chrysophytes and their cysts is by birds, in the plumage of waterfowl, although dispersal by humans has also been suggested in some cases (Kristiansen, 2010). The unusual presence of chrysophyta cysts in sediments Outside GS1, could be attributed to birds. Their presence Inside GS1, however, might as well be due to human activity, such as transport and usage of water from a close oligotrophic water body, in this case the Norman River and its tributaries in the past.

3.4.1.1 Phytolith indices

In general, the results of the D/P and FI-t indices from non-archaeological sediment deposit Outside GS1 showed that the savannah vegetation in the GS1 study area was denser in the past (Table T3.2, Figures F3.8 and F3.11). The indices were the lowest at shallow depths (0−40 cm) (D/P range 0.31−1.13). This suggests that the area has been dominated by more open savannah for approximately the last 2000 years, based on the established chronology in Chapter 2 for the sediment deposit expanding outside the GS1 rockshelter. The increased values of both indices in samples from depths 80−120 cm below the surface (D/P generally >2.5; Table 3.2) suggest that there was greater tree cover in the period between 4000 and 10,000 years ago during the early and mid-Holocene. It is likely that thicker cover characterized the area in the early and mid-Holocene, which gradually opened to reach its current state. A slight decrease in D/P and FI-t indices in samples from depths below 120 cm (Table T3.2) could indicate a more open forest in the Pleistocene–Holocene transition period. These findings align well with other palaeoenvironmental studies from the Australian tropical northeast (e.g. James et al., 2024, Li et al., 2022, Moss et al., 2012, 2017, Reeves et al., 2013a).

Similar D/P values to those reported in this study have been reported from forest–savannah transects in Cameroon, tropical Africa (Bremond et al., 2005, Sangen et al., 2011). There, the lowest range (0.33−1.16) was associated with shrub and tall-grass savannah, while the medium and higher values were with young or mature and gallery forest. In many other forest–savannah ecotones studies, the D/P values were generally much lower (e.g. Alexandré et al., 1997a, Calegari et al., 2013, Chueng et al., 2019, Neumann et al., 2009). The indices, however, represent a relative estimate and the results depend on many factors, such as the sample size or, as in our case, the nominated constraint of morphotype 5% representativeness and the fact that phytolith analysis is always subjected to observer bias and relative experience (Díez-Pastor et al., 2020). Therefore, the results can vary accordingly between studies.

Nonetheless, the phytolith indices exhibit some inconsistencies. For example, the trends shown in the PA_10-M pit profile (Figure F3.11b) do not definitely align with the trends exhibited by other pits and auger holes and some calculations resulted in exaggerated peaks (Figure F3.11a,e). In the case of pit PA_10-M, the shift in trend may be a consequence of sediment mixing subsequent to deposition, discussed elsewhere (refer to: Chapter 1, section 1.4.1.2 and Chapter 2, section 2.4.3). The exaggerated peaks might alternatively be a consequence of the sample preparation procedure (ex-situ), which can influence the distribution of phytoliths and the sample size (e.g. a higher number of counts would probably reduce the peaks).

In contrast, the D/P and FI-t index from the archaeological deposit Inside GS1 exhibit an irregular pattern characterized by alternating increases and decreases and with a major decrease in the uppermost

sample (i.e. from the shallowest depth 3.1 cm), indicated as the first point on the graph Figure F3.12. A pulsating vegetation density pattern like this is highly unlikely to occur in nature, especially considering all the factors and drivers involved in determining the position of tropical forest–savannah ecotones (Oliveras and Malhi, 2016). The recurrent ups and downs in Inside GS1 D/P and FI-t values are more likely connected with changes in human and/or concentrated macropod inputs to the assemblage. Closer examination of the Inside GS1 phytolith assemblages reveals that it is the rondel morphotype driving the alternating pattern (Figure F3.9), causing the D/P index to drop in favour of grasses and vice versa (Figure F3.12). As mentioned in previous paragraphs (section 3.4.1), macropods can contribute significantly to phytolith assemblages inside rockshelters (Wallis, 2000) and these animals may be distorting the phytolith natural signal Inside GS1. Unfortunately, rondels occur in various grass sub-families and it is impossible to interpret this signal more specifically. Additionally, with a modern phytolith reference collection we might be able to gain better information about the origins of the two dominant morphotypes Inside GS1, i.e. Spheroid and Ovate psilate attributed to tree, shrub and herb vegetation. The insight into their possible origin might show if they can be linked to plant species that humans preferably transported for use inside rockshelters. This would additionally support the hypothesis of anthropogenic influence on phytolith assemblage Inside GS1. Finally, these findings question the usage of phytoliths from sediments within rockshelter interiors as sole proxies for vegetation reconstruction and changes in vegetation structure in a study area through time. The record appears to be strongly influenced by factors other than vegetation change outside the shelter.

3.4.2 $\delta^{13}C$ and carbon abundance evidence

The $\delta^{13}C_{SPAC}$ values from the non-archaeological sediment deposit expanding beyond the GS1 dripline (Outside GS1) suggest a savannah type of vegetation has dominated the study area for the last ~15 ka (Figure F3.13). The $\delta^{13}C_{SPAC}$ values from the archaeological sequence Inside GS1 also indicate that savannah vegetation has been predominant throughout the Holocene (Figure F3.13). This outcome is in good agreement with the phytolith evidence. The $\delta^{13}C_{SPAC}$ ranges indicate derivation from a mixed C_3 and C_4 vegetation source, with a predominance of C_3 plants, most likely woody elements (Boutton, 1991, Bremond et al., 2017, Calegari et al., 2013, Coe et al., 2014, Desjardins et al., 1996, Pessenda et al., 1997, 1998, Sangen et al., 2011). From approximately 120−90 cm below the surface the $\delta^{13}C_{SPAC}$ values Outside GS1 and Inside GS1 are relatively similar and consistent (from -23 to -22‰). Above 90 cm, the two collections gradually diverge, with the Outside GS1 samples showing a trend towards a stronger grass C_4 signal. In contrast, the Inside GS1 samples exhibit the opposite trend, towards a stronger C_3 tree signal

(Figure F3.13). This trend suggests that the savannah tree vegetation Outside GS1 was denser during the early and mid-Holocene until approximately 4000 years ago but has gradually changed into a more open savannah. Again, this aligns well with the trend obtained from phytolith indices (section 3.4.1.1) and suggests that the region was subject to a wetter and warmer climate throughout the early and mid-Holocene, as indicated by a denser tree vegetation signal. Over time, the climate gradually shifted to conditions similar to those experienced today, characterized by a more open savannah woodland. In the upper 15 cm, however, the $\delta^{13}C_{SPAC}$ trend changes again with the $\delta^{13}C_{SPAC}$ values in all samples ranging between -23 and -22 ‰ (Figure F3.13). Below 120 cm, the $\delta^{13}C_{SPAC}$ values Outside GS1 and Inside GS1 exhibit considerable variation. They are considered unreliable due to very low amounts of SPAC in deeper samples (<0.05%) resulting in potentially extreme bias towards a single large SPAC particle (Tables T3.2 and T3.3).

In both collections, the $\delta^{13}C_{TOC}$ signal is generally inclined towards tree vegetation (average -23– - 24‰) (Figure F3.14, Tables T3.2, T3.3). This is most probably due to the C_3 signal being created by the roots of the savannah trees and, therefore, the larger presence of deeper-rooted arboreal organic matter in the sediment profiles. Savannah trees produce finer and larger roots extending up to 150 cm deep (e.g. February and Higgins, 2010, Mordelet et al., 1997). Thus, carbon from tree roots and arboreal organic detritus likely influences the $\delta^{13}C_{TOC}$ signature in favour of C_3 vegetation. A comparison between the percentage of TOC Outside GS1 and Inside GS1 shows that the general amount of organic matter in the analysed samples is very low (<1%) and decreases with depth. However, the TOC amounts are higher throughout samples from Inside GS1 than those from Outside GS1.

Similarly to the TOC abundances, the SPAC abundances are generally very low in samples from both collections, not exceeding 0.15% (Figure F3.15b), particularly at greater depths. The exception represents the four distinctively high SPAC peaks Inside GS1, specifically in the two samples (C1-03, C1-05) from depths 24 cm and 42.2 cm, where SPAC accounts for a larger proportion (41% and 69%) of the recorded TOC (Figure F3.15b,c). The clearly higher values of TOC and SPAC from the two outlier samples represent a substantial deviation from the average TOC and SPAC proportions in the surrounding environment, as represented by the Outside GS1 collection at the same depths. These peaks are associated with human activity and are indicative of anthropogenic fires in the GS1 rockshelter interior. This statement is supported by the stronger C_3 signal (lower $\delta^{13}C_{SPAC}$ values) Inside GS1 (Figure F3.13) and macro-charcoal results recorded in these samples (Lowe and Wallis, 2020, Figure 2).

3.5 Conclusions

Phytoliths and the $\delta^{13}C$ isotopic composition of total organic carbon (TOC) and stable polycyclic aromatic carbon (SPAC) were used to reconstruct late Quaternary vegetation at the Gledswood Shelter 1 (GS1) archaeological site in the tropical Australian savannah. The abundance of TOC and SPAC in sediments was also examined. Phytoliths and SPAC were chosen because they are durable and able to preserve in unfavourable semi-arid environments for millennia, compared to other more conventional approaches (Ascough et al., 2020, Bird and Ascough, 2012, Bird et al., 2015, Calegari et al., 2017, Hart, 2016, Rashid et al., 2019, Strömberg et al., 2018, Wurster et al., 2015, Zurro et al., 2016). This study is the first to use this combination of proxies in open-site sediments in Australia for vegetation reconstruction and confirmed the effectiveness of the chosen approach in locales where pollen does not preserve.

Two collections of sediments were analysed for past vegetation evidence from phytoliths and the $\delta^{13}C$ signature in TOC and SPAC. One collection (44 samples) was collected from open-site, non-archaeological sediment deposits surrounding the GS1 rockshelter, up to 73 m beyond the GS1 dripline (Outside GS1). The other collection (64 samples) was collected from the preserved archaeological sequence inside the GS1 rockshelter (named Inside GS1).

In general, the phytolith and $\delta^{13}C$ results from Outside GS1 confirmed the presence of savannah vegetation throughout the Holocene. The calculated phytolith indices indicate denser tree cover during the early and mid-Holocene, followed by a gradual transition to a more open savannah woodland in the last 2000 years. This might point to a wetter and warmer climate in the region during the early and mid-Holocene compared to current conditions.

The archaeological sequence from the rockshelter's interior, Inside GS1, recorded a different vegetation signal, showing an overall higher presence of forest indicators from that of the sediment deposit Outside GS1. Even though grasses have been recorded Inside GS1, their general proportion is noticeably lower than those Outside GS1, suggesting a strong prevalence of forest indicators, i.e. arboreal vegetation. This difference has been recorded through phytolith analysis (Figure F3.10) and $\delta^{13}C_{SPAC}$ analysis (Figure F3.13). The phytolith evidence showed with reasonable confidence that the phytolith signal Inside GS1 has been influenced by additional factors, such as human activity bringing wood to the shelter to make campfires and kangaroo dung. Although it is doubtful that both macropods and humans would have been present inside the shelter at the same time, they would likely each have used the site in periods when the other was absent. Therefore, the presence of one does not exclude the other. The presence of hearth remains inside the GS1 rockshelter was also confirmed by the significantly higher SPAC

content of some sediments, compared to the natural signal recorded in Outside GS1 sediments (Figure F3.13)

Finally, the comparative analysis of the past vegetation records from Outside and Inside GS1 rockshelter indicates that a robust reconstruction of past vegetation and possibly also of coeval human activities should include both a rockshelter interior along with its surroundings. The results also indicated some important issues that need to be addressed in the future. A modern phytolith collection from the local area would assist as a reference to strengthen the interpretation of the results. Further research is needed to better understand the impact of natural processes, particularly bioturbation, on phytolith movement and mixing dynamics in analogous environments. This would minimize their impact on the results and help achieve a more robust interpretation. Furthermore, in the case of very low SPAC quantities in sediments, an isolation technique, such as heavy liquid floatation, should be considered to increase the sample representativeness.

3.6 Acknowledgements

The authors express their gratitude to the Traditional Owners, represented by Woolgar Valley Aboriginal Corporation and especially Uncle Lavin Keyes, Jasmine Keyes and Tameika Keyes as well as Helen Smith and William Smith for their partnership, guidance and help. The authors are very thankful to the Hinze family for their generous support and assistence throughout the field work. We also thank Costijn Zwart, Michael Brandt, Tina Nemec and Raul Hernandez Font for their invaluable help at field work. Their commitment and positive attitude contributed importantly to the outcome of this study. The authors express special thanks to Scott Merrington from Leica Microsystems for his help with Leica Software for microscopy analysis. We are grateful to the University of Nova Gorica, Unit Ajdovščina for the use of their laboratory equipment. We are very thankful to Rainy Comley for his indispensable help and friendly support of laboratory analysis, Cassandra Rowe and Janelle Stevenson for their professional help and valuable advice and Jen Whan for her assistance at scanning electron microscopy. A big thanks to Chris Würster for sharing his expertise.

Chapter 4 Bridging palaeoenvironmental archives from outside to the inside: Gledswood Shelter 1 (GS1), North Queensland, Australia

Mojca Zega[1,2], Michael Bird[1,2], Lynley A. Wallis[3], Christian Reepmeyer[4], Maria Rivera-Araya[2,5], Kelsey Lowe[6], Robert Wasson[1]

[1]College of Science and Engineering, James Cook University, QLD, Australia

[2]ARC Centre of Excellence of Australian Biodiversity and Heritage CABAH

[3]Griffith Centre for Social and Cultural Research, Griffith University, Nathan, Australia

[4]Deutsches Archäologisches Institut, Kommission für Archäologie Außereuropäischer Kulturen (KAAK), Bonn, Germany

[5]Department of Environment and Science, Queensland Government, Australia

[6]School of Social Science, The University of Queensland, Brisbane, QLD, Australia

Statement of contribution of others:

MZ, MB, LW and CR designed the study. MZ conducted the field work and laboratory analysis for the Outside GS1 part of the study. LW conducted the archaeological research for the inside GS1 part of the study. MZ performed all the outside GS1 analysis, the outside–inside GS1 comparison and drafted the manuscript. MB, LW, CR, BW and KL provided support with the interpretation of results. BW provided support in interpreting geomorphologic evidence, KL provided details on magnetic susceptibility analysis Inside GS1 and overall support with interpreting magnetic susceptibility results. MRA carried out the age-depth modelling. All authors edited the manuscript.

Abstract

Rockshelters and caves are sedimentary and environmental archives. They form natural sediment traps in which deposits are protected from the effects of erosion and subaerial weathering. Rockshelter and cave sediments have been studied for as long as there has been scientific interest in caves. Early studies primarily focused on cave formation processes, speleothems as well as fossil and cultural material remains. The palaeoclimatic significance of the clastic sediments in caves was first acknowledged in European alpine caves by Schmid (1958). Today, it is widely recognized that rockshelter and cave sediments contain important palaeoenvironmental evidence, and as such, constitute a potentially valuable archive of Quaternary environmental change. However, rockshelters and caves are not discrete entities. Instead, they are part of wider proximal and distal sediment systems and are, therefore, inseparably connected to their surroundings. Hence, an increasing number of studies suggest that stratigraphic and environmental research based on the clastic sediments in rockshelters and caves should expand beyond the 'dripline' to include the sedimentary record from their surrounding environment. An approach that still lacks full implementation.

The Gledswood Shelter 1 (GS1) is an archaeological rockshelter located in semi-arid inland North Queensland, Australia. This study interrogates the links between the sedimentary record inside GS1 and the sedimentary record in its surrounds. The study area encompasses the archaeological deposit within the GS1 rockshelter (referred to as "Inside GS1") and the non-archaeological open-site sediment deposit that extends south-southwest beyond the dripline of the GS1 (referred to as "Outside GS1"). Here the findings from previous archaeological research conducted inside the GS1 rockshelter are compared with findings from geologic, geomorphic and palaeoenvironmental research conducted in the sediment deposit outside GS1. By bridging the two archives, we present a more reliable and nuanced sedimentary and palaeoenvironmental record for the study area. This allows for a comparison and correlation of the complemented GS1 record with other known records from the Australian tropical north.

Geomorphologic evidence indicates that the immediate study area constitutes part of a larger, weathered sandstone outcrop, possibly a residual hill. GPR analysis and measurements of subsurface bedrock depth reveal an uneven, undulating subsurface bedrock and a depression that extends from the interior of the GS1 rockshelter to approximately 15 m southward beyond the dripline. The depression was possibly formed by foot scarp erosion and was afterwards filled with sediment when weathering processes, such as granular disintegration and arenisation, became dominant. Stratigraphic and sedimentologic evidence, including colour, particle size and microscopic elements, from sediments

Outside GS1 and Inside GS1, confirms that the sediment in the study area originates from the weathering of the Jurassic Hampstead sandstone, which is the dominant lithology in the area. Evidence of post-depositional mixing by bioturbation is evident in sediments from both Outside GS1 and Inside GS1 deposits. Sedimentologic microscopic analysis, however, suggests that certain characteristics observed in sediments Inside GS1, such as increased abundance of charcoal and the presence of iron oxide nodules, differ from those in sediments Outside GS1. These differences may be attributed to the impact of human activity Inside GS1, specifically hearth fires.

The sediments in both archives, Outside GS1 and Inside GS1, were dated using OSL and radiocarbon dating (^{14}C) techniques. Results show that the last sediment accumulation cycle outside GS1 began approximately 15 ka years ago, while the sequence Inside GS1 is much deeper and older, with a maximum age of approximately 38 ka. Age-depth modelling was used to correlate the two chronologies, demonstrating a strong alignment between them.

Magnetic susceptibility analysis and vegetation analysis, the latter involving phytoliths and $\delta^{13}C$, corroborated the impact of human as well as animal (particularly macropod) activities on the sediment record inside GS1. This confirmed the recognised likelihood that the sediment record inside rockshelters will differ from the 'natural' sediment record outside rockshelters due to human and animal presence and modifications.

Finally, the results show that bridging the sediment archives outside and inside of the GS1 rockshelter lad to a more rounded and comprehensive dataset that enables a more robust interpretation, and, therefore, a more reliable palaeoenvironmental reconstruction, for the local area. The study suggests recommendations for future research of the GS1 site as well as other rockshelter sites of archaeological and palaeoenvironmental importance.

4.1 Introduction

4.1.1 Rockshelters as palaeoenvironmental archives and the role of their surroundings

In Australia, as elsewhere, investigations in caves and rockshelters dominate research in prehistoric archaeology. These types of deposits have been considered superior to the study of open-sites mainly owing to the good preservation of stratified sequences (Kibler, 1998). Rockshelters and caves form natural sediment traps in which, in contrast to open sites, deposits are protected from the effects of erosion and

subaerial weathering (Gunn, 2003). Therefore, sediment deposits in rockshelters and caves are often thought to represent relatively complete sequences, which retain environmental signals and archaeological evidence in well-defined, discrete, and datable contexts directly associated with specific moments of the past (Butzer, 2008, Sandweiss and Kelley, 2012).

In the last decade, however, an increasing number of studies have argued that important information could be missed by focusing only on records from confined spaces inside rockshelters and caves, while ignoring the broader outside area beyond their dripline (e.g. Angelucci et al., 2018, Barbieri et al., 2018, Kindermann et al., 2018, Ulm, 2013, Ward et al., 2006). Although rockshelters and caves provide better chronostratigraphic resolution compared to open-site deposits, their sedimentary record is space confined, often discontinuous and usually biased (Langley et al., 2011, O'Connor et al., 2017, Schiffer, 1987, Ulm, 2013, Vannieuwenhuyse, 2016, Walthall, 1998, Ward et al., 2016). There is a recognized risk of forming biased views not only about past human activities and behaviours, but also about past environmental conditions and natural processes that occurred outside the rockshelters and caves (Kindermann et al., 2018). Schiffer (1987) and Walthall (1998), for example, emphasized that deposits inside rockshelters and caves may be subjected to different natural events and post-depositional modification processes compared to those outside their confines, due to the restricted space and long, intense periods of use (Figure F4.1). Ultimately, rockshelters and caves are not isolated nor closed systems. They are fundamental parts of the environment in which they are located, inseparably connected to their surroundings and, as such, represent just one part of the wider proximal and distal sediment systems (Woodward and Goldberg, 2001). The investigation of rockshelters and caves should therefore be expanded beyond the dripline into their surroundings and both sedimentary records, from inside and outside, should be compared and correlated (Woodward and Bailey, 2000).

However, comparative studies of sedimentary records from inside rockshelters and caves with sedimentary records from their surrounding environment are rare (Barbieri et al., 2018, Kindermann et al., 2018, Ward et al., 2006). In Australia, reviews of archaeological research practices reveal that rockshelters and caves represent more than 60% of all published archaeological sites (Langley et al., 2011, Ward et al., 2016). Out of these, only one comprehensive comparative study was performed in tropical north Australia, in the Keep River region of northwest Australia (Ward, 2003, Ward et al., 2006). Stratigraphic sequences of three occupation sites comprising rockshelters and their adjacent sand sheets were compared, questioning the assumption that rockshelters necessarily provide better preservation conditions or longer records of human occupation than open sandy environments. The authors

demonstrated that in the Keep River study area, open sandy environments provide better preservation conditions and longer records than rockshelters, contrary to commonly held assumptions.

This chapter presents a comparative case study conducted at the Gledswood Shelter 1 (GS1) archaeological site in North Queensland, Australia. Evidence obtained through archaeological research from archaeological sediment deposit inside GS1 (referred to as "Inside GS1") is compared with the evidence acquired through geologic, geomorphologic and palaeovegetation investigation of non-archaeological open - site sediments deposited outside the GS1 rockshelter, expanding south-southwest beyond the dripline (referred to as "Outside GS1"). The dripline is used to demark the boundary between the Inside GS1 and the Outside GS1 sediment archives (Figure F4.1). The intent is to link both archives, Outside GS1 and Inside GS1, by comparing and correlating the results and producing a robust interpretation of site formation and palaeoenvironmental history.

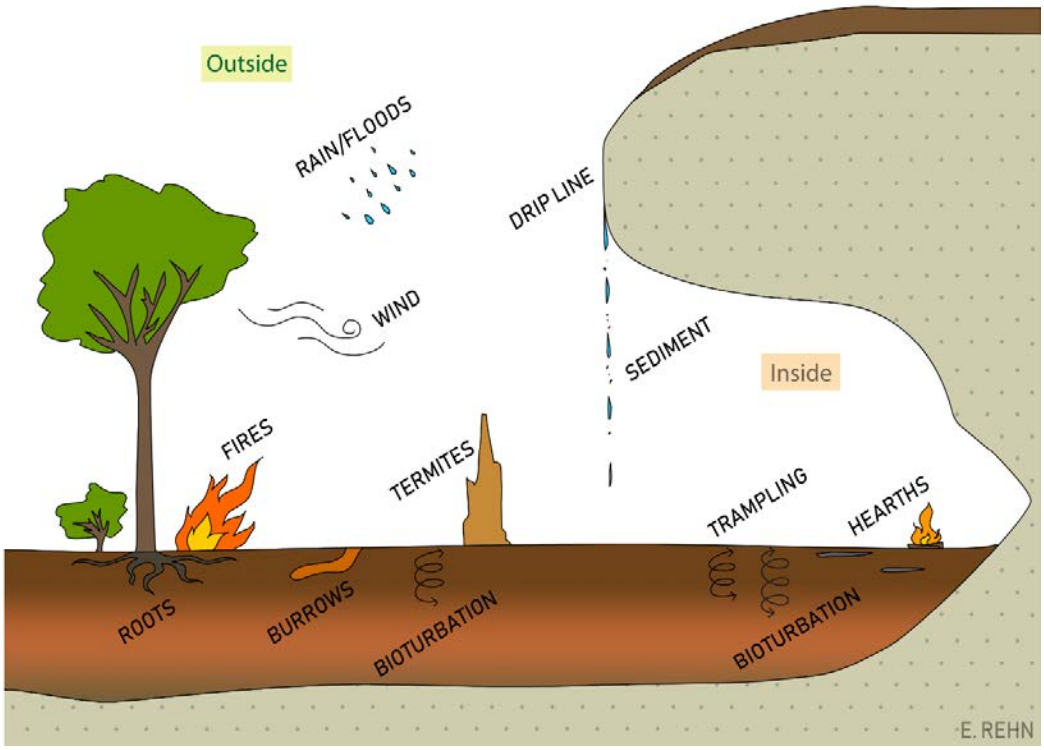

Figure F4.1: The impact of natural events and post-depositional modification processes on sediment records outside and inside rockshelters; note the dripline demarcating the inside space from the outside surrounding environment (author: Emma Rehn).

This integrated approach to site formation processes and palaeoenvironmental reconstruction allows us to examine how the sedimentary records from Inside GS1 complement the sedimentary records from Outside GS1 and vice-versa. It also enables us to observe in what way, and to what degree, the evidence

in the two archives is similar and/or differs. Finally, the establishment of a geomorphologic, geologic and palaeoenvironmental context for the study area will enable a more nuanced interpretation of the significance of the GS1 study area in the wider archaeological and palaeoenvironmental context of the Australian tropical north.

4.1.2 Formation and development of sandstone rockshelters: Cavernous weathering, tafoni and honeycombs

Under the tropical and semi-arid conditions in interior northern Australia, most sandstone rockshelters form on the margins of sandstone hills and escarpments, in lithologies that are themselves remnants of old river deposits (e.g. Clarkson et al., 2015, David et al., 2007, also Chapter 1 of this work). Between these outcrops, extensive and largely stabilized sand plains or sand sheets that now support open savannah woodlands formed. In this environment, various forms and sizes of sandstone rockshelters have developed. To give an example, more than 700 rockshelters were examined by Gunn et al. (2020) on the Arnhem Land Plateau and they were able to identify 13 distinct classes of shelter forms. The most common results from cavernous weathering, through which GS1 also formed.

Cavernous weathering or cavernous features is a collective expression for variously shaped and arranged cavities and hollows on the exposed vertical and steeply inclined surfaces of rocks. These cavities range in size from several millimetres to several meters. Many descriptive terms have been used through time to describe cavernous features on rock surfaces, of which tafoni, alveoli and honeycomb are the most popular. The terminology, however, is highly inconsistent and entangled (a detailed review is given in Groom et al., 2015). There has been a general tendency in recent decades, after Robinson and Williams (1994), to use tafoni for cavernous features on decimetre to metre scale and alveoli or honeycomb for smaller size features (≤ centimetre). Larger tafoni, meter to decametre scale cavities, are called rockshelters, and synonyms include rock overhangs, alcoves or abri (when referring to French sites) (Klimchouk, 2018). Despite the variability in size, morphology and patterns, tafoni and honeycomb features are recognizable (Figure F4.2).

In terms of formation, cavernous features are still some of the most enigmatic and puzzling geomorphologic phenomena. They are mostly found on vertical cliffs, sub-vertical outcrops and boulders in a wide range of rock types, including sandstone, limestone, quartzite, granite, greywacke, dolerite, rhyolite, greenschist, conglomerate and tuff. Tafoni and honeycombs have been described from various climatic zones and environments on all the continents, from deserts to humid areas, coasts and lowlands to high mountains and Antarctic valleys (Turkington, 1998) and even on Mars (Rodriguez-Navarro, 1998).

Studies of these features and the process of cavernous weathering contributed to a large body of literature, particularly in the field of weathering research and sandstone landscapes. Notable works and recent reviews include, among others, Brandmeier et al. (2011), Goudie and Viles (1997), Groom et al. (2015), Huinink et al. (2004), Martini (1978), McBride and Picard (2004), Mustoe (1983), Paradise (2013), Siedel (2015), Turkington (2004), Turkington and Paradise (2005), Turkington and Phillips (2004), Viles (2005), and Young and Young (1992).

Tafoni and honeycomb are considered to form by selective weathering on exposure to atmospheric conditions. Various processes have been invoked to explain their formation, including aeolian deflation, weathering through insolation, frost action, wetting and drying, chemical and salt weathering and decay by biological action. Case hardening and/or core softening have also been suggested to play a major part. Although all these processes contribute to granular disintegration and flaking, the resultant rock decay and formation of cavernous features, none of them, alone or in combination, has yet to explain the principal mechanisms behind cavernous weathering phenomena adequately (Brandmeier et al., 2011, Groom et al., 2015, Klimchouk, 2018, Turkington, 2004, Turkington and Paradise, 2005). Their global occurrence, across a wide range of lithologies and environmental conditions, suggests that their formation is determined by a factor that exceeds variations in these conditions and weathering processes (Klimchouk, 2018, Turkington, 1998, Turkington and Paradise, 2005).

Figure F4.2: Cavernous weathering in Hampstead sandstone. **Top left**: the GS1 rockshelter. **Top right and bottom**: tafoni and honeycombs in outcrops surrounding the GS1 site.

Recently, Klimchouk (2018) proposed a new conceptual model. Based on a study conducted in the Crimean Piedmont, he argued that the primary factor of tafoni and honeycomb formation is the pre-exposure alteration of rocks along fractures and/or karst conduits as a result of fluid-rock interactions. Under this model, the local or regional characteristics of a weathering system are irrelevant or only of

secondary importance in determining the localization and morphology of cavernous features. The proposed model aligns well with the main characteristics of cavernous weathering features described in different rocks around the world that have been challenging to explain by applying the traditional weathering paradigm, which assumes that external agencies (the weathering system) acting on exposed rock surfaces are the primary factor in their formation. According to Klimchouk (2018), the model opens up exciting possibilities for revisiting a number of conspicuous features of sandstone geomorphology in many regions worldwide.

4.1.2 A complex relationship: Rockshelters and related sediment deposits

A major factor governing the processes of sedimentation in rockshelters and caves is the shape of the rockshelter or cave. In simple terms, rockshelters are shallow niches in the hillside, while caves penetrate deeper into the ground forming underground chambers, passages and channels (Lowe and Walker, 2015, pg. 141). Hence, caves, being more enclosed and protected environments not directly exposed to daily and seasonal changes, are modified only by significant and long-term climatic changes that affect the mode of sedimentation, apart from water-lain sediments in conduits (Figure F4.3). Rockshelters, on the other hand, are more open and exposed spaces where sedimentation is directly affected by the open-air daily conditions (Figure F4.3). The stratigraphy of rockshelter deposits is, therefore, often complex and complicated by the fact that several different depositional processes may be acting simultaneously, resulting in a mix of endogenous (internally derived) and exogenous (externally-derived) sediments and a discontinuous stratigraphy (Kibler, 1998) (Figure F4.3).

Three main types of materials contribute to rockshelter and cave sediment sequences: clastic sediments, chemical (precipitated) sediments and organic detritus (Lowe and Walker, 2015, White, 2007) (Figure F4.3). Clastic sediments may include rock rubble, cave earth or water-lain material. They are moved mechanically, whereas chemical sediments are formed in place and precipitated from solution by seeping, dripping or flowing water, such as speleothems or cave breccias (O'Connor et al., 2017). Organic detritus consists of plant and animal remains or materials of anthropogenic origin (Figure F4.3).

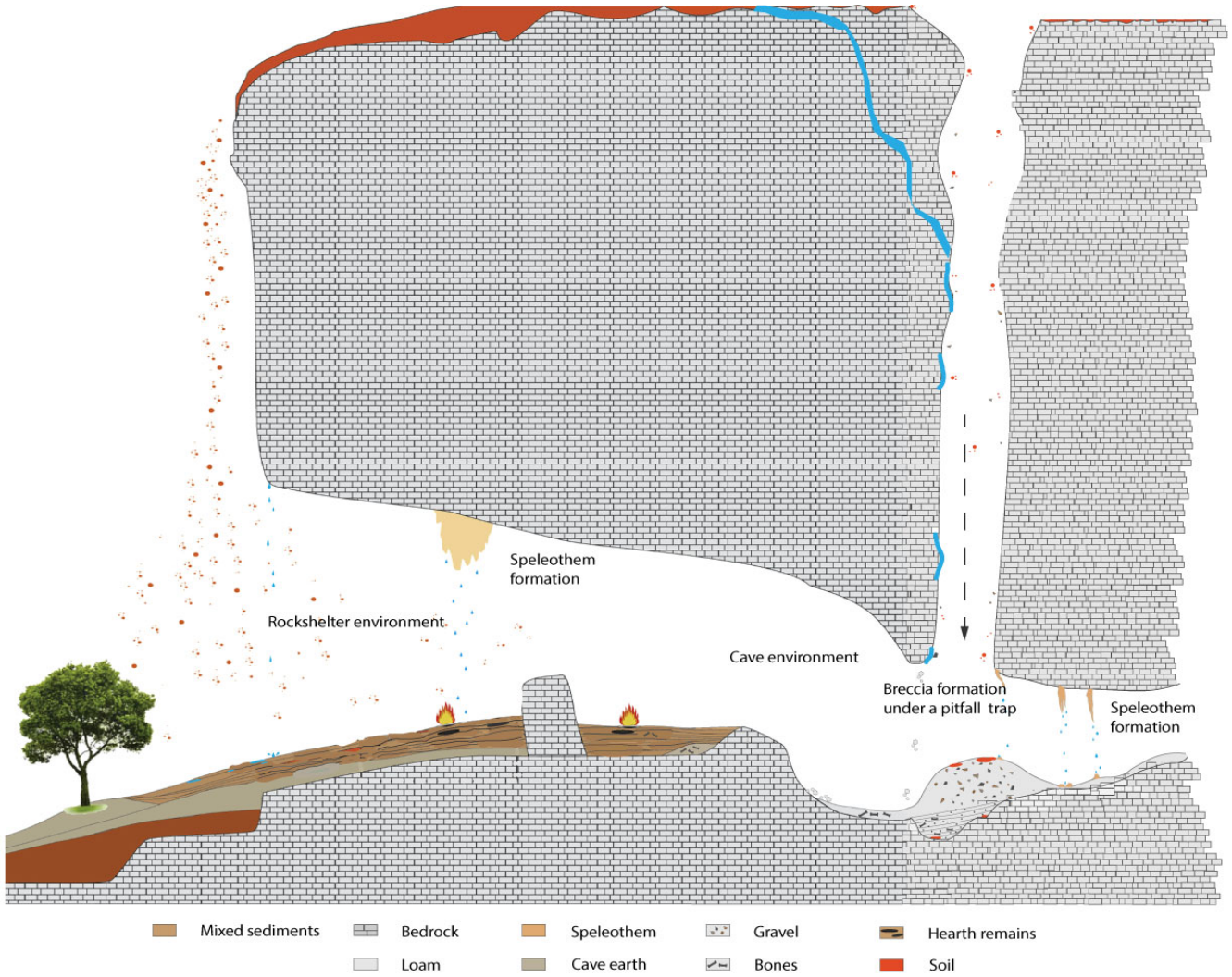

Figure F4.3: Complex sedimentation conditions of rockshelter and cave environment (Figure adapted from Villagran et al. (2017) and rearranged for the purposes of this introduction).

These materials become part of rockshelter and cave deposits via an agent transfer, such as wind, animal, water, or via various mass wasting or weathering processes operating on rock faces at different scales (Carson and Kirkby, 1972, pg. 112-128). Macroscale processes, such as slab failure and rock (roof) fall, are primarily related to primary jointing and fracturing patterns as well as the mechanical strength of the rock unit. They deposit large blocks or fragments into rockshelters and caves. Granular disintegration, on the other hand, acts on a microscale level. Granular disintegration is widespread in sandstones in semi-arid to arid regions (Turkington and Paradise, 2005, Zhang et al., 2011). Weathering usually takes the form of the slow release of individual grains from the rock surface through the destruction of the cement bond that ultimately results in the rock returning to sand and forming deposits inside rockshelters along with the surrounding sand plains.

4.1.3 Study area and sampling locations

The GS1 rockshelter is located in tropical North Queensland (Figure F4.4). Detailed geographic, geomorphic and geologic descriptions of the area are given in previous chapters (sections: I.2A,B; 1.1; 3.2.1). The GS1 is a small overhang developed in an 8 m high sandstone outcrop (Figure F4.2 top left). The distance from the shelter's floor to the dripline is 3–5 m and the interior surface is about 15 m^2 (Figure F4.5). The maximum depth from the shelter's inside ground surface to the bedrock is approximately 250 cm (Lowe et al., 2018, Wallis et al., 2009). Two sediment archives were used for this comparative study (analogous to the two collections in Chapter 3):

1) **Outside GS1**, which encompasses records from sediment samples collected in the years 2008, 2019 and 2020 from pits and auger holes excavated in non-archaeological open-site sediment deposit expanding south-southwest beyond the GS1 dripline (marked by a red circle in Figure F4.4, shown in Figure F4.6), and
2) **Inside GS1**, which encompasses records from sediment samples collected from squares C0 and C1 in the GS1 interior archaeological sediment deposit excavated between 2006 and 2008 (marked by a yellow rectangle in Figure F4.4 and outlined in Figure F4.5).

4.2 Materials and methods

Details of the materials and methods used in the investigations of the Outside GS1 sediment record and for comparison in this study are provided in previous chapters (sections: 1.2, 2.2 and 3.2). Whereas details about the materials and methods used in the investigations of the Inside GS1 archaeological sediment record and for comparison in this study are provided in the previous research (Lowe et al., 2016,

2018, Lowe and Wallis, 2020, Wallis et al., 2009) and reports (Wallis, 2008, Wallis et al., 2014a). A summary of previous studies conducted on Inside GS1 sediment record is also provided in the introductory part of this thesis (section I.2C). An abbreviated version of materials and methods only relevant to the comparison of the Outside GS1 and Inside GS1 archives, is provided below. In addition, Table T4.1 summarises the sample IDs, their location and depth and the materials and methods used to compare the two archives.

Figure F4.4: The map of the study area and sampling sites for both archives – Outside GS1 and Inside GS1. **Outside GS1** is marked by a dashed red circle; purple circles represent the pits and auger holes excavated in 2019 and 2020, blue rectangles represent pits excavated in 2008. **Inside GS1** marked by a yellow rectangle.

Figure F4.5: The inside GS1 archaeological excavation squares marked in yellow.

Figure F4.6: A bird's eye view of the study area. Note the sandstone outcrop with the GS1 rockshelter and the pink arrow indicating the dripline as well as the sediment deposit expanding south-southwest and the red arrow indicating the pit PA_10-M (size of the tarpaulin is approx. 2.7 x 4m).

4.2.1 Subsurface morphology, stratigraphy and sedimentology

Ground-penetrating radar (GPR) data (Lowe and Wallis, 2020) and the results from 17 pits and auger holes were used to obtain information about the subsurface bedrock morphology.

Stratigraphic and sedimentologic characteristics of Outside GS1 and Inside GS1 sediment deposits were examined and documented through pits, auger holes and archaeological stratigraphic units (SUs). A total of 24 bulk sediment samples from Outside GS1, from pits PA_10-M, TP01, TP02 and TP05 (Table T4.1, Figure F4.4), and 24 from Inside GS1, from squares C0 and C1 (Table T4.1, Figure F4.5), were compared. Munsell soil colour charts (1994) were used for sediment colour determination and Malvern Mastersizer MS3000 analyser as well as Endecotts sieves with a Geolab Systems mechanical sieve shaker were used for the Outside GS1 and Inside GS1 sediments' particle size analysis, respectively.

Optical microscopy was applied using a standard petrographic microscope for sedimentologic analysis of Outside GS1 and Inside GS1 sediment thin sections. The optical microscopy results were compared for mineralogical composition, structure and texture of sediments and examined for evidence of post-depositional disturbance and the presence of allochthonous materials, such as charcoal, that might not be discernible at a macroscopic level. Altogether, four sediment thin sections from Outside GS1 (PA_10-M pit south profile) were compared with five sediment thin sections from corresponding depths from Inside GS1 squares C0 and C1 (Table T4.1) collected and analysed in previous archaeological studies (Lowe et al., 2018).

4.2.2. Magnetic susceptibility

Magnetic susceptibility measures how 'magnetisable' a material is. In the natural environment, magnetic susceptibility tells us about the minerals found in rocks, sediments, soils and dusts, particularly Fe-bearing minerals. Magnetism derives from various processes, including primary minerals of geological origin, secondary minerals such as magnetite and maghemite formed through chemical weathering, bacterial processes forming magnetite or produced during burning and pollution dusts containing magnetic spherules (Ellwood et al., 1997, Dalan and Banerjee, 1998, Dearing et al., 1996, Herries and Fisher, 2010, Linford et al., 2005, Thompson and Oldfield, 1986). Magnetic mineral analysis can, therefore, be used, for example, to help characterise sediments and sediment sources, reconstruct palaeoclimatic signatures, identify combustion features and uncover spatial patterning in archaeological sites (Herries, 2006, Herries and Fisher, 2010, Herries and Latham, 2003).

Geologically, northern Queensland comprises an old continental craton of granitic rocks overlain by Proterozoic to Mesozoic quartzose sandstones that are originally only weakly magnetic (Bain & Draper, 1997). However, when sediment or soil is exposed to fire, changes to mineralogy occur that can affect magnetic susceptibility. The nature of these changes are related to the temperature and duration of exposure to fire, the organic content of the sediments and the type and relative abundance of iron-bearing minerals present in the material (Bellomo, 1993, Linford and Canti, 2001, Longworth et al., 1979, McClean and Kean, 1993, Oldfield et al., 1981). A range of mineral grain sizes form in response to exposure to fire, among them ultrafine superparamagnetic (SP) grains (magnetic grain size <0.03 μm) and fine stable single-domain (SD) grains (0.03–0.1 μm), that can potentially be linked to increases in magnetic susceptibility caused by fire (Dearing et al., 1996, Thompson and Oldfield, 1986, Tite and Mullins, 1971).

In environmental samples, low-field magnetic susceptibility (χ_{LF}) is routinely measured to determine the concentration of ferrimagnetic minerals (e.g. magnetite and maghemite) (Thompson and Oldfield, 1986). It is, however, a measurement that in isolation, does not discriminate well between magnetic grain sizes nor mineral type (Dearing et al., 1996). Meanwhile, the frequency dependence of susceptibility (χ_{FD}) is a highly diagnostic measurement with many environmental applications. χ_{FD} is a magnetic parameter that represents the difference between the measured magnetic susceptibilities of sediment at low (χ_{LF}) and high (χ_{HF}) field frequency. χ_{FD} is expressed either as:

1) a relative loss of susceptibility $\chi_{FD} = \chi_{LF} - \chi_{HF}$, or
2) a percentage loss of the low-frequency value $\chi_{FD}\% = \chi_{LF} - \chi_{HF} / \chi_{LF} \times 100$

(Dearing et al., 1996, Maher, 1986). This measurement is used to reveal the contribution of ultrafine superparamagnetic (SP) grains (Dalan and Banerjee, 1998, Dearing et al., 1996, Maher, 1986) and therefore also reveal the potential presence of burned sediments or pedogenic processes (Dearing et al., 1996, Herries and Fisher, 2010). Hence, χ_{FD} may provide information about climate as well as fire usage by humans.

In this study, sediment magnetic properties were measured in the laboratory using a Bartington Instruments MS2B sensor. Magnetic analysis of Outside GS1 and Inside GS1 bulk sediment samples was performed using 10 cm^3 plastic pots provided by Bartington. Each sample was carefully weighed to a three decimal places. Low-field mass-normalized magnetic susceptibility readings at the maximum sensitivity were taken using both low (460 Hz) (χ_{LF}) and high (4,600 Hz) (χ_{HF}) frequencies for frequency dependence of susceptibility (χ_{FD} and $\chi_{FD}\%$) according to the formulas 1) and 2) above.

The potential for using sediment magnetic properties at the GS1 study area to determine human activity was previously investigated by Lowe et al. (2016, 2018) and Lowe and Wallis (2020). Their findings relevant to our comparison of sediment records from Outside GS1 and Inside GS1 are used in this study.

Table T4.1 Materials and Methods used for the comparison Outside GS1 *vs.* Inside GS1: Outside GS1 sediment record

* SPAC - a highly resistant form of micro-charcoal (Stable Polycyclic Aromatic Carbon)

Sample ID	Sampling site	Sampling method	Depth (cm)	Distance from GS1 dripline (m)	Sample form	Particle size (µm)	Colour Munsell Chart	Optical microscopy	Magnetic susceptibility (χ_{LF}) (SI)	Chronolgy	Vegetation (material used)
PA_1-M	Outside GS1	auger hole	10	68	bulk				Bartington MS2B		Phytoliths and $\delta^{13}C$ (SPAC*)
PA_2-M	"	"	25	73	bulk				"		"
PA_3-M	"	"	50-60	45	bulk				"		"
PA_4-M	"	"	30-37	52	bulk				"		"
PA_5-M	"	"	15	37	bulk				"		"
PA_6-M	"	"	50-60	37	bulk				"		"
PA_7-M	"	"	55-65	32	bulk				"		"
PA_8-M	"	"	122-140	29	bulk				"		"
PA_9-M	"	"	150-160	22	bulk				"		"
PA_10-M 42	"	pit PA_10-M	42-43	19	bulk	Mastersizer MS3000	10YR 5/3		"	OSL and ^{14}C	"
PA_10-M 50	"	"	50-52	"	bulk	"	10YR 5/3		"	OSL	"
PA_10-M 60	"	"	60-65	"	bulk	"	10YR 5/4		"	OSL	"
PA_10-M 65	"	"	65-67	"	bulk	"	10YR 5/4		"	OSL and ^{14}C	"
PA_10-M 80	"	"	80-82	"	bulk	"	7.5YR 6/4		"	OSL and ^{14}C	"
PA_10-M 100	"	"	100-105	"	bulk / core	"	7.5YR 6/6		"	OSL	"
PA_10-M 102	"	"	100-102	"	bulk	"	7.5YR 6/7		"	OSL and ^{14}C (SPAC)	"
PA_10-M 120	"	"	120-122	"	bulk	"	7.5YR 6/8		"	OSL and ^{14}C (SPAC)	"
PA_10-M 150	"	"	150-152	"	bulk	"	7.5YR 6/9		"	OSL	"
PA_10-M 160	"	"	160-162	"	bulk	"	7.5YR 6/10		"	OSL	NA
PA_10-M 172	"	"	168-172	"	bulk	"	7.5YR 6/4			OSL and ^{14}C (SPAC)	"
PA_11-M 60	"	auger hole	60 ±5	25	bulk				Bartington MS2B		"
PA_11-M 140	"	auger hole	140-160	"	bulk				"		"
TP01 0	"	pit TP01	0	10	bulk	Mastersizer MS3000			"		"
TP01 40	"	"	40	"	bulk	"			"		"
TP01 60	"	"	60	"	bulk	"			"		"
TP01 80	"	"	80	"	bulk	"			"		"
TP01 120	"	"	120	"	bulk	"			"		"
TP02 20	"	pit TP02	20	20	bulk	"			"		"
TP02 40	"	"	40	"	bulk	"			"	^{14}C (SPAC)	"
TP02 60	"	"	60	"	bulk	"			"		"
TP02 100	"	"	100	"	bulk	"			"		"
TP02 120	"	"	120	"	bulk	"			"	^{14}C (SPAC)	"
TP03 60	"	pit TP03	60	30	bulk				"	^{14}C (SPAC)	"
TP03 120	"	"	120	"	bulk				"		"
TP04 20	"	pit TP04	20	40	bulk				"		"
TP04 80	"	"	80	"	bulk				"		"
TP05 0	"	pit TP05	0	50	bulk	Mastersizer MS3000			"		"
TP05 40	"	"	40	"	bulk	"			"		"
TP05 60	"	"	60	"	bulk	"			"	^{14}C (SPAC)	"
TP05 80	"	"	80	"	bulk	"			"		"
TP05 100	"	"	100	"	bulk	"			"		"
TP05 120	"	"	120	"	bulk	"			"	^{14}C (SPAC)	"
C_1-CR 100	"	pit C_1-CR	100	68	bulk / core				"	^{14}C (SPAC)	"
C_1-CR 135	"	"	135	"	bulk / core				"	^{14}C (SPAC)	"
C_1-CR 200	"	core C_1-CR	200	"	bulk / core				"		"
PA_10-M 1	"	pit PA_10-M; S-face	64-71.8	NA	hard sample			Thin secion			NA
PA_10-M 2	"	"	82.8-90.8	NA	hard sample			Thin secion			NA
PA_10-M 3	"	"	124-130.4	NA	hard sample			Thin secion			NA
PA_10-M 4	"	"	153.2-161	NA	hard sample			Thin secion			NA

Table T4.1 Materials and Methods used for the comparison Outside GS1 *vs. I* nside GS1: Inside GS1 sediment record

*SPAC - a highly resistant form of micro-charcoal (Stable Polycyclic Aromatic Carbon)

Sample ID	Sampling site	Sampling method	Depth (cm)	Sample form	Particle size (µm)	Colour Munsell Chart	Optical microscopy	Magnetic susceptibility (χLF) (SI)	Chronology	Vegetation (material used)
C0-01	Inside GS1	spit / Square C0	2.5	bulk	Geolab Systems					
C0-03	"	"	10						^{14}C (macro-charcoal)	
C0-05	"	"	20	bulk	Geolab Systems				^{14}C (macro-charcoal)	
C0-06	"	"	25						^{14}C (macro-charcoal)	
C0-08	"	"	35						^{14}C (macro-charcoal)	
C0-09	"	"	40	bulk	Geolab Systems				^{14}C (macro-charcoal)	
C0-12	"	"	55	bulk	Geolab Systems				^{14}C (macro-charcoal)	
C0-14	"	"	65	bulk	Geolab Systems					
C0-16	"	"	75						^{14}C (macro-charcoal)	
C0-17/2	"	"	80	bulk	Geolab Systems					
C0-20	"	"	95						^{14}C (macro-charcoal)	
C0-21/2	"	"	100	bulk	Geolab Systems					
C0-25/2	"	"	120	bulk	Geolab Systems				^{14}C (macro-charcoal)	
C0-26	"	"	125						^{14}C (macro-charcoal)	
C0-38B	"	"	145	bulk	Geolab Systems					
C0-41	"	"	170	bulk	Geolab Systems					
C0-47	"	"	200	bulk	Geolab Systems					
C0-54	"	"	235	bulk	Geolab Systems					
MM05	"	Square C0; W-face	59-69	hard sample			thin section			
MM04	"	"	133-143	hard sample			thin section			
MM03	"	"	165-175	hard sample			thin section			
C1-01	Inside GS1	spit / Square C1	3.1	bulk	Geolab Systems	10YR 4/1				Phytoliths and δ^{13}C (SPAC*)
C1-02	"	"	8.6	bulk		10YR 3/1				Phytoliths
C1-04	"	"	18.9	bulk	Geolab Systems					Phytoliths
C1-08	"	"	37.6	bulk	Geolab Systems					Phytoliths
C1-09	"	"	42.4	bulk		7.5YR 4/2		Bartington MS2B		Phytoliths and δ^{13}C (SPAC*)
C1-11	"	"	52.2	bulk	Geolab Systems					Phytoliths
C1-12	"	"	57.0	bulk		2.5YR 3/1				Phytoliths
C1-13	"	"	61.5	bulk	Geolab Systems	10YR 4/2				Phytoliths
C1-14	"	"	66.3	bulk				Bartington MS2B		Phytoliths and δ^{13}C (SPAC*)
C1-17B	"	"	80.5	bulk	Geolab Systems			Bartington MS2B		Phytoliths and δ^{13}C (SPAC*)
C1-19	"	"	88.7	bulk		7.5YR 4/2				Phytoliths
C1-22	"	"	100.6	bulk	Geolab Systems			Bartington MS2B		Phytoliths and δ^{13}C (SPAC*)
C1-23	"	"	105.5	bulk		10YR 3/2				Phytoliths
C1-25	"	"	115.5	bulk		10YR 4/2				Phytoliths
C1-26	"	"	120.4	bulk	Geolab Systems			Bartington MS2B		Phytoliths and δ^{13}C (SPAC*)
C1-27A	"	"	125.4	bulk		10YR 4/3				Phytoliths
C1-29	"	"	135.3	bulk						Phytoliths
C1-30	"	"	140.4	bulk					^{14}C (macro-charcoal)	
C1-32A	"	"	149.6	bulk		10YR 5/4				
C1-32B	"	"	149.6	bulk	Geolab Systems					
C1-34A/B	"	"	163.4	bulk				Bartington MS2B		δ^{13}C (SPAC*)
C1-35A	"	"	168.5	bulk		10YR 6/4				
C1-35B	"	"	168.5	bulk	Geolab Systems					
C1-36B	"	"	173.5	bulk				Bartington MS2B		δ^{13}C (SPAC*)
C1- 41A	"	"	198.0	bulk					^{14}C (macro-charcoal)	
C1-41B	"	"	198.0	bulk						
C1-42	"	"	202.6	bulk	Geolab Systems			Bartington MS2B		δ^{13}C (SPAC*)

C1- 43	"	"	207.3	bulk					^{14}C (macro-charcoal)	
C1-48	"	"	232.1	bulk				Bartington MS2B		$\delta^{13}C$ (SPAC*)
C1- 49	"	"	235.8	bulk		10YR 6/6				
C1-52	"	"	248.9	bulk	Geolab Systems			Bartington MS2B		$\delta^{13}C$ (SPAC*)
MM13	"	Square C1; E-face	100-110	hard sample			thin section			
MM08	"	"	120-130	hard sample			thin section			

4.2.3 Chronology of the sediments

The chronology for non-archaeological sediments Outside GS1 was established using two methods: 1) single-grain optically stimulated luminescence dating (OSL), and 2) the radiocarbon dating (^{14}C) on macro-charcoal (refer to Chapter 2). Open-site terrestrial deposits tend to have an unknown history of stability and disturbance, the stratigraphy is often fragmented and incomplete and sediments are generally mixed post-depositionally. Thus, the two-method approach was applied to cross-check results and determine the reliability of the chosen methods.

The chronology for the archaeological sequence Inside GS1 was determined using ^{14}C dating on macro-charcoal. Radiocarbon dates obtained from earlier studies (Wallis et al., 2009, Wallis et al., 2014a) were recalibrated using OxCal 4.4 and the IntCal20 calibration curve (Ramsey et al., 2010, Reimer et al., 2020).

An age-depth model was built to correlate the Outside GS1 and Inside GS1 sequence chronologies using the *rbacon* software package with Bayesian statistics (Blaauw and Christen, 2011).

4.2.4 Vegetation reconstruction

Plant phytoliths and $\delta^{13}C$ isotopic signature from a highly resistant form of microcharcoal, i.e. Stable Polycyclic Aromatic Carbon (SPAC), were used for the reconstruction of past vegetation in the study area (refer to Chapter 3). The two-proxy method approach was applied to cross-check the results and investigate the potential of each proxy for vegetation reconstruction in analogous environments. The vegetation reconstruction was generated using sediment samples from both archives Outside GS1 and Inside GS1, provided as a separate study in Chapter 3. This chapter presents and discusses only the vegetation reconstruction results relevant to the overall interpretation of the palaeoenvironmental signal.

In brief, 44 samples from sediments Outside GS1 were used for phytolith analysis and 64 samples from the archaeological sequence (square C1) Inside GS1. The same 44 sediment samples from Outside GS1 and 13 from Inside GS1 were also used to obtain $\delta^{13}C$ isotopes of SPAC. Phytolith indices D/P (Dicot/Poaceae = tree/grass) and FI-t (Forest Indicators - time) were also calculated for both collections (for details, refer to Chapter 3).

4.2.5 Other materials

Other excavated materials from the archaeological sequence Inside GS1 include stone artefacts and ochre (Lowe et al., 2018). Wood charcoal was collected from the 7- and 3-mm sediment fractions, weighed and volumetrically corrected.

4.3 Evidence from Outside GS1 and Inside GS1

4.3.1 Subsurface evidence

Evidence from pits and auger holes Outside GS1 demonstrates an uneven, undulating subsurface composed of fallen rock parts, bedrock slabs and intermediate depressions. A general shallowing of the bedrock layer occurs as the distance from the GS1 dripline increases towards the south (Figure F4.7). A general tendency of the subsurface bedrock to dip towards the southwest is also evident (Figure F4.7). The GPR results showed the bedrock is more visible in the subsurface moving away from the GS1 rockshelter wall and several large boulders of roof material were identified in the subsurface (Lowe and Wallis, 2020). A depression or small basin at a depth of around 220 cm was identified extending from inside GS1 approximately 15 m beyond the dripline, then a gradual shallowing of the subsurface bedrock layer occurs further away from the shelter (Lowe and Wallis, 2020) (Figure F4.7). Figure F4.7 shows the projection of GPR imagery onto the drone image of the study area and the evidence of the undulating subsurface obtained from pits and auger holes Outside GS1.

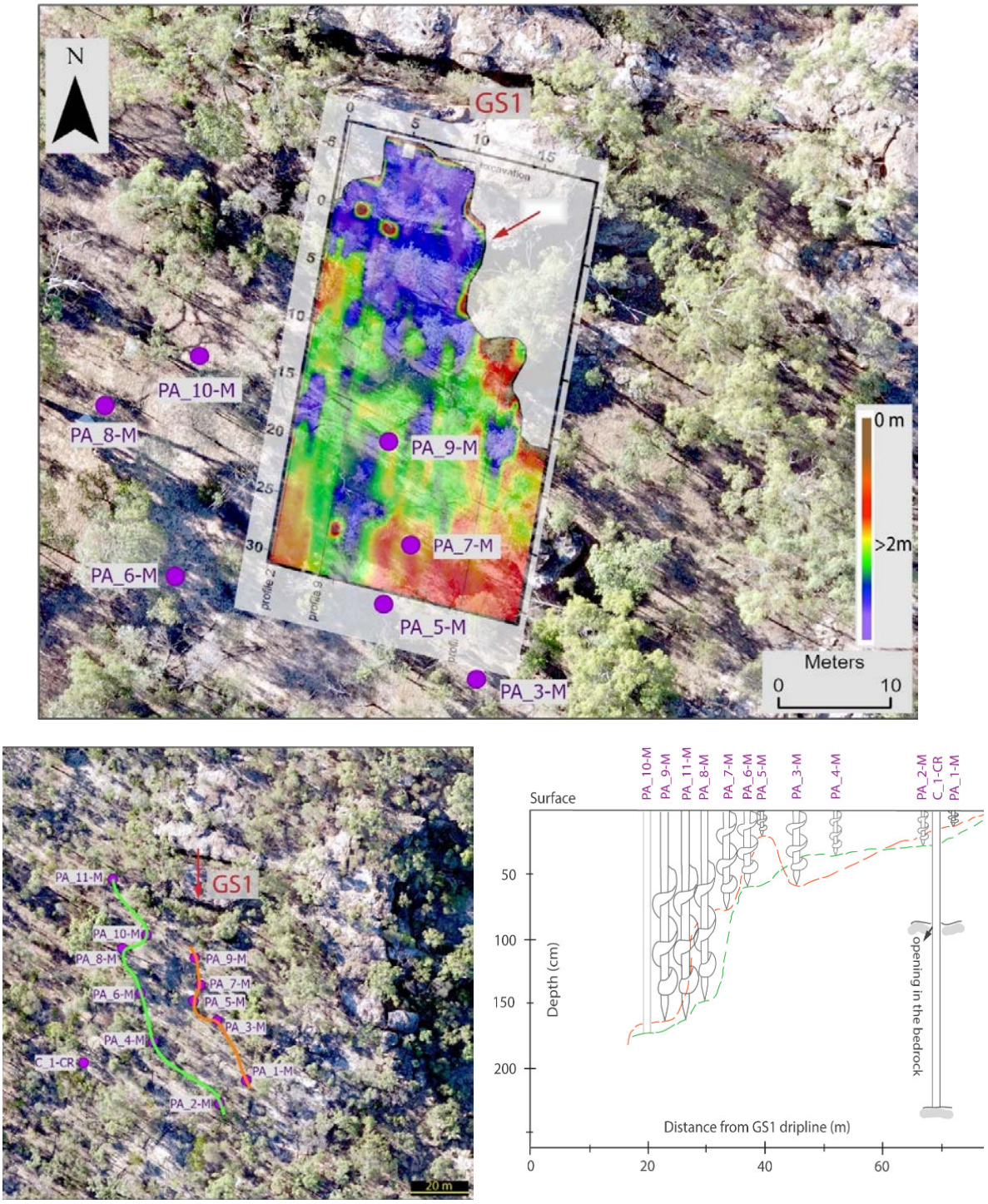

Figure F4.7: Subsurface morphology of the study area as demonstrated by GPR analysis and depths of pits and auger holes. The purple circles mark the Outside GS1 sampling locations (see Figure F4.4). **Upper:** Georeferenced GPR image positioned on the drone image of the study area. Note the depression extending from GS1 interior further south beyond the GS1 dripline. The red arrow indicates the dripline and the scale on the right marks the depth below the surface. **Lower:** Outside GS1 view of pits and auger holes in relation to distance from the GS1 dripline. Pits and auger holes are linked by a green and orange contour on the left side image and same colour dashed lines on the right image of the

Outside GS1 side profile. The orange line connects the auger holes on the east line, the green line connects the pit and auger holes on the west line of the sampling locations; apart from the pit C_1-CR which could not be connected to the two lines because of its offline position. On the right image the two contours show the Outside GS1 side profile and the uneven subsurface bedrock that dips towards the west. The sediment deposit also thickens towards the west as exhibited by the depth of pit C_1-CR.

4.3.2 Stratigraphic evidence

The PA_10-M pit south profile in the non-archaeological sediment deposit Outside GS1 and the square C1 east profile in the archaeological sequence Inside GS1, appear in the field to be stratigraphically homogeneous (Figure F4.8a). No stratification in the form of paleosols, hardened sediment layers (i.e. duricrusts), change in particle size/orientation or any other form was visible in either of the two profiles. A gradual change in colour was recorded in the PA_10-M pit profile Outside GS1, from greyish and greyish brown in the upper 40 cm to brighter pale brown, pinkish or yellowish brown below depth 100 cm (Figure F4.8a,b; Table T4.1). The sediment Inside GS1 in square C1 profile, on the other hand, was generally darker and more grey in hue in the upper part of the profile. At about 150 cm depth a noticeable change in colour occurs to yellowish brown and brownish yellow, also perceived as reddish with the naked eye (Figure F4.8a,b; Table T4.1). Additionally, the presence of roof fall material in the form of scattered rocks and gravel material was recorded in the square C1 profile Inside GS1 (Figure F4.8a)

Both profiles, PA_10-M Outside GS1 and square C1 Inside GS1, showed macroscopic evidence of bioturbation, post-deposition disturbance by plant roots, and animal activity (termites, ants) in the form of soft decomposing root material, burrows, circular and ellipsoidal structures with crust rims (Figure F4.8c).

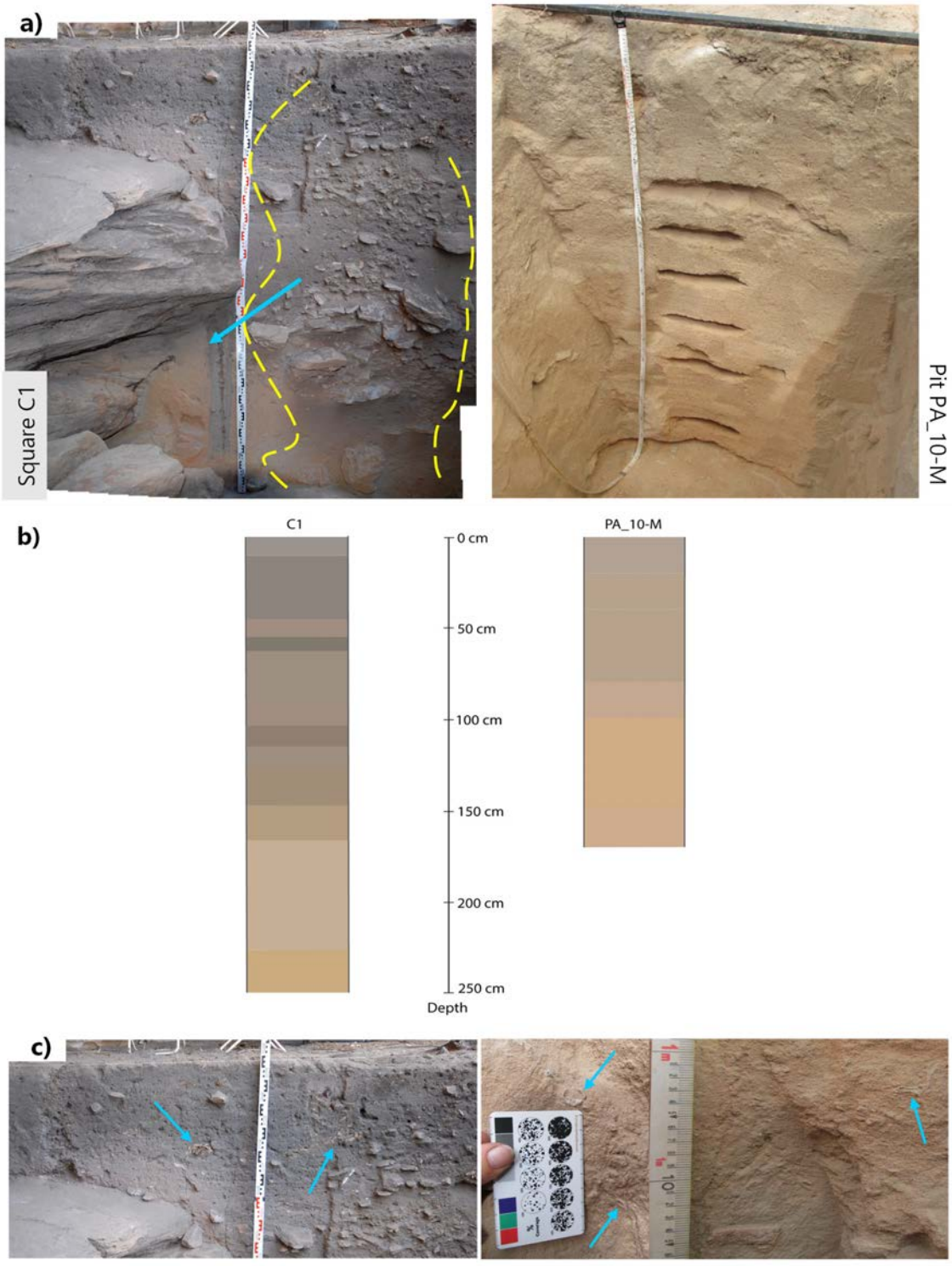

Figure F4.8: a) View of the square C1 eastern profile Inside GS1 and pit PA_10-M south profile Outside GS1. Yellow dashed line marks the roof fall and the blue arrow the abrupt change in colour. **b)** Change in profile colour (Munsell) with depth Inside GS1 (C1) *vs*. Outside GS1 (PA_10-M). **c)** Bioturbation evidence (blue arrows) Inside (left) and Outside GS1 (right).

4.3.3 Sedimentologic evidence

Particle size analysis did reveal a difference between Outside GS1 and Inside GS1 sediment samples, specifically in the fine (62.5−250 µm) and medium (250−500 µm) sand fractions. In the Outside GS1 sediments fine and medium sand-sized particles are the dominant fractions, constituting 80−90%, while the coarse sand component accounts for the lowest percentage, less than 6% (Figure F4.9a). In the Inside GS1 sediment sequence, on the other hand, the fine sand fraction solely accounts for 75−83% (Figure F4.9b), while medium sand represents less than 20% of the total. In both collections, Inside GS1 and Outside GS1, clay (<3.9 µm) and silt (3.9−62.5 µm) particles together make up 6–17% (Figure F4.9a,b). In general, a slight increase with depth in clay content was noticed in Outside GS1 samples, whereas this is not the case in samples Inside GS1 (Figure F4.9c,d). In contrast, in the Inside GS1 samples a slight general increase with depth in the medium sand fraction was observed (Figure F4.9c,d).

a

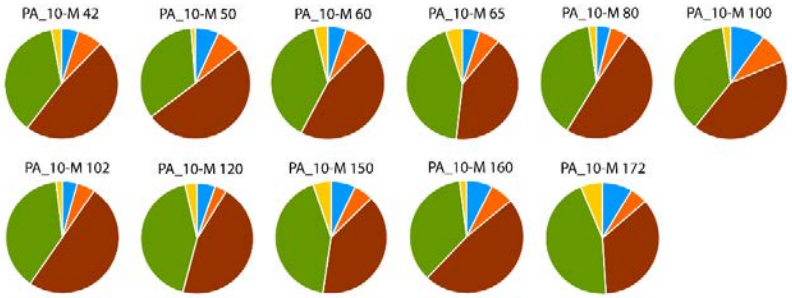

Particle size	PA_10-M 42	PA_10-M 50	PA_10-M 60	PA_10-M 65	PA_10-M 80	PA_10-M 100	PA_10-M 102	PA_10-M 120	PA_10-M 150	PA_10-M 160	PA_10-M 172
clay	4.85%	6.91%	5.23%	4.99%	4.06%	4.25%	9.83%	5.22%	7.07%	7.32%	8.50%
silt	7.25%	7.54%	7.17%	6.03%	5.35%	5.20%	8.81%	3.42%	5.61%	6.64%	5.05%
fine sand	48.20%	50.32%	45.37%	40.75%	49.38%	50.15%	42.11%	45.46%	39.68%	48.14%	35.45%
medium sand	36.85%	33.98%	38.39%	43.45%	38.98%	38.60%	37.00%	42.45%	42.42%	35.94%	44.75%
coarse sand	2.85%	1.25%	3.84%	4.78%	2.23%	1.80%	2.25%	3.45%	5.22%	1.96%	6.25%

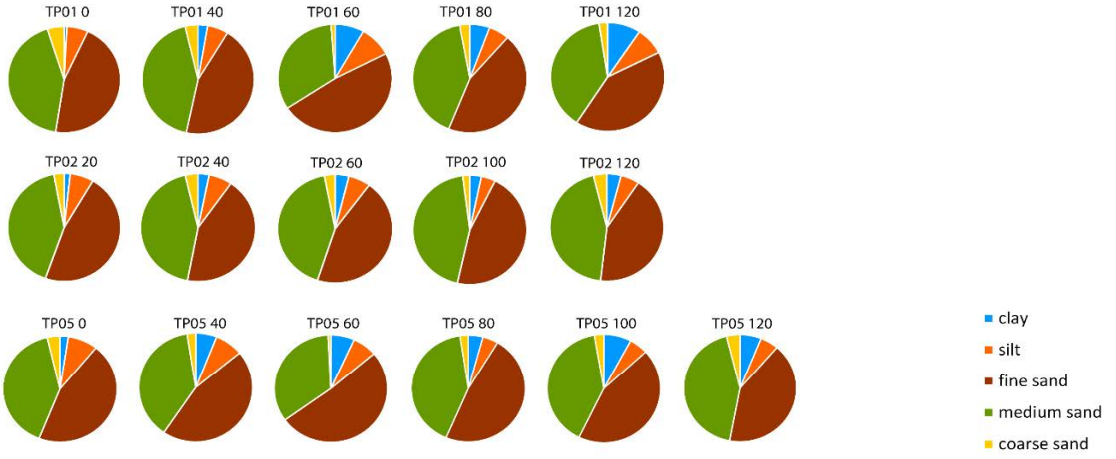

Particle size	TP01 0	TP01 40	TP01 60	TP01 80	TP01 120	TP02 20	TP02 40	TP02 60	TP02 100	TP02 120
clay	0.80%	2.74%	8.25%	5.59%	9.40%	1.71%	3.11%	3.88%	3.27%	4.01%
silt	6.10%	6.04%	9.20%	5.82%	8.18%	6.77%	6.57%	6.22%	4.05%	5.31%
fine sand	45.53%	44.62%	48.30%	44.64%	41.55%	46.93%	43.28%	44.88%	46.22%	42.47%
medium sand	42.73%	42.85%	33.10%	41.06%	38.42%	41.63%	43.45%	42.00%	44.44%	44.36%
coarse sand	4.84%	3.75%	1.15%	2.89%	2.45%	2.96%	3.59%	3.02%	2.02%	3.85%

Particle size	TP05 0	TP05 40	TP05 60	TP05 80	TP05 100	TP05 120
clay	2.35%	5.98%	6.75%	4.13%	7.85%	6.06%
silt	8.50%	8.07%	7.01%	4.44%	5.37%	5.26%
fine sand	45.11%	45.45%	51.30%	47.81%	44.00%	41.65%
medium sand	40.44%	38.04%	34.14%	41.27%	40.07%	43.15%
coarse sand	3.60%	2.46%	0.80%	2.35%	2.71%	3.88%

b

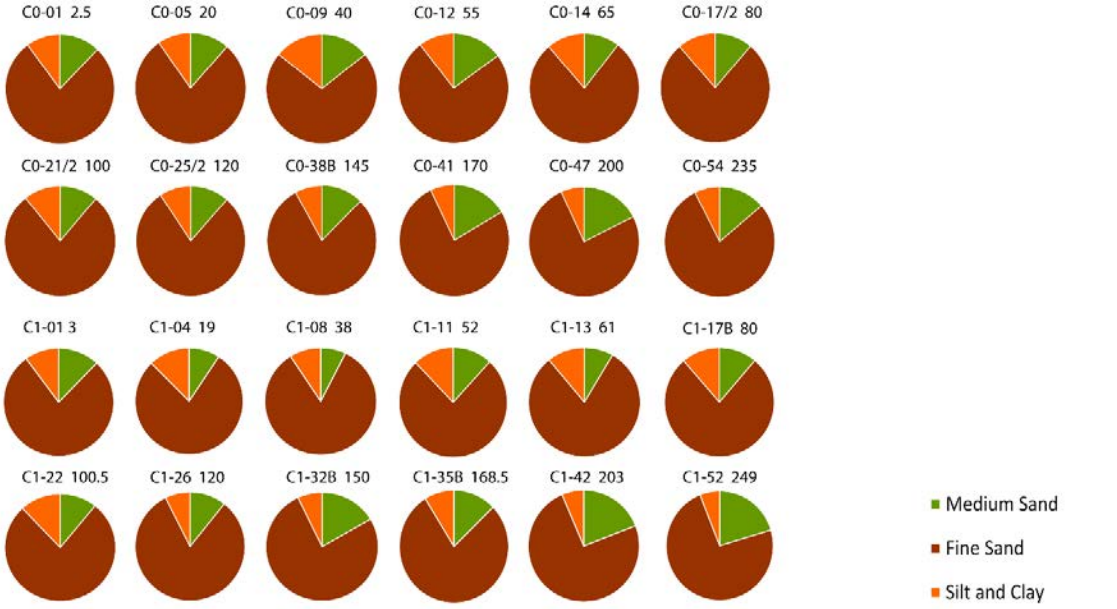

Particle size	C0-1 2.5	C0-5 20	C0-9 40	C0-12 55	C0-14 65	C0-17/2 80	C0-21/2 100	C0-25/2 120	C0-38B 145	C0-41 170	C0-47 200	C0-54 235
medium sand	12.12%	11.45%	14.18%	14.87%	10.46%	11.18%	11.13%	11.52%	12.38%	16.53%	17.52%	13.71%
fine sand	77.81%	78.87%	71.68%	74.74%	78.28%	77.51%	78.10%	79.15%	79.62%	76.40%	75.68%	78.88%
silt and clay	10.07%	9.68%	14.14%	10.39%	11.26%	11.31%	10.77%	9.33%	8.00%	7.07%	6.80%	7.41%

Particle size	C1-01 3	C1-04 19	C1-08 38	C1-11 52	C1-13 61	C1-17B 80	C1-22 100.5	C1-26 120	C1-32B 150	C1-35B 168.5	C1-42 203	C1-52 249
medium sand	12.12%	9.26%	7.31%	11.82%	8.42%	11.18%	10.83%	10.69%	16.53%	12.72%	19.10%	20.38%
fine sand	77.81%	78.36%	83.59%	75.97%	80.66%	77.51%	77.21%	81.90%	76.40%	78.44%	74.49%	73.60%
silt and clay	10.07%	12.37%	9.10%	12.21%	10.92%	11.31%	11.97%	7.40%	7.07%	8.84%	6.41%	6.02%

Figure F4.9a: Particle size results from samples Outside GS1 shown as pie charts. Note the major proportion shared between the fine sand and medium sand fraction. **b:** Particle size results from sediment samples Inside GS1 shown as pie charts. Note the major proportion represented throughout by the fine sand fraction and a general slight increase with depth in medium sand fraction. **c:** Particle size results from the same pits Outside GS1 arranged in stacked bar charts to show a general slight increase in clay content with depth. **d:** Particle size results from the same two squares (C0, C1) Inside GS1 arranged in stacked bar charts to show a general slight increase with depth in medium sand fraction.

Under the microscope, the sediment mineral composition Outside GS1 and Inside GS1 is generally very similar. Quartz of various forms, mono-, poly-, microcrystalline and metamorphic, is the dominant mineral in both groups of samples (~80%). Feldspars and lithic grains are present in minor abundance, the latter composed of chert, quartzite, sandstone and siltstone. The matrix is made up of clay and silt. Clay coatings surround the mineral grains (Figure F4.10). Authigenic clays were also recorded in both collections of samples, Outside GS1 and Inside GS1 (Figure F4.11b,f).

Some distinctions, however, were noted between the analysed sediment thin sections from Outside GS1 and Inside GS1. Charcoal, particularly coarse fragments, were significantly more abundant in thin sections from the Inside GS1 archaeological sequence, compared to the thin sections from similar depths from the Outside GS1 sediments. Larger charcoal particles are absent in the analysed thin sections from the Outside GS1, with rare exceptions (Figure F4.10a). In general, charcoal in the Outside GS1 samples is rare, very fine, mixed with clay-silt matrix and difficult to identify (Figure F4.11a).

Opaque iron-bearing minerals, such as hematite, goethite and pyrite, observed in sediment samples Inside GS1 (Lowe et al., 2018) are very rare in samples Outside GS1. Hematite, however, was identified as part of the matrix of one of the rock samples from Outside GS1 (Figure F4.11c). Moreover, 'iron concretion fragments' or 'iron oxide nodules' (Figure F4.11g,i,j,l) and 'gravel-sized sediment aggregates' (Figure F4.11k) documented in sediment thin sections from Inside GS1 (Lowe et al., 2018) were not recorded in the analysed sediment thin sections from Outside GS1. The sediment aggregates are composed of sand-sized materials cemented or bound together with infillings of silt and clay, where the latter was rich in iron (Lowe et al., 2018). The aggregates were interpreted as reworked fragments that may represent remnants of an older phase of sediment deposition within the shelter or external material sourced from the Bt horizon of the soil. Microscopic evidence of bioturbation in the form of root cross sections and infilled burrows were recorded in sediment thin sections of both collections (Figure F4.11d,h). Finally, no evidence of allochthonous sediment material was found either macroscopically or at the microscopic scale Outside GS1 or Inside GS1.

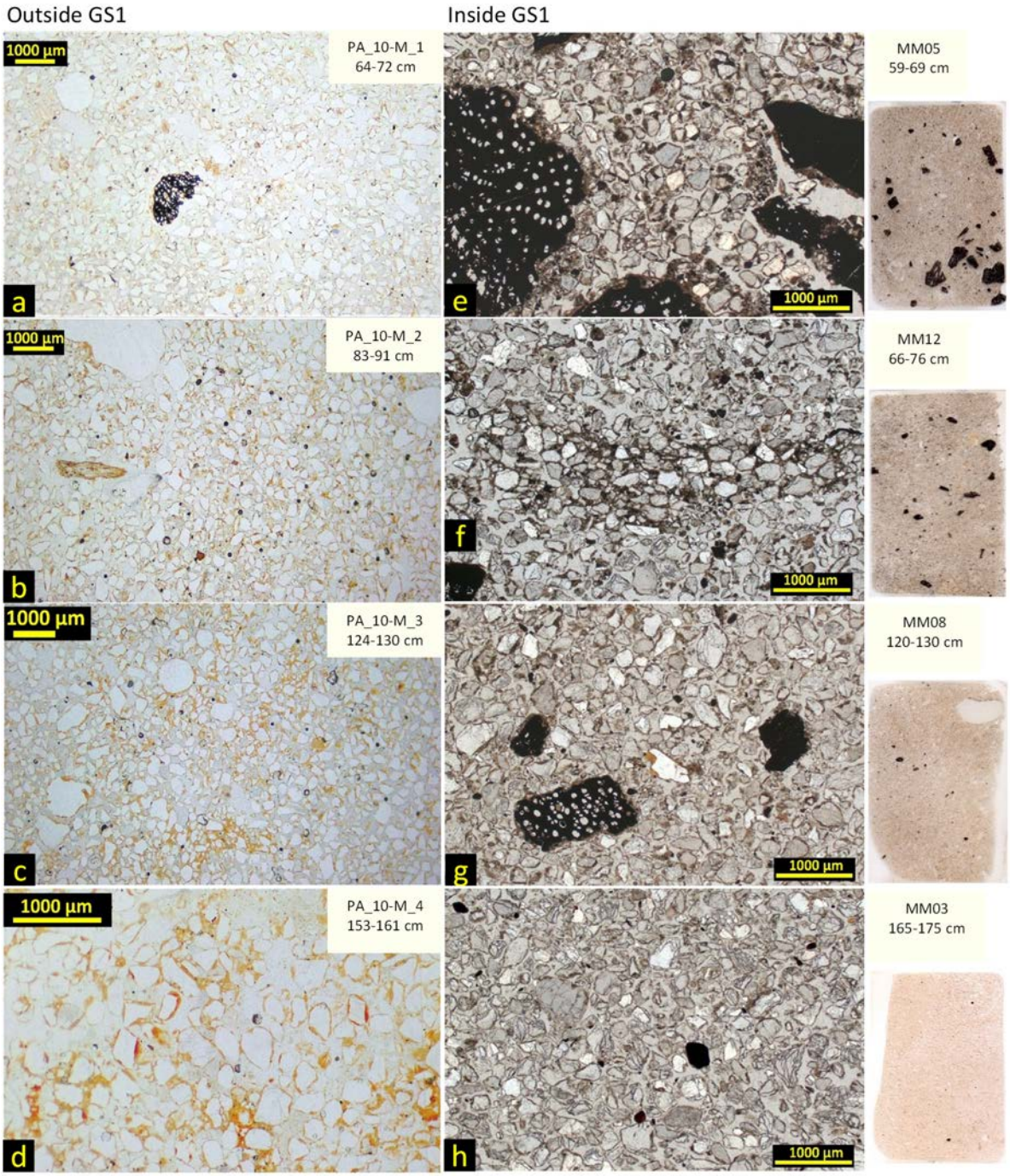

Figure F4.10: A view under the microscope. The comparison of sedimentological microscopic structure of samples from similar depths in Outside GS1 (left side) and Inside GS1 (middle and right side) sediments. All samples from Inside GS1 belong to culturally influenced layers. The mineral composition and sediment structure are very similar in both collections but note the significantly higher content of charcoal and opaque grains Inside GS1. The charcoal is shown as coarser, dark brown to black, porous particles with irregular, obfuscated margins in images a, e, f and g. Three opaque grains shown in image h are iron oxides, not charcoal. Images of the thin sections on the utmost right side are to show the coarse charcoal content Inside GS1 and its gradual diminishment with depth. Scale bar is 1000 µm.

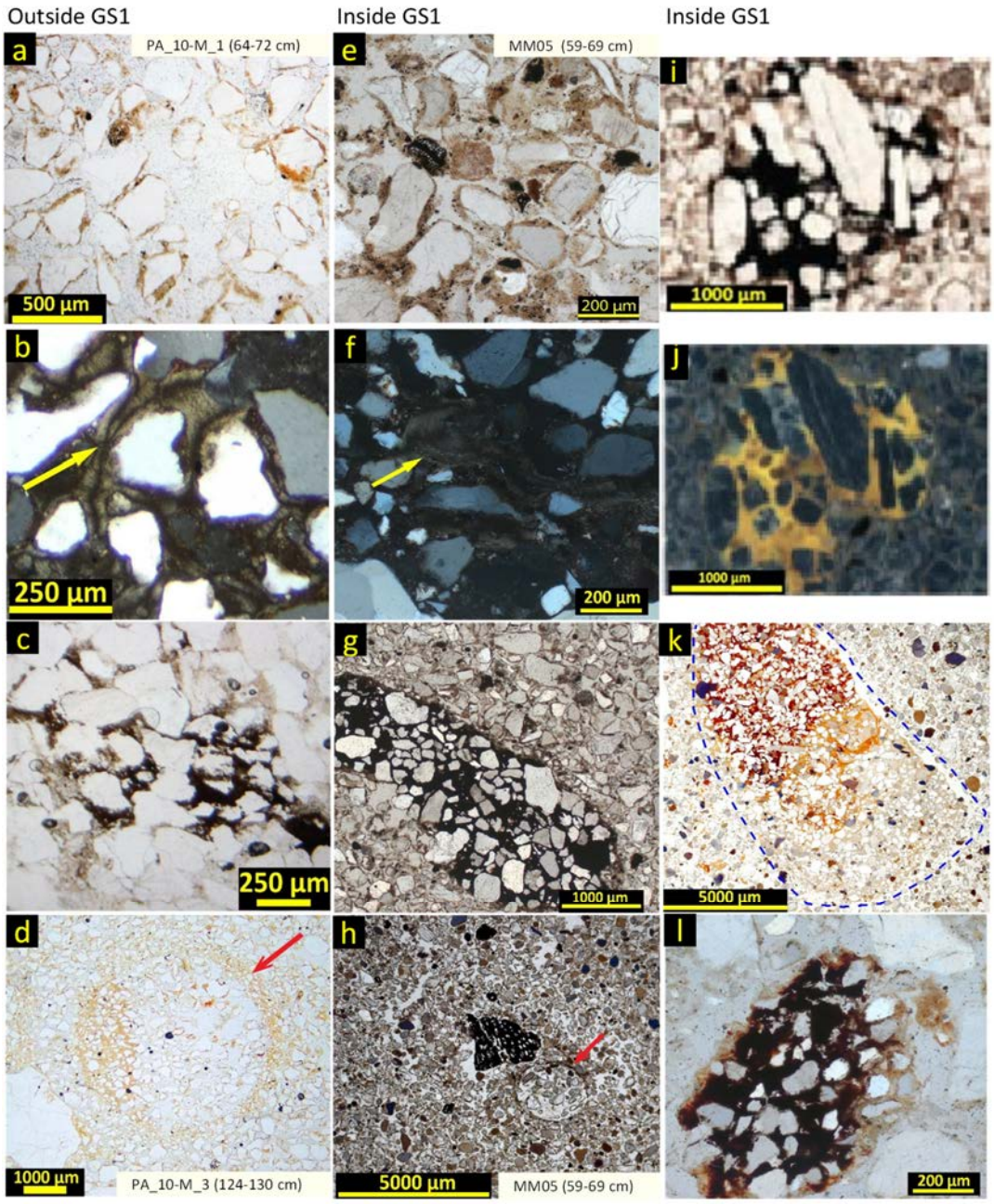

Figure F4.11: The comparison of microscopic characteristics between Outside GS1 (left column) and Inside GS1 collections (middle and right column). **a, e)** rare, very fine charcoal particles mixed with clay−silt matrix and difficult to identify in the sample Outside GS1 *vs.* more abundant and coarser charcoal particles from similar depth in the sample Inside GS1; **i, j)** iron concretion fragment with quartz grain inclusions from Inside GS1 (from Lowe et al., 2018, p. 290); **b, f)** yellow arrows point to authigenic clays recorded in samples Outside GS1 and Inside GS1; **c)** iron oxide (hematite) matrix in a bedrock sample from Outside GS1; **g)** iron concretion fragment Inside GS1 (Wallis doc.); **k)** blue dashed line shows the gravel-size sediment aggregate Inside GS1 (Wallis doc.); **d, h)** red arrows pointing to the rims of infilled burrows, signs of bioturbation in samples Outside GS1 and Inside GS1; **l)** iron oxide nodule Inside GS1 (Wallis doc.)

4.3.4 Magnetic susceptibility evidence

In this study, measurements of frequency-dependent susceptibility involved making two readings in magnetic fields at two different frequencies: low χ_{LF} and high χ_{HF}, 0.46 and 4.6 kHz, respectively. The two frequency measurements are used to detect the presence of ultrafine (<0.03 µm), superparamagnetic ferrimagnetic SP grains or grains near the SP-SD (single-domain) (~0.03 µm) boundary, occurring as crystals produced largely by biochemical processes in sediments or soils, such as by fire or weathering. Samples where SP minerals are present will show slightly lower values when measured at high frequency χ_{HF} (Dearing, 1994).

The magnetic susceptibility results are presented in Table T4.2 and Figure F4.12. The low frequency χ_{LF} magnetic susceptibility values were generally higher in the sediment samples from Inside GS1 compared to those from Outside GS1, apart for two samples (no. 53, 54) that belong to the deepest, basal, culturally sterile units Inside GS1 (Lowe et al., 2016) (Figure F4.12a). This means that the magnetic susceptibility signal in the archaeological sediment sequence Inside GS1 is overall stronger compared to the natural signal measured in non-archaeological open-site sediments Outside GS1.

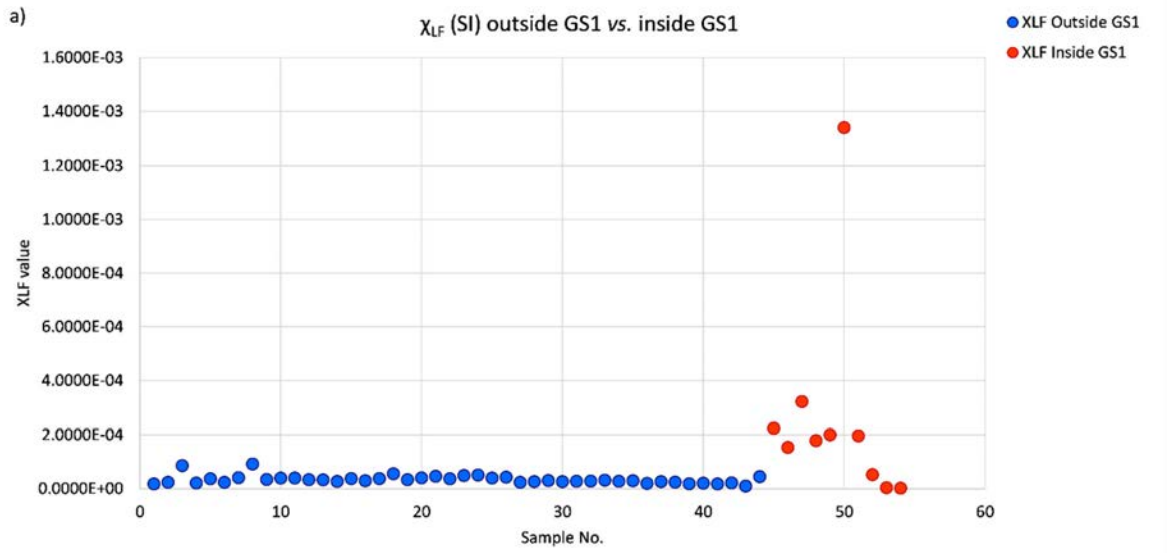

Figure F4.12a): Magnetic susceptibility values χ_{LF} measured in Outside GS1 (blue) and Inside GS1 (red) sediment samples. Note the enhanced magnetic signal in the archaeological sequence Inside GS1 compared to the culturally sterile layers Inside GS1 (sample no. 53, 54) and to the natural signal Outside GS1.

Table T4.2 Magnetic Susceptibilty analysis results

Sample ID	Sample No.	Location (Dataset)	Depth (cm)	χ_{LF}	χ_{HF}	χ_{FD} (χ_{LF} - χ_{HF})	χ_{FD} %
PA_1-M	1	Outside GS1	10	1.85398E-05	1.74905E-05	1.04929E-06	5.65
PA_2-M	2	Outside GS1	25	2.44881E-05	2.21526E-05	2.33546E-06	9.49
PA_3-M	3	Outside GS1	50-60	8.63234E-05	7.74283E-05	8.89511E-06	10.30
PA_4-M	4	Outside GS1	30-37	2.21922E-05	1.91694E-05	3.02284E-06	13.54
PA_5-M	5	Outside GS1	15	3.7662E-05	3.37017E-05	3.96029E-06	10.52
PA_6-M	6	Outside GS1	50-60	2.45176E-05	2.24687E-05	2.04895E-06	8.35
PA_7-M	7	Outside GS1	55-65	4.15626E-05	3.60573E-05	5.50533E-06	13.25
PA_8-M	8	Outside GS1	122-140	9.26167E-05	8.92847E-05	3.33197E-06	3.60
PA_9-M	9	Outside GS1	150-160	3.53781E-05	3.2403E-05	2.97509E-06	8.40
PA_10-M 42	10	Outside GS1	42-43	4.02677E-05	3.63784E-05	3.88929E-06	9.64
PA_10-M 50	11	Outside GS1	50-52	4.0678E-05	3.54698E-05	5.20813E-06	12.80
PA_10-M 60+-5	12	Outside GS1	60-65	3.47492E-05	3.10584E-05	3.69074E-06	10.62
PA_10-M 65	13	Outside GS1	65-67	3.37256E-05	2.94801E-05	4.24555E-06	12.55
PA_10-M 80	14	Outside GS1	80-82	2.78075E-05	2.48048E-05	3.00273E-06	10.80
PA_10-M 100-105	15	Outside GS1	100-105	3.83036E-05	3.30772E-05	5.22635E-06	13.64
PA_10-M 102	16	Outside GS1	100-102	3.06318E-05	2.77535E-05	2.87833E-06	9.39
PA_10-M 120	17	Outside GS1	120-122	3.86686E-05	3.36772E-05	4.99136E-06	12.91
PA_10-M 150	18	Outside GS1	150-152	5.58638E-05	4.89466E-05	6.91716E-06	12.38
PA_10-M 168-172	19	Outside GS1	168-172	3.43653E-05	2.88053E-05	5.55999E-06	16.15
PA_11-M 60+-5	20	Outside GS1	60 ±5	4.09406E-05	3.53687E-05	5.57193E-06	13.61
PA_11-M 140-160	21	Outside GS1	140-160	4.7247E-05	4.17185E-05	5.52857E-06	11.70
TP01 0	22	Outside GS1	0	3.76658E-05	3.40297E-05	3.63608E-06	9.65
TP01 40	23	Outside GS1	40	4.9908E-05	4.4669E-05	5.23892E-06	10.48
TP01 60	24	Outside GS1	60	5.13487E-05	4.62298E-05	5.11891E-06	9.97
TP01 80	25	Outside GS1	80	4.01414E-05	3.57105E-05	4.4309E-06	11.04
TP01 120	26	Outside GS1	120	4.36417E-05	3.87308E-05	4.91094E-06	11.25
TP02 20	27	Outside GS1	20	2.44114E-05	2.11498E-05	3.2616E-06	13.33
TP02 40	28	Outside GS1	40	2.71031E-05	2.56555E-05	1.44765E-06	5.34
TP02 60	29	Outside GS1	60	3.13958E-05	2.68022E-05	4.59364E-06	14.63
TP02 100	30	Outside GS1	100	2.7438E-05	2.22111E-05	5.22698E-06	19.04
TP02 120	31	Outside GS1	120	2.8794E-05	2.51265E-05	3.6675E-06	12.71
TP03 60	32	Outside GS1	60	2.90447E-05	2.58032E-05	3.2415E-06	11.15
TP03 120	33	Outside GS1	120	3.26732E-05	2.99419E-05	2.7313E-06	8.36
TP04 20	34	Outside GS1	20	2.84276E-05	2.48305E-05	3.59712E-06	12.67
TP04 80	35	Outside GS1	80	3.04031E-05	2.82825E-05	2.12058E-06	6.95
TP05 0	36	Outside GS1	0	2.04782E-05	1.68867E-05	3.59147E-06	17.54
TP05 40	37	Outside GS1	40	2.74098E-05	2.44403E-05	2.96943E-06	10.83
TP05 60	38	Outside GS1	60	2.51252E-05	2.21784E-05	2.94681E-06	11.73
TP05 80	39	Outside GS1	80	1.91951E-05	1.55465E-05	3.64865E-06	18.83
TP05 100	40	Outside GS1	100	2.11423E-05	1.98448E-05	1.29748E-06	6.11
TP05 120	41	Outside GS1	120	1.88401E-05	1.51978E-05	3.64236E-06	19.31
C_1-CR 100	42	Outside GS1	100	2.25428E-05	2.14891E-05	1.05369E-06	4.65
C_1-CR 135	43	Outside GS1	135	1.05698E-05	8.85659E-06	1.71317E-06	15.07
C_1-CR 200	44	Outside GS1	200	4.58729E-05	4.35601E-05	2.31284E-06	5.03
C1 09	45	Inside GS1	42.4	2.24486E-04	2.01741E-04	2.27451E-05	10.13
C1 14	46	Inside GS1	66.3	1.54051E-04	1.39223E-04	1.48283E-05	9.63
C1 17B	47	Inside GS1	80.5	3.22447E-04	3.15454E-04	6.99319E-06	2.17
C1 22	48	Inside GS1	100.6	1.78876E-04	1.61032E-04	1.78442E-05	9.97
C1 26	49	Inside GS1	120.4	2.00628E-04	1.83827E-04	1.68012E-05	8.37
C1 34B	50	Inside GS1	163.4	1.34014E-03	1.33323E-03	6.91150E-06	0.52
C1 36B	51	Inside GS1	173.5	1.96419E-04	1.82608E-04	1.38104E-05	7.03
C1 42	52	Inside GS1	202.6	5.29069E-05	4.70259E-05	5.88106E-06	11.12
C1 48	53	Inside GS1	232.1	4.61707E-06	3.95577E-06	6.61305E-07	14.30
C1 52	54	Inside GS1	248.9	2.75367E-06	2.94832E-06	-1.94653E-07	-8.45

The comparison of the dual frequency values χ_{LF} and χ_{HF} showed a generally slightly lower χ_{HF} values for samples Outside GS1 and Inside GS1 (Table T4.2). This confirmed the presence of SP grains in the samples. The slight drop is caused by the presence of SP grains that at high frequency have relaxation times shorter than the measurement time, are blocked magnetically, and do not contribute to the measured signal (Dearing et al., 1996, Sangode et al., 2010).

The calculated frequency dependent susceptibility χ_{FD} values, expressed as $\chi_{LF} - \chi_{HF}$, in general confirmed a higher amount of SP grains in samples from Inside GS1 compared to the samples from Outside GS1, apart for (as stated previously) the two samples, no. 53 and 54, from the deepest, culturally sterile units inside GS1 (Figure F4.12b,c). As shown in Figures F4.1b,c, after the χ_{FD} calculation (subtraction of χ_{HF}) the magnetic susceptibility signal Inside GS1 lowers in value to a range much closer to the natural signal. This suggests that the contribution of SP grains is in large part responsible for the enhancement of the magnetic susceptibility signal in culturally impacted sediment units Inside GS1.

Additionally, a bivariate plot of χ_{LF} to frequency dependent susceptibility χ_{FD} ($\chi_{LF} - \chi_{HF}$) is provided for Outside GS1 and Inside GS1 samples (Figure F4.12d,e). This correlation is a good estimate of the SP grain concentration in samples. The more linear the correlation, the higher the contribution of SP grains (Dearing et al., 1997, Eyre, 1997, Jordanova et al., 2001). In general, the χ_{LF} shows a positive linear relationship with the frequency dependent susceptibility χ_{FD} ($\chi_{LF} - \chi_{HF}$) in both sediment collections. Inside GS1 values, however, exhibit a strong positive linear correlation (R^2=0.94) (Figure F4.12e) compared to the moderate positive linear correlation (R^2=0.69) in Outside GS1 values (Figure F4.12d), indicating a great contribution of SP grains to the susceptibility signal in the Inside GS1 archaeological sediment sequence (Dearing et al., 1997, Jordanova et al., 2001). The weaker correlation in sediments Outside GS1 suggests other grain sizes besides SP grains and/or other materials, such as the paramagnetic minerals pyroxene and biotite, may also contribute to the magnetic susceptibility of the sediments.

The magnetic susceptibility results obtained in this study are generally in agreement with the findings from previous studies that investigated the magnetic properties in sediments at the GS1 site, i.e. Lowe et al. (2016, 2018) and Lowe and Wallis (2020). They also showed that the samples in the basal, culturally sterile layers inside the GS1 are very weakly magnetic with susceptibilities similar to those in sediments located outside GS1, beyond the dripline (Lowe et al., 2016). The χ_{FD}% measurements in these lower basal units averaged ~16%, a high value attributed to measurement error due to very low magnetic susceptibility signals in these layers. Whereas, sediment samples from anthropogenically impacted layers from depths ≤220 cm inside GS1, similarly to this study, showed significantly higher susceptibility values (Lowe et al., 2016) and at the same time a positive relationship with the occurrence of artefacts, wood charcoal and other indicators of occupation. Overall, the highest magnetic susceptibility values were measured in the upper part of the Inside GS1 sequence where also more charcoal and organics were present.

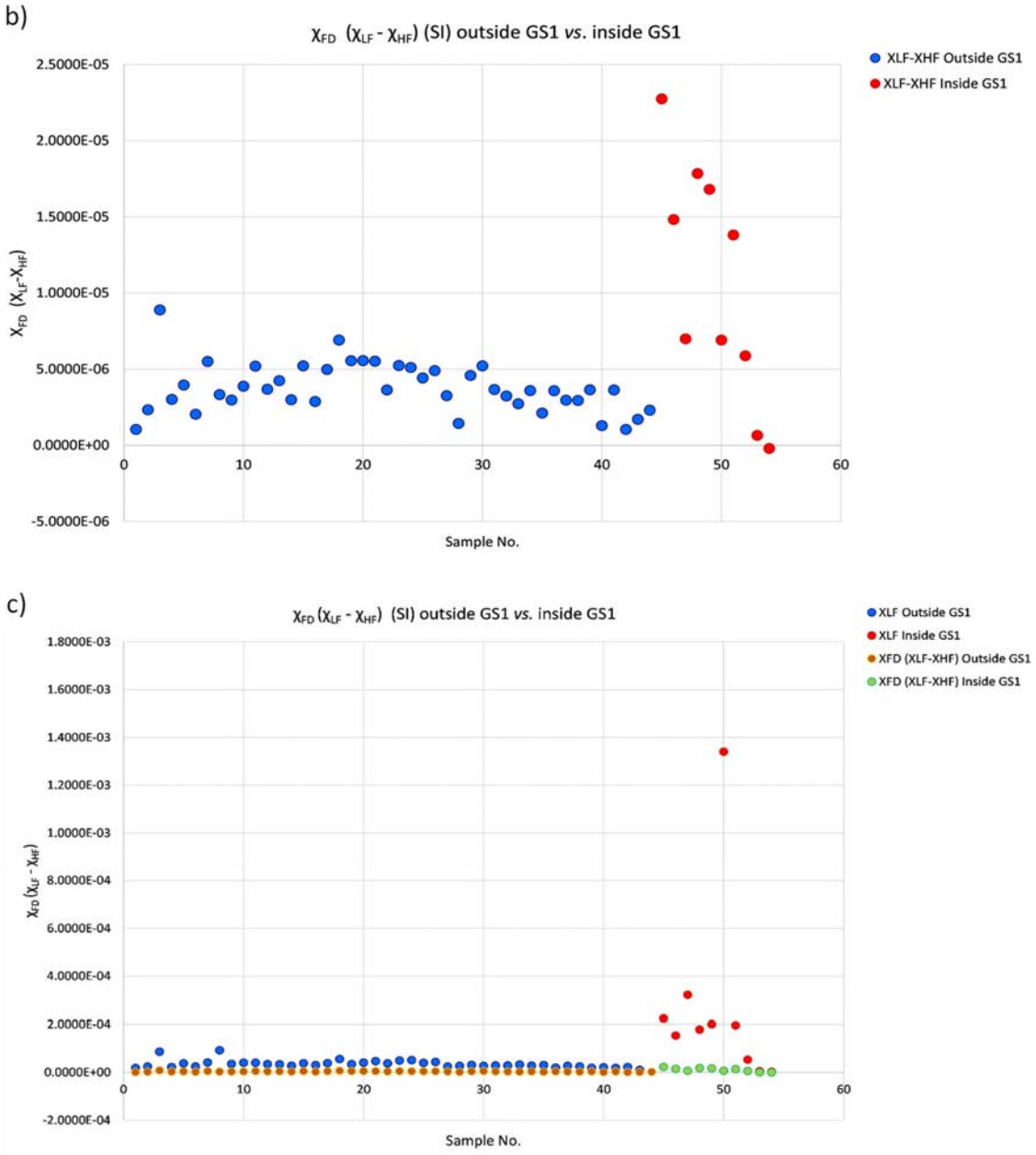

Figure F4.12b), c): The presence and contribution of SP grains to the magnetic susceptibility signal Outside GS1 and Inside GS1. **b)** graph shows a significant drop in magnetic signal in samples Inside GS1 (red) after χ_{FD} calculation, i.e. the removal of SP grains contribution expressed in χ_{HF} value. Although the magnetic signal from culturally impacted layers Inside GS1 (red) is still higher compared to the natural signal from non-archaeologic sediments Outside GS1 (blue), it is considerably lower compared to graph **a)**. The significant drop in magnetic susceptibility signal Inside GS1 after χ_{FD} calculation to values similar to Outside GS1 values is shown in graph **c)**. The Inside GS1 values are shown in red and green circles, where red are the measured χ_{LF} values and green are the calculated χ_{FD} values. The Outside GS1 shown in blue are the measured χ_{LF} values and orange are the calculated χ_{FD} values. The drop in magnetic susceptibility signal Outside GS1 is less meaningful compared to the Inside GS1 samples. However, even a slight drop shows that the natural signal in Outside GS1 sediments is also influenced by the presence of SP grains.

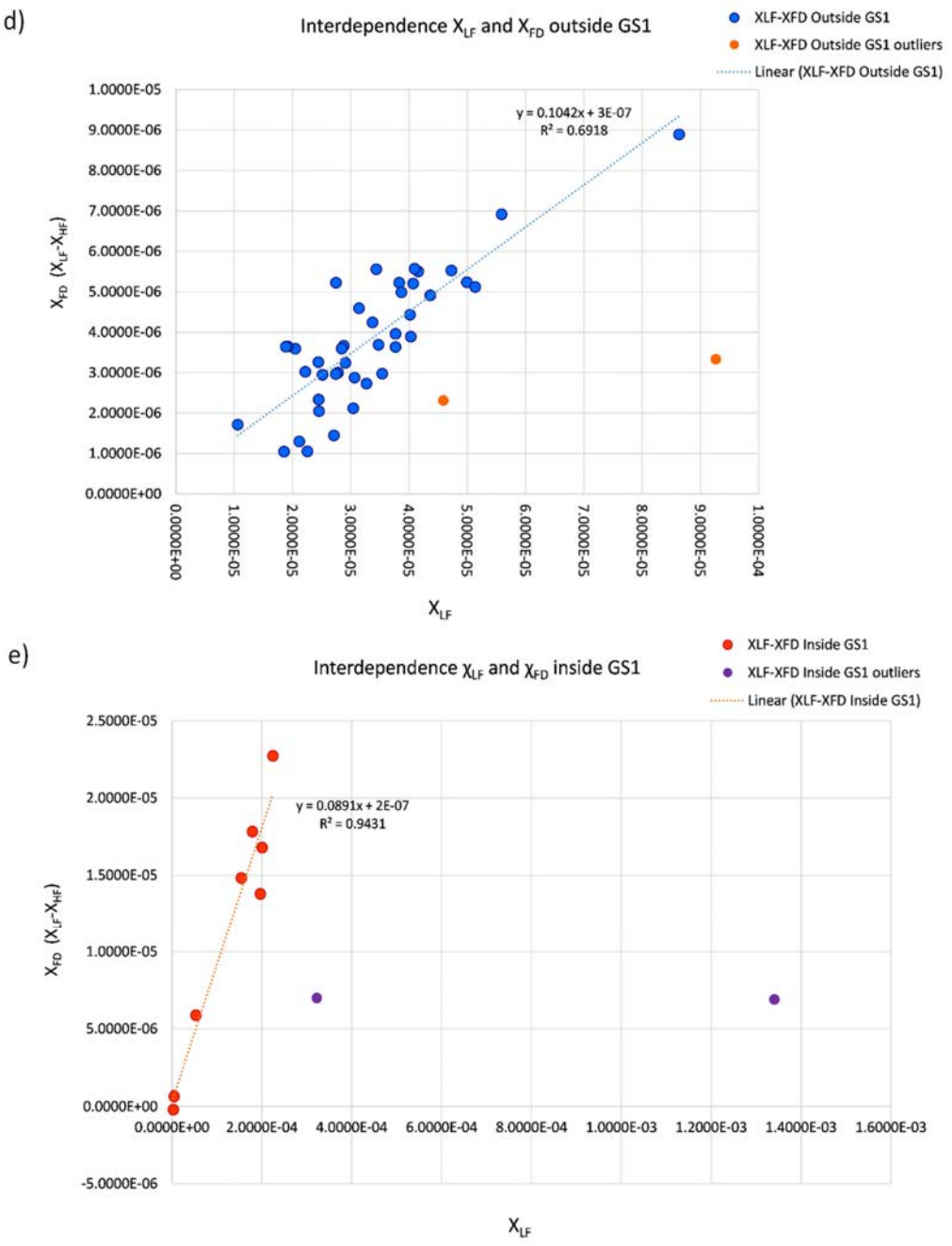

Figure F4.12d), e): Two bivariate plots of χ_{LF} to frequency dependent susceptibility χ_{FD} ($\chi_{LF} - \chi_{HF}$), Outside GS1 and Inside GS1. **e)** Strong positive linear correlation Inside GS1 indicates the major contribution of SP grains to the magnetic susceptibility signal; **d)** Moderate correlation value Outside GS1 suggests the magnetic susceptibility signal (χ_{LF}) is influenced by other grain sizes, apart from SP grains, or/and materials such as paramagnetic minerals pyroxene or biotite. Outliers marked in orange colour in **d)** and purple in **e)** graph mark the values that were excluded from the calculation to avoid misleading and overdispersion.

The magnetic susceptibility measurements of the sediment samples from Outside GS1, according to Lowe et al. (2016), showed a very low enhancement of magnetic susceptibility due to the presence of SP grains, which is also in agreement with the findings in this study (Figure F4.12c). However, contrary to this study, the χ_{FD}% from sediment samples outside GS1 in Lowe et al. (2016) showed a range of only 3–6%. Based on their results, almost all samples inside GS1 had a higher χ_{FD}% (9–12%), indicating they contain a greater percentage of SP grains. The latter was confirmed in this study by χ_{FD} ($\chi_{LF} - \chi_{HF}$) values but not by χ_{FD}% values (Table T4.2, Figure F4.12c). The reason for this might be the overall very low magnetic susceptibility signal at the limit of detection along with the different number of analysed samples Outside GS1 (44 samples) and Inside GS1 (10 samples) in this study compared to Lowe et al. (2016) study (outside ~20 samples; inside ~120 samples).

4.3.5 Chronological evidence

The chronology results of the two sequences−Outside GS1 and Inside GS1, that were constructed in previous independent studies are compared here. Single-grain OSL on quartz grains and ^{14}C on macro-charcoal, both from pit PA_10-M, were used to establish the chronology for the Outside GS1 sequence (Chapter 2 of this thesis). Macro-charcoal collected in squares C0 and C1 was used to build the ^{14}C chronology for the archaeological sequence inside GS1 (Wallis et al., 2009, 2014a). The samples IDs, depths and age results used for comparison and correlation are given in Table T4.3.

The deepest and oldest measurement of non-archaeologic sediment deposit outside GS1 was from pit PA_10-M at depth ~172 cm (Table T4.3, Figure F4.13) dates to approximately 15 ka, indicating the last accumulation cycle outside GS1 began about that time. However, the presence of quartz grains older than 50 ka in the Outside GS1 profile (Table T4.3) suggests that old grains from a previous deposit were reworked into the younger deposit without being exposed to sunlight during the process. This indicates that the dynamics of the sedimentary processes in the study area are much older than 15 ka.

The deepest and oldest measurement from the archaeological sequence inside GS1 was obtained from square C1 at a depth of ~205 cm and showed an age of ~38 ka (Table T4.3, Figure F4.13). At about this depth, signs of human occupation in the GS1 interior appear in the form of stone artefacts. The result indicates that the sediment has been accumulating inside the GS1 rockshelter without noticeable disruption for more than 38 ka (the entire sequence is ~250 cm deep), which is in good agreement with the presence of older quartz grains (>50 ka) found in sediment samples beyond the dripline, outside GS1.

These findings suggest that the sediment in the study area began to form most recently more than 50 ka ago.

Table T4.3 Chronology results used for comparison of Outside GS1 and Inside GS1 sequences

Sample ID	Depth (cm)	Location (Dataset)	Dating method	**Age used for comparison**	OSL age result from other grain population
PA_10-M 42	42-43	Outside GS1	OSL	**1200 ± 200**	
"	"	"	OSL		8700 ± 1300
"	"	"	OSL		55900 ± 8600
"	"	"	^{14}C (macro-charcoal)	**2247 ± 90 cal BP**	
PA_10-M 50	50-52	Outside GS1	OSL	**2000 ± 200**	
PA_10-M 65.7	65-67	Outside GS1	OSL	**2600 ± 200**	
"	"	"	^{14}C (macro-charcoal)	**3591 ± 99 cal BP**	
PA_10-M 71	70-71	Outside GS1	^{14}C (macro-charcoal)	**4064 ± 81 cal BP**	
PA_10-M 80	80-82	Outside GS1	OSL	**3900 ± 300**	
"	"	"			19400 ± 2100
"	"	"	^{14}C (macro-charcoal)	**3807 ± 85 cal BP**	
PA_10-M 102	100-102	Outside GS1	OSL	**7300 ± 500**	
PA_10-M 120	120-122	Outside GS1	OSL	**10800 ± 700**	
PA_10-M 135	135-137	Outside GS1	OSL	**13200 ± 900**	
PA_10-M 150	150-152	Outside GS1	OSL	**12700 ± 1500**	
PA_10-M 160	160-162	Outside GS1	OSL	**11500 ± 1200**	
"	"	"	OSL		34500 ± 4600
"	"	"	OSL		2400 ± 400
PA_10-M 172	168-172	Outside GS1	OSL	**14600 ± 1500**	
"	"	"	OSL		3800 ± 500
"	"	"	OSL		50900 ± 6400
C0-03	10	Inside GS1	^{14}C (macro-charcoal)	**603 ± 62 cal BP**	
C0-05	25	Inside GS1	^{14}C "	**1432 ± 87 cal BP**	
C0-06	27	Inside GS1	^{14}C "	**1469 ± 70 cal BP**	
C0-08	42	Inside GS1	^{14}C "	**3324 ± 115 cal BP**	
C0-09	47	Inside GS1	^{14}C "	**3804 ± 153 cal BP**	
C0-12	61	Inside GS1	^{14}C "	**4116 ± 131 cal BP**	
C0-16	80	Inside GS1	^{14}C "	**3878 ± 181 cal BP**	
C0-20	103	Inside GS1	^{14}C "	**9572 ± 90 cal BP**	
C0-25	125	Inside GS1	^{14}C "	**10478 ± 182 cal BP**	
C0-26	139	Inside GS1	^{14}C "	**15832 ± 233 cal BP**	
C1-30	145	Inside GS1	^{14}C "	**12221 ± 248 cal BP**	
C1-wall	170	Inside GS1	^{14}C "	**18363 ± 264 cal BP**	
C1-41	198	Inside GS1	^{14}C "	**38470 ± 1005 cal BP**	
C1-43	205	Inside GS1	^{14}C "	**37300 ± 964 cal BP**	

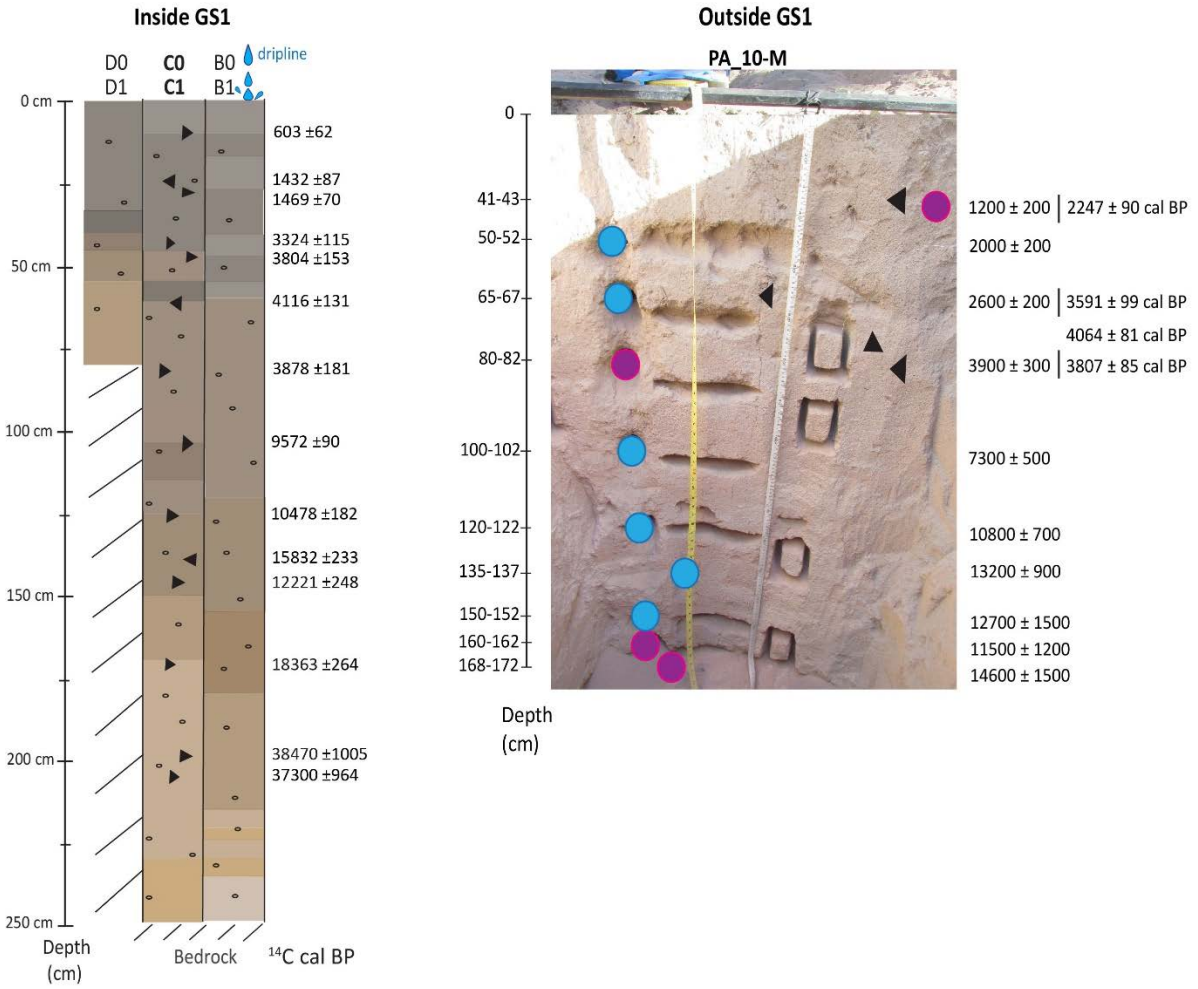

Figure F4.13: The constructed chronologies for the study area are in agreement between the Inside GS1 and Outside GS1 sequences. **Left:** archaeological chronological sequence Inside GS1 constructed using ^{14}C dating on macro-charcoal, represented as black triangles. **Right**: Outside GS1 chronology using single-grain OSL (blue and purple circles) and ^{14}C dating on macro-charcoal (black triangles). Blue circles represent samples where a single population of OSL results was identified, purple circles represent samples where multiple age populations of quartz grains were present (Table T4.3). Detailed chronological analysis of sediments outside GS1 is provided in Chapter 2 of this thesis.

A good correlation between the two chronologies, Outside GS1 and Inside GS1, was confirmed by the constructed age-depth models for each sequence (Figure F4.14). This outcome indicates that the approach used in this study can provide reliable chronologies in settings with complex depositional histories and reveal pivotal information about site formation dynamics.

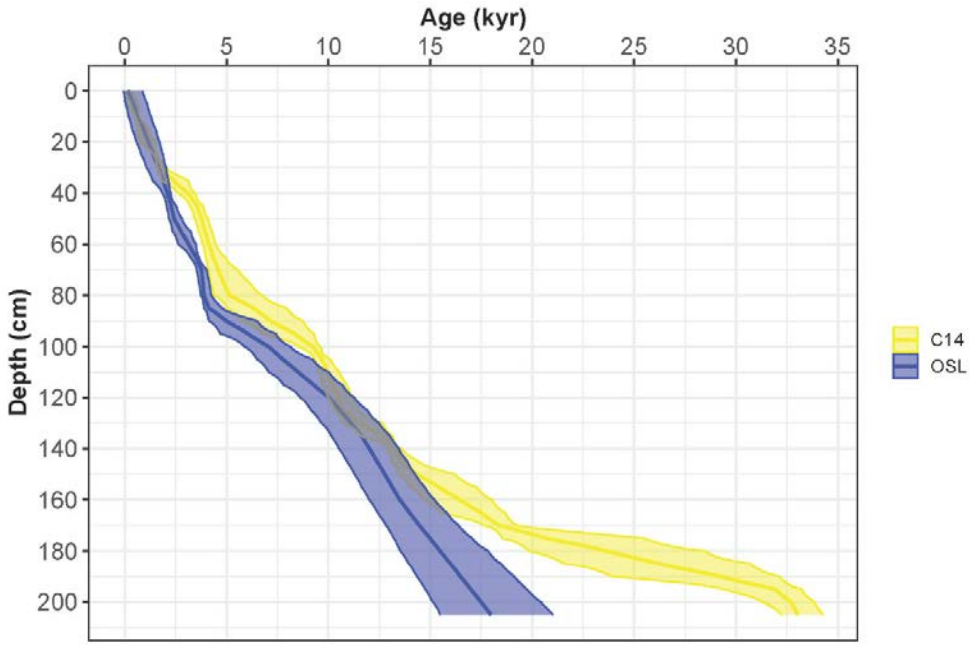

Figure F4.14: Age-depth model of the two chronologic sequences, Outside GS1 and Inside GS1, constructed using Bayesian age modelling with rbacon package in R. The blue band represents the Outside GS1 chronology based on single-grain OSL and ^{14}C macro-charcoal ages, the yellow band displays the Inside GS1 chronology based on ^{14}C macro-charcoal ages using data from Wallis et al. (2009, 2014a).

4.3.6 Vegetation evidence

A comprehensive reconstruction of past vegetation in the study area was conducted using phytoliths and $\delta^{13}C$ isotope signature on SPAC (Stable Polycyclic Aromatic Carbon, a highly resistant form of micro charcoal) from sediment collections from Outside GS1 and Inside GS1 (Figures F4.4, F4.5). The second proxy, $\delta^{13}C_{SPAC}$ isotope signature, was used for the purpose of comparison with phytolith result, given the complicated, post-depositionally disturbed terrestrial sedimentary context of the study area. Phytoliths and SPAC were chosen because they are durable and able to be preserved in unfavourable semi-arid environments for millennia, in comparison to other more conventional approaches (Ascough et al., 2020, Bird and Ascough, 2012, Bird et al., 2015, Calegari et al., 2017, Hart, 2016, Rashid et al., 2019, Strömberg et al., 2018, Wurster et al., 2015, Zurro et al., 2016). Two phytolith indices, D/P (tree/grass) and FI-t (forest indicators-time), were calculated to inform about the tree vs. grass ratio as well as the change in tree cover over time. The applied approach, results and implications are presented and discussed in detail in Chapter 3 of this thesis. To avoid repetition, only a brief summary of the vegetation

reconstruction is provided here, necessary for a coherent continuation of this 'outside – inside comparison' chapter.

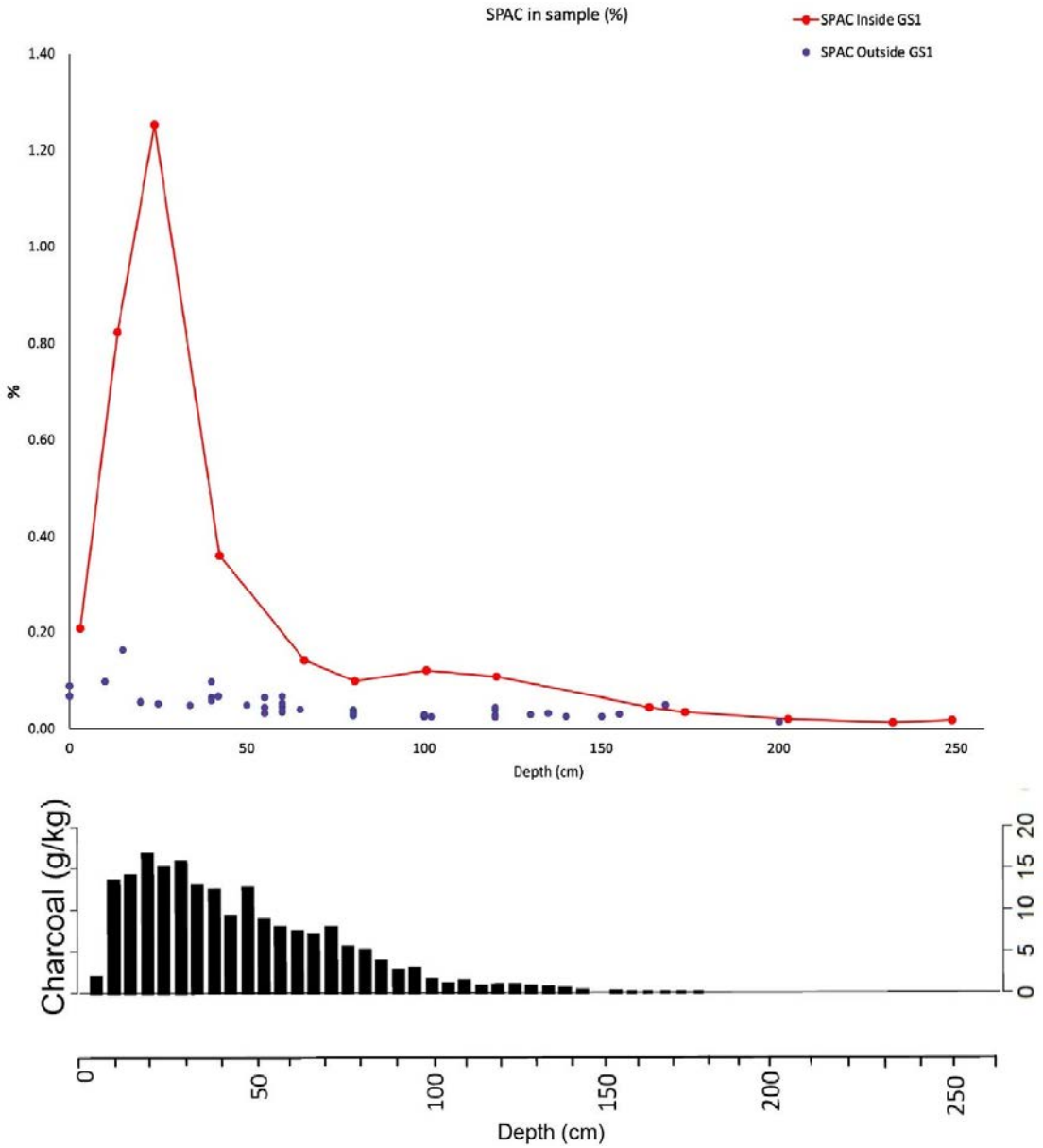

Figure F4.16: Higher SPAC (%) content in some sediment samples from Inside GS1 shown as red line on the upper graph. It aligns with the charcoal amounts obtained from the inside GS1 deposit, as shown on the lower graph from Lowe et al. (2016, 2018).

During the vegetation reconstruction analysis a significantly higher SPAC content was detected in some sediment samples from Inside GS1 in comparison to the SPAC content recorded in the Outside GS1 sediments (Figure F4.16). The occurrence was attributed to the presence of hearths in samples from inside GS1, which was additionally supported by the evidence of wood charcoal data from the GS1 rockshelter interior reported in previous studies (Lowe et al., 2016, 2018).

In summary, our vegetation reconstruction confirmed the effectiveness of using phytoliths and $\delta^{13}C_{SPAC}$ isotope signature to investigate past changes in plant structure in environments where no pollen is preserved, such as semi-arid Australian savannah. The phytolith and $\delta^{13}C_{SPAC}$ results from the Outside GS1 demonstrated the presence of savannah vegetation throughout the Holocene (Figure F4.17a,b,c). The calculated phytolith indices and $\delta^{13}C_{SPAC}$ results indicate denser tree cover during the early and mid-Holocene, between 4000 and 10,000 years ago, followed by a gradual transition to a more open savannah woodland in the last 2000 years (Figure F4.17a,c).

The evidence from Inside GS1, however, showed a generally higher forest indicators signal and lower grass signal compared to Outside GS1, implying a stronger prevalence of arboreal vegetation contributing to the record Inside GS1. This was recorded in both phytolith and in $\delta^{13}C_{SPAC}$ analysis (Figure F4.17b,c). The phytolith evidence showed with reasonable confidence that the phytolith signal Inside GS1 has been influenced by animal activity (macropod faeces) and human activity concentrated inside the GS1 rockshelter, such as accumulating plants for various purposes. Finally, the comparative analysis of sedimentary records from Outside GS1 and Inside GS1 showed that a solid vegetation reconstruction for a rockshelter site should include both−the rockshelter interior and its surroundings.

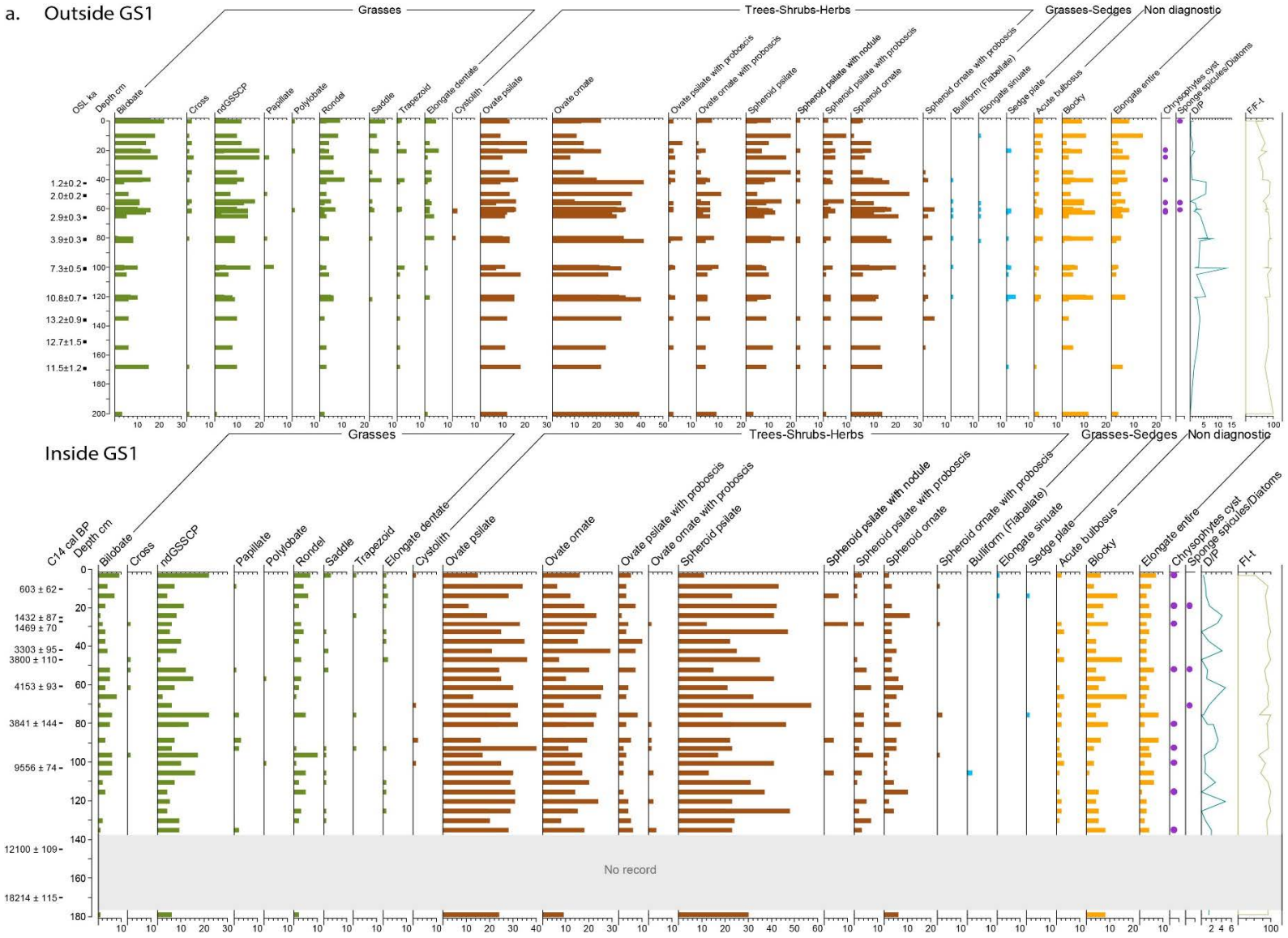
a. Outside GS1
Grasses
Trees-Shrubs-Herbs
Grasses-Sedges
Non diagnostic
OSL ka
Depth cm
Bilobate
Cross
rdGSSCP
Papillate
Polylobate
Rondel
Saddle
Trapezoid
Elongate dentate
Cystolith
Ovate psilate
Ovate ornate
Ovate psilate with proboscis
Ovate ornate with proboscis
Spheroid psilate
Spheroid psilate with nodule
Spheroid psilate with proboscis
Spheroid ornate
Spheroid ornate with proboscis
Bulliform (Fiabellate)
Elongate sinuate
Sedge plate
Acute bulbosus
Blocky
Elongate entire
Chrysophytes cyst
Sponge spicules/Diatoms
D/P
FF-I
1.2±0.2
2.0±0.2
2.9±0.3
3.9±0.3
7.3±0.5
10.8±0.7
13.2±0.9
12.7±1.5
11.5±1.2
Inside GS1
Grasses
Trees-Shrubs-Herbs
Grasses-Sedges
Non diagnostic
C14 cal BP
Depth cm
Bilobate
Cross
rdGSSCP
Papillate
Polylobate
Rondel
Saddle
Trapezoid
Elongate dentate
Cystolith
Ovate psilate
Ovate ornate
Ovate psilate with proboscis
Ovate ornate with proboscis
Spheroid psilate
Spheroid psilate with nodule
Spheroid psilate with proboscis
Spheroid ornate
Spheroid ornate with proboscis
Bulliform (Fiabellate)
Elongate sinuate
Sedge plate
Acute bulbosus
Blocky
Elongate entire
Chrysophytes cyst
Sponge spicules/Diatoms
D/P
FI-I
603 ± 62
1432 ± 87
1469 ± 70
3303 ± 95
3800 ± 110
4153 ± 93
3841 ± 144
9556 ± 74
12100 ± 109
18214 ± 115
No record

Figure F4.17a: Phytolith analysis results from Outside GS1 (upper graph) and Inside GS1 (bottom graph) show the presence of savannah type of vegetation from the Pleistocene−Holocene transition and throughout the Holocene. The time frame is given on the left side of the graphs. Green colour represents the grass phytolith morphotypes, brown the forest indicator morphotypes, blue sedge phytolith morphotypes and yellow morphotypes that are not diagnostic of any group of plants. The calculated phytolith indices (D/P and FI-t) are shown on the right side of both graphs. The 'No record' zone marks the depth gap with no representative phytolith record.

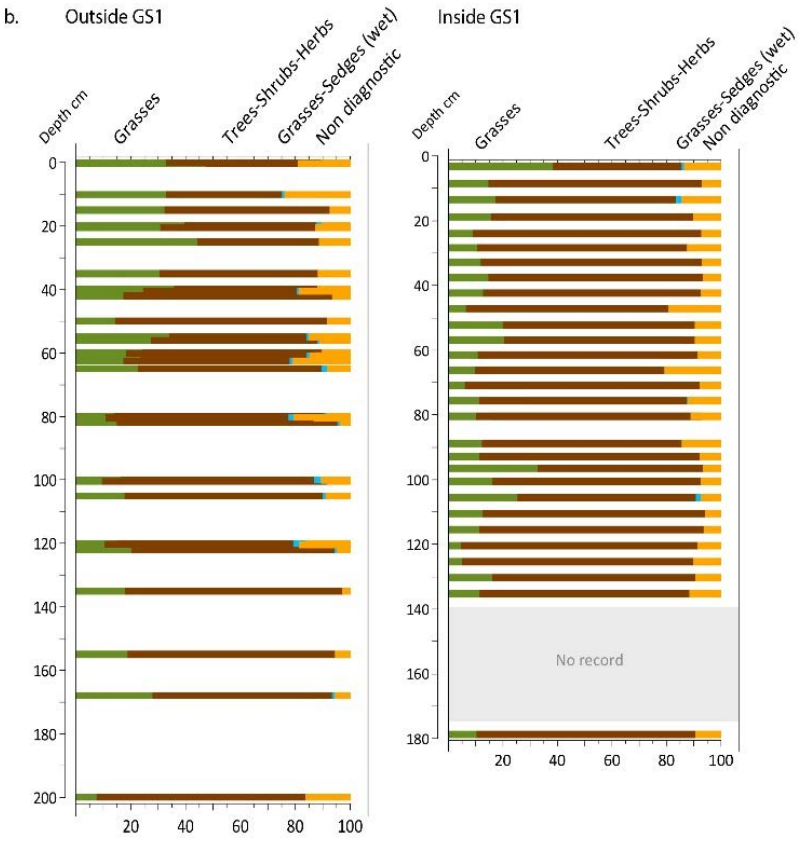

Figure F4.17b.: Percentage phytolith diagrams Outside GS1 (left) and Inside GS1 (right) show a generally higher percentage of forest indicator morphotypes (brown) and lower percentage of grass morphotypes (green) in the Inside GS1 collection compared to the Outside GS1 phytolith collection signal. The 'No record' zone marks the depth gap with no representative phytolith record.

c.

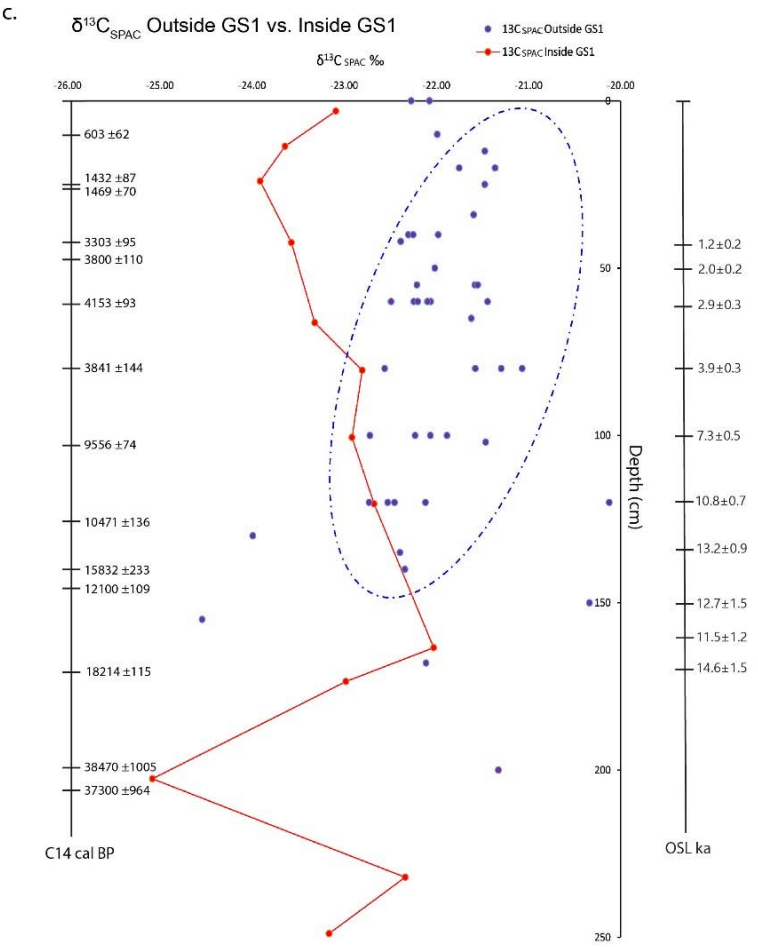

Figure F4.17c.: $\delta^{13}C_{SPAC}$ results in ‰ from Outside GS1 (blue dots) and Inside GS1 (red line). The ages for the Outside GS1 collection are given on the right side (OSL ka) and for the Inside GS1 on the left (^{14}C cal BP) The dashed line marks the cluster of higher $\delta^{13}C_{SPAC}$ values recorded in samples Outside GS1 outstretching towards the grass signal, compared to the values recorded in samples Inside GS1. Both collections exhibit unreliable result patterns below depth 120 cm. This graph also shows that the vegetation signal from the archaeological anthropogenically impacted Inside GS1 (red) sediments differs from the non-archaeologic 'natural environmental' vegetation signal reflected in the Outside GS1 sediment record (blue dots). Although both archives comply with a mixture of forest and grass vegetation, thus a savannah environment, the Outside GS1 δ^{13}C signal inclines towards higher values (-20–-22 ‰) indicating a higher presence of grasses, particularly in mid- to late Holocene. The Inside GS1 signal is overall lower than -22.5 ‰ suggesting a woodier vegetation. Furthermore, the inclination of the Outside GS1 signal (blue dots) towards higher values at lower depths (~20–70 cm), while being closer to the Inside GS1 signal (red line) at greater depths (~110–80 cm) indicates the presence of more woody vegetation during early to mid-Holocene. As the depth diminishes (above ~70 cm depth) a stronger signal of grass vegetation emerges, possibly indicating a shift towards a more open savannah woodland, similar to the present-day landscape. For more details refer to Chapter 3, section 3.4.3.1.

4.4 Interpreting the GS1 site: evidence and conjectures

This study investigates how evidence from the archaeological sediment deposit inside the GS1 rockshelter aligns with and complements evidence from non-archaeological sediments deposited outside the GS1, beyond the dripline in the immediate surroundings of the shelter. The aim is to evaluate whether bridging the 'outside and inside' evidence results in the production of a more reliable interpretation of formation processes and palaeoenvironmental record for the GS1 site. The geomorphic, sedimentologic, and palaeoenvironmental evidence obtained from the collections of sediment samples from Outside GS1 and Inside GS1 was evaluated and compared.

4.4.1 Site formation processes of GS1

The GS1 shelter has developed in the lithology that dominates the area, i.e. the quartzose Jurassic Hampstead sandstone, formed in a fluvial environment during the Late Jurassic, approximately 165−145 million years ago. After being submerged and covered by Cretaceous marine sediments, the sea retreated and the entire region was first subjected to a general uplift due to rifting of the Eastern Australian margin and subsequently, multiple cycles of erosion, deposition and weathering events occurred throughout the Tertiary and Quaternary times (details in section 1.1.1). Lithologically, the Hampstead sandstone is described as fine, medium and coarse quartzose sandstone, and interbedded micaceous siltstone, mudstone and very fine sandstone (Smart and Senior, 1980). The sediments resulting from its weathering can therefore present in various mineralogies and grain sizes, corresponding to single packages in the original rock. The Hampstead sandstone at the GS1 site and the surrounding area is characterized by its strong cross-bedding and a dark tone. Rugged outcrops reveal distinct structures such as honeycombs, tafoni, rockshelters, mushrooms and large vertical cracks (Figures F4.2, F4.18).

Sandstones are ubiquitous rocks on the Earth surface able to develop striking relief (Young et al., 2009). Lithological and structural diversity within sandstone packages influenced by weathering processes foster the development of a wide array of landforms, including some that hardly have parallels elsewhere, on other lithologies (Migoń, 2021). The variety of these features, such as tafoni, honeycombs, mushroom rocks, hoodoos, alcoves and rock arches, on exposed rock surfaces in sandstone areas is impressive. They have been long known and studied (Turkington and Paradise, 2005) (also section 4.1.1), resulting in the multitude of names and various classification approaches (e.g. Mikuláš, 2007, Urban and Górnik, 2017), but their understanding remains incomplete.

In the last decade, important contributions, such as Bruthans et al. (2014), Ostanin et al. (2017) and Řihošek et al. (2019), demonstrated that these shapes could have been the result of the negative feedback between stress and erosion that originates in fundamental laws of friction between the rock's constituent particles. The way this mechanism works is that denudation, abrasion and/or wind deflation remove the granular material in the regions subjected to relatively small compressive stresses inside the sandstone packages, leaving more stressed and consolidated material intact, which, after many episodes of erosion, leads to a distinctive, exotic natural geostructure.

Figure F4.18: Examples of a rock fall and a slab break (left) and a vertical, parallel crack (right) in Jurassic Hampstead sandstone outcrops in the proximity of the GS1 site.

Along with climate, the speed and effect of weathering are largely influenced by the structure and texture of sandstones (Peña-Monné et al., 2022). While quartz provides greater resistance to weathering, the composition of the matrix also plays a crucial role in determining the effectiveness of many exogenous processes that affect sandstone bodies (Migoń, 2021). However, in order to gain a deeper understanding of the origin and development of some medium- and large-scale landforms on sandstones, subsurface processes appear to be of key importance. Although subsurface processes are typically associated with carbonate and sulphate karst contexts, they have been demonstrated to create a variety of impressive landforms in sandstone regions, also known as sandstone karst (Jennings, 1983, 1988, Migoń, 2021, Wray, 1997, 2009, Young, 1986). Central to this approach is the theory of 'arenization', defined as disintegration of sandstone into sand through preferential dissolution along crystal boundaries so that the bulk of rock is less bonded and may become entirely fragmented (Martini, 1979, Mecchia et al., 2014, Piccini and

Mecchia, 2009, Sauro, 2014, Wray, 2009). This makes the remaining sand grains susceptible to physical removal. Importantly, arenization may affect both sandstones with carbonate cement as well as silica-cemented quartz sandstones (Young et al., 2009). It is however more important for the latter type of bedrock, being the key mechanism triggering disintegration, compared to other types of sandstone, of lower strength, where other processes prevail (Migoń, 2021). Wray and Sauro (2017, p. 552) acknowledged that arenization and development of subterranean landforms is not likely to apply to all sandstones, but preferably to a rock of high quartz content. They emphasized additional environmental conditions favouring the development of quartz sandstone subterranean landforms, including a high volume of rainwater, best fulfilled in humid tropical and subtropical regions, in terrains exposed on long timescales and a general stability of rock surfaces. The most evident examples of these landforms come from low latitude areas, which experience wet climate today, or at times in the Cenozoic, including wet intervals of the Quaternary, such as northern Australia, parts of the Sahara, and central and south-eastern Brazil (Migoń, 2021, Wray and Sauro, 2017).

The GS1 rockshelter developed in the sandstone outcrop by cavernous weathering as a small overhang with approximately 15 m^2 interior space and 250 cm deep sedimentary floor sequence (Figure F4.4). The subsurface depression that extends from the interior of GS1 for approximately 15 m beyond the dripline towards the south (Figures F4.7, F4.20) may have been formed by a combination of surface and subsurface weathering, particularly by the denudation of the bedrock at the scarp foot of the sandstone outcrop. Denudation is defined as rock removal by chemical dissolution (arenization and grain disintegration) and physical erosion (transport). Precipitation percolating on the outcrop scarp wall and falling from the dripline directly on the exposed bedrock surface would have ensured continued activity at the weathering front (Twidale, 2014). The immediate scarp foot zone is the site of maximum and locally deep weathering, because the accumulated moisture in scarp foot zones causes weathering followed by physical erosion and the shaping of scarp foot depressions (Twidale, 2014). We can speculate that the accumulated moisture contributed to the formation of the depression in the of interior GS1 and under the dripline (Figure F4.7). Weathering by arenization, granular disintegration and physical removal caused denudation of the surface and subsurface bedrock, where moisture content increased in the wet season by percolation, seepage and flowing water. No recorded evidence of substantial surface runoff or aeolian activity in the excavated archaeological sequence Inside GS1 suggests that the denuded material remained nearly in place, eventually leading to the accumulation of sediment in the developed depression.

The GS1 study area is characterized by sandstone outcrops, scarps, lag gravel and fallen rocks, patches of sediment accumulation and plane surfaces of smooth bedrock. On a smaller scale, these characteristics recall erosional surfaces, such as pediments, stripped bedrock surfaces and planation surfaces. The formation mechanisms of these surfaces are connected to the erosion of the constituting rock (Mabbutt, 1966, Oard, 2013, Twidale, 2014) (Figure F4.19). The weathering of the outcrop causes scarp retreat and scarp foot depression retreat. Thus, the depression in the GS1 interior diminishes as the distance from the scarp wall increases and the bedrock becomes shallower as the distance from the GS1 dripline increases (Figures F4.7, F4.20), indicative of scarp foot depression retreat. The direction and effectiveness of subsurface weathering depends on subsurface moisture seepage and therefore depends on the subsurface morphology that directs the moisture as well as the particle movement and transport. Subsurface moisture action is constant. Etching eradicates all but the most resistant irregularities to produce smooth bedrock surfaces (Twidale, 2014). This explains the smooth surfaces observed in the study area on the subsurface bedrock at the bottom of the pits as well as plane bedrock exposures on the surface (Chapter 1, section 1.3.1, Figure F1.17). Finally, typical for sandstone landscapes, there were most probably large lag gravel particles lying on the surface as well as rock slabs and occasional rock falls from the surrounding outcrops that impacted denudation and sediment accumulation in the study area in the past, causing what we today observe as an undulating subsurface.

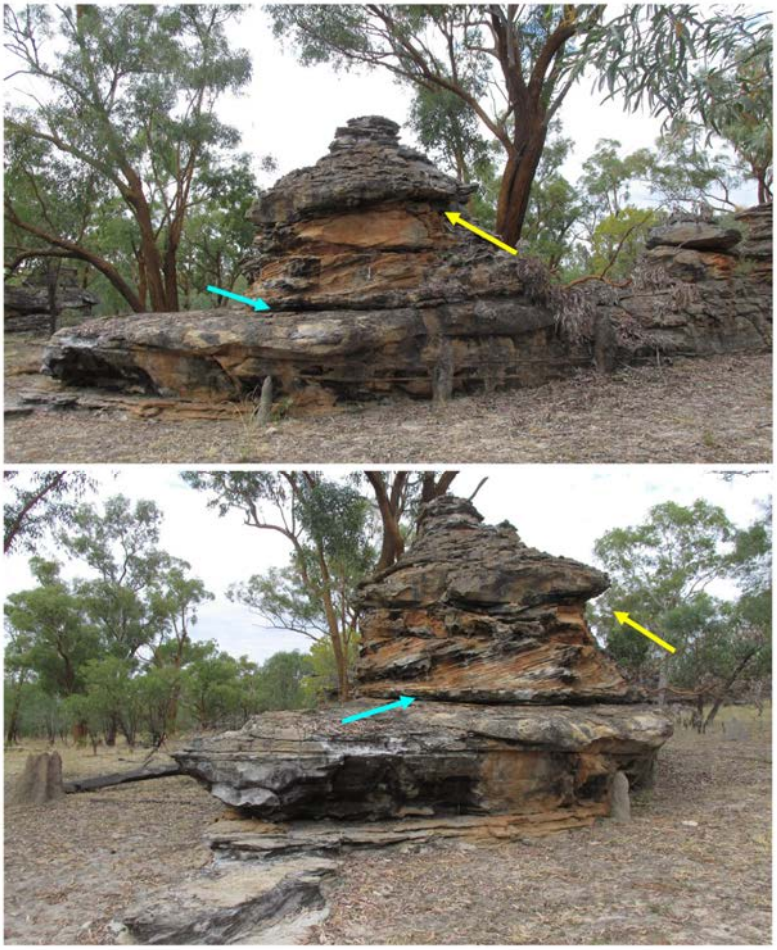

Figure F4.19: A typical Jurassic Hampstead sandstone outcrop the GS1 site. A vertical stack is positioned on a planar bedrock surface, resembling a miniature version of geomorphic forms that can occur in analogous environments on a larger scale. In such cases, a rockshelter can form in the steep wall of the stack scarp and a depression can develop at its base. This recreates a situation of ultimate stage of residual hills, i.e. residual boulders spread (Migoń et al., 2020), much like the one observed in this study. The yellow arrow indicates a capping under which weathering has formed a niche, while the turquoise arrow points to a hypothetical erosion point at the base of the scarp.

4.4.2 Palaeoenvironmental reconstruction of the GS1 area

Sediments in the GS1 study area can be divided into three groups: a) autochthonous, originating by denudation of Jurassic Hampstead sandstone that constitutes the site, b) autochthonous originating by rock fall and roof fall, and c) altered by human activity. All three categories are found within the archaeological deposit Inside GS1 in roughly similar proportions. In contrast, the non-archaeological open-site sediments outside GS1 primarily correspond to categories a) and b) since no evidence can be

confidently attributed to human activity. The absence of evidence of any allochthonous sediment material corroborates the interpretation of site formation by weathering of the constituting rock through processes of arenization, granular disintegration, physical transport and accumulation.

The darker and greyer sediment colour in the upper part of the C1 sequence Inside GS1 compared to the brownish sediment colour in PA_10-M pit profile of Outside GS1 is indicative of the presence of hearths in GS1 (Figure 4.8a). The abrupt change to reddish (yellowish brown) in the lower part of the profile belonging to Inside GS1 indicates oxidation processes (Figure 4.8a). The latter could be attributed to pedogenesis, i.e. oxidation coloration with depth. Oxidation processes could also be evidence of high severity burns and extreme heating. According to Parsons et al. (2010) and Ulery and Graham (1993), localized red (oxidized) soil was found to underlie a thick, powdery layer of grey and white ash near a burned out stump or log, indicating extreme heating.

The comparison of particle size results shows the dominance of the fine sand fraction (75−85%) in sediments from Inside GS1, whereas in sediments from Outside GS1 the prevalence (80−90%) is shared between fine and medium sand (Figure F4.9). Other fractions, smaller and bigger, do not exhibit much difference between the two archives. We attribute the prevalence of the fine sand fraction in sediments Inside GS1 to the lithology of the GS1 sandstone outcrop, where at the given level the fine sand fraction prevails therefore contributing most of the sediment material. The sediments from Outside GS1, on the other hand, exhibit a more diverse range of particle sizes, due to the larger and varying sediment contributing area. In sediment samples from Outside GS1 the clay fraction increases slightly with the sample depth, due to clay illuviation down the profile (Chapter 1, section 1.4.1.1), while in samples from Inside GS1 the medium sand fraction shows a slight increase with sample depth (F4.9a,b). This suggests that gravitational processes potentially affect particle movement and raises the possibility of trampling impact on particle size distribution inside the GS1 rockshelter (Williams, 2018b, pg. 431). The slight increase in medium sand fraction with sample depth in Inside GS1 sediments, however, might simply be related to the lithology of the GS1 outcrop. Although a more in-depth examination is beyond the scope of this study, it may be worthwhile investigating whether a similar pattern in particle size distribution is observed in other rockshelter sites within the northern Australia.

Optical microscopy confirmed that the sediments from Outside GS1 and Inside GS1 originate from the Jurassic Hampstead sandstone. Under the microscope, the mineralogy and grain morphology in sediment thin sections from both collections were very much alike. Evidence of bioturbation was also observed in the thin sections from both sample collections. The two sediment collections, however, differ

in some aspects. Iron bearing fragments and gravel-sized sediment aggregates were only observed in thin sections from Inside GS1. Additionally, thin sections from the Inside GS1 sediments contained a considerably larger number of charcoal grains compared to the Outside GS1 thin sections (Figures F4.10, F4.11). Various studies, predominantly in connection with the effects of natural fires on soils and prehistoric pigment production (i.e. ochre), report that conversion of Fe-oxides, such as goethite to hematite, is easily achieved with simple campfires (Lin et al., 2021 and citations therein). They describe that burning causes a decrease in the clay content of soils and formation of coarse sand-sized aggregates (Datta, 2021 and citations therein, Ulery and Graham, 1993). Hence, the higher charcoal content, the presence of iron-bearing fragments and the coarse gravel-sand-sized aggregates in sediment thin sections from Inside GS1 (Lowe et al., 2018) could indicate the influence of human activity, specifically hearth fires, on the sediment record in the archaeological deposit inside GS1, and perhaps even more so because these features were not observed in the Outside GS1 sediment thin sections.

The effect of hearth fires on the sediment record from Inside GS1 is additionally corroborated by magnetic susceptibility values. Susceptibility itself largely depends upon the concentrations of ferrimagnetic grains in sediments, i.e. Fe-oxides predominantly magnetite, maghemite and hematite. The concentration of iron oxides in a sediment profile is influenced by many factors, such as its parent material, physicochemical properties, age, biological activity, but also weathering and fire (Dearing et al., 1996, Maher, 1986, Spassov et al., 2004). Hence, it was expected that weathering and natural fire events, a regular occurrence in the Australian savannah, would result in changes to the magnetic properties of the Outside GS1 sediment samples. The Outside GS1 samples did in fact show a general very slight enhancement in magnetic susceptibility, reflecting in this way the natural signal. These values, however, were significantly lower compared with the magnetic susceptibility values in sediments from the archaeological sequence from Inside GS1 (Figure F4.12). The latter therefore indicate an altered or enhanced natural magnetic signal. Furthermore, the frequency dependent susceptibility analysis χ_{FD} showed that the enhancement in sediment magnetic properties in samples from Outside GS1 and particularly from Inside GS1 is associated with the presence of SP grains (Figure F4.12b,c,d,e).

The presence of SP grains is a diagnostic tool for many environmental applications. Particularly the heating of sediments causes the conversion of weaker magnetic phases to stronger magnetic phases in a similar way to pedogenesis or weathering (Herries and Fisher, 2010). Experimental data have shown that natural fires generally do not alter soil/sediment temperature and/or mineralogy to the same extent as hearth fires (cf. Bellomo, 1993, McClean and Kean, 1993, Linford and Canti, 2001). The impact of fire on

soil/sediment differs depending on the nature of the soil/sediment. Sediments like sand and silt have a higher heat tolerance and are usually affected by combustion when temperatures exceed 400°C for at least 1 hour (Datta, 2021, Ketterings et al., 2000), conditions not typically met in natural fires. High intensity fire that exhibits extreme fire behaviour (high flame length, rapid rate of spread or overstory crown consumption) might result in low- to moderate-degree effects on the soil/sediment due to short heat residence time and because bark acts as an insulator, reducing the amount of heat transferred to the ground (Parsons et al., 2010). Typical examples are crown fires in forests or shrub or grassland fires. As a result, the surrounding sediments are rarely oxidized. In contrast, a low intensity fire, such as smouldering log, can produce intense heat and can be of long duration, resulting in high sediment/soil burn severity in the area under the log (Parsons et al., 2010). Mineral alterations in sediments and soils from forest fires therefore occur in rather restricted areas where fuel sources, such as logs and stumps, are concentrated (Ulery et al., 1996).

Analogously, human controlled hearth fires require a significant amount of fuel to burn regularly for extended periods of time and they tend to maintain higher temperatures. These campfires almost always produce an oxidizing or mixed environment of heating (Herries et al., 2007, Lin et al., 2021). This suggests, in accordance with Lowe et al. (2016), the co-occurrence of enhanced magnetic susceptibility in sediments from Inside GS1 with human occupation of the GS1 is not coincidental. It also ties together all the evidence from the sediments Inside GS1 connected with hearth fires and therefore human activity, including the darker and grey in hue sediment colour, the documented presence of a higher amount of microcharcoal and SPAC, iron-bearing minerals and coarse sized aggregates and significantly higher magnetic susceptibility.

Finally, there is also a strong relationship between the change in the magnetic properties and the onset of human occupation of the associated sediments in the GS1 rockshelter interior as defined by the presence of stone artefacts (Lowe et al., 2016). According to Lowe et al. (2016), the magnetic susceptibility results showed that modifications to the natural sedimentary sequence inside the GS1 began to take place once humans started using the site (at a depth of approximately 206 cm), which preceded the appearance of the first stone artefacts. The enhancement of magnetic susceptibility through anthropogenic burning in the GS1 rockshelter is probably a better indicator of the first use of the site by humans than is the appearance of the first stone artefacts, whose presence is particularly affected by sampling issues in small excavations (Lowe and Wallis, 2020).

Two chronological sequences were compared in this study: the Outside GS1 chronology constructed from PA_10-M pit south profile, using OSL on quartz grains and ^{14}C on macro-charcoal pieces, and the Inside GS1 chronology, using ^{14}C on macro-charcoal fragments from the archaeological sequence, squares C0 and C1, in the GS1 interior (Figure F4.13). In general, the two chronologies align well (Figure F4.14). The Outside GS1 quartz grains yielded the age of ~15 ka for the 172 cm deep profile, suggesting that the last sediment accumulation cycle outside the GS1 rockshelter confines commenced about that time. The Inside GS1 sequence is significantly deeper and older reaching ~38 ka at depth 205 cm. As anticipated, the Inside GS1 archaeological sequence provided older basal dates. However, despite the shallower depth, two populations of quartz grains from the Outside GS1 sequence exhibited ages as old as ~55 ka. These results indicate that the sediment deposits surrounding the GS1 rockshelter are being generated by weathering of the constituting sandstone, deposited, occasionally removed and redeposited for at least that long.

This statement, however, raises a question: where did the removed pre-15 ka sediment go? One possibility is that it was blown away during the LGM due to generally dry conditions and low vegetation cover, as discussed in the introductory section I.2E of this thesis. However, there is no evidence of intensified eolian activity recorded in sediment deposits from Outside GS1 or Inside GS1. Another possibility is that the accumulated sediment was washed away during intense rainfall episodes before and during the LGM, a common occurrence in arid environments. In this case, the sediment would have been carried away to (and by) the Norman River, resulting in higher water flow and sediment load as well as the formation of intermittent tributary channels and river aggradation. Evidence of these phenomena was observed in the Norman River terraces and discussed in Chapter 1 and Chapter 2 of this thesis, confirming a period of Norman River aggradation of at least 35 ka.

A study of fluvial activity during the last glacial cycle in the Fitzroy River Basin, a large river basin in tropical northeastern Australia about 700 km southeast of the GS1, revealed several discrete phases of active bedload sedimentation among which at: ~50−40 ka (MIS 3) and ~30−10 ka (MIS 3/2) (Croke et al., 2011). Our observations from the Norman River terraces align with the timing of the Fitzroy fluvial activity during the period immediately before, during and after the LGM and together present evidence on fluvial response to reduced rainfall and vegetation cover suggested by regional palaeoclimate indicators (Croke et al., 2011). However, Croke et al. (2011) report about the absence of a strong Holocene signal in the Fitzroy basin which does not align with previous accounts from other parts of Australia (Nanson et al.,

2008), including our observations from the youngest terrace of the Norman River (Chapter 2, section 2.4.1).

Considerable post-depositional mixing of sediments in the Outside GS1 PA_10-M pit was confirmed with the OSL analysis. The post-depositional mixing was in large part attributed to bioturbation by both plants and animals. Evidence of both was recorded in sediment profiles Outside GS1 and Inside GS1 macroscopically during the field work as well as under the microscope (chapter 4.3.2.2). However, trampling by human feet or larger animals, e.g. macropods, can also cause a more subtle disturbance of sediments (Cropper, 2018, Williams, 2018a). Evidence of the presence of both animals and people inside the GS1 rockshelter was corroborated by phytolith indices and $\delta^{13}C$ analysis in Chapter 3 (3.4.2.2; 3.4.3.1) and summarized here (section 4.3.6). Human (or larger animal) trampling is a form of bioturbation, which occurs when people walk across a site, step on artefacts and push them below the surface, or kick up soil or sand to mix the sediments and bury artefacts. Various studies have been conducted on the influence of bioturbation on OSL dating (e.g. Araujo, 2013, Bateman et al., 2003, Chazan et al., 2013, Gliganic et al., 2016, Johnson et al., 2014, Kristensen et al., 2015, Rink et al., 2013, Williams et al., 2021) as well as human trampling on artefact movement in sediments (e.g. Driscoll et al., 2016, Eren et al., 2010, Marwick et al., 2017, Reynard and Henshilwood, 2018, Stockton, 1973, Thulman, 2012, Williams, 2018b). There is however very little knowledge about the effect of human and animal trampling of sediments on OSL dating. It might be worth considering in future research a comparison of single grain OSL De values in radial distribution graphs from inside and outside rockshelters, where evidence of trampling has been already confirmed by other means.

Finally, the vegetation reconstruction presented in Chapter 3 of this thesis has shown the presence of savannah type of vegetation in the study area since the Pleistocene-Holocene transition and throughout the Holocene. Phytolith indices and $\delta^{13}C_{SPAC}$ analysis, however, indicated the forest cover was denser during early to mid-Holocene followed by a gradual transition to a current open woodland savannah. Both proxies, the phytoliths and $\delta^{13}C_{SPAC}$ isotopic signature, showed a difference in results between the Inside GS1 and Outside GS1 assemblages, where Inside GS1 did not reflect the same signal from the surrounding environment reflected in the Outside GS1 signal. Using the phytolith indices (D/P and FI-t) we determined that the proxies from the archaeological sequence Inside GS1 were biased due to human and animal usage of the shelter. More specifically, the grass phytolith assemblage Inside GS1 was influenced by macropod dung, while the tree-shrub-herb phytolith assemblage was affected by people bringing in leaves, branches and bark for fibre, bedding and fires.

The vegetation reconstruction in this study demonstrated with great confidence that both palaeoenvironmental archives, Outside and Inside GS1, should be combined to obtain a reliable outcome. To summarise the findings of this study two figures have been provided. Figure F4.20 illustrates the evidence preserved in sediments from Inside GS1 and Outside GS1 as well as the comparison of the results. Figure F4.21, on the other hand, depicts the reconstruction of the formation processes and the palaeoenvironment produced in this study.

A final comment should be made. The dated commencement of sediment accumulation and human occupation of the GS1 rockshelter does not necessarily reflect the earliest human presence at the site. Instead, it signifies the earliest preserved evidence of human activity. The GS1 study location is a dynamic, constantly changing site, impacted by weathering and gravitational processes such as cracking, rock-fall, slope collapse and shifts in periods of bedrock exposure (sediment removal) and sediment accumulation. A period of bedrock exposure, or 'bare rock', indicates a state where physical erosion is dominant and leaves hardly any evidence of human or other activity in the form of a sediment record. However, this does not mean that the study area was not utilized. In fact, several bare floor rockshelters were discovered in the wider GS1 area containing well preserved rock art. This further confirms the presence of humans in the area over a long period of time.

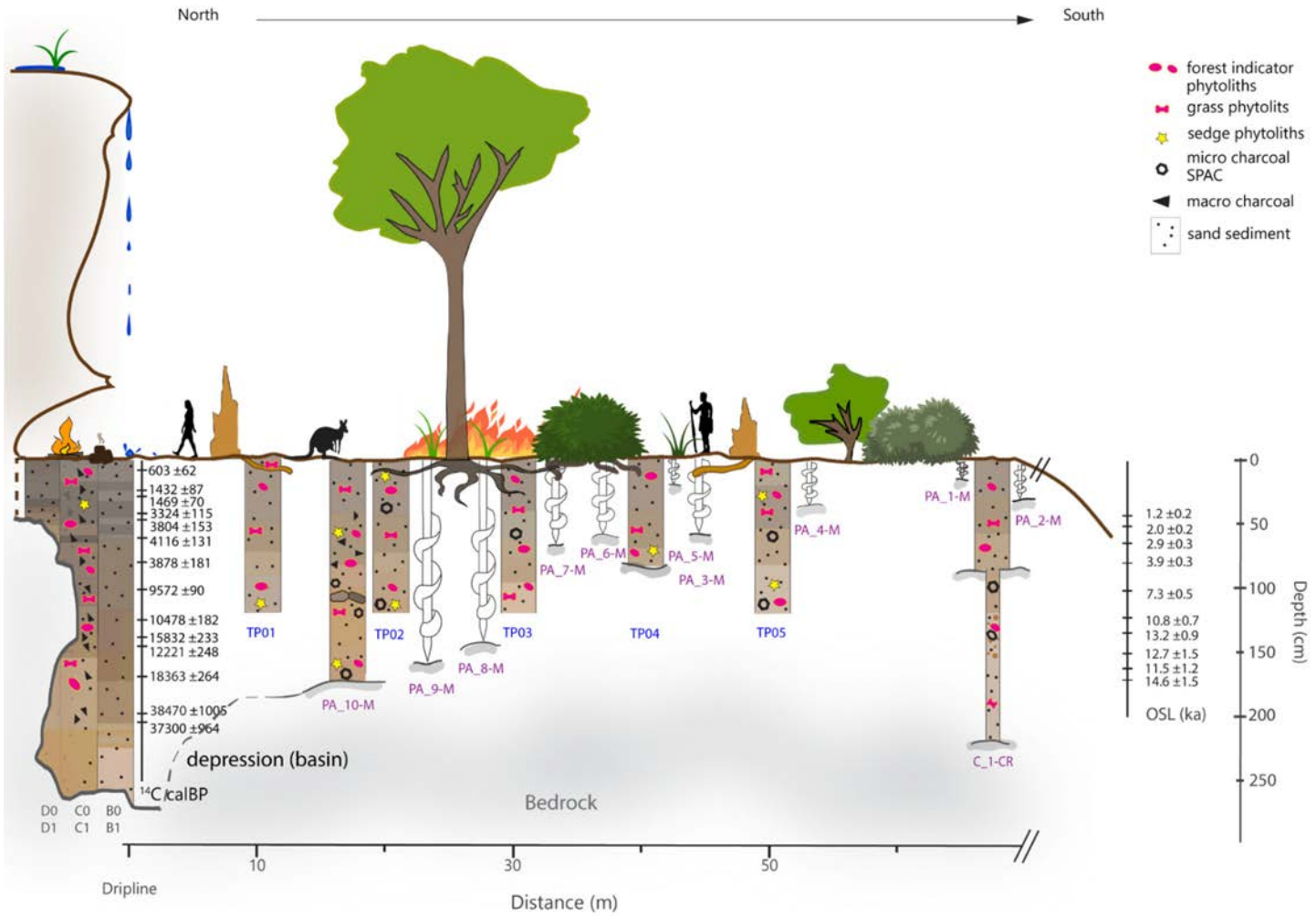

Figure F4.20: The visualisation of the Outside GS1 vs. Inside GS1 comparison study. Geomorphic and sedimentologic evidence is shown along with the established chronologies and the savannah vegetation reconstruction in the study area. Some proxies used for comparison are also shown. **From the left:** outline of the GS1 rockshelter with the dripline and the ^{14}C chronology of the archaeological sequence Inside GS1. The evidence of human and animal impact on the Inside GS1 sediment record is shown in the form of a hearth fire and kangaroo dung. Beyond the dripline, the OSL chronology for the Outside GS1 sequence is given along with the depth scale. Natural fire record is presented in the form of macro- and micro-charcoal in the Outside GS1 sediments. Evidence of bioturbation is shown as termite mounds and plant roots. The stone-line of possible anthropogenic or natural origin found in pit PA_10-M is also shown.

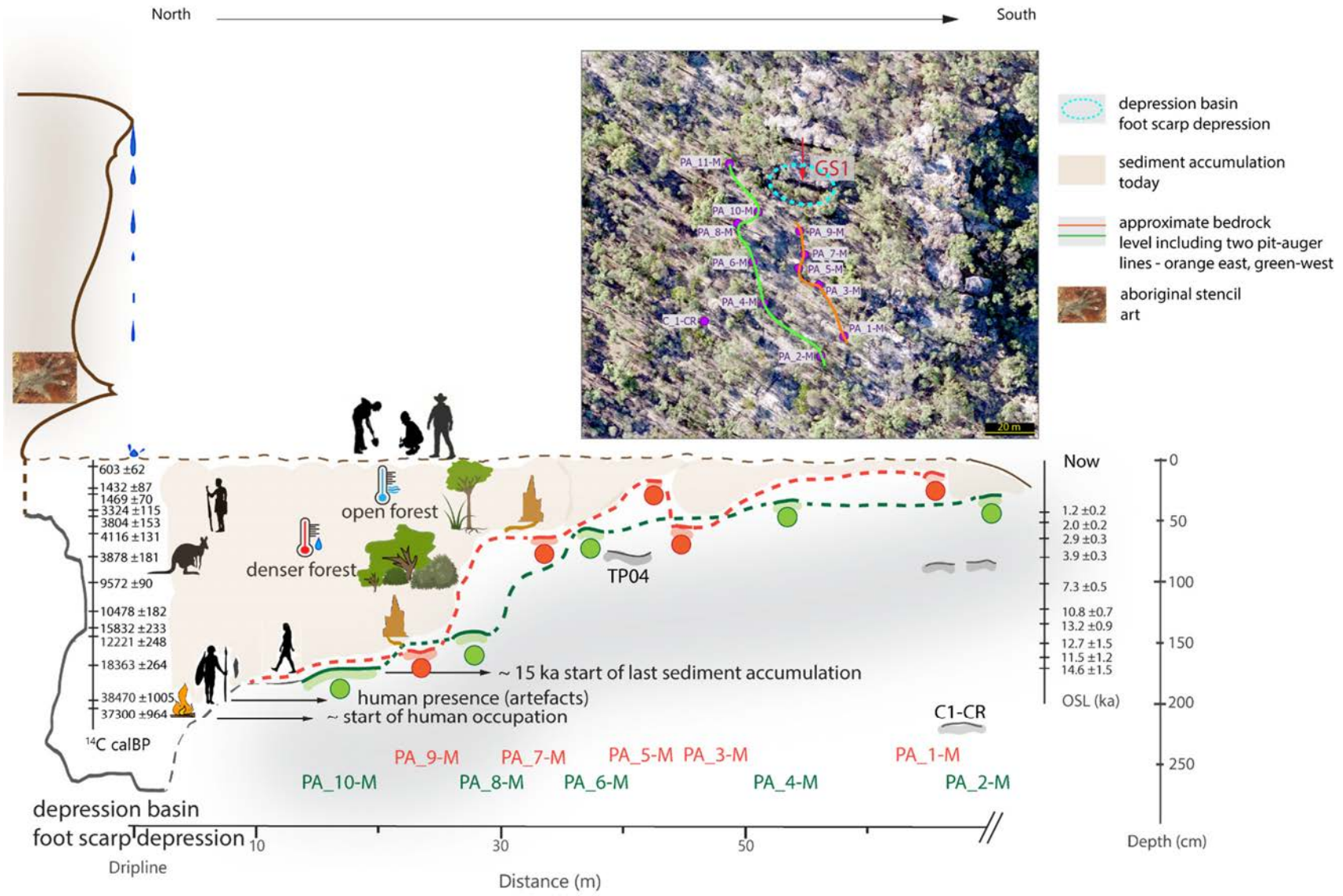
North
South
depression basin
foot scarp depression
sediment accumulation today
approximate bedrock level including two pit-auger lines - orange east, green-west
aboriginal stencil art
PA_11-M
GS1
PA_10-M
PA_8-M
PA_9-M
PA_7-M
PA_6-M
PA_5-M
PA_3-M
PA_4-M
C_1-CR
PA_1-M
PA_2-M
20 m
603 ±62
1432 ±87
1469 ±70
3324 ±115
3804 ±153
4116 ±131
3878 ±181
9572 ±90
10478 ±182
15832 ±233
12221 ±248
18363 ±264
38470 ±1005
37300 ±964
14C calBP
open forest
denser forest
TP04
~ 15 ka start of last sediment accumulation
human presence (artefacts)
~ start of human occupation
Now
1.2 ±0.2
2.0 ±0.2
2.9 ±0.3
3.9 ±0.3
7.3 ±0.5
10.8 ±0.7
13.2 ±0.9
12.7 ±1.5
11.5 ±1.2
14.6 ±1.5
OSL (ka)
C1-CR
PA_9-M
PA_7-M
PA_5-M
PA_3-M
PA_1-M
PA_10-M
PA_8-M
PA_6-M
PA_4-M
PA_2-M
depression basin
foot scarp depression
Dripline
10
30
50
Distance (m)
0
50
100
150
200
250
Depth (cm)

Figure F4.21: The GS1 study area reconstruction of formation processes and palaeoenvironment. Pivotal events in the past are also marked. **Top right:** the ground plan of the study area, the red arrow points to the drip-line. **Main image:** on the left the GS1 rockshelter with marked dripline and the depression basin with foot scarp erosion. Beyond the dripline, the horizontal ground shows the current sediment accumulation level, the orange and green dashed lines depict the subsurface bedrock level as inferred by excavated pits and auger holes (orange and green circles). The start of the current accumulation cycle outside GS1 began approx. 15 ka ago based on OSL evidence. The onset of human occupation (ca. 206 cm depth) based on magnetic susceptibility results is represented by the hearth fire. Human presence, further confirmed by artefacts and charcoal records found inside the GS1 rockshelter, is represented by the silhouettes. Termite mounds represent bioturbation and post-depositional mixing recorded in sedimentological and chronological analysis, while the kangaroo represents the impact of macropods on the palaeovegetation record in sediments from inside GS1. Based on evidence discussed in this and previous chapters the two thermometers indicate a warmer and wetter climate resulting in a denser tree cover during early to mid-Holocene (approx. 10–4 ka years ago) and a cooler and drier climate resulting in a transition to a more open savannah woodland that we experience today.

4.5 The significance of the GS1 study area

The study area, which includes the GS1 rockshelter and its immediate surroundings, has significant potential as a sedimentological, palaeoenvironmental and archaeological case study in the terrestrial sediments of the Australian tropical north savannah interior. The significance of the site is clearly demonstrated by the new knowledge that has been generated through the research carried out to date. The work conducted to date also alludes to the implications for future research.

This study bridges the sedimentological and palaeoenvironmental record obtained from the non-archaeological sediments surrounding the GS1 rockshelter (Outside GS1), with the sedimentological and palaeoenvironmental record obtained from the archaeological deposit within the GS1 interior (Inside GS1). The aim was to investigate how the two palaeoenvironmental archives (Outside GS1 and Inside GS1) complement and question each other and whether bridging the two archives enables the production of a more reliable palaeoenvironmental record for the study area. This will eventually provide much needed palaeoenvironmental data for the savannah environment that characterises most of the interior of tropical north Australia.

One important outcome of this study is the review of site formation processes. The development of the scarp foot zone at the base of the outcrop explains the existing depression (basin) that extends from the GS1 interior approximately 15 m beyond the dripline (Figure F4.21). The structure of the Jurassic Hampstead sandstone that constitutes the study area conditions its response to surface and subsurface weathering mechanisms, such as cavernous weathering, arenization, granular disintegration, the moisture effect and bedrock denudation, which further explains the site characteristics, particularly the rockshelter development, uneven subsurface morphology and smoothed bedrock surfaces. With no recorded evidence, either Inside GS1 or Outside GS1, of wind or flooding, these mechanisms appear to be the main processes that shape the GS1 study area and govern the occurrence, transport and accumulation of sediment.

Another important outcome is the establishment of a chronologic framework for the area of study. It shows the last cycle of sediment accumulation commenced approximately 15 ka ago, but the overall site formation dynamics started long before that, at least 55 ka ago. It also suggests the possibility of interchanging periods of sediment accumulation and sediment stripping, the latter probably linked to time intervals of enhanced erosional conditions in the area. Inside the GS1 rockshelter, to the contrary, the niche and the development of the foot scarp depression caused the GS1 interior to function as a sediment trap that allowed sediment to continuously deposit for at least 38 ka without noticeable interruption or removal. Despite the relatively homogeneous nature of the sediments, with poor temporal resolution and severe post-depositional disturbance, the constructed age-depth model supports the assumption that a reliable chronology can be established for the GS1 study area through a multi method approach and the combination of the two archives (Inside and Outside GS1).

Magnetic susceptibility results along with sediment microscopic analysis support the evidence of human presence inside the GS1 rockshelter for at least ~38 ka, which aligns well with the evidence of stone artefacts (Lowe et al., 2016, 2018). Moreover, it appears that the enhancement of magnetic susceptibility through anthropogenic burning is as good as (if not a better) indicator of the first use of the site by humans as the appearance of the first stone artefacts. Finally, the combination of the two archives for the reconstruction of past vegetation structure showed that human and animal (macropods) activity bias the sediment record of the archaeological deposit inside the GS1 rockshelter. It also demonstrated the presence of savannah woodland on the study area since the Pleistocene-Holocene transition suggesting that the area was a viable refugia and a pleasant place to be, at least for the last 12 ka.

The GS1 study area has potential for future research. One inevitable question relates to the general dilemma about sediment accumulation inside rockshelters being influenced by human activity and to what degree. Hughes (1977: 192-198), almost 50 years ago, concluded that human use of rockshelters either led to increased rates of weathering and roof fall or to increased accumulation of roof fall in the rockshelters, or both. Prior to Hughes, the possibility of human impact on the accumulation of rockshelter deposits was considered by Mulvaney and Joyce (1965: 170), but no mechanisms were postulated. At the GS1 study area, to resolve this dilemma, we argue it is essential to first understand the current dynamics of sedimentation. For this purpose, sediment traps were installed during the two-year field work from 2018 to 2020. The preliminary results showed a noticeable difference in accumulated sediment between the GS1 interior and the area outside GS1. Pursuing these results was not the objective of this study, nonetheless, we believe that this research direction has potential and could be pursued.

Finally, during the course of this study it became apparent that despite numerous stone artefacts being documented in the archaeological deposit Inside GS1, not one single artefact was recorded Outside GS1 in any of the pits or auger holes excavated beyond the dripline. It appears highly improbable that not a single artefact would have been lost or dropped or intentionally thrown away during the daily activities on the site. This raises a question whether there is a behavioural pattern that should be investigated or whether a deeper study of subsurface morphology, sedimentation mechanisms, trampling and bioturbation effects might provide an answer to this rather peculiar occurrence. Other rockshelter sites across northern Australia, such as Madjedbebe, could be profitably examined in this regard.

To conclude, this study shows that expanding the existing records from known archaeological rockshelters into their surroundings represents a valid approach to start filling the gap in palaeoenvironmental record for the Australian tropical north interior. The existing data from known rockshelter sites provide an excellent starting point and by bridging this data with their surroundings it is possible to obtain more reliable and solid records to fill the gap.

4.6 Acknowledgements

The authors express their gratitude to the Traditional Owners represented by Woolgar Valley Aboriginal Corporation, especially Uncle Lavin Keyes, Jasmine Keyes and Tameika Keyes as well as Helen Smith and William Smith for their partnership, guidance and help. The authors are very thankful to the Hinze family for their generous support and assistance throughout the fieldwork. We also thank Costijn Zwart, Michael Brandt, Tina Nemec and Raul Hernandez Font for their invaluable help with fieldwork. Their commitment and positive attitude contributed importantly to the outcome of this study. The authors express special thanks to Lawrence Conyers for providing use of the GPR data collected from the GS1 site and to David Heslop and Ian Roach for their expertise in interpreting magnetic susceptibility results. We thank Rainy Comley for his invaluable assistance and support during laboratory analysis.

II Thesis Summary

II.1 Summary of thesis conclusions

This project recognised, and sought to fill, a significant gap in late Quaternary palaeoenvironmental knowledge from the tropical semi-arid savannahs that cover much of the north Australian interior. The majority of the existing records come from lake, swamp and estuarine deposits found in the coastal part of northern Australia as well as the marine domain. The extent of palaeoenvironmental research into the interior tropical Australian savannah is greatly hindered by poor sediment stratigraphies and unfavourable preservation conditions for organic materials, such as pollen, and bones. These limitations can be partially addressed through the integrated palaeoenvironmental investigation of sediment records inside and outside rockshelters. Proxies that are preserved in these conditions can be studied, while using a multi-method approach for interpreting the results can add valuable insight.

This thesis aimed to produce a palaeoenvironmental reconstruction for the area within the semi-arid tropical Australian savannah in Northern Queensland, where the Gledswood Shelter 1 (GS1) archaeological rockshelter site is located. This location provides an exceptional opportunity to bridge the sediment records from two palaeoenvironmental archives: the archaeological deposit inside the GS1 and the non-archaeological, open-site terrestrial sediments extending south-southwest beyond the GS1 dripline. Additionally, evidence from nearby Norman River, flowing 1.6 km south of GS1, contributes to a valuable case study for addressing the main scientific questions proposed in this thesis.

Four research questions are addressed: (1) What were the main geologic and geomorphic processes that created the surrounding landscape and GS1? (2) What is the chronology of the non-archaeological sediments outside GS1? (3) How has the environment changed in the study area? And (4) How do sedimentary records from deposits inside and outside GS1 complement or differ from each other and how does this contribute to a better, broader, understanding of sedimentary and palaeoenvironmental archives at the GS1 site?

Chapter 1 ('the landscape layer') addresses the (1) research question. Aerial imagery, digital elevation modelling, stratigraphy, sedimentology, and cosmogenic nuclide methods were used to identify the geomorphic and geologic processes that formed and shaped the study area, providing a landscape context for more detailed investigations of the study area. Geomorphic evidence shows an uneven subsurface bedrock morphology and a surface composed of sandstone outcrops, escarpments, collapsed slopes and patches of accumulated sediments. The results suggest that the

area where GS1 is located represents a large, weathered erosion remnant of a residual hill partially covered by sandy sediment accumulation. The GS1 rockshelter has formed in a residual sandstone outcrop. The sedimentologic characteristics of sediments outside the GS1 rockshelter indicate derivation from the Jurassic Hampstead sandstone by chemical weathering and physical erosion of the local bedrock and outcrops. Post-depositional disturbance due to bioturbation was documented and attributed to termite, ant and root activity. In addition, a stone line was observed in the PA_10-M pit approximately 19 m beyond the GS1 dripline, which could be attributed to animal bioturbation, physical processes or could represent evidence of human activity in the area during the mid-Holocene.

Sedimentologic evidence from Norman River terraces demonstrates that the river sediments originate from the Jurassic Hampstead sandstone. A palaeochannel adjacent to the modern Norman River channel and the elevation of the investigated terraces indicate that river levels were higher at some times in the past. The cross profile of the river channel matches a *fill-cut* terrace, where the subsequent incision of the stream channel occurs into the river's aggraded material. This geomorphic evidence of the river dynamics history infers that prior to the present-day incising, the Norman River was aggrading. Additionally, the particle size distribution pattern in the sediment sample from the lowermost and oldest terrace suggests a lower flow strength during the period of formation of this terrace compared to the younger upper terrace, where the particle size distribution pattern indicates an increase in flow strength. Overall, the evidence from the Norman River site indicates shifts in water flow and sediment supply, potentially linked with changes in palaeoclimate. An increase in water flow can be due to more intense precipitation and may indicate monsoon intensification. On the other hand, an increase of incision can also be due to a decrease in sediment supply because of reduced erosion. It may, therefore, indicate less intense precipitation and a monsoon decrease.

The work done here shows the importance of understanding the geomorphic processes and geologic evolution of the study area to interpret the evidence obtained from stratigraphic and sedimentologic analyses around and in the rockshelter itself. The results of this study establish a sedimentological and geomorphological framework that help interpret the records from the GS1 rockshelter.

In Chapter 2 ('the chronology layer') the (2) research question: What is the chronology of the non-archaeological sediments outside GS1?, is addressed. A multi-method dating approach was used to obtain ages for sediment deposits outside GS1 and the subsidiary Norman River site. Single-grain OSL dating on quartz grains and radiocarbon dating on two charcoal fractions, macro-charcoal and Stable Polycyclic Aromatic Carbon (SPAC), enabled the production of a reliable chronology despite the poor stratigraphic differentiation and noticeable post-depositional mixing of the deposits. OSL dating revealed that the last deposition cycle commenced approximately 15 ka ago, shaping the sediment

accumulation we observe at the GS1 site today. The presence of grains older than 50 ka alongside the youngest grains (<2ka) within the same chronological sequence (pit PA_10-M), however, indicates that some of the sediment pool at the GS1 site is much older. Likely, the sediments have been exposed to periods of translocation, removal and deposition. Post-depositional mixing due to bioturbation (termite, ant and plant roots) was responsible for a substantial scatter in dose distributions observed in OSL radial plots. Yet, the evidence from the GS1 outside chronological sequence (from pit PA_10-M) suggests another process, apart from bioturbation, may be needed to account for the introduction of the oldest (≥50 ka) intrusive grains into the sequence.

The radiocarbon dating (^{14}C) results on four pieces of macro-charcoal exhibited a good correlation with the OSL results. On the other hand, SPAC did not provide reliable chronological information for the GS1 outside sediments, possibly due to a combination of reasons connected with unfavourable conditions for charcoal preservation and a fine particle size that makes the material susceptible to downward translocation in the sandy matrix. The final age-depth model confirmed a good correlation between the OSL and ^{14}C macro-charcoal ages. The calculated sedimentation rates revealed a significant increase in sedimentation rate during the last ~3 ka.

Important information was also obtained from the OSL results from the Norman River terraces. Considerably less scatter in dose distributions in the OSL radial plots from the Norman River sediments can be attributed to a relative lack of termite and ant activity due to the proximity of water. The lowermost and oldest exposed terrace is ~40 ka old, while the bottom of the upmost and youngest terrace suggests an age of ~11 ka. The latter coincides with the Pleistocene–Holocene boundary and indicates that the Norman River was aggrading in this period. Moreover, the river deposited another 124 cm of alluvium during the Holocene, forming the upmost terrace before it shifted to the incision phase we see today.

This work has shown that establishing a reliable chronology in post-depositionally mixed, open-site terrestrial sediments in semi-arid Australian savannah is possible but complex. The results are highly significant for advancing palaeoenvironmental research in the vast interior of the northern Australian continent. They highlight the necessity of employing multiple techniques to establish a reliable chronology. Palaeoclimatically, the results of this work suggest a change in climatic conditions in the late Holocene, possibly a monsoon lessening. The increase in sedimentation rate in the non-archaeological deposits beyond the GS1 dripline, approximately 3 ka ago, may be linked to a reduction in precipitation, which would result in a decrease in sediment erosion off-site and subsequently lead to an increase in sedimentation. The evidence from the Norman River terraces also shows a change in river dynamics in the late Holocene, considering the 124 cm of accumulated Holocene alluvium before

the shift from aggradation to incision. This shift to incision (discussed in Chapter 1) may be linked to a reduction in sediment supply due to a decrease in erosion because of a decrease in monsoon intensity.

The (3) research question: How has the environment changed in the study area?, is addressed in Chapter 3 ('the vegetation layer'). This chapter outlines a vegetation reconstruction study, utilising a combination of proxies−phytoliths and $\delta^{13}C$ of SPAC ($\delta^{13}C_{SPAC}$), from outside and inside the GS1 rockshelter. The evidence from outside GS1 shows the continuous existence of savannah vegetation throughout the Holocene, confirmed by the shared presence of both tree and grass phytolith morphotypes in the sediments. The results, however, indicate denser tree cover between 10 and 4 ka ago, during the early and mid-Holocene, followed by a gradual transition to a more open savannah woodland during the last 2 ka. In contrast, analyses from inside the GS1 rockshelter suggest a substantial prevalence of tree vegetation which, in general, is not consistent with the natural vegetation signal represented by the sediment records from outside GS1. This difference between the outside and inside GS1 results was recorded in both phytolith and the $\delta^{13}C_{SPAC}$ values. Further investigation showed that animal and human activity probably influenced the phytolith and $\delta^{13}C_{SPAC}$ signal inside GS1. More precisely, the recorded grass peaks were augmented by inputs from macropod faeces and the woody vegetation peaks from hearth fires lit by human occupants of the shelter.

This work is the first to use this combination of proxies for vegetation reconstruction, which is necessary in the absence of more traditional proxies such as pollen. The outcome confirmed the effectiveness of this approach in reconstructing past environmental conditions. It also demonstrated how the records from inside rockshelters could be biased due to animal and human activity. This study demonstrates the need to expand the research on rockshelters beyond the dripline into their surroundings to obtain a more reliable and comprehensive result. Finally, the denser tree cover during the early and mid-Holocene may indicate a wetter and warmer climate in the region. This aligns with observations regarding changes in sedimentation rates on the Norman River, all of which suggest a shift in climatic conditions, likely caused by monsoon weakening over the last ~3 ka, hence following the mid-Holocene wet phase. Records of a wet period between 9 and 7 ka were also found in the western part of the Australian tropics, specifically in the Kimberley region.

Chapter 4 ('the integration layer') addresses the last research question (4) by bringing together the results from the two main palaeoenvironmental archives, outside and inside GS1 rockshelter. Specifically, this chapter compares and correlates the geomorphic, stratigraphic, sedimentologic, chronologic and vegetation results outside and inside GS1 and investigates how do sedimentary records from deposits inside and outside GS1 complement or differ from each other. This work

demonstrates how bridging the outside and inside rockshelters archives contributes to a more nuanced and holistic understanding of the formation processes and function of the GS1 site as well as to developing a palaeoenvironmental record in the context of early human presence.

This study shows that the structure of the Jurassic Hampstead sandstone conditioned the site response to surface and subsurface weathering processes. The development of a scarp foot zone at the base of the GS1 outcrop explains the existing depression in subsurface morphology, now covered by sediment. Moreover, the combination of the two archives (Outside and Inside GS1) provided a reliable chronological framework for the GS1 site as a whole, despite the relatively homogenous sediments of poor stratigraphic resolution and significant post-depositional disturbances. Surprisingly, among various methods applied throughout this research, magnetic susceptibility analysis was revealed to have great potential as a palaeoenvironmental tool, particularly as an indicator of anthropogenic burning.

Finally, when placing this study within the regional archaeological framework and in the context of late Quaternary palaeoenvironmental changes in tropical north Australia, the evidence gathered at the GS1 site suggests a good agreement in the duration of human occupation compared to other regional archaeological sites. Examples of such sites include the Gregory River at Riversleigh and Mickey Springs (chapter I.1D). Additionally, the sedimentary records from terrestrial open-site sequences outside GS1 as well as the Norman River terraces, provide evidence of a broader pattern of past environmental change that can be discerned. The change in river dynamics from aggrading to incising discussed in Chapter 1, the significant increase in sedimentation rate demonstrated in Chapter 2 and the difference in the savannah tree density between the early and late Holocene discussed in Chapter 3, suggest a relatively wet Pleistocene–Holocene, transition period leading to a wetter early and mid-Holocene subsequently changing to a drier period of decreased monsoon activity, around 3 ka ago, and continuing to the present. This pattern generally agrees with the broader literature, which suggests that the early to mid-Holocene climates on the coastal margin of eastern Australia were significantly wetter than present, but they have gradually become drier over the last 5 ka. The El Niño–Southern Oscillation (ENSO) is the most prominent driver suggested for this late Holocene drying. In particular, the strengthening of ENSO (notably the El Niño phase) has been used to explain climate drying for latitudes ~10 to 45°S.

II.2 Future work

This project was part of the larger ARC Centre of Excellence for Australian Biodiversity and Heritage–CABAH. The results presented in this study will ultimately be combined with a number of additional studies being conducted elsewhere in the Australasian tropics, such as Arnhem Land, the

Gulf of Carpentaria, Cape York, Papua New Guinea, a variety of Indonesian islands as well as the Australian subtropical and temperate regions. One aim of CABAH is to provide new, long, replicated, high-resolution records extending from beyond the early human arrival to the present that will enable a robust disentangling of climate and anthropogenic drivers of environmental change in deep time for the extensive Australian tropical savannah. For the savannah region very few records currently exist.

Future geomorphic and geologic transects (transverse sections) extending from the GS1 site to the Norman River, as well as a comprehensive study of terraces on the Norman River and Woolgar River (~30 km south of GS1), would be very worthwhile, based on the results presented in this thesis. These will provide new sediment records to support a better understanding of the processes that formed the landscapes of the area and the origin and more detailed timing of the (large) changes in river dynamics that have occurred in the past, in turn, linked to changes in rainfall and vegetation. In addition, the chronologic results in Chapter 2 exhibit a good correlation between OSL ages at the GS1 study area and the Norman River terraces OSL chronology. Whether this is a matter of coincidence or possibly valuable evidence that could allow the establishment of a chronological framework for the wider area should be examined in the future. These investigations, combined with the development of a modern phytolith collection from the area (unfortunately not possible in this thesis), will strengthen our understanding of the drivers of, and responses to, past environmental changes in the region. Ultimately, this will deepen our knowledge of palaeoenvironmental change in the North Queensland tropical interior, a large region inhabited by humans for tens of millennia.

The results of this work have also opened new avenues to address what is arguably one of the most important dilemmas in Australian rockshelter formation mechanisms: *Is there a direct relationship between the rate of sediment accumulation and the intensity of human usage of rockshelters?* The experimental placement of sediment traps outside and inside GS1 gave promising results but was very preliminary. The installation of sediment traps and a particle size analysis of the sediments could be used to better characterise the amounts and types of trapped particles and provide useful information about their dynamics and mechanisms of movement in and around the shelter. The groundwork initiated in Chapter 1 of this thesis, which involved field survey, cosmogenic nuclide analysis and sedimentology has also opened new avenues for conducting a more comprehensive study of the numerous axe-grinding grooves documented in bedrock exposures along the Norman River and Woolgar River. These grooves were mentioned in the introductory archaeological context provided for the region and it is possible that they have considerable antiquity. They are likely to have been re-exposed by incision of the Norman River into its bed, and hence likely pre-date the Holocene.

References

ADAMIEC, G. & AITKEN, M. J. 1998. Dose-rate conversion factors: update. *Ancient TL,* 16, 37-50.

AGAFONOFF, V. 1936. *Les sols de France au point de vue pédologique*, Dunod, pp.154.

AITKEN, M. J. 1985. *Thermoluminescence dating* London, Academic Press, pp.351.

AITKEN, M. J. 1998. *Introduction to Optical Dating: the Dating of Quaternary Sediments by the Use of Photon-stimulated Luminescence*, Clarendon Press, pp.280

AITKEN, M. J. 2003. Radiocarbon dating. *In:* ELLIS, L. (ed.) *Archaeological Method and Theory.* New York: Garland Publishing.

ALA-Atlas of Living Australia [Online]. Available: https://biocache.ala.org.au/explore/your-area [Accessed 19.01. 2022].

ALBERT, R. M. & CABANES, D. 2007. Fire in prehistory: An experimental approach to combustion processes and phytolith remains. *Israel Journal of Earth Sciences,* 56,175-189.

ALBERT, R. M., LAVI, O., ESTROFF, L., WEINER, S., TSATSKIN, A., RONEN, A. & LEV-YADUN, S. 1999. Mode of occupation of Tabun Cave, Mt Carmel, Israel during the Mousterian period: a study of the sediments and phytoliths. *Journal of Archaeological Science,* 26, 1249-1260.

ALEMAN, J. C., HENNEBELLE, A., VANNIÈRE, B., BLARQUEZ, O. & THE GLOBAL PALEOFIRE WORKING GROUP. 2018. Sparking New Opportunities for Charcoal-Based Fire History Reconstructions. *Fire,* 1(1), 7.

ALEMAN, J. C., SAINT-JEAN, A., LEYS, B., CARCAILLET, C., FAVIER, C. & BREMOND, L. 2013. Estimating phytolith influx in lake sediments. *Quaternary Research,* 80, 341-347.

ALEXANDRE, A., BASILE-DOELSCH, I., DELHAYE, T., BORSHNECK, D., MAZUR, J.-C., REYERSON, P. & SANTOS, G. 2015. New highlights of phytolith structure and occluded carbon location: 3-D X-ray microscopy and NanoSIMS results. *Biogeosciences,* 12, 863-873.

ALEXANDRE, A., COLIN, F. & MEUNIER, J. 1994. Phytoliths as indicators of the biogeochemical turnover of silicon in equatorial rain-forest. *Comptes Rendus de l'Academie des Sciences serie II,* 319, 453-458.

ALEXANDRE, A., CRESPIN, J., SYLVESTRE, F., SONZOGNI, C. & HILBERT, D. 2012. The oxygen isotopic composition of phytolith assemblages from tropical rainforest soil tops (Queensland, Australia): validation of a new paleoenvironmental tool. *Climate of the Past,* 8, 307-324.

ALEXANDRE, A., MEUNIER, J.-D., COLIN, F. & KOUD, J.-M. 1997b. Plant impact on the biogeochemical cycle of silicon and related weathering processes. *Geochimica et cosmochimica acta,* 61, 677-682.

ALEXANDRÉ, A., MEUNIER, J.-D., LÉZINE, A.-M., VINCENS, A. & SCHWARTZ, D. 1997a. Phytoliths: indicators of grassland dynamics during the late Holocene in intertropical Africa. *Palaeogeography, Palaeoclimatology, Palaeoecology,* 136, 213-229.

ALEXANDRE, A., MEUNIER, J.-D., MARIOTTI, A. & SOUBIES, F. 1999. Late Holocene phytolith and carbon-isotope record from a latosol at Salitre, South-Central Brazil. *Quaternary Research,* 51, 187-194.

ALLAN, R., LINDESAY, J. & PARKER, D. 1996. *El Niño Southern Oscillation & climatic variability*, Aubrey Books Intl. Ltd, pp.405.

ALLAN, R. J. 1988. El Niño southern oscillation influences in the Australasian region. *Progress in Physical Geography,* 12, 313-348.

ALLEN, J. & O'CONNELL, J. F. 2008. Getting from Sunda to Sahul. *In:* CLARK, G., LEACH, F. & O'CONNOR, S. (eds.) *Islands of Inquiry, Colonization, Seafaring and the Archaeology of Maritime Landscapes.* Canberra: ANU Press, 31-46.

ALLEN, J. P. & FIELDING, C. R. 2007a. Sedimentology and stratigraphic architecture of the Late Permian Betts Creek Beds, Queensland, Australia. *Sedimentary Geology,* 202, 5-34.

ALLEN, J. P. & FIELDING, C. R. 2007b. Sequence architecture within a low-accommodation setting: An example from the Permian of the Galilee and Bowen basins, Queensland, Australia. *AAPG Bulletin,* 91**,** 1503-1539.

ALLEN, P. A. 2008. From landscapes into geological history. *Nature,* 451, 274-276.

ALLEN, P. A. & ARMITAGE, J. J. 2012. Cratonic Basins. *In:* BUSBY, C. & AZOR, A. (eds.) *Tectonics of Sedimentary Basins: Recent advantages.* UK: Blackwell Publishing Ltd, pp.633.

ALON, D., MINTZ, G., COHEN, I., WEINER, S. & BOARETTO, E. 2002. The use of Raman spectroscopy to monitor the removal of humic substances from charcoal: quality control for ^{14}C dating of charcoal. *Radiocarbon,* 44, 1-11.

ANDERSEN, A. N., MAINWARING, J. P., MORRIS, I., DAWES-GROMADZKI, T. 2005. *Termites of Northern Australia*. Alice Springs, NT: Barker Souvenirs, pp.44.

ANDERSON, R. S., REPKA, J. L. & DICK, G. S. 1996. Explicit treatment of inheritance in dating depositional surfaces using in situ ^{10}Be and ^{26}Al. *Geology,* 24, 47-51.

ANGELUCCI, D. E., ANESIN, D., SUSINI, D., VILLAVERDE, V., ZAPATA, J. & ZILHÃO, J. 2018. A tale of two gorges: Late Quaternary site formation and surface dynamics in the Mula basin (Murcia, Spain). *Quaternary International,* 485, 4-22.

ARAUJO, A. G. 2013. Bioturbation and the upward movement of sediment particles and archaeological materials: comments on Bueno et al. *Journal of Archaeological Science,* 40, 2124-2127.
ARNOLD, L. J. & ROBERTS, R. G. 2009. Stochastic modelling of multi-grain equivalent dose (De) distributions: Implications for OSL dating of sediment mixtures. *Quaternary Geochronology,* 4, 204-230.
ARNOLD, L. J., ROBERTS, R. G., GALBRAITH, R. F. & DELONG, S. 2009. A revised burial dose estimation procedure for optical dating of young and modern-age sediments. *Quaternary Geochronology,* 4, 306-325.
ASCOUGH, P., BIRD, M. I., BROCK, F., HIGHAM, T., MEREDITH, W., SNAPE, C. & VANE, C. H. 2009. Hydropyrolysis as a new tool for radiocarbon pre-treatment and the quantification of black carbon. *Quaternary Geochronology,* 4, 140-147.
ASCOUGH, P., BIRD, M. I., MEREDITH, W., WOOD, R., SNAPE, C. E., BROCK, F., HIGHAM, T. F., LARGE, D. & APPERLEY, D. 2010. Hydropyrolysis: implications for radiocarbon pretreatment and characterization of black carbon. *Radiocarbon,* 52, 1336-1350.
ASCOUGH, P. L., BIRD, M. I., MEREDITH, W., SNAPE, C., LARGE, D., TILSTON, E., APPERLEY, D., BERNABÉ, A. & SHEN, L. 2018. Dynamics of Charcoal Alteration in a Tropical Biome: A Biochar-Based Study. *Frontiers in Earth Science,* 6, 61.
ASCOUGH, P. L., BROCK, F., COLLINSON, M. E., PAINTER, J. D., LANE, D. W. & BIRD, M. I. 2020. Chemical characteristics of macroscopic pyrogenic carbon following millennial-scale environmental exposure. *Frontiers in Environmental Science*, 7, 203.
ASSCHER, Y. & BOARETTO, E. 2019. Charred micro-particles characterization in archaeological contexts: Identifying mixing between sediments with implications for stratigraphy. *Journal of Archaeological Science,* 107, 32-39.
ASSCHER, Y. & GOREN, Y. 2016. A Rapid On-Site Method for Micromorphological Block Impregnation and Thin Section Preparation. *Geoarchaeology,* 31, 324-331.
ATHANASSAS, C. D. & WAGNER, G. A. 2016. Geochronology beyond radiocarbon: optically stimulated luminescence dating of palaeoenvironments and archaeological sites. *Elements,* 12, 27-32.
AUBRY, T., DIMUCCIO, L. A., ALMEIDA, M., NEVES, M. J., ANGELUCCI, D. E. & CUNHA, L. 2011. Palaeoenvironmental forcing during the Middle–Upper Palaeolithic transition in central-western Portugal. *Quaternary Research,* 75, 66-79.
BAIN, J. H. & DRAPER, J. (eds.) 1997. *North Queensland Geology,* Australian Geological Survey Organisation.
BALCO, G. 2020a. A prototype transparent-middle-layer data management and analysis infrastructure for cosmogenic-nuclide exposure dating. *Geochronology,* 2, 169-175.
BALCO, G. 2020b. *Version 3 erosion rate calculator benchmarked, finally* [Online]. https://cosmognosis.wordpress.com/2020/10/10/version-3-erosion-rate-calculator-benchmarked-finally/: WordPress.com. [Accessed 30.11. 2022].
BALCO, G., STONE, J. O., LIFTON, N. A. & DUNAI, T. J. 2008. A complete and easily accessible means of calculating surface exposure ages or erosion rates from ^{10}Be and ^{26}Al measurements. *Quaternary geochronology,* 3, 174-195.
BALDOCK, J. A. & SMERNIK, R. J. 2002. Chemical composition and bioavailability of thermally altered Pinus resinosa (Red pine) wood. *Organic Geochemistry,* 33**,** 1093-1109.
BALEK, C. L. 2002. Buried artifacts in stable upland sites and the role of bioturbation: a review. *Geoarchaeology: An International Journal,* 17, 41-51.
BALESDENT, J., MARIOTTI, A. & GUILLET, B. 1987. Natural ^{13}C abundance as a tracer for studies of soil organic matter dynamics. *Soil biology and biochemistry,* 19, 25-30.
BALFE, P. E. 1979. Stratigraphic drilling report-GSQ Hughenden 7. *Queensland Government Mining Journal* 80, 282-293.
BALLARINI, M., WINTLE, A. & WALLINGA, J. 2006. Spatial variation of dose rate from beta sources as measured using single grains. *Ancient TL,* 24, 1-7.
BARBIERI, A., LEVEN, C., TOFFOLO, M. B., HODGINS, G. W. L., KIND, C.-J., CONARD, N. J. & MILLER, C. E. 2018. Bridging prehistoric caves with buried landscapes in the Swabian Jura (southwestern Germany). *Quaternary International,* 485, 23-43.
BARBONI, D., BONNEFILLE, R., ALEXANDRE, A. & MEUNIER, J.-D. 1999. Phytoliths as paleoenvironmental indicators, west side Middle Awash Valley, Ethiopia. *Palaeogeography, Palaeoclimatology, Palaeoecology,* 152, 87-100.
BARBONI, D., BREMOND, L. & BONNEFILLE, R. 2007. Comparative study of modern phytolith assemblages from inter-tropical Africa. *Palaeogeography, Palaeoclimatology, Palaeoecology,* 246, 454-470.
BARROWS, T. T., STONE, J. O., FIFIELD, L. K. & CRESSWELL, R. G. 2001. Late Pleistocene glaciation of the Kosciuszko massif, snowy mountains, Australia. *Quaternary Research,* 55, 179-189.
BATEMAN, M., BOULTER, C., CARR, A., FREDERICK, C., PETER, D. & WILDER, M. 2007b. Preserving the palaeoenvironmental record in drylands: bioturbation and its significance for luminescence-derived chronologies. *Sedimentary Geology,* 195, 5-19.

BATEMAN, M. D., BOULTER, C. H., CARR, A. S., FREDERICK, C. D., PETER, D. & WILDER, M. 2007a. Detecting post-depositional sediment disturbance in sandy deposits using optical luminescence. *Quaternary geochronology,* 2, 57-64.

BATEMAN, M. D., FREDERICK, C. D., JAISWAL, M. K. & SINGHVI, A. K. 2003. Investigations into the potential effects of pedoturbation on luminescence dating. *Quaternary Science Reviews,* 22, 1169-1176.

BELLOMO, R. V. 1993. A methodological approach for identifying archaeological evidence of fire resulting from human activities. *Journal of Archaeological Science,* 20, 525-553.

BENDER, M. M. 1971. Variations in the $^{13}C/^{12}C$ ratios of plants in relation to the pathway of photosynthetic carbon dioxide fixation. *Phytochemistry,* 10, 1239-1244.

BENNETT, C. L., BEUKENS, R. P., CLOVER, M. R., GOVE, H. E., LIEBERT, R. B., LITHERLAND, A., PURSER, K. H. & SONDHEIM, W. E. 1977. Radiocarbon dating using electrostatic accelerators: negative ions provide the key. *Science,* 198, 508-510.

BENVENUTO, M. L., HONAINE, M. F., OSTERRIETH, M. L. & MOREL, E. 2015. Differentiation of globular phytoliths in Arecaceae and other monocotyledons: morphological description for paleobotanical application. *Turkish Journal of Botany,* 39, 341-353.

BIANCHI, V., ZHOU, F., PISTELLATO, D., MARTIN, M., BOCCARDO, S. & ESTERLE, J. 2018. Mapping a coastal transition in braided systems: an example from the Precipice Sandstone, Surat Basin. *Australian Journal of Earth Sciences,* 65, 483-502.

BIERMAN, P. R. & CAFFEE, M. 2002. Cosmogenic exposure and erosion history of Australian bedrock landforms. *Geological Society of America Bulletin,* 114, 787-803.

BIERMAN, P. R. & NICHOLS, K. K. 2004. Rock to sediment slope to sea with 10 Be rates of landscape change. *Annual Review of Earth and Planetary Sciences,* 32, 215-255.

BIRD, M. 1997. Report on the archaeological survey and assessment of a proposed 66 kV Transmission Line, Richmond-Julia Creek, north west Queensland. *Unpublished report prepared for the North Queensland Electricity Corporation.* Townsville.

BIRD, M. 1998. Cultural heritage desktop study, Flinders River Dam pre-feasibility study, Richmond District, north Queensland. *Unpublished report prepared for McIntyre and Associates on behalf of the Department of Natural Resources, Queensland.* Townsville.

BIRD, M. 1999. Cultural heritage desktop study for a proposed NORQEB 66 kV Transmission Line, Hughenden-Richmond, north Queensland. *Unpublished report prepared for Sinclair Knight Merz on behalf of NORQEB.*

BIRD, M. 2000. Progress report #10 to Ergon Energy cultural heritage reconnaissance Mid-Western SWER powerline refurbishment project Richmond South SWER area April-June 2000. *Unpublished report prepared for Ergon Energy Corporation, Townsville and the Wanamara Traditional Owners.*

BIRD, M., AYLIFFE, L., FIFIELD, L., TURNEY, C., CRESSWELL, R., BARROWS, T. & DAVID, B. 1999a. Radiocarbon dating of "old" charcoal using a wet oxidation, stepped-combustion procedure. *Radiocarbon,* 41, 127-140.

BIRD, M., MOYO, C., VEENENDAAL, E., LLOYD, J. & FROST, P. 1999b. Stability of elemental carbon in a savanna soil. *Global biogeochemical cycles,* 13, 923-932.

BIRD, M. I. 2007. Radiocarbon Dating | Charcoal. *In:* ELIAS, S. A. (ed.) *Encyclopedia of Quaternary Science.* Oxford: Elsevier.

BIRD, M. I. & ASCOUGH, P. L. 2012. Isotopes in pyrogenic carbon: a review. *Organic Geochemistry,* 42, 1529-1539.

BIRD, M. I., BEAMAN, R. J., CONDIE, S. A., COOPER, A., ULM, S. & VETH, P. 2018. Palaeogeography and voyage modelling indicates early human colonization of Australia was likely from Timor-Roti. *Quaternary science reviews,* 191, 431-439.

BIRD, M. I., BRAND, M., DIEFENDORF, A. F., HAIG, J. L., HUTLEY, L. B., LEVCHENKO, V., RIDD, P. V., ROWE, C., WHINNEY, J. & WURSTER, C. M. 2019a. Identifying the 'savanna' signature in lacustrine sediments in northern Australia. *Quaternary Science Reviews,* 203, 233-247.

BIRD, M. I., CONDIE, S. A., O'CONNOR, S., O'GRADY, D., REEPMEYER, C., ULM, S., ZEGA, M., SALTRÉ, F. & BRADSHAW, C. J. A. 2019b. Early human settlement of Sahul was not an accident. *Scientific reports,* 9, 8220-10.

BIRD, M. I. & GRÖCKE, D. R. 1997. Determination of the abundance and carbon isotope composition of elemental carbon in sediments. *Geochimica et Cosmochimica Acta,* 61, 3413-3423.

BIRD, M. I., HAIG, J., HADEEN, X., RIVERA-ARAYA, M., WURSTER, C. M. & ZWART, C. 2020. Stable isotope proxy records in tropical terrestrial environments. *Palaeogeography, Palaeoclimatology, Palaeoecology,* 538, 109445.

BIRD, M. I., O'GRADY, D. & ULM, S. 2016. Humans, water, and the colonization of Australia. *Proceedings of the National Academy of Sciences of the United States of America,* 113, 11477-11482.

BIRD, M. I., TAYLOR, D. & HUNT, C. 2005. Palaeoenvironments of insular Southeast Asia during the Last Glacial Period: a savanna corridor in Sundaland? *Quaternary Science Reviews,* 24, 2228-2242.

BIRD, M. I., TURNEY, C. S. M., FIFIELD, L. K., JONES, R., AYLIFFE, L. K., PALMER, A., CRESSWELL, R. & ROBERTSON, S. 2002. Radiocarbon analysis of the early archaeological site of Nauwalabila I, Arnhem Land, Australia: implications for sample suitability and stratigraphic integrity. *Quaternary Science Reviews,* 21, 1061-1075.

BIRD, M. I., WYNN, J. G., SAIZ, G., WURSTER, C. M. & MCBEATH, A. 2015. The pyrogenic carbon cycle. *Annual Review of Earth and Planetary Sciences,* 43, 273-298.
BIRDSELL, J. B. 1977. The recalibration of a paradigm for the first peopling of Greater Australia. *Sunda and Sahul: Prehistoric Studies in Southeast Asia, Melanesia, and Australia*, 113-167.
BLAAUW, M. & CHRISTEN, J. A. 2011. Flexible paleoclimate age-depth models using an autoregressive gamma process. *Bayesian analysis,* 6, 457-474.
BLACKMAN, E. 1971. Opaline silica bodies in the range grasses of southern Alberta. *Canadian Journal of Botany,* 49, 769-781.
BLOG, M. S. 2013. *Examining Radiocarbon dating* [Online]. Available: https://matthew2262.wordpress.com/2013/02/18/examining-radiocarbon-dating/ [Accessed 31.05. 2022].
BLOOD, D., MITCHELL, A. & ADDISON, J. 2015. *Field Guide to Common Grasses of the. Southern Rangelands,* Perth, WA, Rangelands NRM.
BORRELLI, N., OSTERRIETH, M. & MARCOVECCHIO, J. 2008. Interrelations of vegetal cover, silicophytolith content and pedogenesis of Typical Argiudolls of the Pampean Plain, Argentina. *Catena,* 75, 146-153.
BØTTER-JENSEN, L., ANDERSEN, C., DULLER, G. A. & MURRAY, A. S. 2003. Developments in radiation, stimulation and observation facilities in luminescence measurements. *Radiation Measurements,* 37, 535-541.
BOUTTON, T. W. 1991. Stable carbon isotope ratios of natural materials: II. Atmospheric, terrestrial, marine, and freshwater environments. *In:* COLEMAN, D. C. (ed.) *Carbon Isotope Techniques.* Academic Press, 173-183
BOWDERY, D. 1989. Phytolith analysis: Introduction and applications. *In:* BECK, W., CLARKE, A. & HEAD, L. M. (eds.) *Plants in Australian Archaeology.* Anthropology Museum, University of Queensland, St. Lucia: Archaeology and Material Culture Studies in Anthropology. Tempus 1, 161-196.
BOWDERY, D., HART, D. M., LENTFER, C. & WALLIS, L. A. 2001. A universal phytolith key. *In:* MEUNIER, J. D. & COLIN, F. (eds.) *Phytoliths: Applications in Earth Sciences and Human History.* Lisse: AA Balkema, 267-278.
BOWDLER, S. 1977. The coastal colonisation of Australia. *In:* ALLEN, J., GOLSON, J. & JONES, R. (eds.) *Sunda and Sahul: Prehistoric Studies in Southeast Asia, Melanesia and Australia.* London: Academic Press, 205-246.
BOWLER, J., HOPE, G., JENNINGS, J., SINGH, G. & WALKER, D. 1976. Late quaternary climates of Australia and New Guinea. *Quaternary Research,* 6, 359-394.
BOWLER, J. & WASSON, R. 1984. Glacial age environments of inland Australia. *In:* VOGEL, J. C. (ed.) *Late Cainozoic palaeoclimates of the Southern Hemisphere.* Rotterdam: Balkema, 183-208.
BOWLER, J. M. 1976. Aridity in Australia: Age, origins and expression in aeolian landforms and sediments. *Earth-science reviews,* 12, 279-310.
BOWLER, J. M., GILLESPIE, R., JOHNSTON, H. & BOLJKOVAC, K. 2012. Wind v water: glacial maximum records from the Willandra Lakes. *Peopled landscapes: Archaeological and biogeographic approaches to landscapes,* 34**,** 271-296.
BOWLER, J. M. & HAMADA, T. 1971. Late Quaternary stratigraphy and radiocarbon chronology of water level fluctuations in Lake Keilambete, Victoria. *Nature,* 232, 330-332.
BOWLER, J. M., WYRWOLL, K.-H. & LU, Y. 2001. Variations of the northwest Australian summer monsoon over the last 300,000 years: the paleohydrological record of the Gregory (Mulan) Lakes System. *Quaternary International,* 83, 63-80.
BOWMAN, S. 1990. *Radiocarbon dating (Interpreting the Past)*, British Museum and University of California Press, pp.64.
BOYD, M. 2002. Identification of anthropogenic burning in the paleoecological record of the northern prairies: a new approach. *Annals of the Association of American Geographers,* 92, 471-487.
BOZARTH, S. R. 1992. Classification of opal phytoliths formed in selected dicotyledons native to the Great Plains. *In:* RAPP, G. & MULHOLLAND, S. C. (eds.) *Phytolith Systematics: Emerging Issues.* Boston, MA: Springer US, 193-214.
BRADSHAW, C. J. A., NORMAN, K., ULM, S., WILLIAMS, A. N., CLARKSON, C., CHADŒUF, J., LIN, S. C., JACOBS, Z., ROBERTS, R. G., BIRD, M. I., WEYRICH, L. S., HABERLE, S. G., O'CONNOR, S., LLAMAS, B., COHEN, T. J., FRIEDRICH, T., VETH, P., LEAVESLEY, M. & SALTRÉ, F. 2021. Stochastic models support rapid peopling of Late Pleistocene Sahul. *Nature Communications,* 12, 2440.
BRANDMEIER, M., KUHLEMANN, J., KRUMREI, I., KAPPLER, A. & KUBIK, P. 2011. New challenges for tafoni research. A new approach to understand processes and weathering rates. *Earth Surface Processes and Landforms,* 36, 839-852.
BRANDT, J. 1988. The Transformation of Rainfall Energy by a Tropical Rain Forest Canopy in Relation to Soil Erosion. *Journal of Biogeography,* 15, 41-48.
BRAUCHER, R., LIMA, C., BOURLÈS, D., GASPAR, J. & ASSAD, M. 2004. Stone-line formation processes documented by in situ-produced 10Be distribution, Jardim River basin, DF, Brazil. *Earth and Planetary Science Letters,* 222, 645-651.

BREMOND, L., ALEXANDRE, A., HÉLY, C. & GUIOT, J. 2005. A phytolith index as a proxy of tree cover density in tropical areas: calibration with Leaf Area Index along a forest–savanna transect in southeastern Cameroon. *Global and Planetary Change,* 45, 277-293.

BREMOND, L., ALEXANDRE, A., PEYRON, O. & GUIOT, J. 2008. Definition of grassland biomes from phytoliths in West Africa. *Journal of Biogeography,* 35, 2039-2048.

BREMOND, L., ALEXANDRE, A., VÉLA, E. & GUIOT, J. 2004. Advantages and disadvantages of phytolith analysis for the reconstruction of Mediterranean vegetation: an assessment based on modern phytolith, pollen and botanical data (Luberon, France). *Review of Palaeobotany and Palynology,* 129, 213-228.

BREMOND, L., BODIN, S., BENTALEB, I., FAVIER, C. & CANAL, S. 2017. Past tree cover of the Congo Basin recovered by phytoliths and $\delta^{13}C$ along soil profiles. *Quaternary International,* 434, 91-101.

BRIDGE, B. & ROSS, P. 1983. Water erosion in vegetated sand dunes at Cooloola, south-east Queensland. *Zeitschrift für Geomorphologie. Supplementband,* 45, 227-244.

BRIMHALL, G. H., CHADWICK, O. A., LEWIS, C. J., COMPSTON, W., WILLIAMS, I. S., DANTI, K. J., DIETRICH, W. E., POWER, M. E., HENDRICKS, D. & BRATT, J. 1992. Deformational mass transport and invasive processes in soil evolution. *Science,* 255, 695-702.

BROWN, D. A. 1984. Prospects and limits of a phytolith key for grasses in the central United States. *Journal of Archaeological Science,* 11, 345-368.

BRUTHANS, J., SOUKUP, J., VACULIKOVA, J., FILIPPI, M., SCHWEIGSTILLOVA, J., MAYO, A. L., MASIN, D., KLETETSCHKA, G. & RIHOSEK, J. 2014. Sandstone landforms shaped by negative feedback between stress and erosion. *Nature Geoscience,* 7, 597-601.

BUFFINGTON, J. M. 2012. Changes in Channel Morphology Over Human Time Scales. *In:* CHURCH, M., BIRON, P. M. & ROY, A. G. (eds.) *Gravel-Bed Rivers: Processes, Tools, Environments.* John Wiley & Sons, Ltd, 433-463.

BULL, W. B. 1990. Stream-terrace genesis: implications for soil development. *Geomorphology,* 3, 351-367.

BURROWS, M., HEIJNIS, H., GADD, P. & HABERLE, S. 2016. A new late Quaternary palaeohydrological record from the humid tropics of northeastern Australia. *Palaeogeography, Palaeoclimatology, Palaeoecology,* 451, 164-182.

BUTZER, K. W. 2008. Challenges for a cross-disciplinary geoarchaeology: The intersection between environmental history and geomorphology. *Geomorphology,* 101, 402-411.

CABANES, D. & SHAHACK-GROSS, R. 2015. Understanding fossil phytolith preservation: the role of partial dissolution in paleoecology and archaeology. *PloS one,* 10, e0125532.

CABANES, D., WEINER, S. & SHAHACK-GROSS, R. 2011. Stability of phytoliths in the archaeological record: a dissolution study of modern and fossil phytoliths. *Journal of Archaeological Science,* 38, 2480-2490.

CAHEN, D. & MOEYERSONS, J. 1977. Subsurface movements of stone artefacts and their implications for the prehistory of Central Africa. *Nature,* 266, 812-815.

CALEGARI, M. R., MADELLA, M., BRUSTOLIN, L. T., PESSENDA, L. C. R., BUSO JR, A. A., FRANCISQUINI, M. I., BENDASSOLLI, J. A. & VIDAL-TORRADO, P. 2017. Potential of soil phytoliths, organic matter and carbon isotopes for small-scale differentiation of tropical rainforest vegetation: a pilot study from the campos nativos of the Atlantic Forest in Espírito Santo State (Brazil). *Quaternary International,* 437, 156-164.

CALEGARI, M. R., MADELLA, M., VIDAL-TORRADO, P., PESSENDA, L. C. R. & MARQUES, F. A. 2013. Combining phytoliths and $\delta^{13}C$ matter in Holocene palaeoenvironmental studies of tropical soils: an example of an Oxisol in Brazil. *Quaternary International,* 287, 47-55.

CARSON, M. A. & KIRKBY, M. J. 1972. *Hillslope Form and Process*, Cambridge Geographical Studies No.3, Cambridge University Press, pp.475.

CARTER, J. A. 2009. Atmospheric carbon isotope signatures in phytolith-occluded carbon. *Quaternary International,* 193, 20-29.

CHARLTON, R. 2007. *Fundamentals of Fluvial Geomorphology,* London and New York, Routledge, pp.264.

CHAZAN, M., PORAT, N., SUMNER, T. A. & HORWITZ, L. K. 2013. The use of OSL dating in unstructured sands: The archaeology and chronology of the Hutton Sands at Canteen Kopje (Northern Cape Province, South Africa). *Archaeological and Anthropological Sciences,* 5, 351-363.

CHEN, S. T. & SMITH, S. Y. 2013. Phytolith variability in Zingiberales: a tool for the reconstruction of past tropical vegetation. *Palaeogeography, Palaeoclimatology, Palaeoecology,* 370, 1-12.

CHEN, S. T., SMITH, S. Y., SHELDON, N. D. & STRÖMBERG, C. A. 2015. Regional-scale variability in the spread of grasslands in the late Miocene. *Palaeogeography, Palaeoclimatology, Palaeoecology,* 437, 42-52.

CHUENG, K. F., COE, H. H. G., AUGUSTIN, C. H. R. R., MACARIO, K. D., RICARDO, S. D. F. & VASCONCELOS, A. M. C. 2019. Landscape paleodynamics in siliciclastic domains with the use of phytoliths, sponge spicules and carbon isotopes: The case of southern Espinhaço Mountain Range, Minas Gerais, Brazil. *Journal of South American Earth Sciences,* 95, 102232.

CLARK, R. L., EAST, T. J., GUPPY, J., JOHNSTON, A., LEANEY, F., MCBRIDE, P. & WASSON, R. J. 1992. Late Quaternary Stratigraphy of the Magela plain. *In:* WASSON, R. J. (ed.) *Modern sedimentation and late Quaternary evolution of the Magela plain.* Darwin, NT: NTU Printing/Publishing Services, 28-80.

CLARKE, J. 2003. The occurrence and significance of biogenic opal in the regolith. *Earth-Science Reviews,* 60, 175-194.

CLARKSON, C., JACOBS, Z., MARWICK, B., FULLAGAR, R., WALLIS, L., SMITH, M., ROBERTS, R. G., HAYES, E., LOWE, K., CARAH, X., FLORIN, S. A., MCNEIL, J., COX, D., ARNOLD, L. J., HUA, Q., HUNTLEY, J., BRAND, H. E. A., MANNE, T., FAIRBAIRN, A., SHULMEISTER, J., LYLE, L., SALINAS, M., PAGE, M., CONNELL, K., PARK, G., NORMAN, K., MURPHY, T. & PARDOE, C. 2017. Human occupation of northern Australia by 65,000 years ago. *Nature,* 547, 306-306.

CLARKSON, C., SMITH, M., MARWICK, B., FULLAGAR, R., WALLIS, L. A., FAULKNER, P., MANNE, T., HAYES, E., ROBERTS, R. G., JACOBS, Z., CARAH, X., LOWE, K. M., MATTHEWS, J. & FLORIN, S. A. 2015. The archaeology, chronology and stratigraphy of Madjedbebe (Malakunanja II): A site in northern Australia with early occupation. *Journal of Human Evolution,* 83, 46-64.

CLARKSON, C. & WALLIS, L. 2003. The search for El Niño/Southern Oscillation in archaeological sites: Recent phytolith analysis at Jugali-ya rock shelter, Wardaman Country, Australia. *Phytolith and starch research in the Australian-Pacific-Asian regions: The state of the art*, 137-152.

COCKBURN, H. A. & SUMMERFIELD, M. A. 2004. Geomorphological applications of cosmogenic isotope analysis. *Progress in Physical Geography: Earth and Environment,* 28, 1-42.

CODILEAN, A. T., FÜLÖP, R. H., MUNACK, H., WILCKEN, K. M., COHEN, T. J., ROOD, D. H., FINK, D., BARTLEY, R., CROKE, J. & FIFIELD, L. K. 2021. Controls on denudation along the East Australian continental margin. *Earth-Science Reviews,* 214, 103543.

COE, H. H., MACARIO, K., GOMES, J. G., CHUENG, K. F., OLIVEIRA, F., GOMES, P. R., CARVALHO, C., LINARES, R., ALVES, E. & SANTOS, G. M. 2014. Understanding Holocene variations in the vegetation of Sao Joao River basin, southeastern coast of Brazil, using phytolith and carbon isotopic analyses. *Palaeogeography, Palaeoclimatology, Palaeoecology,* 415, 59-68.

COHEN-OFRI, I., WEINER, L., BOARETTO, E., MINTZ, G. & WEINER, S. 2006. Modern and fossil charcoal: aspects of structure and diagenesis. *Journal of Archaeological Science,* 33, 428-439.

COHEN, T., NANSON, G., JANSEN, J. D., JONES, B., JACOBS, Z., LARSEN, J., MAY, J.-H., TREBLE, P., PRICE, D. & SMITH, A. 2012. Late Quaternary mega-lakes fed by the northern and southern river systems of central Australia: varying moisture sources and increased continental aridity. *Palaeogeography, Palaeoclimatology, Palaeoecology,* 356, 89-108.

COHEN, T. J. & NANSON, G. C. 2007. Mind the gap: an absence of valley-fill deposits identifying the Holocene hypsithermal period of enhanced flow regime in southeastern Australia. *The Holocene,* 17, 411-418.

COHEN, T. J., NANSON, G. C., JANSEN, J. D., JONES, B. G., JACOBS, Z., TREBLE, P., PRICE, D. M., MAY, J.-H., SMITH, A. M. & AYLIFFE, L. K. 2011. Continental aridification and the vanishing of Australia's megalakes. *Geology,* 39, 167-170.

COLLURA, L. V. & NEUMANN, K. 2017. Wood and bark phytoliths of West African woody plants. *Quaternary International,* 434, 142-159.

CONEDERA, M., TINNER, W., NEFF, C., MEURER, M., DICKENS, A. F. & KREBS, P. 2009. Reconstructing past fire regimes: methods, applications, and relevance to fire management and conservation. *Quaternary Science Reviews,* 28, 555-576.

COOK, A., BRYAN, S. & DRAPER, J. 2013. Post-orogenic Mesozoic basins and magmatism. *In:* JELL, P. (ed.) *Geology of Queensland*, Geological Survey of Queensland, Australia, 515-575.

COOKE, P. 1995. Draft Report: Richmond Land Purchase. Unpublished report to the Central Queensland Land Council.

COPE, M. J. & CHALONER, W. G. 1980. Fossil charcoal as evidence of past atmospheric composition. *Nature,* 283, 647-649.

COPPOLA, A. I. & DRUFFEL, E. R. 2016. Cycling of black carbon in the ocean. *Geophysical Research Letters,* 43, 4477-4482.

CORBETT, L. B., BIERMAN, P. R. & ROOD, D. H. 2016b. An approach for optimizing in situ cosmogenic 10Be sample preparation. *Quaternary Geochronology,* 33, 24-34.

CORNELIS, J.-T., DUMON, M., TOLOSSA, A. R., DELVAUX, B., DECKERS, J. & VAN RANST, E. 2014. The effect of pedological conditions on the sources and sinks of silicon in the Vertic Planosols in south-western Ethiopia. *Catena,* 112, 131-138.

COTRUFO, M. F., BOOT, C. M., KAMPF, S., NELSON, P. A., BROGAN, D. J., COVINO, T., HADDIX, M. L., MACDONALD, L. H., RATHBURN, S. & RYAN-BUKETT, S. 2016. Redistribution of pyrogenic carbon from hillslopes to stream corridors following a large montane wildfire. *Global Biogeochemical Cycles,* 30, 1348-1355.

COTTON, J. M., SHELDON, N. D. & STRÖMBERG, C. A. 2012. High-resolution isotopic record of C4 photosynthesis in a Miocene grassland. *Palaeogeography, Palaeoclimatology, Palaeoecology,* 337, 88-98.

COVENTRY, R. J. 1976. Abandoned shorelines and the late quaternary history of Lake George, New South Wales. *Journal of the Geological Society of Australia,* 23, 249-273.

CRESSLER, W. L. 2001. Evidence of earliest known wildfires. *Palaios,* 16, 171-174.

CRIFÒ, C. & STRÖMBERG, C. A. 2020. Small-scale spatial resolution of the soil phytolith record in a rainforest and a dry forest in Costa Rica: applications to the deep-time fossil phytolith record. *Palaeogeography, Palaeoclimatology, Palaeoecology,* 537, 109107.

CROKE, J., JANSEN, J. D., AMOS, K. & PIETSCH, T. J. 2011. A 100 ka record of fluvial activity in the Fitzroy River Basin, tropical northeastern Australia. *Quaternary Science Reviews,* 30, 1681-1695.

CROPPER, D. 2018. Excavations at Jundaru (HN-A9) Rockshelter. *In:* CROPPER, D. & LAW, B. W. (eds.) *Rockshelter Excavations in the East Hamersley Range, Pilbara Region, Western Australia.* Summertown, Oxford: Archaeopress Publishing Ltd, 91-171.

CROTHERS, L. 1997. A documentation of Aboriginal cultural heritage sites located in the Richmond region, northwest Queensland. *Unpublished report prepared for the Central Queensland Aboriginal Land Council.*

DALAN, R. A. & BANERJEE, S. K. 1998. Solving archaeological problems using techniques of soil magnetism. *Geoarchaeology: An International Journal,* 13, 3-36.

DALSGAARD, K. & ODGAARD, B. V. 2001. Dating sequences of buried horizons of podzols developed in wind-blown sand at Ulfborg, Western Jutland. *Quaternary International,* 78, 53-60.

DARVILL, C. M. 2013. Cosmogenic nuclide analysis. *In: Geomorphological Techniques.* London, UK: British Society for Geomorphology, 1-25.

DARWIN, C. 1809-1882 (1959). *The voyage of the Beagle,* London: New York: Dent, Dutton.

DATTA, R. 2021. To extinguish or not to extinguish: The role of forest fire in nature and soil resilience. *Journal of King Saud University - Science,* 33, 101539.

DAVID, B., ROBERTS, R. G., MAGEE, J., MIALANES, J., TURNEY, C., BIRD, M., WHITE, C., FIFIELD, L. K. & TIBBY, J. 2007. Sediment mixing at Nonda Rock: investigations of stratigraphic integrity at an early archaeological site in northern Australia and implications for the human colonisation of the continent. *Journal of Quaternary Science,* 22, 449-479.

DAVIDSON, D. S. 1935. Archaeological Problems of Northern Australia. *The Journal of the Royal Anthropological Institute of Great Britain and Ireland,* 65, 145-183.

DAVIDSON, I., CLIFF, R. & SULIVAN, T. 1991. Burke River Pipeline. A survey on the impact of archaeological sites. *Unpublished report to Cyprus Gold Australia Corporation.*

DAVIDSON, I. & FIFE, R. 1994. Archaeological Investigations: Osborne Project, North West Central Queensland. *Unpublished report. Department of Archaeology and Palaeoanthropology, University of New England, Armidale.*

DAVIDSON, I., SUTTON, S. & GALE, S. 1993. The human occupation of Cuckadoo 1 Rockshelter, northwest central Queensland. *In:* SMITH, M., SPRIGGS, M. & FANKHAUSER, B. (eds.) *Sahul in Review. Occasional Papers in Prehistory No. 24.* Canberra: Research School of Pacific and Asian Studies, The Australian National University, 164-172.

DAWSON, T., MCTAVISH, K. & ELLIS, B. 2004. Diets and foraging behaviour of red and eastern grey kangaroos in arid shrub land: is feeding behaviour involved in the range expansion of the eastern grey kangaroo into the arid zone? *Australian Mammalogy,* 26, 169-178.

DE CARITAT, P. & BRAUN, J. 1992. Cyclic development of sedimentary basins at convergent plate margins − 1. Structural and tectono-thermal evolution of some gondwana basins of eastern Australia. *Journal of Geodynamics,* 16, 241-282.

DE DECKKER, P. 1982. Holocene ostracods, other invertebrates and fish remains from cores of four maar lakes in southeastern Australia. *Proceedings of the Royal Society of Victoria,* 94, 183-220.

DE DECKKER, P., ARNOLD, L. J., VAN DER KAARS, S., BAYON, G., STUUT, J.-B. W., PERNER, K., LOPES DOS SANTOS, R., UEMURA, R. & DEMURO, M. 2019. Marine Isotope Stage 4 in Australasia: A full glacial culminating 65,000 years ago – Global connections and implications for human dispersal. *Quaternary Science Reviews,* 204, 187-207.

DE VRIES, H. & BARENDSEN, G. 1954. Measurements of age by the carbon-14 technique. *Nature,* 174, 1138-1141.

DEARING, J. 1994. *Environmental magnetic susceptibility. Using the Bartington MS2 system,* Kenilworth, Chi Publications.

DEARING, J., BIRD, P., DANN, R. & BENJAMIN, S. F. 1997. Secondary ferrimagnetic minerals in Welsh soils: a comparison of mineral magnetic detection methods and implications for mineral formation. *Geophysical Journal International,* 130, 727-736.

DEARING, J. A., DANN, R., HAY, K., LEES, J., LOVELAND, P., MAHER, B. A. & O'GRADY, K. 1996. Frequency-dependent susceptibility measurements of environmental materials. *Geophysical Journal International,* 124, 228-240.

DEMEYER, A., NKANA, J. V. & VERLOO, M. 2001. Characteristics of wood ash and influence on soil properties and nutrient uptake: an overview. *Bioresource Technology,* 77, 287-295.

DENIRO, M. J. & EPSTEIN, S. 1978. Influence of diet on the distribution of carbon isotopes in animals. *Geochimica et cosmochimica acta,* 42, 495-506.

DERRY, L. A., KURTZ, A. C., ZIEGLER, K. & CHADWICK, O. A. 2005. Biological control of terrestrial silica cycling and export fluxes to watersheds. *Nature,* 433, 728-731.

DESJARDINS, T., MARIOTTI, A., GIRARDIN, C. & CHAUVEL, A. 1996. Changes of the forest-savanna boundary in Brazilian Amazonia during the Holocene revealed by stable isotope ratios of soil organic carbon. *Oecologia,* 108, 749-756.

DEVRIENDT, L. S. J. 2011. *Late quaternary environment of Palaeolake Carpentaria inferred from the chemistry of ostracod valves.* Master of Science - Research, University of Wollongong.
DICKSON, J. & COLEMAN, M. 1990. Changes in carbon and oxygen isotope composition during limestone diagenesis. *In:* TUCKER, M. E. & BATHURST, R. G. C. (eds.) *Carbonate Diagenesis*, Blackwell Scientific Publications, 259-270.
DÍEZ-PASTOR, J.-F., LATORRE-CARMONA, P., ARNAIZ-GONZÁLEZ, Á., RUIZ-PÉREZ, J. & ZURRO, D. 2020. "You Are Not My Type": An Evaluation of Classification Methods for Automatic Phytolith Identification. *Microscopy and Microanalysis,* 26, 1158-1167.
DOMETT, K., WALLIS, L. A., KYNUNA, D., KYNUNA, A. & SMITH, H. 2006. Late Holocene human remains from northwest Queensland, Australia: archaeology and palaeopathology. *Archaeology in Oceania,* 41, 25-36.
DONNELLY, T. & WASSON, R. 1989. CLIMANZ 3: Proceedings of the Third Symposium on the Late Quaternary Climatic History of Australasia. Parkville, Vic., 28-29, November 1987: CSIRO, Division of Water Resources, Canberra, ACT, pp.158.
DORRONSORO, C. & AGUILAR, J. El proceso de iluviación de arcilla. Anales de edafologia y agrobiologia, 1988. 311-350.
DORTCH, C. E. 1986. Excavations outside the Former (North) Entrance to Devil's Lair, Southwestern Australia. *Australian Archaeology*, 62-69.
DORTCH, J., BALME, J., MCDONALD, J., MORSE, K., O'CONNOR, S. & VETH, P. 2019. Settling the West: 50 000 years in a changing land. *Journal of the Royal Society of Western Australia,* 102, 30-44.
DRAPER, J. J. & MINES, Q. D. O. N. R. A. 2002. *Geology of the Cooper and Eromanga basins, Queensland* Brisbane, Queensland Department of Natural Resources and Mines, pp. 93.
DRISCOLL, K., ALCAINA, J., ÉGÜEZ, N., MANGADO, X., FULLOLA, J.-M. & TEJERO, J.-M. 2016. Trampled under foot: A quartz and chert human trampling experiment at the Cova del Parco rock shelter, Spain. *Quaternary International,* 424, 130-142.
DULLER, G. 2003. Distinguishing quartz and feldspar in single grain luminescence measurements. *Radiation measurements,* 37, 161-165.
DULLER, G. A. 2004. Luminescence dating of Quaternary sediments: recent advances. *Journal of Quaternary Science,* 19, 183-192.
DULLER, G. A. 2008. Single-grain optical dating of Quaternary sediments: why aliquot size matters in luminescence dating. *Boreas,* 37, 589-612.
DUNBAR, G., DICKENS, G. & CARTER, R. 2000. Sediment flux across the Great Barrier Reef Shelf to the Queensland Trough over the last 300 ky. *Sedimentary Geology,* 133, 49-92.
DUNN, R. E., STRÖMBERG, C. A. E., & LE, T.-Y. 2015. Light environment and epidermal cell morphology in grasses. *International Journal of Plant Sciences,* 176, 832-847.
EARGLE, D. H. 1940. The relations of soils and surface in the South Carolina Piedmont. *Science,* 91**,** 337-338.
ECKMEIER, E., VAN DER BORG, K., TEGTMEIER, U., SCHMIDT, M. W. & GERLACH, R. 2009. Dating charred soil organic matter: comparison of radiocarbon ages from macrocharcoals and chemically separated charcoal carbon. *Radiocarbon,* 51, 437-443.
EHLERINGER, J. R. & CERLING, T. E. 2002. C3 and C4 Photosynthesis. *In:* MOONEY, H. A. & CANADELL, J. G. (eds.) *Encyclopedia of Global Environmental Change.* Chichester: John Wiley & Sons, Ltd, 186-190.
ELBAUM, R., WEINER, S., ALBERT, R. M. & ELBAUM, M. 2003. Detection of burning of plant materials in the archaeological record by changes in the refractive indices of siliceous phytoliths. *Journal of Archaeological Science,* 30, 217-226.
ELLWOOD, B. B., PETRUSO, K. M., HARROLD, F. B. & SCHULDENREIN, J. 1997. High-resolution paleoclimatic trends for the Holocene identified using magnetic susceptibility data from archaeological excavations in caves. *Journal of Archaeological Science,* 24, 569-573.
ENACHE, M. D. & CUMMING, B. F. 2006. Tracking recorded fires using charcoal morphology from the sedimentary sequence of Prosser Lake, British Columbia (Canada). *Quaternary Research,* 65, 282-292.
ENGLISH, P., SPOONER, N., CHAPPELL, J., QUESTIAUX, D. & HILL, N. 2001. Lake Lewis basin, central Australia: environmental evolution and OSL chronology. *Quaternary International,* 83, 81-101.
EPSTEIN, E. 1999. Silicon. *Annual review of plant biology,* 50, 641-664.
EREN, M. I., DURANT, A., NEUDORF, C., HASLAM, M., SHIPTON, C., BORA, J., KORISETTAR, R. & PETRAGLIA, M. 2010. Experimental examination of animal trampling effects on artifact movement in dry and water saturated substrates: a test case from South India. *Journal of Archaeological Science,* 37, 3010-3021.
EVANS, P. 1980. Geology of the Galilee Basin. *The geology and geophysics of northeastern Australia: Geological Society of Australia,* 2, 299-305.
EYRE, J. K. 1997. Frequency dependence of magnetic susceptibility for populations of single-domain grains. *Geophysical Journal International,* 129, 209-211.
FAIRBRIDGE, R. W. & FINKL JR, C. W. 1984. Tropical stone lines and podzolized sand plains as paleoclimatic indicators for weathered cratons. *Quaternary Science Reviews,* 3, 41-72.

FARQUHAR, G. D., EHLERINGER, J. R. & HUBICK, K. T. 1989. Carbon isotope discrimination and photosynthesis. *Annual review of plant biology,* 40, 503-537.
FARQUHAR, G. D., VON CAEMMERER, S. V. & BERRY, J. A. 1980. A biochemical model of photosynthetic CO2 assimilation in leaves of C3 species. *Planta,* 149, 78-90.
FEBRUARY, E. C. & HIGGINS, S. I. 2010. The distribution of tree and grass roots in savannas in relation to soil nitrogen and water. *South African Journal of Botany,* 76, 517-523.
FENG, Z. D., RAN, M. & YANG, Q. 2013. Geomorphological and sedimentological precautions in radiocarbon dating of eolian and lacustrine sequences in arid Asia. *Quaternary International,* 286, 126-137.
FIELD, J. H., KEALHOFER, L., COSGROVE, R. & COSTER, A. C. 2016. Human-environment dynamics during the Holocene in the Australian Wet Tropics of NE Queensland: A starch and phytolith study. *Journal of Anthropological Archaeology,* 44, 216-234.
FISHKIS, O., INGWERSEN, J., LAMERS, M., DENYSENKO, D. & STRECK, T. 2010. Phytolith transport in soil: a field study using fluorescent labelling. *Geoderma,* 157, 27-36.
FISHKIS, O., INGWERSEN, J. & STRECK, T. 2009. Phytolith transport in sandy sediment: experiments and modeling. *Geoderma,* 151, 168-178.
FITZSIMMONS, K. E. & BARROWS, T. T. 2010. Holocene hydrologic variability in temperate southeastern Australia: an example from Lake George, New South Wales. *The Holocene,* 20, 585-597.
FITZSIMMONS, K. E., COHEN, T. J., HESSE, P. P., JANSEN, J., NANSON, G. C., MAY, J.-H., BARROWS, T. T., HABERLAH, D., HILGERS, A., KELLY, T., LARSEN, J., LOMAX, J. & TREBLE, P. 2013. Late Quaternary palaeoenvironmental change in the Australian drylands. *Quaternary Science Reviews,* 74, 78-96.
FITZSIMMONS, K. E., RHODES, E. J., MAGEE, J. W. & BARROWS, T. T. 2007. The timing of linear dune activity in the Strzelecki and Tirari Deserts, Australia. *Quaternary Science Reviews,* 26, 2598-2616.
FLORIN, S. A., FAIRBAIRN, A. S., NANGO, M., DJANDJOMERR, D., MARWICK, B., FULLAGAR, R., SMITH, M., WALLIS, L. A. & CLARKSON, C. 2020. The first Australian plant foods at Madjedbebe, 65,000–53,000 years ago. *Nature communications,* 11, 1-8.
FOLK, R. L. 1980. *Petrology of Sedimentary Rocks,* Austin, Texas, Hemphill Pub. Co.
FÖLSTER, H., KALK, E. & MOSHREFI, N. 1971. Complex pedogenesis of ferrallitic savanna soils in South Sudan. *Geoderma,* 6, 135-149.
FREDLUND, G. G. 1993. Paleoenvironmental interpretations of stable carbon, hydrogen, and oxygen isotopes from opal phytoliths, Eustis Ash Pit, Nebraska. *MASCA research papers in science and archaeology,* 10, 37-46.
FREDLUND, G. G. & TIESZEN, L. L. 1997. Phytolith and carbon isotope evidence for late Quaternary vegetation and climate change in the southern Black Hills, South Dakota. *Quaternary Research,* 47, 206-217.
FREDLUND, G. G. & TIESZEN, L. T. 1994. Modern phytolith assemblages from the North American Great Plains. *Journal of Biogeography*, 21, 321-335.
FREI, E. & CLINE, M. G. 1949. Profile studies of normal soils of New York: II. Micromorphological studies of the gray-brown podzolic—brown podzolic soil sequence. *Soil Science,* 68, 333-344.
FRY, B. & SHERR, E. B. 1989. $\delta^{13}C$ Measurements as Indicators of Carbon Flow in Marine and Freshwater Ecosystems. *In:* RUNDEL, P. W., EHLERINGER, J. R. & NAGY, K. A. (eds.) *Stable Isotopes in Ecological Research. Ecological Studies.* New York: Springer, 196-229.
FUJIOKA, T. & CHAPPELL, J. 2011. Desert landscape processes on a timescale of millions of years, probed by cosmogenic nuclides. *Aeolian Research,* 3, 157-164.
FULLAGAR, R. & WALLIS, L. A. 2012. Usewear and phytoliths on bedrock grinding patches, Pilbara, north-western Australia. *The Artefact: the Journal of the Archaeological and Anthropological Society of Victoria,* 35, 75-87.
GABET, E. J., REICHMAN, O. & SEABLOOM, E. W. 2003. The effects of bioturbation on soil processes and sediment transport. *Annual Review of Earth and Planetary Sciences,* 31, 249-273.
GAGAN, M. K., HENDY, E. J., HABERLE, S. G. & HANTORO, W. S. 2004. Post-glacial evolution of the Indo-Pacific warm pool and El Nino-Southern Oscillation. *Quaternary International,* 118, 127-143.
GALBRAITH, R., ROBERTS, R. & YOSHIDA, H. 2005. Error variation in OSL palaeodose estimates from single aliquots of quartz: a factorial experiment. *Radiation Measurements,* 39, 289-307.
GALBRAITH, R. F. 1988. Graphical Display of Estimates Having Differing Standard Errors. *Technometrics,* 30**,** 271-281.
GALBRAITH, R. F. & ROBERTS, R. G. 2012. Statistical aspects of equivalent dose and error calculation and display in OSL dating: an overview and some recommendations. *Quaternary Geochronology,* 11, 1-27.
GALBRAITH, R. F., ROBERTS, R. G., LASLETT, G. M., YOSHIDA, H. & OLLEY, J. M. 1999. Optical dating of single and multiple grains of quartz from Jinmium rock shelter, northern Australia: Part I, experimental design and statistical models. *Archaeometry,* 41, 339-364.
GALLEGO, L. & DISTEL, R. A. 2004. Phytolith assemblages in grasses native to Central Argentina. *Annals of Botany,* 94**,** 865-874.
GALLOWAY, R. 1965. Late quaternary climates in Australia. *The Journal of Geology,* 73, 603-618.
GARNIER, A., NEUMANN, K., EICHHORN, B. & LESPEZ, L. 2013. Phytolith taphonomy in the middle-to late-Holocene fluvial sediments of Ounjougou (Mali, West Africa). *The Holocene,* 23**,** 416-431.

GILLESPIE, R., HAMMOND, A., GOH, K., TONKIN, P., LOWE, D., SPARKS, R. & WALLACE, G. 1992. AMS dating of a late Quaternary tephra at Graham's Terrace, New Zealand. *Radiocarbon,* 34, 21-27.

GIMENO, L., DRUMOND, A., NIETO, R., TRIGO, R. M. & STOHL, A. 2010. On the origin of continental precipitation. *Geophysical Research Letters,* 37, L13804.

GLIGANIC, L. A., COHEN, T. J., SLACK, M. & FEATHERS, J. K. 2016. Sediment mixing in aeolian sandsheets identified and quantified using single-grain optically stimulated luminescence. *Quaternary Geochronology,* 32**,** 53-66.

GLIGANIC, L. A., MAY, J. H. & COHEN, T. J. 2015. All mixed up: Using single-grain equivalent dose distributions to identify phases of pedogenic mixing on a dryland alluvial fan. *Quaternary International,* 362, 23-33.

GOERGEN, E. & DAEHLER, C. C. 2001. Reproductive ecology of a native Hawaiian grass (Heteropogon contortus; Poaceae) versus its invasive alien competitor (Pennisetum setaceum; Poaceae). *International Journal of Plant Sciences,* 162, 317-326.

GOLSON, J., HART, D. M. & WALLIS, L. A. 2003. *Phytolith and starch research in the Australian-Pacific-Asian regions: the state of the art. Papers from a conference held at the ANU, August 2001, Canberra, Australia,* Canberra, ACT, Pandanus Books, Research School of Pacific and Asian Studies.

GORECKI, P. & GRANT, M. Grinding patches from the Croydon region, Gulf of Carpentaria. Archaeology in the North: Proceedings of the 1993 Australian Archaeological Association Conference, 1994. North Australia Research Unit (ANU), 227-46.

GORECKI, P., GRANT, M. & SALMON, M. 1992. The 1992 archaeological surveys on Esmeralda Station, Gulf of Carpentaria: preliminary results. *Queensland Archaeological Research,* 9, 54-58.

GORECKI, P., GRANT, M. & SALMON, M. 1996. Rock art from the Gregory Range, Gulf of Carpentaria. *In:* ULM, S., LILLEY, I. & ROSS , A. (eds.) *Australian Archaeology '95: Proceedings of the 1995 Australian Archaeological Association Annual Conference.* St Lucia, Anthropology Museum: University of Queensland. Tempus 6, 219-229.

GOSSE, J. C. & KLEIN, J. 2020. Terrestrial cosmogenic nuclide dating. *In:* RINK, W. J. & THOMPSON, J. (eds.) *Encyclopedia of Scientific Dating Methods.* Dordrecht: Springer Netherlands.

GOSSE, J. C. & PHILLIPS, F. M. 2001. Terrestrial in situ cosmogenic nuclides: theory and application. *Quaternary Science Reviews,* 20, 1475-1560.

GOUDIE, A. & VILES, H. A. 1997. *Salt Weathering Hazards*, Wiley & Sons Ltd, pp. 256.

GRAY, A. R. G. 1977. Stratigraphic drilling in the Hughenden 1:250000 sheet area, 1974-75. *Queensland Government Mining Journal,* 78, 382-892.

GUNN, J. (ed.) 2003. *Encyclopedia of Caves and Karst Science,* Great Britain: Fitzroy Dearborn.

GRIFFITHS, M. L., DRYSDALE, R. N., GAGAN, M., ZHAO, J.-X., AYLIFFE, L., HELLSTROM, J. C., HANTORO, W., FRISIA, S., FENG, Y.-X. & CARTWRIGHT, I. 2009. Increasing Australian–Indonesian monsoon rainfall linked to early Holocene sea-level rise. *Nature Geoscience,* 2, 636-639.

GRIFFITHS, M. L., DRYSDALE, R. N., GAGAN, M. K., FRISIA, S., ZHAO, J.-X., AYLIFFE, L. K., HANTORO, W. S., HELLSTROM, J. C., FISCHER, M. J. & FENG, Y.-X. 2010a. Evidence for Holocene changes in Australian–Indonesian monsoon rainfall from stalagmite trace element and stable isotope ratios. *Earth and Planetary Science Letters,* 292, 27-38.

GRIFFITHS, M. L., DRYSDALE, R. N., VONHOF, H. B., GAGAN, M. K., ZHAO, J.-X., AYLIFFE, L. K., HANTORO, W. S., HELLSTROM, J. C., CARTWRIGHT, I. & FRISIA, S. 2010b. Younger Dryas–Holocene temperature and rainfall history of southern Indonesia from δ18O in speleothem calcite and fluid inclusions. *Earth and Planetary Science Letters,* 295, 30-36.

GRIMES, K. 1979. The stratigraphic sequence of old land surfaces in northern Queensland. *Bureau of Mineral Resources Australian Journal of Geology and Geophysics,* 4, 33-46.

GRIMES, K. & DOUTCH, H. 1978. The late Cainozoic evolution of the Carpentaria Plains, north Queensland. *BMR Journal of Australian Geology and Geophysics,* 3, 101-112.

GRINDROD, J., MOSS, P. & KAARS, S. V. D. 1999. Late Quaternary cycles of mangrove development and decline on the north Australian continental shelf. *Journal of Quaternary Science: Published for the Quaternary Research Association,* 14, 465-470.

GRINDROD, J. F., MOSS, P. & VAN DER KAARS, S. 2002. Late Quaternary mangrove pollen records from continental shelf and ocean cores in the North Australian-Indonesian region. *Advances in Geoecology, Special issue: Bridging Wallace's Line: the environmental and cultural history and dynamics of the Australian-Southeast Asian region,* No.34, 119-146.

GROOM, K. M., ALLEN, C. D., MOL, L., PARADISE, T. R. & HALL, K. 2015. Defining tafoni: Re-examining terminological ambiguity for cavernous rock decay phenomena. *Progress in Physical Geography,* 39, 775-793.

GUNN, R. G., DOUGLAS, L. C. & WHEAR, R. L. 2020. Rockshelter development on the Arnhem Land plateau (Australia) and its implications for rock art research. *Rock Art Research,* 37, 19-34.

GURALNIK, B., LI, B., JAIN, M., CHEN, R., PARIS, R. B., MURRAY, A. S., LI, S.-H., PAGONIS, V., VALLA, P. G. & HERMAN, F. 2015. Radiation-induced growth and isothermal decay of infrared-stimulated luminescence from feldspar. *Radiation Measurements,* 81, 224-231.

HAJDAS, I., ASCOUGH, P., GARNETT, M. H., FALLON, S. J., PEARSON, C. L., QUARTA, G., SPALDING, K. L., YAMAGUCHI, H. & YONEDA, M. 2021. Radiocarbon dating. *Nature Reviews Methods Primers,* 1, 62.

HALFEN, A. & HASIOTIS, S. Downward thinking: rethinking the" up" in soil bioturbation. 19th World Congress of Soil Science, Soil Solutions for a Changing World, 2010. Citeseer, 1-6.

HALL, G., WOODBORNE, S. & SCHOLES, M. 2008. Stable carbon isotope ratios from archaeological charcoal as palaeoenvironmental indicators. *Chemical Geology,* 247, 384-400.

HAMMES, K., SCHMIDT, M. W., SMERNIK, R. J., CURRIE, L. A., BALL, W. P., NGUYEN, T. H., LOUCHOUARN, P., HOUEL, S., GUSTAFSSON, Ö. & ELMQUIST, M. 2007. Comparison of quantification methods to measure fire-derived (black/elemental) carbon in soils and sediments using reference materials from soil, water, sediment and the atmosphere. *Global Biogeochemical Cycles,* 21, GB3016.

HARDEN, C. 2004. Stream terraces. *In:* GOUDIE, A. S. (ed.) *Encyclopedia of Geomorphology.* London and New York: Routledge.

HART, D. 1988. A safe method for the extraction of plant opal from sediments. *Search,* 19, 293-294.

HART, D. & HUMPHREYS, G. The mobility of phytoliths in soils; pedological considerations. First European meeting on phytolith research. Centro de Ciencias Medioambientales del Con sejo Superior de Investigaciones Cientificas Serrano, Madrid, 1997. 93-100.

HART, D. M. & HUMPHREYS, G. S. 2003. Phytolith depth functions in surface regolith materials. *In:* ROACH, I. C. (ed) *Advances in Regolith.* Bentley, Australia: Cooperative Research Centre for Landscape Environments and Mineral Exploration, 159-163.

HART, T. C. 2015. Phytoliths: the storytelling stones inside plants: these microscopic structures, which arise from silica present in plant tissues, are finding a wide variety of uses, from archaeology to forensics. *American Scientist,* 103, 136-144.

HART, T. C. 2016. Issues and directions in phytolith analysis. *Journal of Archaeological Science,* 68**,** 24-31.

HATCH, M. D. 1987. C4 photosynthesis: a unique elend of modified biochemistry, anatomy and ultrastructure. *Biochimica et Biophysica Acta (BBA)-Reviews on Bioenergetics,* 895, 81-106.

HATTÉ, C., MORVAN, J., NOURY, C. & PATERNE, M. 2001. Is classical acid-alkali-acid treatment responsible for contamination? An alternative proposition. *Radiocarbon,* 43, 177-182.

HAWTHORNE, D., MUSTAPHI, C. J. C., ALEMAN, J. C., BLARQUEZ, O., COLOMBAROLI, D., DANIAU, A.-L., MARLON, J. R., POWER, M., VANNIERE, B. & HAN, Y. 2018. Global Modern Charcoal Dataset (GMCD): A tool for exploring proxy-fire linkages and spatial patterns of biomass burning. *Quaternary International,* 488, 3-17.

HAYES, E., FIELD, J., COSTER, A., FULLAGAR, R., MATHESON, C., FLORIN, S., NANGO, M., DJANDJOMERR, D., MARWICK, B. & WALLIS, L. 2021. Holocene grinding stones at Madjedbebe reveal the processing of starchy plant taxa and animal tissue. *Journal of Archaeological Science: Reports,* 35, 102754.

HEDGES, J. I., EGLINTON, G., HATCHER, P. G., KIRCHMAN, D. L., ARNOSTI, C., DERENNE, S., EVERSHED, R. P., KÖGEL-KNABNER, I., DE LEEUW, J. W. & LITTKE, R. 2000. The molecularly-uncharacterized component of nonliving organic matter in natural environments. *Organic geochemistry,* 31, 945-958.

HEIMSATH, A. M., CHAPPELL, J. & FIFIELD, K. 2010. Eroding Australia: rates and processes from Bega Valley to Arnhem land. *Geological Society, London, Special Publications,* 346, 225-241.

HEIMSATH, A. M., CHAPPELL, J., SPOONER, N. A. & QUESTIAUX, D. L. G. 2002. Creeping soil. *Geology,* 30, 111-114.

HEIMSATH, A. M., FINK, D. & HANCOCK, G. R. 2009. The "humped" soil production function: eroding Arnhem Land, Australia. *Earth Surface Processes and Landforms,* 34, 1674-1684.

HERRIES, A., KOVACHEVA, M., KOSTADINOVA, M. & SHAW, J. 2007. Archaeo-directional and-intensity data from burnt structures at the Thracian site of Halka Bunar (Bulgaria): The effect of magnetic mineralogy, temperature and atmosphere of heating in antiquity. *Physics of the Earth and Planetary Interiors,* 162, 199-216.

HERRIES, A. & LATHAM, A. 2003. 'Environmental Archaeomagnetism': Evidence for climatic change during the Later Stone Age using the magnetic susceptability of cave sediments from Rose Cottage Cave, South Africa. *In:* MITCHELL, P., HAOUR, A. & HOBART, J. (eds.) *Researching Africa's Past: New Contributions from British Archaeologists* Oxford, University School of Archaeology monograph, 57, 25-34.

HERRIES, A. I. 2006. Archaeomagnetic evidence for climate change at Sibudu Cave. *Southern African Humanities,* 18, 131-147.

HERRIES, A. I. & FISHER, E. C. 2010. Multidimensional GIS modeling of magnetic mineralogy as a proxy for fire use and spatial patterning: Evidence from the Middle Stone Age bearing sea cave of Pinnacle Point 13B (Western Cape, South Africa). *Journal of Human Evolution,* 59, 306-320.

HESSE, P. P., MAGEE, J. W. & VAN DER KAARS, S. 2004. Late Quaternary climates of the Australian arid zone: a review. *Quaternary International,* 118, 87-102.

HIGHAM, T. F., BARTON, H., TURNEY, C. S., BARKER, G., RAMSEY, C. B. & BROCK, F. 2009. Radiocarbon dating of charcoal from tropical sequences: results from the Niah Great Cave, Sarawak, and their broader implications. *Journal of Quaternary Science: Published for the Quaternary Research Association,* 24, 189-197.

HISCOCK, P. 1988. Prehistoric settlement patterns and artefact patterns at Lawn Hill, Northwest Queensland. *Unpublished PhD thesis, Department of Anthropology and Sociology, School of Social Science, University of Queensland, St Lucia*.

HISCOCK, P. 2008. *Archaeology of Ancient Australia,* New York, Routledge, pp.360.

HISCOCK, P. & WALLIS, L. A. 2005 Pleistocene settlement of deserts from an Australian perspective. *In:* VETH, P., SMITH, M. & HISCOCK, P. (eds.) *Desert Peoples: Archaeological Perspectives.* Maiden: Blackwell Publishing, 34-57.

HOCKADAY, W. C., GRANNAS, A. M., KIM, S. & HATCHER, P. G. 2006. Direct molecular evidence for the degradation and mobility of black carbon in soils from ultrahigh-resolution mass spectral analysis of dissolved organic matter from a fire-impacted forest soil. *Organic Geochemistry,* 37, 501-510.

HOGG, A., TURNEY, C., PALMER, J., SOUTHON, J., KROMER, B., RAMSEY, C. B., BOSWIJK, G., FENWICK, P., NORONHA, A. & STAFF, R. 2013. The New Zealand kauri (Agathis australis) research project: a radiocarbon dating intercomparison of Younger Dryas wood and implications for IntCal13. *Radiocarbon,* 55, 2035-2048.

HOGG, A. G., HEATON, T. J., HUA, Q., PALMER, J. G., TURNEY, C. S., SOUTHON, J., BAYLISS, A., BLACKWELL, P. G., BOSWIJK, G. & RAMSEY, C. B. 2020. SHCal20 Southern Hemisphere calibration, 0–55,000 years cal BP. *Radiocarbon,* 62, 759-778.

HOLBOURN, A., KUHNT, W., KAWAMURA, H., JIAN, Z., GROOTES, P., ERLENKEUSER, H. & XU, J. 2005. Orbitally paced paleoproductivity variations in the Timor Sea and Indonesian Throughflow variability during the last 460 kyr. *Paleoceanography,* 20, PA3002.

HONAINE, M. F., OSTERRIETH, M. L. & ZUCOL, A. F. 2009. Plant communities and soil phytolith assemblages relationship in native grasslands from southeastern Buenos Aires province, Argentina. *Catena,* 76, 89-96.

HORTON, D. R. 1981. Water and woodland: The peopling of Australia. *Australian Institute of Aboriginal Studies Newsletter* 16, 21-27.

HOVERS, E., EKSHTAIN, R., GREENBAUM, N., MALINSKY-BULLER, A., NIR, N. & YESHURUN, R. 2014. Islands in a stream? Reconstructing site formation processes in the late Middle Paleolithic site of 'Ein Qashish, northern Israel. *Quaternary International,* 331, 216-233.

HOY, D. & ROSENBAUM, G. 2017. Episodic behavior of Gondwanide deformation in eastern Australia: Insights from the Gympie Terrane. *Tectonics,* 36, 1497-1520.

HOY, D., ROSENBAUM, G., MORTIMER, N. & SHAANAN, U. 2018. Hunter–Bowen deformation in south Percy island, northeastern Australia. *Australian Journal of Earth Sciences,* 65, 175-190.

HU, Y., LI, B. & JACOBS, Z. 2019. Single-grain quartz OSL characteristics: Testing for correlations within and between sites in Asia, Europe and Africa. *Methods and protocols,* 3, 2.

HUANG, P. M. & HARDIE, A. G. 2011. Role of Abiotic Catalysis in the Transformation of Organics, Metals, Matalloids, and Other Inorganics. *In:* HUANG, P. M., LI, Y. & SUMNER, M. E. (eds.) *Handbook of Soil Sciences: Properties and Processes.* London, New York: CRC Press, Taylor & Francis Group, pp. 1436.

HUGHEN, K., LEHMAN, S., SOUTHON, J., OVERPECK, J., MARCHAL, O., HERRING, C. & TURNBULL, J. 2004. ^{14}C activity and global carbon cycle changes over the past 50,000 years. *Science,* 303, 202-207.

HUGHES, P. 1977. *A geomorphological interpretation of selected archaeological sites in southern coastal New South Wales.* PhD Doctorate, University of New South Wales, Sydney.

HUININK, H. P., PEL, L. & KOPINGA, K. 2004. Simulating the growth of tafoni. *Earth Surface Processes and Landforms: The Journal of the British Geomorphological Research Group,* 29, 1225-1233.

HUTTON, J., PRESCOTT, J. & TWIDALE, C. 1984. Thermoluminescence dating of coastal dune sand related to a higher stand of Lake Woods, Northern Territory. *Soil Research,* 22, 15-21.

HYLAND, E. G. 2014. Phytoliths as Tracers of Recent Environmental Change. *In:* HEMBREE, D. I., PLATT, B. F. & SMITH, J. J. (eds.) *Experimental Approaches to Understanding Fossil Organisms: Lessons from the Living.* Dordrecht: Springer Netherlands, 207-225.

ICPT-International Comitee for Phytolith Taxonomy, 2019. International code for phytolith nomenclature (ICPN) 2.0. *Annals of Botany,* 124, 189-199.

IRIARTE, J. & PAZ, E. A. 2009. Phytolith analysis of selected native plants and modern soils from southeastern Uruguay and its implications for paleoenvironmental and archeological reconstruction. *Quaternary International,* 193, 99-123.

IVY-OCHS, S. & KOBER, F. 2008. Surface exposure dating with cosmogenic nuclides. *E&G Quaternary Sci. J.,* 57, 179-209.

IVY-OCHS, S., SCHLÜCHTER, C., PRENTICE, M., KUBIK, P. W. & BEER, J. 1997. ^{10}Be and ^{26}Al exposure ages for the Sirius group at Mount Fleming, Mount Feather and Table Mountain and the plateau surface at Table Mountain. *In:* RICCI, C. A. (ed.) *The Antarctic Region: Geological Evolution and Processes*, *Proceedings of the 7th international symposium on Antarctic earth sciences, Sienna, 1995,* Terra Antarctica, 1153-1158.

JACOBS, Z., DULLER, G. A. & WINTLE, A. G. 2006a. Interpretation of single grain De distributions and calculation of De. *Radiation Measurements,* 41, 264-277.

JACOBS, Z., DULLER, G. A., WINTLE, A. G. & HENSHILWOOD, C. S. 2006b. Extending the chronology of deposits at Blombos Cave, South Africa, back to 140 ka using optical dating of single and multiple grains of quartz. *Journal of Human Evolution,* 51, 255-273.

JACOBS, Z., MEYER, M. C., ROBERTS, R. G., ALDEIAS, V., DIBBLE, H. & EL HAJRAOUI, M. A. 2011. Single-grain OSL dating at La Grotte des Contrebandiers ('Smugglers Cave'), Morocco: improved age constraints for the Middle Paleolithic levels. *Journal of Archaeological Science,* 38, 3631-3643.

JACOBS, Z. & ROBERTS, R. G. 2007. Advances in optically stimulated luminescence dating of individual grains of quartz from archeological deposits. *Evolutionary Anthropology: Issues, News, and Reviews,* 16, 210-223.

JACOBS, Z., SAKTURA, M. W. & LI, B. 2022. *Optical dating - Theory, Methods and Applications. Practical guide for the user,* ARC Centre of Excellence for Australian Biodiversity and Heritage (CABAH), University of Wollongong.

JACOBS, Z., WINTLE, A. G., DULLER, G. A., ROBERTS, R. G. & WADLEY, L. 2008. New ages for the post-Howiesons Poort, late and final Middle stone age at Sibudu, South Africa. *Journal of Archaeological Science,* 35, 1790-1807.

JAMES, J., COMLEY, R., WURSTER, C. M., LEVCHENKO, V., GADD, P. & BIRD, M. I. 2024. Holocene savanna hydroclimate record from Kinrara Lake, north-east Queensland, Australia. *Palaeogeography, Palaeoclimatology, Palaeoecology,* 637, 111985.

JASPER, J. P. & GAGOSIAN, R. B. 1989. Glacial–interglacial climatically forced $\delta^{13}C$ variations in sedimentary organic matter. *Nature,* 342, 60-62.

JENNINGS, J. N. 1983. Sandstone pseudokarst or karst. *In:* YOUNG, R. W. & NANSON, G. C. (eds.) *Aspects of Australian sandstone landscapes.* Wollongong: Australian and New Zealand Geomorphology Group.

JENSEN, K., LYNCH, E. A., CALCOTE, R. & HOTCHKISS, S. C. 2007. Interpretation of charcoal morphotypes in sediments from Ferry Lake, Wisconsin, USA: do different plant fuel sources produce distinctive charcoal morphotypes? *The Holocene,* 17, 907-915.

JOHNSON, D. 2006. Why have Pedogenic Stonelayers (Stone-lines, Nappes de Gravats, etc.) been interpreted as Geogenic by so many Geologists, Pedologists and Others? *2006 International Meetings, Nov. 12-16, Indianapolis* American Society of Agronomy, Crop Science Society of America, Soil Science Society of America.

JOHNSON, D. L. 1989. Subsurface stone lines, stone zones, artifact-manuport layers, and biomantles produced by bioturbation via pocket gophers (Thomomys bottae). *American Antiquity,* 54, 370-389.

JOHNSON, D. L. 1990. Biomantle evolution and the redistribution of earth materials and artifacts. *Soil Science,* 149**,** 84-102.

JOHNSON, D. L. 1993. Dynamic denudation evolution of tropical, subtropical and temperate landscapes with three tiered soils: toward a general theory of landscape evolution. *Quaternary International,* 17, 67-78.

JOHNSON, D. L., DOMIER, J. & JOHNSON, D. 2005. Reflections on the nature of soil and its biomantle. *Annals of the Association of American Geographers,* 95, 11-31.

JOHNSON, M. O., MUDD, S. M., PILLANS, B., SPOONER, N. A., KEITH FIFIELD, L., KIRKBY, M. J. & GLOOR, M. 2014. Quantifying the rate and depth dependence of bioturbation based on optically-stimulated luminescence (OSL) dates and meteoric 10Be. *Earth Surface Processes and Landforms,* 39, 1188-1196.

JONES, A. 2004. *Sedimentological record of the late Palaeozoic Gondwanan glaciation in Queensland.* PhD Thesis, The University of Queensland.

JONES, B. G., WOODROFFE, C. D. & MARTIN, G. R. 2003. Deltas in the Gulf of Carpentaria, Australia: Forms, Processes, and Products. *In:* SIDI, H. F., NUMMEDAL, D., IMBERT, P., DARMAN, H. & POSAMENTIER, H. W. (eds.) *Tropical Deltas of Southeast Asia–Sedimentology, Stratigraphy, and Petroleum Geology.* Tulsa: Society for Sedimentary Geology (SEPM), 21-45.

JONES, L. & HANDRECK, K. 1967. Silica in soils, plants, and animals. *Advances in Agronomy,* 19, 107-149.

JONES, L. & MILNE, A. 1963. Studies of silica in the oat plant. *Plant and Soil,* 18, 207-220.

JORDANOVA, N., PETROVSKY, E., KOVACHEVA, M. & JORDANOVA, D. 2001. Factors determining magnetic enhancement of burnt clay from archaeological sites. *Journal of Archaeological Science,* 28, 1137-1148.

JORRY, S. J., DROXLER, A. W., MALLARINO, G., DICKENS, G. R., BENTLEY, S. J., BEAUFORT, L., PETERSON, L. C. & OPDYKE, B. N. 2008. Bundled turbidite deposition in the central Pandora Trough (Gulf of Papua) since Last Glacial Maximum: Linking sediment nature and accumulation to sea level fluctuations at millennial timescale. *Journal of Geophysical Research: Earth Surface,* 113, F01S19.

JUNGERS, M. C., BIERMAN, P. R., MATMON, A., NICHOLS, K., LARSEN, J. & FINKEL, R. 2009. Tracing hillslope sediment production and transport with in situ and meteoric 10Be. *Journal of Geophysical Research: Earth Surface,* 114, F04020.

KACZOREK, D., PUPPE, D., BUSSE, J. & SOMMER, M. 2019. Effects of phytolith distribution and characteristics on extractable silicon fractions in soils under different vegetation – An exploratory study on loess. *Geoderma,* 356, 113917.

KASTE, J. M., HEIMSATH, A. M. & BOSTICK, B. C. 2007. Short-term soil mixing quantified with fallout radionuclides. *Geology,* 35, 243-246.

KEALHOFER, L. 1996. The human environment during the terminal Pleistocene and Holocene in northeastern Thailand: phytolith evidence from Lake Kumphawapi. *Asian Perspectives*, 35, 229-254.

KEALHOFER, L. & PIPERNO, D. R. 1998. Opal phytoliths in Southeast Asian flora. *Annals of the Smithsonian Institution. Smithsonian contributions to botany, Number 88, pp. 43*.

KEALY, S., LOUYS, J., & O'CONNOR S. 2018. Least-cost pathway models indicate northern human dispersal from Sunda to Sahul. *Journal of Human Evolution*, 125, 59-70.

KELLY, E. F., AMUNDSON, R. G., MARINO, B. D. & DENIRO, M. J. 1991. Stable isotope ratios of carbon in phytoliths as a quantitative method of monitoring vegetation and climate change. *Quaternary Research,* 35, 222-233.

KEMP, J. & RHODES, E. 2010. Episodic fluvial activity of inland rivers in southeastern Australia: Palaeochannel systems and terraces of the Lachlan River. *Quaternary Science Reviews,* 29, 732-752.

KENDRICK, K. J. 2005. Pedogenic Silica Accumulation. *In:* RATTAN, L. (ed.) *Encyclopedia of Soil Science.* Boca Raton: Taylor & Francis CRC Press, 1251–1253.

KERSHAW, A. 1978. Record of last interglacial–glacial cycle from northeastern Queensland. *Nature,* 272, 159-161.

KERSHAW, A. P. 1974. A long continuous pollen sequence from north-eastern Australia. *Nature,* 251**,** 222-223.

KERSHAW, A. P. 1976. A late Pleistocene and Holocene pollen diagram from Lynch's Crater, northeastern Queensland, Australia. *New Phytologist,* 77, 469-498.

KERSHAW, A. P. 1981. Quaternary vegetation and environments *In:* KEAST, A. (ed.) *Ecological Biogeography of Australia.* The Hague: Dr W. Junk, 81-101.

KERSHAW, A. P. 1986. Climatic change and Aboriginal burning in north-east Australia during the last two glacial/interglacial cycles. *Nature,* 322, 47-49.

KERSHAW, A. P., BRETHERTON, S. C. & VAN DER KAARS, S. 2007. A complete pollen record of the last 230 ka from Lynch's Crater, north-eastern Australia. *Palaeogeography, Palaeoclimatology, Palaeoecology,* 251, 23-45.

KERSHAW, A. P. & NANSON, G. 1993. The last full glacial cycle in the Australian region. *Global and Planetary Change,* 7, 1-9.

KERSHAW, A. P. & VAN DER KAARS, S. 2012. Australia and the southwest Pacific *In:* METCALFE, S. E. & NASH, D. J. (eds.) *Quaternary Environmental Change in the Tropics.* UK: John Wiles & Sons, Ltd, 236-262.

KETTERINGS, Q. M., BIGHAM, J. M. & LAPERCHE, V. 2000. Changes in soil mineralogy and texture caused by slash-and-burn fires in Sumatra, Indonesia. *Soil Science Society of America Journal,* 64, 1108-1117.

KEYS, B. O. 2009. *Engrained in the Past: Using Geoarchaeology to Understand Site Formation Processes at the Gledswood Shelter 1 Site, Northwest Queensland.* Honours Thesis, Flinders University.

KIBLER, K. W. 1998. Late Holocene environmental effects on sandstone rockshelter formation and sedimentation on the Southern Plains. *Plains Anthropologist,* 43, 173-186.

KINDERMANN, K., KEHL, M., HAUCK, T. & KLASEN, N. 2018. Inside – Outside: Integrating cave and open-air archives. *Quaternary International,* 485, 1-3.

KLIMCHOUK, A. 2018. Tafoni and honeycomb structures as indicators of ascending fluid flow and hypogene karstification. *Geological Society, London, Special Publications,* 466, 79-105.

KOHN, M. J. 2010. Carbon isotope compositions of terrestrial C3 plants as indicators of (paleo) ecology and (paleo) climate. *Proceedings of the National Academy of Sciences,* 107, 19691-19695.

KONDO, R. 1977. Opal phytoliths, inorganic, biogenic particles in plants and soils. *Japan Agricultural Research Quarterly,* 11, 198-203.

KONDO, R., CHILDS, C. W., ATKINSON, I. A. E. & PRITCHARD, T. 1994. *Opal Phytoliths of New Zealand,* Lincoln, N.Z.: Manaaki Whenua Press, pp.85.

KONG, P., NA, C., FINK, D., DING, L. & HUANG, F. 2007. Erosion in northwest Tibet from in-situ-produced cosmogenic 10Be and 26Al in bedrock. *Earth Surface Processes and Landforms: The Journal of the British Geomorphological Research Group,* 32, 116-125.

KRISTENSEN, J. A., THOMSEN, K. J., MURRAY, A. S., BUYLAERT, J.-P., JAIN, M. & BREUNING-MADSEN, H. 2015. Quantification of termite bioturbation in a savannah ecosystem: Application of OSL dating. *Quaternary Geochronology,* 30, 334-341.

KRISTIANSEN, J. 2010. Chrysophytes - Golden Algae. *In:* LIKENS, G. E. (ed.) *Plankton of Inland waters. (A Derivative of Encyclopedia of Inland Waters).* Academic Press, 124-131.

KRULL, E. S., SKJEMSTAD, J. O., GRAETZ, D., GRICE, K., DUNNING, W., COOK, G. & PARR, J. F. 2003. ^{13}C-depleted charcoal from C4 grasses and the role of occluded carbon in phytoliths. *Organic Geochemistry,* 34, 1337-1352.

KRULL, E. S., SWANSTON, C. W., SKJEMSTAD, J. O. & MCGOWAN, J. A. 2006. Importance of charcoal in determining the age and chemistry of organic carbon in surface soils. *Journal of Geophysical Research: Biogeosciences,* 111, G04001.

KUBIËNA, W. L. 1943. Gefügeuntersuchungen an tropischen und subtropischen Rotlehmen. *Beiträge zur Kolonialforschung,* 3, 48-58.

KUHNT, W., HOLBOURN, A., XU, J., OPDYKE, B., DE DECKKER, P., RÖHL, U. & MUDELSEE, M. 2015. Southern Hemisphere control on Australian monsoon variability during the late deglaciation and Holocene. *Nature communications,* 6, 5916.

LA CROIX, A. D., WANG, J., HE, J., HANNAFORD, C., BIANCHI, V., ESTERLE, J. & UNDERSHULTZ, J. R. 2019. Widespread nearshore and shallow marine deposition within the Lower Jurassic Precipice Sandstone and Evergreen Formation in the Surat Basin, Australia. *Marine and Petroleum Geology,* 109, 760-790.

LAL, D. 1991. Cosmic ray labeling of erosion surfaces: in situ nuclide production rates and erosion models. *Earth and Planetary Science Letters,* 104, 424-439.

LAL, D., HARRIS, N. B., SHARMA, K. K., GU, Z., DING, L., LIU, T., DONG, W., CAFFEE, M. W. & JULL, A. 2003. Erosion history of the Tibetan Plateau since the last interglacial: constraints from the first studies of cosmogenic 10Be from Tibetan bedrock. *Earth and Planetary Science Letters,* 217, 33-42.

LANE, E. W. 1955. Importance of fluvial morphology in hydraulic engineering. *American Society of Civil Engineers Proceedings,* 81, 1-17.

LANGLEY, M. C., CLARKSON, C. & ULM, S. 2011. From small holes to grand narratives: The impact of taphonomy and sample size on the modernity debate in Australia and New Guinea. *Journal of Human Evolution,* 61, 197-208.

LARSON, P. H., DORN, R. I., FAULKNER, D. J. & FRIEND, D. A. 2015. Toe-cut terraces: A review and proposed criteria to differentiate from traditional fluvial terraces. *Progress in Physical Geography,* 39, 417-439.

LECOMTE, P. 1988. Stone line profiles: Importance in geochemical exploration. *Journal of Geochemical Exploration,* 30, 35-61.

LEE, K. & WOOD, T. 1971. Physical and chemical effects on soils of some Australian termites, and their pedological significance. *Pedobiologia,* 11, 376-409.

LEES, B. G. 1992b. Geomorphological evidence for late Holocene climatic change in northern Australia. *The Australian Geographer,* 23, 1-10.

LEES, B. G., STANNER, J., PRICE, D. M. & YANCHOU, L. 1995. Thermoluminescence dating of dune podzols at Cape Arnhem, northern Australia. *Marine Geology,* 129, 63-75.

LEES, B. G., YANCHOU, L. & HEAD, J. 1990. Reconnaissance thermoluminescence dating of northern Australian coastal dune systems. *Quaternary Research,* 34, 169-185.

LEES, B. G., YANEHOU, L. & PRICE, D. M. 1992a. Thermoluminescence dating of dunes at Cape St. Lambert, East Kimberleys, northwestern Australia. *Marine Geology,* 106, 131-139.

LEIGH, D. S. 1998. Evaluating artifact burial by eolian versus bioturbation processes, South Carolina Sandhills, USA. *Geoarchaeology: An International Journal,* 13, 309-330.

LENTFER, C. 2003a. *Plants, people and landscapes in prehistoric Papua New Guinea: a compendium of phytolith (and starch) analyses.* PhD Thesis, Southern Cross University.

LENTFER, C. J., COTTER, M. M. & BOYD, W. E. 2003b. Particle settling times for gravity sedimentation and centrifugation: A practical guide for palynologists. *Journal of Archaeological Science,* 30, 149-168.

LEWIS, R. O. 1978. Use of opal phytoliths in paleo-environmental reconstruction. *Wyoming Contributions to Anthropology,* 1, 127-132.

LEWIS, R. O. 1979. *Use of opal phytoliths in paleo-environmental reconstruction*. Master of Arts Thesis, University of Wyoming.

LEWIS, S. C., GAGAN, M. K., AYLIFFE, L. K., ZHAO, J.-X., HANTORO, W. S., TREBLE, P. C., HELLSTROM, J. C., LEGRANDE, A. N., KELLEY, M. & SCHMIDT, G. A. 2011. High-resolution stalagmite reconstructions of Australian–Indonesian monsoon rainfall variability during Heinrich stadial 3 and Greenland interstadial 4. *Earth and Planetary Science Letters,* 303, 133-142.

LEWIS, S. E., SLOSS, C. R., MURRAY-WALLACE, C. V., WOODROFFE, C. D. & SMITHERS, S. G. 2013. Post-glacial sea-level changes around the Australian margin: a review. *Quaternary Science Reviews,* 74, 115-138.

LI, B., JACOBS, Z., ROBERTS, R. G., GALBRAITH, R. & PENG, J. 2017. Variability in quartz OSL signals caused by measurement uncertainties: Problems and solutions. *Quaternary Geochronology,* 41, 11-25.

LI, N., XIE, M., SACK, D., DUBOIS, N., YANG, X., GAO, G., LI, D., LIU, L., LIU, H. & LENG, C. 2021. Continuous aridification since the mid-Holocene as the main cause of C3/C4 dynamics in the grasslands of northeastern China. *European Journal of Soil Science,* 72, 356-371.

LI, T., COMLEY, R., ZHANG, E., ZHOU, Y., ZHOU, X., MUNKSGAARD, N. C., ZHU, Z., HAIG, J., ZHENG, F. & BIRD, M. I. 2023. Paleo-temperature inferred from brGDGTs over the past 18 cal ka BP from Lake Barrine, tropical NE Australia. *Quaternary Science Reviews,* 310, 108125.

LI, T., WURSTER, C. M., HAIG, J., ZHOU, Y., ZWART, C., REN, J., COMLEY, R., MUNKSGAARD, N. C., GADD, P. S. & BIRD, M. I. 2022. Environmental change inferred from multiple proxies from an 18 cal ka BP sediment record, Lake Barrine, NE Australia. *Quaternary Science Reviews,* 294, 107751.

LIBBY, W. F. 1955. *Radiocarbon dating (Vol. 2),* Chicago, University of Chicago Press, pp. 175.

LIBBY, W. F. 1961. Radiocarbon Dating: The method is of increasing use to the archeologist, the geologist, the meteorologist, and the oceanographer. *Science,* 133, 621-629.

LIBBY, W. F., ANDERSON, E. C. & ARNOLD, J. R. 1949. Age determination by radiocarbon content: world-wide assay of natural radiocarbon. *science,* 109, 227-228.

LICHTE, M. & BEHLING, H. 1999. Dry and cold climatic conditions in the formation of the present landscape in Southeastern Brazil An interdisciplinary approach to a controversially discussed topic. *Zeitschrift für Geomorphologie*, 341-358.
LIFTON, N., SATO, T. & DUNAI, T. J. 2014. Scaling in situ cosmogenic nuclide production rates using analytical approximations to atmospheric cosmic-ray fluxes. *Earth and Planetary Science Letters,* 386, 149-160.
LIN, Z., NATOLI, J. M., PICURI, J. C., SHAW, S. E. & BOWYER, W. J. 2021. Replication of the conversion of goethite to hematite to make pigments in both furnace and campfire. *Journal of Archaeological Science: Reports,* 39, 103134.
LINFORD, N. & CANTI, M. G. 2001. Geophysical evidence for fires in antiquity: preliminary results from an experimental study. Paper given at the EGS XXIV General Assembly in The Hague, April 1999. *Archaeological Prospection,* 8, 211-225.
LINFORD, N., LINFORD, P. & PLATZMAN, E. 2005. Dating environmental change using magnetic bacteria in archaeological soils from the upper Thames Valley, UK. *Journal of Archaeological Science,* 32, 1037-1043.
LINSLEY, B. K., ROSENTHAL, Y. & OPPO, D. W. 2010. Holocene evolution of the Indonesian throughflow and the western Pacific warm pool. *Nature Geoscience,* 3, 578-583.
LIU, L., JIE, D., LIU, H., GAO, G., LI, D. & LI, N. 2021. Phytolith transport and its influence factor in different soil types in northern temperate region. *Quaternary International,* 599, 170-183.
LIU, L., LI, D., JIE, D., LIU, H., GAO, G. & LI, N. 2019. Translocation of phytoliths within natural soil profiles in Northeast China. *Frontiers in Plant Science*, 10, 1254.
LLOYD, J., BIRD, M. I., VELLEN, L., MIRANDA, A. C., VEENENDAAL, E. M., DJAGBLETEY, G., MIRANDA, H. S., COOK, G. & FARQUHAR, G. D. 2008. Contributions of woody and herbaceous vegetation to tropical savanna ecosystem productivity: a quasi-global estimate. *Tree Physiology,* 28, 451-468.
LOCKE, W. W. 1986. Fine particle translocation in soils developed on glacial deposits, southern Baffin Island, NWT, Canada. *Arctic and Alpine Research,* 18, 33-43.
LONGWORTH, G., BECKER, L., THOMPSON, R., OLDFIELD, F., DEARING, J. & RUMMERY, T. 1979. Mössbauer effect and magnetic studies of secondary iron oxides in soils. *Journal of Soil Science,* 30, 93-110.
LOURANDOS, H. & ROSS, A. 1994. The great 'intensification debate': its history and place in Australian archaeology. *Australian Archaeology,* 39, 54-63.
LOWE, J. J. & WALKER, M. J. C. 2015. *Reconstructing Quaternary Environments,* London, Taylor and Francis Group, Ruthledge, pp.568.
LOWE, K. M., MENTZER, S. M., WALLIS, L. A. & SHULMEISTER, J. 2018. A multi-proxy study of anthropogenic sedimentation and human occupation of Gledswood Shelter 1: exploring an interior sandstone rockshelter in Northern Australia. *Archaeological and Anthropological Sciences,* 10, 279-304.
LOWE, K. M., SHULMEISTER, J., FEINBERG, J. M., MANNE, T., WALLIS, L. A. & WELSH, K. 2016. Using soil magnetic properties to determine the onset of Pleistocene human settlement at Gledswood Shelter 1, Northern Australia. *Geoarchaeology,* 31, 211-228.
LOWE, K. M. & WALLIS, L. A. 2020. Exploring ground-penetrating radar and sediment magnetic susceptibility analyses in a sandstone rockshelter in northern Australia. *Australian Archaeology,* 86, 63-74.
LU, H.-Y., WU, N.-Q., YANG, X.-D., JIANG, H., LIU, K.-B. & LIU, T.-S. 2006. Phytoliths as quantitative indicators for the reconstruction of past environmental conditions in China I: phytolith-based transfer functions. *Quaternary Science Reviews,* 25, 945-959.
LULY, J., GRINDROD, J. & PENNY, D. 2006. Holocene palaeoenvironments and change at Three-Quarter Mile Lake, Silver Plains Station, Cape York Peninsula, Australia. *The Holocene,* 16, 1085-1094.
MABBUTT, J. 1965. Stone distribution in a stony tableland soil. *Soil Research,* 3, 131-142.
MABBUTT, J. A. 1966. Mantle-controlled planation of pediments. *American Journal of Science,* 264, 78-91.
MADELLA, M. & LANCELOTTI, C. 2012. Taphonomy and phytoliths: a user manual. *Quaternary International,* 275, 76-83.
MADELLA, M., POWERS-JONES, A. H. & JONES, M. K. 1998. A simple method of extraction of opal phytoliths from sediments using a non-toxic heavy liquid. *Journal of Archaeological Science,* 25, 801-803.
MAHER, B. 1986. Characterisation of soils by mineral magnetic measurements. *Physics of the Earth and Planetary Interiors,* 42, 76-92.
MALEY, J., DOUMENGE, C., GIRESSE, P., MAHÉ, G., PHILIPPON, N., HUBAU, W., LOKONDA, M. O., TSHIBAMBA, J. M. & CHEPSTOW-LUSTY, A. 2018. Late Holocene forest contraction and fragmentation in central Africa. *Quaternary Research,* 89, 43-59.
MALONEY, T., O'CONNOR, S., WOOD, R., APLIN, K. & BALME, J. 2018. Carpenters Gap 1: A 47,000 year old record of indigenous adaption and innovation. *Quaternary Science Reviews,* 191, 204-228.
MARTíNEZ, J. I., DE DECKKER, P. & BARROWS, T. T. 1999. Palaeoceanography of the last glacial maximum in the eastern Indian Ocean: planktonic foraminiferal evidence. *Palaeogeography, Palaeoclimatology, Palaeoecology,* 147, 73-99.

MARTINI, J. 1979. Karst in black reef quartzite near Kaapsehoop, Eastern Transvaal. *Ann. Geol. Surv. (S. Afr),* 13, 115-128.
MARTINI, P. 1978. Tafoni weathering, with examples from Tuscany. *Zeitschrift fuer Geomorphologie,* 22, 44-67.
MARWICK, B., HAYES, E., CLARKSON, C. & FULLAGAR, R. 2017. Movement of lithics by trampling: An experiment in the Madjedbebe sediments, northern Australia. *Journal of Archaeological Science,* 79, 73-85.
MARX, S. K., KAMBER, B. S., MCGOWAN, H. A. & DENHOLM, J. 2011. Holocene dust deposition rates in Australia's Murray-Darling Basin record the interplay between aridity and the position of the mid-latitude westerlies. *Quaternary Science Reviews,* 30, 3290-3305.
MARX, S. K., MCGOWAN, H. A. & KAMBER, B. S. 2009. Long-range dust transport from eastern Australia: A proxy for Holocene aridity and ENSO-type climate variability. *Earth and Planetary Science Letters,* 282, 167-177.
MASIELLO, C. A. 2004. New directions in black carbon organic geochemistry. *Marine Chemistry,* 92**,** 201-213.
MAZUMDAR, J. 2011. Phytoliths of pteridophytes. *South African Journal of Botany,* 77, 10-19.
MCBEATH, A. V., WURSTER, C. M. & BIRD, M. I. 2015. Influence of feedstock properties and pyrolysis conditions on biochar carbon stability as determined by hydrogen pyrolysis. *Biomass and Bioenergy,* 73, 155-173.
MCBREARTY, S. 1990. Consider the humble termite: termites as agents of post-depositional disturbance at African archaeological sites. *Journal of Archaeological Science,* 17, 111-143.
MCBRIDE, E. F. & PICARD, M. D. 2004. Origin of honeycombs and related weathering forms in Oligocene Macigno Sandstone, Tuscan coast near Livorno, Italy. *Earth Surface Processes and Landforms,* 29, 713-735.
MCCLEAN, R. G. & KEAN, W. 1993. Contributions of wood ash magnetism to archaeomagnetic properties of fire pits and hearths. *Earth and Planetary Science Letters,* 119, 387-394.
MCCORKLE, D. C., EMERSON, S. R. & QUAY, P. D. 1985. Stable carbon isotopes in marine porewaters. *Earth and Planetary Science Letters,* 74, 13-26.
MCGREGOR, H. V. & GAGAN, M. K. 2004. Western Pacific coral δ18O records of anomalous Holocene variability in the El Niño–Southern Oscillation. *Geophysical Research Letters,* 31, L11204.
MCIVOR, J., WILLIAMS, J. & GARDENER, C. 1995. Pasture management influences runoff and soil movement in the semi-arid tropics. *Australian Journal of Experimental Agriculture,* 35, 55-65.
MCMICHAEL, C. H., BUSH, M. B., PIPERNO, D. R., SILMAN, M. R., ZIMMERMAN, A. R. & ANDERSON, C. 2012. Spatial and temporal scales of pre-Columbian disturbance associated with western Amazonian lakes. *The Holocene,* 22, 131-141.
MECCHIA, M., SAURO, F., PICCINI, L., DE WAELE, J., SANNA, L., TISATO, N., LIRA, J. & VERGARA, F. 2014. Geochemistry of surface and subsurface waters in quartz-sandstones: significance for the geomorphic evolution of tepui table mountains (Gran Sabana, Venezuela). *Journal of Hydrology,* 511, 117-138.
MELLETT, C. L. 2013. Luminescence dating. *In:* CLARKE, L. E. (ed.) *Geomorphical techniques (online edition).* London: British Society for Geomorphology, 1–11.
MERCADER, J., BENNETT, T., ESSELMONT, C., SIMPSON, S. & WALDE, D. 2009. Phytoliths in woody plants from the Miombo woodlands of Mozambique. *Annals of Botany,* 104, 91-113.
MERCADER, J., BENNETT, T., ESSELMONT, C., SIMPSON, S. & WALDE, D. 2011. Soil phytoliths from miombo woodlands in Mozambique. *Quaternary Research,* 75, 138-150.
MEREDITH, W., ASCOUGH, P. L., BIRD, M. I., LARGE, D. J., SNAPE, C. E., SUN, Y. & TILSTON, E. L. 2012. Assessment of hydropyrolysis as a method for the quantification of black carbon using standard reference materials. *Geochimica et Cosmochimica Acta,* 97, 131-147.
MERRITTS, D. J., VINCENT, K. R. & WOHL, E. E. 1994. Long river profiles, tectonism, and eustasy: A guide to interpreting fluvial terraces. *Journal of Geophysical Research: Solid Earth,* 99, 14031-14050.
METCALFE, C. R. 1960. *Anatomy of the Monocotyledons. I. Gramineae*, Clarendon Press: Oxford University Press, pp.731.
METCALFE, C. R. 1971. *Anatomy of the Monocotyledons: V. Cyperaceae*, Oxford at the Clarendon, pp.610.
METCALFE, S. E. & NASH, D. J. 2012. Introduction. Why Tropics matter. *In:* METCALFE, S. E. & NASH, D. J. (eds.) *Quaternary Environmental Change in the Tropics.* UK: John Wiley & Sons, Ltd, 3-8.
MIDDLETON, M. F. 1989. A model for the formation of intracratonic sag basins. *Geophysical Journal International,* 99, 665-676.
MIGOŃ, P. 2021. Sandstone geomorphology – Recent advances. *Geomorphology,* 373, 107484.
MIGOŃ, P., DUSZYŃSKI, F., JANCEWICZ, K. & KOTWICKA, W. 2020. Late evolutionary stages of residual hills in tablelands (Elbsandsteingebirge, Germany). *Geomorphology,* 367, 107308.
MIKULÁŠ, R. 2007. Microforms of the sandstone relief. *In:* HÄRTEL, H., CÍLEK, V., HERBEN, T., JACKSON, A. & WILLIAMS, R. (eds.) *Sandstone Landscapes.* Prague: Academia, 66-75.
MILLER, G. H., FOGEL, M. L., MAGEE, J. W. & GAGAN, M. K. 2016. Disentangling the impacts of climate and human colonization on the flora and fauna of the Australian arid zone over the past 100 ka using stable isotopes in avian eggshell. *Quaternary Science Reviews,* 151, 27-57.
MOEYERSONS, J. 1989. A possible causal relationship between creep and sliding on Rwaza hill, Southern Rwanda. *Earth Surface Processes and Landforms,* 14, 597-614.

MOEYERSONS, J., NYSSEN, J., POESEN, J., DECKERS, J. & HAILE, M. 2006. On the origin of rock fragment mulches on Vertisols: a case study from the Ethiopian highlands. *Geomorphology,* 76, 411-429.

MOONEY, S. D., HARRISON, S. P., BARTLEIN, P. J., DANIAU, A.-L., STEVENSON, J., BROWNLIE, K. C., BUCKMAN, S., CUPPER, M., LULY, J. & BLACK, M. 2011. Late Quaternary fire regimes of Australasia. *Quaternary Science Reviews,* 30, 28-46.

MOORE, P. 2005. *Guide to plants of inland Australia.* Sydney: Reed New Holland, pp. 503.

MORALES, V. L., ZHANG, W., GAO, B., LION, L. W., BISOGNI JR, J. J., MCDONOUGH, B. A. & STEENHUIS, T. S. 2011. Impact of dissolved organic matter on colloid transport in the vadose zone: deterministic approximation of transport deposition coefficients from polymeric coating characteristics. *Water Research,* 45, 1691-1701.

MORAVEK, S., LULY, J., GRINDROD, J. & FAIRFAX, R. 2013. The origin of grassy balds in the Bunya Mountains, southeastern Queensland, Australia. *The Holocene,* 23, 305-315.

MORDELET, P., MENAUT, J. C. & MARIOTTI, A. 1997. Tree and grass rooting patterns in an African humid savanna. *Journal of Vegetation Science,* 8, 65-70.

MORRÁS, H., MORETTI, L., PÍCCOLO, G. & ZECH, W. 2009. Genesis of subtropical soils with stony horizons in NE Argentina: Autochthony and polygenesis. *Quaternary international,* 196, 137-159.

MORWOOD, M. 1990. The prehistory of Aboriginal landuse on the upper Flinders River, north Queensland highlands. *Queensland Archaeological Research,* 7, 3-56.

MORWOOD, M. 1992. Changing art in a changing landscape: a case study from the Upper Flinders Region of the North Queensland Highland. *In:* MCDONALD, J. & HASKOVEC, I. (eds.) *State of the Art: Regional Rock Art Studies in Australia and Melanesia.* Melbourne: Australian Rock Art Research Association, 60-70.

MORWOOD, M. 2002. *Visions from the Past: The archaeology of Australian Aboriginal Art.* Crows Nest, NSW: Allen & Unwin, pp.347.

MORWOOD, M. & GODWIN, L. 1982. Aboriginal Sites in the Hughenden Region, North Queensland Highlands: Research Prospects. *Australian Archaeology*, 15, 49-53.

MOSS, P. T., COSGROVE, R., FERRIER, A. & HABERLE, S. G. 2012. Holocene environments of the sclerophyll woodlands of the Wet Tropics of northeastern Australia. *Peopled Landscapes. Archaeological and Biogeographic Approaches to Landscapes. Terra Australis,* 34, 329-341.

MOSS, P. T., DUNBAR, G. B., THOMAS, Z., TURNEY, C., KERSHAW, A. P. & JACOBSEN, G. E. 2017. A 60 000-year record of environmental change for the Wet Tropics of north-eastern Australia based on the ODP 820 marine core. *Journal of Quaternary Science,* 32, 704-716.

MOSS, P. T. & KERSHAW, A. P. 2007. A late Quaternary marine palynological record (oxygen isotope stages 1 to 7) for the humid tropics of northeastern Australia based on ODP Site 820. *Palaeogeography, Palaeoclimatology, Palaeoecology,* 251, 4-22.

MULVANEY, D. J. & JOYCE, E. B. Archaeological and geomorphological investigations on Mt. Moffatt station, Queensland, Australia. Proceedings of the Prehistoric Society, 1965. Cambridge University Press, 147-212.

MUNSELL COLOR ,1994. Soil Color Charts (revised edition). Macbeth Division of Kollmorgen Instruments Corporation. New Windsor, New York, USA.

MUNT, S. 2013. Axe grinding grooves in central and northwest Queensland, with a case study from Rocks Crossing. *Unpublished study*.

MURRAY, A., WOHL, E. & EAST, J. 1992. Thermoluminescence and excess 226Ra decay dating of late Quaternary fluvial sands, East Alligator River, Australia. *Quaternary Research,* 37, 29-41.

MURRAY, A. S. & WINTLE, A. G. 2000. Luminescence dating of quartz using an improved single-aliquot regenerative-dose protocol. *Radiation measurements,* 32, 57-73.

MURRAY, A. S. & WINTLE, A. G. 2003. The single aliquot regenerative dose protocol: potential for improvements in reliability. *Radiation measurements,* 37, 377-381.

MURUNGI, M. L. & BAMFORD, M. K. 2020. Revised taxonomic interpretations of Cyperaceae phytoliths for (paleo) botanical studies with some notes on terminology. *Review of Palaeobotany and Palynology,* 275, 104189.

MUSCHELER, R., BEER, J., KUBIK, P. W. & SYNAL, H.-A. 2005. Geomagnetic field intensity during the last 60,000 years based on 10Be and 36Cl from the Summit ice cores and ^{14}C. *Quaternary Science Reviews,* 24, 1849-1860.

MUSTAPHI, C. J. C. & PISARIC, M. F. 2014. A classification for macroscopic charcoal morphologies found in Holocene lacustrine sediments. *Progress in Physical Geography,* 38, 734-754.

MUSTOE, G. 1983. The origin of honeycomb weathering. *GSA Bulletin* 93, 108-115.

NANSON, G. C., EAST, T. J. & ROBERTS, R. G. 1993. Quaternary stratigraphy, geochronology and evolution of the Magela Creek catchment in the monsoon tropics of northern Australia. *Sedimentary Geology,* 83, 277-302.

NANSON, G. C., JONES, B. G., PRICE, D. M. & PIETSCH, T. J. 2005. Rivers turned to rock: Late Quaternary alluvial induration influencing the behaviour and morphology of an anabranching river in the Australian monsoon tropics. *Geomorphology,* 70, 398-420.

NANSON, G. C., PRICE, D. M., JONES, B. G., MAROULIS, J. C., COLEMAN, M., BOWMAN, H., COHEN, T. J., PIETSCH, T. J. & LARSEN, J. R. 2008. Alluvial evidence for major climate and flow regime changes during the middle and late Quaternary in eastern central Australia. *Geomorphology,* 101, 109-129.

NANSON, G. C., PRICE, D. M. & SHORT, S. A. 1992. Wetting and drying of Australia over the past 300 ka. *Geology,* 20, 791-794.

NANSON, G. C., PRICE, D. M., SHORT, S. A., YOUNG, R. W. & JONES, B. G. 1991. Comparative uranium-thorium and thermoluminescence dating of weathered Quaternary alluvium in the tropics of northern Australia. *Quaternary Research,* 35, 347-366.

NEETHIRAJAN, S., GORDON, R. & WANG, L. 2009. Potential of silica bodies (phytoliths) for nanotechnology. *Trends in Biotechnology,* 27, 461-467.

NEHREN, U., KIRCHNER, A. & HEINRICH, J. 2016. What do yellowish-brown soils and stone layers tell us about Late Quaternary landscape evolution and soil development in the humid tropics? A field study in the Serra dos Órgãos, Southeast Brazil. *Catena,* 137, 173-190.

NEHREN, U. M., KIRCHNER, A., SATTLER, D., TURETTA, A. P. & HEINRICH, J. 2013. Impact of natural climate change and historical land use on landscape development in the Atlantic Forest of Rio de Janeiro, Brazil. *Anais da Academia Brasileira de Ciências,* 85, 497-518.

NELLE, O., ROBIN, V. & TALON, B. 2013. Pedoanthracology: Analysing soil charcoal to study Holocene palaeoenvironments. *Quaternary International,* 289, 1-4.

NELSON, D. E., KORTELING, R. G. & STOTT, W. R. 1977. Carbon-14: direct detection at natural concentrations. *Science,* 198, 507-508.

NEUMANN, K., FAHMY, A., LESPEZ, L., BALLOUCHE, A. & HUYSECOM, E. 2009. The Early Holocene palaeoenvironment of Ounjougou (Mali): phytoliths in a multiproxy context. *Palaeogeography, Palaeoclimatology, Palaeoecology,* 276, 87-106.

NEUMANN, K., FAHMY, A. G., MÜLLER-SCHEEßEL, N. & SCHMIDT, M. 2017. Taxonomic, ecological and palaeoecological significance of leaf phytoliths in West African grasses. *Quaternary International,* 434, 15-32.

NICHOLLS, K. H. & WUJEK, D. E. 2003. Chrysophycean algae. *In:* WEHR, J. D. & SHEATH, R. G. (eds.) *Freshwater Algae of North America.* Burlington: Academic Press, 471-509.

NISHIIZUMI, K., LAL, D., KLEIN, J., MIDDLETON, R. & ARNOLD, J. 1986. Production of 10Be and 26Al by cosmic rays in terrestrial quartz in situ and implications for erosion rates. *Nature,* 319, 134-136.

NORMAN, K., INGLIS, J., CLARKSON, C., FAITH, J. T., SHULMEISTER, J. & HARRIS, D. 2018. An early colonisation pathway into northwest Australia 70-60,000 years ago. *Quaternary science reviews,* 180, 229-239.

NOTT, J. & PRICE, D. 1994. Plunge pools and paleoprecipitation. *Geology,* 22, 1047-1050.

NOTT, J. & PRICE, D. 1999. Waterfalls, floods and climate change: evidence from tropical Australia. *Earth and Planetary Science Letters,* 171, 267-276.

NOTT, J. F., PRICE, D. M. & BRYANT, E. A. 1996. A 30,000 year record of extreme floods in tropical Australia from relict plunge-pool deposits: Implications for future climate change. *Geophysical Research Letters,* 23, 379-382.

NOVELLO, A., BARBONI, D., BERTI-EQUILLE, L., MAZUR, J.-C., POILECOT, P. & VIGNAUD, P. 2012. Phytolith signal of aquatic plants and soils in Chad, Central Africa. *Review of Palaeobotany and Palynology,* 178, 43-58.

NYE, P. H. 1955. Some soilforming processes in the humid tropics: IV. The action of the soil fauna. *Journal of Soil Science,* 6, 73-83.

O'CONNELL, J. F. & ALLEN, J. 2004. Dating the colonization of Sahul (Pleistocene Australia–New Guinea): a review of recent research. *Journal of Archaeological Science,* 31, 835-853.

O'CONNELL, J. F. & ALLEN, J. 2012. The restaurant at the end of the universe: Modelling the colonisation of Sahul. *Australian Archaeology*, 74, 5-17.

O'CONNELL, J. F. & ALLEN, J. 2015. The process, biotic impact, and global implications of the human colonization of Sahul about 47,000 years ago. *Journal of Archaeological Science,* 56, 73-84.

O'CONNELL, J. F., ALLEN, J., WILLIAMS, M. A., WILLIAMS, A. N., TURNEY, C. S., SPOONER, N. A., KAMMINGA, J., BROWN, G. & COOPER, A. 2018. When did Homo sapiens first reach Southeast Asia and Sahul? *Proceedings of the National Academy of Sciences,* 115, 8482-8490.

O'CONNOR, S. 1995. Carpenter's Gap rockshelter 1: 40,000 years of Aboriginal occupation in the Napier Ranges, Kimberley, WA. *Australian Archaeology,* 40, 58-59.

O'CONNOR, S. 2007. New evidence from East Timor contributes to our understanding of earliest modern human colonisation east of the Sunda Shelf. *Antiquity,* 81, 523-535.

O'CONNOR, S., BARHAM, A., APLIN, K. & MALONEY, T. 2017. Cave stratigraphies and cave breccias: Implications for sediment accumulation and removal models and interpreting the record of human occupation. *Journal of Archaeological Science,* 77, 143-159.

O'CONNOR, S. & VETH, P. 2000. The world's first mariners: Savannah dwellers in an island continent. *In:* O'CONNOR, S. & VETH, P. (eds.) *East of Wallace's Line: Studies of past and present maritime cultures of the Indo-Pacific region.* Rotterdam: AA Balkema, 99-139.

O'CONNOR, S., VETH, P. & HUBBARD, N. 1993. Changing interpretations of postglacial human subsistence and demography in Sahul. *In:* SMITH, M. A., SPRIGGS, M. & FANKHAUSER, B. (eds.) *Sahul in Review: Pleistocene Archaeology in Australia, New Guinea and Island Melanesia, Occasional Papers in Prehistory 24.* Canberra: Department of Prehistory, Research School of Pacific Studies, Australian National University, 95-105.

O'LEARY, M. H. 1981. Carbon isotope fractionation in plants. *Phytochemistry,* 20, 553-567.
O'LEARY, M. H. 1988. Carbon isotopes in photosynthesis. *Bioscience,* 38, 328-336.
OARD, M. J. 2013. *Earth's Surface Shaped by Genesis Flood Runoff* [Online]. Available: http://michael.oards.net/pdf/Book/Front_material.pdf [Accessed 20.8. 2023].
OESTMO, S., SCHOVILLE, B. J., WILKINS, J. & MAREAN, C. W. 2014. A Middle Stone Age Paleoscape near the Pinnacle Point caves, Vleesbaai, South Africa. *Quaternary International,* 350, 147-168.
OJANUGA, A. & WIRTH, K. 1977. Threefold stonelines in southwestern Nigeria: evidence of cyclic soil and landscape development. *Soil Science,* 123, 249-257.
OLDFIELD, F., THOMPSON, R. & DICKSON, D. 1981. Artificial magnetic enhancement of stream bedload: a hydrological application of superparamagnetism. *Physics of the Earth and Planetary Interiors,* 26, 107-124.
OLIVERAS, I. & MALHI, Y. 2016. Many shades of green: the dynamic tropical forest–savannah transition zones. *Philosophical Transactions of the Royal Society B,* 371 (1703), 20150308.
OLLEY, J., CAITCHEON, G. G. & ROBERTS, R. 1999. The origin of dose distributions in fluvial sediments, and the prospect of dating single grains from fluvial deposits using optically stimulated luminescence. *Radiation Measurements,* 30, 207-217.
OLLEY, J. M., ROBERTS, R. G., YOSHIDA, H. & BOWLER, J. M. 2006. Single-grain optical dating of grave-infill associated with human burials at Lake Mungo, Australia. *Quaternary Science Reviews,* 25, 2469-2474.
OLLIER, C. D. 1988. Deep Weathering, Groundwater and Climate. *Geografiska Annaler. Series A, Physical Geography,* 70, 285-290.
OPALINSKA, B. & COWLING, S. 2015. Modelling the movement of biogenic silica from terrestrial vegetation to riverine systems within the continental USA. *Ecological Modelling,* 312, 104-113.
OPPO, D. W. & FAIRBANKS, R. G. 1989. Carbon isotope composition of tropical surface water during the past 22,000 years. *Paleoceanography,* 4, 333-351.
OSBORNE, C. P., SALOMAA, A., KLUYVER, T. A., VISSER, V., KELLOGG, E. A., MORRONE, O., VORONTSOVA, M. S., CLAYTON, W. D. & SIMPSON, D. A. 2014. A global database of C4 photosynthesis in grasses. *New Phytologist,* 204, 441-446.
OSHEBI, F. M., EL ADLI, M. B., SHALTAMI, O. R. & FARES, F. F. 2017. Alluvial terraces as a measure of vertical movements and neotectonics: Evidences from Wadi Zazah, Al Jabal Al Akhdar, NE Libya. *Journal of Science & Technology,* 6, 19-24.
OSMOND, C., ALLAWAY, W., SUTTON, B., TROUGHTON, J., QUEIROZ, O., LÜTTGE, U. & WINTER, K. 1973. Carbon isotope discrimination in photosynthesis of CAM plants. *Nature,* 246, 41-42.
OSTANIN, I., SAFONOV, A. & OSELEDETS, I. 2017. Natural erosion of sandstone as shape optimisation. *Scientific Reports,* 7, 17301.
PARADISE, T. R. 2013. Tafoni and other rock basins. *In:* SHRODER, J. (ed.) *Treatise on Geomorphology.* San Diego, CA: Academic Press, 111-126.
PARIZEK, E. & WOODRUFF, J. 1957. Description and origin of stone layers in soils of the southeastern states. *The Journal of Geology,* 65, 24-34.
PARR, J. F. 2006. Effect of fire on phytolith coloration. *Geoarchaeology,* 21, 171-185.
PARR, J. F. & CARTER, M. 2003. Phytolith and starch analysis of sediment samples from two archaeological sites on Dauar Island, Torres Strait, northeastern Australia. *Vegetation History and Archaeobotany,* 12, 131-141.
PARR, J. F. & SULLIVAN, L. A. 2005. Soil carbon sequestration in phytoliths. *Soil Biology and Biochemistry,* 37, 117-124.
PARSONS, A., ROBICHAUD, P. R., LEWIS, S. A., NAPPER, C. & CLARK, J. T. 2010. Field guide for mapping post-fire soil burn severity. *General Techical Report.* Fort Collins.
PATON, T. R., HUMPHREYS, G. S. & MITCHELL, P. B. 1995. *Soils: A new global view,* Boca Raton, Taylor & Francis Group CRC Press, pp.234.
PEARSALL, D. M. 1978. Phytolith analysis of archeological soils: evidence for maize cultivation in formative Ecuador. *Science,* 199, 177-178.
PEARSALL, D. M. 1982. Phytolith Analysis: Applications of a New Paleoethnobotanical Technique in Archeology. *American Anthropologist,* 84, 862-871.
PEÑA-MONNÉ, J. L., SAMPIETRO-VATTUONE, M. M., BÁEZ, W. A., GARCÍA-GIMÉNEZ, R., STÁBILE, F. M., MARTÍNEZ STAGNARO, S. Y. & TISSERA, L. E. 2022. Sandstone weathering processes in the painted rock shelters of Cerro Colorado (Córdoba, Argentina). *Geoarchaeology,* 37, 332-349.
PENG, J., DONG, Z., HAN, F., LONG, H. & LIU, X. 2013. R package numOSL: numeric routines for optically stimulated luminescence dating. *Ancient TL,* 31, 41-48.
PERRY, R., SLEEMAN, J., TWIDALE, C., COLLINS, F., SLATYER, R., LAZARIDES, M. & PRICHARD, C. 1964. No. 11 General Report on Lands of the Leichhardt–Gilbert Area, Queensland, 1953–54. *CSIRO Land Research Surveys,* 2010, 1-236.
PESSENDA, L. C., GOUVEIA, S. E. & ARAVENA, R. 2001. Radiocarbon dating of total soil organic matter and humin fraction and its comparison with ^{14}C ages of fossil charcoal. *Radiocarbon,* 43, 595-601.

PESSENDA, L. C. R., GOMES, B. M., ARAVENA, R., RIBEIRO, A. D. S., BOULET, R. & GOUVEIA, S. E. 1998. The carbon isotope record in soils along a forest-cerrado ecosystem transect: implications for vegetation changes in the Rondonia state, southwestern Brazilian Amazon region. *The Holocene,* 8, 599-603.

PESSENDA, L. C. R., GOUVEIA, S. E. M., ARAVENA, R., GOMES, B. M., BOULET, R. & RIBEIRO, A. D. S. 1997. ^{14}C dating and stable carbon isotopes of soil organic matter in forest–savanna boundary areas in the southern Brazilian Amazon region. *Radiocarbon,* 40, 1013-1022.

PETHERICK, L., BOSTOCK, H., COHEN, T. J., FITZSIMMONS, K., TIBBY, J., FLETCHER, M.-S., MOSS, P., REEVES, J., MOONEY, S. & BARROWS, T. 2013. Climatic records over the past 30 ka from temperate Australia–a synthesis from the Oz-INTIMATE workgroup. *Quaternary Science Reviews,* 74, 58-77.

PETTIJOHN, F. J., POTTER, P. E. & SIEVER, R. 2012. *Sand and Sandstone.* NY: Springer New York, pp.553.

PHILLIPS, J. D. & MARION, D. A. 2006. Biomechanical effects of trees on soil and regolith: beyond treethrow. *Annals of the Association of American Geographers,* 96, 233-247.

PHILLIPS, L., ESTERLE, J. & EDWARDS, S. 2017a. Review of Lopingian (upper Permian) stratigraphy of the Galilee Basin, Queensland, Australia. *Australian Journal of Earth Sciences,* 64, 283-300.

PICCINI, L. & MECCHIA, M. 2009. Solution weathering rate and origin of karst landforms and caves in the quartzite of Auyan-tepui (Gran Sabana, Venezuela). *Geomorphology,* 106, 15-25.

PIETIKÄINEN, J., KIIKKILÄ, O. & FRITZE, H. 2000. Charcoal as a habitat for microbes and its effect on the microbial community of the underlying humus. *Oikos,* 89, 231-242.

PIPERNO, D. R. 1983. *The application of Phytolith analysis to the reconstruction of plant subsistence and environments in prehistoric Panama.* PhD Dissertation, Temple University, Philadelphia, PA.

PIPERNO, D. R. 1988. *Phytolith Analysis: An Archaeological and Geological Perspective,* San Diego, Academic Press, pp. 280.

PIPERNO, D. R. 2006. *Phytoliths: A Comprehensive Guide for Archaeologists and Paleoecologists*, AltaMira Press, pp. 238.

PIPERNO, D. R. & PEARSALL, D. M. 1998. The Silica Bodies of Tropical American Grasses: Morphology, Taxonomy, and Implications for Grass Systematics and Fossil Phytolith Identification. *Smithsonian contributions to Botany,* Number 85, 1-40.

PORUBCAN, A. A. & XU, S. 2011. Colloid straining within saturated heterogeneous porous media. *Water Research,* 45**,** 1796-1806.

PREBBLE, M., SIM, R., FINN, J. & FINK, D. 2005. A Holocene pollen and diatom record from Vanderlin Island, Gulf of Carpentaria, lowland tropical Australia. *Quaternary Research,* 64, 357-371.

PRESCOTT, J. R. & HUTTON, J. T. 1994. Cosmic ray contributions to dose rates for luminescence and ESR dating: Large depths and long-term time variations. *Radiation Measurements,* 23, 497-500.

PREUSSER, F., DEGERING, D., FUCHS, M., HILGERS, A., KADEREIT, A., KLASEN, N., KRBETSCHEK, M., RICHTER, D. & SPENCER, J. Q. 2008. Luminescence dating: basics, methods and applications. *E&G Quaternary Science Journal,* 57, 95-149.

PURSER, K. H., LIEBERT, R., LITHERLAND, A., BEUKENS, R., GOVE, H. E., BENNETT, C., CLOVER, M. & SONDHEIM, W. 1977. An attempt to detect stable N-ions from a sputter ion source and some implications of the results for the design of tandems for ultra-sensitive carbon analysis. *Revue de Physique Appliquée,* 12, 1487-1492.

QUIGLEY, M., SANDIFORD, M., FIFIELD, L. K. & ALIMANOVIC, A. 2007. Landscape responses to intraplate tectonism: Quantitative constraints from 10Be nuclide abundances. *Earth and Planetary Science Letters,* 261, 120-133.

RAMSEY, C. B., DEE, M., LEE, S., NAKAGAWA, T. & STAFF, R. A. 2010. Developments in the Calibration and Modeling of Radiocarbon Dates. *Radiocarbon,* 52, 953-961.

RASHID, I., MIR, S. H., ZURRO, D., DAR, R. A. & RESHI, Z. A. 2019. Phytoliths as proxies of the past. *Earth-Science Reviews,* 194, 234-250.

REEVES, J. M., BARROWS, T. T., COHEN, T. J., KIEM, A. S., BOSTOCK, H. C., FITZSIMMONS, K. E., JANSEN, J. D., KEMP, J., KRAUSE, C., PETHERICK, L., PHIPPS, S. J., STOCKHOLMS, U., NATURVETENSKAPLIGA, F. & INSTITUTIONEN FÖR NATURGEOGRAFI OCH, K. 2013b. Climate variability over the last 35,000 years recorded in marine and terrestrial archives in the Australian region: an OZ-INTIMATE compilation. *Quaternary Science Reviews,* 74, 21-34.

REEVES, J. M., BOSTOCK, H. C., AYLIFFE, L. K., BARROWS, T. T., DE DECKKER, P., DEVRIENDT, L. S., DUNBAR, G. B., DRYSDALE, R. N., FITZSIMMONS, K. E., GAGAN, M. K., GRIFFITHS, M. L., HABERLE, S. G., JANSEN, J. D., KRAUSE, C., LEWIS, S., MCGREGOR, H. V., MOONEY, S. D., MOSS, P., NANSON, G. C., PURCELL, A. & VAN DER KAARS, S. 2013a. Palaeoenvironmental change in tropical Australasia over the last 30,000 years – a synthesis by the OZ-INTIMATE group. *Quaternary Science Reviews,* 74, 97-114.

REHN, E., REHN, A. & POSSEMIERS, A. 2019. Fossil charcoal particle identification and classification by two convolutional neural networks. *Quaternary Science Reviews,* 226, 106038.

REHN, E., ROWE, C., ULM, S., GADD, P., ZAWADZKI, A., JACOBSEN, G., WOODWARD, C. & BIRD, M. 2021a. Multiproxy Holocene fire records from the tropical savannas of northern Cape York Peninsula, Queensland, Australia. *Frontiers in Ecology and Evolution,* 9, 16.

REHN, E., ROWE, C., ULM, S., WOODWARD, C. & BIRD, M. 2021b. A late-Holocene multiproxy fire record from a tropical savanna, eastern Arnhem Land, Northern Territory, Australia. *The Holocene,* 31, 870-883.
REIMER, P. J., AUSTIN, W. E., BARD, E., BAYLISS, A., BLACKWELL, P. G., RAMSEY, C. B., BUTZIN, M., CHENG, H., EDWARDS, R. L. & FRIEDRICH, M. 2020. The IntCal20 Northern Hemisphere radiocarbon age calibration curve (0–55 cal kBP). *Radiocarbon,* 62, 725-757.
REIMER, P. J., BARD, E., BAYLISS, A., BECK, J. W., BLACKWELL, P. G., RAMSEY, C. B., BROWN, D. M., BUCK, C. E., EDWARDS, R. L. & FRIEDRICH, M. 2013. Selection and treatment of data for radiocarbon calibration: an update to the International Calibration (IntCal) criteria. *Radiocarbon,* 55, 1923-1945.
REISSER, M., PURVES, R. S., SCHMIDT, M. W. & ABIVEN, S. 2016. Pyrogenic carbon in soils: a literature-based inventory and a global estimation of its content in soil organic carbon and stocks. *Frontiers in Earth Science,* 4**,** 80.
REPKA, J. L., ANDERSON, R. S. & FINKEL, R. C. 1997. Cosmogenic dating of fluvial terraces, Fremont River, Utah. *Earth and Planetary Science Letters,* 152, 59-73.
REYNARD, J. P. & HENSHILWOOD, C. S. 2018. Using Trampling Modification to Infer Occupational Intensity During the Still Bay at Blombos Cave, Southern Cape, South Africa. *African Archaeological Review,* 35, 1-19.
RIEBE, C. S., KIRCHNER, J. W., GRANGER, D. E. & FINKEL, R. C. 2001. Strong tectonic and weak climatic control of long-term chemical weathering rates. *Geology,* 29, 511-514.
ŘIHOŠEK, J., SLAVÍK, M., BRUTHANS, J. & FILIPPI, M. 2019. Evolution of natural rock arches: A realistic small-scale experiment. *Geology,* 47, 71-74.
RINK, W. J., DUNBAR, J. S., TSCHINKEL, W. R., KWAPICH, C., REPP, A., STANTON, W. & THULMAN, D. K. 2013. Subterranean transport and deposition of quartz by ants in sandy sites relevant to age overestimation in optical luminescence dating. *Journal of Archaeological Science,* 40, 2217-2226.
RINK, W. J., KANDEL, A. W. & CONARD, N. J. 2002. The ESR geochronology and geology of the open-air Palaeolithic deposits in Bollschweil, Germany. *Archaeometry,* 44, 635-650.
RITTER, D. F., KOCHEL, R. C. & MILLER, J. R. 2002. *Process Geomorphology* Long Grove, Waveland Press Inc, pp.652.
RIVERA-ARAYA, M., ROWE, C., LEVCHENKO, V., ULM, S. & BIRD, M. I. 2022. A radiocarbon chronology for Sanamere Lagoon, Cape York Peninsula, using multiple organic fractions. *Quaternary Geochronology,* 70, 101273.
ROBERTS, H. M. 2008. The development and application of luminescence dating to loess deposits: a perspective on the past, present and future. *Boreas,* 37, 483-507.
ROBERTS, R., BIRD, M., OLLEY, J., GALBRAITH, R., LAWSON, E., LASLETT, G., YOSHIDA, H., JONES, R., FULLAGAR, R. & JACOBSEN, G. 1998. Optical and radiocarbon dating at Jinmium rock shelter in northern Australia. *Nature,* 393, 358-362.
ROBERTS, R. G., GALBRAITH, R., YOSHIDA, H., LASLETT, G. & OLLEY, J. M. 2000. Distinguishing dose populations in sediment mixtures: a test of single-grain optical dating procedures using mixtures of laboratory-dosed quartz. *Radiation Measurements,* 32, 459-465.
ROBERTS, R. G., JACOBS, Z., LI, B., JANKOWSKI, N. R., CUNNINGHAM, A. C. & ROSENFELD, A. B. 2015. Optical dating in archaeology: thirty years in retrospect and grand challenges for the future. *Journal of Archaeological Science,* 56, 41-60.
ROBINSON, D. & WILLIAMS, R. Sandstone weathering and landforms in Britain and Europe. Rock weathering and landform evolution, 1994. 371-391.
RODRIGUEZ-NAVARRO, C. 1998. Evidence of honeycomb weathering on Mars. *Geophysical Research Letters,* 25, 3249-3252.
ROHDENBURG, H. 1982. Geomorphologisch-bodenstratigraphischer Vergleich zwischen dem nordostbrasilianischen Trockengebiet und immerfeucht-tropischen Gebieten Südbrasiliens. *Beiträge zur Geomorphologie der Tropen Ostafrika, Brasilien, Zentral-und Westafrika. Catena Suppl,* 2, 73-122.
ROUSSEEUW, P. J. & CROUX, C. 1993. Alternatives to the median absolute deviation. *Journal of the American Statistical Association,* 88, 1273-1283.
ROUSSEEUW, P. J., DEBRUYNE, M., ENGELEN, S. & HUBERT, M. 2006. Robustness and outlier detection in chemometrics. *Critical reviews in analytical chemistry,* 36, 221-242.
ROVNER, I. 1971. Potential of opal phytoliths for use in paleoecological reconstruction. *Quaternary Research,* 1, 343-359.
ROWE, C. 2007. Vegetation change following mid-Holocene marine transgression of the Torres Strait shelf: a record from the island of Mua, northern Australia. *The Holocene,* 17, 927-937.
ROWE, C., BRAND, M., HUTLEY, L. B., ZWART, C., WURSTER, C., LEVCHENKO, V. & BIRD, M. 2019. Understanding Australian tropical savanna: environmental history from a pollen perspective. *Northern Territory Naturalist,* 29, 2-11.
ROWE, C., WURSTER, C. M., ZWART, C., BRAND, M., HUTLEY, L. B., LEVCHENKO, V. & BIRD, M. I. 2021. Vegetation over the last glacial maximum at Girraween Lagoon, monsoonal northern Australia. *Quaternary Research,* 102, 39-52.
RUHE, R. V. 1959. Stone lines in soils. *Soil Science,* 87, 223-231.

RULE, S. 2020. *Millennial Perspectives on Tropical Climate Variability from the Last Glacial through to the Holocene: a palaeoecological analysis from Lynch's Crater, northeast Queensland, Australia.* Doctorate Thesis, Monash University.

RUNGE, E. C. A. 1973. Soil development sequences and energy models. *Soil Science,* 115, 183-193.

RUNGE, F. 1998. The effect of dry oxidation temperatures (500-800°C) and of natural corrosion on opal phytoliths. *In:* MEUNIER, J. D., COLIN, F. & Faure-Denard, L. (eds.) *Deuxième congrès international de recherche sur les phytolithes*, 73. Aix-en-Provence: Cerge.

RUNGE, F. 1999. The opal phytolith inventory of soils in central Africa−quantities, shapes, classification, and spectra. *Review of Palaeobotany and Palynology,* 107, 23-53.

SAGE, R. F. 2004. The evolution of C4 photosynthesis. *New Phytologist,* 161, 341-370.

SALDARRIAGA, J. G. & WEST, D. C. 1986. Holocene fires in the northern Amazon basin. *Quaternary Research,* 26, 358-366.

SALGADO, E. T., MIZUSAKI, A. M. P., CHUENG, K. F., COE, H. H. G., EVALDT, A. C. P. & BAUERMANN, S. G. 2021. Holocene palaeoenvironmental and palaeoclimatic reconstruction of a native ecosystem on the coastal plain of southern Brazil through multi-proxy analysis. *Journal of South American Earth Sciences,* 106, 103067.

SANDWEISS, D. H. & KELLEY, A. R. 2012. Archaeological contributions to climate change research: The archaeological record as a paleoclimatic and paleoenvironmental archive. *Annual Review of Anthropology,* 41, 371-391.

SANGEN, M., NEUMANN, K. & EISENBERG, J. 2011. Climate-induced fluvial dynamics in tropical Africa around the last glacial maximum? *Quaternary Research,* 76, 417-429.

SANGODE, S. J., VHATKAR, K., PATIL, S. K., MESHRAM, D. C., PAWAR, N. J., GUDADHE, S. S., BADEKAR, A. G. & KUMARAVEL, V. 2010. Magnetic susceptibility distribution in the soils of Pune Metropolitan Region: implications to soil magnetometry of anthropogenic loading. *Current Science,* 98, 516-527.

SANGSTER, A., WILLIAMS, S. & HODSON, M. 1997. Silica deposition in the needles of the gymnosperms. II Scanning electron microscopy and X-Ray microanalysis. *In:* PINILLA, A., JUAN-TRESSERRAS, J. & MACHADO, M. J. (eds.) *The State-of-the-Art of Phytoliths in Soils and Plants. First European Meeting on Phytolith Research.* Centro de Ciencas Medioambientales. CSIC Monografias 4, 135-146.

SANTÍN, C., DOERR, S. H., KANE, E. S., MASIELLO, C. A., OHLSON, M., DE LA ROSA, J. M., PRESTON, C. M. & DITTMAR, T. 2016. Towards a global assessment of pyrogenic carbon from vegetation fires. *Global Change Biology,* 22, 76-91.

SANTOS, G. M. & ALEXANDRE, A. 2017. The phytolith carbon sequestration concept: fact or fiction? A comment on "Occurrence, turnover and carbon sequestration potential of phytoliths in terrestrial ecosystems by Song et al. *Earth-Science Reviews,* 164, 251-255.

SANTOS, G. M., GOMES, P. R. S., ANJOS, R. M., CORDEIRO, R. C., TURCQ, B. J., SIFEDDINE, A., DI TADA, M. L., CRESSWELL, R. G. & FIFIELD, L. K. 2000. ^{14}C AMS dating of fires in the central Amazon rain forest. *Nuclear Instruments and Methods in Physics Research Section B: Beam Interactions with Materials and Atoms,* 172, 761-766.

SANTOS, G. M., MASION, A. & ALEXANDRE, A. 2018. When the carbon being dated is not what you think it is: Insights from phytolith carbon research. *Quaternary Science Reviews,* 197, 162-174.

SAURO, F. 2014. Structural and lithological guidance on speleogenesis in quartz–sandstone: Evidence of the arenisation process. *Geomorphology,* 226, 106-123.

SCHAEFER, J. M., CODILEAN, A. T., WILLENBRING, J. K., LU, Z.-T., KEISLING, B., FÜLÖP, R.-H. & VAL, P. 2022. Cosmogenic nuclide techniques. *Nature Reviews Methods Primers,* 2, 1-22.

SCHAETZL, R. J. & FOLLMER, L. R. 1990. Longevity of treethrow microtopography: implications for mass wasting. *Geomorphology,* 3, 113-123.

SCHAETZL, R. J., JOHNSON, D. L., BURNS, S. F. & SMALL, T. W. 1989. Tree uprooting: review of terminology, process, and environmental implications. *Canadian Journal of Forest Research,* 19, 1-11.

SCHIFFER, M. B. 1987. *Formation Processes of the Archaeological Record,* Albuquerque, NM, University of New Mexico Press, pp. 428.

SCHIMMELPFENNIG, S. & GLASER, B. 2012. One Step Forward toward Characterization: Some Important Material Properties to Distinguish Biochars. *Journal of Environmental Quality,* 41, 1001-1013.

SCHIRMER, W. 2020. Edifice of Fluvial Terrace Flights, Stacks and Rows. *Geosciences,* 10, 501.

SCHMIDT, M. W., SKJEMSTAD, J. O., CZIMCZIK, C. I., GLASER, B., PRENTICE, K. M., GELINAS, Y. & KUHLBUSCH, T. A. 2001. Comparative analysis of black carbon in soils. *Global Biogeochemical Cycles,* 15, 163-167.

SCHOENEBERGER, P. J., WYSOCKI, D. A. & BENHAM, E. C. 2012. *Field book for describing and sampling soils, Version 3.0.,* Lincoln, NE, Natural Resources Conservation Service, National Soil Survey Center.

SCHOLLE, P. A. 1979. *M 28: A Color Illustrated Guide to Constituents, Textures, Cements, and Porosities of Sandstones and Associated Rocks,* Tulsa, Oklahoma, American Association of The American Association of Petroleum Geologists Foundation, pp. 193.

SCHROEDTER, T. M., DREIBRODT, S., HOFMANN, R., LOMAX, J., MÜLLER, J. & NELLE, O. 2013. Interdisciplinary interpretation of challenging archives: Charcoal assemblages in Drina Valley alluvial and colluvial sediments (Jagnilo, Bosnia and Herzegovina). *Quaternary International,* 289, 36-45.

SCHUMM, S. A. 1977. *The Fluvial System*, The Blackburn Press, pp. 338.

SÉGALEN, P. 1969. Le remaniement des sols et la mise en place de la stone-line en Afrique. *Cahiers ORSTOM, série Pédolologique,* 7, 113-131.

SELKIN, P. A., STRÖMBERG, C. A., DUNN, R., KOHN, M. J., CARLINI, A. A., DAVIES-VOLLUM, K. S. & MADDEN, R. H. 2015. Climate, dust, and fire across the Eocene-Oligocene transition, Patagonia. *Geology,* 43, 567-570.

SHARON, G., ZAIDNER, Y. & HOVERS, E. 2014. Opportunities, problems and future directions in the study of open-air Middle Paleolithic sites. *Quaternary International,* 331, 1-5.

SHEN, Z., TÖRNQVIST, T. E., AUTIN, W. J., MATEO, Z. R. P., STRAUB, K. M. & MAUZ, B. 2012. Rapid and widespread response of the Lower Mississippi River to eustatic forcing during the last glacial-interglacial cycle. *GSA Bulletin,* 124, 690-704.

SHIPTON, C., COHEN, T., FORBES, M., BOESL, F., JACOBS, Z., DIXON, R. D., DIXON, E., KINGSTON, S., ALBERT, C. & O'CONNOR, S. 2021. Diverse stone artefacts around Lake Woods, Central Northern Territory, Australia. *Australian Archaeology,* 87, 156-178.

SHULMEISTER, J. 1999. Australasian evidence for mid-Holocene climate change implies precessional control of Walker Circulation in the Pacific. *Quaternary International,* 57, 81-91.

SHULMEISTER, J. & LEES, B. G. 1992. Morphology and chronostratigraphy of a coastal dunefield; Groote Eylandt, northern Australia. *Geomorphology,* 5, 521-534.

SHULMEISTER, J. & LEES, B. G. 1995. Pollen evidence from tropical Australia for the onset of an ENSO-dominated climate at c. 4000 BP. *The Holocene,* 5, 10-18.

SIEDEL, H. 2015. Cavernous Weathering Features. *In:* HARGATAI, H. & KERESZTURI, A. (eds.) *Encyclopedia of Planetary Landforms.* Berlin: Springer, 231-236

SIVIA, D., BURBIDGE, C., ROBERTS, R. G. & BAILEY, R. A Bayesian approach to the evaluation of equivalent doses in sediment mixtures for luminescence dating. AIP Conference Proceedings, 2004. American Institute of Physics, 305-311.

SKJEMSTAD, J. O., CLARKE, P., TAYLOR, J., OADES, J. & MCCLURE, S. 1996. The chemistry and nature of protected carbon in soil. *Soil Research,* 34, 251-271.

SLACK, M. J., FULLAGAR, R. L., FIELD, J. H. & BORDER, A. 2004. New Pleistocene ages for backed artefact technology in Australia. *Archaeology in Oceania,* 39, 131-137.

SLACK, M. J., LAW, W. B. & GLIGANIC, L. A. 2018. Pleistocene settlement of the eastern Hamersley Plateau: A regional study of 22 rock-shelter sites. *Archaeology in Oceania,* 53, 191-204.

SMART, J. 1973 Gilberton, Queensland 1:250,000 Geological Series, Explanatory Notes, Sheet SE54-16. Canberra: Australian Government Publishing Service.

SMART, J., GRIMES, K., DOUTCH, H. & PINCHIN, J. 1980. The Mesozoic Carpentaria and the Cainozoic Karumba Basin, Northern Queensland. Bureau of Mineral Resources, Australia. *BMR Bulletin,* 202.

SMART, J., INGRAM, J. A., DOUTCH, H. F. & GRIMES, K. G. 1971. Recent mapping in the Carpentaria Basin − New stratigraphic names. *Queensland Government Mining Journal,* 72, 227-233.

SMART, J. & SENIOR, B. R. 1980. Jurassic-Cretaceous basins of northeastern Australia. *In:* HENDERSON, R. A. & STEPHENSON, P. J. (eds.) *The Geology and Geophysics of Northeastern Australia.* Brisbane, Queensland, Australia: Geological Society of Australia, Queensland Division.

SMITH, M. 1993. Biogeography, human ecology and prehistory in the sandridge deserts. *Australian Archaeology,* 37, 35-50.

SMITH, M. 2005. Palaeoclimates: An archaeology of climate change. *In:* SHERRAT, T., GRIFFITHS, T. & ROBIN, L. (eds.) *A change in the weather: Climate and culture in Australia.* Canberra: National Museum of Australia, 176-186.

SMITH, M. 2013. *The Archaeology of Australia's Deserts*, Cambridge University Press, pp. 406.

SMITH, M., WARD, I. & MOFFAT, I. 2021. Letter to the editors on termite stone lines. *Geoarchaeology,* 36, 363-365.

SMITH, M. A., VELLEN, L. & PASK, J. 1995. Vegetation history from archaeological charcoals in central Australia; the late Quaternary record from Puritjarra rock shelter. *Vegetation History and Archaeobotany,* 4, 171-177.

SMITH, M. A., WARD, I. & MOFFAT, I. 2020. How do we distinguish termite stone lines from artefact horizons? A challenge for geoarchaeology in tropical Australia. *Geoarchaeology,* 35, 232-242.

SOIL SCIENCE SOCIETY OF AMERICA, 2001. Glossary of Soil Science Terms, Madison, Soil Science Society of America.

SOLEREDER, H. 1908. *Systematic Anatomy of the Dicotyledons: A Handbook for Laboratories of Pure and Applied Botany. Vol. 2,* Oxford: Clarendon Press.

SOMMER, M., JOCHHEIM, H., HÖHN, A., BREUER, J., ZAGORSKI, Z., BUSSE, J., BARKUSKY, D., PUPPE, D., WANNER, M. & KACZOREK, D. 2012. Si cycling in a forest biogeosystem–the importance of anthropogenic perturbation and induced transient state of biogenic Si pools. *Biogeosciences Discussions,* 9, 18865-18906.

SOMMER, M., KACZOREK, D., KUZYAKOV, Y. & BREUER, J. 2006. Silicon pools and fluxes in soils and landscapes—a review. *Journal of Plant Nutrition and Soil Science,* 169, 310-329.

SONETT, C. & FINNEY, S. 1990. The spectrum of radiocarbon. *Philosophical Transactions of the Royal Society of London. Series A, Mathematical and Physical Sciences,* 330, 413-426.
SONG, Z., MCGROUTHER, K. & WANG, H. 2016. Occurrence, turnover and carbon sequestration potential of phytoliths in terrestrial ecosystems. *Earth-Science Reviews,* 158, 19-30.
SORENG, R. J., PETERSON, P. M., ROMASCHENKO, K., DAVIDSE, G., TEISHER, J. K., CLARK, L. G., BARBERÁ, P., GILLESPIE, L. J. & ZULOAGA, F. O. 2017. A worldwide phylogenetic classification of the Poaceae (Gramineae) II: An update and a comparison of two 2015 classifications. *Journal of Systematics and Evolution,* 55, 259-290.
SPASSOV, S., EGLI, R., HELLER, F., NOURGALIEV, D. & HANNAM, J. 2004. Magnetic quantification of urban pollution sources in atmospheric particulate matter. *Geophysical Journal International,* 159, 555-564.
SPENCER, T. 1994. A documentation of archaeological sites on the 1:250 000 sheets for Richmond, Julia Creek, Camooweal and some adjoining areas. *Unpublished report to the Queensland Museum, Brisbane.*
SPOONER, M. I., BARROWS, T. T., DE DECKKER, P. & PATERNE, M. 2005. Palaeoceanography of the Banda Sea, and late Pleistocene initiation of the northwest monsoon. *Global and Planetary Change,* 49, 28-46.
SPOONER, M. I., DE DECKKER, P., BARROWS, T. T. & FIFIELD, L. K. 2011. The behaviour of the Leeuwin Current offshore NW Australia during the last five glacial–interglacial cycles. *Global and Planetary Change,* 75, 119-132.
SQUIRES, V. R. 1982. Competitive interactions in the dietary preference of kangaroos and sheep, cattle and goats in inland Australia. *Journal of Arid Environments,* 5, 337-345.
STOCKING, M. A. 1978. Interpretation of Stone-Lines. *South African Geographical Journal,* 60, 121-134.
STOCKMANN, U., MINASNY, B., PIETSCH, T. & MCBRATNEY, A. 2013. Quantifying processes of pedogenesis using optically stimulated luminescence. *European Journal of Soil Science,* 64, 145-160.
STOCKTON, E. D. 1973. Shaw's Creed Shelter: Human Displacement of Artefacts and its Significance. *The Australian Journal of Anthropology,* 9, 112-117.
STONE, J. O. 2000. Air pressure and cosmogenic isotope production. *Journal of Geophysical Research: Solid Earth,* 105**,** 23753-23759.
STOOPS, G., MARCELINO, V. & MEES, F. (eds.) 2018. *Interpretation of Micromorphological Features of Soils and Regoliths*, Elsevier Science, pp. 752.
STOTT, L., TIMMERMANN, A. & THUNELL, R. 2007. Southern Hemisphere and deep-sea warming led deglacial atmospheric CO2 rise and tropical warming. *Science,* 318, 435-438.
STRÖMBERG, C. 2007. Can slide preparation methods cause size biases in phytolith assemblages?: Results from a preliminary study. *In:* MANDELLA, M. & ZURRO, D. (ed) *Places, People and Plants: Recent studies in phytolith analysis.* Oxford: Oxbow Books*,* 1-12.
STRÖMBERG, C. A. 2002. The origin and spread of grass-dominated ecosystems in the late Tertiary of North America: preliminary results concerning the evolution of hypsodonty. *Palaeogeography, Palaeoclimatology, Palaeoecology,* 177, 59-75.
STRÖMBERG, C. A. 2003. *The origin and spread of grass-dominated ecosystems during the Tertiary of North America and how it relates to the evolution of Hypsodonty in Equids.* Doctorate Thesis, University of California, Berkeley.
STRÖMBERG, C. A. 2004. Using phytolith assemblages to reconstruct the origin and spread of grass-dominated habitats in the great plains of North America during the late Eocene to early Miocene. *Palaeogeography, Palaeoclimatology, Palaeoecology,* 207, 239-275.
STRÖMBERG, C. A. 2005. Decoupled taxonomic radiation and ecological expansion of open-habitat grasses in the Cenozoic of North America. *Proceedings of the National Academy of Sciences,* 102, 11980-11984.
STRÖMBERG, C. A. 2009. Methodological concerns for analysis of phytolith assemblages: does count size matter? *Quaternary International,* 193, 124-140.
STRÖMBERG, C. A., DUNN, R. E., CRIFÒ, C. & HARRIS, E. B. 2018. Phytoliths in Paleoecology: Analytical considerations, current use, and future directions. *Methods in Paleoecology.* Springer, 235-287.
STRÖMBERG, C. A., DUNN, R. E., MADDEN, R. H., KOHN, M. J. & CARLINI, A. A. 2013. Decoupling the spread of grasslands from the evolution of grazer-type herbivores in South America. *Nature Communications,* 4, 1-8.
STRÖMBERG, C. A., FRIIS, E. M., LIANG, M.-M., WERDELIN, L. & ZHANG, Y.-U. 2007b. Palaeoecology of a Middle Miocene lake in China: preliminary interpretations based on phytoliths from the Shanwang Basin. *Vertebrata PalAsiatica,* 45, 145-160.
STRÖMBERG, C. A., WERDELIN, L., FRIIS, E. M. & SARAÇ, G. 2007a. The spread of grass-dominated habitats in Turkey and surrounding areas during the Cenozoic: phytolith evidence. *Palaeogeography, Palaeoclimatology, Palaeoecology,* 250, 18-49.
STUIVER, M., BRAZIUNAS, T. F., BECKER, B. & KROMER, B. 1991. Climatic, solar, oceanic, and geomagnetic influences on late-glacial and Holocene atmospheric $^{14}C/^{12}C$ change. *Quaternary Research,* 35, 1-24.
STURMAN, A. P. & TAPPER, N. J. 1996. *The Weather and Climate of Australia and New Zealand,* USA, Oxford University Press, pp.541.
TACHIKAWA, K., VIDAL, L., SONZOGNI, C. & BARD, E. 2009. Glacial/interglacial sea surface temperature changes in the Southwest Pacific ocean over the past 360 ka. *Quaternary Science Reviews,* 28, 1160-1170.

TESTÉ, M., GARNIER, A., LIMONDIN-LOZOUET, N., OXLAJ, E., CASTANET, C., PURDUE, L., LEMONNIER, E., DUSSOL, L. & NONDÉDÉO, P. 2020. The phytoliths of Naachtun (Petén, Guatemala): Development of a modern reference for the characterization of plant communities in the Maya Tropical Lowlands. *Review of Palaeobotany and Palynology,* 272, 104130.

THACKWAY, R. & CRESSWELL, I. D. 1995. An Interim Biogeographic Regionalisation for Australia: a Framework for Establishing the National System of Reserves. Australian Nature Conservation Agency, Canberra.

THOMAS, M. F. 1974. *Tropical Geomorphology: A Study of Weathering and Landform Development in Warm Climates,* London: Macmillian, pp. 332.

THOMAS, M. F., NOTT, J. & PRICE, D. M. 2001. Late Quaternary stream sedimentation in the humid tropics: a review with new data from NE Queensland, Australia. *Geomorphology,* 39, 53-68.

THOMPSON, R. & OLDFIELD, F. 1986. *Environmental Magnetism.* London: Allen and Unwin Ltd, pp. 228.

THORN, V. C. 2004. Phytolith evidence for C4-dominated grassland since the early Holocene at Long Pocket, northeast Queensland, Australia. *Quaternary Research,* 61, 168-180.

THULMAN, D. K. 2012. Bioturbation and the Wakulla Springs Lodge site artifact distribution. *The Florida Anthropologist,* 65, 25-34.

TIBBY, J. 2012. The Younger Dryas: relevant in the Australian region? *Quaternary International,* 253**,** 47-54.

TIESZEN, L. L. & BOUTTON, T. W. 1989. Stable Carbon Isotopes in Terrestrial Ecosystem Research. *In:* RUNDEL, P. W., EHLERINGER, J. R. & NAGY, K. A. (eds.) *Stable Isotopes in Ecological Research, vol 68.* New York: Springer, 167-195.

TIESZEN, L. L., BOUTTON, T. W., TESDAHL, K. G. & SLADE, N. A. 1983. Fractionation and turnover of stable carbon isotopes in animal tissues: implications for $\delta^{13}C$ analysis of diet. *Oecologia,* 57, 32-37.

TINDALE, N. B. 1981. Prehistory of the Aborigines: Some interesting considerations. *In:* KEAST, A. (ed.) *Ecological Biogeography of Australia.* The Hague: Dr W Junk Publishers, 1761-1796.

TITE, M. S. & MULLINS, C. 1971. Enhancement of the magnetic susceptibility of soils on archaeological sites. *Archaeometry,* 13 The Hague 209-219.

TODD, C. N. 2020. *The sedimentary evolution of Permian to Cretaceous basins in Queensland, Australia: insights from lithostratigraphy, U–Pb zircon geochronology, sedimentary facies, and provenance analysis.* PhD Thesis, James Cook University.

TOFELDE, S., SAVI, S., WICKERT, A. D., BUFE, A. & SCHILDGEN, T. F. 2019. Alluvial channel response to environmental perturbations: fill-terrace formation and sediment-signal disruption. *Earth Surf. Dynam.,* 7, 609-631.

TOMBEUR, F. D., TURNER, B., LALIBERTÉ, E., LAMBERS, H., MAHY, G., FAUCON, M.-P., ZEMUNIK, G. & CORNELIS, J.-T. 2020. Plants sustain the terrestrial silicon cycle during ecosystem retrogression. *Science,* 369, 1245-1248.

TRICART, J. 1972. *Landforms of the Humid Tropics, Forests and Savannas*. London: Longman, pp.306.

TRIPATHI, D., KOTLIA, B. S., TIWARI, M., POKHARIA, A. K., AGRAWAL, S., KUMAR, P., LONG, T., PAULRAMASAMY, M., THAKUR, B. & PAL, J. 2021. New evidence of mid-to late-Holocene vegetation and climate change from a Neolithic settlement in western fringe of Central Ganga Plain: Implications for Neolithic to Historic phases. *The Holocene,* 31, 392-408.

TRUMBORE, S. E. & ZHENG, S. 1996. Comparison of fractionation methods for soil organic matter ^{14}C analysis. *Radiocarbon,* 38, 219-229.

TSARTSIDOU, G., LEV-YADUN, S., ALBERT, R.-M., MILLER-ROSEN, A., EFSTRATIOU, N. & WEINER, S. 2007. The phytolith archaeological record: strengths and weaknesses evaluated based on a quantitative modern reference collection from Greece. *Journal of Archaeological Science,* 34, 1262-1275.

TUCKER, R. T., ROBERTS, E. M., DARLINGTON, V. & SALISBURY, S. W. 2017. Investigating the stratigraphy and palaeoenvironments for a suite of newly discovered mid-Cretaceous vertebrate fossil-localities in the Winton Formation, Queensland, Australia. *Sedimentary Geology,* 358, 210-229.

TUCKER, R. T., ROBERTS, E. M., HENDERSON, R. A. & KEMP, A. I. 2016. Large igneous province or long-lived magmatic arc along the eastern margin of Australia during the Cretaceous? Insights from the sedimentary record. *GSA Bulletin,* 128, 1461-1480.

TUDHOPE, A. W., CHILCOTT, C. P., MCCULLOCH, M. T., COOK, E. R., CHAPPELL, J., ELLAM, R. M., LEA, D. W., LOUGH, J. M. & SHIMMIELD, G. B. 2001. Variability in the El Niño-Southern Oscillation through a glacial-interglacial cycle. *Science,* 291, 1511-1517.

TURKINGTON, A. 1998. Cavernous weathering in sandstone: lessons to be learned from natural exposure. *Quarterly Journal of Engineering Geology and Hydrogeology,* 31, 375-383.

TURKINGTON, A. V. 2004. Cavernous Weathering. *In:* GOUDIE, A. S. (ed.) *Encyclopedia of Geomorphology.* London: Routledge,Taylor & Francis Group, 128-130.

TURKINGTON, A. V. & PARADISE, T. R. 2005. Sandstone weathering: a century of research and innovation. *Geomorphology,* 67, 229-253.

TURKINGTON, A. V. & PHILLIPS, J. D. 2004. Cavernous weathering, dynamical instability and self-organization. *Earth Surface Processes and Landforms,* 29, 665-675.

TURNEY, C. S., BIRD, M. I., FIFIELD, L. K., KERSHAW, A. P., CRESSWELL, R., SANTOS, G., DI TADA, M., HAUSLADEN, P. & YOUPING, Z. 2001. Development of a robust ^{14}C chronology for Lynch's Crater (North Queensland, Australia) using different pretreatment strategies. *Radiocarbon,* 43, 45-54.

TURNEY, C. S., KERSHAW, A. P., LOWE, J. J., VAN DER KAARS, S., JOHNSTON, R., RULE, S., MOSS, P., RADKE, L., TIBBY, J. & MCGLONE, M. S. 2006. Climatic variability in the southwest Pacific during the Last Termination (20–10 kyr BP). *Quaternary Science Reviews,* 25, 886-903.

TWIDALE, C. R. 1966. Geomorphology of the Leichardt-Gilbert Area of North-west Queensland. *Land Research Series, No.16.* Melbourne, Australia: Commonwealth Scientific and Industrial Research Organization.

TWIDALE, C. R. 2014. Pediments and platforms: problems and solutions. *Géomorphologie: relief, processus, environnement,* 20, 43-56.

TWISS, P. C. 1992. Predicted World Distribution of C3 and C4 Grass Phytoliths. *In:* RAPP, G. & MULHOLLAND, S. C. (eds.) *Phytolith Systematics. Advances in Archaeological and Museum Science, vol 1.* . Boston: Springer, 113-128.

UA, 2022. *The Carbon cycle* [Online]. Available:http://www.atmo.arizona.edu/students/courselinks/fall16/atmo336s2/lectures/sec3/carbon.html [Accessed 15.04. 2023].

ULERY, A., GRAHAM, R. & BOWEN, L. 1996. Forest fire effects on soil phyllosilicates in California. *Soil Science Society of America Journal,* 60, 309-315.

ULERY, A. L. & GRAHAM, R. C. 1993. Forest Fire Effects on Soil Color and Texture. *Soil Science Society of America Journal,* 57, 135-140.

ULM, S. 2013. 'Complexity' and the Australian continental narrative: Themes in the archaeology of Holocene Australia. *Quaternary International,* 285, 182-192.

URBAN, J. & GÓRNIK, M. 2017. Some aspects of lithological and exogenic control of sandstone morphology, the Świętokrzyskie (Holy Cross) Mts. case study, Poland. *Geomorphology,* 295, 773-789.

UTHMEIER, T. & CHABAI, V. 2018. Formation processes at sites with high-resolution sequences in the Crimean Middle Paleolithic: The Kabazi V rock shelter and the open-air site of Kabazi II compared. *Quaternary International,* 485, 44-67.

VAN DER KAARS, S. & DE DECKKER, P. 2002. A Late Quaternary pollen record from deep-sea core Fr10/95, GC17 offshore Cape Range Peninsula, northwestern Western Australia. *Review of Palaeobotany and Palynology,* 120**,** 17-39.

VAN DER MEER, J. J. & MENZIES, J. 2011. The micromorphology of unconsolidated sediments. *Sedimentary Geology,* 238, 213-232.

VAN DER MEER, J. J., MÜCHER, H. J. & HÖFLE, H. C. 1993. Micromorphological Observations on Till Samples from Shackleton Range and North Victoria Land, Antarctica. *Polarforschung,* 62, 57-65.

VAN GEEL, B., VAN DER PLICHT, J. & RENSSEN, H. 2003. Major $\Delta^{14}C$ excursions during the late glacial and early Holocene: changes in ocean ventilation or solar forcing of climate change? *Quaternary International,* 105, 71-76.

VAN HEESWIJCK, A. 2004. The structure and hydrocarbon potential of the northern Drummond Basin and northeastern Galilee Basin, central Queensland, Australia. *In:* BOULT, P. J., JOHNS, D. R. & LANG, S. C. (eds.) PESA's Eastern Australasian Basin Symposium II. Conference Proceedings, 2004 Adelaide, South Australia.

VAN HEESWIJCK, A. 2010. Late Paleozoic to early Mesozoic deformation in the northeastern Galilee Basin, Australia. *Australian Journal of Earth Sciences,* 57, 431-451.

VANNIEUWENHUYSE, D. 2016. *Mind the gap: Geoarchaeology and micromorphology of cave and rockshelter sequences from the Kimberley, north-west Australia.* PhD Thesis, University of Western Australia.

VEEVERS, J. 2006. Updated Gondwana (Permian–Cretaceous) earth history of Australia. *Gondwana Research,* 9, 231-260.

VEIT, H. & VEIT, H. 1985. Relief, Gestein und Boden im Gebiet von Conceição dos Correias (S Brasilien). *Fankf. Geow. Arb. Serie D. Phys. Geogr.,* 5, 1-98.

VEPRASKAS, M. J. 2015. Redoximorphic Features for Identifying Aquic Conditions. *Technical Bulletin 301, North Carolina Agricultural Research Service, Raleigh*, 33.

VEPRASKAS, M. J. & VAUGHAN, K. L. 2016. Morphological features of hydric and reduced soils. *In:* VEPRASKAS, M. J. & CRAFT, C. B. (eds.) *Wetland soils: Genesis, Hydrology, Landscapes and Classification.* Boca Raton: Lewis Publisher, 189-217.

VETH, P., O'CONNOR, S. & WALLIS, L. A. 2000. Perspectives on ecological approaches in Australian archaeology. *Australian Archaeology,* 50, 54-66.

VETH, P., SMITH, M., BOWLER, J., FITZSIMMONS, K., WILLIAMS, A. & HISCOCK, P. 2009. Excavations at Parnkupirti, Lake Gregory, great sandy desert: OSL ages for occupation before the last glacial maximum. *Australian Archaeology,* 69, 1-10.

VETH, P., WARD, I., MANNE, T., ULM, S., DITCHFIELD, K., DORTCH, J., HOOK, F., PETCHEY, F., HOGG, A., QUESTIAUX, D., DEMURO, M., ARNOLD, L., SPOONER, N., LEVCHENKO, V., SKIPPINGTON, J., BYRNE, C., BASGALL, M.,

ZEANAH, D., BELTON, D., HELMHOLZ, P., BAJKAN, S., BAILEY, R., PLACZEK, C. & KENDRICK, P. 2017. Early human occupation of a maritime desert, Barrow Island, North-West Australia. *Quaternary Science Reviews,* 168, 19-29.

VETH, P. M. 1993. *Islands in the Interior: The Dynamics of Prehistoric Adaptations Within the Arid Zone of Australia*, International Monographs in Prehistory, pp. 144.

VILES, H. 2005. Self-organized or disorganized? Towards a general explanation of cavernous weathering. *Earth Surface Processes and Landforms,* 30, 1471-1473.

VILES, H. A., GOUDIE, A. S. & GOUDIE, A. M. 2021. Ants as geomorphological agents: A global assessment. *Earth-Science Reviews,* 213, 103469.

VILLAGRAN, X. S., STRAUSS, A., MILLER, C., LIGOUIS, B. & OLIVEIRA, R. 2017. Buried in ashes: Site formation processes at Lapa do Santo rockshelter, east-central Brazil. *Journal of Archaeological Science,* 77, 10-34.

VOGT, J. 1966. Le complexe da la stone-line. Mise an point. *Bull. Bur. Rèch. Géol. Min.,* 4, 3-51.

VON BLANCKENBURG, F. 2005. The control mechanisms of erosion and weathering at basin scale from cosmogenic nuclides in river sediment. *Earth and Planetary Science Letters,* 237, 462-479.

VRYDAGHS, L., BALL, T. B. & DEVOS, Y. 2016. Beyond redundancy and multiplicity. Integrating phytolith analysis and micromorphology to the study of Brussels Dark Earth. *Journal of Archaeological Science,* 68, 79-88.

WAINMAN, C., HANNAFORD, C., MANTLE, D. & MCCABE, P. 2018a. Utilizing U–Pb CA-TIMS dating to calibrate the Middle to Late Jurassic spore-pollen zonation of the Surat Basin, Australia to the geological time-scale. *Alcheringa: An Australasian Journal of Palaeontology,* 42, 402-414.

WAINMAN, C., MCCABE, P., CROWLEY, J. & NICOLL, R. 2015. U−Pb zircon age of the Walloon Coal Measures in the Surat Basin, southeast Queensland: implications for paleogeography and basin subsidence. *Australian Journal of Earth Sciences,* 62, 807-816.

WAINMAN, C. C. & MCCABE, P. J. 2019. Evolution of the depositional environments of the Jurassic Walloon Coal Measures, Surat Basin, Queensland, Australia. *Sedimentology,* 66, 1673-1699.

WAINMAN, C. C., MCCABE, P. J. & CROWLEY, J. L. 2018b. Solving a tuff problem: Defining a chronostratigraphic framework for Middle to Upper Jurassic nonmarine strata in eastern Australia using uranium–lead chemical abrasion–thermal ionization mass spectrometry zircon dates. *AAPG Bulletin,* 102, 1141-1168.

WALLIS, A. L. 2018. Phytolith Analysis of Sediment Samples from Djadjiling (HD07-1A-04), Jundaru (HN-A9) and HD07-3A-PAD13, Pilbara, Western Australia. *In:* CROPPER, D. & LAW, W. B. (eds.) *Rockshelter Excavations in the East Hamersley Range, Pilbara Region, Western Australia.* Oxford: Archaeopress Publishing Ltd, 359-384.

WALLIS, L. 2003. An overview of leaf phytolith production patterns in selected northwest Australian flora. *Review of Palaeobotany and Palynology,* 125, 201-248.

WALLIS, L. A. 2000. *Phytoliths, Late Quaternary environment and archaeology in tropical semi-arid northwest Australia.* PhD Thesis, The Australian National University.

WALLIS, L. A. 2001. Environmental history of northwest Australia based on phytolith analysis at Carpenter's Gap 1. *Quaternary International,* 83, 103-117.

WALLIS, L. A. 2002. AMS dates and phytolith data from mud wasp and bird nests at Carpenter's Gap 1, Northern Australia. *Australian Archaeology*, 55, 35-39.

WALLIS, L. A. 2008. Archaeological Excavations at Gledswood 1 Shelter, Northwest Queensland. Unpublished final report prepared for the Woolgar Valley Aboriginal Corporation and Australian Institute of Aboriginal and Torres Strait Islander Studies (Grant Number G2007/7270).

WALLIS, L. A., FITZSIMMONS, K., LOWE, K. M., KEYS, B. O., MOFFAT, I., CARAH, X., WRIGHT, N. & MENTZER, S. 2014a. Unpublished site report on Gledswood Shelter 1.

WALLIS, L. A., KEYS, B., MOFFAT, I. & FALLON, S. 2009. Gledswood Shelter 1: Initial radiocarbon dates from a Pleistocene aged rockshelter site in northwest Queensland. *Australian Archaeology*, 69, 71-74.

WALLIS, L. A., LOWE, K. M., POPELKA-FILCOFF, R., BENNETT, J. W., ST GEORGE, C., WATSON, C., FITZSIMMONS, K., LENEHAN, C., WATCHMAN, A., WIGHT, C. & MATTHEWS, J. 2014b. Ochre through the late Quaternary at Gledswood Shelter 1, northwest Queensland *Australasian Quaternary Association Biennial Conference.* Mildura.

WALLIS, L. A., SMITH, D. & SMITH, H. 2004a. Recent Archaeological Surveys on Middle Park Station, Northwest Queensland. *Australian Archaeology*, 59, 43-50.

WALLIS, L. A., SMITH, H. & SMITH, D. 2004b. Investigations of Aboriginal hearth sites along the Finders River, inland north west Queensland. *The Artefact: the Journal of the Archaeological and Anthropological Society of Victoria,* 27, 59-76.

WALTHALL, J. A. 1998. Rockshelters and hunter-gatherer adaptation to the Pleistocene/Holocene transition. *American Antiquity,* 63, 223-238.

WANG, J., LA CROIX, A. D., GONZALEZ, S., HE, J. & UNDERSCHULTZ, J. 2019. Sequence stratigraphic analysis of the Lower Jurassic Precipice Sandstone and Evergreen Formation in the Surat Basin, Australia: Implications for the architecture of reservoirs and seals for CO2 storage. *Marine and Petroleum Geology,* 102, 829-843.

WANG, Y.-J., CHENG, H., EDWARDS, R. L., AN, Z., WU, J., SHEN, C.-C. & DORALE, J. A. 2001. A high-resolution absolute-dated late Pleistocene monsoon record from Hulu Cave, China. *Science,* 294, 2345-2348.

WANG, Y., AMUNDSON, R. & TRUMBORE, S. 1996. Radiocarbon dating of soil organic matter. *Quaternary Research,* 45, 282-288.

WARD, I. & LARCOMBE, P. 2003. A process-orientated approach to archaeological site formation: application to semi-arid Northern Australia. *Journal of Archaeological Science,* 30, 1223-1236.

WARD, I., NANSON, G. C., HEAD, L. M., FULLAGAR, R. L. K., PRICE, D. M. & FINK, D. 2005. Late Quaternary landscape evolution in the Keep River region, northwestern Australia. *Quaternary Science Reviews,* 24, 1906-1922.

WARD, I., WINTER, S. & DOTTE-SAROUT, E. 2016. The lost art of stratigraphy? A consideration of excavation strategies in Australian Indigenous Archaeology. *Australian Archaeology,* 82**,** 263-274.

WARD, I. A. 2003. *Hidden in the sands of time: Geoarchaeology of sandstone landscapes in the Keep River region, Northern Territory, Australia.* PhD Thesis, University of Wollongong

WARD, I. A. K., FULLAGAR, R. L. K., BOER-MAH, T., HEAD, L. M., TAÇON, P. S. C. & MULVANEY, K. 2006. Comparison of sedimentation and occupation histories inside and outside rock shelters, Keep-River region, northwestern Australia. *Geoarchaeology,* 21, 1-27.

WATLING, J. & IRIARTE, J. 2013. Phytoliths from the coastal savannas of French Guiana. *Quaternary International,* 287, 162-180.

WEBSTER, P. J. & STRETEN, N. A. 1978. Late Quaternary Ice Age Climates of Tropical Australasia: Interpretations and Reconstructions. *Quaternary Research,* 10, 279-309.

WESLEY, D., LITSTER, M., MOFFAT, I. & O'CONNOR, S. 2018. Indigenous built structures and anthropogenic impacts on the stratigraphy of Northern Australian rockshelters: insights from Malarrak 1, north western Arnhem Land. *Australian Archaeology,* 84, 3-18.

WHITAU, R., BALME, J., O'CONNOR, S. & WOOD, R. 2017. Wood charcoal analysis at Riwi cave, Gooniyandi country, Western Australia. *Quaternary International,* 457, 140-154.

WHITE, A. F., VIVIT, D. V., SCHULZ, M. S., BULLEN, T. D., EVETT, R. R. & AAGARWAL, J. 2012. Biogenic and pedogenic controls on Si distributions and cycling in grasslands of the Santa Cruz soil chronosequence, California. *Geochimica et Cosmochimica Acta,* 94, 72-94.

WILD, S. 1986. Voyaging to Australia: 30,000 years ago. *Computers & Graphics,* 10, 207-212.

WILKINS, D., GOURAMANIS, C., DE DECKKER, P., FIFIELD, L. K. & OLLEY, J. 2013. Holocene lake-level fluctuations in Lakes Keilambete and Gnotuk, southwestern Victoria, Australia. *The Holocene,* 23, 784-795.

WILKINSON, M. T., RICHARDS, P. J. & HUMPHREYS, G. S. 2009. Breaking ground: pedological, geological, and ecological implications of soil bioturbation. *Earth-Science Reviews,* 97, 257-272.

WILLIAMS, A. N., ULM, S., COOK, A. R., LANGLEY, M. C. & COLLARD, M. 2013. Human refugia in Australia during the Last Glacial Maximum and Terminal Pleistocene: a geospatial analysis of the 25–12 ka Australian archaeological record. *Journal of Archaeological Science,* 40, 4612-4625.

WILLIAMS, A. N., VETH, P., STEFFEN, W., ULM, S., TURNEY, C. S. M., REEVES, J. M., PHIPPS, S. J. & SMITH, M. 2015. A continental narrative: Human settlement patterns and Australian climate change over the last 35,000 years. *Quaternary Science Reviews,* 123, 91-112.

WILLIAMS, F. 2018a. Report on Optically Stimulated Luminescence (OSL) Dating of a Further Four Samples from HD07-3A-PAD13 Rockshelter, Pilbara, Western Australia. *In:* CROPPER, D. & LAW, B. W. (eds.) *Rockshelter Excavations in the East Hamersley Range, Pilbara Region, Western Australia.* Oxford: Archaeopress Publishing Ltd, 421-429.

WILLIAMS, M. A. 2019. Termites and stone lines-traps for the unwary archaeologist. *Quaternary Science Reviews,* 226, 106028.

WILLIAMS, M. A., SPOONER, N. A., MCDONNELL, K. & O'CONNELL, J. F. 2021. Identifying disturbance in archaeological sites in tropical northern Australia: Implications for previously proposed 65,000-year continental occupation date. *Geoarchaeology,* 36, 92-108.

WILLIAMS, M. A. J. 1969. Prediction of Rainsplash Erosion in the Seasonally Wet Tropics. *Nature,* 222, 763-765.

WILLIAMS, M. A. J. 1976. Erosion in the Alligator Rivers area. *In:* STORY, R., GALLOWAY, R. W., MCALPINE J. R., ALDRICK, J. M., WILLIAMS, M. A. J. (eds.) *Lands of the Alligator Rivers Area Northern Territory.* Melbourne: CSIRO Land Research, 112-125.

WILLIAMS, M. A. J. 2018b. Report on the Geomorphology and Quaternary Geology of HD07-3A-PAD13 Rockshelter, Pilbara, Western Australia. *In:* CROPPER, D. & LAW, B. W. (eds.) *Rockshelter Excavations in the East Hamersley Range, Pilbara Region, Western Australia.* Oxford: Archaeopress Publishing Ltd, 429-435.

WILLIAMS, P. W. 1996. A 230 ka record of glacial and interglacial events from Aurora Cave, Fiordland, New Zealand. *New Zealand Journal of Geology and Geophysics,* 39, 225-241.

WILSON, M. D. & PITTMAN, E. D. 1977. Authigenic clays in sandstones; recognition and influence on reservoir properties and paleoenvironmental analysis. *Journal of Sedimentary Research,* 47, 3-31.

WINTLE, A. G. 1997. Luminescence dating: laboratory procedures and protocols. *Radiation Measurements,* 27**,** 769-817.

WOOD, R., JACOBS, Z., VANNIEUWENHUYSE, D., BALME, J., O'CONNOR, S. & WHITAU, R. 2016. Towards an accurate and precise chronology for the colonization of Australia; the example of Riwi, Kimberley, Western Australia. *PloS one,* 2016**,** e0160123-e0160123.

WOOD, W. R. & JOHNSON, D. L. 1978. A survey of disturbance processes in archaeological site formation. *Advances in Archaeological Method and Theory,* 1, 315-381.

WOODROFFE, C. D., THOM, B. G. & CHAPPELL, J. 1985. Development of widespread mangrove swamps in mid-Holocene times in northern Australia. *Nature,* 317, 711-713.

WOODWARD, J. C. & BAILEY, G. N. 2000. Sediment sources and terminal Pleistocene geomorphological processes recorded in rockshelter sequences in Northwest Greece. *In:* Foster, I. D. L (ed.) *Tracers in Geomorphology*. Chichester: John Wiley & Sons, 473-501.

WOODWARD, J. C. & GOLDBERG, P. 2001. The sedimentary records in Mediterranean rockshelters and caves: archives of environmental change. *Geoarchaeology,* 16, 327-354.

WRAY, R. A. 1997. A global review of solutional weathering forms on quartz sandstones. *Earth-Science Reviews,* 42, 137-160.

WRAY, R. A. 2009. Phreatic drainage conduits within quartz sandstone: evidence from the Jurassic Precipice Sandstone, Carnarvon Range, Queensland, Australia. *Geomorphology,* 110, 203-211.

WRAY, R. A. & SAURO, F. 2017. An updated global review of solutional weathering processes and forms in quartz sandstones and quartzites. *Earth-Science Reviews,* 171, 520-557.

WURSTER, C. M., LLOYD, J., GOODRICK, I., SAIZ, G. & BIRD, M. I. 2012. Quantifying the abundance and stable isotope composition of pyrogenic carbon using hydrogen pyrolysis. *Rapid Communications in Mass Spectrometry,* 26, 2690-2696.

WURSTER, C. M., MCBEATH, A. V. & BIRD, M. I. 2015. The carbon isotope composition of semi-labile and stable pyrogenic carbon in a thermosequence of C3 and C4 derived char. *Organic Geochemistry,* 81, 20-26.

WURSTER, C. M., ROWE, C., ZWART, C., SACHSE, D., LEVCHENKO, V. & BIRD, M. I. 2021. Indigenous impacts on north Australian savanna fire regimes over the Holocene. *Scientific Reports,* 11, 1-8.

WURSTER, C. M., SAIZ, G., SCHNEIDER, M. P. W., SCHMIDT, M. W. I. & BIRD, M. I. 2013. Quantifying pyrogenic carbon from thermosequences of wood and grass using hydrogen pyrolysis. *Organic Geochemistry,* 62, 28-32.

WYRWOLL, K.-H., DONG, B. & VALDES, P. 2000. On the position of southern hemisphere westerlies at the Last Glacial Maximum: an outline of AGCM simulation results and evaluation of their implications. *Quaternary Science Reviews,* 19**,** 881-898.

WYRWOLL, K.-H. & MILLER, G. H. 2001. Initiation of the Australian summer monsoon 14,000 years ago. *Quaternary International,* 83, 119-128.

YOUNG, R. 1986. Tower karst in sandstone: Bungle Bungle massif, northwestern Australia. *Zeitschrift für Geomorphologie*, 189-202.

YOUNG, R. 1988. Quartz etching and sandstone karst: examples from the East Kimberleys, northwestern Australia. *Zeitschrift für Geomorphologie*, 409-423.

YOUNG, R. & YOUNG, A. R. M. 1992. *Sandstone Landforms*, Springer-Verlag, pp.163.

YOUNG, R. W., WRAY, R. A. L. & YOUNG, A. R. M. 2009. *Sandstone Landforms,* New York, Cambridge University Press, pp.304.

ZACKRISSON, O., NILSSON, M.-C. & WARDLE, D. A. 1996. Key ecological function of charcoal from wildfire in the Boreal forest. *Oikos*, 10-19.

ZHANG, Z., YANG, Z., WANG, S. & ZHANG, L. 2011. Weathering rates of a sandstone structure in a semi arid environment: a case study of the ancient city of Pingyao (world cultural heritage), China. *Bulletin of Engineering Geology and the Environment,* 70, 231-237.

ZUCOL, A., BREA, M. & BELLOSI, E. 2010. Phytolith studies in Gran Barranca (central Patagonia): the middle-late Eocene. *In:* MADDEN, R., CARLINI, A., VUCETICH, M. & KAY, R. (eds.) *The Paleontology of Gran Barranca. Evolution and environmental change through the Middle Cenozoic of Patagonia.* Cambridge University Press, 317-341.

ZURRO, D. 2018. One, two, three phytoliths: assessing the minimum phytolith sum for archaeological studies. *Archaeological and Anthropological Sciences,* 10, 1673-1691.

ZURRO, D., GARCÍA-GRANERO, J. J., LANCELOTTI, C. & MADELLA, M. 2016. Directions in current and future phytolith research. *Journal of Archaeological Science,* 68, 112-117.

Appendices

Appendix A3.1: Extraction of phytoliths from sediment and slides preparation, protocol adapted from L. Wallis (2000, pg. 429-432) and Aleman et al. (2013)

Materials and equipment

Distilled water (also de-ionised if possible)	0.5 cm mesh sieve
10% Calgon $(NaPO)_6$	Weighing papers
33% Hydrogen peroxide H_2O_2	10 cm plastic lidded tubes
100% Ethanol	50 ml centrifuge tubes
50% Ethanol	Glass stirring rods
Sodium polytungstate (sg 2.35)	0.425 mm mesh sieve
Siphon (Vacuum flask)	15 mL centrifuge tubes
Beakers	Drying oven
Storage vials	Ultrasonic bath
Centrifuge	Pipettes
Water bath or sand bath	Fumehood
	Weighing balance

An example of a sample worksheet used at this study for the phytoliths extraction can be found at the end of this document.

Procedure

1. Dry sediment in drying oven at 70°C overnight
2. Sieve through a 0.425 mm sieve
3. Place 5.0 g of sediment in a plastic lidded tube 10 cm

Deflocculation

4. I. Add 10% (5%) Calgon
   II. Stir thoroughly and place in ultrasonic bath for 1 hour or shaker for 12 hours
   III. Remove from ultrasonic bath/shaker and allow to settle for 6 hours
   IV Siphon off supernatant
   V. Add distilled water and stir thoroughly
   VI. Allow to settle for 6 hours
   VII. Siphon off supernatant
   Repeat steps 4.V. – VII. until supernatant is clear of clay particles.

5. I. Wash residual material into clean labelled 50 ml centrifuge tube using distilled water
   II. Top up all samples with distilled water to the same level
   III. Centrifuge at 3000 rpm for 10 minutes
   IV. Decant
   Repeat step 5.III. - IV. two times

For all following stages of the procedure the researcher must wear safety glasses, a lab coat and protective gloves.

Organic matter removal - Stage 6 should be carried out in a fume hood

6. I. Add 20 m l of 33% hydrogen peroxide (H_2O_2) and stir
   II. Place in water bath at 70°C for at least one hour, or until reaction stops (top up with fresh hydrogen peroxide if necessary). Stir occasionally or use the shaker
   III. Remove from water bath and allow to cool
   IV. Top up all samples with distilled water to the same level
   V. Centrifuge at 3000 rpm for 10 minutes
   VI. Decant.

7. I. Add 30 ml distilled water to the tube and stir well
   II. Centrifuge at 3000 rpm for 10 minutes
   III. Decant

If there are carbonates present in the samples proceed to Carbonates removal step using. 15% HCl. In this study this step was skipped.

Clays removal

8. I. Fill the tube with 10% Calgon and stir
   II. Place in a water bath at 70°C and shake for 12 hours
   III. Remove from water bath and allow to cool
   IV. Top up all samples with distilled water to the same level
   V. Centrifuge at 3000 rpm for 10 minutes
   VI. Decant

9. I. Wash sample through a 0.425 mm sieve into a clean labelled 50 ml centrifuge tube using distilled water.
   II. Top all samples up with distilled water to the same level.
   III. Centrifuge at 3000 rpm for 10 minutes.
   IV Decant.
   V. Material in sieve can be dried and weighed if required or discarded.

10. I. Wash sediment into clean labelled 15 ml centrifuge tubes using ethanol.
    II. Top up all samples with ethanol to the same level.
    III. Shake gently and centrifuge at 3000 rpm for 10 minutes.
    IV. Decant.
    Repeat step 10.II. – IV. two times and let ethanol evaporate for 20 min at 30°C.

Extraction of phytoliths

11. I. Add 8 ml sodium polytungstate ($Na_6O_{39}W_{12}$) (s.g. 2.3) to tube and mix well.
    II. Centrifuge for 20 minutes at 3000 rpm.
    III. Pipette supernatant and interface off into clean labelled 15 ml centrifuge tube (this will become the phytolith tube).
    Repeat steps 11.II. – III. as necessary until all supernatant and interface has been removed.
    Top up with fresh sodium polytungstate as required.

12. I. Top up all phytolith/polytungstate mix with distilled water to the same level (using at least 5 ml distilled water).
    II. Centrifuge at 3000 rpm for 10 minutes.
    III. Decant polytungstate into a clean beaker and set aside for recovery.

Repeat steps 12.I. – III. for the sediment/polytungstate mix.

13. I. Add 10 ml 50% ethanol to the phytolith tube and mix well.
    II. Centrifuge at 3000 rpm for 10 minutes.
    III. Decant.

Repeat steps 13.I. – III. for the sediment tube.

14. I. Add 10 ml 100% ethanol to the phytolith tube and mix well.
    II. Centrifuge at 3000 rpm for 10 minutes.
    III. Decant.

Repeat steps 14.I. – III. for the sediment tube.

15. Weigh and label clean storage vials for remaining sediment and phytoliths.
16. Transfer sediment and phytoliths to separate storage vials using 100% ethanol.
17. Place in fume hood with fan on and allow ethanol to evaporate.
18. Weigh phytolith fraction.

Preparation of phytolith smear slides for light microscopy analysis

Materials and equipment required

Eukitt UV
100% Ethanol
Slide warmer
Pipettes 5 µl
UV light
Glass coverslips (22 x 40mm; size '0' thickness)
Standard 1 mm thick glass slides
labels

Procedure:

1. I. Add 2 ml of 100% ethanol to the storage vial containing the dried phytolith residue.
   II. Mix well.
   III. If necessary, immerse the sample in an ultrasonic bath to aid disaggregation and ensure complete mixing.

2. I. Pipette 5 µl of the sample out.
   II. Place on the centre of a glass coverslip (22 x 40mm; size '0' thickness).
   III. Spread thinly over the central portion of the coverslip using the disposable pipette tip.

3. I. Warm the coverslip (with sample in place) on a slide warmer at 60°C until the ethanol evaporates.
   II. While the sample (on the coverslip) is drying, apply a few drops of Eukitt to a standard 1mm thick glass slide.
   III. Invert the slide carefully and lower onto the coverslip.
   IV. Once the coverslip is attached to the slide, reinvert the slide to an upright position.

4. Label the slide and allow to dry with small lead weights placed atop the coverslip.

Sample work sheet: Extraction of phytoliths from sediments

Sample ID	Date commenced	Weight initial (g)	Deflocculation	Settle in dH2O 7h (#repeats)	dH2O wash	H2O2 (#days)	dH2O wash (repeat 2x)	10% Calgon (#days)	dH2O wash (repeat 2x)	ETOH wash	Measure (ml)	H/L process (#repeats)	dH2O wash	50% ETOH wash	100% ETOH wash	Slide name

Appendix A3.2: General description of identified phytolith morphotypes and their potential confusers

A3.2.1 Grass Morphotypes (Plate P3.1)

Grass Short Silica Cell Phytoliths (GSSCP) (Plate P3.1a-ad)

- *Bilobate (BIL) (Plate P3.1a-d)*

The shape consists of two lobes separated by two indentations or a distinct castula. Bilobate ends can be convex, straight or concave. The castula can break during sedimentation and in that case only one lobe can be observed (Unilobe). Long axis is typically 10-25 µm, occasionally up to 40 µm. Bilobates have been described from nearly all subfamilies of grasses and they have been often subdivided to distinguish forms produced by different subclades (Piperno and Pearsall, 1998, Strömberg et al., 2013).

- *Cross (CRO) (Plate P3.1f-h)*

The cross shape typically consists of four roughly equal lobes separated by four indentations. Occasionally, three-lobed or five-lobed forms can occur. Length and width in planar view is approximately equal and the ends can have a different look, e.g. sharp like facets, or smooth like tubercles. Longest axis is 8-25 µm. Same as Bilobate, Cross morphotype can be subdivided more finely (Neumann et al., 2017, Novello et al., 2012, Piperno and Pearsall, 1998, Strömberg, 2003), which is however beyond the aim of this study.

- *Not-defined Grass silica short cell Phytoliths (ndGSSCP) (Plate P3.1i-r)*

This morphotype consists of different grass silica short cell phytoliths that are clearly grass belonging short silica cell phytoliths but could not be attributed to any of the other grass morphotypes. This can occur due to phytolith's position within the sample, the viewing angle under the microscope or if the phytoliths are damaged or have an atypical shape.

- *Polylobate (POL) (Plate P3.1s)*

This morphotype consists of two end-lobes separated by a castula, along which additional distinctly separated lobes are inserted. Castula lobes can be of similar size or smaller than the end lobes and either unpaired or paired (present on both sides of the castula). The surface can be smooth (psilate) or ornamented (e.g. ridges, tubercles). Long axis is typically 20-40 µm.

- *Rondel (RON) (Plate P3.1t-y)*

The Rondel morphotype consists of an approximately circular or oval shape in planar view, which can be slightly indented or flattened along one aspect. Other views show variability in shape, size and ornamentation. Shape varies from rounded to angular, pointed or carinate and ornamentation can comprise ridges, tubercles, spikes. In side view sides are typically concave. Diameter is generally 8-20 µm. As in the cases of Bilobate and Cross, Rondel encompasses a wide range of sub-morphotypes that can be commonly subdivided to distinguish rondel produced by different subclades (Novello et al., 2012, Piperno and Pearsall, 1998, Strömberg, 2003). The latter is beyond the aim of this study.

- *Saddle (SAD) (Plate P3.1aa-ac)*

The Saddle is a symmetrical morphotype resembling a saddle (Metcalfe, 1960). In planar view the shape consists of two more or less convex faces connected by concave faces, while in side view both are concave and in the end view both faces are convex. In planar view the faces have the same, or nearly the same size and shape, giving the body a symmetrical look. Typically, the longest axis is 8-20 µm. The saddle

morphotype is most commonly found in chloridoid grasses, typically associated with arid tropical and subtropical grasslands, and it is frequently used as diagnostic of C_4 grasses in the Chloridoideae subfamily (Fredlund and Tieszen, 1994, Soreng et al., 2017, Twiss, 1992). However, saddles are found in other grass subfamilies as well, so having a knowledge of local grass communities and an understanding of the (palaeo)environmental context of the study site is recommended before drawing any conclusions.

- *Trapezoid (TRZ) (Plate P3.1ad)*

The morphotype is a quadratic to rectangular or even oblong in planar view, with at least the two longer faces (sides) parallel, and with ends that can be straight, convex or oblique. The cross section is trapezoidal and typically smooth (psilate). Trapezoids can be distinguished from rondels by the latter having concave sides in side view and lacking parallel faces in planar view. Trapezoids are often abundantly produced in many pooid grasses (Pooidae) and frequently used as diagnostic of this clade (Fredlund and Tieszen, 1994, Kondo et al., 1994, Twiss, 1992). Pooid grasses are the largest subfamily in grass family and they include some major cereals as well as lawn and pasture grasses (Soreng et al., 2017). All of them use the C_3 photosynthetic pathway and they are often referred to as cool-season grasses.

Grass Morphotypes that are not GSSCP(Plate P3.1ae-ai)

- *Papillate (PAP) (Plate 3.1ae-af)*

This morphotype forms in, and takes the shape of, a specialized trichome found primarily in the inflorescence bracts of grasses. The term 'papillate' refers to the overall nipple-like shape. Papillates are circular to oval with a short, conical, blunt or pointy protrusion in the centre where the plate is thickest. The protrusion points obliquely at an angle $<90^0$ with the plane of the plate. The plate is smooth and homogenous and ranges from being very thin and transparent to being thickened and laminated. In cases where the entire plate is silicified its edges can be sinuate, sometime showing small circular holes. Papillates are typically ~10-20 µm in diameter. They can be differentiated from Sedge-plates usually because the apex of Papillate points at an oblique angle and is often offset from the plate centre.

- *Elongate dentate (ELO_DET) (Plate 3.1ag-ai)*

This morphotype consist of an elongated shape and dentate margins. 'Dentate' is the appropriate descriptor for margin features. The outline is rectilinear or nearly rectilinear in 2D and L:W is ≥2. The long side margins have acute–tooth like (dentate) or occasionally carinate projections. Thickness can range from thinly tabular to robustly thick. Surface texture is typically psilate (smooth) but can also be granulate or papillar. Elongate dentate are commonly formed in the epidermis of *Poaceae* leaves (ICPT, 2019). Although they have been observed in other plant families, this morphotype is common in the inflorescence of *Poaceae* (ICPT, 2019). Length can vary from 20-250 µm and transitional forms with Elongate entire, Elongate sinuate and Elongate dendritic occur.

A3.2.2 Grass and Sedge Morphotypes

- *Bulliform flabellate (BUL_FLA) (Plate 3.2a-d)*

The name of this morphotype is attributed to the intracellular silicification of bulliform cells of grasses (*Poaceae*) and sedges (*Cyperaceae*) and the general flabellate shape of the morphotype (ICPT, 2019). Phytoliths are solid and heavily built with the lower part markedly narrower compared to the generally convex upper part. In some cases, the upper part can be truncated, therefore showing a flat or concave shape. The sides of the lower part can be straight or concave and the body is often symmetrical along the top-to-base axes. Vertical length from top to base can vary from 40-200 µm. The Bulliform flabellate morphotype is easily recognizable, although sometimes it can be mistakenly attributed to the Blocky morphotype, if lacking the distinctive flabellate shape.

- *Elongate sinuate (ELO_SIN) (Plate 3.2e-h)*

The Elongate sinuate morphotype is characterised by an elongate shape and sinuate margins. The outline (nearly) rectilinear in 2D and L:W is ≥2. Undulations can range from slightly to very well developed, becoming clavate or columnar. Surface texture can vary broadly, from psilate to granulate and striate and length can vary as well from 50-200 µm. Elongate sinuate has been observed in several groups of plants, from grasses, sedges to pines (Pinaceae) and arrowroots (*Marantaceae*) and even ferns (*Polypodiopsida*) (Gallego and Distel, 2004, Honaine et al., 2009, Mazumdar, 2011, Metcalfe, 1960, Metcalfe, 1971, Sangster et al., 1997, Strömberg, 2003). The latter three however cannot be attributed to our study site and therefore we connected this morphotype with grasses and sedges particularly when in the presence of other typical grass and sedge morphotypes (ICPT, 2019, Metcalfe, 1960, Metcalfe, 1971).

A3.2.3 Sedge Morphotypes

- *Sedge plate (SED_PLA) (Plate 3.2i-l)*

This morphotype is not listed among the current standard phytolith morphotypes in the ICPN 2.0 nomenclature although it is mentioned as a recognisable shape (ICPT, 2019, Supplementary Information, pg. 4). In this study the Sedge plate was classified as a separate morphotype to distinguish the sedge counts from other similar conical shapes and the Papillate. The shape consists of a plate with one or multiple short protrusions. The plate can vary in shape from circular and oval to angular and protrusions can vary from one to multiple nodules and tubercules that can be blunt or pointy or anything in between (Metcalfe, 1971, Murungi and Bamford, 2020, Piperno, 1988, Piperno, 2006, Wallis, 2000). Size along the long axis is ~20-60 µm. Sedge plate can be distinguished from Papillate by size, the latter being generally smaller, and by the angle and position of the apex. The differences however are not always straightforward.

A3.2.4 Tree, shrub and herb Morphotypes (Forest indicators)

Ovate (Plate P3.3)

The group of ovate morphotypes includes ovate shaped phytoliths along with all transitional forms from ovate to ellipsoidal, reniform and oblong. The surface can be psilate or ornamented, like granulate, tuberculate, nodulate or verrucate. Although the ovate morphotypes share some characteristics with the spheroidal morphotypes (described below), they are at the same time as distinct and representative as the spheroids. The ovates were therefore counted as a separate group in this study and classified into four sub-types:

- *Ovate psilate (OVA_PSI) (Plate P3.3a,b)*

This morphotype consists of all transitional ovate shapes - from ovate to ellipsoidal, reniform and oblong, with smooth surface or without distinguishable surface ornamentation. Size along the long axis is ~10-25 µm.

- *Ovate ornate (OVA_ORN) (Plate P3.3c-e,g)*

This includes all transitional ovate shapes with a distinguishable ornamentation (tuberculate, nodulate, granulate or verrucate). They measure ~10-25 µm along the long axis.

- *Ovate psilate with proboscis (OVA_PSI_prob) (Plate P3.3f)*

This morphotype represents the Ovate psilate (OVA_PSI) morphotype with a clearly visible proboscis or stalk. The actual origin of the proboscis or stalk is not clear. It could represent either a protrusion that marks a site of attachment to a host structure (Piperno, 2006, pg. 39) or a bent upper part of a cone or an exaggerated tubercula.

- *Ovate ornate with proboscis (OVA_ORN_prob) (Plate P3.3f)*

This is the morphotype Ovate ornate (OVA_ORN) with a visible proboscis or stalk. As in the previous case the origin of the stalk is not clear although ornamented ovates or irregular spheroids with a stalk might sometimes be cystoliths.

- *Cystoliths (CYS) (Plate P3.3h-i)*

Cystoliths are outgrowths of the cell walls of specialized cells called lithocysts, which occur in the epidermis and ground tissue of plant leaves. They are impregnated with silica and/or calcium carbonate and resemble a cluster. The cystoliths' phytoliths are usually large, distinctive bodies with various kinds of surface ornamentation, such as verrucate, echinate or tuberculate, and very often they have a characteristic stalk where the outgrowths were attached to the cell wall (Piperno, 1988, 2006). Studies describe cystoliths from different tropical plant families around the world all belonging to dicots (Bozarth, 1992, Lentfer, 2003a, Piperno, 1988, 2006, Solereder, 1908, Runge, 1999). When recovered from sediments cystoliths can be valuable indicators of plant families and genera. This, however, is beyond the aims of this study. In this study the potential cystoliths were counted as a separate morphotype, when there was enough confidence to do so, otherwise they were included in Ovate ornate or Ovate ornate with proboscis morphotypes.

Spheroid (Plate P3.4)

In this study the group of spheroids, sphere-like bodies, encompasses a broad range of variations from perfect spheres to subspheroidal or spheroidal irregular, where the basic shape is closer to a sphere than an ovate. We differentiated five spheroid sub-types:

- *Spheroid psilate (SPH_PSI) (Plate P3.4a-c)*

The morphotype consists of spheroidal and subspheroidal phytoliths with a relatively smooth surface. Texture can be homogenous translucent silica or granular. Diameter can vary from 3-30 µm. Spheroid psilate morphotype has been identified repeatedly in connection with woody dicots (e.g. Iriarte and Paz, 2009, Piperno, 1988, 2006, Watling and Iriarte, 2013) as well as some monocots (e.g. Bremond et al., 2004, Runge, 1999). However, it has been often used as evidence for non-grass plants, for example as part of a 'forest indicators' group (ICPT, 2019).

- *Spheroid psilate with nodule (SPH_PSI_nod) Plate (P3.4c)*

This is a spheroid psilate morphotype with one or two visual projections that resembles a small nodule, tubule or papilla. A similar shape has been described in Collura and Neumann (2017, Fig. 3. c,g) in connection with wood phytoliths. It can, however, also be a phytolith confuser – a Chrysophyceae stomatocyst (ICPT, 2019) (refer to A3.2.7).

- *Spheroid psilate with proboscis (SPH_PSI_prob) (Plate P3.4f)*

This morphotype is similar to the previous, the only difference being a proboscis or stalk rather than a nodule. This shape too exhibits similarities with wood phytoliths presented in Collura and Neumann (2017, Fig. 3. h,i). This morphotype can also be confused with potential non-phytoliths (ICPT, 2019) (refer to A3.2.7).

- *Spheroid ornate (SPH_ORN) (Plate P3.4d,e)*

This consists of spheroids with complex surface ornamentation, including tuberculate, nodulate, verrucate or granulate and various combinations or transitional forms of all these. The ornamented spheroids described in literature are found predominantly in different tissues and structures of woody dicots (e.g. Alexandré et al., 1997a, Barboni et al., 1999, Collura and Neumann, 2017, Garnier et al., 2013, Iriarte and Paz, 2009, Kealhofer and Piperno, 1998, Mercader et al., 2009, 2011, 2019, Piperno, 1988, 2006, Testé et al., 2020). They were, however, found also in herbaceous monocots (Piperno, 2006, pg. 39). According to Piperno (2006, pg. 39) some studies agree that the ornamented spheroids from

monocots usually range from 9-25 µm in size or even larger (Chen and Smith, 2013, Crifò and Strömberg, 2020), with those from dicots being much smaller 3-9 µm. In this study the spheroid ornate was associated with woody vegetation regardless of the size.

- *Spheroid ornate with proboscis (SPH_ORN with prob) (Plate P3.4f-g)*

Basically consists of the previous morphotype Spheroid ornate (SPH_ORN) with a visible proboscis or stalk.

- *Spheroid echinate (SPH_ECH) (Plate P3.4k)*

Spheroid echinate represents a spheroidal phytolith with conical projections distributed over the entire surface. This phytolith morphotype is typically associated with palms (Arecaceae) (Benvenuto et al., 2015, ICPT, 2019, Piperno, 1988, 2006).

A3.2.5 Non diagnostic Morphotypes

Due to the wide distribution in different plants, the diagnostic value of this morphotypes is very low.

- *Acute Bulbosus (ACU_BUL) (Plate 3.5a-c)*

This morphotype in this study is assigned to hair cells or trichomes. These are fine appendages on plants that serve protective and secretory functions. Hair cell phytoliths consist of a solid body with a generally narrower acute part (apex) and a wider base (antapex). The apex can be straight or curved, with a sharp or rounded tip, while the antapex can be of various shapes from subspheroidal, subspheroidal truncated, oblong, ellipsoidal or near parallelepipedal to fusiform, sometimes with pointed ends. The apex often forms an angle of less than 90° with the antapex resulting in an asymmetrical or kind of triangular shape in side view (ICPT, 2019). The body from base to top is generally ~25-100 µm long and consists of homogenous or granular silica. Hair cells display immense diversity and they have been found in dicots (Kealhofer and Piperno, 1998, Kondo et al., 1994, Lentfer, 2003a, Mercader et al., 2009, Piperno, 1988, 2006) and many grasses (Alexandré et al., 1997a, Barboni et al., 2007, Brown, 1984, Piperno, 1988, 2006, Zucol et al., 2010), but also sedges (Piperno, 1983, 1988, Strömberg, 2003) and palms (Piperno, 1988, Fig. 46, Strömberg, 2003).

- *Blocky (BLO) (Plate 3.5d-i)*

Blocky was introduced by ICPT (2019) as a commonly accepted term best describing, but not restricted to, phytoliths with more or less parallelepipedal shapes . Blocky encompasses compact, heavily built, solid phytoliths with length/width <2. Some Blocky have projections on the edges, ridges, facets or protrusions that may appear as dentate margins. In literature Blocky are reported as very common in leaves of sedges and grasses. They are, however, commonly found in other monocots, dicots and conifers (Strömberg, 2003) as well as in bark from the Mediterranean (Albert et al., 1999, Tsartsidou et al., 2007) and Africa (Collura and Neumann, 2017).

- *Elongate entire (ELO_ENT) (Plate 3.5j-k)*

This morphotype has an overall rectilinear outline with L:W ≥2 and highly variable sizes (20-700 µm). It also includes slightly arcuate elongated phytoliths with more or less parallel long margins. Surface texture is generally psilate or granulate. Long margins are generally smooth, sometimes slightly uneven or velloate, with the transverse section ranging from angular or circular to oblong. Ends can be straight, concave or convex, rounded or tapering and thickness ranges from thin to robust. The Elongate entire is one of the most commonly produced phytolith morphotypes among land plants. It has been reported from lycophytes, conifers, monocots and dicots (ICPT, 2019).

A3.2.6 Irregular bodies

Irregular bodies in this study come in different shapes (e.g. tabular, nodular, geniculate) and sizes, from large (≥25 µm) to small (10-15 µm). Irregular bodies were counted separately in each sample (Table T3.2, T3.3), but the counts did not add to the sample size.

A3.2.7 Potential confusers

Three potential confusers, as defined in ICPT 2.0 (2019), were observed in this study: the chrysophyte cysts (Chrysophyceae stomatocysts), sponge spicules, and diatoms (Plate 3.6l-t).

The chrysophyte algae or Golden Algae are potential confusers for phytolith Spheroid morphotypes. They produce morphologically distinctive, siliceous, microscopic cysts during a resting stage of their life cycles. The cysts are more or less globular and can be smooth or have various ornamentation. They can be best distinguished from Spheroid psilate by a distinct pore, sometimes with a collar, or resembling a proboscis or a flagella (Plate P3.6, l-n). Sponge spicules on the other hand can be confused with the Elongate entire morphotype (refer to A3.2.5), because they tend to present as translucent elongates, but they can be distinguished by a distinct axial canal (Plate P3.6, p). The diatoms are single celled algae that come in all shapes and forms from elongate to globular. Their cells range in size from 2-500 µm. Diatoms tend to have a thick frustule with a very distinct ornamentation pattern that usually distinguish them from phytoliths (Plate P3.6, o).

Appendix A3.3 Number of counts per morphotype per sample Outside GS1

FINAL MORPHOTYPES	ICPN 2.0 CODE	VEGETATION TYPE	PA_1-M	PA_2-M	PA_3-M	PA_4-M	PA_5-M	PA_6-M	PA_7-M	PA_8-M	PA_9-M	PA_10-M 42	PA_10-M 50	PA_10-M 60±5	PA_10-M 65	PA_10-M 80	PA_10-M 100±5	PA_10-M 102	PA_10-M120	PA_10-M 150	PA_10-M 160	PA_11-M 60±5	PA_11-M 140-160	TP01 0	TP01 40	TP01 60	TP01 80	TP01 120	TP02 20	TP02 40	TP02 60	TP02 100	TP02 120	TP03 60	TP03 120	TP04 20	TP04 80	TP05 0	TP05 40	TP05 60	TP05 80	TP05 100	TP05 120	C_1-CR 100	C_1-CR 135	C_1-CR 200
Acute bulbosus	ACU_BUL	mixed (ICPN - grasses; Piperno - dicots)	4	2	1	2	3	0	1	0	0	0	2	4	2	1	1	0	2	0	1	4	0	3	2	2	1	1	4	1	1	0	3	2	0	0	4	4	1	4	4	1	1	2	0	2
Bilobate, Bilobate (Aristida)	BIL	grasses GSSCP	18	19	11	12	14	11	10	1	6	4	6	6	5	8	5	2	6	1	15	14	0	16	16	4	1	7	12	13	10	4	7	13	2	16	8	22	12	16	2	10	10	4	6	3
Blocky	BLO	mixed; low diagnostic value	11	3	10	5	2	10	5	1	5	4	4	6	3	1	5	3	3	0	0	15	0	4	4	5	4	11	4	6	3	6	2	4	2	9	14	9	14	9	5	7	14	4	3	12
Bulliform (Flabellate)	BUL_FLA	grasses GSSCP and Sedges (Cyperaceae)	0	0	1	0	0	0	0	0	0	0	0	0	1	0	0	0	0	0	0	0	0	0	0	0	1	1	0	0	0	1	0	0	0	0	1	0	1	1	0	0	0	0	0	0
Circular small Type B	SPH_PSI_nodular	woody	0	0	1	1	0	0	0	0	1	0	0	0	0	1	0	0	0	0	1	0	0	1	0	0	0	0	1	0	0	0	0	0	0	0	1	0	1	0	0	0	0	0	1	
Cross	CRO	grasses GSSCP	1	3	2	2	2	1	0	0	0	0	0	2	0	0	0	0	0	0	1	0	0	0	0	0	0	0	0	1	0	0	0	0	0	1	1	2	1	0	0	0	0	0	0	
Cystolith	CYS	TSH (trees, shrubs, herbs)	0	0	0	0	0	0	0	0	0	0	0	2	0	0	0	0	0	0	0	0	0	0	0	0	0	1	0	0	0	0	0	0	0	0	0	0	0	0	0	0	0	0	0	
Elongate entire	ELO_ENT	mixed; low diagnostic value	14	8	6	6	3	2	5	1	0	3	4	4	5	2	2	0	0	0	5	4	1	4	7	4	4	6	3	4	2	3	5	8	2	5	4	8	6	3	2	2	6	1	0	
Elongate dentate	ELO_DET	Grasses/Poaceae	0	1	2	3	2	3	2	0	0	1	0	2	4	0	0	0	0	0	0	0	0	3	3	1	4	0	6	1	1	0	0	1	1	0	0	5	2	0	0	1	2	1	0	
Elongate sinuate	ELO_SIN	grasses/Poaceae & Sedges (e.g. Cyperus sp.)	1	0	0	0	0	1	0	0	0	0	0	0	1	1	0	0	0	0	0	0	0	0	0	0	0	0	0	0	0	1	0	0	0	0	0	0	0	0	0	0	0	0	0	
Grass silica short cell Phytoliths	GSSCP	grasses/Poaceae	10	20	18	10	12	13	10	0	8	10	7	15	15	9	6	5	9	2	10	3	0	5	10	9	9	4	20	13	6	5	2	7	3	4	4	12	3	6	3	16	8	2	10	
Ovate psilate	OVA_PSI	forest indicator	9	10	16	13	21	7	15	4	11	9	13	10	11	13	18	8	15	1	18	12	2	12	13	10	10	15	8	17	16	11	15	15	3	21	13	13	15	11	9	4	6	7	12	
Ovate ornate	OVA_ORN	TSH (trees, shrubs, herbs)	11	8	10	14	14	31	29	8	24	41	36	22	29	41	25	21	40	3	22	27	4	22	20	33	32	30	14	13	32	21	21	23	16	22	14	13	9	32	22	26	33	31	31	35
Ovate psilate with proboscis	OVA_PSI_prob	TSH (trees, shrubs, herbs)	0	3	0	3	6	2	2	1	2	1	0	0	0	1	0	0	0	0	0	0	0	0	0	1	0	1	2	1	0	2	1	2	0	2	2	2	3	0	6	3	3	1	2	2
Ovate ornate with proboscis	OVA_ORN_prob	TSH (trees, shrubs, herbs)	0	1	2	2	1	6	1	1	4	4	11	3	6	4	5	4	5	1	4	3	0	7	2	6	8	5	4	5	6	10	4	2	1	2	4	1	6	6	3	5	4	7	6	9
Papillate	PAP	grasses /inflorescence Trichome	0	2	0	0	0	0	0	0	0	0	1	0	0	0	0	0	0	0	0	0	0	0	0	0	0	0	0	0	0	4	0	0	0	0	1	0	0	0	0	0	0	0	0	0
Polylobate	POL	grasses GSSPC	0	0	0	0	0	0	0	0	0	0	0	0	0	0	0	0	0	0	0	0	0	0	0	0	0	0	1	0	0	0	0	1	0	1	0	1	0	0	0	0	0	0	0	0
Rondel	RON	grasses GSSPC	8	6	5	6	4	2	1	0	3	3	3	2	3	0	4	2	6	0	3	2	0	9	10	6	1	5	2	11	7	1	0	1	3	4	3	3	2	2	4	3	6	1	2	2
Saddle	SAD	grasses GSSPC	3	0	1	1	0	0	1	0	0	0	0	0	0	0	0	0	1	0	0	0	0	0	0	0	0	0	1	0	0	0	0	2	1	4	1	7	5	1	0	0	0	0	0	0
Sedge plate/Conical (squat ornate or smooth)	SED	sedges	0	0	0	0	0	0	0	0	0	0	0	2	0	0	1	0	1	0	1	1	0	0	0	0	0	0	4	2	0	0	1	1	0	0	0	1	0	0	0	0	2	0	0	0
Spheroid psilate	SPH_PSI	low diagnostic value; general forest indicators	20	18	16	20	10	9	5	1	12	8	5	12	8	11	10	8	5	1	9	13	0	11	12	2	11	8	7	13	4	7	11	10	4	7	17	5	10	7	10	8	9	9	9	3
Spheroid psilate with nodule (or pore, or collar)	SPH_PSI_nod	low diagnostic value; general forest indicators or Chrysophyta cyst	0	0	1	1	0	0	0	0	1	0	0	0	0	1	0	0	0	0	1	0	0	1	0	0	0	0	1	0	0	0	0	0	0	0	1	0	1	0	0	0	0	0	1	0
Spheroid psilate with proboscis	SPH_PSI_prob	low diagnostic value; wood or forest indicator or possible confuser Chrysophyta cyst with flagelatte	10	5	9	4	4	2	3	0	3	4	0	5	2	1	1	4	3	0	1	2	0	2	0	2	0	1	5	1	2	0	3	1	0	3	3	0	3	1	1	4	1	1	3	1
Spheroid ornate	SPH_ORN	TSH (trees, shrubs, herbs)	1	6	2	5	9	10	16	6	13	17	26	10	21	18	5	12	11	1	14	10	2	5	10	18	16	10	9	8	8	8	12	15	6	5	9	4	14	8	11	20	9	14	14	14
Spheroid ornate with proboscis	SPH_ORN_prob	TSH (trees, shrubs, herbs)	0	0	0	1	0	0	0	0	1	0	0	0	2	0	1	0	1	0	0	0	0	0	0	5	4	2	0	1	3	1	0	0	0	0	1	0	2	0	1	1	1	0	5	0
Trapezoid (short cell rectangular)	TRZ	grasses GSSPC	0	0	0	0	1	0	2	1	1	1	0	0	0	0	1	2	0	0	1	0	0	2	0	0	0	1	0	0	2	0	0	0	0	4	0	1	3	1	0	3	0	0	1	0

Appendix A3.4 Number of counts per morphotype per sample Inside GS1

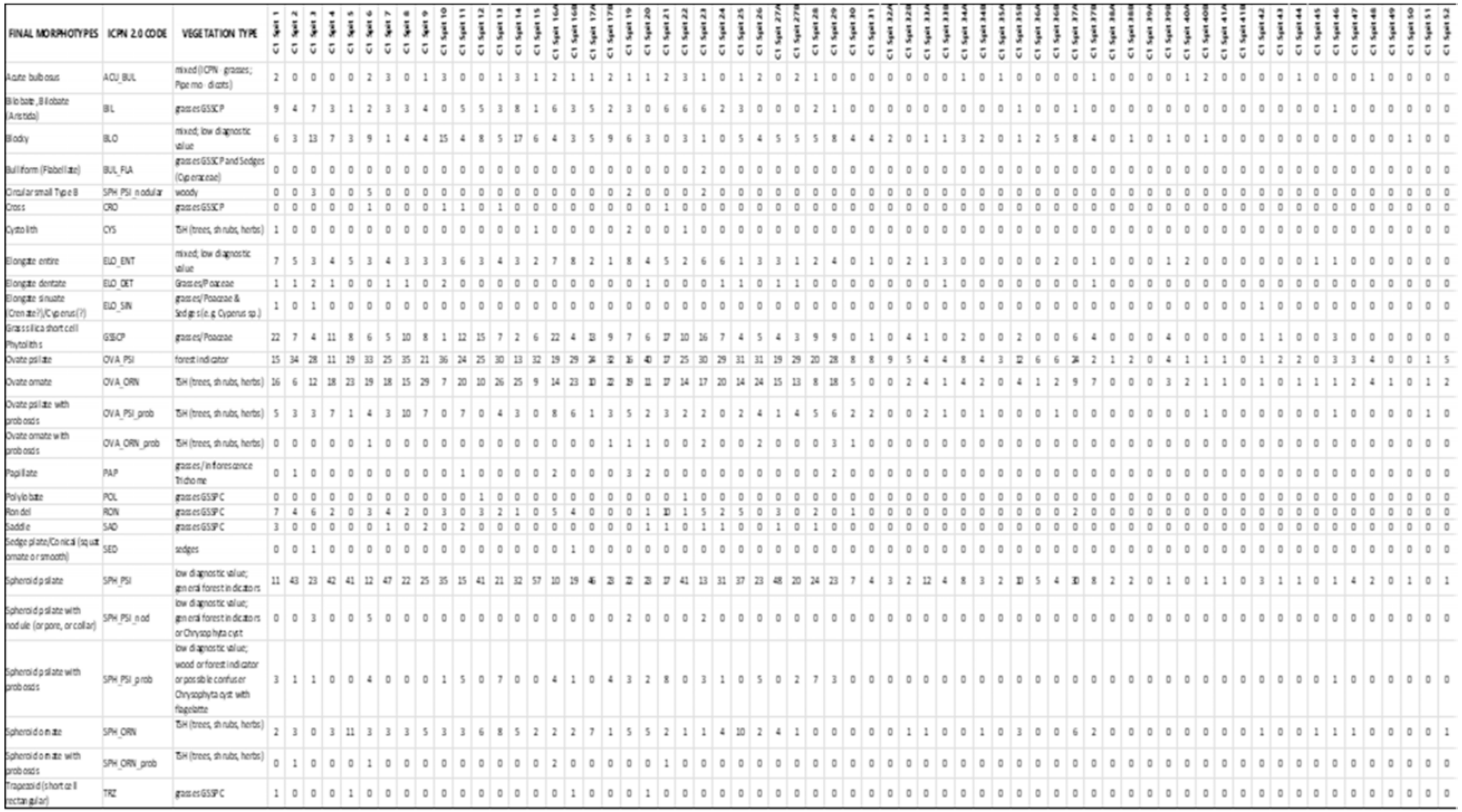

FINAL MORPHOTYPES	ICPN 2.0 CODE	VEGETATION TYPE	C1 Spit 1	C1 Spit 2	C1 Spit 3	C1 Spit 4	C1 Spit 5	C1 Spit 6	C1 Spit 7	C1 Spit 8	C1 Spit 9	C1 Spit 10	C1 Spit 11	C1 Spit 12	C1 Spit 13	C1 Spit 14	C1 Spit 15	C1 Spit 16A	C1 Spit 16B	C1 Spit 17A	C1 Spit 17B	C1 Spit 19	C1 Spit 20	C1 Spit 21	C1 Spit 22	C1 Spit 23	C1 Spit 24	C1 Spit 25	C1 Spit 26	C1 Spit 27A	C1 Spit 27B	C1 Spit 28	C1 Spit 29	C1 Spit 30	C1 Spit 31	C1 Spit 32A	C1 Spit 32B	C1 Spit 33A	C1 Spit 33B	C1 Spit 34A	C1 Spit 34B	C1 Spit 35A	C1 Spit 35B	C1 Spit 36A	C1 Spit 36B	C1 Spit 37A	C1 Spit 37B	C1 Spit 38A	C1 Spit 38B	C1 Spit 39A	C1 Spit 39B	C1 Spit 40A	C1 Spit 40B	C1 Spit 41A	C1 Spit 41B	C1 Spit 42	C1 Spit 43	C1 Spit 44	C1 Spit 45	C1 Spit 46	C1 Spit 47	C1 Spit 48	C1 Spit 49	C1 Spit 50	C1 Spit 51	C1 Spit 52
Acute bulbosus	ACU_BUL	mixed (ICPN - grasses; Piperno - dicots)	2	0	0	0	0	2	3	0	1	3	0	0	1	3	1	2	1	1	2	1	1	2	3	1	0	1	2	0	2	1	0	0	0	0	0	0	0	1	0	1	0	0	0	0	1	0	0	0	0	1	2	0	0	0	0	1	0	0	0	1	0	0	0	0
Bilobate, Bilobate (Aristida)	BIL	grasses GSSCP	9	4	7	3	1	2	3	3	4	0	5	5	3	8	1	6	3	5	2	3	0	6	6	6	2	3	0	0	0	2	1	0	0	0	0	0	0	0	0	0	1	0	0	1	0	0	0	0	0	0	0	0	0	0	0	0	0	1	0	0	0	0	0	0
Blocky	BLO	mixed; low diagnostic value	6	3	13	7	3	9	1	4	4	15	4	8	5	17	6	4	3	5	9	6	3	0	3	1	0	5	4	5	5	5	8	4	4	2	0	1	1	3	2	0	1	2	5	8	4	0	1	0	1	0	1	0	0	0	0	0	0	0	0	0	0	1	0	0
Bulliform (Flabellate)	BUL_FLA	grasses GSSCP and Sedges (Cyperaceae)	0	0	0	0	0	0	0	0	0	0	0	0	0	0	0	0	0	0	0	0	0	0	0	2	0	0	0	0	0	0	0	0	0	0	0	0	0	0	0	0	0	0	0	0	0	0	0	0	0	0	0	0	0	0	0	0	0	0	0	0	0	0	0	0
Circular small Type B	SPH_PSI_nodular	woody	0	0	3	0	0	5	0	0	0	0	0	0	0	0	0	0	0	0	0	2	0	0	0	2	0	0	0	0	0	0	0	0	0	0	0	0	0	0	0	0	0	0	0	0	0	0	0	0	0	0	0	0	0	0	0	0	0	0	0	0	0	0	0	0
Cross	CRO	grasses GSSCP	0	0	0	0	0	1	0	0	0	1	1	0	1	0	0	0	0	0	0	0	0	1	0	0	0	0	0	0	0	0	0	0	0	0	0	0	0	0	0	0	0	0	0	0	0	0	0	0	0	0	0	0	0	0	0	0	0	0	0	0	0	0	0	0
Cystolith	CYS	TSH (trees, shrubs, herbs)	1	0	0	0	0	0	0	0	0	0	0	0	0	0	1	0	0	0	0	2	0	0	1	0	0	0	0	0	0	0	0	0	0	0	0	0	0	0	0	0	0	0	0	0	0	0	0	0	0	0	0	0	0	0	0	0	0	0	0	0	0	0	0	0
Elongate entire	ELO_ENT	mixed; low diagnostic value	7	5	3	4	5	3	4	3	3	3	6	3	4	3	2	7	8	2	1	8	4	5	2	6	6	1	3	3	1	2	4	0	1	0	2	1	3	0	0	0	0	0	2	0	1	0	0	0	1	2	0	0	0	0	0	0	1	1	0	0	0	0	0	0
Elongate dentate	ELO_DET	Grasses/Poaceae	1	1	2	1	0	0	1	1	0	2	0	0	0	0	0	0	0	0	0	0	1	0	0	0	1	1	0	1	1	0	0	0	0	0	0	0	1	0	0	0	0	0	0	0	1	0	0	0	0	0	0	0	0	0	0	0	0	0	0	0	0	0	0	0
Elongate sinuate (Crenate?)/Cyperus(?)	ELO_SIN	grasses/Poaceae & Sedges (e.g. Cyperus sp.)	1	0	1	0	0	0	0	0	0	0	0	0	0	0	0	0	0	0	0	0	0	0	0	0	0	0	0	0	0	0	0	0	0	0	0	0	0	0	0	0	0	0	0	0	0	0	0	0	0	0	0	0	0	1	0	0	0	0	0	0	0	0	0	0
Grass silica short cell Phytoliths	GSSCP	grasses/Poaceae	22	7	4	11	8	6	5	10	8	1	12	15	7	2	6	22	4	13	9	7	6	17	10	16	7	4	5	4	3	9	9	0	1	0	4	1	0	2	0	0	2	0	0	6	4	0	0	0	4	0	0	0	0	1	1	0	0	3	0	0	0	0	0	0
Ovate psilate	OVA_PSI	forest indicator	15	34	28	11	19	33	25	35	21	36	24	25	30	13	32	19	29	24	32	16	40	17	25	30	29	31	31	19	29	20	28	8	8	9	5	4	4	8	4	3	12	6	6	24	2	1	2	0	4	1	1	1	0	1	2	2	0	3	3	4	0	0	1	5
Ovate ornate	OVA_ORN	TSH (trees, shrubs, herbs)	16	6	12	18	23	19	18	15	29	7	20	10	26	25	9	14	23	10	22	19	11	17	14	17	20	14	24	15	13	8	18	5	0	0	2	4	1	4	2	0	4	1	2	9	7	0	0	0	3	2	1	1	0	1	0	1	1	1	2	4	1	0	1	2
Ovate psilate with proboscis	OVA_PSI_prob	TSH (trees, shrubs, herbs)	5	3	3	7	1	4	3	10	7	0	7	0	4	3	0	8	6	1	3	5	2	3	2	2	0	2	4	1	4	5	6	2	2	0	0	2	1	0	1	0	0	0	1	0	0	0	0	0	0	0	1	0	0	0	0	0	0	1	0	0	0	0	1	0
Ovate ornate with proboscis	OVA_ORN_prob	TSH (trees, shrubs, herbs)	0	0	0	0	0	1	0	0	0	0	0	0	0	0	0	0	0	0	1	1	1	0	0	2	0	0	2	0	0	0	3	1	0	0	0	0	0	0	0	0	0	0	0	0	0	0	0	0	0	0	0	0	0	0	0	0	0	0	0	0	0	0	0	0
Papillate	PAP	grasses/ inflorescence Trichome	0	1	0	0	0	0	0	0	0	0	1	0	0	0	0	2	0	0	0	3	2	0	0	0	0	0	0	0	0	0	2	0	0	0	0	0	0	0	0	0	0	0	0	0	0	0	0	0	0	0	0	0	0	0	0	0	0	0	0	0	0	0	0	0
Polylobate	POL	grasses GSSPC	0	0	0	0	0	0	0	0	0	0	0	1	0	0	0	0	0	0	0	0	0	0	1	0	0	0	0	0	0	0	0	0	0	0	0	0	0	0	0	0	0	0	0	0	0	0	0	0	0	0	0	0	0	0	0	0	0	0	0	0	0	0	0	0
Rondel	RON	grasses GSSPC	7	4	6	2	0	3	4	2	0	3	0	3	2	1	0	5	4	0	0	0	1	10	1	5	2	5	0	3	0	2	0	1	0	0	0	0	0	0	0	0	0	0	0	2	0	0	0	0	0	0	0	0	0	0	0	0	0	0	0	0	0	0	0	0
Saddle	SAD	grasses GSSPC	3	0	0	0	0	0	1	0	2	0	2	0	0	0	0	0	0	0	0	0	1	1	0	1	1	0	0	1	0	1	0	0	0	0	0	0	0	0	0	0	0	0	0	0	0	0	0	0	0	0	0	0	0	0	0	0	0	0	0	0	0	0	0	0
Sedge plate/Conical (squat ornate or smooth)	SED	sedges	0	0	1	0	0	0	0	0	0	0	0	0	0	0	0	0	1	0	0	0	0	0	0	0	0	0	0	0	0	0	0	0	0	0	0	0	0	0	0	0	0	0	0	0	0	0	0	0	0	0	0	0	0	0	0	0	0	0	0	0	0	0	0	0
Spheroid psilate	SPH_PSI	low diagnostic value; general forest indicators	11	43	23	42	41	12	47	22	25	35	15	41	21	32	57	10	19	46	23	22	23	17	41	13	31	37	23	48	20	24	23	7	4	3	2	12	4	8	3	2	10	5	4	30	8	2	2	0	1	0	1	1	0	3	1	1	0	1	4	2	0	1	0	1
Spheroid psilate with nodule (or pore, or collar)	SPH_PSI_nod	low diagnostic value; general forest indicators or Chrysophyta cyst	0	0	3	0	0	5	0	0	0	0	0	0	0	0	0	0	0	0	0	2	0	0	0	2	0	0	0	0	0	0	0	0	0	0	0	0	0	0	0	0	0	0	0	0	0	0	0	0	0	0	0	0	0	0	0	0	0	0	0	0	0	0	0	0
Spheroid psilate with proboscis	SPH_PSI_prob	low diagnostic value; wood or forest indicator or possible confuser Chrysophyta cyst with flagelatte	3	1	1	0	0	4	0	0	0	1	5	0	7	0	0	4	1	0	4	3	2	8	0	3	1	0	5	0	2	7	3	0	0	0	0	0	0	0	0	0	0	0	0	0	0	0	0	0	0	0	0	0	0	0	0	0	0	1	0	0	0	0	0	0
Spheroid ornate	SPH_ORN	TSH (trees, shrubs, herbs)	2	3	0	3	11	3	3	3	5	3	3	6	8	5	2	2	2	7	1	5	5	2	1	1	4	10	2	4	1	0	0	0	0	0	1	1	0	0	1	0	3	0	0	6	2	0	0	0	0	0	0	0	0	1	0	0	1	1	1	0	0	0	0	1
Spheroid ornate with proboscis	SPH_ORN_prob	TSH (trees, shrubs, herbs)	0	1	0	0	0	1	0	0	0	0	0	0	0	0	0	2	0	0	0	0	0	1	0	0	0	0	0	0	0	0	0	0	0	0	0	0	0	0	0	0	0	0	0	0	0	0	0	0	0	0	0	0	0	0	0	0	0	0	0	0	0	0	0	0
Trapezoid (short cell rectangular)	TRZ	grasses GSSPC	1	0	0	0	1	0	0	0	0	0	0	0	0	0	0	0	1	0	0	0	1	0	0	0	0	0	0	0	0	0	0	0	0	0	0	0	0	0	0	0	0	0	0	0	0	0	0	0	0	0	0	0	0	0	0	0	0	0	0	0	0	0	0	0